PUNCHING SHEAR STRENGTH OF UNBONDED PRESTRESSED FLAT SLABS AT EDGE COLUMN CONNECTIONS

by

Seyed Hashem Musavi, B.Eng., M.Sc.

A thesis submitted for the degree of

Doctor of philosophy

Department of Civil Engineering

University of Glasgow

May , 1992

CONTENTS

CHAPTER 3– DESIGN METHOD OF PRESTRESSED FLAT SLAB

CHAPTER 4– THE FINITE ELEMENT METHOD

ACKNOWLEDGEMENTS

The work presented in this thesis was carried out in the department of Civil Engineering at Glasgow University under the general direction of Professor A. Coull whose help and encouragement is gratefully acknowledged.

I wish to express my indebtedness to my supervisor, Dr. P. Bhatt for his valuable guidance, advice and constant encouragement throughout the work.

I wish to express my thanks to Professor D. R. Green and professor D. Muirwood, past and present heads of the Department of Civil Engineering for making the facilities available.

Many thanks are also to:

– The staff of the Concrete Laboratory, in particular, Mr. A. Burnett, Mr. R. McCaskie, Mr. I. Gardner , Mr. R. Thornton, Mr. B. Thomson, Mr. A. Yuille, I. Dickson and Mr. Ken Ryan for their assistance in preparing and testing the models.

– The research staff and students of Civil Engineering Department, Dr. Zhang Binsheng and Dr. B. Famiyesin and Mr. A. M. Bensalem for their useful discussions.

– The Iranian Goverment for the financial support during the period of the research.

Finally, my thanks are reserved to my wife and family for their boundless patience and moral support throughout the years.

SUMMARY

This thesis presents an experimental and theoretical study of the punching shear strength of unbonded prestressed flat slabs at edge column junction. Six tests were conducted under monotonic loading and two under cyclic loading. The models were approximately 1000 × 1000 × 130 mm and prestressed in two directions by unbonded tendons. The main parameters of study were:

a) Prestress level,

b) Column aspect ratio,

c) Wind shear moment/wind shear, (M_W/V_W).

The following data were collected:

i) Load– deflection relationship,

ii) Strain development in reinforcing bars and at the compressive face of concrete

iii) Variation of force in prestressing bars.

For design of the models, the slab element was regarded as consisting of two outer layers separated by an unreinforced concrete filling. The slab was analysed as an elastic plate subjected to ultimate design loads. The moments (M_x, M_y, M_{xy}) were replaced by two equal and opposite forces acting at the mid– depth of the outer layers. These forces were combined with inplane forces (N_x, N_y, N_{xy}) divided equally between the two layers. Each layer was considered as a membrane element and designed using Direct Design Method using Nielsen's yield criterion.

A 3– dimensional nonlinear finite element program based on 20 node isoparametric brick element was developed. The constitutive laws of concrete proposed by Kotsovos and embedded representation of unstressed steel were adopted. Shear transfer across crack was allowed. Forces due to prestressing were included using the concept of

equivalent loads. Steel reinforcement including prestressing steel was modelled as elastic— perfectly plastic material. 'Smeared' cracking model was used.

Finally, Comparative study was carried out between the experimental and the theoretical results for the models tested by the author and by other investigators. Comparison of the experimental and theoretical failure loads with that predicted by the BS8110 and the ACI codes were included. It was concluded that the finite element method can predict failure load and behaviour of the junctions satisfactorily.

NOTATIONS

Symbols used in the text are defined wherever they appear. But for convenience, a summary of those symbols is presented below as follows:

Chapter Two

A_c	critical cross-sectional area of concrete
A_s	steel area
A_{so}	ordinary steel area
A_{sp}	prestressed steel area
c	side dimension for cubic column
c_1, c_2	dimensions of the column
d	effective depth of slab
d_{ps}	effective depth of tendon profile
e_x	eccentricity of tendon in x-direction
e_y	eccentricity of tendon in y-direction
f'_c	the design compressive cylinder strength of concrete
f_t	split cylinder tensile strength of concrete
f_{cp}	average compressive stress of concrete due to prestressing
f_{cu}	cube strength of concrete
f_{pu}	ultimate stregth of tendon
f_y	yield stress of steel
f_{pb}	proof stress of prestressing bars
h	slab thickness
H	compressive membrane force
J	polar moment of inertia of critical section

l_p	a multiple of (0.75d)
L_x, L_y	slab spans in X and Y-directions
M	moment transfered to the column
M_o	ultimate capacity of critical section for moment transfer only
M_t	moment transfered to the column
γM	fraction of moment transfered by torsion
m_u	moment per unit width at the critical section
P_x, P_y	prestressing forces per unit length in X and Y-directions
P_o	decompression load of prestressed slab
P_{ol}	decompression load of slab prestressed in longitudinal direction
P_{ur}	punching strength of geometrically similar reinforced concrete slab
P_{url}	is 'P_{ur}' but only in longitudinal direction
P_{urt}	is 'P_{ur}' but only in transverse irection
P_{up}	punching strength of prestressed slab
u	length of critical perimeter
u_o	length of the perimeter which touches column faces
v	shear strength
v_{shear}	shear stress due to pure shear
$v_{torsion}$	shear stress due to torsion
v_{max}	maximum shear strength in critical area
V_c	punching shear strength
v_c	permissible shear stress of concrete
V_p	vertical component of prestressing force crossing the critical section
V^*	design shear force
V_o	ultimate capacity of critical section for shear transfer only

V_g	shear force due to gravity loads
V_{eff}	effective shear strength
V_t	shear force transfered to the column
w_b	uniformly distributed load to be balanced by prestressing loads
w_{px}	upward load exerted by tendon in x-direction
w_{py}	upward load exerted by tendon in y-direction
X	side length of the perimeter parallel to the axis of bending
β_c	ratio of the longside to the shortside of the column
γ_m	partial safety factor for concrete in shear
ρ	steel ratio
ρ_s	ordinary steel ratio
ρ_e	equivalent steel ratio
ρ_{ps}	prestressed steel ratio

Chapter Three

A_{xt}	steel area at top layer in x-direction
A_{xb}	steel area at bottom layer in x-direction
A_{yt}	steel area at top layer in y-direction
A_{yb}	steel area at bottom layer in y-direction
[B]	strain matrix
[D]	rigidity matrix
e	eccentricity of tensile reinforcement
f_{cu}	cube strength of concrete
f_{cp}	compressive stress of concrete due to prestressing
f_t	tensile stress of concrete
h	slab thickness

N	inplane force of slab
N_x, N_y	inplane force of slab in X an Y-direction
N_{xy}	inplane shear force
N_i	shape function at the i^{th} node
n_c	principle compressive membrane force in concrete
n_f	load capacity of unreinforced filling layer
n_u	ultimate compressive force in concrete
n_x, n_y	inplane forces in layer element in X and Y-directions
n_{xt}, n_{yt}	inplane forces in top layer in X and Y-directions
n_{xb}, n_{yb}	inplane forces in bottom layer in X and Y-directions
n_{xy}	inplane shear force
n_{xyt}	inplane shear force in top layer
n_x^*	design force in X-direction
n_y^*	design force in Y-direction
M	bending moment
M_x, M_y	bending moments in X and Y-directions
M_{xy}	twisting moment
S	outer layers thickness
v_c	permissible shear stress of concrete
W	displacement in Z-direction
$\partial W/\partial x$	rotation about y-axis
$\partial W/\partial y$	rotation about x-axis
σ_c	permissible compressive stress of concrete
σ_y	yield stress of reinforcement
$[\delta]$	element nodal displacement

Chapter Four

$[B]$	strain matrix

$[D]$	rigidity matrix
$[D]_c$	rigidity matrix for cracked concrete
$[D]_{x,y,x}$	rigidity matrix in x,y,z space
E	Young's modulus
f'_c	cylinder compressive strength of concrete
f_{cu}	cube strength of concrete
$[F^e]$	vector of element nodal force
$[F_u]$	vector of residual force
G_o	initial value of shear modulus
I_1	first stress invariant
I_2	second stress invariant
I_3	third stress invariant
J_2	second deviatoric stress invariant
J_3	third deviatoric stress invariant
$[J]$	jacobian matrix
K_o	initial value of bulk modulus
K_s	second bulk modulus
$[K]$	stiffness matrix
ℓ,m,n	the direction cosines of a principal stress
$[N]$	shape functions
$[P]$	body force per unit volume
$[P_i]$	total equivalent nodal forces
$[P_i]_{conc}$	equivalent nodal force carried by concrete
$[P_i]_{steel}$	equivalent nodal force carried by steel
$[q]$	applied surface loads
q,r,θ	cylindrical coordinate system
$[R]$	vector of external nodal forces
S	loaded surface area

$[T]$	transformation matrix
u,v,w	components of displacement in x,y,z-directions respectively
V	volume of the stracture
β	shear retention factor
γ_{oct}	octahedral shear strain
$\gamma_{xy},\gamma_{yz},\gamma_{zx}$	shear strain components
ξ,η,ζ	local coordinate axis
$\epsilon_1,\epsilon_2,\epsilon_3$	principal strains
ϵ_{oct}	octahedral normal strain
$\epsilon_{od},\epsilon_{oh}$	volumetric strain, deviatoric and hydrostatic
$\epsilon_x,\epsilon_y,\epsilon_z$	components of normal strains
$[\epsilon]$	vector of normal and shear strain components
$[\epsilon_o]$	vector of initial strains
υ	poisson's ratio
π	total potential energy
$\sigma_1,\sigma_2,\sigma_3$	principal stresses
σ_{int}	internal stresses
σ_{oct}	octahedral normal stress
$\sigma_x,\sigma_y,\sigma_z$	normal stress component
$[\sigma]$	vector of normal and shear stress components
$[\sigma_o]$	vector of initial stresses
τ_{oct}	octahedral shear stress

<u>Chapter Six and Seven</u>

C_x,C_y	column side dimensions in X and Y directions
E_c	Young's modulus of concrete

f_{cu}	cube strength of concrete
f_{pe}	effective prestress
f_{pu}	ultimate strength of tendons
f_t	tensile strength of concrete
L_x, L_y	slab dimensions in X and Y directions respectively
M_b	bending moment
M_g	moment due to gravity loads
M_t	twisting moment
M_w	bending moment due to wind loads
t	slab thickness
V_g	gravity shear
V_w	wind shear

<u>Chapter Eight</u>

S. D.	standard deviation
V_{exp}	experimental failure load
V_{theo}	theoretical failure load
β	shear retention factor

CHAPTER ONE

INTRODUCTION

1.1 General

In the past few decades, reinforced and prestressed concrete flat slabs have been widely used for various structural applications such as multi– story car parking, apartments, long– span bridges and industrial buildings. Flat slab floors have many advantages over the beam– slab floors. Simple formwork and reduced storey height are some major advantages. Windows can extend right up to the underside of the slab, and there are no beam to obstruct the light and the circulation of air. Figure 1.1 shows a typical plan of flat slab– column structures used in multi– story buildings.

For designers of flat slab– column structures, punching shear failure of slab in the vicinity of column or concentrated load is an important problem. Punching is critical when the slab– column connection is subjected to moment as well as shear forces. This is particularly important at an edge column connections because of the reduction of critical perimeter around the column and the presence of twisting moment. Unfortunately, very few guide lines are available in some Codes of practice for designers of this type of structures. For instance, in the British Code (BS8110) there is no information about prestressed flat slabs at all, and designers are referred to appropriate specialist literatures(1).

The majority of investigations which are reported on punching shear strength of prestressed flat slabs have been done experimentally considering interior slab– column connections(25,26,27,40). To the author's knowledge, no information is available on nonlinear theoretical analysis of prestressed concrete slabs using 3– dimensional finite element method.

1.2 Purpose of This Study

Lack of theoretical investigation on the general behaviour of prestressed flat slabs at column connections was the main motivation for this work. This study was conducted in the following order:

a)– Developing the 3–dimensional nonlinear finite element programme for the analysis and prediction of the overall behaviour of prestressed flat slabs such as deflections, strains, stresses and ultimate strength of the slab–column connections.

b)– Developing the two–dimensional finite element programme for designing of prestressed concrete slabs using plate bending elements. This programme is capable of handling both inplane and out–of–plane forces acting on the slab due to prestressing, lateral and gravity loads. The detailed description of this method is presented in Chapter three.

c)– Experimental and theoretical study of behaviour of unbonded prestressed flat slab at edge column junction. In this connection both monotonic and cyclic loading conditions are considered.

d)– Analysis of prestressed flat slab with interior column connection which have been tested by other investigators and comparison of analytical results with their experimental counterparts.

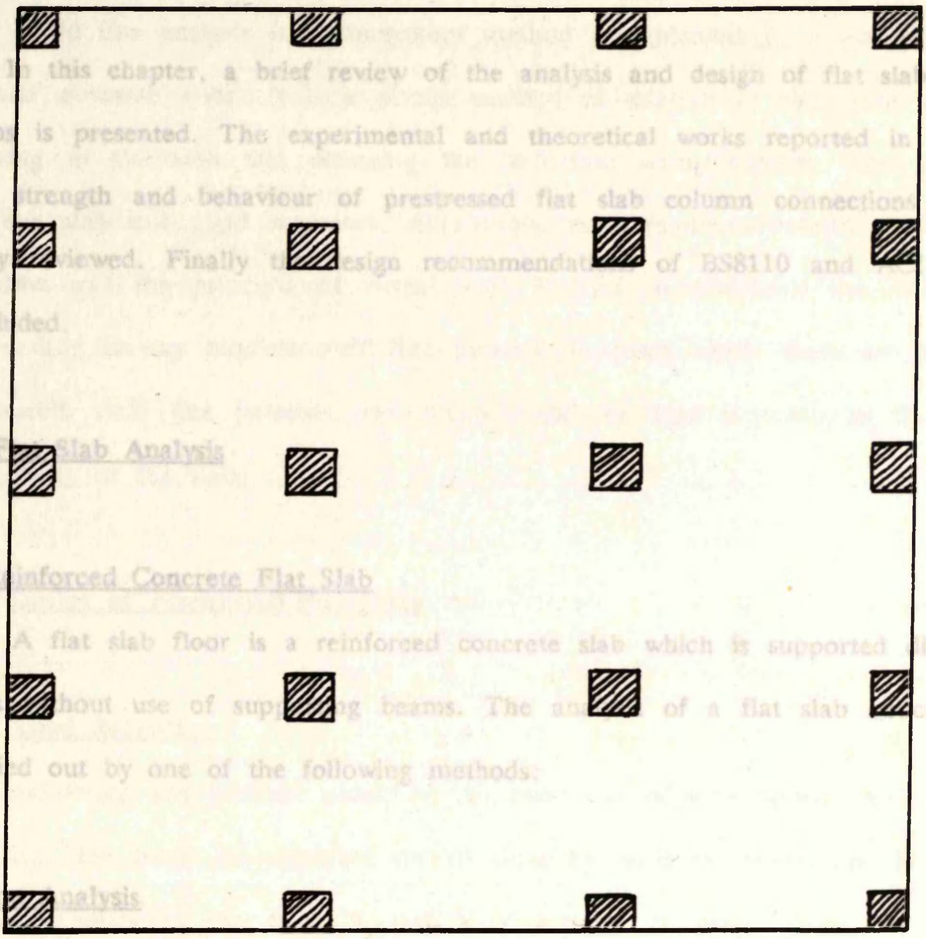

Figure 1.1 : Typical plan of Flat Slab– Column Structure.

CHAPTER TWO

LITERATURE REVIEW

2.1 Introduction

In this chapter, a brief review of the analysis and design of flat slab–column junctions is presented. The experimental and theoretical works reported in literature on the strength and behaviour of prestressed flat slab column connections are also critically reviewed. Finally the design recommendations of BS8110 and ACI 318–83 are included.

2.2 Flat Slab Analysis

2.2.1 Reinforced Concrete Flat Slab

A flat slab floor is a reinforced concrete slab which is supported directly by columns without use of supporting beams. The analysis of a flat slab structure may be carried out by one of the following methods:

a) Frame Analysis

In this method the structure is idealized into a set of parallel two–dimensional frames in each of two orthogonal directions through the structure. Each frame consists of a series of columns spanned by equivalent beams. An equivalent beam is an idealization of the slab strip so that the width of the beam on each side of the column line equals to half of the distance to the adjacent parallel row of columns.

The moment in these frames may be determined by either a method of frame analysis or simplified method using shear and moment coefficients which are suggested in some codes of practice (such as BS8110).

b) Yield line Analysis

Yield line analysis is a convenient method for calculating the collapse load of reinforced concrete slabs. It is a plastic method of analysis of slab with yield lines developing in the slab and changing the slab into a mechanism. The yield lines divide the slab into rigid segments. At collapse each segments rotates about an axis of rotation and the principle of virtual work is used to determine the collapse load corresponding to any possible yield line pattern. In cases where there are more than one possible yield line patterns, the smallest collapse load is taken as the ultimate load capacity of the slab.

2.2.2 Design of Prestressed Flat Slabs

2.2.2.1 Load Balancing

Considering the internal panel of the two-way edge-supported slab shown in Figure 2.1, the panel is supported on all sides by walls or beams and contains the parabolic tendons in the both X and Y-directions. If the tendons are uniformly spaced, the upward load which is exerted by the tendons to the slab will be :

$$w_{px} = \frac{8P_x e_x}{L_x^2} \qquad w_{py} = \frac{8P_y e_y}{L_y^2} \qquad 2.1$$

where : w_{px} and w_{py} are upward loads exerted by the tendons.

P_x and P_y are prestressing forces per unit width in the X and Y directions.

e_x and e_y are the cable eccentricity in X and Y directions.

If w_b is assumed to be uniformly distributed applied load to be balanced by prestressing loads, then :

$$w_b = w_{px} + w_{py}$$

The slab tendons may be distributed arbitrarily between X and Y– directions provided that adequate additional tendons are placed in the column strips to balance the line loads $w_{px}L_x$ and $w_{py}L_y$ as shown on the column lines in Figure 2.2. The column line tendons have to be placed within the width of the slab in which the slab tendons have reverse curvature. The downward load from slab tendons should be in balance with the upward load exerted by column line tendons (Figure 2.3). These tendons are frequently spread out over a width of slab as large as one half of the shorter span of panel as shown in Figure 2.4. For example, in the slab shown in Figure 2.4(a) the entire load to be balanced is carried by slab tendons in the X– direction, $w_{px} = w_b$ and $w_{py} = 0$. This entire load is deposited as a line load on the column lines in the Y– direction and must be balanced by column line tendons in this vicinity. This slab is in fact treated as a one– way slab spanning in the X– direction and being supported by shallow, heavily stressed, slab strips on the Y– direction column lines.

The two– way system shown in Figure 2.4(b) is more likely to perform better under unbalanced loads, perticularly when L_x and L_y are similar and the panel is roughly square. In practice, steel concentration over the supporting columns and minimum spacing requirements make the distribution of tendons on the column lines impossible. Figure 2.4(c) shows a more practical and generally acceptable layout. Approximately, 75% of the tendons in each direction are located in the column strips, the remainder being uniformly spread across the middle strip regions[3].

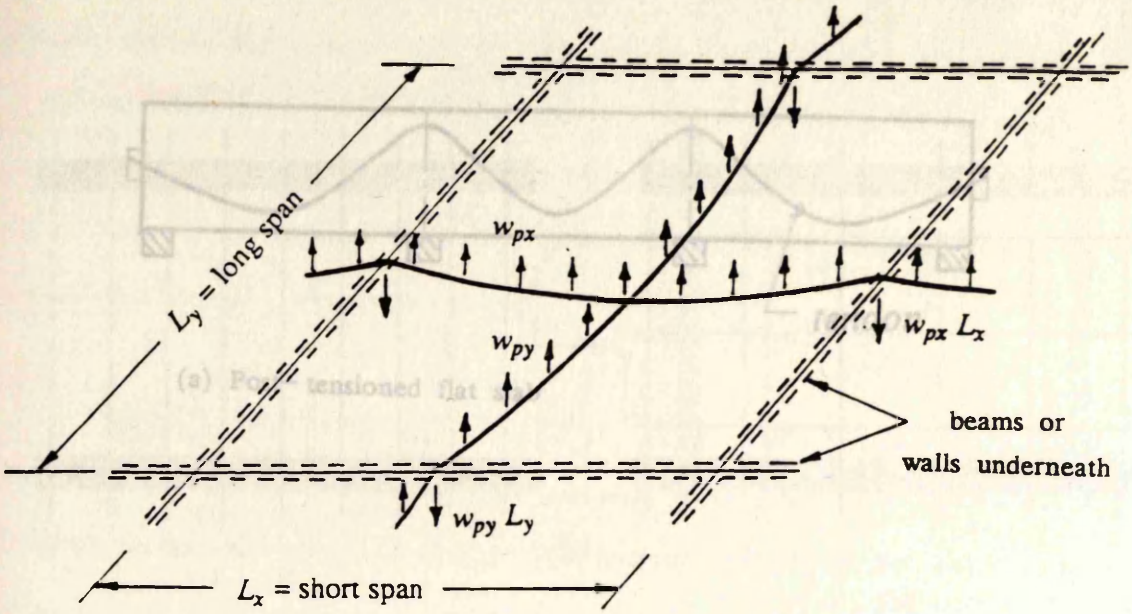

Figure 2.1 : Edge– supported slab panel

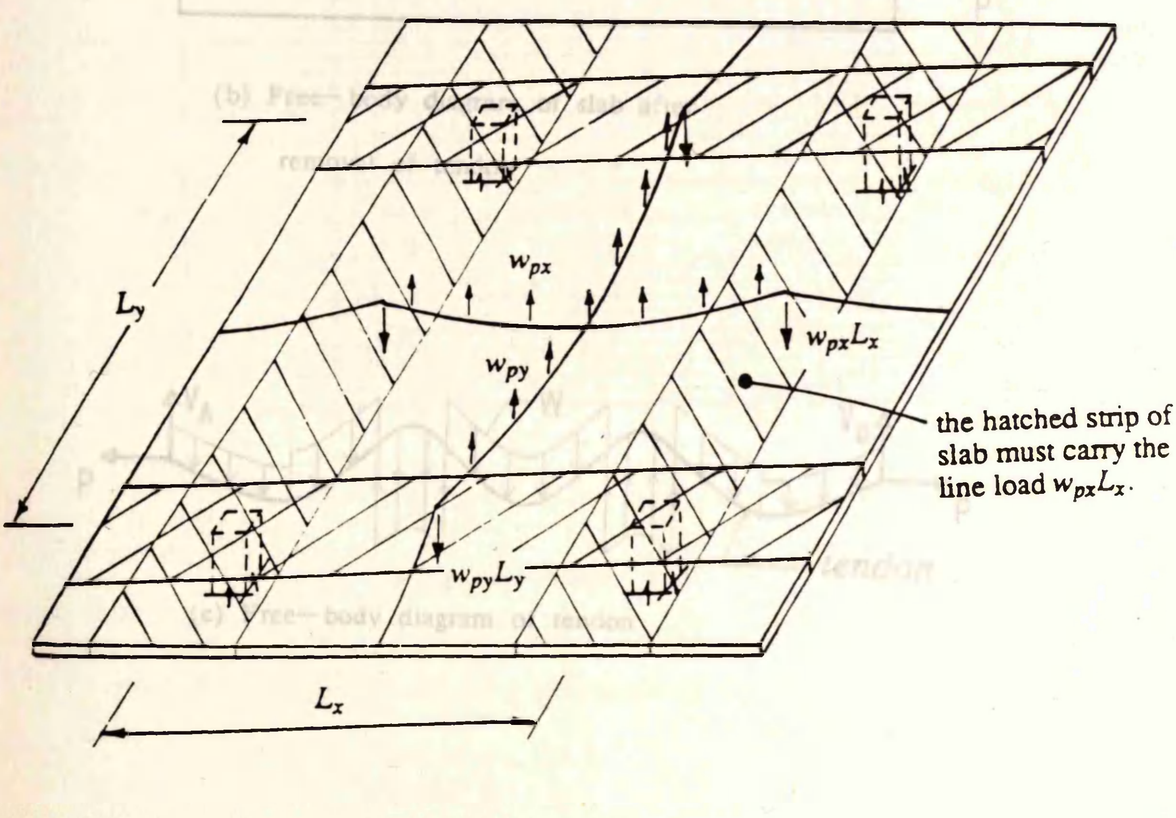

Figure 2.2 : Flat slab panel

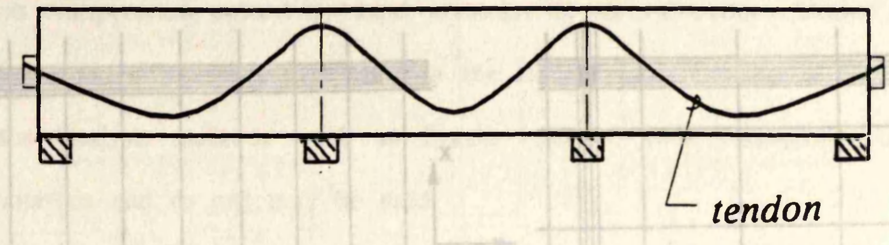

(a) Post– tensioned flat slab

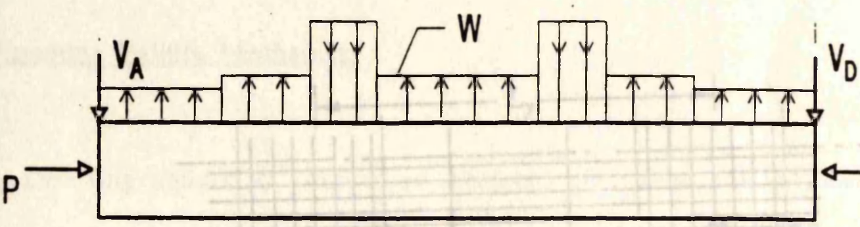

(b) Free– body diagram of slab after removal of tendon

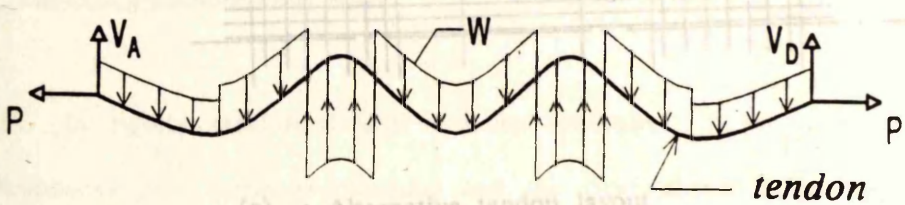

(c) Free– body diagram of tendon

Figure 2.3 : Force system between tendon and slab

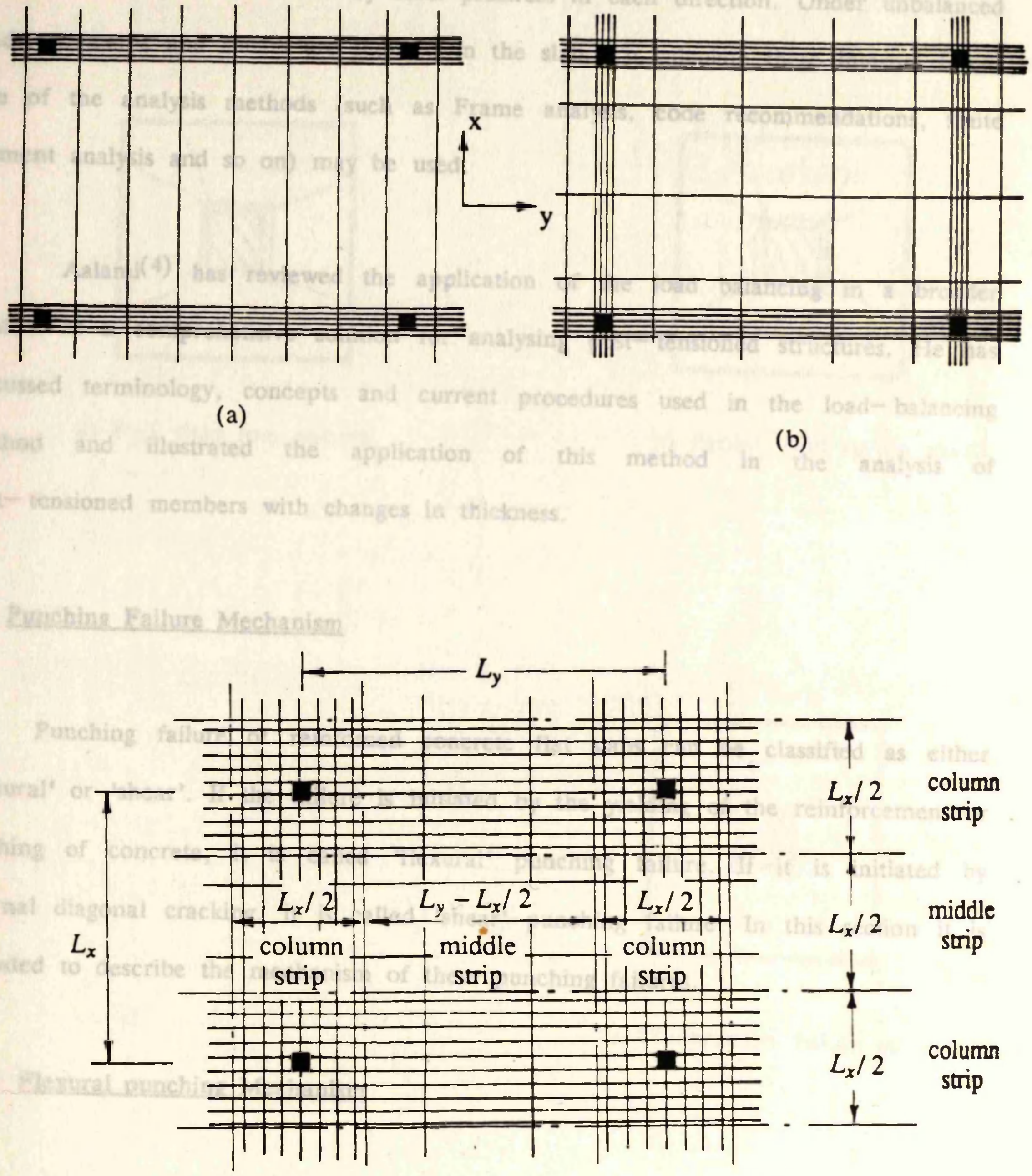

(c) : Alternative tendon layout

Figure 2.4

If the tendon layout is such that the upward force on the slab is approximately uniform, then at the balance load the slab has zero deflection and is subjected only to uniform compression caused by axial prestress in each direction. Under unbalanced loads, moments and shears are induced in the slab. To calculate these internal forces one of the analysis methods (such as Frame analysis, code recommendations, finite element analysis and so on) may be used.

Aalami[4] has reviewed the application of the load balancing in a broader context as a comprehensive solution for analysing post–tensioned structures. He has discussed terminology, concepts and current procedures used in the load–balancing method and illustrated the application of this method in the analysis of post–tensioned members with changes in thickness.

2.3 Punching Failure Mechanism

Punching failure of reinforced concrete flat slabs can be classified as either 'flexural' or 'shear'. If the failure is initiated by the yielding of the reinforcement or crushing of concrete, it is called 'flexural' punching failure. If it is initiated by internal diagonal cracking, it is called 'shear' punching failure. In this section it is intended to describe the mechanism of these punching failures.

2.3.1 Flexural punching Mechanism

In lightly reinforced slab–column specimens, it is more likely that the reinforcements yield prior to punching and the yield pattern might approach the full yield–line pattern as shown in Figure 2.5a. Conversely, in heavily reinforced slabs, yielding becomes more localized and the failure mode approaches the compression failure of concrete around the column (Figure 2.5c). Thus depending on the ductility,

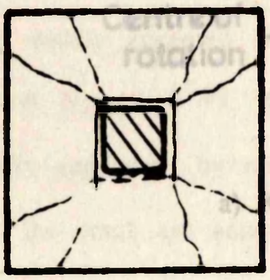

a) Full yield line pattern

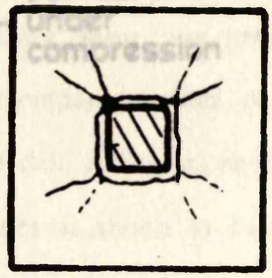

b) Partial yield failure mode

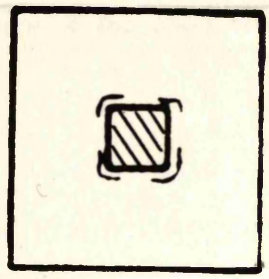

c) Compression failure mode

Figure 2.5 :

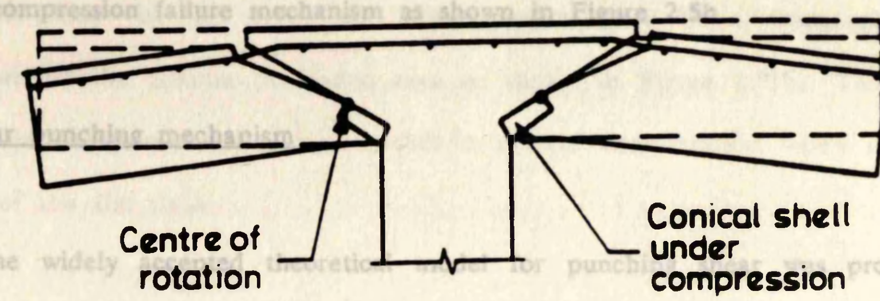

a) Kinnunen/Nylander model

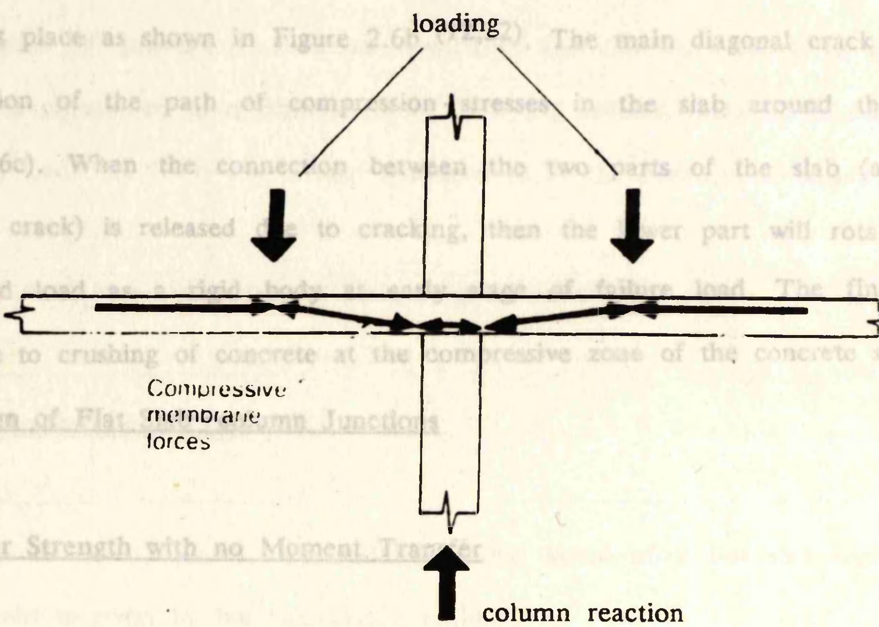

b) Load transfer through the slab to the column

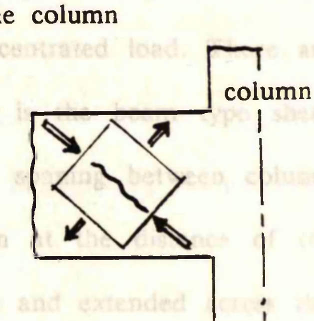

c) Diagonal shear crack around the column

Figure 2.6 :

the 'flexural' punching mechanism is something between the full yield–line and localized compression failure mechanism as shown in Figure 2.5b.

2.3.2 Shear punching mechanism

The widely accepted theoretical model for punching shear was proposed by Kinnunen and Nylander[5,6]. This is based on the observation of tests on circular slabs centrally supported by circular columns. In this model, radial segments of the slab outside the crack are assumed to rotate as rigid bodies as shown in Figure 2.6a. The basic idea is that the transmission of the applied loads to column through the slab takes place as shown in Figure 2.6b [12,22]. The main diagonal crack occurs in the direction of the path of compression stresses in the slab around the column (Figure 2.6c). When the connection between the two parts of the slab (above and below the crack) is released due to cracking, then the lower part will rotate due to the applied load as a rigid body at early stage of failure load. The final failure occurs due to crushing of concrete at the compressive zone of the concrete shell.

2.4 Design of Flat Slab– column Junctions

2.4.1 Shear Strength with no Moment Transfer

In the design of prestressed flat slabs, shear strength usually controls the thickness of the slab particularly around the column or concentrated load. There are two kinds of shear failure that may be critical. The first is the beam type shear failure which is based on the slab acting as a wide beam spaning between column strips shown in Figure 2.7(a). The critical section is taken at the distance of (d) ,where 'd' is effective depth of slab , from the column face and extended across the entire width of the slab.

Another type of shear failure may happen in the vicinity of a column or concentrated load. In this type, the failure surface may be a truncated cone or pyramid around the column or loaded area as shown in Figure 2.7(b). This is called punching shear failure and it often needs a critical consideration when determining thickness of the flat slabs.

The critical section is assumed to be perpendicular to the plane of slab. The shape of critical perimeter is taken (in some codes of practice) to be the same as column or the loaded area while some other codes round off the corners of perimeters around rectangular columns or loaded areas (Figure 2.8). In most of the current codes of practice (such as American and German Codes), the critical perimeter is considered at a distance (d/2) from the column faces or loaded area. In the British Code (BS8110) the critical perimeter is at the distance of (1.5d).

2.4.1.1 Recommendations of ACI-318-83[2]

a) Non-prestressed slab

In ACI-318-83, the punching shear stress of a flat slab without shear reinforcement is given by the following equation:

$$V_c = v_c \times u \times d \qquad 2.2$$

where v_c is the permissible shear strength of concrete which is given by lesser of the following equations:

$$v_c = \varphi (0.166 + 0.33/\beta_c) \sqrt{f'_c}$$

$$v_c = \varphi\ (\ 0.33\ \surd\ f'_c\ )$$

where: β_c = the ratio of the long side to the short side of the column or loaded area.

f'_c = the design compressive cylinder strength of concrete.

u = the length of critical perimeter taken at distance of d/2 from faces of the column or loaded area.

d = effective depth of slab

φ = 0.85 for shear

It is evident that in the above expressions, the effect of flexural reinforcement on the punching strength has not been taken into account.

b) Prestressed Flat Slab

For two-way prestressed flat slabs, the punching shear strength of the slab without shear reinforcement is also given by equation 2.2. But the permissible shear stress of concrete ,v_c, is given by :

$$v_c = \varphi\ (0.29\ \surd\ f'_c + 0.3\ f_{cp} + V_p/ud\ ) \qquad 2.3$$

in which : φ = 0.85 for shear

f_{cp} = The average value of effective prestress at the critical area.

V_p = The vertical component of all effective prestressing forces crossing the critical area.

f_c should not be taken greater than 35 N/mm^2 and f_{cp} in each direction should not be less than 1 N/mm^2 nor greater than 3.5 N/mm^2. Because the tendons at the critical section are fairly horizontal and the vertical component of the prestressing force ,V_p, is small, it may be taken conservatively as zero.

2.4.1.2 British Code Recommendations (BS8110)[1]

a) Non-prestressed Flat Slab

According to BS8110-1985, punching failure occurs on the inclined faces of a truncated cone or pyramid depending on the shape of the loaded area. However, for practical purposes it is satisfactory to consider rectangular failure perimeter as shown in Figure 2.9. In this Code, the critical perimeter is at 1.5d from the loaded area and punching shear strength of the slab is given by the following equation:

$$V = v_c \times u \times d \qquad 2.4$$

where $v_c = 0.79(f_{cu}/25)^{1/3}\,(100A_s/ud)^{1/3}\,(400/d)^{1/4}\,/\,\gamma_m$

f_{cu} = Cube strength of concrete

d = Effective depth of slab

u = Length of the critical perimeter taken at distance 1.5d from faces of the column or loaded area

A_s = Area of all the tension reinforcement crossing the critical area (CIRIA 110 , page 19)

γ_m = Partial safety factor for concrete in shear

The limitations are;

$\gamma_m = 1.25$

$f_{cu} \not> 40\ \text{N/mm}^2$

$(100A_s/ud) \ngtr 3.0$

$(400/d) \nless 1.0$

In all cases with or without shear reinforcement, V should not exceed the maximum shear capacity of slab given by the following equation;

$(V_{max}/u_o d) > 0.8 \sqrt{f_{cu}}$ or 5 N/mm2 [whichever is smaller]

where u_o is effective length of the perimeter which touches the loaded area.

If the shear stress exceeds v_c , shear reinforcement should be provided. Design procedure is to check the failure zone adjacent to a loaded area (zone 1) first, as shown in Figure 2.10. If this zone does not require shear reinforcement then no further checks are required. Otherwise the successive zones (Figure 2.10) are checked until a zone is reached which does not require shear reinforcement.

b) Prestressed Flat Slab

In BS8110[1] no special recommendation is given concerning design of prestressed concrete flat slabs. So the analysis and design of prestressed flat slabs have been referred to specialist literature. So far only relevant reference for the design of prestressed flat slabs is the recommendations of the Concrete Society[7,64].

2.4.1.3 Recommendations of The Concrete Society[7,64]

According to these recommendations, the following two cases should be considered to calculate the punching shear resistance of flat slab– column connections.

<u>Case 1</u> – The shear strength of a section at a perimeter 0.75h from the column face based on the tensile strength of concrete is given by equation:

$$V = v_c \times u \times h \qquad 2.5$$

where v_c: is given in Table 2.1

h : is the slab thickness.

The figures in Table 2.1 is calculated by the following equation:

$$v_c = 0.67 \sqrt{f_t^2 + 0.8 f_{cp} f_t}$$

where : f_t = Tensile strength of concrete

f_{cp} = Average prestress of concrete at the critical area

<u>Case 2</u> – The shear strength of a section at the critical surface is calculated in accordance with BS8110 recommendations for non–prestressed flat slab except that the values of permissible shear strength of concrete ,v_c, may be calculated using A_s, where :

$$A_s = A_{so} + A_{sp}(f_{pu}/f_y) \qquad 2.6$$

in which,

A_{so} = cross–section area of ordinary steel crossing the critical surface.

A_{sp} = cross–section area of prestressing bars crossing the critical surface.

f_{pu} = proof stress of prestressing bars

f_y = Yield stress of ordinary steel

TABLE 2.1 : Permissible shear strength of concrete in accordance with the Concrete Society Recommendations (Ref. 7).

f_{cp}* N/mm²	Concrete Grade (f_{cu})		
	25	30	40
	N/mm²	N/mm²	N/mm²
1·0	1·05	1·10	1·25
1·5	1·15	1·20	1·35
2·0	1·25	1·30	1·45
2·5	1·30	1·40	1·55
3·0	1·40	1·50	1·65
3·5	1·45	1·55	1·70

*) f_{cp} = average compression stress of concrete due to prestressing

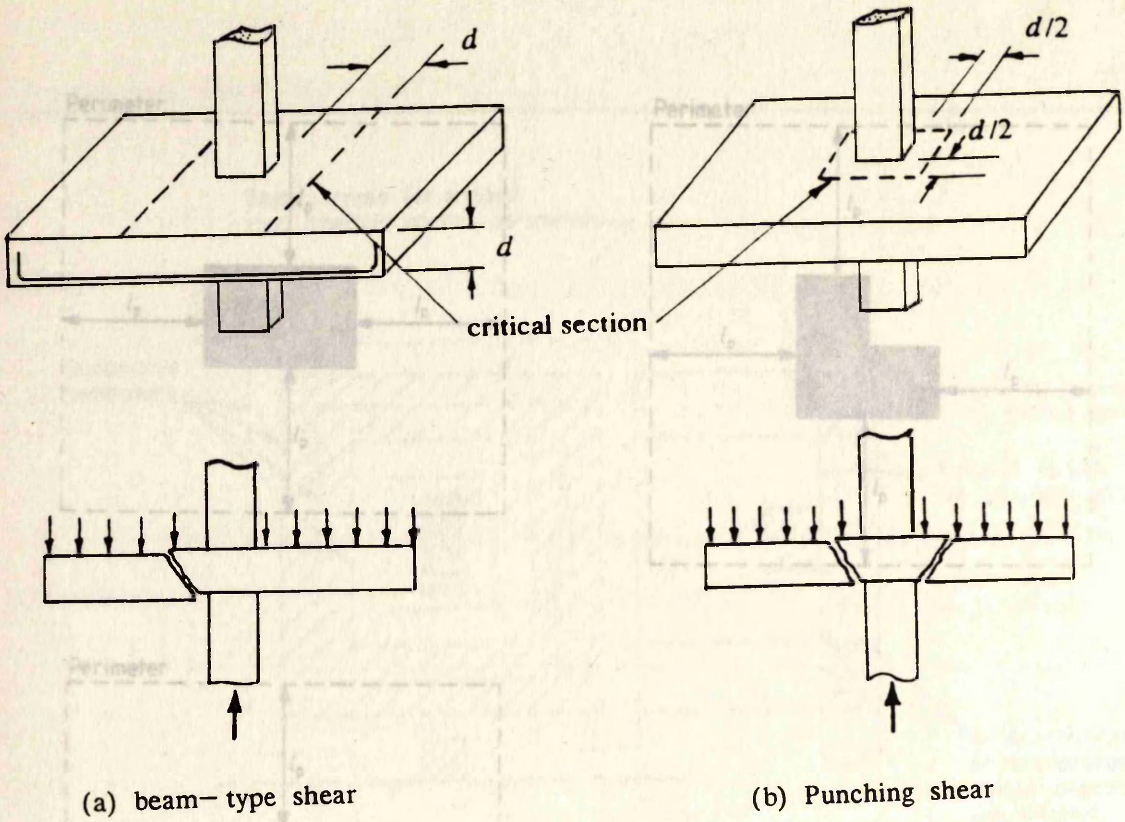

Figure 2.7 : Shear failure surface in a slab.

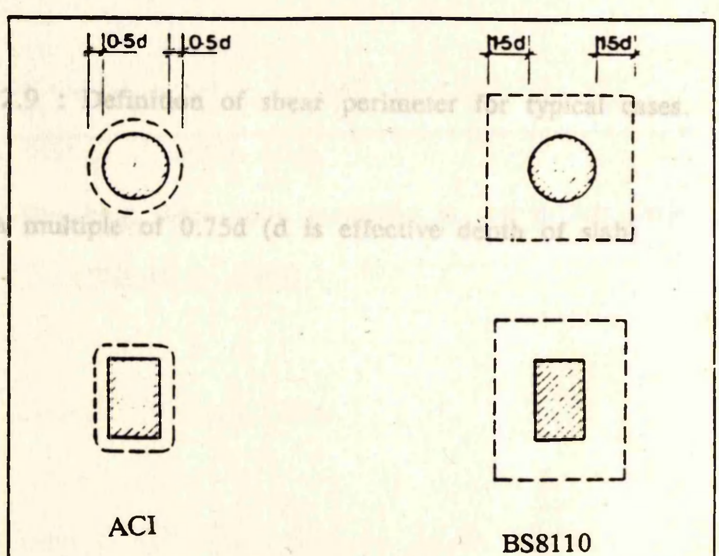

Figure 2.8 : Definition of shear perimeter.

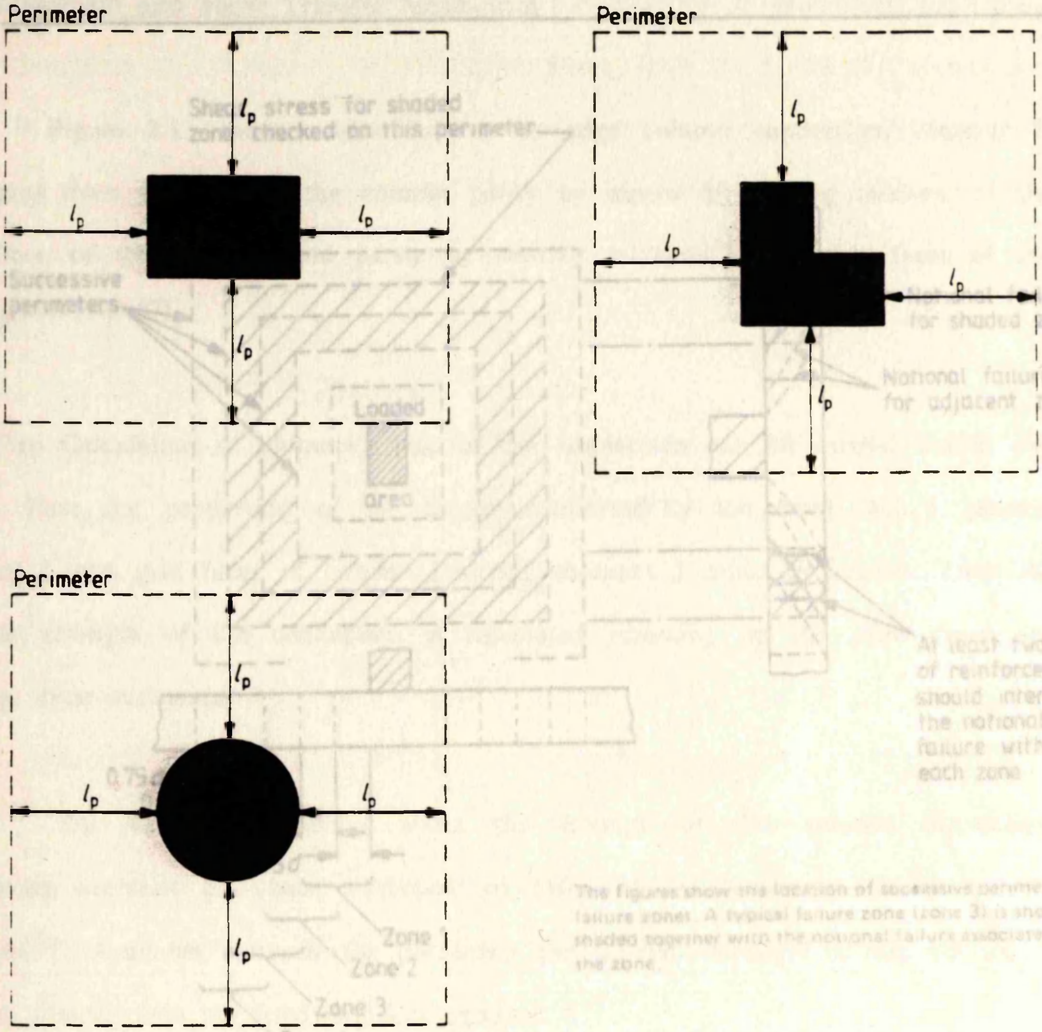

Figure 2.9 : Definition of shear perimeter for typical cases.

l_p = A multiple of 0.75d (d is effective depth of slab)

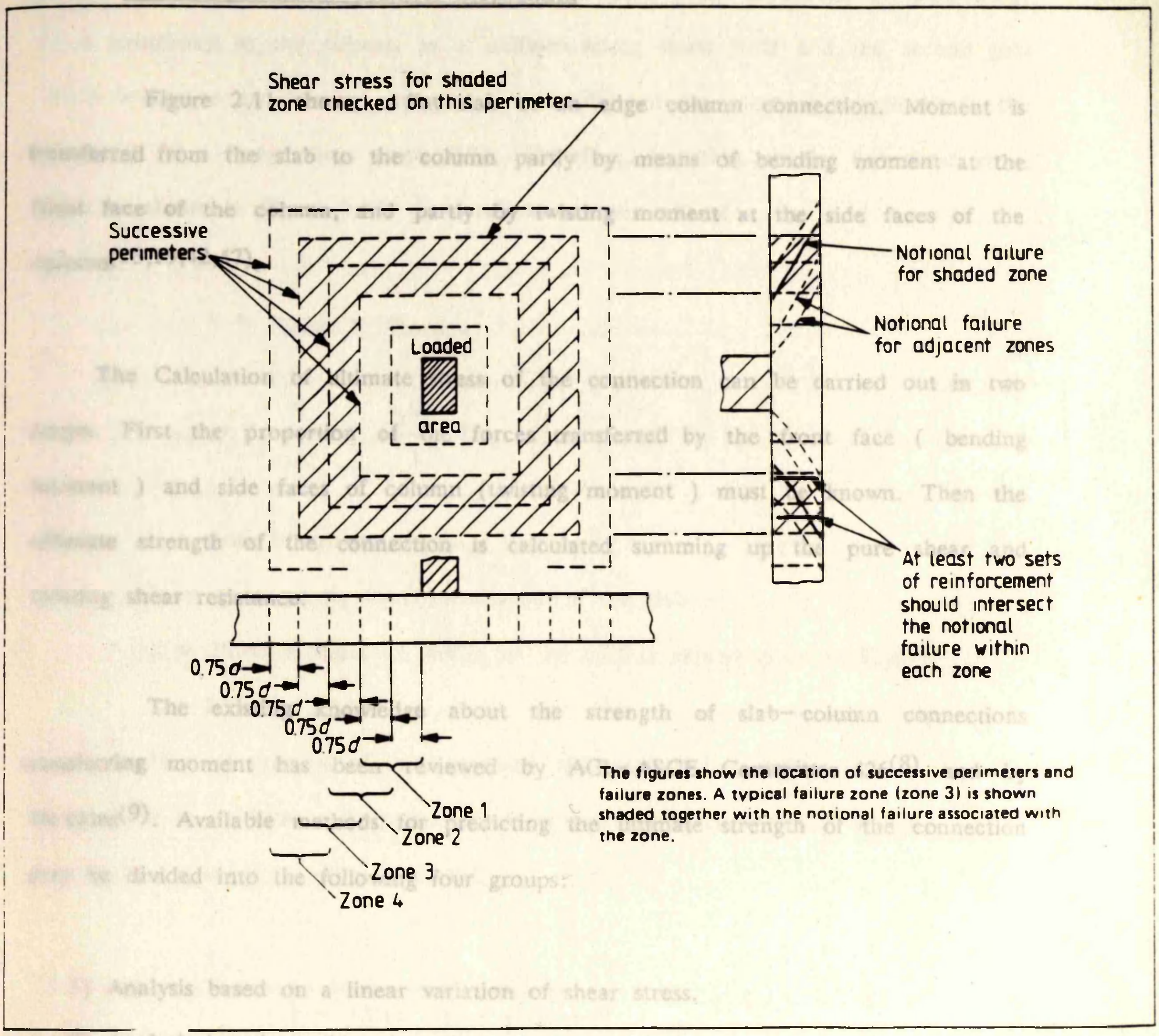

Figure 2.10 : Punching shear zone according to the British Code (BS8110 – 1985).

2.4.2 Shear Strength with Moment Transfer

2.4.2.1 Moment and Shear Transfer Mechanism

Figure 2.11 shows a flat slab at an edge column connection. Moment is transferred from the slab to the column partly by means of bending moment at the front face of the column, and partly by twisting moment at the side faces of the column(18,19,42,47).

The Calculation of ultimate stress of the connection can be carried out in two stages. First the proportion of the forces transferred by the front face (bending moment) and side faces of column (twisting moment) must be known. Then the ultimate strength of the connection is calculated summing up the pure shear and twisting shear resistance.

The existing knowledge about the strength of slab–column connections transferring moment has been reviewed by ACI–ASCE Committee 426[8] and by Hawkins[9]. Available methods for predicting the ultimate strength of the connection may be divided into the following four groups:

1) Analysis based on a linear variation of shear stress.
2) Analysis based on thin plate theory.
3) Beam analogy method.
4) Finite element method.

2.4.2.2 Linear Variation in Shear Stress

This method was first introduced by D Stasio and V Buren[10] in 1960.

Figure 2.12 shows the model suggested by them for internal and edge column connections. In this method it is assumed that the distribution of shear stress around the connection is sum of two parts. The first part which is caused by pure shear force transferred to the column as a uniform shear stress field and the second part which is caused by twisting moment (a fraction of the moment transferred to the column), is a linear shear stress field. Therefore, summing up the two shear stress fields as shown in Figure 2.12, the total shear stress will be:

$$v = v_{shear} + v_{torsion}$$

$$v(x) = \frac{V}{A} + \frac{\gamma M}{J}(x) \qquad 2.7$$

where : A = Area of critical section.

V = pure gravity load transferred to the slab

J = Polar moment of inertia of the critical section given in Figures 2.13a to 2.13d.

γM = A fraction of total moment ,M, transferred by torsion.

x = A distance from the centre of rotation to the point at which stress is being calculated.

and $$\gamma = 1 - \frac{1}{1 + (2/3)\sqrt{(c_1 + d)/(c_2 + d)}}$$

According to ACI−318−83[2], the moment−shear interaction relationship of equation (2.7) for an interior column connection is shown in Figure 2.14. Which is a linear interaction between V/V_o and $\gamma M/M_o$ where;

$$V_o = v_c \times A$$

$$M_o = v_c \times [2J/(c_1 + d)]$$

where, $A = 2d(c_1 + c_2 + 2d)$

v_c= permissible shear stress of concrete

c_1= Column side perpendicular to moment direction

c_2= Column side parallel to moment direction

The stress diagrams on Figure 2.14 also show idealized shear stress distributions for the different points along the line 'ab'. The line 'cd' represents the possible limitation imposed by the flexural reinforcement. That is, before γM reaches M_o there is a possibility for flexural reinforcement to yield and consequently the slab fails in flexural mode.

Test results(8) indicated that the behaviour of specimens is not far from the above idealization. Hawkins et. al.(9) have shown that the measured shear strength of specimens lie along curve such as 'amn'. For a concrete of 21 N/mm^2 cube strength, that curve lies progressively further outside the envelope 'acd' as the reinforcement ratio within lines 1.5h either side of the column increases to above 0.8%. The reverse is true as the ratio decreases below 0.8%.

The British Code BS8110, was also based on the approach of 'linear variation in shear stress' proposed by Regan(40). The BS8110 specifies the critical section at a distance of 1.5d from the column perimeter and it has square corners whether the column is square or circular (Figure 2.8). The detailed information about the recommendations of ACI-318 83 and BS8110 will be discussed in a later section.

2.4.2.3 <u>Thin Plate Method</u>

Method of analysis based on elastic thin plate theory has been proposed by

Mast[13]. The loading and boundary conditions of the flat plate used by Mast are shown in Figure 2.15 . Shear and moment distribution predicted for the above plate at a section 0.05L (L is the span) are compared in Figure 2.16 with the distributions appropriate for equation 2.6.

The distribution of stresses both transverse and parallel to the direction of the applied moment in this method are nonlinear. It is evident that the flexural moment M_x calculated from equation 2.7 are much higher than that given by thin plate method and the contribution of the torsional moment M_{yx} is underestimated by the straight line shear distribution hypothesis.

Mast found that, in contrast to the assumptions made in ACI Code 318–71 formulation, the relative participation of torsional , flexural and shear stresses to moment transfer varied with the shape, size of the column, dimensions and boundary conditions of the plate. He also found that, for square columns the stresses calculated from his theoretical method and that predicted from the linear–stress method (equation 2.7) give similar results. But for columns for which their aspect ratio in the direction of unbalanced moment is greater than 1.0, flexural plate theory gave better agreement with the experiments than the linear–stress method.

Long et al[14,15] developed a theoretical method of analysis for the calculation of the punching load of a column–flat slab connection with two–way reinforcement without shear reinforcement based on elastic thin–plate theory. They idealized the problem as an axi–symmetric slab–column specimen having a column radius equal to 0.6 times the side length of square column. An octahedral shear stress criterion of failure was used to find the corresponding failure stresses. It was assumed that the initial modulus of elasticity remains approximately constant up to ultimate load. Distribution of bending stresses in the compressive zone of the slab was linear.

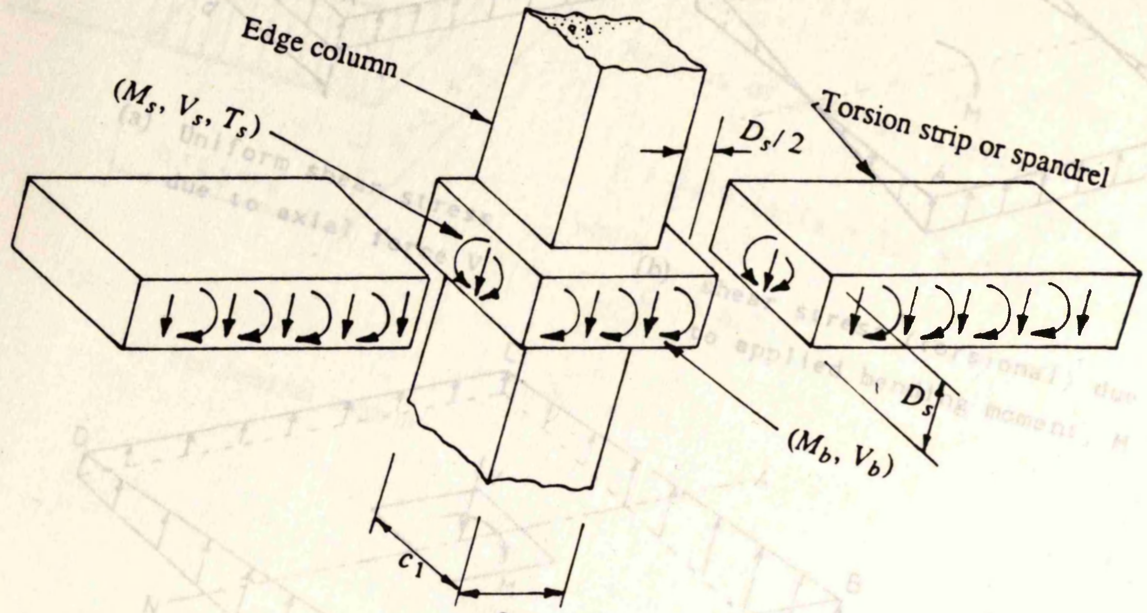

Figure 2.11 : Forces at an edge column– slab connection

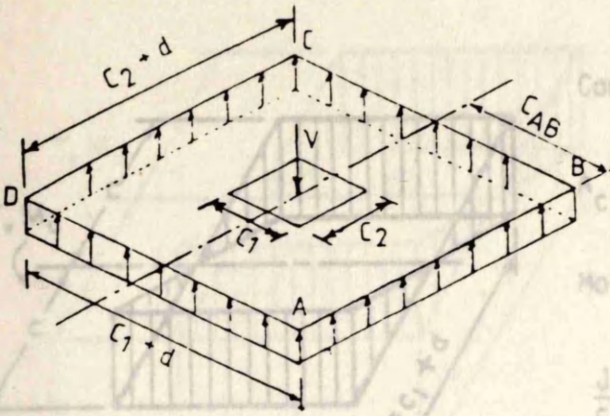

(a) Uniform shear stress due to axial force, V

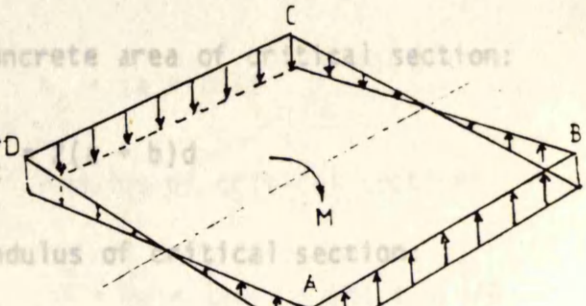

(b) shear stress (torsional) due to applied bending moment, M

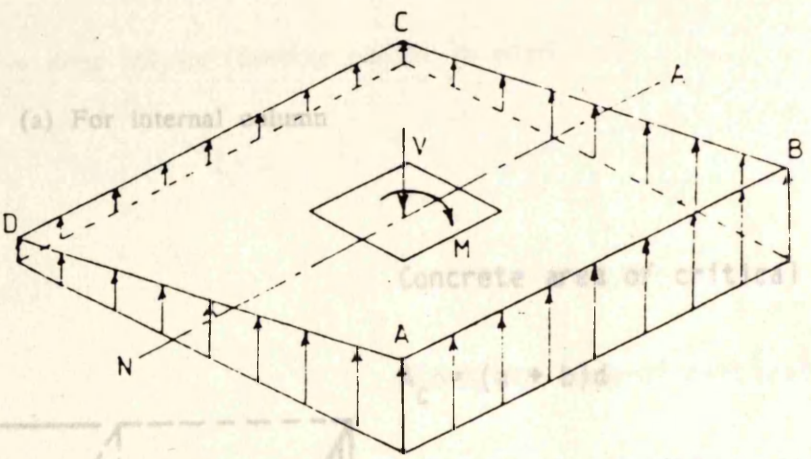

(c) Net shear stress around the critical perimeter

Figure 2.12 : Theory of linear variation in shear stress.

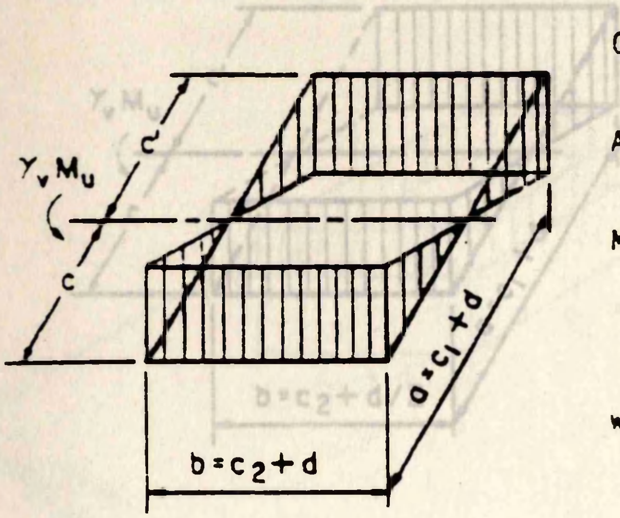

Concrete area of critical section:

$$A_c = 2(a + b)d$$

Modulus of critical section:

$$\frac{J}{c} = \frac{J}{c'} = \left[ad(a + 3b) + d^3\right]/3$$

where

$$c = c' = a/2$$

(a) For internal column

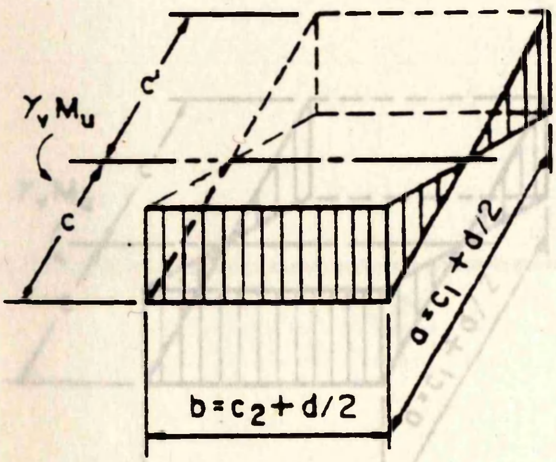

Concrete area of critical section:

$$A_c = (a + b)d$$

Modulus of critical section:

$$\frac{J}{c} = \left[ad(a + 4b) + d^3(a + b)/a\right]/6$$

$$\frac{J}{c'} = \left[a^2d(a + 4b) + d^3(a + b)\right] / \left[6(a + 2b)\right]$$

where

$$c = a^2 / \left[2(a + b)\right]$$

$$c = a(a + 2b) / \left[2(a + b)\right]$$

(b) For corner column

Figure 2.13 :Section properties for shear stress calculations (ACI 318–83)

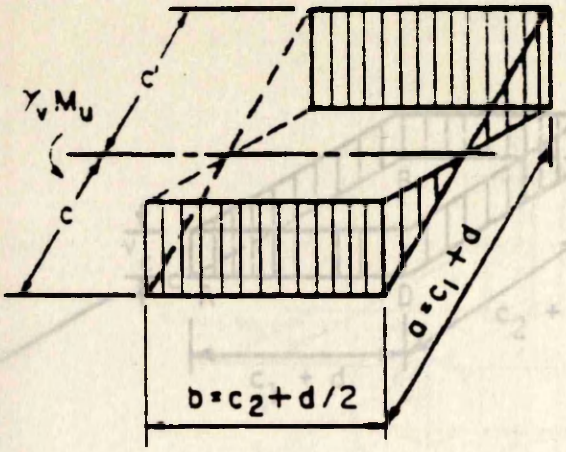

Concrete area of critical section:

$$A_c = (a + 2b)d$$

Modulus of critical section:

$$\frac{J}{c} = \frac{J}{c'} = \left[ad(a + 6b) + d^3\right]/6$$

where

$$c = c' = a/2$$

(c) For edge column (bending parallel to edge)

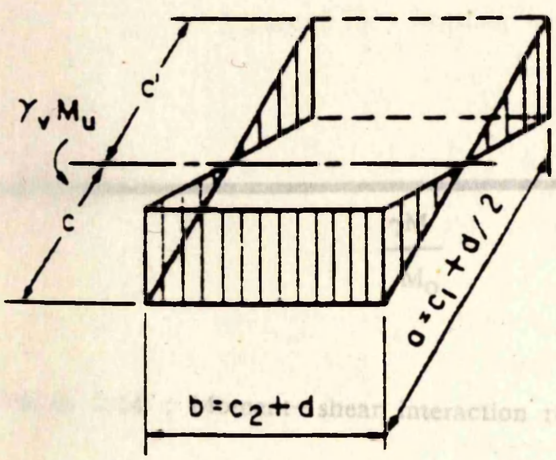

Concrete area of critical section:

$$A_c = (2a + b)d$$

Modulus of critical section:

$$\frac{J}{c} = \left[2ad(a + 2b) + d^3(2a + b)/a\right]/6$$

$$\frac{J}{c'} = \left[2a^2d(a + 2b) + d^3(2a + b)\right]/\left[6(a + b)\right]$$

where

$$c = a^2/(2a + b)$$

$$c' = a(a + b)/(2a + b)$$

(d) for edge column (bending perpendicular to edge)

Figure 2.13 : (continued)

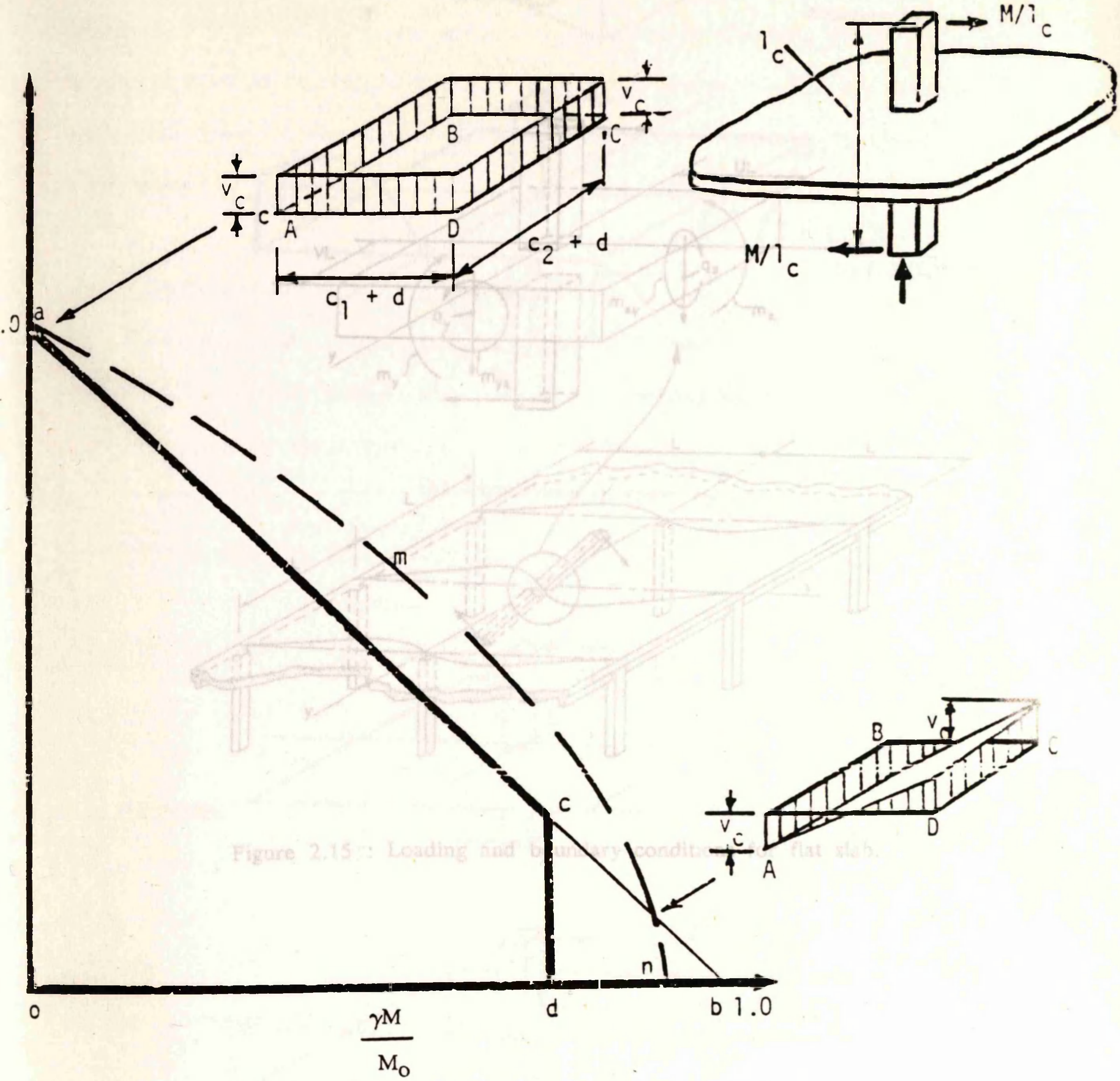

Figure 2.14 : Moment– shear interaction relationship for interior column connections.

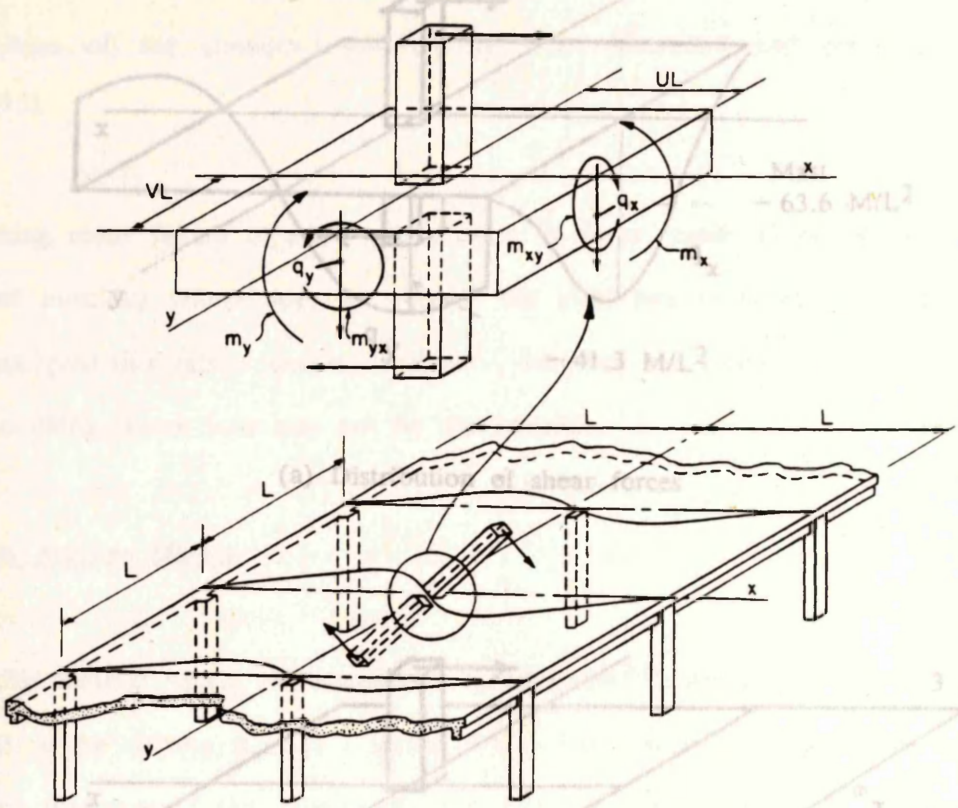

Figure 2.15 : Loading and boundary conditions for flat slab.

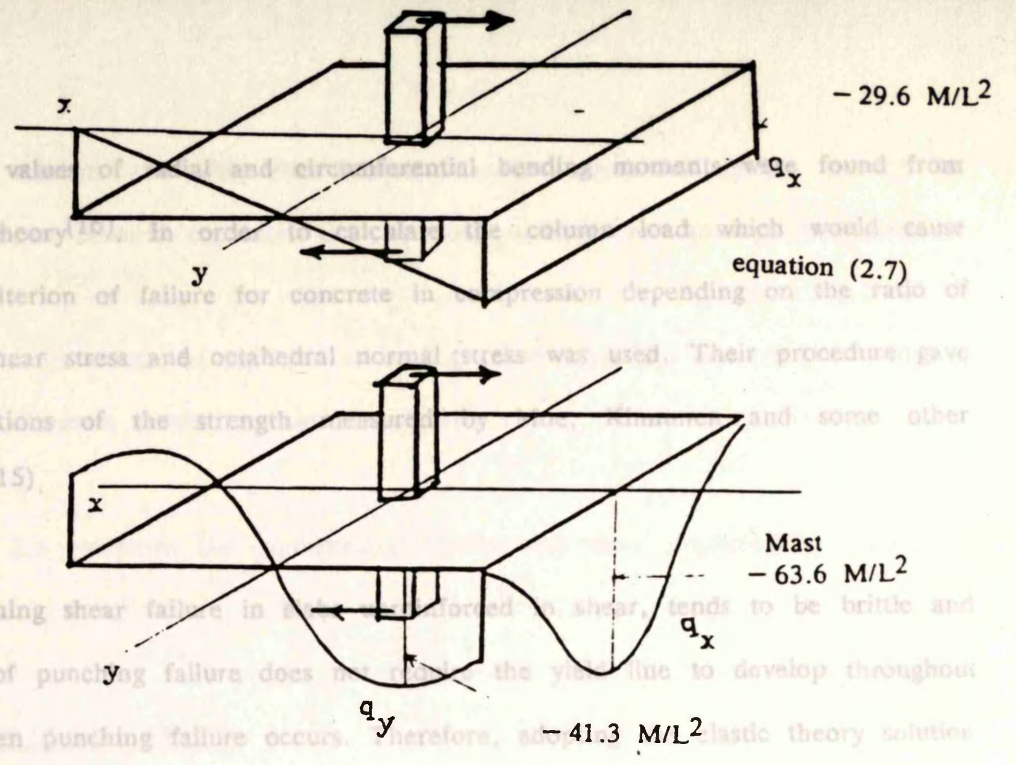

(a) Distribution of shear forces

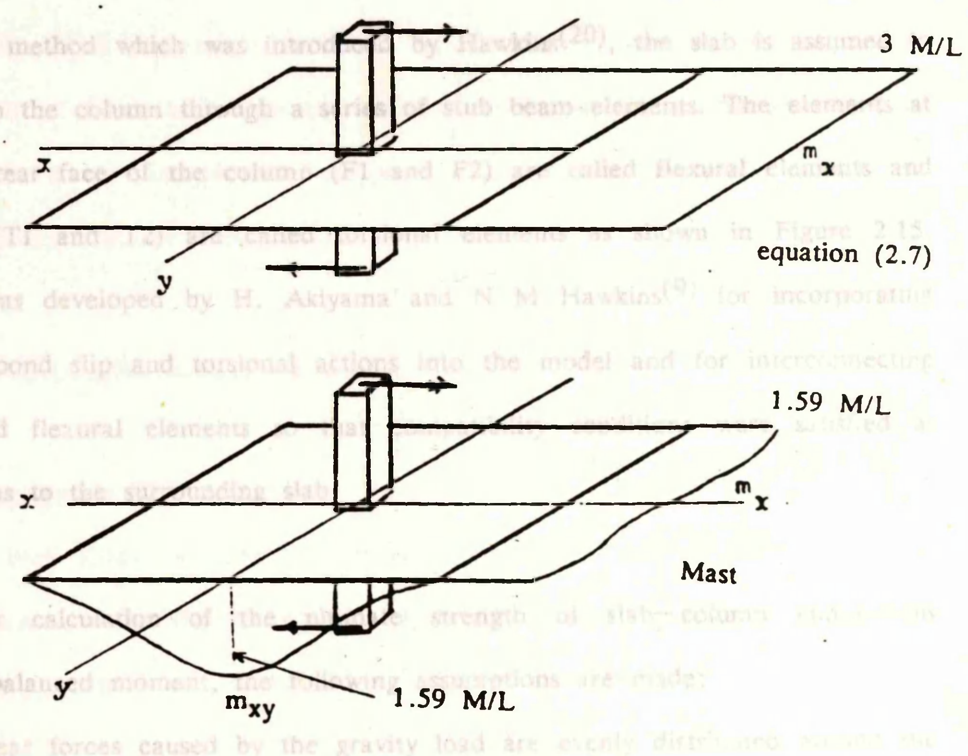

(b) Distribution of moments

Figure 2.16 : Comparison between the linear distribution and the elastic thin plate theory(13) at a section 0.05L (L is the span) from the centre of an interior column.

The values of radial and circumferential bending moments were found from thin plate theory[16]. In order to calculate the column load which would cause failure, a criterion of failure for concrete in compression depending on the ratio of octahedral shear stress and octahedral normal stress was used. Their procedure gave good predictions of the strength measured by Moe, Kinnunen and some other investigators[15].

Punching shear failure in slabs unreinforced in shear, tends to be brittle and the nature of punching failure does not require the yield line to develop throughout the slab when punching failure occurs. Therefore, adopting the elastic theory solution to predict punching failure load may not be unreasonable.

2.4.2.4 <u>Beam Analogy Method</u>

In this method which was introduced by Hawkins[20], the slab is assumed to be connected to the column through a series of stub beam elements. The elements at the front and rear face of the column (F1 and F2) are called flexural elements and side elements (T1 and T2) are called torsional elements as shown in Figure 2.15. This method was developed by H. Akiyama and N M Hawkins[9] for incorporating the effects of bond slip and torsional actions into the model and for interconnecting the torsion and flexural elements so that compatibility conditions were satisfied at their connections to the surrounding slab.

For calculation of the ultimate strength of slab–column connections transferring unbalanced moment, the following assumptions are made:

a)– The shear forces caused by the gravity load are evenly distributed around the column.

b)– The moment caused by lateral load is transfered to the column first through the flexural element and after the flexural element looses its rigidity through its attainment of its flexural capacity, that moment is transfered through the torsional element.

c)– A connection can be regarded as having failed when the front or rear side of the torsional elements reaches its ultimate strength.

Table 2.3 compares the experimental results with those predicted by theoretical method.

2.4.2.5 Finite Element Method

Finite element procedure can be used to calculate and more accurately assess the strength of slab– column connections(48). Elnounu(23) developed a three– dimensional finite element method for nonlinear stress analysis of reinforced concrete structures. This programme was used by Elnounu(23) and Bari(24) to predict the ultimate load of shear wall– slab connections. As far as the author is aware no one has used the three– dimensional finite element to analyse prestressed slabs. This aspect will be pursued in the later sections of this work.

2.4.2.6 American Code Recommendations (ACI 318– 83)

a) Non– prestressed Flat Slab

When both shear ,V, and unbalanced moment ,M, are transfered from the slab to the column, ACI 318– 83 suggests that the maximum shear stress on the critical section ,v_{max}, may be calculated from equation 2.7:

$$v_{max} = \frac{V}{A} + \frac{\gamma M}{J} C_{AB} \qquad 2.8$$

Table 2.3

No. of tests	Type of slab-column connection	Shear reinforcement used	M_{pred} / M_{test} *	
			mean	standard deviation
7	Interior	No	1.00	0.07
8	Interior	Yes	1.12	0.07
2	Exterior: moment parallel to the edge	No	0.99	0.06
3	Exterior: moment parallel to the edge	Yes	1.07	0.05
3	Exterior: moment normal to the edge	No	1.00	0.09
5	Exterior: moment normal to the edge	Yes	1.03	0.07
3	corner	No	0.99	0.07
2	corner	Yes	0.91	0.00

* M_{pred} = Predicted moment transfer capacity

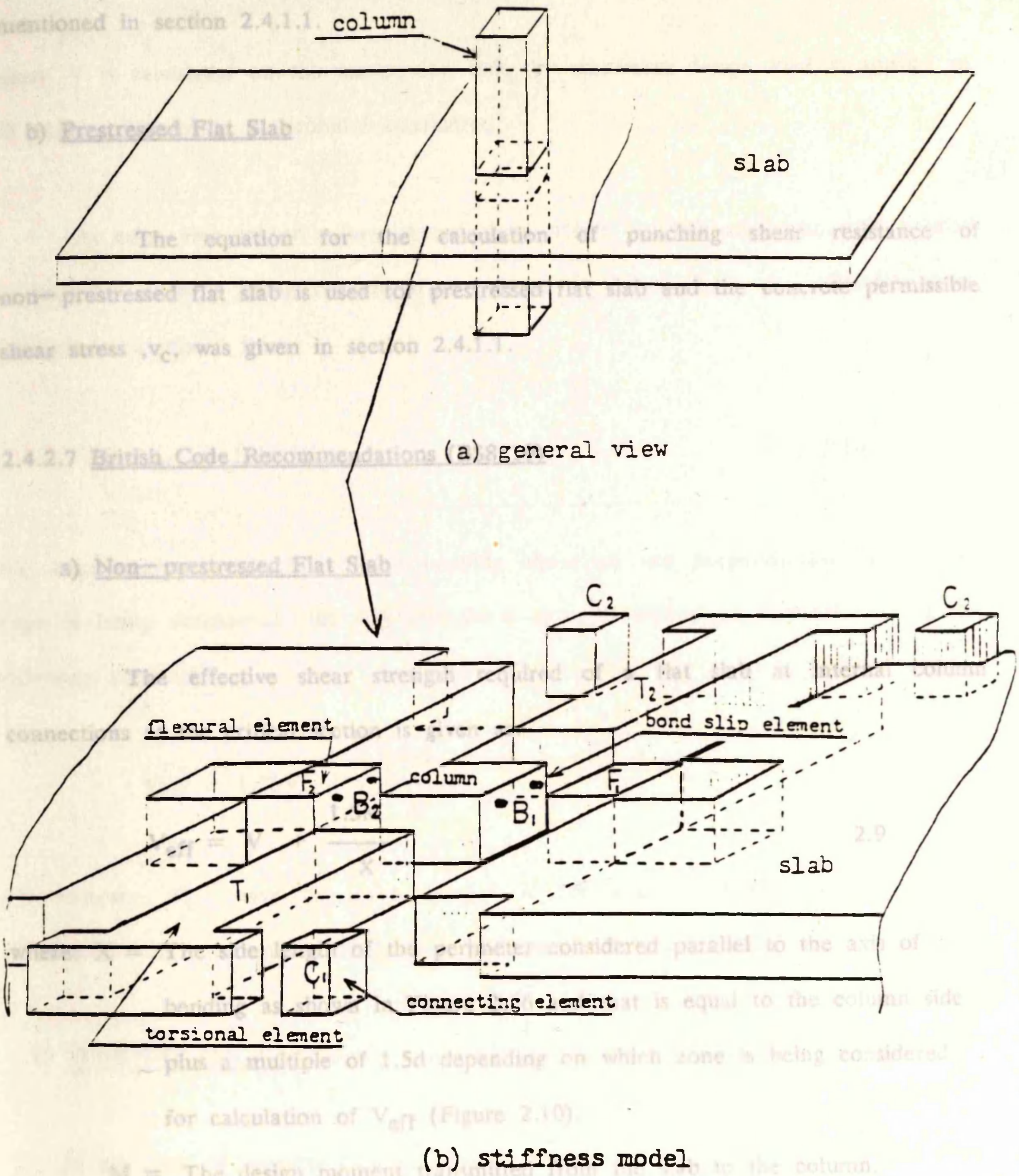

Figure 2.17 : Stiffness model for interior column connections.

The ACI 318−83 design requirement for slabs containing no shear reinforcement is that the v_{max} does not exceed a permissible shear stress v_c carried by concrete. as mentioned in section 2.4.1.1.

b) Prestressed Flat Slab

The equation for the calculation of punching shear resistance of non−prestressed flat slab is used for prestressed flat slab and the concrete permissible shear stress ,v_c, was given in section 2.4.1.1.

2.4.2.7 British Code Recommendations (BS8110)

a) Non−prestressed Flat Slab

The effective shear strength required of a flat slab at internal column connections at the critical section is given as:

$$V_{eff} = V + \frac{1.5M}{X} \qquad 2.9$$

where: X = The side length of the perimeter considered parallel to the axis of bending as shown in Figure 2.16 and that is equal to the column side plus a multiple of 1.5d depending on which zone is being considered for calculation of V_{eff} (Figure 2.10).

M = The design moment transmitted from the slab to the column.

V = The design shear force transfered to the column.

In the absence of calculations, for internal columns in braced structures with approximately equal spans, it will be satisfactory to take V_{eff} from the following equation:

$$V_{eff} = 1.15 \; V$$

where V is calculated on the assumption that the maximum design load is applied to all panels adjacent to the column considered.

At edge and corner column connections where bending about an axis parallel to the free edge is being considered, as shown in Figure 2.19, the effective shear strength is calculated from:

$$V_{eff} = 1.25 \; V \qquad 2.10$$

For edge column connections when bending about an axis perpendicular to the free edge is being considered, the effective shear strength should be calculated using the following equation:

$$V_{eff} = 1.25V + \frac{1.5M}{X} \qquad 2.11$$

Alternatively, V_{eff} may be taken as 1.4 V for approximately equal spans. The permissible shear strength of concrete is given in Table 3.9 in BS8110(1).

b) <u>Prestressed Flat Slab</u>(65)

In the case of moment transfer, the equation for non– prestressed flat slab shear strength calculation is also applicable to predict the shear strength of prestressed flat slab– column connections. The only difference is that, the permissible shear stress is dependent on the area of total steel crossing the critical perimeter and account should be taken of both prestressing and reinforcing bars as shown in equation 2.6 in

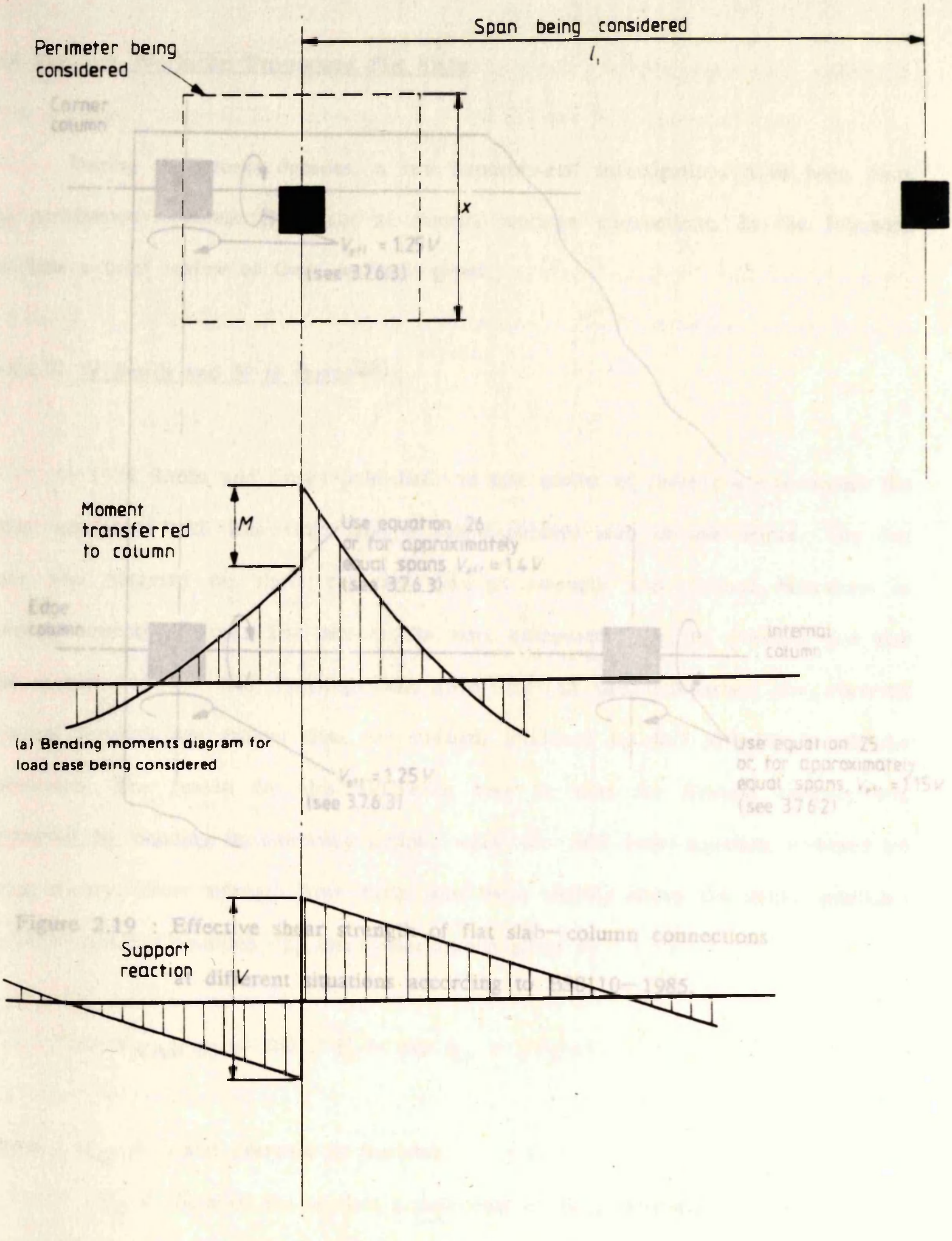

Figure 2.18 : Shear and moment diagram at slab– column connection.

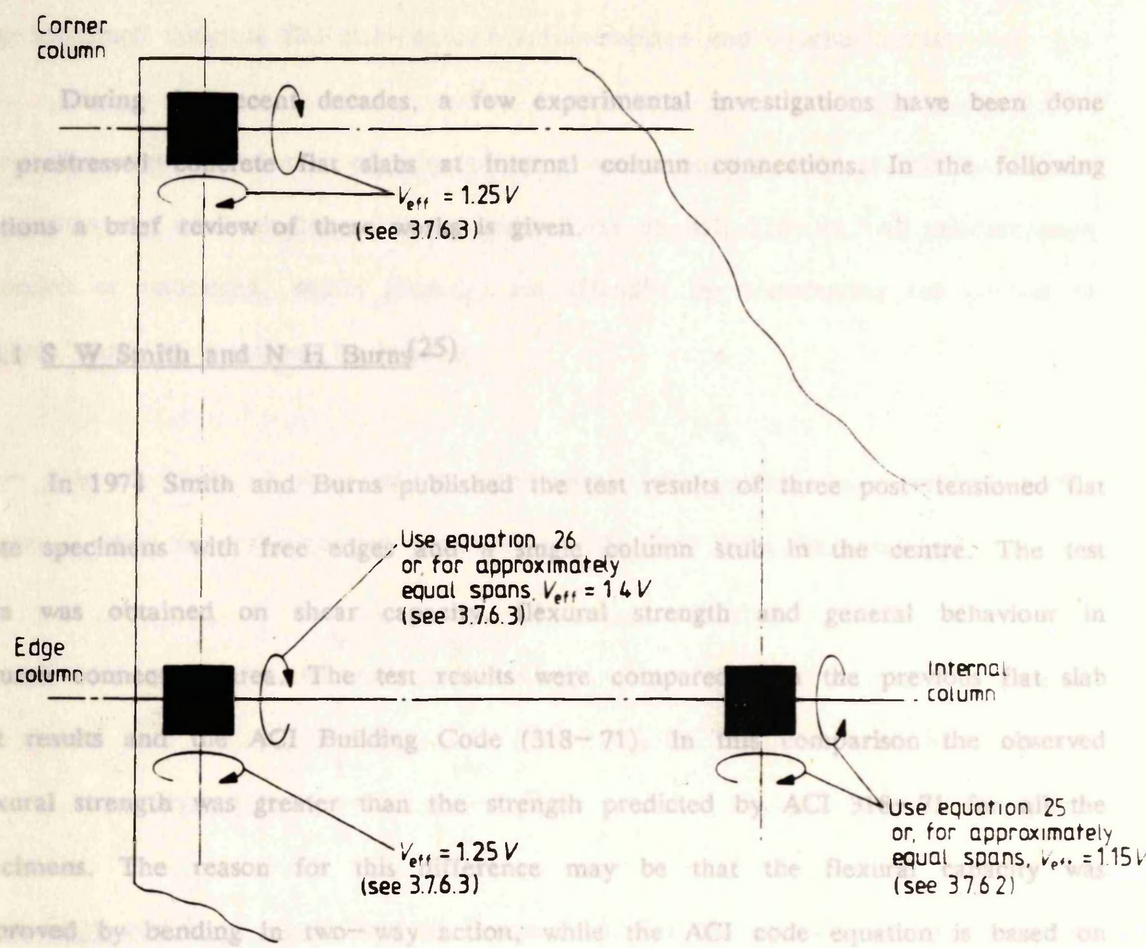

Figure 2.19 : Effective shear strength of flat slab– column connections at different situations according to BS8110– 1985.

section 2.4.1.2.

2.5 Previous Works on Prestressed Flat Slabs

During the recent decades, a few experimental investigations have been done on prestressed concrete flat slabs at internal column connections. In the following sections a brief review of these works is given.

2.5.1 S W Smith and N H Burns[25]

In 1974 Smith and Burns published the test results of three post–tensioned flat plate specimens with free edges and a single column stub in the centre. The test data was obtained on shear capacity, flexural strength and general behaviour in column connection area. The test results were compared with the previous flat slab test results and the ACI Building Code (318–71). In this comparison the observed flexural strength was greater than the strength predicted by ACI 318–71 for all the specimens. The reason for this difference may be that the flexural capacity was improved by bending in two–way action, while the ACI code equation is based on beam theory. Shear strength from these tests were slightly above the values predicted by ACI–ASCE Commitee 423 Recommendations given by:

$$V_{u(ASCE)} = 0.3\sqrt{f'_c} + 0.3\,f_{cp} + (V_p/ud) \qquad 2.13$$

where, f_{cp} = Axial prestress in the slab.

V_p = Sum of the vertical components of all prestressing tendons crossing the critical section for shear.

The average value of the ratio [$V_{u(test)}/V_{u(ASCE)}$] was 0.98.

2.5.2 N M Hawkins[26]

In 1981 Hawkins published an investigation on six full-scale unbonded post-tensioned concrete flat slab-column subassemblage and concluded that:

1)- The moment transfer capacity of prestressed concrete slab at interior column connections can be evaluated using the procedures of ACI 318-77. All reinforcement, bonded or unbonded, within $(3d+c_1)$ are effective for transferring the portion of moment which is transfered by bending.

2)- For all kinds of slab-column connections, shear stress on a critical section located at (d/2) from the column perimeter is calculated from the formulae:

$$v_{(AB)} = \frac{V}{A} + \frac{\gamma M}{J} C_{AB} \qquad 2.14(a)$$

or

$$v_{(CD)} = \frac{V}{A} - \frac{\gamma M}{J} C_{CD} \qquad 2.14(b)$$

where C_{AB} and C_{CD} are defined in Figure 2.14. For the interior column connection $|v_{(AB)}|$ is always greater than $|v_{(CD)}|$. But for the exterior column connection transfering moment normal to the discontinuous edge, the centroid of the critical section lies further from the slab edge than the centroid of the column so that $|v_{(CD)}|$ can be greater than $|v_{(AB)}|$ when M is large. In this case, the bonded reinforcement detailed so that it can act as torsional reinforcement, should be provided at the discontinuous edge when the shear stress given by equation 2.14(b) exceeds $0.17 \sqrt{f_c'}$ N/mm2.

3)- Tendons bundled through the column are an effective means of increasing the moment transfer strength of slab at interior column connections.

2.5.3 S O Franklin and A E Long[27]

In 1982, Franklin and Long presented the results of tests on seven unbonded post– tensioned flat slabs with internal columns. The main parameters in these tests were the level of eccentricity and slab boundary conditions. The experimental failure loads were compared with those predicted by the relevant British and American design recommendations (recommendations of the Concrete Society[7] and ACI– ASCE 423[29]).

They found that the average ratio of (V_{test} / V_{ACI}) is 1.41 and that of (V_{test} / V_{CS}) is 1.36 with Standard Deviation of 0.15 and 0.07 respectively. Accordingly, they concluded that the ACI– ASCE 423[29] design method and the Concrete Society[7] approach significantly underestimate the failure load of all the models. They also reported that the increase in tendon stress at the failure load was normally within 12% of the initial tendon stress and extra bonded reinforcement is required at all critical locations to ensure that the structure has sufficient strength and ductility.

Later on, Franklin, Cleland and Long[30] presented a theoretical method for predicting the ultimate punching capacity of post– tensioned slabs at internal connections subjected to a pure gravity load. This method is based on flexural criterion of failure in which punching is assumed to occur when the slab moment at the column face causes rupture of the concrete compression zone. From previous test results[27, 30, 31] they came to realize that the flexural strength can be expected to have a considerable effect on the punching strength because the slab– column connection is a location of both maximum shear and bending moment.

They[30] mentioned considerable experimental evidence to prove that the slab moment at the column face is a critical moment for punching failure. Therefore for pure gravity loading the relationship between the vertical load (V_f) and the slab moment per unit width at the critical section (m) was proposed to be:

$$V_f = k_1 \, m_u \qquad 2.15$$

where k_1 is dependent on the slab boundary conditions and the ratio C/L (column dimension to slab span) and its calculation is described in References (66). For normal range of column size to slab span ratio (c/L = 0.04 to 0.12), k_1 is given by :

$$k_1 = 6 + 32c/L - (6-16c/L)(\rho f_y/f_c)^{0.5}$$

'm_u' is the resistance moment per unit width at the critical section which can be taken as:

$$m_u = \rho_s \, f_y \, d^2 \, (1.0 - 0.6 \frac{\rho_s f_y}{f_{cu}}) \qquad 2.16$$

The equivalent equation for post-tensioned slab is given by:

$$m_u = \rho_e \, f_y \, d^2 \, (1.0 - 0.6 \frac{\rho_e f_y}{f_{cu}}) \qquad 2.17$$

where ρ_e is equivalent reinforcement ratio given by:

$$\rho_e = \rho_s + \rho_{ps} \frac{f_{pb}}{f_y} \frac{d_{ps}}{d} \qquad 2.18$$

where : ρ_s = Ratio of ordinary reinforcement at the critical cross-section to the area of concrete.

ρ_{ps} = Ratio of prestressing steel to the critical cross-section area of concrete.

f_{pb} = Tensile stress in tendon at slab failure.

f_y = Yield stress of ordinary bonded reinforcement.

d_{ps} = Effective depth of tendon profile.

d = Effective depth of ordinary reinforcement.

Combining equation 2.15 and 2.17 the punching capacity can be obtained and a comparison of this method with experimental tests is shown in Figure 2.20.

In order to achieve good agreement with all the relevant test results, Franklin et. al.[30] took the enhancing effect of compressive membrane action into account. The relationship between the vertical load (V_f) and the slab moment per unit width at the critical section (m_u) after incorporating the effect of compressive membrane force is given by:

$$V_f = \left(1 + \frac{H}{2T_o} \right) k_1 m_u \qquad 2.19$$

where H, the compressive membrane force, is given by:

$$H = \frac{R^2 - (0.125L)^2}{R^2 + (0.125L)^2} \left(f_t + f_{cp} \right) h$$

where ; f_t = split cylinder tensile strength of concrete.

f_{cp} = initial stress at centroidal axis due to prestress.

L = slab span

R = outer radius of thick cylinder (for more details see Ref. 27).

h = overall slab depth

and T_o, the normal force in the reinforcement can be taken as:

$$T_o = \rho_e f_y d$$

The ultimate flexural punching load predicted by equation 2.19 are compared with test results in Figure 2.21.

In 1987 Rankin and Long(66,67), in addition to the flexural method for predicting the punching capacity of prestressed concrete flat slabs, proposed a method for the prediction based on internal diagonal cracking prior to the development of yielding of the reinforcement or crushing of the concrete. This is called 'shear punching' capacity of the internal slab—column junctions ,V_s, and given by:

$$V_s = 1.66 \sqrt{f'_c}\,(c + d)d(100\rho_s)^{0.25} \qquad 2.20$$

where : c = Length of column side

d = Average effective depth to tensile reinforcement

f_c = Cylinder compressive strength of concrete (taken as 80% of cube compressive strength)

ρ_s = Reinforcement ratio

For the prestressed slabs 'ρ_s' should be replaced by 'ρ_e' given by:

$$\rho_e = \rho_s + \rho_{ps}(f_{pe}/f_y)$$

in which : f_{pe} = Effective prestress in unbonded tendon

f_y = Yield stress reinforcement

The enhanced shear punching strength can be found by taking into account the increase in the depth of the concrete compression zone due to the compressive membrane action. Rankin and Long proposed that, effect of the increase in the compression zone is equivalent to considering a higher reinforcement index (ω =

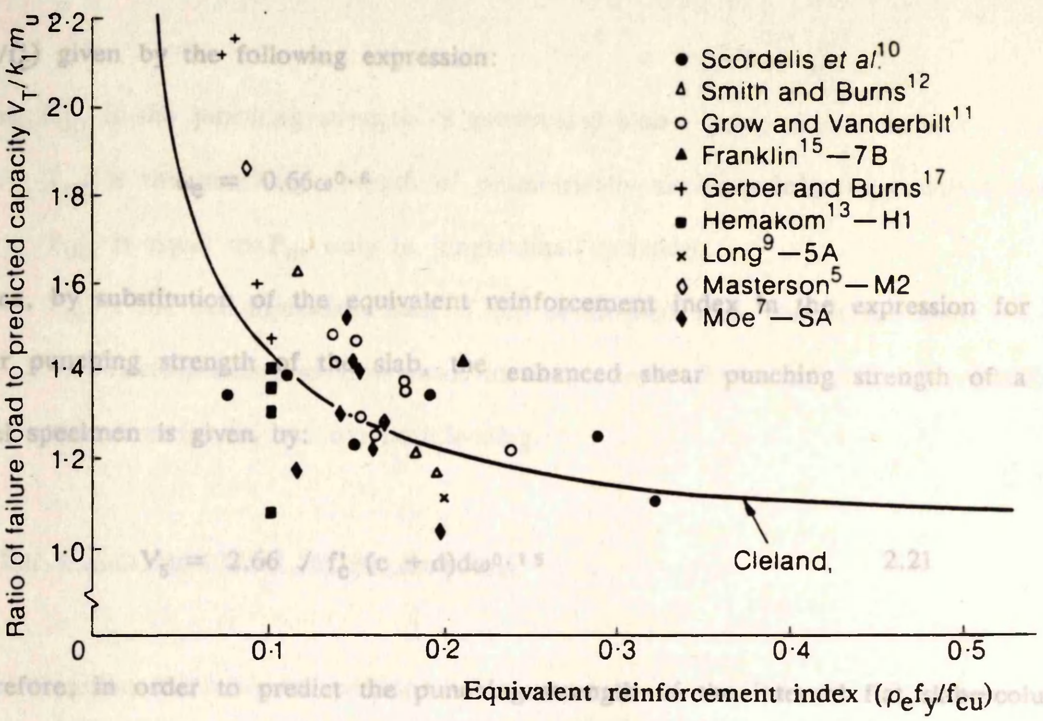

Figure 2.20 : Comparison of finite element predictions with test results.

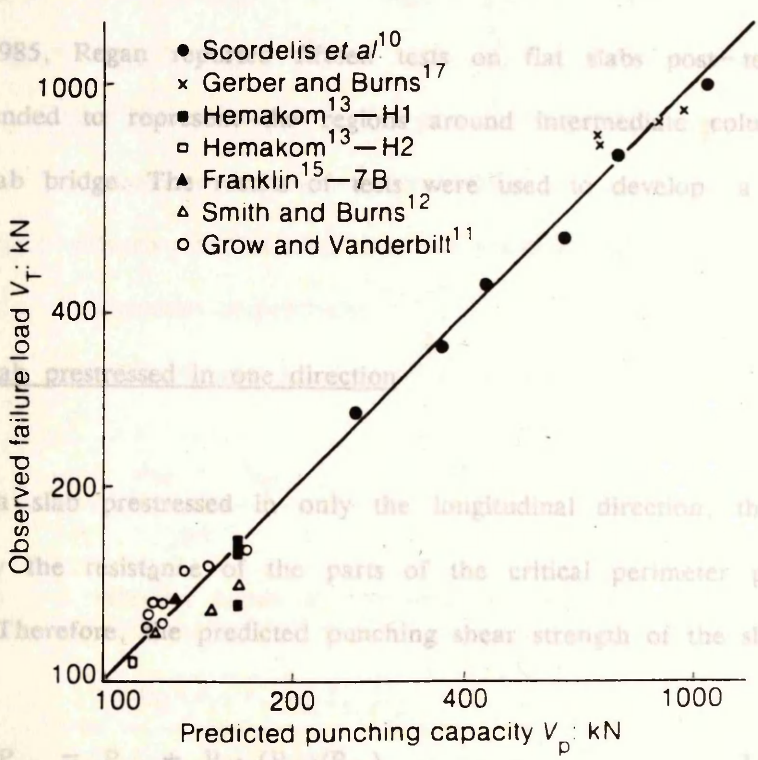

Figure 2.21 : Comparison of proposed flexural approuch with test results.

$\rho_s f_y / f'_c$) given by the following expression:

$$\omega_e = 0.66\omega^{0.6}$$

Hence, by substitution of the equivalent reinforcement index in the expression for the shear punching strength of the slab, the enhanced shear punching strength of a full panel specimen is given by:

$$V_s = 2.66 \sqrt{f'_c}\,(c + d)d\omega^{0.15} \qquad 2.21$$

Therefore, in order to predict the punching strength of the internal flat slab– column junction both the flexural punching strength and shear punching strength are calculated and the lesser of these two values is the predicted ultimate load.

2.5.4 P E Regan[40]

In 1985, Regan reported fifteen tests on flat slabs post– tensioned in one direction intended to represent the regions around intermediate column supports of prestressed slab bridge. The results of tests were used to develop a design equation as follows:

a)– For a slab prestressed in one direction

For a slab prestressed in only the longitudinal direction, the prestress can influence only the resistance of the parts of the critical perimeter perpendicular to the tendons. Therefore, the predicted punching shear strength of the slab is given by:

$$P_{up} = P_{ur} + P_{ol}\,(P_{url}/P_{ur}) \qquad 2.22$$

where P_{up} is the punching strength of prestressed slab

P_{ur} is the punching strength of geometrically similar reinforced concrete slab.

P_{url} is equal to P_{ur} only in longitudinal direction.

P_{ol} is the decompression load of the prestressed slab, that is the load corresponding to zero stress at the extreme fibre tensioned in longitudinal direction by the external loading.

b)— <u>For a slab prestressed in two directions</u>

Equation 2.21 can be extended to treat slabs prestressed in two directions:

$$P_{up} = P_{ur} + P_{ol}(P_{url}/P_{ur}) + P_{ot}(P_{urt}/P_{ur}) \qquad 2.23$$

where, $P_{url} = 0.27\,(500/d_l)^{1/4}\,(100\rho f_{cu})^{1/3}\,[2d_l(c_t + 3d_t)]$

$P_{urt} = 0.27\,(500/d_t)^{1/4}\,(100\rho f_{cu})^{1/3}\,[2d_t(c_l + 3d_l)]$

$P_{ur} = P_{url} + P_{urt}$

c_l, c_t = side dimensions of loaded area in longitudinal and transverse directions respectively.

d_l, d_t = effective depths of slab in longitudinal and transverse directions respectively.

ρ = ratio of reinforcement which is given by:

$$\rho = \frac{A_{sr} + A_{sp}}{ud}$$

d = effective depth of slab which is defined by:

$$d = \frac{A_{sr}f_y d_r + A_{sp}f_{0.2}d_p}{A_{sr}f_y + A_{sp}f_{0.2}}$$

where $f_{0.2}$ is 0.2% proof stress of prestressed reinforcement. The subscripts r and p refer to the ordinary and prestressed reinforcement respectively. A_{sr} and A_{sp} are corresponding steel area.

For slabs with equal reinforcement and equal prestressing in both directions subjected to equal orthogonal bending, equation 2.23 reduces to :

$$P_{up} = P_{ur} + P_o \qquad 2.24$$

where P_o is the decompression load of the prestressed slab.

Comparison between the punching strength predicted by this procedure for slabs prestressed in one direction and the result of the tests and also with those of tests which were carried out by Nylander et al are shown in Figure 2.22(a). The calculated strengths were approximately equal to mean of experimental strengths. The average ratios of P_{exp}/P_{cal} were 0.97 , 1.05 and 0.99 for the bonded slabs, DT Series and EL Series[40] respectively.

Punching strength predicted by equation 2.21 for the slabs prestressed in two directions were compared with the results of experimental studies carried out by Pralong et al, Grow and Vanderbilt, Shehata , Gerber and Burns. The agreement between calculated and experimental punching strength was generally good even though the tendons were unbonded in most of the cases [Figure 2.22(a)].

2.5.5 <u>V G Johannes and C S Alexander</u>[46]

In 1983, Johannes and Alexander used a numerical method for the material

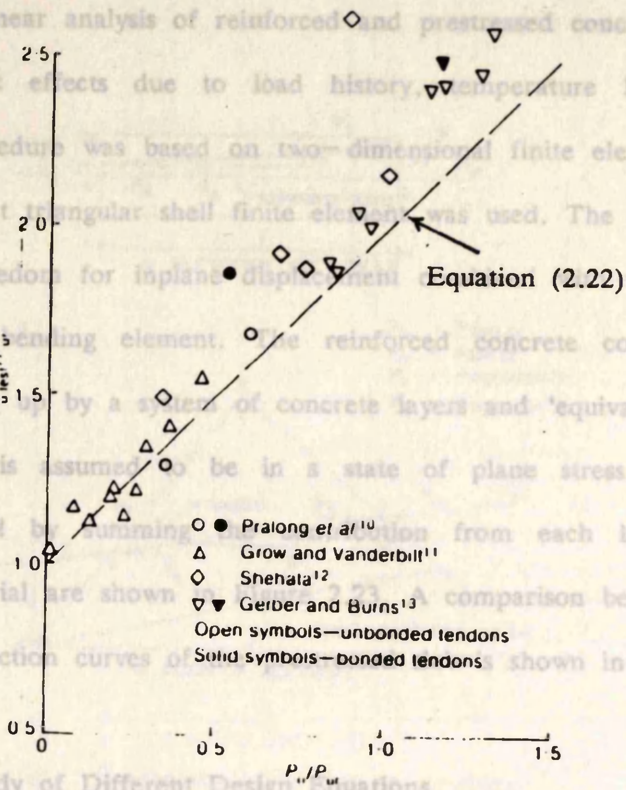

Figure 2.22(b) : Comparison of calculated and experimental strength for slabs with two– way prestress in Ref. (40).

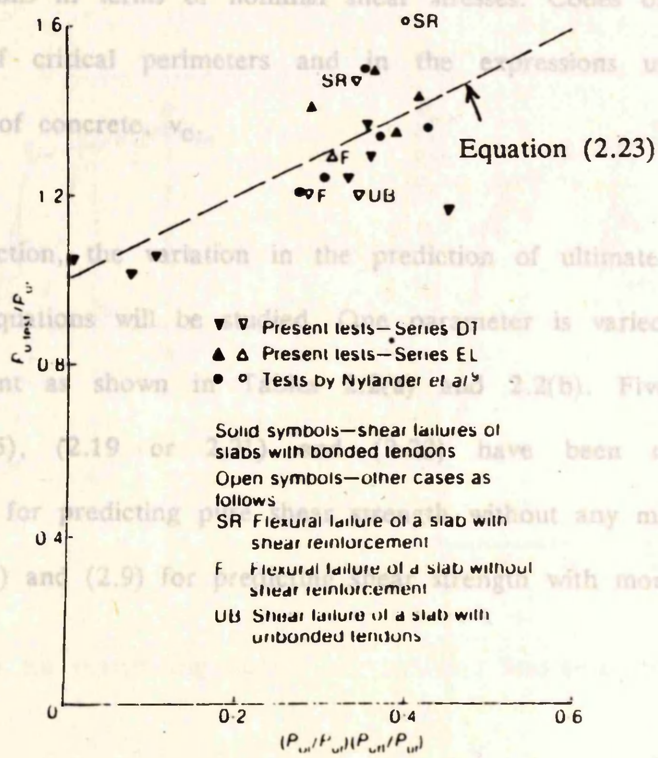

Figure 2.22(a) : Comparison of calculated and experimental strength for slabs with one– way prestress in Ref. (40).

and geometric nonlinear analysis of reinforced and prestressed concrete slabs including the time dependent effects due to load history, temperature history, creep and shrinkage. The procedure was based on two-dimensional finite element method using layer element. A flat triangular shell finite element was used. The element consists of the 6 degree of freedom for inplane displacement combined with the nine degree of freedom for plate bending element. The reinforced concrete composite section is assumed to be made up by a system of concrete layers and 'equivalent smeared' steel layers. Each layer is assumed to be in a state of plane stress and the material matrix was obtained by summing the contribution from each layer. Stress-strain curves for the material are shown in Figure 2.23. A comparison between the test and analytical load-deflection curves of the prestressed slab is shown in Figure 2.24.

2.6 Comparative Study of Different Design Equations

Concerning the causes for punching shear failure, there are various views and wide divergencies between different empirical formula. Codes of Practice also use empirical expressions in terms of nominal shear stresses. Codes of practice differ in the definitions of critical perimeters and in the expressions used to define the permissible stress of concrete, v_c.

In this section, the variation in the prediction of ultimate shear strength by different design equations will be studied. One parameter is varied keeping all other parameters constant as shown in Tables 2.2(a) and 2.2(b). Five design equations (2.2), (2.4), (2.5), (2.19 or 2.21) and (2.23) have been considered in this comparative study for predicting pure shear strength without any moment transfer and two equations (2.8) and (2.9) for predicting shear strength with moment transfer.

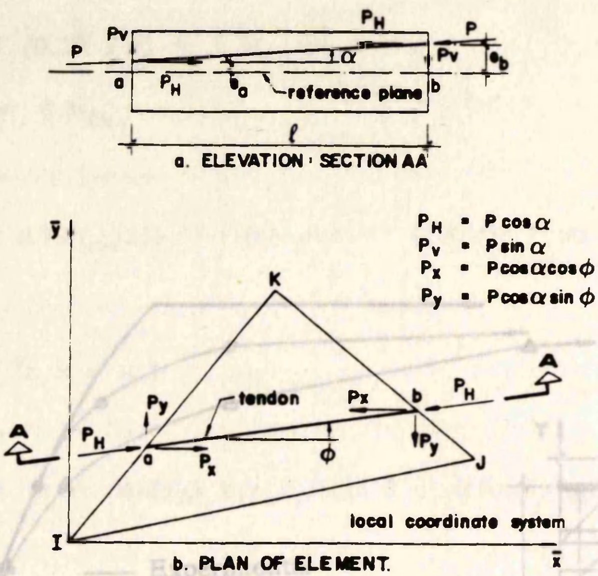

(a) : Equivalent loads due to prestress

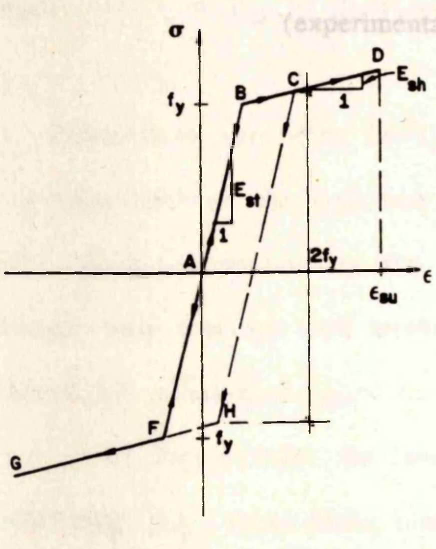

: Stress– strain curve for reinforcing steel

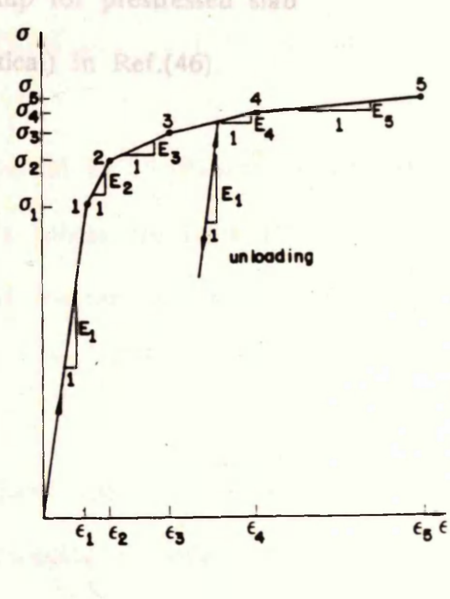

(c) : Stress– strain curve for prestressing steel

Figure 2.23

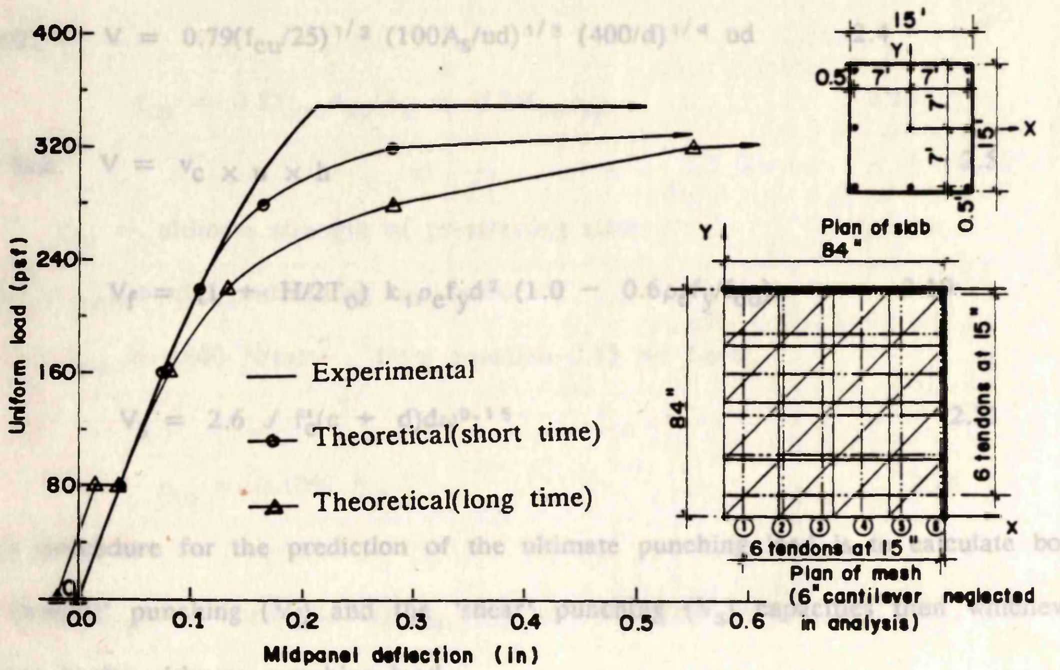

Figure 2.24 : Load– deflection relationship for prestressed slab (experimental and theoretical) in Ref.(46).

2.6.1 The equations for gravity load (without moment transfer)

ACI: $V = (0.29 \surd f_c' + 0.3f_{cp})ud + V_p$ 2.2

where $f_c' = 0.8f_{cu}$

BS8110: $V = 0.79(f_{cu}/25)^{1/3} (100A_s/ud)^{1/3} (400/d)^{1/4}$ ud 2.4

Con. Soc. $V = v_c \times u \times h$ 2.5

Long: $V_f = (1 + H/2T_o)\ k_1\rho_e f_y d^2 (1.0 - 0.6\rho_e f_y/f_{cu})$ 2.19

$V_s = 2.6 \surd f_c'(c + d)d\omega^{0.15}$ 2.21

Long's procedure for the prediction of the ultimate punching load is to calculate both the 'flexural' punching (V_f) and the 'shear' punching (V_s) capacities then whichever is lesser is the ultimate punching load.

Regan: $V = P_{ur} + P_{ol}(P_{url}/Pur) + P_{ot}(P_{urt}/P_{ur})$ 2.23

Calculations were done for f_{cu} varying from 25 to 55 N/mm^2. From figure 2.25 it is clear that all the equations except that proposed by Long et al (Eq. 2.19 or 2.21), predict approximately the same rate of increase in ultimate punching shear strength with concrete cube strength ,f_{cu}. 'V' from Long's formula is insignificantly affected by variation of f_{cu}.

In Figure 2.26, the average compressive axial stress of concrete due to prestressing ,f_{cp}, varies from 1 to 8 N/mm^2 keeping all other parameters constant. 'V' in ACI-83 (Eq. 2.3) is directly dependent on 'f_{cp}' but the other equations are dependent on the prestressing steel area 'A_{sp}'. Assuming the prestress in service equals to $0.55f_{pu}$, prestressing force ,F_p, will be :

$$F_p = 0.55f_{pu}A_{sp}$$

Assuming uniform distribution of prestress, we have:

$$f_{cp} = 0.55f_{pu}A_{sp}/A_c = 0.55f_{pu}\rho_{sp} \qquad 2.13$$

where: f_{pu} = ultimate strength of prestressing steel

ρ_{sp} = the prestressing steel ratio

assuming $f_{pu} = 1800\ N/mm^2$, from equation 2.13 we have:

$$\rho_{sp} = 0.10\%\ f_{cp} \qquad 2.14$$

Having got f_{cp}, the corresponding ρ_{sp} was used in equations 2.4, 2.5, 2.19, 2.21 and 2.23 to calculate the punching capacity.

Figure 2.27 shows the variation of punching shear strength of prestressed slab due to variation of effective depth of slab, d. The influence of this parameter on all the equations is nearly the same except for the equation proposed by Long. In this equation, the increase rate of prediction of punching shear strength is slightly more than the others.

In shear strength study due to pure gravity loads without moment transfer, it is assumed that ,for simplicity, the column sides are equal (e.g. $c_1 = c_2 = c$). Figure 2.28 shows the variation of punching shear strength predicted due to variation of ,c, and indicates that the rate of increase in prediction of punching shear strength is nearly the same for all equations except that proposed by Long. For example, the

TABLE 2.2 (a): Parameters for pure shear equations

Figures	Main Parameter studied	Other Parameters kept constant
2.25	f_{cu} (N/mm2)	f_{cp} = 2.0 N/mm2 , d = 200 mm c = 300 mm , ρ_s = 0.3%
2.26	f_{cp} (N/mm2)	f_{cu} = 40 N/mm2 , d = 200 mm c = 300 mm , ρ_s = 0.3%
2.27	d (mm)	f_{cu} = 40 N/mm2 , c = 300 mm f_{cp} = 2.0 N/mm2 , ρ_s = 0.3%
2.28	c (mm)	f_{cu} = 40 N/mm2 , d = 200 mm f_{cp} = 2.0 N/mm2 , ρ_s = 0.3%
2.29	ρ_s	f_{cu} = 40 N/mm2 , c = 300 mm f_{cp} = 2.0 N/mm2 , d = 200 mm

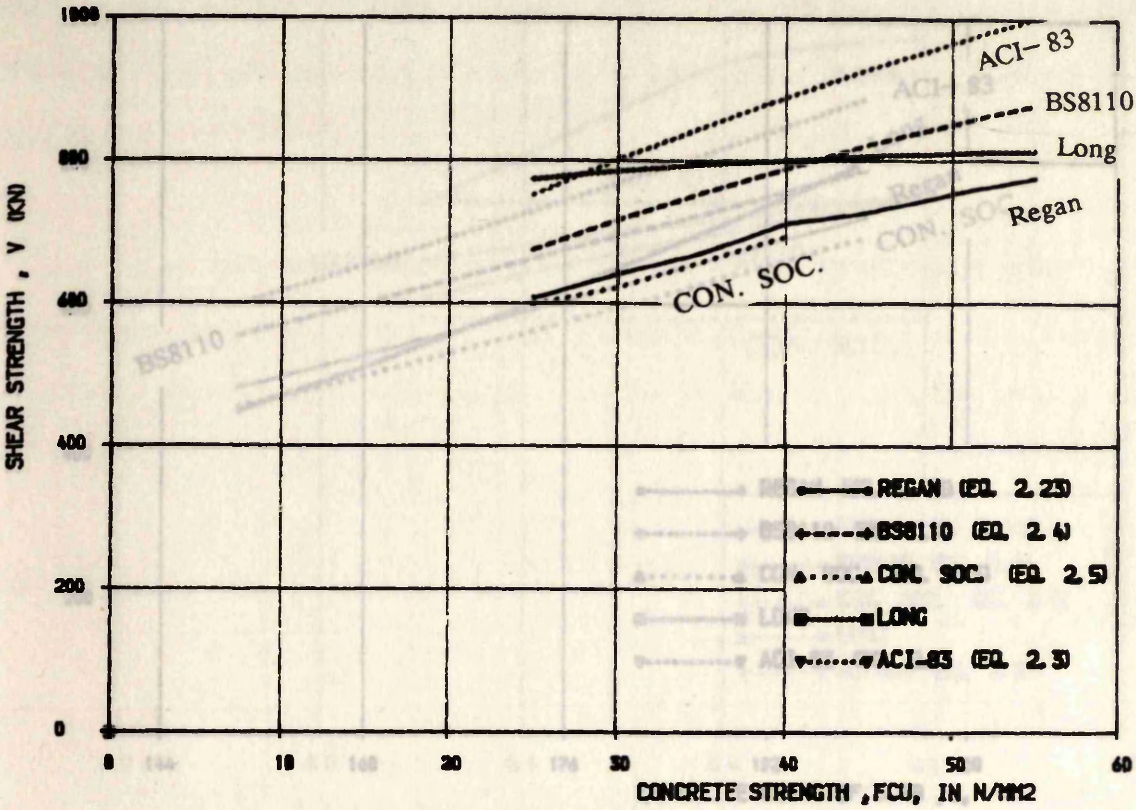

FIG. (2-25), CURVES SHOWING THE EFFECT OF 'FCU' ON THE PUNCHING SHEAR STRENGTH. OTHER PARAMETERS ARE CONSTANT

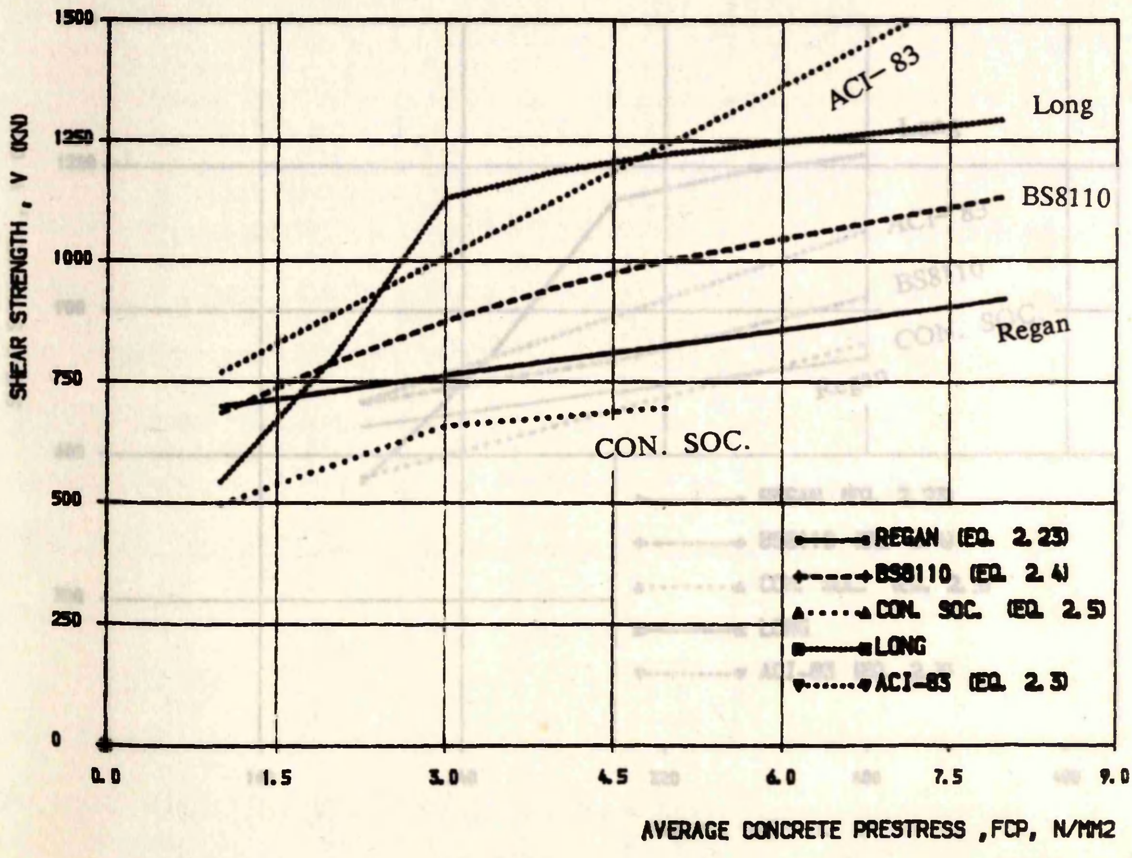

FIG. (2-26), CURVES SHOWING THE EFFECT OF 'FCP' ON THE PUNCHING SHEAR STRENGTH. OTHER PARAMETERS ARE CONSTANT

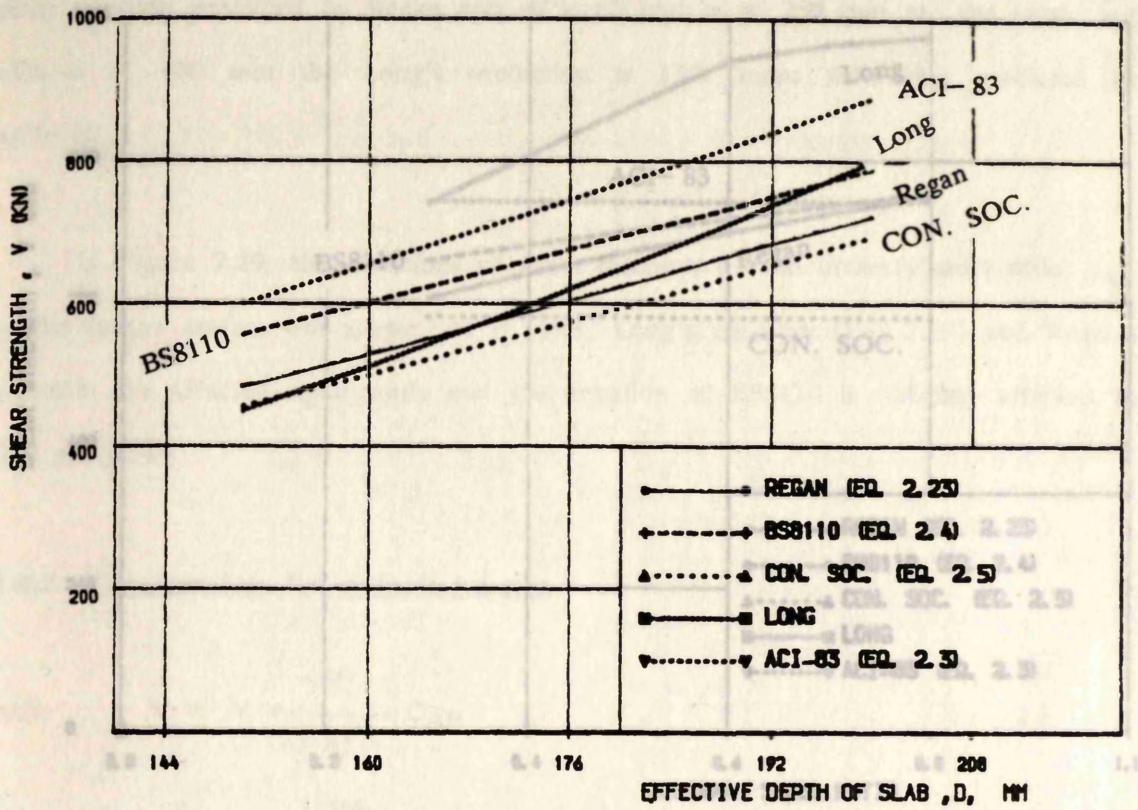

FIG. (2-27), CURVES SHOWING THE EFFECT OF 'D' ON THE PUNCHING SHEAR STRENGTH. OTHER PARAMETERS ARE CONSTANT

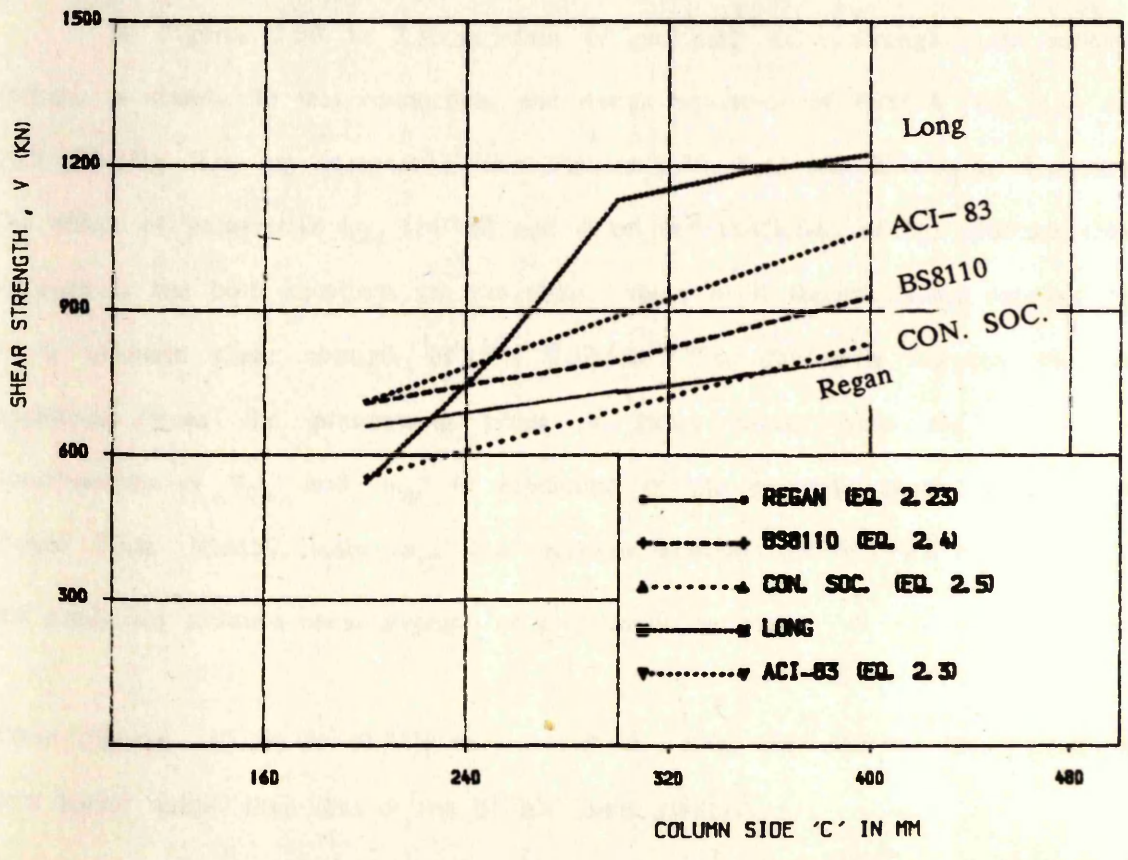

FIG. (2-28), CURVES SHOWING THE EFFECT OF 'C' ON THE PUNCHING SHEAR STRENGTH. OTHER PARAMETERS ARE CONSTANT

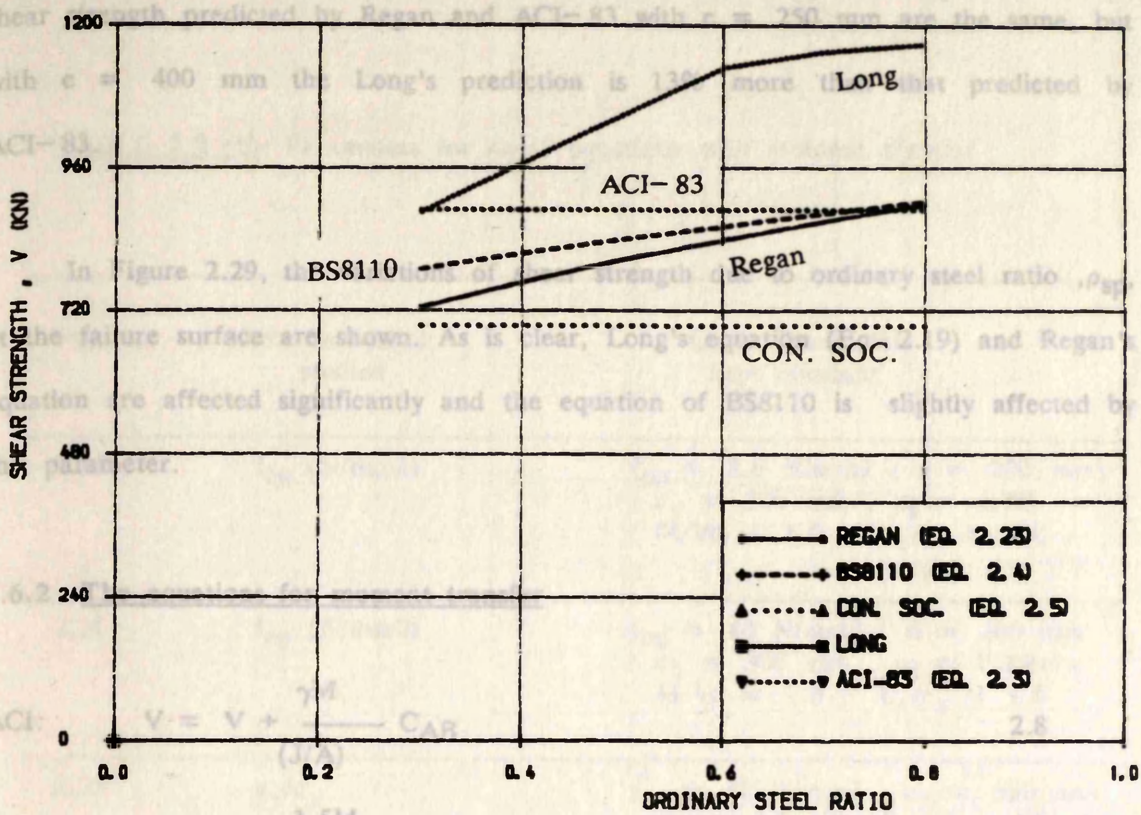

FIG. (2-29), CURVES SHOVING THE EFFECT OF 'AS' ON THE PUNCHING SHEAR STRENGTH. OTHER PARAMETERS ARE CONSTANT shear strength predicted by Regan and ACI−83 with c = 250 mm are the same, but with c = 400 mm the Long's prediction is 13% more than that predicted by ACI−83.

In Figure 2.29, the variations of shear strength due to ordinary steel ratio ,ρ_{sp}, at the failure surface are shown. As is clear, Long's equation (Eq. 2.19) and Regan's equation are affected significantly and the equation of BS8110 is slightly affected by this parameter.

2.6.2 The equations for moment transfer

ACI: $$V = V + \frac{\gamma M}{(J/A)} C_{AB} \qquad 2.8$$

BS8110: $$V = V + \frac{1.5M}{X} \qquad 2.9$$

In Figures 2.30 to 2.35,variation of punching shear strength with moment transfer is shown. In this connection, the design equations of BS8110 (Eq. 2.9) and ACI−83 (Eq. 2.9) are compared. From Figures 2.30, 2.33 and 2.34 it is clear that, the effect of parameters f_{cu}, (M/Vd) and d on the prediction of the ultimate shear strength in the both equations are the same, where M is the unbalanced moment and V is ultimate shear strength of the junction. The difference between the two equations (from the prestressing point of view) comes from the manner of consideration of 'f_{cp}' and 'ρ_{sp}' in prediction of the punching shear strength. The British Code ,BS8110, takes 'ρ_{sp}' into account whereas the ACI−83 considers 'f_{cp}' for predicting ultimate shear strength of prestressed flat slabs.

From Figures (2.25) to (2.35), in most of the cases the ACI−83 Code equations give higher values than that of the British Code ,BS8110. ;

TABLE 2.2 (b): Parameters for shear equations with moment transfer

Figures	Main Parameter studied	Other Parameters kept constant
2.30	f_{cu} (N/mm2)	f_{cp} = 2.0 N/mm2 , d = 200 mm c_2 = 300 mm , ρ_s = 0.3% M/Vd = 1.0 , c_1/c_2 = 1.0
2.31	f_{cp} (N/mm2)	f_{cu} = 40 N/mm2 , d = 200 mm c_2 = 300 mm , ρ_s = 0.3% M/Vd = 1.0 , c_1/c_2 = 1.0
2.32	c_1/c_2	f_{cu} = 40 N/mm2 , c_2 = 300 mm f_{cp} = 2.0 N/mm2 , d = 200 mm M/Vd = 1.0 , ρ_s = 0.3%
2.33	M/Vd	f_{cu} = 40 N/mm2 , d = 200 mm f_{cp} = 2.0 N/mm2 , ρ_s = 0.3% c_2 = 300. , c_1/c_2 = 1.0
2.34	d (mm)	f_{cu} = 40 N/mm2 , c_2 = 300 mm f_{cp} = 2.0 N/mm2 , ρ_{sp} = 0.2% M/Vd= 1.0 , c_1/c_2 = 1.0
2.35	ρ_s	f_{cu} = 40 N/mm^2 , c_2 = 300 mm f_{cp} = 2.0 N/mm^2, d = 200 mm M/Vd = 1.0 , c_1/c_2 = 1.0

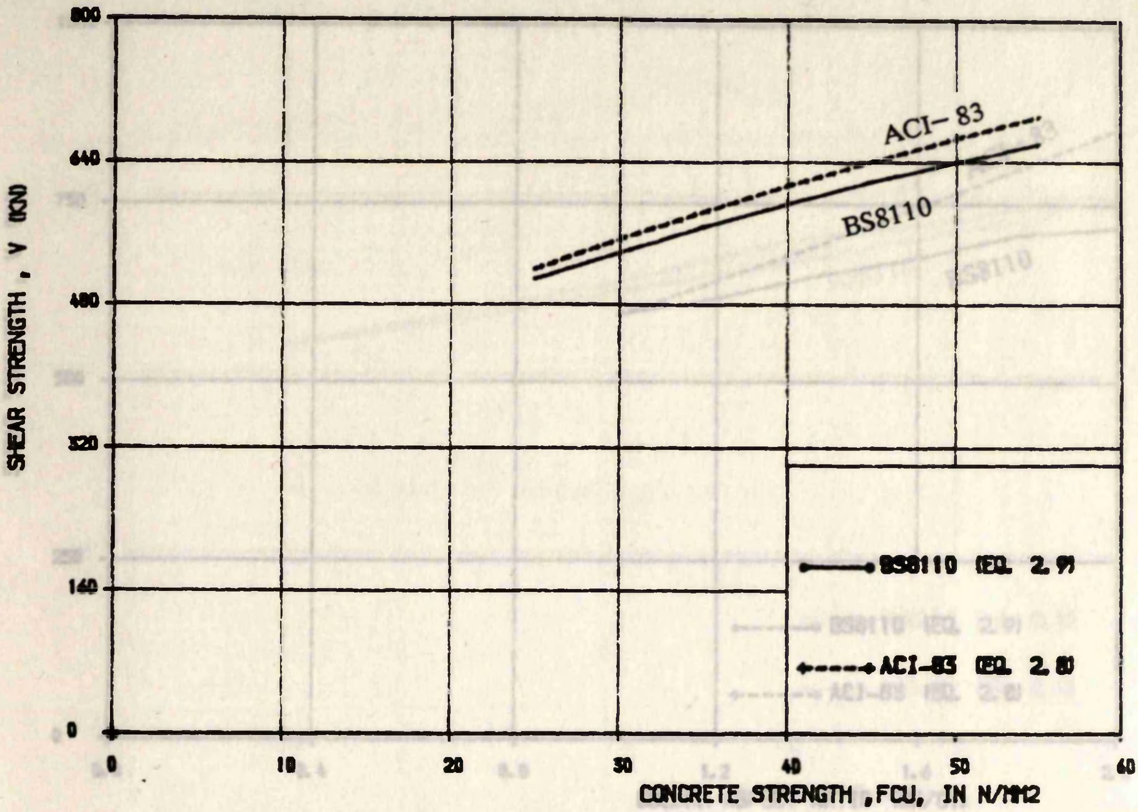

FIG. (2-30), CURVES SHOWING THE EFFECT OF 'FCU' ON THE PUNCHING SHEAR STRENGTH FOR MOMENT TRANSFER CASES.

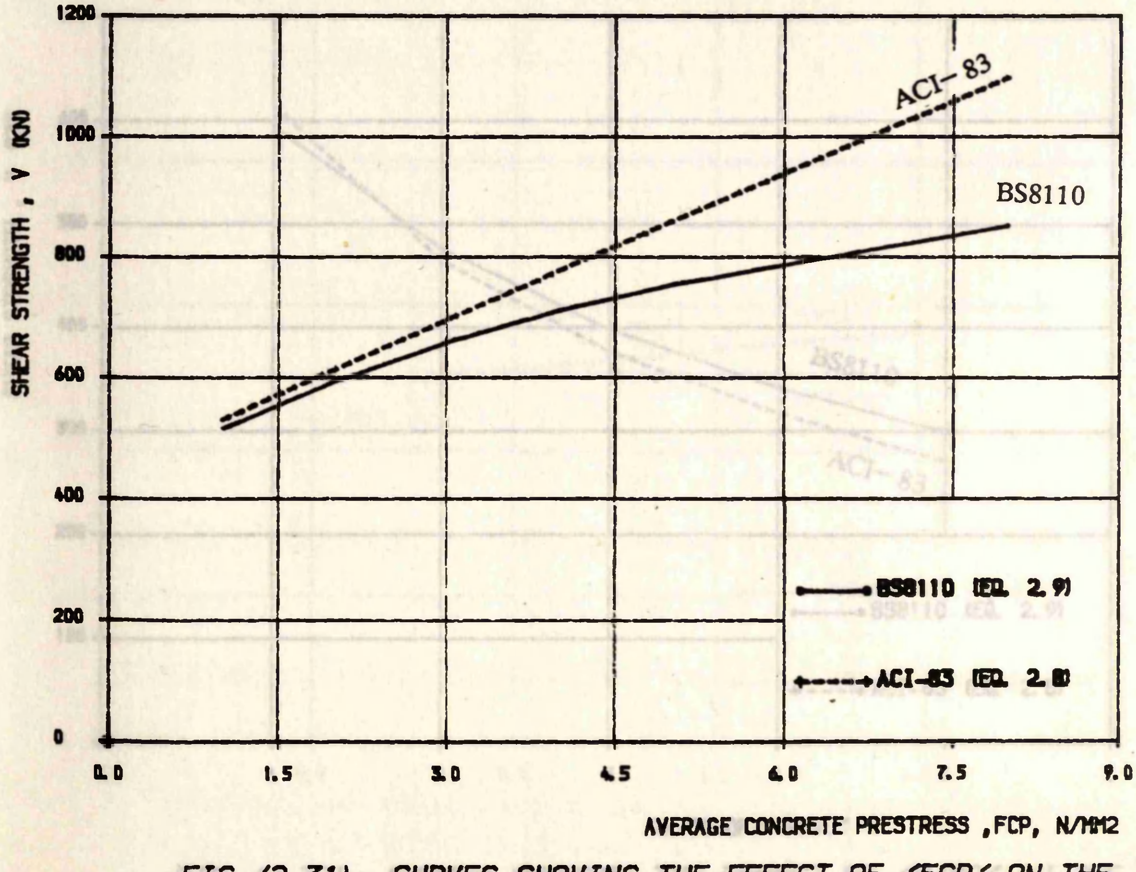

FIG. (2-31), CURVES SHOWING THE EFFECT OF 'FCP' ON THE PUNCHING SHEAR STRENGTH FOR MOMENT TRANSFER CASES.

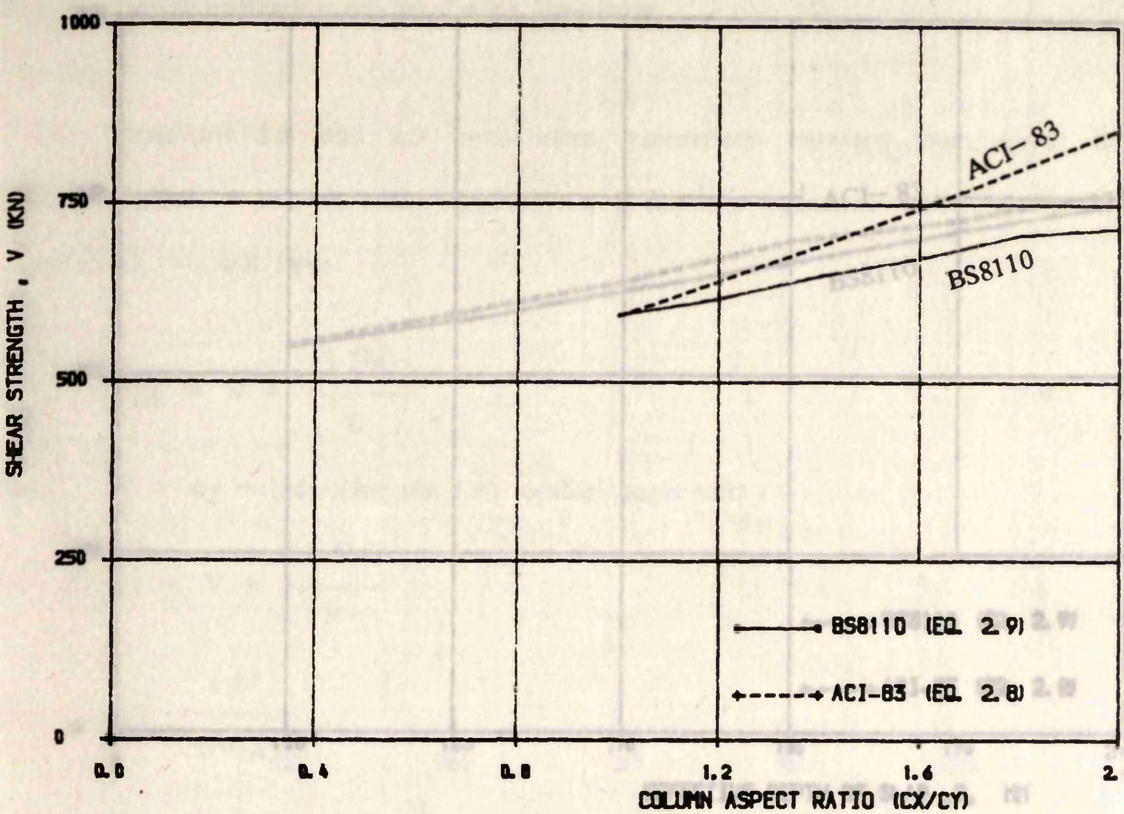

FIG. (2-32), CURVES SHOWING THE EFFECT OF 'CX/CY' ON THE PUNCHING SHEAR STRENGTH. OTHER PARAMETERS ARE CONSTANT

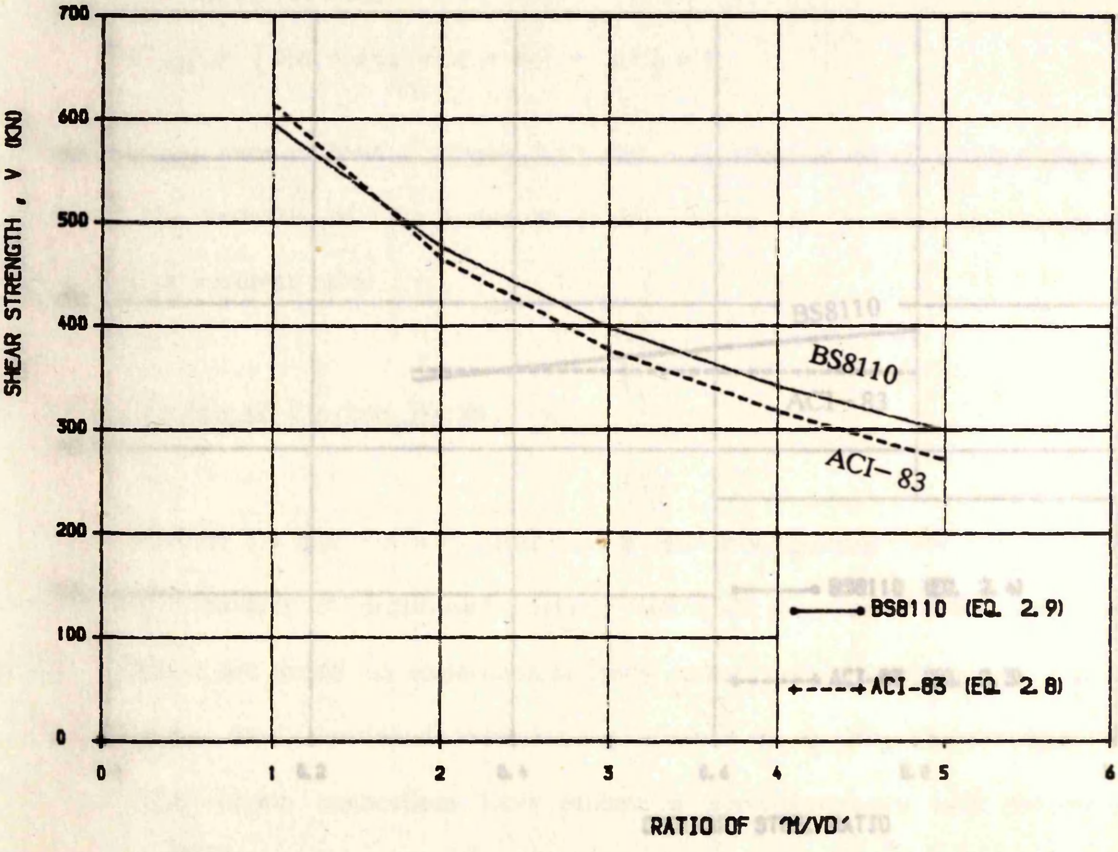

FIG. (2-33), CURVES SHOWING THE EFFECT OF 'M/VD' ON THE PUNCHING SHEAR STRENGTH. OTHER PARAMETERS ARE CONSTANT

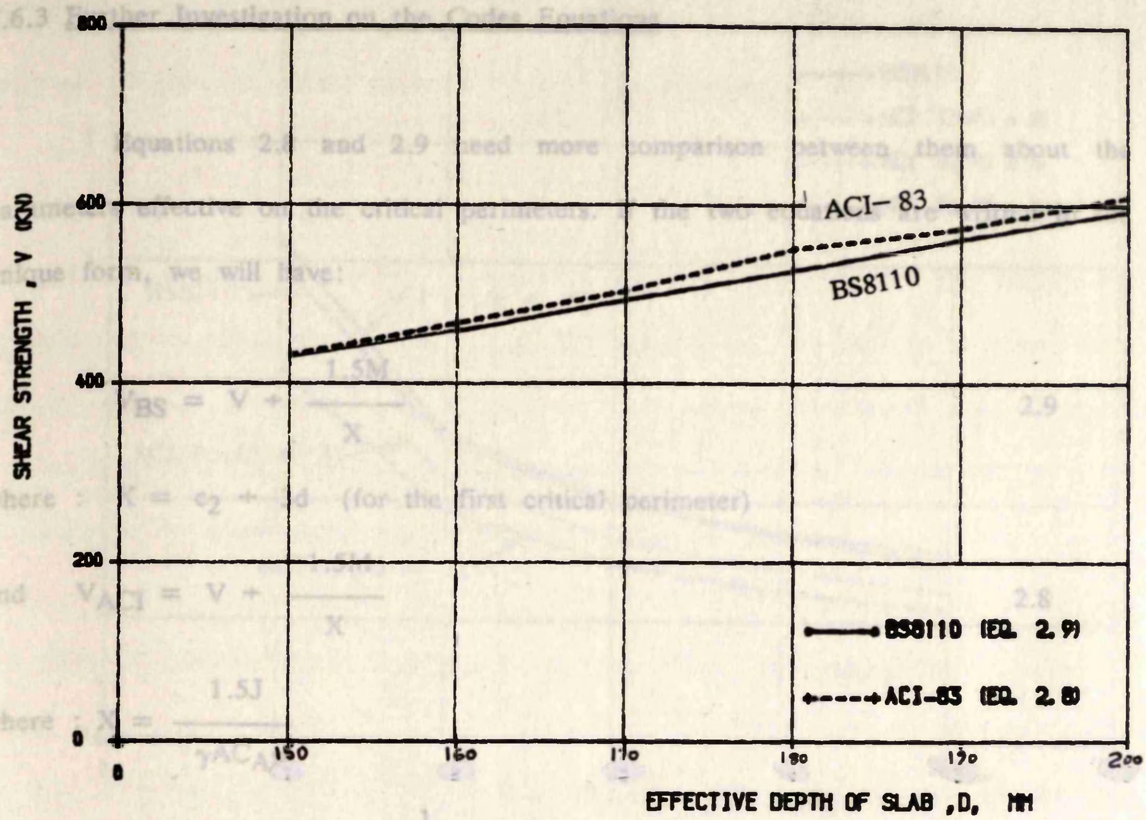

FIG. (2-34), CURVES SHOWING THE EFFECT OF 'D' ON THE PUNCHING SHEAR STRENGTH FOR MOMENT TRANSFER CASES.

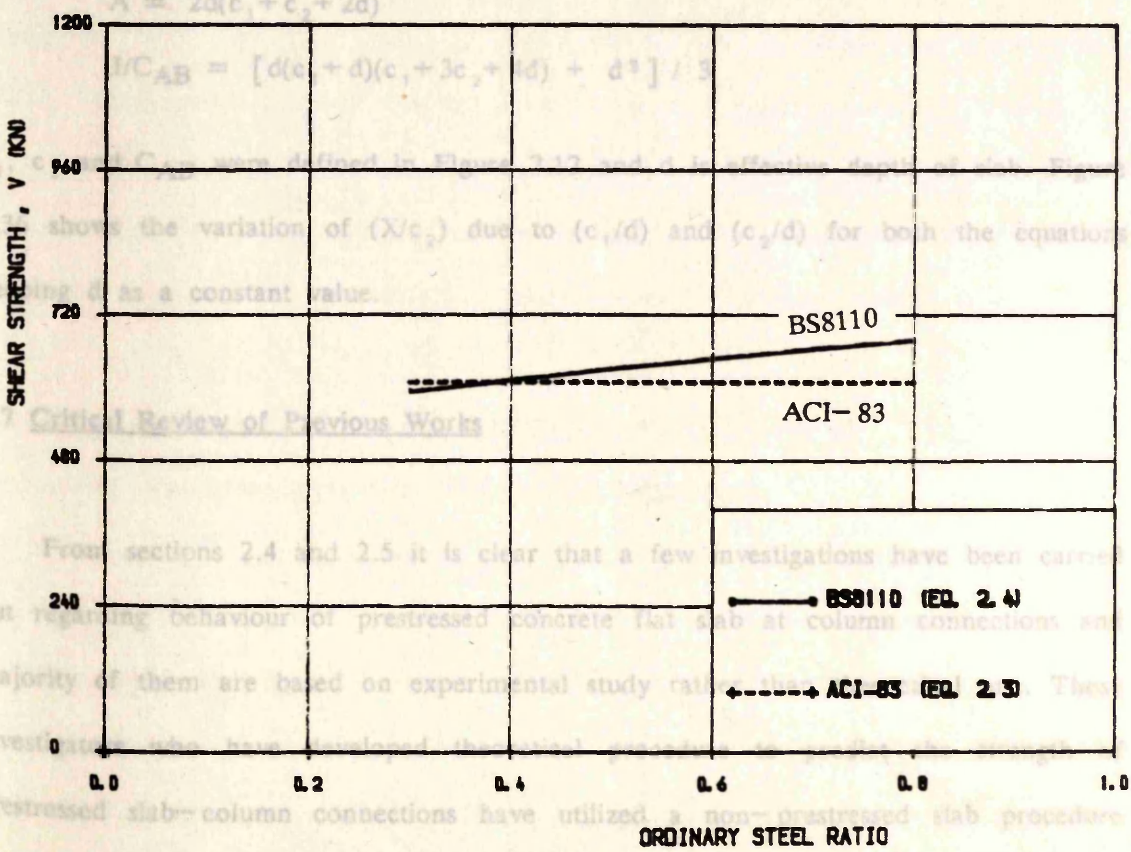

FIG. (2-35), CURVES SHOWING THE EFFECT OF 'AS' ON THE PUNCHING SHEAR STRENGTH. OTHER PARAMETERS ARE CONSTANT

2.6.3 Further Investigation on the Codes Equations

Equations 2.8 and 2.9 need more comparison between them about the parameters effective on the critical perimeters. If the two equations are written in the unique form, we will have:

$$V_{BS} = V + \frac{1.5M}{X} \qquad 2.9$$

where : $X = c_2 + 3d$ (for the first critical perimeter)

and $$V_{ACI} = V + \frac{1.5M}{X} \qquad 2.8$$

where : $X = \dfrac{1.5J}{\gamma A C_{AB}}$

$$\gamma = 1 - \frac{1}{1 + 0.67\sqrt{(c_1 + d)/(c_2 + d)}}$$

$$A = 2d(c_1 + c_2 + 2d)$$

$$J/C_{AB} = [d(c_1 + d)(c_1 + 3c_2 + 4d) + d^3] / 3$$

c_1, c_2 and C_{AB} were defined in Figure 2.12 and d is effective depth of slab. Figure 2.36 shows the variation of (X/c_2) due to (c_1/d) and (c_2/d) for both the equations keeping d as a constant value.

2.7 Critical Review of Previous Works

From sections 2.4 and 2.5 it is clear that a few investigations have been carried out regarding behaviour of prestressed concrete flat slab at column connections and majority of them are based on experimental study rather than theoretical one. Those investigators who have developed theoretical procedure to predict the strength of prestressed slab–column connections have utilized a non–prestressed slab procedure

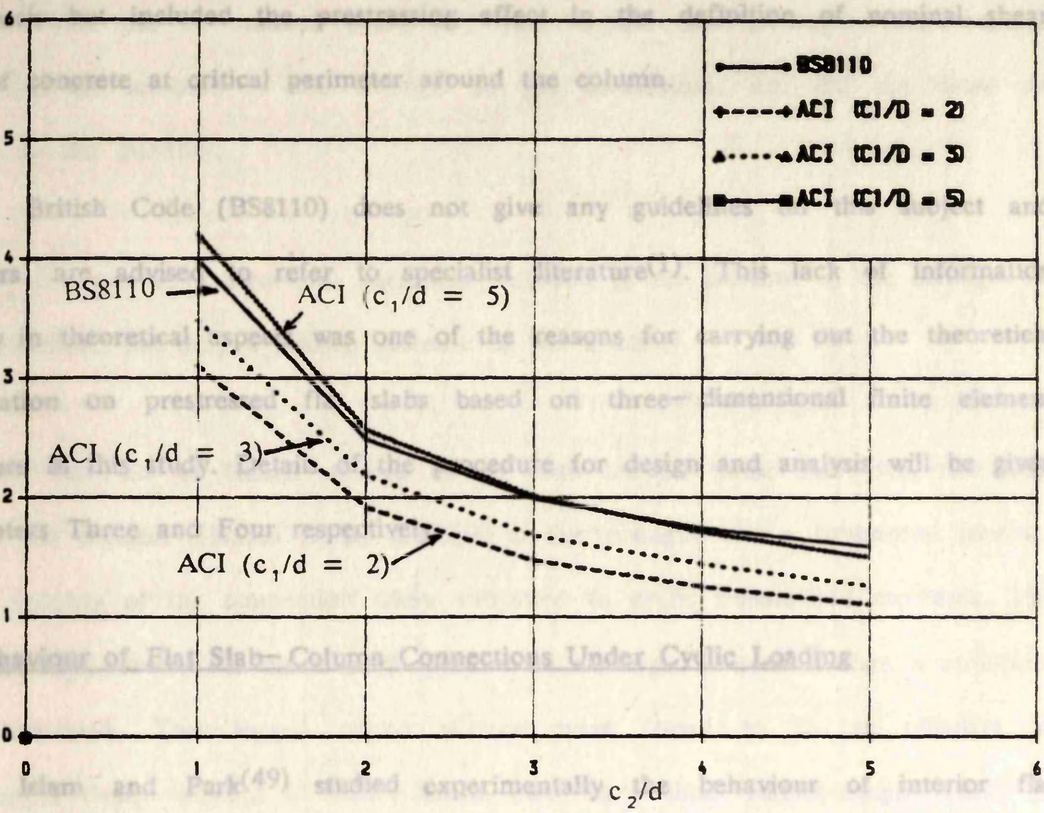
BS8110
ACI (C1/D = 2)
ACI (C1/D = 3)
ACI (C1/D = 5)
BS8110
ACI (c_1/d = 5)
ACI (c_1/d = 3)
ACI (c_1/d = 2)
X/c_2
c_2/d

FIG. (2-36)

as a basis but included the prestressing effect in the definition of nominal shear stress of concrete at critical perimeter around the column.

British Code (BS8110) does not give any guidelines on this subject and designers are advised to refer to specialist literature(1). This lack of information specially in theoretical aspects was one of the reasons for carrying out the theoretical investigation on prestressed flat slabs based on three–dimensional finite element procedure in this study. Details of the procedure for design and analysis will be given in chapters Three and Four respectively.

2.8 Behaviour of Flat Slab–Column Connections Under Cyclic Loading

Islam and Park(49) studied experimentally the behaviour of interior flat slab–column connections. Four of the eight models, were subjected to cyclic loading conditions (combination of gravity and seismic type of loading). A number of specimens tested contained various arrangements of shear reinforcement. The statically applied cyclic loading which caused reversals of unbalanced bending moment was achieved by applying an upward load at one of the sides of the slab and a downward load at the opposite side. The column was axially loaded while concrete blocks were suspended from the slab to simulate a uniformly distributed gravity load.

They summarized the following conclusions from the tests on slab–column connections transfering shear and unbalanced moment;

a)– The slab–column connections without any shear reinforcment had little ductility and failure occurred suddenly by diagonal tension cracking and splitting of the concrete along the bars in the top of the slab on the critical side of the column b)– The use of cranked (bent up) bars in the slab as shear reinforcement resulted in an increase in the strength of the connection, but did not cause an increase in the ductility.

c)– The use of a structural shearhead resulted in an increase in the strength of the connection, but only a limited increase in the ductility.

d)– The use of closed stirrups in the slab around those slab bars that pass through the column resulted in an increase in the strength and a substantial increase in the ductility of the connection when subjected to cyclic unbalanced moments. The closed stirrups resulted in more ductile behaviour at large deflections than a structural steel shearhead. Two–legged closed stirrups were found to be as effective as four–legged closed stirrups at each column face. Such shear reinforcement would be suitable for slab–column connections in earthquake resistant structures when ductile behaviour is essential.

Ahmadi and Gilbert(50) presented an investigation into the behaviour of reinforced concrete flat slab at edge column connections subjected to a combination of cyclic lateral loads and normal gravity loads. Eight 1/3 scale models were tested to study the behaviour of the connections at both the service and the ultimate load stages. The parameters of study were column aspect ratio, percentage of reinforcement in slab and size of structural shearhead reinforcement. The typical plan and boundary conditions for experimental models are shown in Figure 2.37. They(50) adopted a static mode for lateral load application which comprised a predetermined sequence of displacement intervals. A typical cyclic loading programme is shown in Figure 2.38.

It was concluded that increasing the column aspect ratio in the direction of moment transfer proved to be an effective means of enhancing the ultimate lateral load capacity. 60% increase in the ultimate load capacity was achieved by changing the aspect ratio from 1.5 to 2.0. However, increasing the dimension of the column parallel to the free edge by 50%, resulted in a lateral load capacity of only 13%. Variation of the deflection versus the lateral load for models 6 and 7 is shown in Figure 2.39.

Some investigators ,e.g. Derbal[51], have utilized analytical methods of slab–column connections for monotonic loading to predict the strength of the connections under cyclic loading. Derbal reported a review of those analytical procedures and used it to calculate moment and shear capacity of seven edge column–slab connections.

Akiyama and Hawkins[9] utilized the results of the series of experimental investigations on flat slab–column subassemblages subjected to inelastic reversed cyclic lateral loads to develop general beam analogy model for the prediction of strength and behaviour of flat slab concrete structures subjected to lateral loads.

The analytical model[9] was calibrated through comparisons with experimental results of nine interior flat slab–column connections tested at the University of Washington. In addition , a comparison was made between the predicted and experimental results for all the slab–column connections tested at the University of Washington. Those tests included eight interior, thirteen exterior and five corner column–slab connections. Average ratio of the predicted moment transfer capacity to the test results is shown in Table 2.3.

The predictions are in good agreement with experimental results. The stiffness predicted for test specimens were also compared with the test results as characterized by the rotation between the slab edge deformation and the applied lateral load. The stiffness prediction was in comparatively good agreement with the test results.

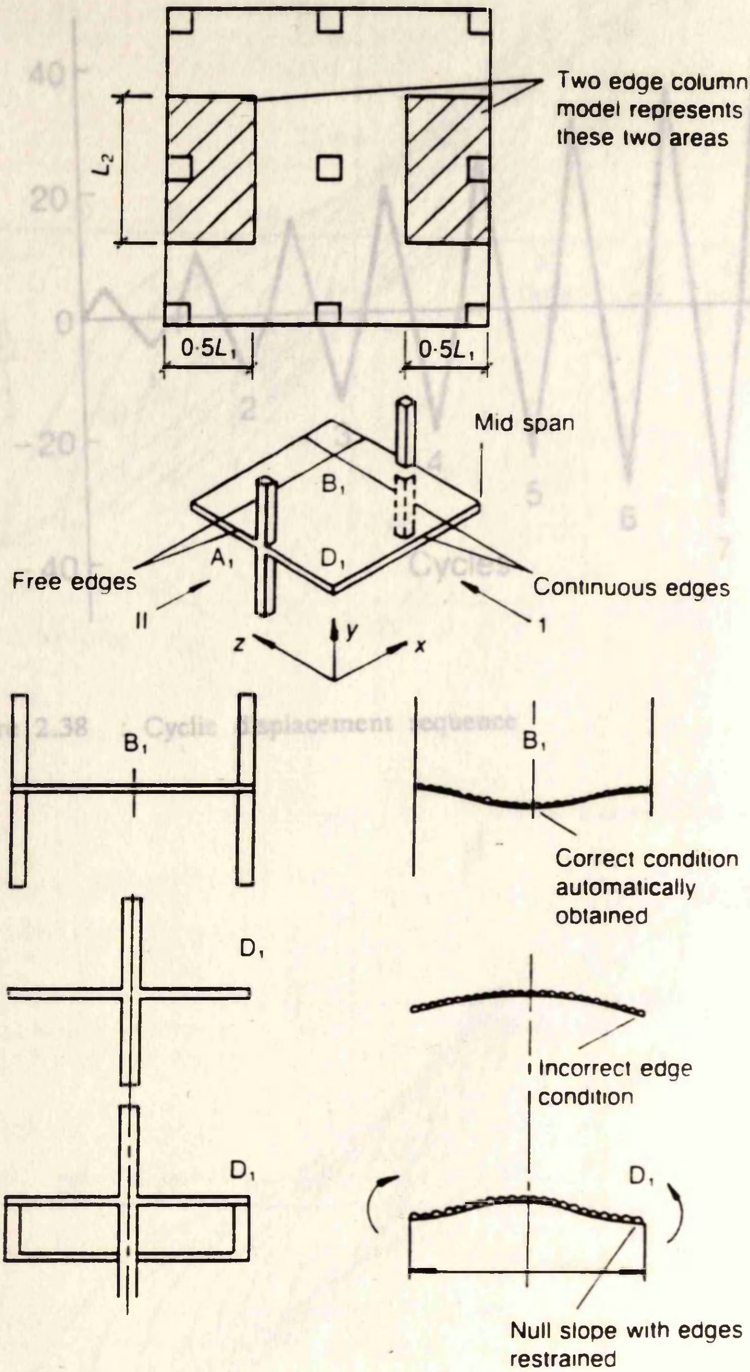

Figure 2.37 : Boundary conditions for the two– column model.

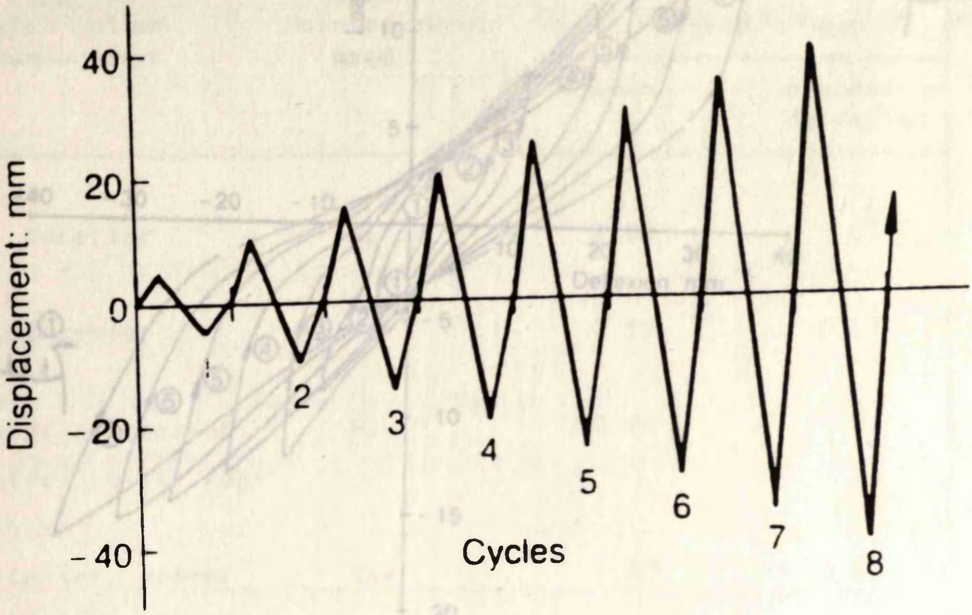

Figure 2.38 : Cyclic displacement sequence

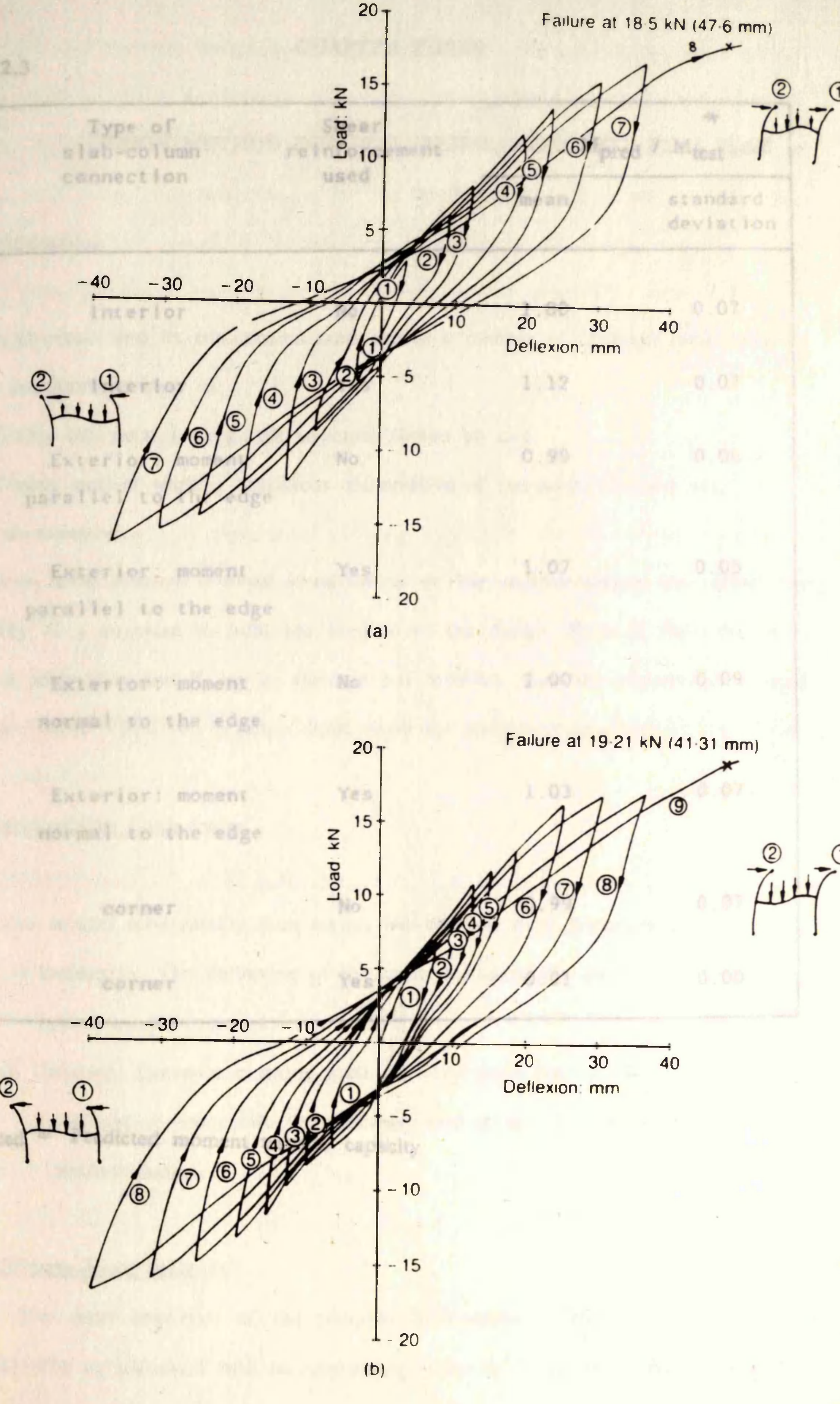

Figure 2.39 : Variation of lateral load with deflection in Ref.(50); (a) model 6 , (b) model 7

Table 2.3

No. of tests	Type of slab-column connection	Shear reinforcement used	M_{pred} / M_{test} * mean	standard deviation
7	Interior	No	1.00	0.07
8	Interior	Yes	1.12	0.07
2	Exterior: moment parallel to the edge	No	0.99	0.06
3	Exterior: moment parallel to the edge	Yes	1.07	0.05
3	Exterior: moment normal to the edge	No	1.00	0.09
5	Exterior: moment normal to the edge	Yes	1.03	0.07
3	corner	No	0.99	0.07
2	corner	Yes	0.91	0.00

* M_{pred} = Predicted moment transfer capacity

CHAPTER THREE

DESIGN METHOD FOR PRESTRESSED CONCRETE FLAT SLAB

3.1 Introduction

A structure and its components must satisfy a number of different limit states or design requirements such as:

1. Under the worst loading, the structure should be safe.
2. During normal working conditions deformation of the structure must not be excessive.

The limit state concept involves identification of the various factors that affect the suitability of a structure to fulfil the purpose of the design. Each of these factors is called a limit state and if any of them is not satisfied, then the structure is deemed to have "failed". The two principal limit states for most structures are:

a)– Serviceability Limit States

There are several serviceability limit states, but the two most important are:

i) Deflection: The deflection of the structure under the service load must not be excessive.

ii) Cracking: Excessive cracking must not take place because the cracks may permit water into the concrete, leading to corrosion of the steel reinforcement.

b)– Ultimate Limit State

The most important of the ultimate limit states is 'strength'. The structure must be able to withstand with an acceptable factor of safety the collapse load. For most prestressed concrete structures, design is carried out considering the serviceability limit state of cracking or deflection, and then the ultimate strength limit state is checked. Reinforced concrete design, by contrast, is usually based on the ultimate strength limit state, with later checks on the serviceability limit states. In this study because the ultimate punching strength of experimental specimens was the main concern, the ultimate strength limit state procedure was used. The method used to design the models will be described in section 3.4.

3.2 Analysis of Prestressed Flat Slab

In the analysis of prestressed concrete flat slabs, the prestressing forces are replaced by external loads calculated on the bases of 'equivalent load' concept. Figure 3.1 shows the prestressed concrete members involving different cases of prestressing and their equivalent loads.

Having replaced the prestressing loads by equivalent loads, the slab is designed for ultimate load conditions.

3.3 Design For Ultimate Limit State

In the theory of plasticity any solution to the ultimate load has to satisfy the following conditions of classical plasticity:

1) The Equilibrium Condition: The internal stresses must be in equilibrium with the externally applied loads.
2) The Yield Condition: The yield criteria defining the strength of the slab section must nowhere be exceeded.
3) The Mechanism Condition: Under the ultimate load, sufficient plastic regions must exist to transform the structure into a mechanism.

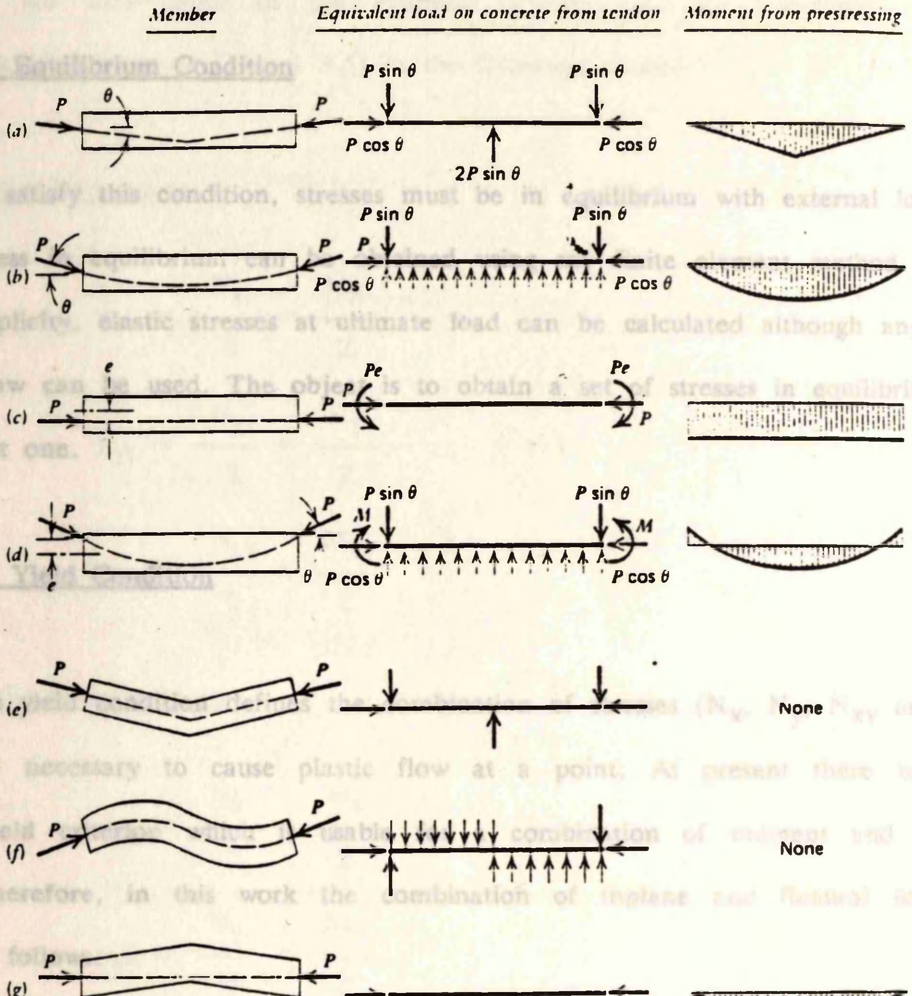

Figure 3.1: Equivalent loads and moments produced by prestressed tendons.

In classical plasticity problems, the solution for ultimate load is obtained for a given structure. However in the case of reinforced and prestressed concrete structures, the very conditions for ultimate loads solution can be used to design (i.e. determining the required reinforcement) for a given structure. This can be done as follows;

3.3.1 The Equilibrium Condition

To satisfy this condition, stresses must be in equilibrium with external loads. A set of stress in equilibrium can be obtained using say finite element method. Owing to its simplicity, elastic stresses at ultimate load can be calculated although any other material law can be used. The object is to obtain a set of stresses in equilibrium not the correct one.

3.3.2 The Yield Condition

The yield condition defines the combination of stresses (N_x, N_y, N_{xy} and M_x, M_y, M_{xy}) necessary to cause plastic flow at a point. At present there is no a general yield criterion which is usable for a combination of moment and inplane forces. Therefore, in this work the combination of inplane and flexural forces is treated as follows.

3.3.2.1 Combination of Bending and inplane stresses

In Figure 3.2 a typical element of slab subjected to a combination of inplane and flexural forces is shown. Normal forces are taken as positive corresponding to tension. The element is regarded as consisting of two outer layers separated by an unreinforced concrete filling as shown in Figure 3.3 and from now on this is termed as 'Sandwich Element'. In this study, the contribution of the unreinforced concrete filling in carrying compressive stress is ignored. Consideration of the share of the filling in the compressive capacity of the section was discussed in reference (55).

The moments M_x, M_y and M_{xy} and the inplane forces N_x, N_y and N_{xy}, acting at the mid-depth of the element (Figure 3.2) are transferred to the mid-depth of each layer (Figure 3.5) in the following manner:

a)- <u>For the Top Layer</u>

$$n_{xt} = \frac{N_x}{2} + \frac{M_x}{Z}$$

$$n_{yt} = \frac{N_y}{2} + \frac{M_y}{Z}$$

$$n_{xyt} = \frac{N_{xy}}{2} + \frac{M_{xy}}{Z}$$

b)- <u>For the Bottom Layer</u>

$$n_{xb} = \frac{N_x}{2} - \frac{M_x}{Z}$$

$$n_{yb} = \frac{N_y}{2} - \frac{M_y}{Z}$$

$$n_{xyb} = \frac{N_{xy}}{2} - \frac{M_{xy}}{Z}$$

where Z is the distance between the centers of the two layers as shown in Figure 3.5.

3.3.2.2 <u>The Yield Criterion</u>

The applied inplane forces n_x, n_y and n_{xy} in the element (Figure 3.9) are to

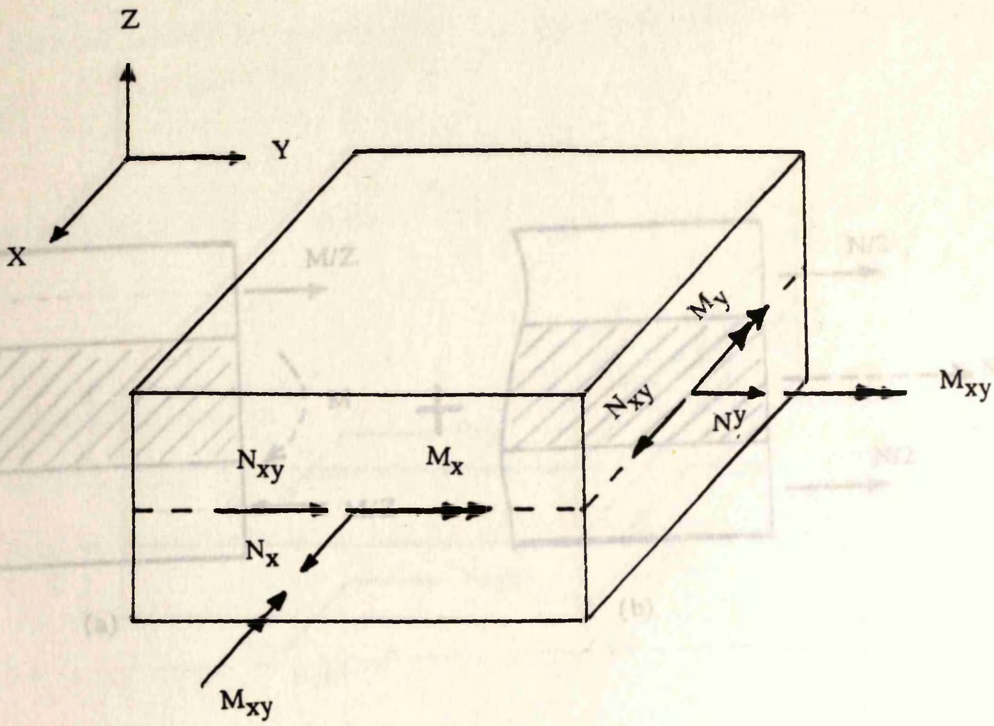

Figure 3.2 : A typical element of slab

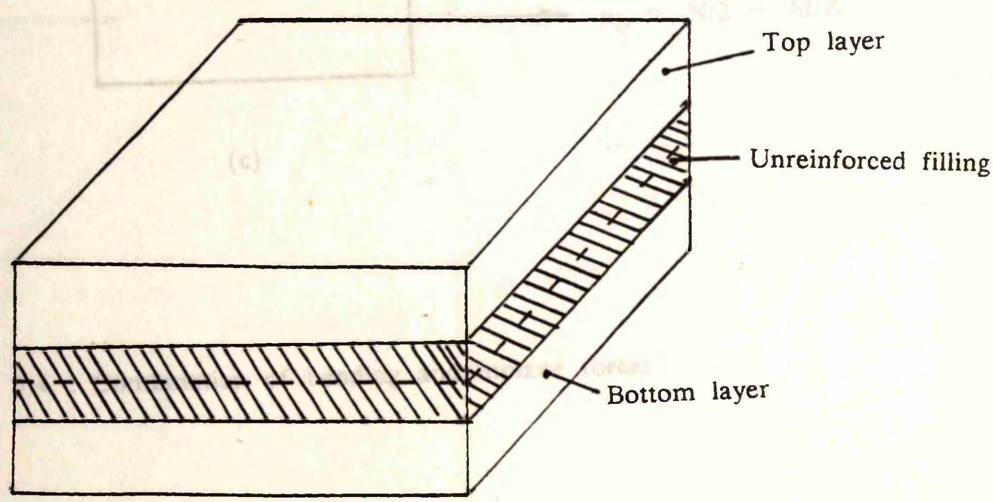

Figure 3.3 : Sandwich Element

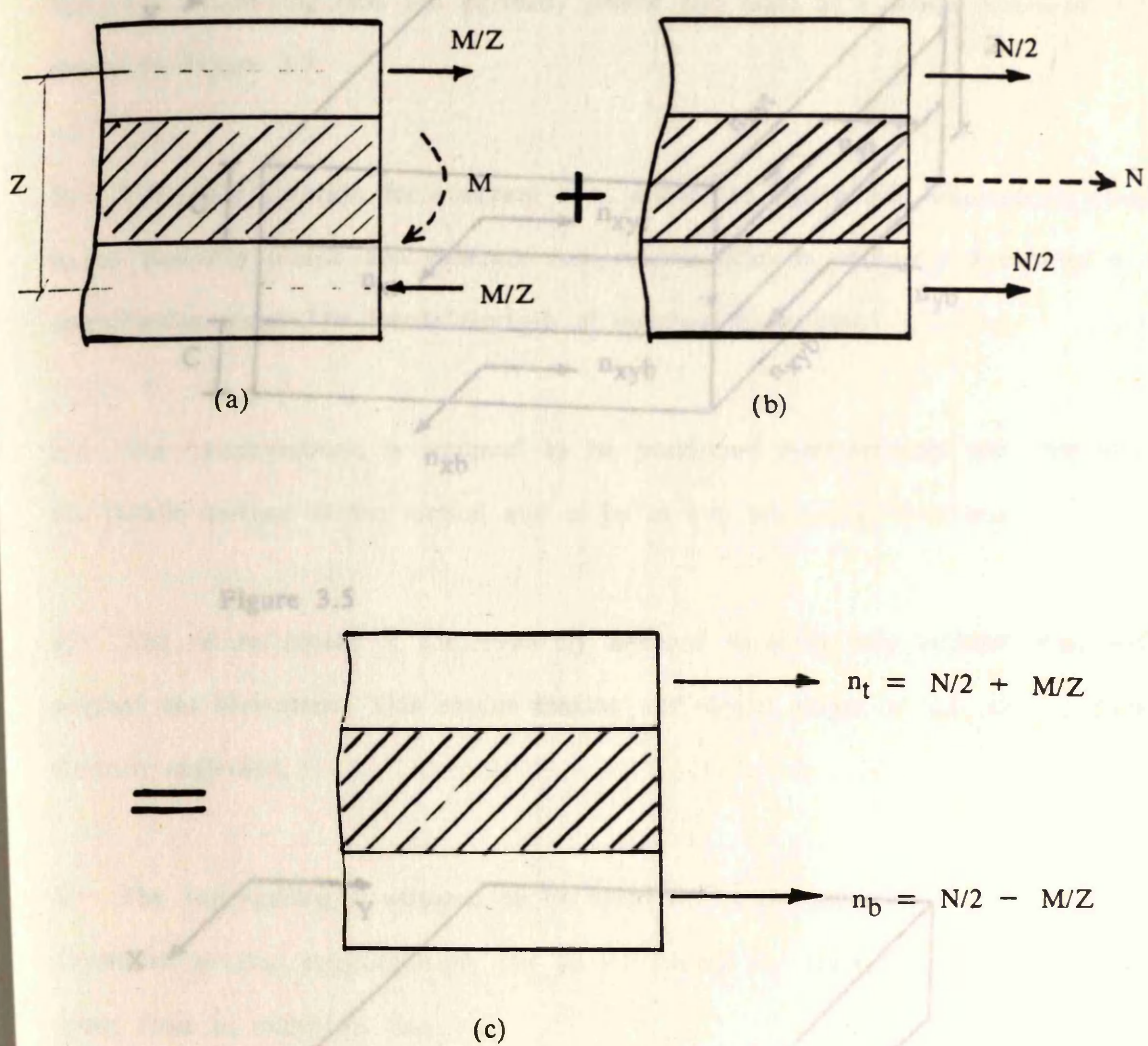

Figure 3.4 : Combination of bending and inplane forces

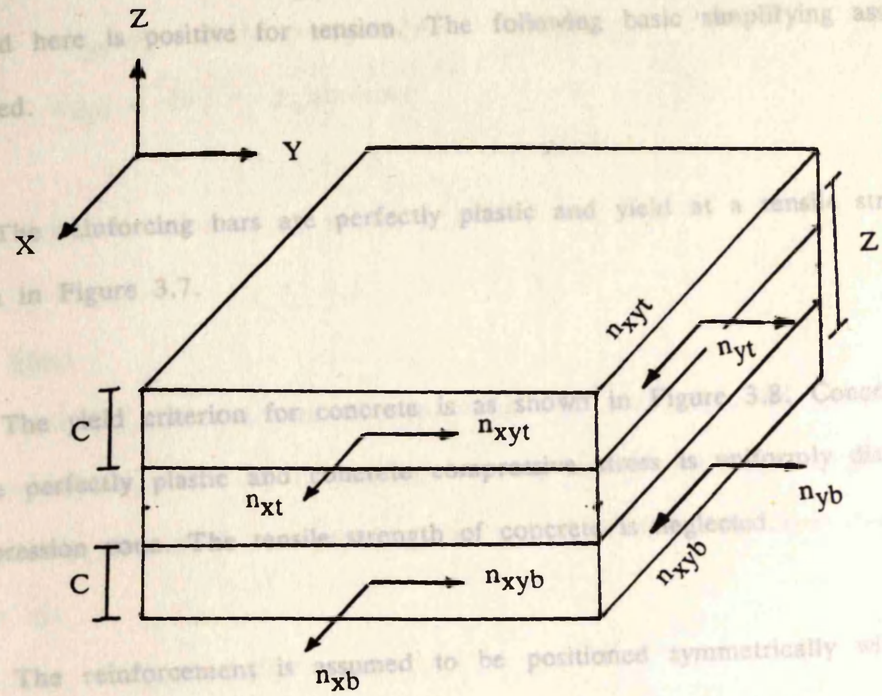

Figure 3.5

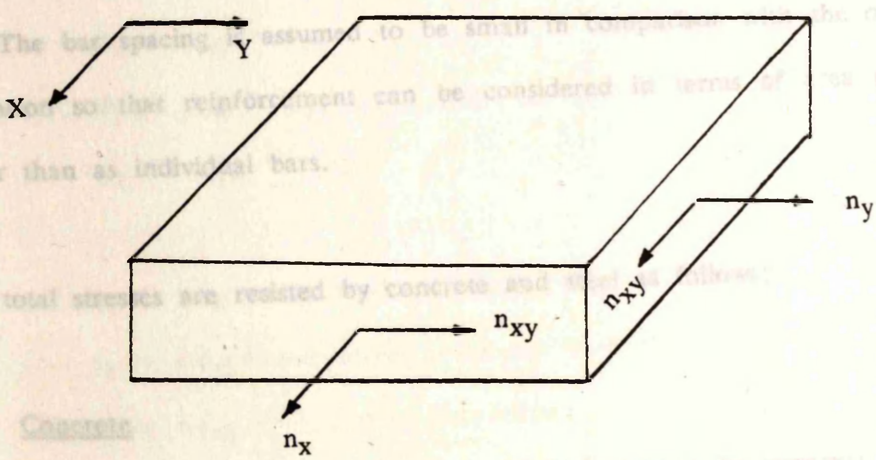

Figure 3.6 : Typical layer element

be resisted by a combination of concrete and reinforcing steel. The sign convention adopted here is positive for tension. The following basic simplifying assumptions are accepted.

1)– The reinforcing bars are perfectly plastic and yield at a tensile stress of 'f_y' as shown in Figure 3.7.

2)– The yield criterion for concrete is as shown in Figure 3.8. Concrete is assumed to be perfectly plastic and concrete compressive stress is uniformly distributed in the compression zone. The tensile strength of concrete is neglected.

3)– The reinforcement is assumed to be positioned symmetrically with reference to the middle surface of the section and to be in two orthogonal directions.

4)– The reinforcement is conservatively assumed to carry only uniaxial stress in the original bar directions. This means kinking and dowel action of the bars in resisting shear is neglected.

5)– The bar spacing is assumed to be small in comparison with the overall structure dimension so that reinforcement can be considered in terms of area per unit length rather than as individual bars.

The total stresses are resisted by concrete and steel as follows;

(a)– <u>Concrete</u>

Assuming σ_1 and σ_2 represent principal stresses in concrete and $\sigma_1 > \sigma_2$, from Figure 3.10(b) the concrete resistance is given as:

$$\sigma_{xc} = \sigma_1 \cos^2\theta + \sigma_2 \sin^2\theta$$

$$\sigma_{yc} = \sigma_1 \sin^2\theta + \sigma_2 \cos^2\theta \qquad 3.1$$

$$\tau_{xyc} = (\sigma_1 - \sigma_2)\sin\theta\cos\theta$$

where θ is orientation of σ_1 to the x– axis.

(b)– Steel

Assuming that the area of reinforcing steel and associated yield stresses in the two orthogonal directions (x and y) are represented by (A_x , A_y) and (f_x , f_y) respectively, the steel resistance in the x and y– directions from Figure 3.10(c) is given by:

$$\sigma_{xs} = A_x f_x/t$$

$$\sigma_{ys} = A_y f_y/t \qquad 3.2$$

$$\tau_{xys} = 0.0$$

where t is the thickness of the element.

Equating applied forces and resistant stresses of the element in Figure 3.10 we have:

$$\sigma_x = \sigma_{xc} + \sigma_{xs}$$

$$\sigma_y = \sigma_{yc} + \sigma_{ys} \qquad 3.3$$

$$\tau_{xy} = \tau_{xyc} + \tau_{xys}$$

or

$$n_x = t\cdot\sigma_x = t\cdot\sigma_1\cos^2\theta + t\cdot\sigma_2\sin^2\theta + A_x\cdot f_x$$

$$n_y = t\cdot\sigma_y = t\cdot\sigma_1\sin^2\theta + t\cdot\sigma_2\cos^2\theta + A_y\cdot f_y \qquad 3.4$$

$$n_{xy} = t\cdot\tau_{xy} = (\sigma_1 - \sigma_2)t\sin\theta\cos\theta$$

Considering σ_1 as a tensile stress, and since concrete cannot carry any tension we set the value of σ_1 = 0.0. Then Equations 3.4 give:

$$n_x = t \cdot \sigma_2 \sin^2\theta + A_x f_x$$

$$n_y = t \cdot \sigma_2 \cos^2\theta + A_y f_y$$

$$n_{xy} = -t \cdot \sigma_2 \sin\theta \cos\theta$$

using the notations : $n_x^* = A_x f_x$ and $n_y^* = A_y f_y$, we have

$$n_x^* - n_x = -t\sigma_2 \sin^2\theta$$

$$n_y^* - n_y = -t\sigma_2 \cos^2\theta \qquad 3.5$$

$$n_{xy} = -t\sigma_2 \sin\theta \cos\theta$$

eliminating θ from Equations 3.5, gives:

$$(n_x^* - n_x)(n_y^* - n_y) = n_{xy}^2 \qquad 3.6$$

$$(n_x^* - n_x) + (n_y^* - n_y) = -t\sigma_2$$

This equation is Nielsen's yield criterion for the element subjected to inplane forces n_x, n_y and n_{xy}.

3.3.2.3 <u>Calculation of Optimum Steel Required</u>

Having calculated n_x , n_y and n_{xy}, the n_x^* and n_y^* must be obtained so as not to violate the yield condition as given by Nielsen criterion (equation 3.6). In this connection, there are four different cases to be considered as follows:

<u>Case 1</u> : Both n_x^* and $n_y^* > 0$

In this case the sum of $(n_x^* + n_y^*)$ in the element along the cracked line , as shown in Figure 3.10, is made a minimum. Hence from equation 3.6 :

$$n_y^* = n_y + n_{xy}^2 / (n_x^* - n_x)$$

$$(n_y^* + n_x^*) = n_x^* + n_y + n_{xy}^2 / (n_x^* - n_x)$$

For minimizing the expression of $(n_x^* + n_y^*)$, we require:

$$\partial(n_x^* + n_y^*) / \partial(n_x^*) = 0$$

i.e. $$1 - n_{xy}^2 / (n_x^* - n_x)^2 = 0$$

or

$$(n_x^* - n_x) = \pm |n_{xy}| \qquad 3.7$$

According to the yield criterion, $(n_x^* - n_x) > 0$ in every point of the element. Hence;

$$n_x^* = n_x + |n_{xy}| \qquad 3.8$$

In a similar manner:

$$n_y^* = n_y + |n_{xy}| \qquad 3.9$$

Equation 3.8 and 3.9 are valid when n_x^* and n_y^* are positive only. That is,

$$n_x \geq - |n_{xy}|$$

$$n_y \geq - |n_{xy}|$$

From equations 3.8 and 3.9 it is clear that :

$$n_x^* = 0. \quad \text{if} \quad n_x = - |n_{xy}|$$

$$n_y^* = 0. \quad \text{if} \quad n_x = - |n_{xy}|$$

substituting the above values into equations 3.4 results in:

$$\tan\theta = 1 \quad \text{so} \quad \theta = 45^0$$

and $$n_{xy} = -\sigma_2 t \sin\theta\cos\theta = -\sigma_2 t/2$$

Then the principal compressive force in the concrete ,n_c, is equal to:

$$n_c = t\sigma_2 = -2|n_{xy}| \qquad 3.10$$

Case 2 : $n_x^* > 0$ and $n_y^* < 0$

Equation 3.8 and 3.9 are no longer valid when $n_y^* < 0$, i.e. , when $n_x < -|n_{xy}|$. In this case reinforcement is only required in the X– direction. Therefore, in equation 3.6 considering $n_y^* = 0$ then n_x^* will be:

$$n_x^* = n_x - n_{xy}^2 / n_y \qquad 3.11$$

Also from equations 3.5 the principal compressive force in concrete is:

$$n_c = t\sigma_2 = n_x + n_{xy}^2 / n_x \qquad 3.12$$

Case 3 : $n_x^* < 0$ and $n_y^* > 0$

In a similar manner which was used in Case 2, the following equation can be obtained:

$$\begin{cases} n_x^* = 0 \\ n_y^* = n_y - n_{xy}^2 / n_x \end{cases} \qquad 3.13$$

and

$$n_c = n_y + n_{xy}^2 / n_y \qquad 3.14$$

Case 4 : $n_x^* < 0$ and $n_y^* < 0$

If both n_x^* and n_y^* are negative and $n_x n_y \geqslant n_{xy}^2$, no reinforcement is required.

$$n_x^* = 0$$

$$n_y^* = 0 \qquad 3.15$$

From equations 3.5 the principle compressive force of concrete is given by:

$$n_c = 0.5\,(n_x + n_y) - 0.5\,\sqrt{(n_x + n_y)^2 + 4n_{xy}^2} \qquad 3.16$$

These four cases discussed above are summarized in Figure 3.8 and the formula indicated in each corresponding part of the diagram apply to the case in question.

After the calculation of ultimate design inplane forces for each of the above-mentioned cases, the required cross-sectional area of reinforcement in the X and the Y-direction for each layer of the element of slab is obtained as follows:

<u>For the top layer:</u>

$$A_{xt} = n_{xt}^*/f_s$$

$$A_{yt} = n_{yt}^*/f_s \qquad 3.17(a)$$

<u>For the bottom layer:</u>

$$A_{xb} = n_{xb}^*/f_s$$

$$A_{yb} = n_{yb}^*/f_s \qquad 3.17(b)$$

where : f_s = Yield stress of reinforcement

Therefore, using the equations 3.7 to 3.16 to calculate steel required will satisfy the yield condition because the yield criterion is nowhere violated throughout the slab. Note that in the above design procedure:

$n_c \ngtr S \cdot \sigma_c$ and $n_{xy} \ngtr 0.5\ S \cdot \sigma_c$

in order not to isolate the yield condition for concrete.

where : S = thickness of the outer layers

σ_c = permissible compressive stress of concrete

n_c = principal compressive force acting on the outer layer.

n_{xy} = shear force acting on the outer layer

3.3.3 Mechanism Condition

When the equilibrium and yield conditions are satisfied, the necessary resistance is made equal to the calculated stresses at every point in the slab. So it is anticipated that all the parts of slab will attain their ultimate strength under the ultimate design load. Consequently, with minimum redistribution, every point will yield at the ultimate load, thus converting the slab into a mechanism.

3.3.4 Ductility Demand

In classical plasticity it is assumed that the material has infinite ductility. Unfortunately reinforced concrete is a material with limited ductility. In using a method based on a classical plasticity, attention has to be paid to minimizing ductility demand. In Direct Design Method because of the fact that the minimum redistribution is needed to achieve failure of the slab in this method, the demand for ductility which depends on the difference between the first and the last yield in the slab will decrease. This has the additional advantage that crackwidth will not create a serious problem at serviceability stage. The steps involved in applying Direct Design Method are as follows:

1)– The prestressing forces are replaced by the equivalent loads and combined with external ultimate design loads.

2)– The elastic distribution of moments (M_x, M_y, M_{xy}) and inplane forces (N_x, N_y, N_{xy}) are determined by two–dimensional finite element computer programme (Figure 3.12).

3)– The slab element is regarded as consisting of two outer layers separated by an unreinforced concrete filling. The bending moments (M_x, M_y) and twisting moment (M_{xy}) are replaced by two equal and opposite forces acting at the mid–depth of outer layers as shown in Figure 3.4a. These forces are combined with the inplane forces (N_x, N_y, N_{xy}) divided equally between the two layers (Figure 3.4b). Each layer is considered as a membrane element subjected to inplane forces n_x, n_y and n_{xy} only.

4)– Having got n_x, n_y and n_{xy}, the ultimate design forces n_x^* and n_y^* are calculated for both top and bottom layers using Nielsen's criterion formula[54]

5)– The required amount of unstressed steel in each layer, corresponding to n_x^* and n_y^*, is obtained (section 3.4). In this connection, prestressing steel is treated as an ordinary steel with an equivalent yield stress equal to the difference between its 0.2% proof stress and effective prestress. Additional unstressed steel over and above that provided by prestressing steel is provided as required.

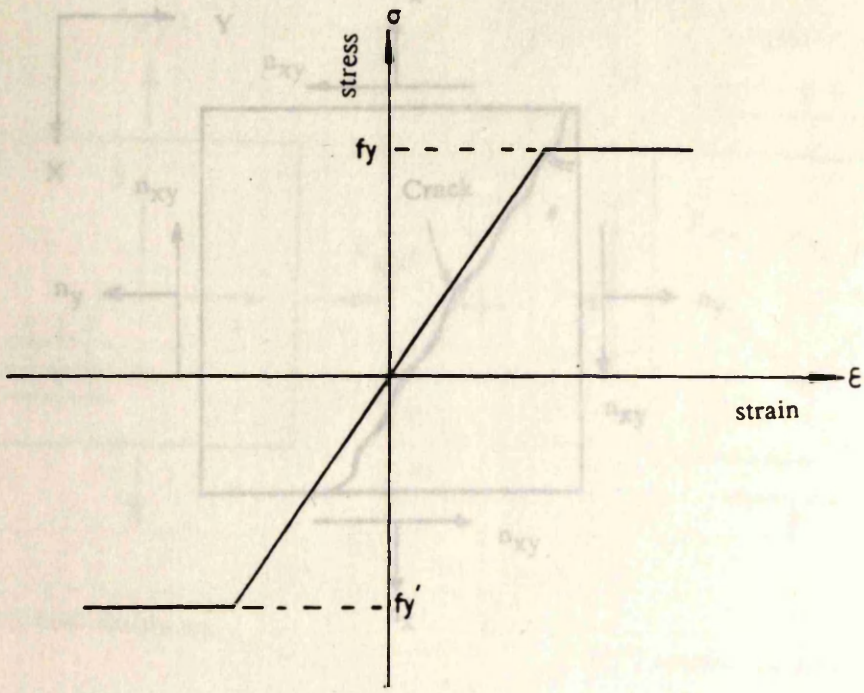

Figure 3.7 : yield strength of steel bar in tension and compression.

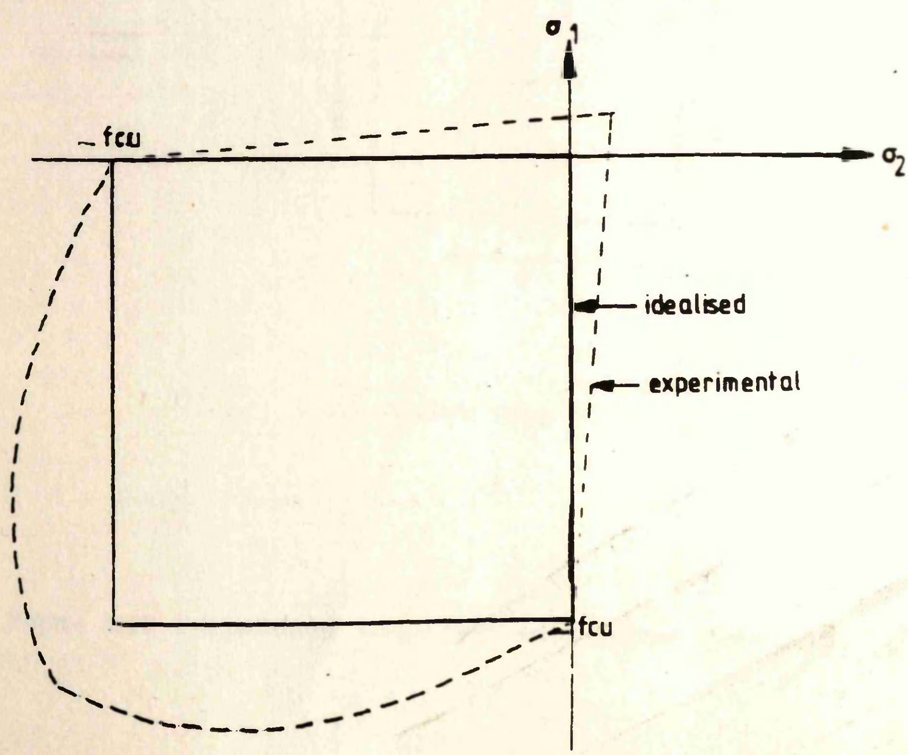

Figure 3.8 : Yield criterion for concrete.

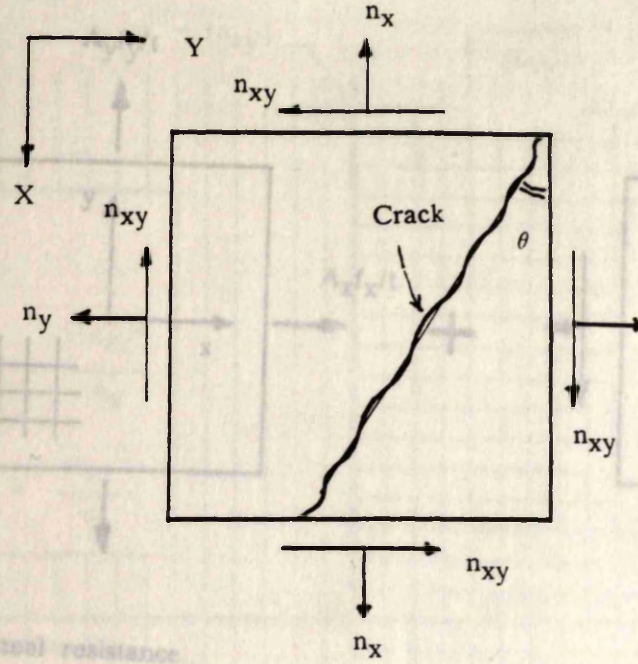

Figure 3.9 : In– plane normal and shear stresses on the layer element.

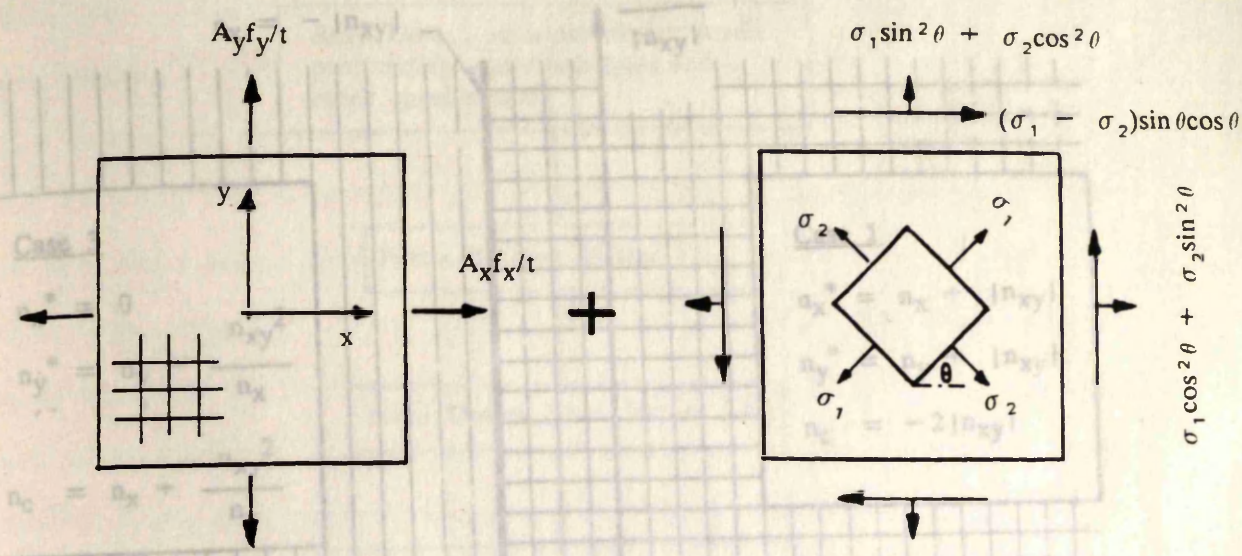

(a) Steel resistance

b) Concrete resistance

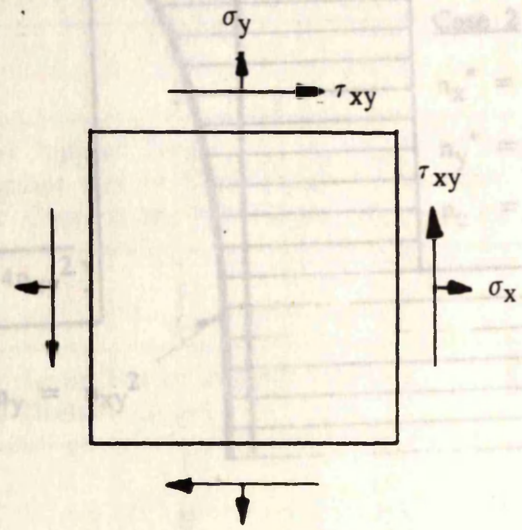

(c) Applied stress

Figure 3.10 : Equilibrium of element under inplane forces.

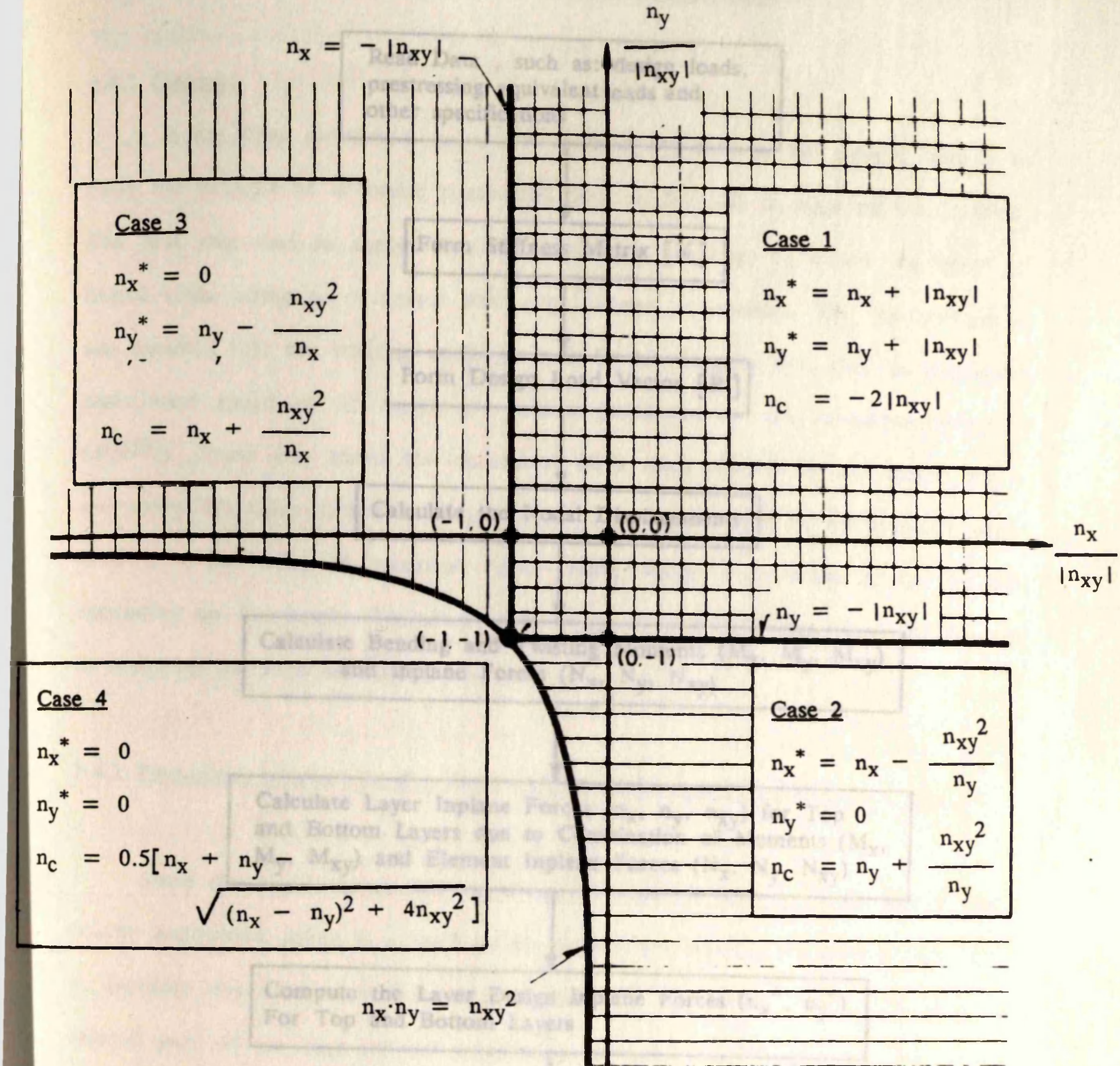

Figure 3.11 : Design formula for any combination of inplane forces.

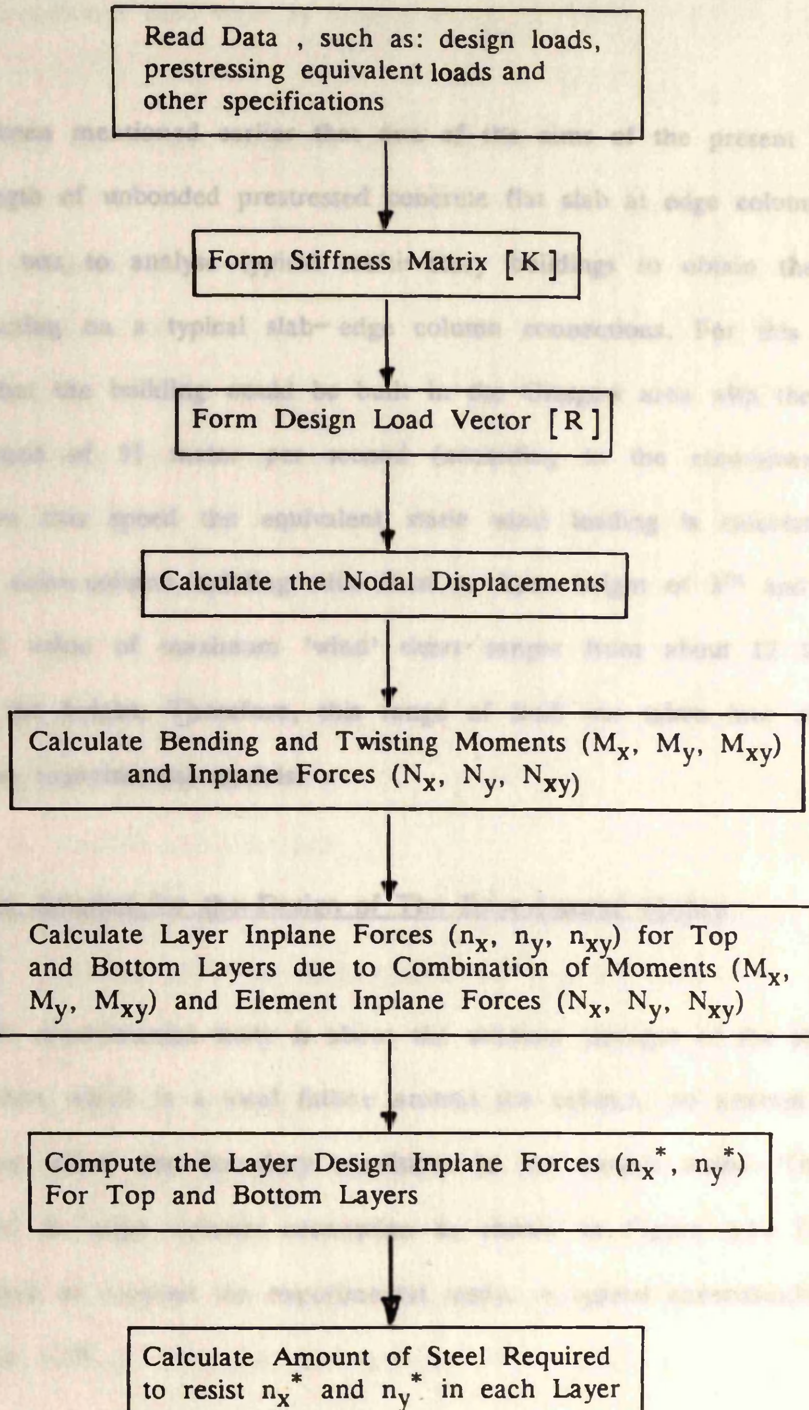

Figure 3.12 : Flow– Chart of the 2– Dimensional Finite Element Program

3.4 Design of Slabs in The Experimental Models in this Study

3.4.1 General

It has been mentioned earlier that one of the aims of the present work is to study the strength of unbonded prestressed concrete flat slab at edge column junction. The first step was to analyse typical multi–story buildings to obtain the range of lateral loads acting on a typical slab–edge column connections. For this purpose it was assumed that the building would be built in the Glasgow area with the maximum basic wind speed of 51 meter per second (according to the recommendations of CP3[56]). From this speed the equivalent static wind loading is calculated. For a ten–story flat slab–column building with floor to floor height of 3^m and bay width of 5 m , the value of maximum 'wind' shear ranges from about 12 to 100 KN depending on the height. Therefore, this range of load was taken into consideration in designing the experimental models.

3.4.2 Procedure Adopted for the Design of The Experimental Models

Since the experimental study is about the ultimate strength of the slab at edge column connection which is a local failure around the column, no attempt was made to duplicate the actual size boundary conditions in the models tested. Therefore an isolated part of an edge column connection as shown in Figure 3.14 (the shaded part) was selected to conduct the experimental study. A typical experimental model is shown in Figure 3.15.

A two–dimensional finite element computer programme for the linear plate bending analysis was developed to consider the combination of bending and prestress equivalent loads and was used for the design of the models. For this purpose, use was made of symmetry so that only one–half of the slab needed to be analysed using 8-node isoparametric element and 16-element mesh as shown in Figure 3.16. The boundary conditions used were as follows:

At all nodes along the column boundary ,abgf, will be:

$$\begin{cases} W = 0 \\ \partial W/\partial x = 0 \\ \partial W/\partial y = 0 \end{cases}$$

and at all nodes along the line 'bc' will be:

$$\partial W/\partial y = 0$$

where W = displacement in z-direction

$\partial W/\partial x$ = rotation about y-axis

$\partial W/\partial y$ = rotation about x-axis

Since we are interested in the local behaviour of the slab at edge column connection, violation of the boundary conditions of real slab was of minor importance.

For the design lateral loads, the maximum wind shear was known but its distribution along the line 'AB' which produced uniform displacement was needed. In the case of flat slab-shear wall junction, Bari[24] has shown that the linear distribution shown in Figure 3.17 causes uniform displacement along the line 'AB'. Figure 3.18 shows the displacement obtained for model MS1. The maximum difference was 2% of the maximum value.

At all the 'Gauss' points of elements, the computer program calculated the moment triad (M_x , M_y , M_{xy}) and inplane forces triad (N_x , N_y , N_{xy}) due to the combination of prestress and design loads. The values of n_x^* and n_y^* were evaluated at the 'Gauss' points of each outer layer element according to the rules given in section 3.5.2. The unstressed steel required to resist these forces at ultimate conditions was calculated using the recommendations of 'BS8110'.

The effective concrete shear stress ,v_c, was calculated for each model and compared with the allowable shear stress ,v_a, given by:

$$v_a = 0.67 \sqrt{(f_t^2 + 0.8 f_{cp} f_t)}$$

where $f_t = 0.24 \sqrt{f_{cu}}$

f_{cp} = average compressive concrete stress due to prestressing

Because the effective shear stress in the critical area around the column didn't exceed the allowable concrete shear stress ,v_a, therefore, shear reinforcement was not necessary.

3.4.3 Strain and Rigidity Matrix for Combined Loads

As previously mentioned, a two-dimensional finite element method based on elastic analysis of the bending plate was developed to consider inplane loads due to prestressing equivalent loads. In this section the combined form of the strain and the rigidity matrix used to obtain the moment triad (M_x , M_y , M_{xy}) and inplane forces triad (N_x , N_y , N_{xy}) is presented in the centre of each element of the slab.

3.4.3.1 Strain Matrix

i)– For bending element

The strains within the bending elements can be expressed in terms of the

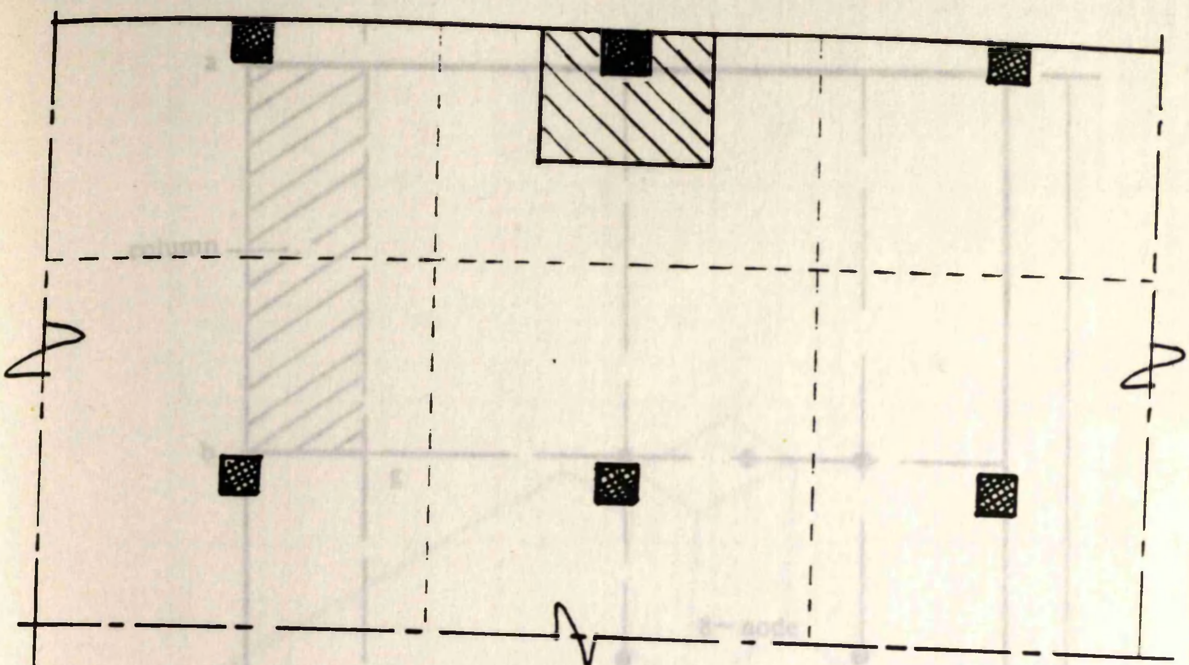

Figure 3.14 : Typical Plan of Flat Slab– Column Structure

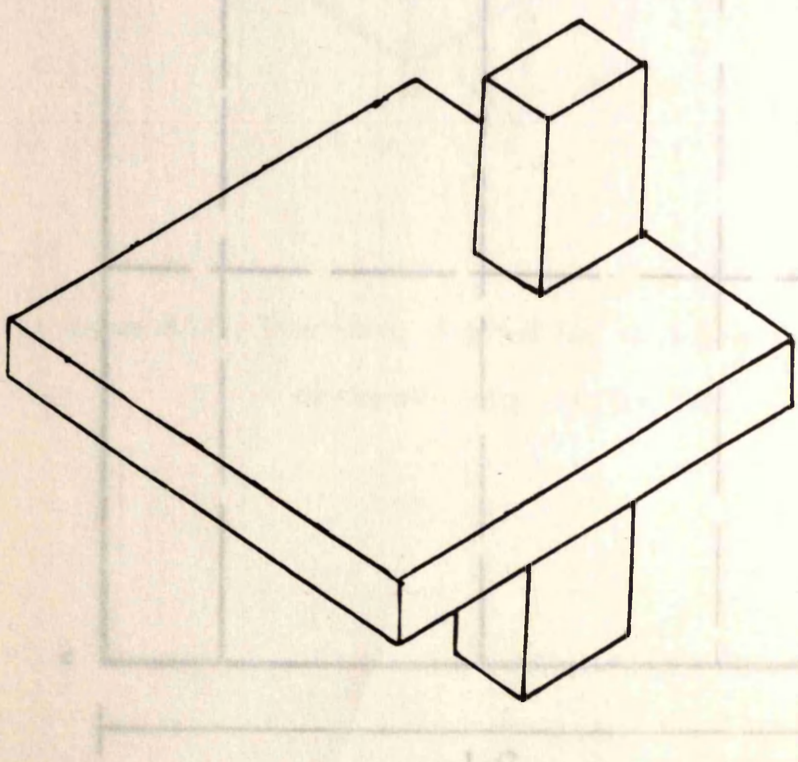

Figure 3.15 : An Isometric View of Typical Experimental Model.

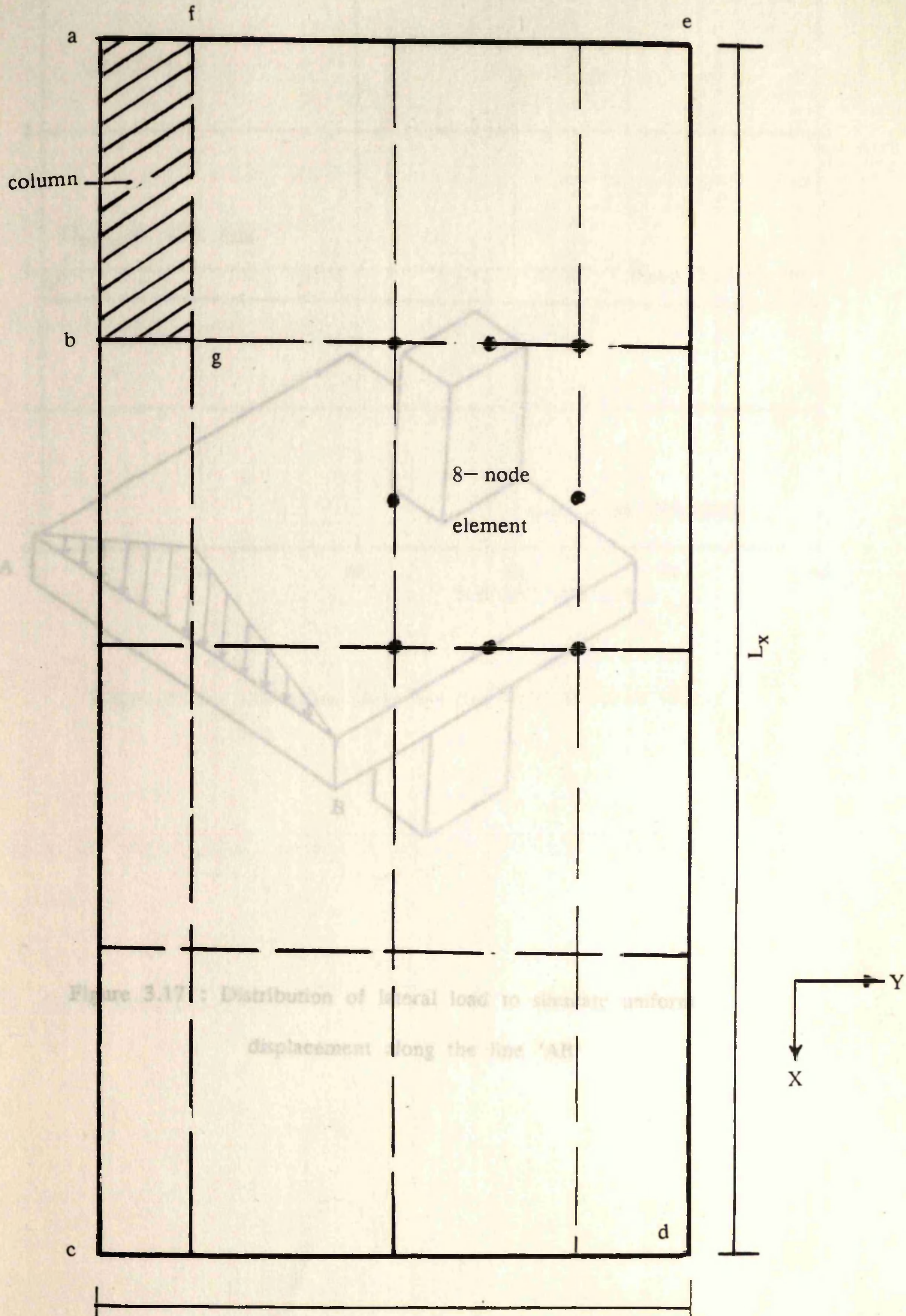

Figure 3.16 : Typical mesh and column boundary conditions.

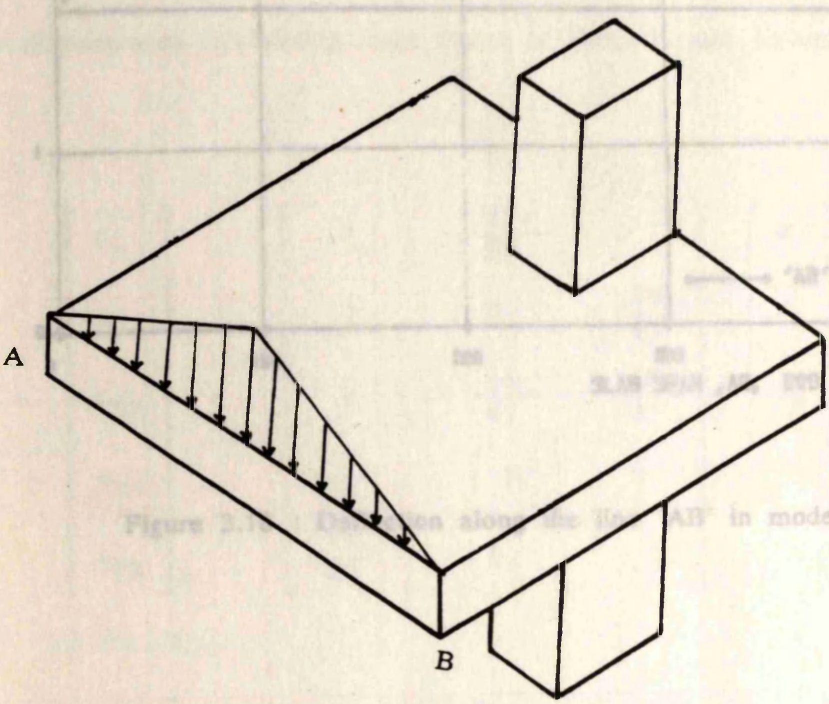

Figure 3.17 : Distribution of lateral load to simulate uniform displacement along the line 'AB'

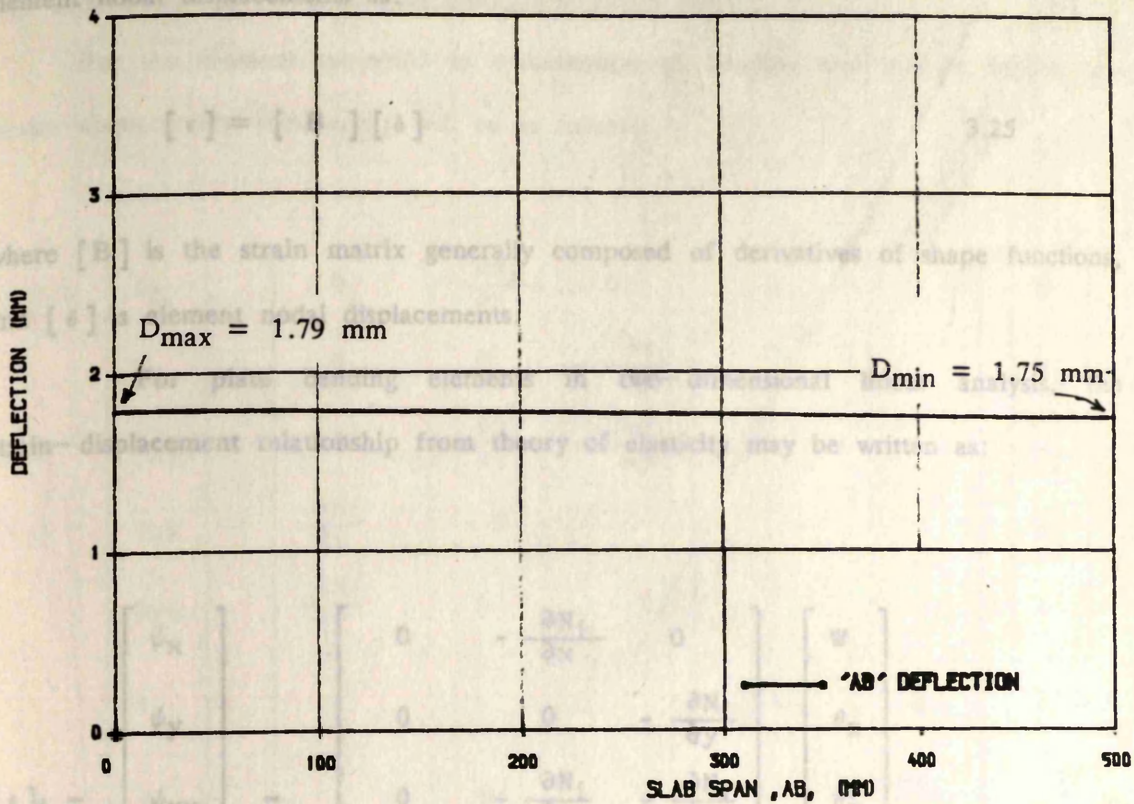

Figure 3.18 : Deflection along the line 'AB' in model MS1.

element nodal displacements as:

$$[\epsilon] = [B][\delta] \tag{3.25}$$

where $[B]$ is the strain matrix generally composed of derivatives of shape functions, and $[\delta]$ is element nodal displacements.

For plate bending elements in two-dimensional linear analysis, the strain-displacement relationship from theory of elasticity may be written as:

$$[\epsilon]_i = \begin{bmatrix} \psi_x \\ \psi_y \\ \psi_{xy} \\ \gamma_{xz} \\ \gamma_{yz} \end{bmatrix}_i = \begin{bmatrix} 0 & -\frac{\partial N_i}{\partial x} & 0 \\ 0 & 0 & -\frac{\partial N_i}{\partial y} \\ 0 & -\frac{\partial N_i}{\partial y} & -\frac{\partial N_i}{\partial y} \\ \frac{\partial N_i}{\partial x} & -N_i & 0 \\ \frac{\partial N_i}{\partial y} & 0 & -N_i \end{bmatrix} \begin{bmatrix} W \\ \theta_x \\ \theta_y \end{bmatrix}_i$$

where N_i is the shape function at the i^{th} node at which the nodal displacements are W_i, θ_{xi} and θ_{yi}.

ii)- <u>For membrane element</u>

$$[\epsilon]_i = \begin{bmatrix} \epsilon_x \\ \epsilon_y \\ \gamma_{xy} \end{bmatrix}_i = \begin{bmatrix} \frac{\partial N_i}{\partial x} & 0 \\ 0 & \frac{\partial N_i}{\partial y} \\ \frac{\partial N_i}{\partial y} & \frac{\partial N_i}{\partial x} \end{bmatrix} \begin{bmatrix} u \\ v \end{bmatrix}_i$$

iii)- <u>Combination of Bending and Membrane Strain Matrix</u>

For the element subjected to combination of bending and inplane forces, the strain- displacement relationship will be as follows:

$$[\epsilon]_i = \begin{bmatrix} \psi_x \\ \psi_y \\ \psi_{xy} \\ \gamma_{xz} \\ \gamma_{yz} \\ \epsilon_x \\ \epsilon_y \\ \gamma_{xy} \end{bmatrix}_i = \left[\begin{array}{ccc|cc} 0 & -\frac{\partial N_i}{\partial x} & 0 & & \\ 0 & 0 & -\frac{\partial N_i}{\partial y} & & \\ 0 & -\frac{\partial N_i}{\partial y} & -\frac{\partial N_i}{\partial y} & & 0 \\ \frac{\partial N_i}{\partial x} & -N_i & 0 & & \\ \frac{\partial N_i}{\partial y} & 0 & -N_i & & \\ \hline & & & \frac{\partial N_i}{\partial x} & 0 \\ & 0 & & 0 & \frac{\partial N_i}{\partial y} \\ & & & \frac{\partial N_i}{\partial y} & \frac{\partial N_i}{\partial x} \end{array}\right] \begin{bmatrix} W \\ \theta_x \\ \theta_y \\ u \\ v \end{bmatrix}$$

3.4.3.2 <u>Rigidity Matrix</u>

The general form of the stress- strain relationship may be written as follows:

$$[\sigma] = [D][\epsilon] \qquad 3.29$$

where $[D]$ is called 'elasticity matrix' or 'rigidity matrix'

Subtituting equation 3.25 into 3.29 results in :

$$[\sigma] = [D][B][\delta] \qquad 3.30$$

a)- The Rigidity Matrix $[D]$ for bending element assuming isotropy is:

$$[D]_b = \begin{bmatrix} \frac{Et^3}{12(1-\nu^2)} & \frac{\nu Et^3}{12(1-\nu^2)} & 0 & 0 & 0 \\ \frac{\nu Et^3}{12(1-\nu^2)} & \frac{Et^3}{12(1-\nu^2)} & 0 & 0 & 0 \\ 0 & 0 & \frac{(1-\nu)Et^3}{24(1-\nu^2)} & 0 & 0 \\ 0 & 0 & 0 & \frac{Et}{2.4(1+\nu)} & 0 \\ 0 & 0 & 0 & 0 & \frac{Et}{2.4(1+\nu)} \end{bmatrix}$$

b)- The Rigidity Matrix $[D]$ for membrane element is:

$$[D]_m = \begin{bmatrix} \frac{E}{1-\nu^2} & \frac{\nu E}{1-\nu^2} & 0 \\ \frac{\nu E}{1-\nu^2} & \frac{E}{1-\nu^2} & 0 \\ 0 & 0 & \frac{E}{2(1+\nu)} \end{bmatrix}$$

c)- The Rigidity Matrix $[D]$ for an element subjected to bending and inplane forces is formed by combination of $[D]_b$ and $[D]_m$ as follows:

$$
[D] = \left[\begin{array}{ccccc|ccc}
\frac{Et^3}{12(1-\nu^2)} & \frac{\nu Et^3}{12(1-\nu^2)} & 0 & 0 & 0 & & & \\
\frac{\nu Et^3}{12(1-\nu^2)} & \frac{Et^3}{12(1-\nu^2)} & 0 & 0 & 0 & & 0 & \\
0 & 0 & \frac{(1-\nu)Et^3}{24(1-\nu^2)} & 0 & 0 & & & \\
0 & 0 & 0 & \frac{Et}{2.4(1+\nu)} & 0 & & & \\
0 & 0 & 0 & 0 & \frac{Et}{2.4(1+\nu)} & & & \\
\hline
 & & & & & \frac{E}{1-\nu^2} & \frac{\nu E}{1-\nu^2} & 0 \\
 & & 0 & & & \frac{\nu E}{1-\nu^2} & \frac{E}{1-\nu^2} & 0 \\
 & & & & & 0 & 0 & \frac{E}{2(1+\nu)}
\end{array}\right]
$$

CHAPTER FOUR

FINITE ELEMENT ANALYSIS

4.1 Introduction

Developments in the finite element method over the last two decades is one of the most significant achievements in the history of engineering. This analysis technique is now used regularly by engineers in the solution of various problems in the context of structural engineering. Using this technique, investigators in many fields of engineering have moved to areas such as nonlinear applications and modelling of complex material behaviour. In the case of reinforced concrete, all nonlinear aspects such as cracking, tension stiffening, nonlinear multiaxial material properties, creep, shrinkage and other parameters which previously were ignored or treated in a very approximate manner, can now be considered rationally by the finite element method

The application of finite element to nonlinear problems increases the numerical work as compared with linear problems. However, development of high speed computers which meet this need have insured that adequate capability is now available. In this chapter, the three– dimensional finite element approach for the analysis of reinforced concrete slab– column connections is presented. The theoretical results and comparison with their experimental counterpart will be shown in Chapter Eight.

4.2 Finite Element Formulation of Slab

Since the finite element analysis is a well known standard procedure, it is not necessary to describe it in detail in this study. But in order to define terms for their applications a brief review of the method will be presented.

4.2.1 General Procedure and Discretisation by Finite Elements

In any continuum, the actual number of degrees of freedom is infinite and an exact analysis of a structure is impossible using a method of discretisation. For any numerical approach it is assumed that the behaviour of the continuum can be represented by a finite number of unknowns. In the finite element method the continuum is divided into a series of elements which are connected together at a finite number of points known as nodal points. This process is called 'discretisation'.

For structural applications, the governing equilibrium equations can be obtained by minimizing the total potential energy of the system. The total potential energy can be expressed as:

$$\pi = 0.5 \int_V [\sigma]^T[\epsilon]dv - \int_V [\delta]^T[p]dv - \int_S [\delta]^T[q]ds -$$

$$\int_\ell [\delta]^T[\omega]d\ell - \Sigma\Delta_i Q_i \qquad (4.1)$$

where $[\sigma]$ and $[\epsilon]$ are the stress and strain vectors respectively, $[\delta]$ the displacement at any point, $[p]$ the body force per unit volume, $[q]$the applied surface tractions, $[\omega]$ is the applied line load and Q_i is the concentrated load. Integrations are carried over the volume 'v' of the structure and loaded surface area 's'. The first term on the right hand side of equation 4.1 represents the internal strain energy and the second to fifth terms are the work contributions of the external forces [p], [q], [w] and Q_i respectively.

In the finite element displacement method, the displacement is assumed to have unknown values only at the nodal points so that the variation within any element is described in terms of the nodal values by means of interpolation functions. Thus

$$[\delta] = [N][\delta^e] \qquad 4.2$$

where $[N]$ is the set of interpolation functions termed as shape functions and $[\delta^e]$ is the vector of nodal displacements of the element. The strains within the element can be expressed in terms of the element nodal displacement as:

$$[\epsilon] = [B][\delta^e] \qquad 4.3$$

where $[B]$ is the strain matrix generally composed of derivatives of shape functions. Finally, the stress may be related to the strains by use of an elasticity matrix $[D]$ as follows:

$$[\sigma] = [D][\epsilon] = [D][B][\delta^e] \qquad 4.4$$

The total potential energy of the continuum will be the sum of the energy contributions of the individual elements. Thus

$$\pi = \Sigma\, \pi_e \qquad 4.5$$

where π_e represents the total potential energy of an element 'e' which, using equation 4.1, can be written as;

$$\pi_e = 0.5 \int_{ve} [\delta^e]^T[B]^T[D][\delta^e]dv - \int_{ve} [\delta^e]^T[N]^T[p]dv - \int_{se} [\delta^e]^T[N]^T[q]ds - \int_{\ell e} [\delta^e]^T[N]^T[\omega]d\ell - \Sigma[\delta^e]^T[N]^T Q_i \qquad (4.6)$$

where v_e is the element volume, s_e is the loaded element surface area and ℓ_e is the loaded line on the element face. Performance of minimisation for element 'e' with respect to the element nodal displacement $[\delta^e]$ results in;

$$\frac{\partial \pi_e}{\partial \delta^e} = \int_{ve} ([B]^T[D][B])[\delta^e]dv - \int_{ve} [N]^T[p]dv - \int_{se} [N]^T[q]ds - \int_{\ell e} [N]^T[\omega]d\ell - \Sigma\, [N]^T Q_i$$

or

$$= [K^e]\,[\delta^e] - [F^e] \qquad (4.7)$$

where :

$$[F^e] = \int_{ve} [N]^T[p]dv + \int_{se} [N]^T[q]ds + \int_{\ell e} [N]^T[\omega]d\ell + \Sigma [N]^T Q_i \qquad (4.8)$$

are the equivalent nodal forces, and

$$[K^e] = \int_{ve} [B]^T[D][B]dv \qquad (4.9)$$

is termed the 'element stiffness matrix'. The summation of the terms in equation 4.7 over all the elements, when equated to zero, results in a system of equilibrium equations for the complete continuum. These equations are then solved by any standard technique to yield the nodal displacements. The strains and therefore the stresses within each element can be calculated from the displacements using equations 4.3 and 4.4. In this study the 'Frontal solution technique' described in section 4.5.5 was used.

4.2.2 Element Type

The selection of the element type is always related to the type of problems to be solved. As three-dimensional nonlinear analysis is the main concern of the analytical part of this study, the 20-noded isoparametric brick element(57) ,as illustrated in Figure 4.1, is used throughout this work to represent concrete. Reinforcing steel is simulated by bars embedded inside the concrete element at their actual locations in the structure without imposing any restrictions on the mesh choice. The mathematical derivations of the stiffness contribution of these bars can be found in Reference (58,59).

This element was chosen to consider the effect of the six stress components σ_x, σ_y, σ_z, τ_{xy}, τ_{yz}, τ_{zx} as shown in Figure 4.2. Each nodal point has three degrees of freedom, that is:

movement in x-direction = u ,

movement in y-direction = v , and

movement in z-direction = w .

Each element has its own local coordinate system (ξ,η,ζ)(Figure 4.1), with the origin at the centre of element such that each local coordinate ranges from -1 to $+1$ only.

4.2.3 Shape Functions

Shape functions are interpolation functions which describe the variation of the displacement within the element in terms of the nodal displacement

$$[\delta] = \sum_{i=1}^{n} [N_i]\ [\delta_i] \tag{4.10}$$

where N_i is the shape function at the i^{th} node at which the nodal displacement is δ_i.

The efficiency of any particular element type will depend on how well the shape functions are capable of representing the true displacement field. The isoparametric family are a group of elements in which the shape functions are used to define the geometry as well as the displacement field. For three dimensional applications, the displacements field at a particular local coordinate (ξ,η,ζ) are $u(\xi,\eta,\zeta)$, $v(\xi,\eta,\zeta)$, $w(\xi,\eta,\zeta)$ and are defined using three displacements degrees of freedom u_i, v_i, w_i at each of the twenty nodes and a quadratic interpolation scheme.

The coordinate values $x(\xi,\eta,\zeta)$, $y(\xi,\eta,\zeta)$ and $z(\xi,\eta,\zeta)$ at any point (ξ,η,ζ) within the element may be defined by the expressions:

$$\begin{aligned} x(\xi,\eta,\zeta) &= \sum_{i=1}^{20} N_i\ (\xi,\eta,\zeta)\ .\ x_i \\ y(\xi,\eta,\zeta) &= \sum_{i=1}^{20} N_i\ (\xi,\eta,\zeta)\ .\ y_i \\ z(\xi,\eta,\zeta) &= \sum_{i=1}^{20} N_i\ (\xi,\eta,\zeta)\ .\ z_i \end{aligned} \tag{4.11}$$

where (x_i,y_i,z_i) are the coordinates of node 'i', and $N_i(\xi,\eta,\zeta)$ are three dimensional

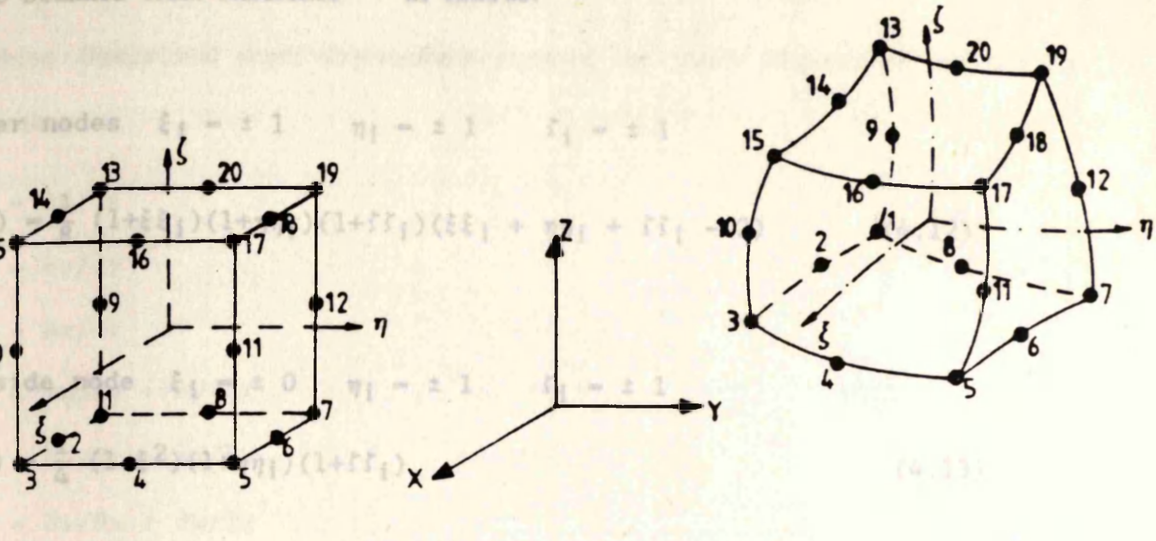

(a) Local coordinates

(b) Cartesian coordinates

Figure (4.1) : 20-Noded isoparametric brick element

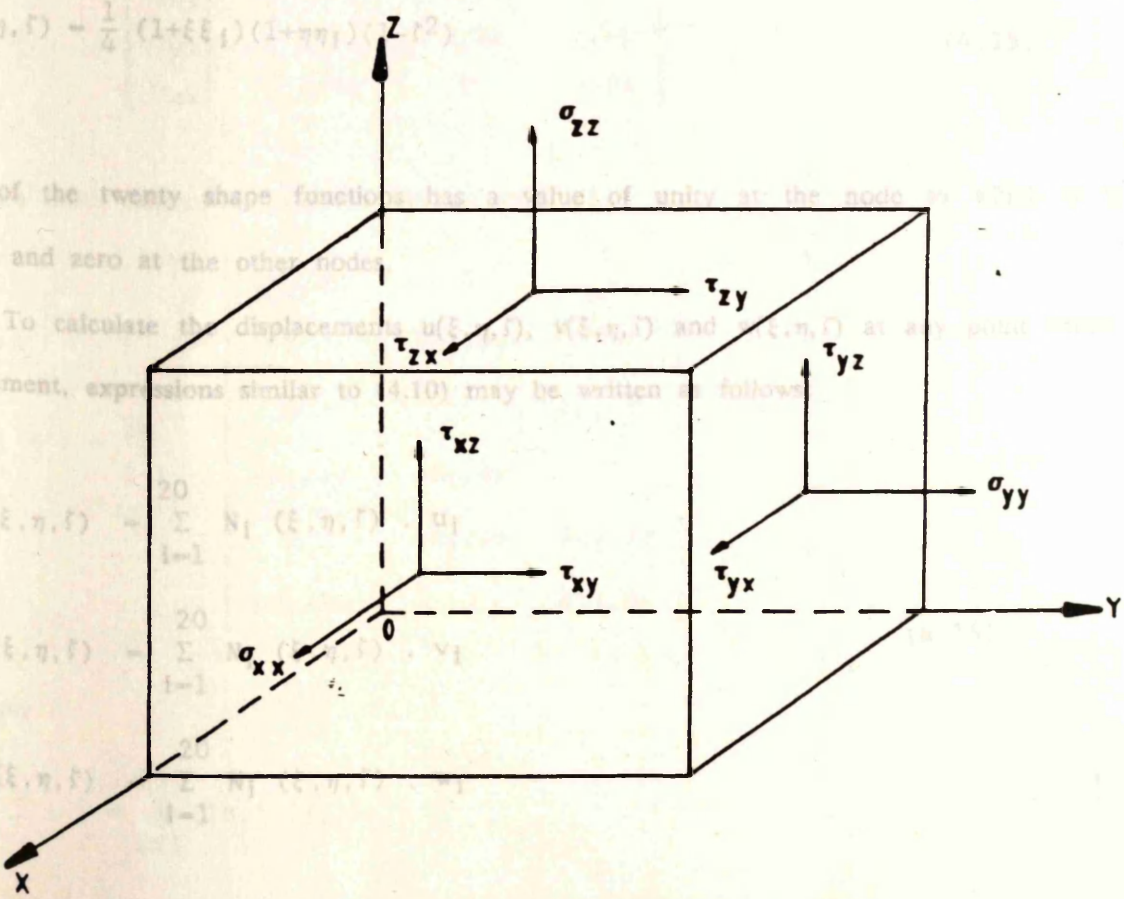

Figure (4.2) : Cartesian stress components quadratic shape functions. In the present work, such shape functions of each of the twenty nodes were obtained from Reference(57) as follows:

For corner nodes $\xi_i = \pm 1 \quad \eta_i = \pm 1 \quad \zeta_i = \pm 1$

$$N_i(\xi,\eta,\zeta) = \frac{1}{8}(1+\xi\xi_i)(1+\eta\eta_i)(1+\zeta\zeta_i)(\xi\xi_i + \eta\eta_i + \zeta\zeta_i - 2) \qquad (4.12)$$

For mid-side node $\xi_i = \pm 0 \quad \eta_i = \pm 1 \quad \zeta_i = \pm 1$

$$N_i(\xi,\eta,\zeta) = \frac{1}{4}(1-\xi^2)(1+\eta\eta_i)(1+\zeta\zeta_i) \qquad (4.13)$$

For mid-side node $\xi_i = \pm 1 \quad \eta_i = \pm 0 \quad \zeta_i = \pm 1$

$$N_i(\xi,\eta,\zeta) = \frac{1}{4}(1+\xi\xi_i)(1-\eta^2)(1+\zeta\zeta_i) \qquad (4.14)$$

For mid-side node $\xi_i = \pm 1 \quad \eta_i = \pm 1 \quad \zeta_i = \pm 0$

$$N_i(\xi,\eta,\zeta) = \frac{1}{4}(1+\xi\xi_i)(1+\eta\eta_i)(1-\zeta^2) \qquad (4.15)$$

Each of the twenty shape functions has a value of unity at the node to which it is related and zero at the other nodes.

To calculate the displacements $u(\xi,\eta,\zeta)$, $v(\xi,\eta,\zeta)$ and $w(\xi,\eta,\zeta)$ at any point within the element, expressions similar to (4.10) may be written as follows:

$$\begin{aligned} u(\xi,\eta,\zeta) &= \sum_{i=1}^{20} N_i(\xi,\eta,\zeta) \cdot u_i \\ v(\xi,\eta,\zeta) &= \sum_{i=1}^{20} N_i(\xi,\eta,\zeta) \cdot v_i \qquad (4.16) \\ w(\xi,\eta,\zeta) &= \sum_{i=1}^{20} N_i(\xi,\eta,\zeta) \cdot w_i \end{aligned}$$

4.2.4 Strain Matrix

In three dimensional small displacement analysis, the strain–displacement relationship may be written as:

$$
\begin{aligned}
\epsilon_x &= \partial u/\partial x \\
\epsilon_y &= \partial v/\partial y \\
\epsilon_z &= \partial w/\partial z \\
\gamma_{xy} &= \partial u/\partial y + \partial v/\partial x \\
\gamma_{yz} &= \partial v/\partial z + \partial w/\partial y \\
\gamma_{zx} &= \partial w/\partial x + \partial u/\partial z
\end{aligned}
\qquad (4.17)
$$

in which ϵ_x , ϵ_y, ϵ_z are the normal strain components and γ_{xy}, γ_{yz}, γ_{zx} are the shear strain components. Equations 4.17 may be written in matrix form as follows:

$$
[\ \epsilon\ ] = \begin{bmatrix} \epsilon_x \\ \epsilon_y \\ \epsilon_z \\ \gamma_{xy} \\ \gamma_{yz} \\ \gamma_{zx} \end{bmatrix} \begin{bmatrix} \partial/\partial x & 0 & 0 \\ 0 & \partial/\partial y & 0 \\ 0 & 0 & \partial/\partial z \\ \partial/\partial y & \partial/\partial x & 0 \\ 0 & \partial/\partial z & \partial/\partial y \\ \partial/\partial z & 0 & \partial/\partial x \end{bmatrix} \begin{bmatrix} u \\ v \\ w \end{bmatrix} \qquad (4.18)
$$

using the finite element idealisation we can write

$$
[\ \epsilon\ ] = \sum_{i=1}^{20} \begin{bmatrix} \partial N_i/\partial x & 0 & 0 \\ 0 & \partial N_i/\partial y & 0 \\ 0 & 0 & \partial N_i/\partial z \\ \partial N_i/\partial y & \partial N_i/\partial x & 0 \\ 0 & \partial N_i/\partial z & \partial N_i/\partial y \\ \partial N_i/\partial z & 0 & \partial N_i/\partial x \end{bmatrix} \begin{bmatrix} u_i \\ v_i \\ w_i \end{bmatrix} \qquad (4.19)
$$

or simply

$$
[\ \epsilon\ ] = \sum_{i=1}^{20} [B_i]\ [\delta_i] \qquad (4.20)
$$

where $[B_i]$ is the 6×3 strain matrix in equation 4.19 which contains the cartesian derivatives of the shape functions. Since the shape functions N_i are defined in terms of the local coordinates of the element (ξ, η, ζ), a transformation from local to global coordinates is required to obtain the $[B]$ matrix in equation 4.19. This is done through the well known Jacobian matrix which is written as:

$$[\ J\ ] = \begin{bmatrix} \partial x/\partial\xi & \partial y/\partial\xi & \partial z/\partial\xi \\ \partial x/\partial\eta & \partial y/\partial\eta & \partial z/\partial\eta \\ \partial x/\partial\zeta & \partial y/\partial\zeta & \partial z/\partial\zeta \end{bmatrix} \tag{4.21}$$

thus

$$[\ J\ ] = \sum_{i=1}^{20} \begin{bmatrix} \frac{\partial N_i}{\partial\xi}.x_i & \frac{\partial N_i}{\partial\xi}.y_i & \frac{\partial N_i}{\partial\xi}.z_i \\ \frac{\partial N_i}{\partial\eta}.x_i & \frac{\partial N_i}{\partial\eta}.y_i & \frac{\partial N_i}{\partial\eta}.z_i \\ \frac{\partial N_i}{\partial\zeta}.x_i & \frac{\partial N_i}{\partial\zeta}.y_i & \frac{\partial N_i}{\partial\zeta}.z_i \end{bmatrix} \tag{4.22}$$

the inverse of the jacobian matrix will be

$$[\ J\ ]^{-1} = \begin{bmatrix} \frac{\partial\xi}{\partial x} & \frac{\partial\eta}{\partial x} & \frac{\partial\zeta}{\partial x} \\ \frac{\partial N_i}{\partial y} & \frac{\partial N_i}{\partial y} & \frac{\partial\zeta}{\partial y} \\ \frac{\partial N_i}{\partial z} & \frac{\partial N_i}{\partial z} & \frac{\partial\zeta}{\partial z} \end{bmatrix} \tag{4.23}$$

therefore the cartesian derivatives are given by

$$\begin{bmatrix} \frac{\partial N_i}{\partial x} \\ \frac{\partial N_i}{\partial y} \\ \frac{\partial N_i}{\partial z} \end{bmatrix} = [\ J\ ]^{-1} \begin{bmatrix} \frac{\partial N_i}{\partial\xi} \\ \frac{\partial N_i}{\partial\eta} \\ \frac{\partial N_i}{\partial\zeta} \end{bmatrix} \tag{4.24}$$

4.2.5 Stress–Strain Relationship

For linear analysis of uncracked concrete, and in the absence of initial stresses and strains, the stress–strain relationship may be written in the form of

$$[\sigma] = [D][\epsilon] \qquad 4.25$$

where $[D]$ is the elasticity matrix which takes the form

$$[D] = \frac{E(1-\nu)}{(1+\nu)(1-2\nu)} \begin{bmatrix} 1 & \frac{\nu}{(1-\nu)} & \frac{\nu}{(1-\nu)} & 0 & 0 & 0 \\ & 1 & \frac{\nu}{(1-\nu)} & 0 & 0 & 0 \\ & & 1 & 0 & 0 & 0 \\ & & & \frac{(1-2\nu)}{2(1-\nu)} & 0 & 0 \\ & \text{Symmetry} & & & \frac{(1-2\nu)}{2(1-\nu)} & 0 \\ & & & & & \frac{(1-2\nu)}{2(1-\nu)} \end{bmatrix} \qquad (4.26)$$

where 'E' is the Young's modulus of elasticity, and 'ν' is Poission's ratio. The concrete nonlinearity as considered in this work is only the material nonlinearity and all changes in material properties enter through the changes in elasticity matrix $[D]$. This will be discussed later in section 4.4.4.3.

4.2.6 Numerical Integration

The element stiffness matrix ,$[K^e]$, in equation 4.9 is given by:

$$[K^e] = \int_{ve} [B]^T[D][B]$$

Since it is difficult to carry out the integration analytically, some form of numerical integration should be specified. In this study, 3×3×3 Gauss–Lengender quadrature rules have been used as shown in Figure 4.3.

4.2.7 Principal Stresses

From equation 4.25 there are six cartesian stress components at each Gauss points that can be evaluated, namely:

$$[\sigma] = [\sigma_x, \sigma_y, \sigma_z, \tau_{xy}, \tau_{yz}, \tau_{zx}] \tag{4.27}$$

Considering uncracked material, there exist three planes on which the shear stresses are zero. These planes are called 'principal planes'. The stresses normal to these planes are called principal stresses. The value of such principal stresses , σ_i, may be obtained by solving the following cubic equation(60).

$$\sigma_i^3 - I_1\sigma_i^2 + I_2 - I_3 = 0 \tag{4.28}$$

in which I_1, I_2 and I_3 are the stress invariants, which may be expressed as follows:

$$I_1 = \sigma_x + \sigma_y + \sigma_z \tag{4.29}$$

$$I_2 = [\sigma_x\sigma_y + \sigma_y\sigma_z + \sigma_z\sigma_x + \tau^2{}_{xy} + \tau^2{}_{yz} + \tau^2{}_{zx}] \tag{4.30}$$

I_3 = determinant of the stress tensor

$$\begin{vmatrix} \sigma_x & \tau_{xy} & \tau_{zx} \\ \tau_{yx} & \sigma_y & \tau_{yz} \\ \tau_{zx} & \tau_{zy} & \sigma_z \end{vmatrix} \tag{4.31}$$

The principal directions which determine the principal planes can be expressed by their respective directions cosines such that:

$$l_i = \cos(\theta x_i) \ , \ m_i = \cos(\theta y_i) \ , \ n_i = \cos(\theta z_i) \tag{4.32}$$

where θ_{xi} , θ_{yi} and θ_{zi} are the angles between the principal direction (i) and x , y and z– axsis respectively. Thus the direction cosines of σ_1 are l_1, m_1, n_1; those for σ_2 are l_2, m_2, n_2 and those for σ_3 are l_3, m_3, n_3.

The method to evaluate these direction cosines is explained in details elsewhere(60) and is briefly presented here. Denoting

$$A = \begin{vmatrix} \sigma_y - \sigma_i & \tau_{zy} \\ \tau_{yz} & \sigma_z - \sigma_i \end{vmatrix} \qquad B = -\begin{vmatrix} \tau_{xy} & \tau_{zy} \\ \tau_{xz} & \sigma_z - \sigma_i \end{vmatrix} \qquad C = \begin{vmatrix} \tau_{xy} & \sigma_y - \sigma_i \\ \tau_{xz} & \tau_{yz} \end{vmatrix} \tag{4.33}$$

it can be shown that the three direction cosines can be expressed as:

$$\frac{l_i}{A} = \frac{m_i}{B} = \frac{n_i}{C} = R \tag{4.34}$$

where R is a non– zero constant to be determined. The subsidiary trigonometric condition:

$$l_i^2 + m_i^2 + n_i^2 = 1 \tag{4.35}$$

gives R as :

$$R = \frac{1}{\sqrt{A^2 + B^2 + C^2}} \tag{4.36}$$

then $l_i = A.R$, $m_i = B.R$ and $n_i = C.R$ (4.37)

4.3 Steel Modelling

4.3.1 Modelling Methods

In developing a finite element model for a reinforced concrete member, at least the following three alternative representations of the reinforcement have been used.

a)– distributed (or smeared)

b)– discrete

c)– embedded

For a distributed representation as shown in Figure 4.4a, the steel is assumed to be distributed as an equivalent layer (among the layers of concrete) which can carry stresses only in the direction of the original bars. The equivalent thickness of the steel layers in any direction is proportional to the corresponding ratio of steel in that particular direction in the element. Perfect bond is assumed between the concrete and steel.

A discrete representation of the reinforcement, using one dimensional element (Figure 4.4b), has been widely used. Axial force members are assumed to be pin-connected with three degrees of freedom at the nodal points. The one dimensional reinforcement element is superimposed on a three-dimensional finite element mesh representing concrete at nodal points. A serious disadvantage of this representation, however, is that the location of reinforcement often dictates the size of concrete mesh. This may result in slender elements where the reinforcing bars are too close together or increases the number of elements which consequently increases the cost of computer analysis.

An embedded representation is shown in Figure 4.4c. In this method the reinforcing bar is considered as an axial member embedded into the isoparametric element such that its strains are consistent with those of the element. In other words, perfect bond is assumed between concrete and steel. The concept of embedded representation of reinforcing bars was first presented for plane stress, strain and axisymmetric analysis(63). It allows an isoparametric element to include as many bars as possible and the bars can be placed in positions corresponding to those in the real structure without imposing any restrictions on mesh size.

In this study, reinforcing bars are embedded in the 20-noded isoparametric brick element used for concrete. The basic two-dimensional theoretical formulation presented by Phillips and Zienkiewicz(63), was extended for three-dimensional element(65) in a similar manner. The derivation requires that bars are restricted to lie along the local coordinate axes of the basic element as shown in Figure 4.5. The details of the theoretical derivation of bar element stiffness can be found in References (23,65).

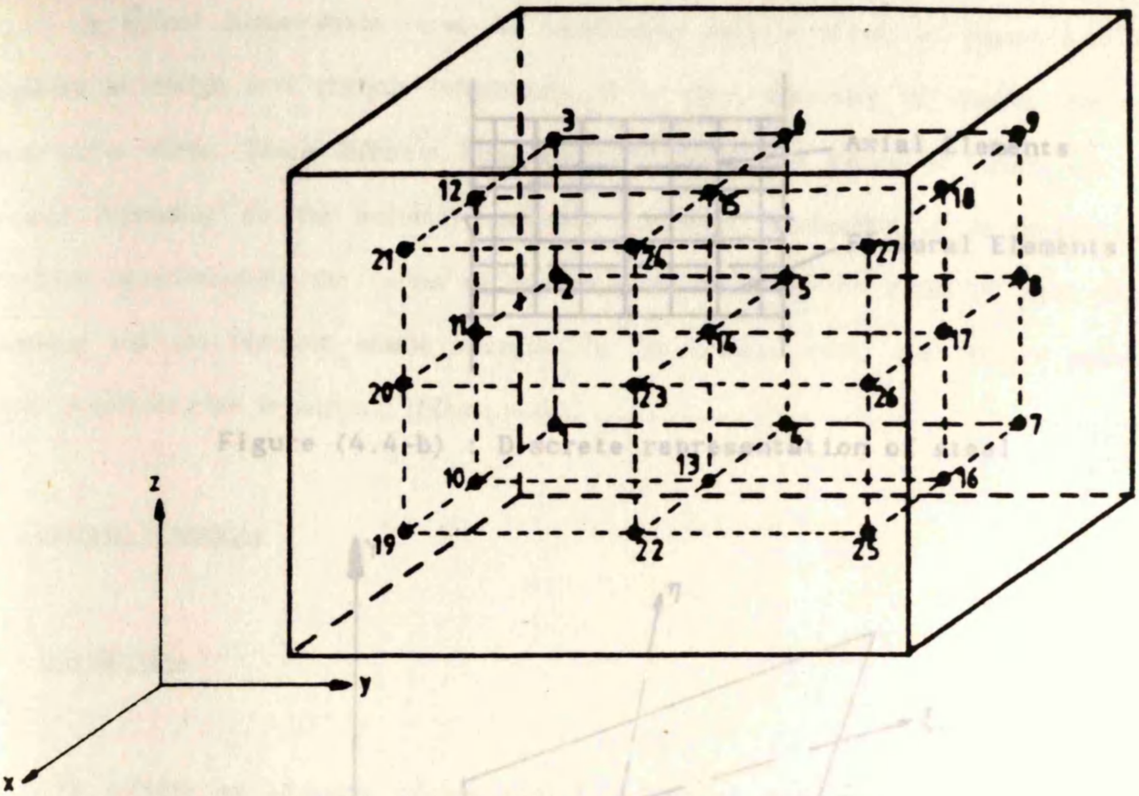

Figure (4.3) : Location of Gauss points for the 3x3x3 integration rule; those for the 2x2x2 and 4x4x4 rules follow the same order

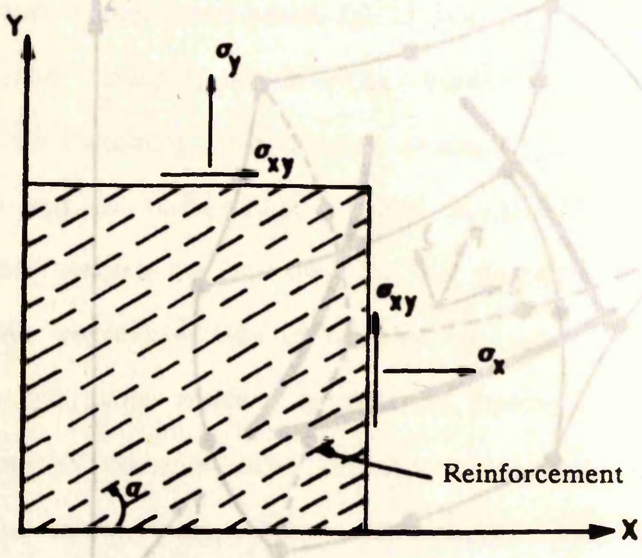

Figure (4.4-a) : Distributed representation of steel

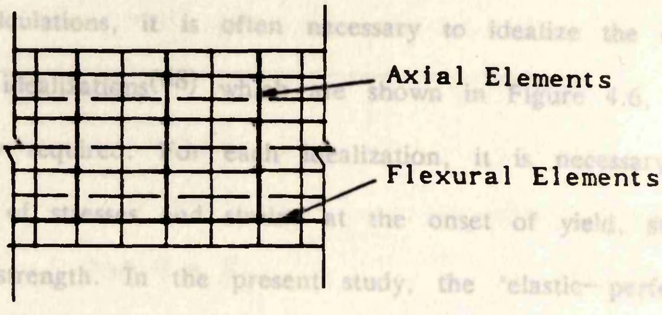

Figure (4.4-b) : Discrete representation of steel

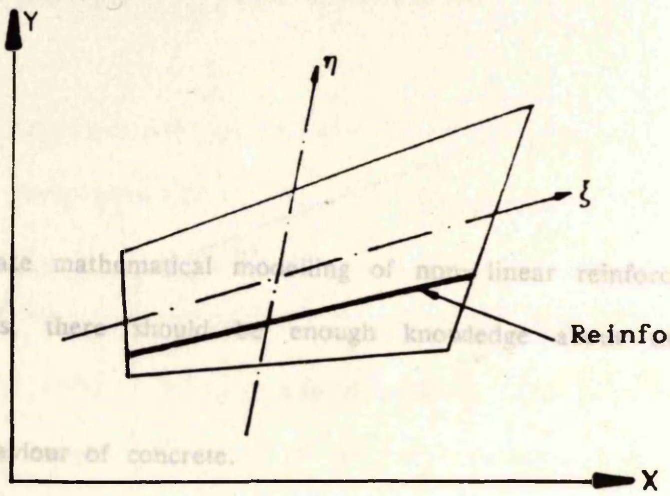

Figure (4.4-c) : Embedded representation of steel

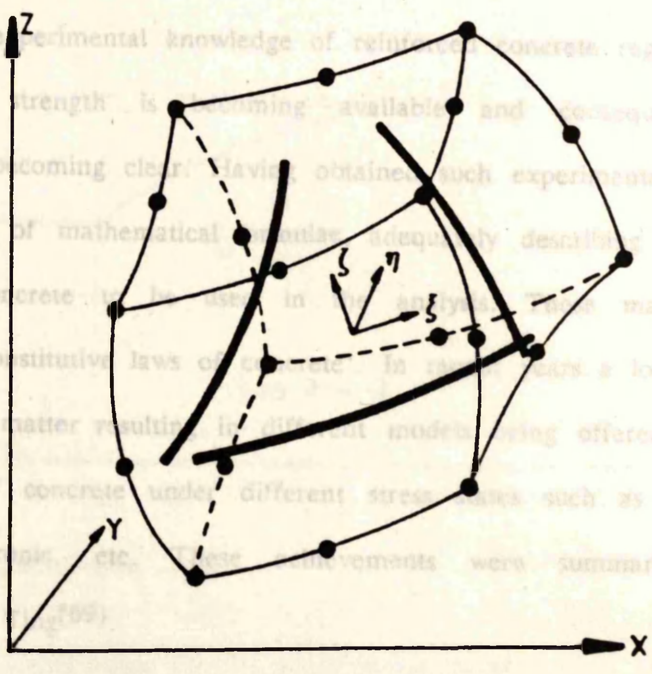

Figure (4.5) : Embedded bars within the 20-noded isoparametric brick element

4.3.2 Characteristic Properties of Unstressed Steel

A typical stress–strain curve for reinforcing steel is shown in Figure 4.5. For simplicity in design and analysis calculations, it is often necessary to idealize the steel stress–strain curve. These different idealizations(68) which are shown in Figure 4.6, can be used depending on the accuracy required. For each idealization, it is necessary to determine experimentally the values of stresses and strains at the onset of yield, strain hardening and the ultimate tensile strength. In the present study, the 'elastic–perfectly plastic' approximation is adopted (Figure 4.6a).

4.4 Concrete Modelling

4.4.1 Introduction

To achieve an adequate mathematical modelling of non–linear reinforced concrete behaviour by finite elements, there should be enough knowledge about the following aspects:

a)– Elastic and inelastic behaviour of concrete.

b)– Behaviour of steel reinforcement

c)– Bond–slip phenomenon between concrete and reinforcement.

Now–a–days more and more experimental knowledge of reinforced concrete regarding the deformational behaviour and strength is becoming available and consequently the above–mentioned subjects are becoming clear. Having obtained such experimental data, it must be transformed into sets of mathematical formulae, adequately describing the basic characteristics of reinforced concrete to be used in the analysis. These mathematical formulae are normally called 'constitutive laws of concrete'. In recent years a lot of work have been carried out on this matter resulting in different models being offered for the description of the behaviour of concrete under different stress states such as nonlinear elastic, elastic–plastic, endochronic, etc. These achievements were summarized and critically evaluated by Chen and Ting(69).

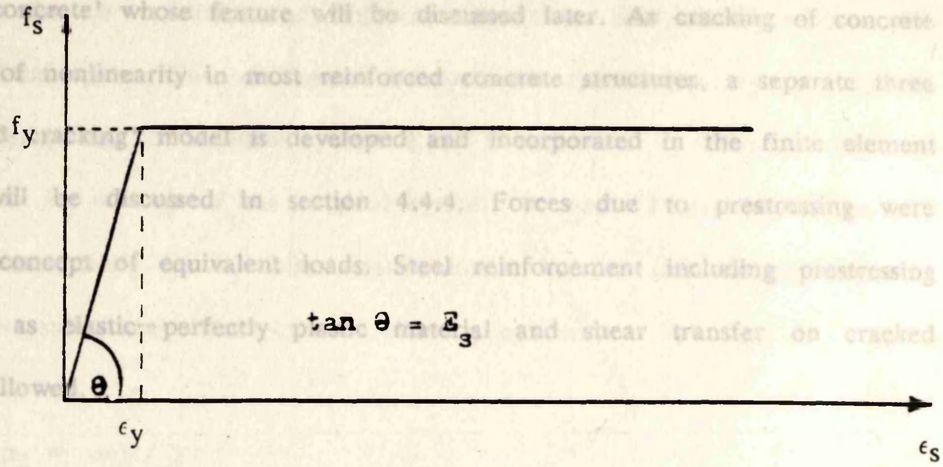

(a) Elastic-perfectly plastic approximation

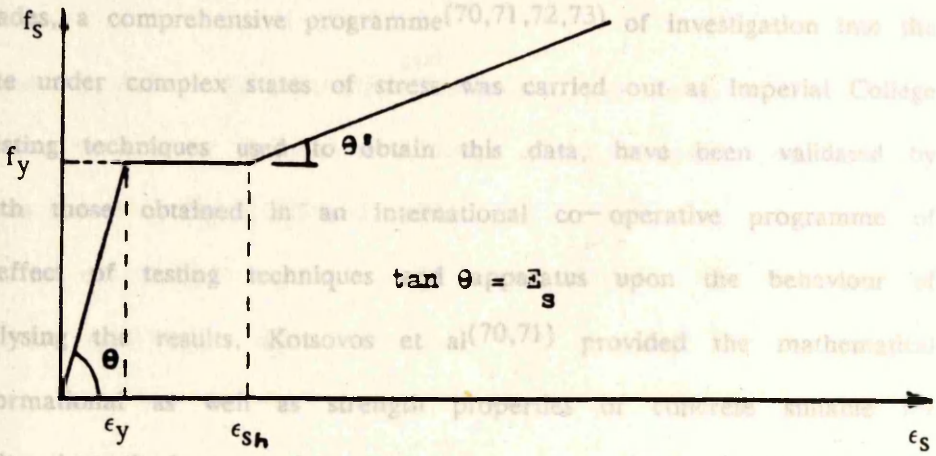

(b) Trilinear approximation

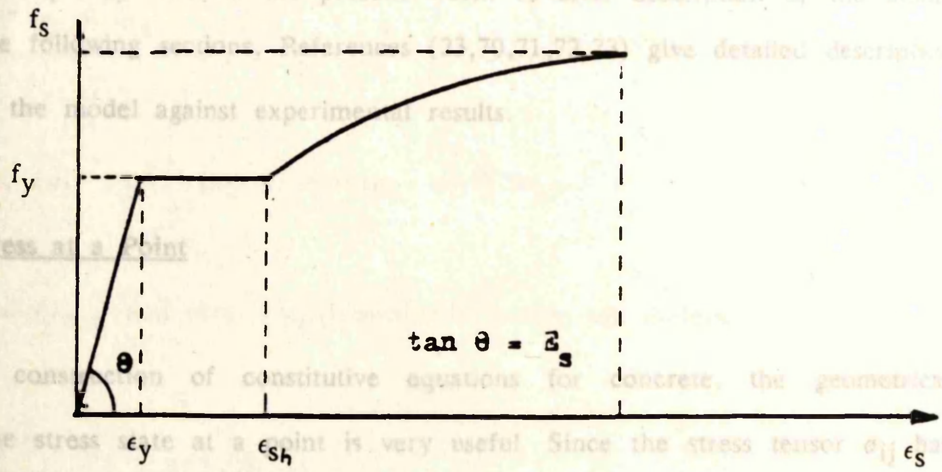

(c) Complete curve

Figure 4.6 : Idealizations for the stress–strain curve for steel in tension or compression.

In this study, concrete properties were modelled based on 'Kotsovos[70,71] constitutive law of concrete' whose feature will be discussed later. As cracking of concrete is the major cause of nonlinearity in most reinforced concrete structures, a separate three dimensional 'smeared cracking' model is developed and incorporated in the finite element programme. This will be discussed in section 4.4.4. Forces due to prestressing were included using the concept of equivalent loads. Steel reinforcement including prestressing steel was modelled as elastic–perfectly plastic material and shear transfer on cracked concrete faces was allowed.

4.4.2 Kotsovos' Constitutive Laws of Concrete

In recent decades, a comprehensive programme[70,71,72,73] of investigation into the behaviour of concrete under complex states of stress was carried out at Imperial College of London. The testing techniques used to obtain this data, have been validated by comparing them with those obtained in an international co–operative programme of research into the effect of testing techniques and apparatus upon the behaviour of concrete. After analysing the results, Kotsovos et al[70,71] provided the mathematical expressions for deformational as well as strength properties of concrete suitable for nonlinear computer based methods to analyse concrete structures. These expressions were successfully implemented in the computer programme by Elnounu[23], then were utilized by Bari[24] and subsequently used in the present work. A brief description of the model will be given in the following sections. References (23,70,71,72,73) give detailed description with verification of the model against experimental results.

4.4.2.1 State of Stress at a Point

For the construction of constitutive equations for concrete, the geometrical representation of the stress state at a point is very useful. Since the stress tensor σ_{ij} has six independent components, it is possible to consider these components as positional co–ordinates in a six–dimensional space. However, it is too difficult to deal with in this study. The simplest alternative is to take the three principal stresses σ_1, σ_2, σ_3 such that $\sigma_1 > \sigma_2 > \sigma_3$ as the co-ordinates and represents the stress state at a point in the three dimensional stress space. This orthogonal co-ordinate system σ_1, σ_2, σ_3 can be transformed into a cylindrical co-ordinate system q, r, θ such that 'q' coincides with the space diagonal ($\sigma_1 = \sigma_2 = \sigma_3$) of the original system, 'r' and 'θ' are the radius and rotational variables respectively on the plane perpendicular to the axis 'q' as shown in Figure 4.7. The two systems are related by the following equations:

$$q = (\sigma_1 + \sigma_2 + \sigma_3)/\surd 3$$

$$r = [(\sigma_1 - \sigma_2)^2 + (\sigma_2 - \sigma_3)^2 + (\sigma_3 - \sigma_1)^2]^{0.5} / \surd 3 \qquad (4.38)$$

$$\cos\theta = (\sigma_1 + \sigma_2 - 2\sigma_3) \;/\; (r\surd 6)$$

The variables 'q' and 'r' define the hydrostatic and deviatoric components of stress state respectively, whereas the variable 'θ' defines the direction of the deviatoric component on the octahedral plane as shown in Figure 4.7 and varies from:

$\theta = 0^\circ$ for $\sigma_1 = \sigma_2 > \sigma_3$

$\theta = 60^\circ$ for $\sigma_1 > \sigma_2 = \sigma_3$

The hydrostatic and deviatoric components can also be expressed in terms of the normal (σ_{oct}) and shear (τ_{oct}) octahedral stresses which are defined as follows:

$$\sigma_{oct} = \frac{\sigma_1 + \sigma_2 + \sigma_3}{3} = q/\surd 3 \qquad (4.39)$$

$$\tau_{oct} = 1/[3\surd\,(\sigma_1 - \sigma_2)^2 + (\sigma_2 - \sigma_3)^2 + (\sigma_3 - \sigma_1)^2] = r/\surd 3$$

Similarly, the normal (ϵ_{oct}) and shear (γ_{oct}) octahedral strains are defined as follows:

$$\epsilon_{oct} = \frac{\epsilon_1 + \epsilon_2 + \epsilon_3}{3}$$

$$\gamma_{oct} = [(\epsilon_1 - \epsilon_2)^2 + (\epsilon_2 - \epsilon_3)^2 + (\epsilon_3 - \epsilon_1)^2]^{0.5} / 3 \qquad 4.40$$

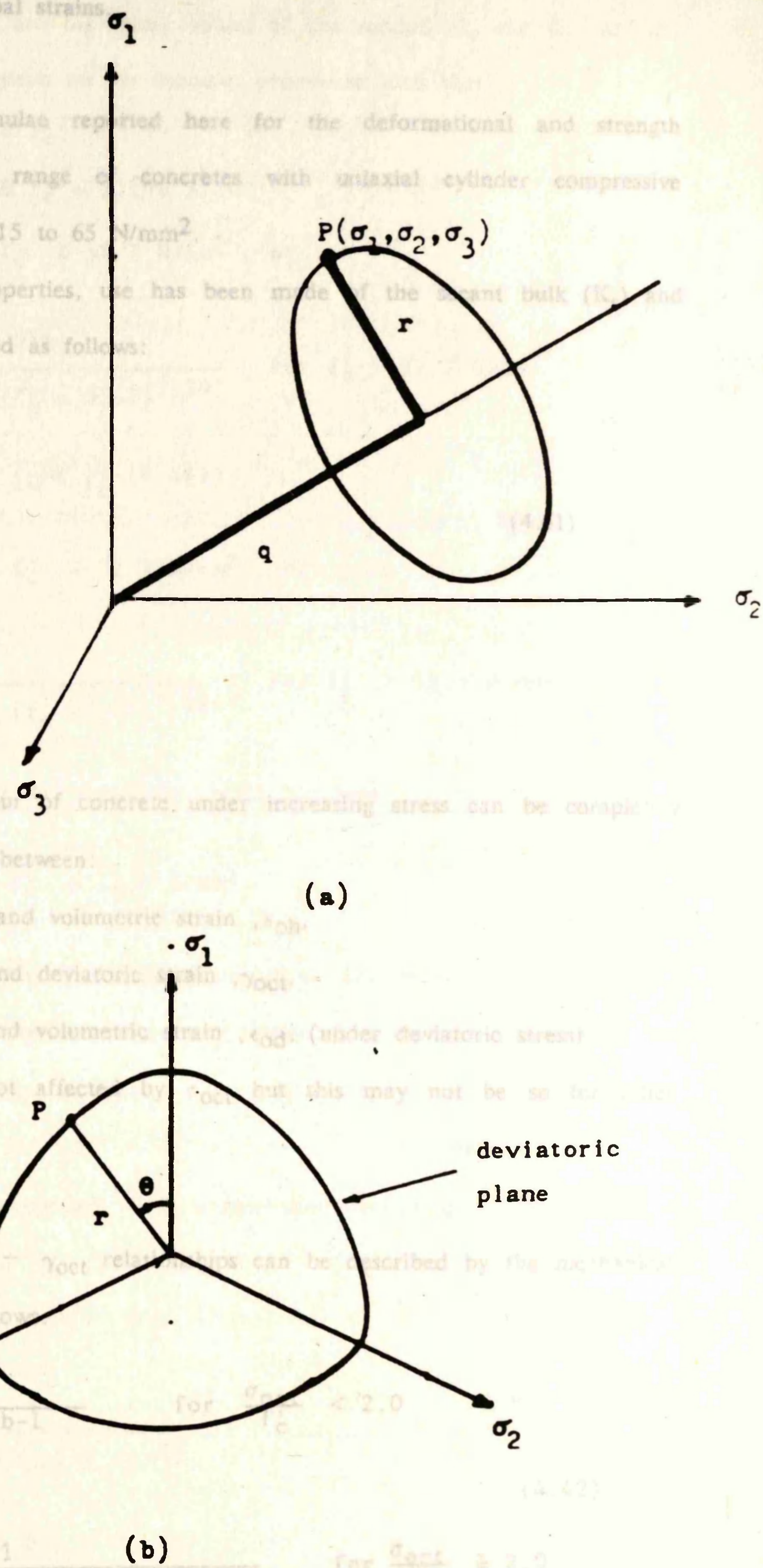

Figure (4.7) : Cylindrical coordinate system where ϵ_1, ϵ_2, ϵ_3 are the principal strains.

The mathematical formulae reported here for the deformational and strength properties are applicable to a range of concretes with uniaxial cylinder compressive strength (f'_c) varying from about 15 to 65 N/mm^2.

For the deformational properties, use has been made of the secant bulk (K_s) and secant shear (G_s) moduli expressed as follows:

$$K_s = \frac{\sigma_{oct}}{3\epsilon_{oct}} \qquad G_s = \frac{\tau_{oct}}{2\gamma_{oct}} \tag{4.41}$$

4.4.2.2 <u>Deformational Properties</u>

The deformational behaviour of concrete under increasing stress can be completely described[70] by the relationships between:

(a)– hydrostatic stress ,σ_{oct}, and volumetric strain ,ϵ_{oh},

(b)– deviatoric stress ,τ_{oct}, and deviatoric strain ,γ_{oct},

(c)– deviatoric stress ,τ_{oct}, and volumetric strain ,ϵ_{od}, (under deviatoric stress)

(Note that for metals, ϵ_{od} is not affected by τ_{oct} but this may not be so for other materials)

The $\sigma_{oct} - \epsilon_{oh}$ and $\tau_{oct} - \gamma_{oct}$ relationships can be described by the mechanical properties of the model[70] as follows:

$$\frac{K_s}{K_o} = \frac{1}{1 + A\left(\frac{\sigma_{oct}}{f'_c}\right)^{b-1}} \qquad \text{for } \frac{\sigma_{oct}}{f'_c} < 2.0 \tag{4.42}$$

$$\frac{K_s}{K_o} = \frac{1}{1 + 2^{(b-1)}\, b\, A - 2^{b}\, (b-1) A \left(\frac{\sigma_{oct}}{f'_c}\right)^{-1}} \qquad \text{for } \frac{\sigma_{oct}}{f'_c} \geq 2.0$$

$$\frac{G_s}{G_o} = \frac{1}{1 + C\left(\frac{\tau_{oct}}{f'_c}\right)^{d-1}} \tag{4.43}$$

where K_o and G_o (in KN/mm2) are the initial values of the moduli K_s and G_s, and A, b, C, d are parameters which depend on the material properties such that

$$K_o = 11.0 + 0.0032\, f_c'^2$$

$$G_o = 9.224 + 0.136\, f_c' + 3.296 \times 10^{-15}\, f_c'^{(8.273)}$$

$$A = 0.516 \quad \text{for } f_c' \leq 31.7 \text{ N/mm}^2 \text{ , or}$$

$$= \frac{0.516}{1.0 + 0.0027(f_c' - 31.7)^{2.397}} \quad \text{for } f_c' > 31.7 \text{ N/mm}^2$$

$$b = 2.0 + 1.81 \times 10^{-8}\, f_c'^{(4.461)}$$

$$C = 3.573 \quad \text{for } f_c' \leq 31.7 \text{ N/mm}^2 \text{ , or} \qquad (4.44)$$

$$= \frac{3.573}{1.0 + 0.0134\,(f_c' - 31.7)^{1.414}} \quad \text{for } f_c' > 31.7 \text{ N/mm}^2$$

$$d = 2.12 + 0.0183\, f_c' \quad \text{for } f_c' > 31.7 \text{ N/mm}^2$$

$$= 2.7 \quad \text{for } f_c' \leq 31.7 \text{ N/mm}^2$$

In order to evaluate the effect of internal stresses on deformation, use is made of the artificial concept that the volumetric strain (ϵ_{od}) under deviatoric stress is due to the hydrostatic component of such stresses so that

$$\sigma_{int} = 3\, K_s\, \epsilon_{od} \qquad 4.45$$

the $\tau_{oct} - \epsilon_{od}$ relationship was expressed(70) in a non-dimensionalised form as follows:

$$\sigma_{int}/f_c' = M\,(\tau_{oct} / f_c')^{d1} \qquad (4.46)$$

where

$$M = \frac{k}{1 + d_2\,(\sigma_{oct} / f_c')^{d3}} \qquad (4.47)$$

and

$$k = \frac{4.0}{1.0 + 1.087\,(f_c' - 15.0)^{0.23}} \qquad (4.47)$$

$$d_1 = 1.0 \quad \text{for } f_c' \leq 31.7 \text{ N/mm}^2 \text{, or}$$

$$= 0.3124 + 0.0217\, f_c' \quad \text{for } f_c' > 31.7 \text{ N/mm}^2$$

$$d_2 = 0.222 + 0.01086 \, f'_c - 0.000122 f'^2_c \tag{4.48}$$

$$d_3 = -2.415 \quad \text{for } f'_c \leq 31.7 \text{ N/mm}^2 \text{ , or}$$

$$= -3.5308 + 0.0352 \, f'_c \quad \text{for } f'_c > 31.7 \text{ N/mm}^2$$

The hydrostatic component (σ_{int}) is equivalent to three principal stresses, $\sigma_1 = \sigma_2 = \sigma_3 = \sigma_{int}$, and its effect on deformation will be the deformational response of the model under these principal stresses.

Equations 4.42 and 4.43 when used with equation 4.41, the total octahedral normal strain will be

$$\epsilon_{oct} = \epsilon_{oh} + \epsilon_{od} \qquad 4.49$$

4.4.2.3 <u>Strength Properties of Concrete</u>

The strength of concrete under multiaxial stresses is a function of the state of stress consisting of six components. Based on an analysis of strength data, Kotsovos(71) derived mathematical expressions to describe the strength properties of concrete under biaxial or triaxial stress states which can be presented as follows:

- τ_{oe} is the value of τ_{oct} at the ultimate strength level for $\theta = 0$ degree;
- τ_{oc} is the value of τ_{oct} at the ultimate strength level for $\theta = 60$ degree;

the value of τ_{of} at the ultimate strength level for any values θ such that $0 < \theta < 60$ degrees, may be given by the following expression:

$$\tau_{of} = \frac{2\tau_{oc}(\tau^2_{oc}-\tau^2_{oe})\cos\theta+\tau_{oc}(2\tau_{oe}-\tau_{oc})[4(\tau^2_{oc}-\tau^2_{oe})\cos^2\theta+5\tau^2_{oe}-4\tau_{oc}\tau_{oe}]^{0.5}}{4(\tau^2_{oc} - \tau^2_{oe})\cos^2\theta + (\tau_{oc} - 2\tau_{oe})^2} \tag{4.50}$$

This expression describes in the deviatoric plane a smooth convex curve with tangents perpendicular to the directions of τ_{oe} and τ_{oc} at $\theta = 0$ and $\theta = 60$ degrees respectively (see Figure 4.8). If isotropic material behaviour is assumed, equation 4.50 may be used to define a six-fold symmetric ultimate strength surface, provided the variations of τ_{oe} and τ_{oc} with σ_{oct} are established.

Figure 4.9 shows the normalized combinations of octahedral stresses (with respect to the uniaxial cylinder compressive strength (f'_c)) at the ultimate strength level obtained from triaxial tests[71]. The envelopes in this Figure are considered to describe adequately the strength of most concretes likely to be encountered in practice[71]. A mathematical description of the above strength envelopes was obtained[71] as follows:

$$\tau_{oc}/f'_c = 0.944\,[(\sigma_o/f'_c) + 0.05]^{0.724}$$
$$\tau_{oe}/f'_c = 0.633\,[(\sigma_o/f'_c) + 0.05]^{0.857} \qquad 4.51$$

Equation 4.51 represents two open ended convex envelopes whose slope tends to become equal to that of the space diagonal as σ_{oct} tends to infinity. These expressions together with equation 4.50 are used in this work to define an ultimate strength surface which conforms with the generally accepted[70] shape requirements such as six-fold symmetry, convexity with respect to the space diagonal, and open ended shape which tends to become cylindrical as σ_o tends to infinity.

4.4.3 Failure Criteria of Concrete

4.4.3.1 Introduction

Criteria such as yielding, initiation of cracking, load carrying capacity and extent of deformation are generally used to define failure. But failure is defined in this study as the ultimate load-carrying capacity of a test specimen. In general, concrete failures can be divided into two types: tensile type and compressive type. Tensile and compressive type of

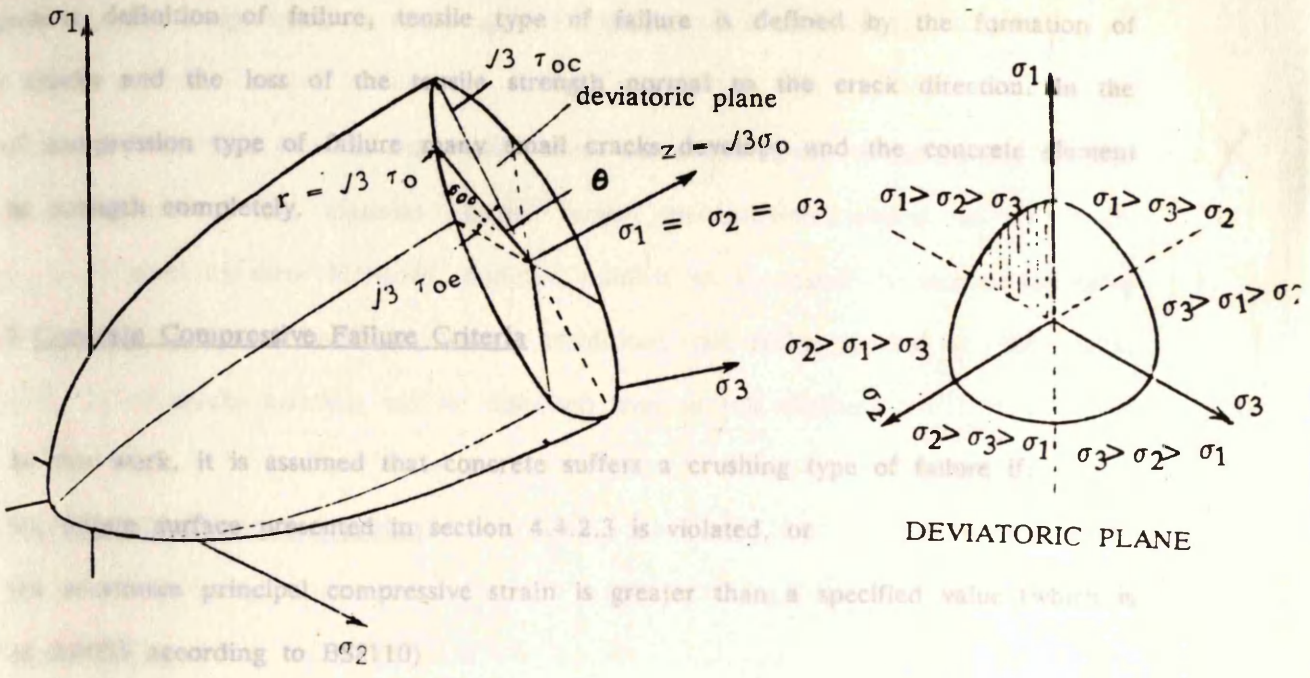

Figure (4.8) : Schematic representation of the ultimate strength surface

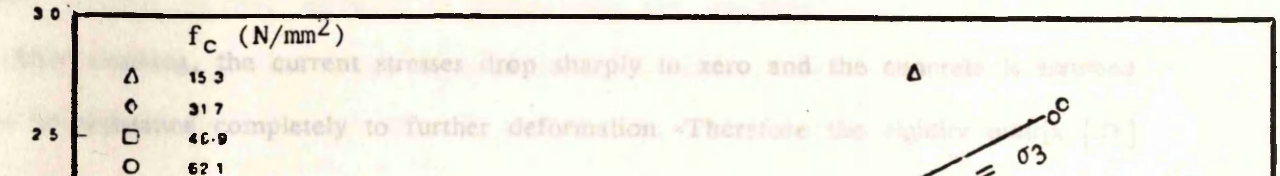

Figure (4.9) : **Combinations of octahedral stresses at ultimate strength for concrete under the axisymmetric stress states $\sigma_1 > \sigma_2 = \sigma_3$ and $\sigma_1 = \sigma_2 > \sigma_3$**

failures are generally characterised by brittleness and ductility, respectively. With respect to the present definition of failure, tensile type of failure is defined by the formation of major cracks and the loss of the tensile strength normal to the crack direction. In the case of compression type of failure many small cracks develop and the concrete element loses its strength completely.

X

4.4.3.2 Concrete Compressive Failure Criteria

In this work, it is assumed that concrete suffers a crushing type of failure if:

(a)– the failure surface presented in section 4.4.2.3 is violated, or

(b)– the maximum principal compressive strain is greater than a specified value (which is taken as 0.0035 according to BS8110)

Condition (a) holds for isotropic (uncracked) concrete material, and it is found that condition (b) will never be satisfied prior to condition (a) as long as the material is isotropic. But when a crack exists, condition (a) is not applicable thus only condition (b) is valid.

After crushing, the current stresses drop sharply to zero and the concrete is assumed to lose its resistance completely to further deformation. Therefore the rigidity matrix [D] will be zero.

4.4.3.3 Concrete Tensile Failure Criteria

In this study, it is assumed that concrete will suffer a cracking type of failure if:

(a)– the failure surface presented in section 4.4.2.3 is violated. or

(b)– the maximum tensile principal stress exceeds a specified value. A value equals $f_t/2$ is approximately the value on the failure surface for uniaxial tensile stress state (f_t is ultimate tensile strength of concrete).

Condition (a) holds for isotropic (uncracked) concrete material. Under multiaxial stress state, condition (b) will never be satisfied prior to condition (a) as long as the material is uncracked. When at least one crack exists at any point due to condition (a), only condition (b) is applicable to check against a second or a third crack.

Once a crack has formed, the tensile stress across the crack drops sharply to zero and the resistance of the material against further deformation normal to the crack direction is reduced to zero. However, material parallel to the crack is assumed to carry stress according to the uniaxial or biaxial conditions prevailing parallel to the crack. Further details of cracks handling will be discussed later in this chapter.

4.4.4 Modelling of Concrete Cracking

4.4.4.1 Introduction

Cracking of concrete is a major factor contributing to nonlinear behaviour of reinforced concrete structures. Early studies on modelling of reinforced concrete nonlinear behaviour resulted in two methods of representing the cracking of concrete. The first approach , termed discrete crack representation(32), uses a predefined discrete crack system. The major disadvantage of this method ,however,is that the topology of the structure has to be continuously altered as cracking progresses and previous knowledge of the crack pattern might be necessary. There is also a lack of generality in the possible crack directions as these are dictated by element boundaries rather than the resulting principal stresses or strains.

The second approach, known as the smeared crack model(63), assumes that the cracked concrete remains a continuum. This implies that an infinite number of parallel cracks occur at a specific point if a certain cracking criterion is satisfied. By using the smeared cracking approach the problem of changing the topology of the structure with crack propagation is overcome. Moreover the initiation, orientation and propagation of cracks at the sampling points are independent of the mesh adopted. Figure 4.10 illustrates both cracking models as applied to the two dimensional analysis.

The selection of which cracking model to use depends largely upon the purpose of the finite element study undertaken and the nature of the output desired[24]. Generally, if the overall load– displacement behaviour, without regarding to local stresses and realistic crack patterns is desired, the smeared crack representation is probably the best choice. If, on the other hand, detailed local behaviour is of prime importance, adoption of the discrete cracking model is useful. The element type, size and grid pattern have significant effects on both the models. The smeared crack approach is the most commonly used because it is easy to implement. Further details on this aspect can be found in References (63,69).

In this study, the overall structural behaviour is of particular importance. Furthermore, the efficient 20– noded isoparametric brick element is used to represent concrete with embedded bars to simulate the reinforcing steel at its exact locations in the structure. Therefore, the smeared crack simulation is adopted.

4.4.4.2 Smeared Cracking Model

The main feature of the present cracking model may be summarized as follows:

a)– cracking in one, two and three direction is allowed

b)– cracks are allowed to open or close during the load increment

c)– no tension stiffening but shear retention is allowed.

d)– variable crack direction is permitted.

In the three dimensional stress space defined by σ_1, σ_2 and σ_3, cracks might occur normal to any of the three principal stresses (Figure 4.11). It is possible for any point to be cracked in more than one direction. Up to three cracks at a point are allowed in this analysis provided that they are orthogonal to one another. Once a crack occurs, its direction in the cartesian xyz space is fixed and retained as such in all subsequent loading. In this method , matrix [D] is modified such that the modulus of elasticity 'E' of the concrete is reduced to zero in the direction normal to the crack. Further, a reduced shear modulus 'G' is assumed on the cracked plane to account for aggregate interlocking.

Because of the fact that shear stress is allowed to act at the cracked surfaces, this procedure allows tensile stress to build up on surface other than the crack direction.

Because of the fact that shear stress is allowed on the cracked planes, for later stages of loading, the principal stress direction changes from the previous one. Gupta and Akbar[33] reported in the analysis of reinforced concrete, that the direction of initial and final cracks do not coincide. In this analysis, instead of fixing the direction of the first crack once it develops , the crack direction is monitored for every iteration in every increment. If the crack rotates by more than ± 10% from its previous direction, that direction is changed and the new correct direction is fixed, until the direction again changes by ± 10% in further iterations.

In order to improve the realism of the present cracking model, the possibility of crack closing is considered. This behaviour may take place due to the redistribution of stresses during an iteration or upon further loading. In the present work, the possibility of cracking of any sampling point is re-examined within each iteration until the numerical solution converges within the permissible limits of convergence. After convergence, the direction of any cracking is fixed. The fictitious principal strain normal to the crack direction is monitored to assess the state of the cracks in the cracked concrete. If this strain has a negative value, then the crack is assumed to close and the modulus of elasticity normal to the crack is restored back to initial value 'E'.

4.4.4.3 <u>Rigidity Matrix for Crack Analysis</u>

It has been reported earlier in this work that the triaxial rigidity matrix for

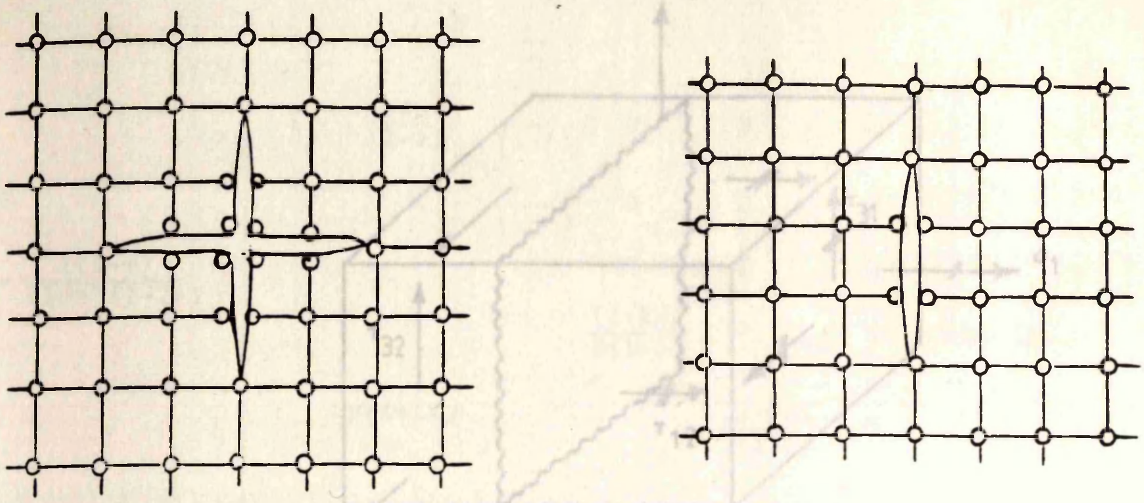

(a) Two - directional cracking

(b) One - directional cracking

(i) Discrete cracking model

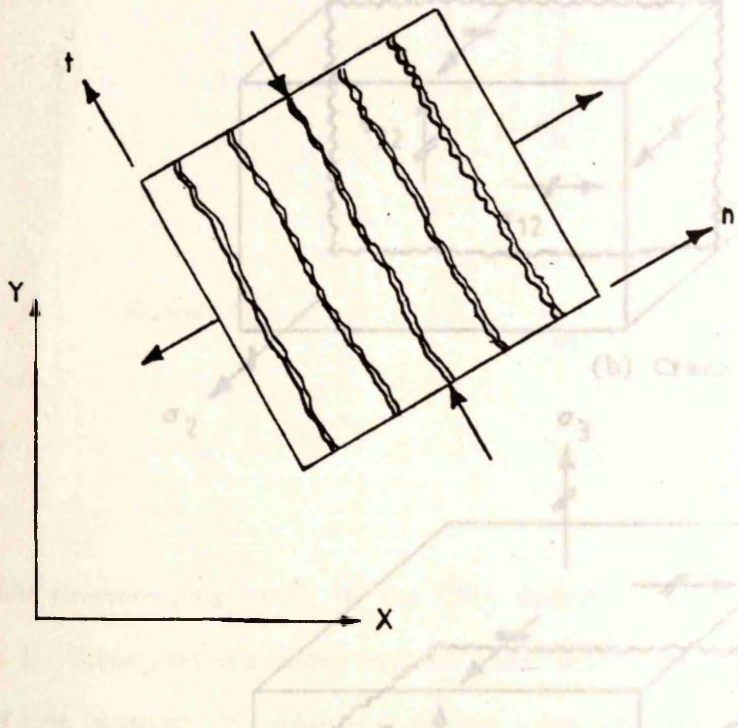

-(ii) Smeared cracking model

Figure (4.10) : **Discrete and smeared cracking models**

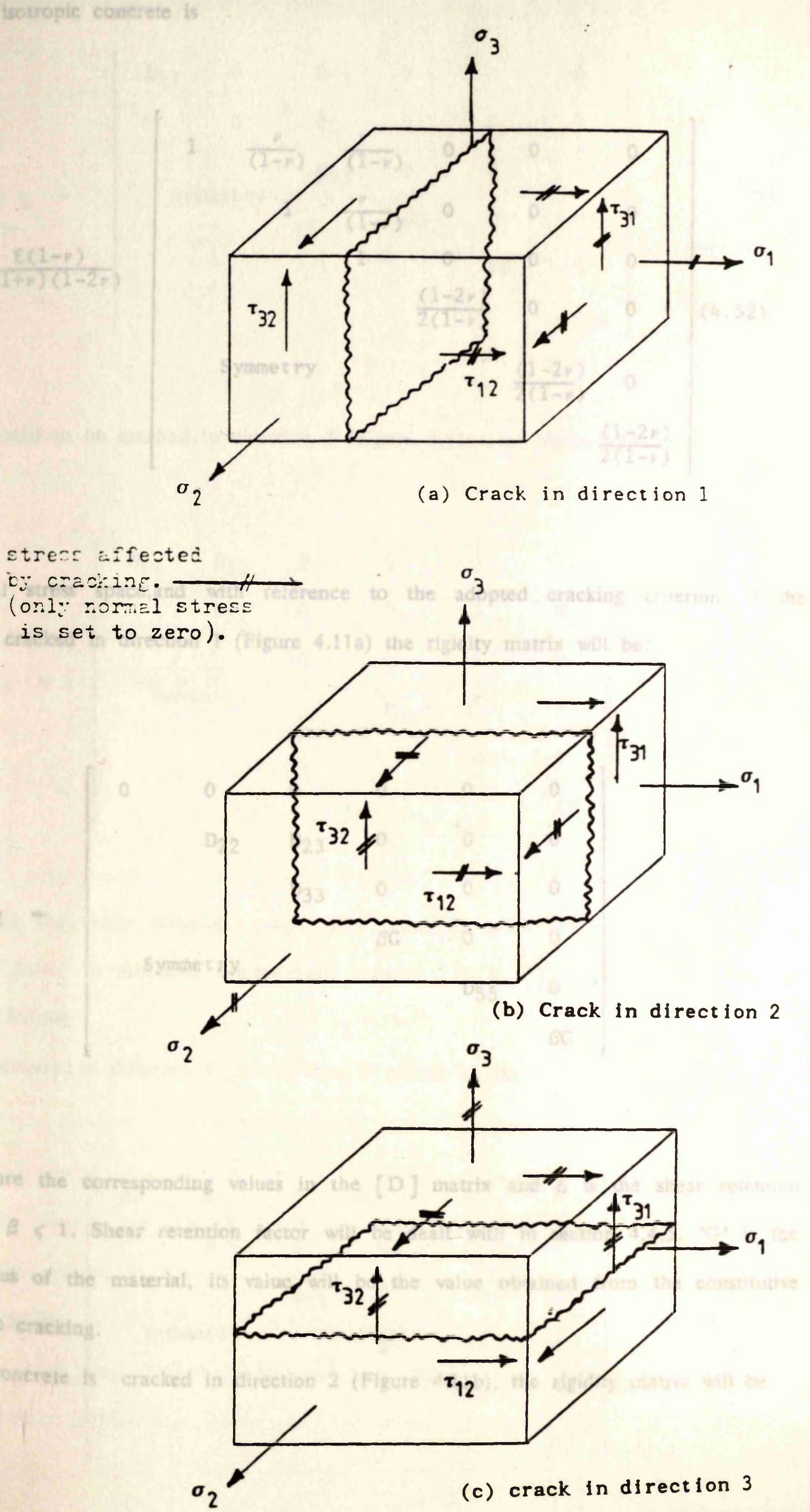

Figure (4.11) : Types of cracks in concrete uncracked isotropic concrete is

$$[D] = \frac{E(1-\nu)}{(1+\nu)(1-2\nu)} \begin{bmatrix} 1 & \frac{\nu}{(1-\nu)} & \frac{\nu}{(1-\nu)} & 0 & 0 & 0 \\ & 1 & \frac{\nu}{(1-\nu)} & 0 & 0 & 0 \\ & & 1 & 0 & 0 & 0 \\ & & & \frac{(1-2\nu)}{2(1-\nu)} & 0 & 0 \\ & \text{Symmetry} & & & \frac{(1-2\nu)}{2(1-\nu)} & 0 \\ & & & & & \frac{(1-2\nu)}{2(1-\nu)} \end{bmatrix} \quad (4.52)$$

In principal stress space,and with reference to the adopted cracking criterion, if the concrete is cracked in direction 1 (Figure 4.11a) the rigidity matrix will be:

$$[\,D_c\,]_1 = \begin{bmatrix} 0 & 0 & 0 & 0 & 0 & 0 \\ & D_{22} & D_{23} & 0 & 0 & 0 \\ & & D_{33} & 0 & 0 & 0 \\ & & & \beta G & 0 & 0 \\ & \text{Symmetry} & & & D_{55} & 0 \\ & & & & & \beta G \end{bmatrix} \quad (4.53)$$

where D_{ij} are the corresponding values in the $[D]$ matrix and β is the shear retention factor, $0 \leqslant \beta \leqslant 1$. Shear retention factor will be dealt with in section 4.4.5. 'G' is the shear modulus of the material, its value will be the value obtained from the constitutive laws prior to cracking.

If the concrete is cracked in direction 2 (Figure 4.11b), the rigidity matrix will be

$$[\,D_c\,]_2 = \begin{bmatrix} D_{11} & 0 & D_{13} & 0 & 0 & 0 \\ & 0 & 0 & 0 & 0 & 0 \\ & & D_{33} & 0 & 0 & 0 \\ & \text{Symmetry} & & \beta G & 0 & 0 \\ & & & & \beta G & 0 \\ & & & & & D_{66} \end{bmatrix} \qquad (4.54)$$

and if it is said to be cracked in direction 3 (Figure 4.11c) the rigidity matrix will be

$$[\,D_c\,]_3 = \begin{bmatrix} D_{11} & D_{12} & 0 & 0 & 0 & 0 \\ & D_{22} & 0 & 0 & 0 & 0 \\ & & 0 & 0 & 0 & 0 \\ & \text{Symmetry} & & D_{44} & 0 & 0 \\ & & & & \beta G & 0 \\ & & & & & \beta G \end{bmatrix} \qquad (4.55)$$

Depending on the stress situation, cracks may occur in more than one direction at a single Gauss point. In this case combinations between $[D_c]_1$, $[D_c]_2$ and $[D_c]_3$ may be necessary as follows:

a) If crack occurred in direction 1 and 2, then D matrix is given by

$$[\,D_c\,]_{1,2} = \begin{bmatrix} 0 & 0 & 0 & 0 & 0 & 0 \\ & 0 & 0 & 0 & 0 & 0 \\ & & D_{33} & 0 & 0 & 0 \\ & \text{Symmetry} & & \beta G & 0 & 0 \\ & & & & \beta G & 0 \\ & & & & & \beta G \end{bmatrix} \qquad (4.56)$$

b) If crack occurred in direction 2 and 3, then D matrix is given by

$$[D_c]_{2,3} = \begin{bmatrix} D_{11} & 0 & 0 & 0 & 0 & 0 \\ & 0 & 0 & 0 & 0 & 0 \\ & & 0 & 0 & 0 & 0 \\ & \text{Symmetry} & & \beta G & 0 & 0 \\ & & & & \beta G & 0 \\ & & & & & \beta G \end{bmatrix} \quad (4.57)$$

c) If crack occurred in direction 3 and 1 , then D matrix is given by

$$[D_c]_{3,1} = \begin{bmatrix} 0 & 0 & 0 & 0 & 0 & 0 \\ & D_{22} & 0 & 0 & 0 & 0 \\ & & 0 & 0 & 0 & 0 \\ & \text{Symmetry} & & \beta G & 0 & 0 \\ & & & & \beta G & 0 \\ & & & & & \beta G \end{bmatrix} \quad (4.58)$$

and finally if crack occurred in all three principal directions it is assumed that this cracked point is incapable of resisting any stress. Therefore,

$$[D_c]_{1,2,3} = [0] \quad 4.59$$

Depending on the number of cracks which occur at a Gauss point at a particular level of loading, the appropriate rigidity matrix will be evaluated at that Gauss point and for simplifying the discussion it will be merely termed hereafter as $[D_c]$ and used in the evaluation of the stiffness matrix.

The rigidity matrix $[D_c]$ is defined with respect to the directions of principal stresses at the Gauss point under consideration. To enable its use in global x, y, z space, a process of transformation must follow using the procedure described in Reference (34) as follows:

$$[\,D_c\,]_{x,y,z} = [\,T_\epsilon\,]^T\,[\,D_c\,]\,[\,T_\epsilon\,] \tag{4.60}$$

where $[T_\epsilon]$ is the transformation matrix for strain tensor which takes the following form:

$$[T_\epsilon] = \begin{bmatrix} \ell_1^2 & m_1^2 & n_1^2 & \ell_1 m_1 & m_1 n_1 & n_1 \ell_1 \\ \ell_2^2 & m_2^2 & n_2^2 & \ell_2 m_2 & m_2 n_2 & n_2 \ell_2 \\ \ell_3^2 & m_3^2 & n_3^2 & \ell_3 m_3 & m_3 n_3 & n_3 \ell_3 \\ 2\ell_1\ell_2 & 2m_1m_2 & 2n_1n_2 & (\ell_1m_2+\ell_2m_1) & (m_1n_2+m_2n_1) & (n_1\ell_2+n_2\ell_1) \\ 2\ell_1\ell_3 & 2m_2m_3 & 2n_2n_3 & (\ell_2m_3+\ell_3m_2) & (m_2n_3+m_3n_2) & (n_2\ell_3+n_3\ell_2) \\ 2\ell_3\ell_1 & 2m_3m_1 & 2n_3n_1 & (\ell_3m_1+\ell_1m_3) & (m_3n_1+m_1n_3) & (n_3\ell_1+n_1\ell_3) \end{bmatrix}$$

where ℓ_1, m_1, n_1, are the direction cosines of the first principal stress, ℓ_2, m_2, n_2 are those for the second principal stress, and ℓ_3, m_3, n_3 are for the third principal stress.

The three principal directions are orthogonal to each other. This may be assured by satisfying the following set of equation[(60)]:

$$\begin{aligned} \ell_1\ell_2 + m_1m_2 + n_1n_2 &= 0 \\ \ell_2\ell_3 + m_2m_3 + n_2n_3 &= 0 \\ \ell_3\ell_1 + m_3m_1 + n_3n_1 &= 0 \end{aligned} \tag{4.62}$$

The three principal directions at a point can vary during loading before cracking is initiated, but they are fixed if at least two cracks exist at the point. One crack fixes only one principal direction but constrains the other two to be perpendicular to the crack.

The process described earlier in section 4.2.7 for the calculation of the principal stresses in three dimensional analysis applies to the case when the direction of one or more principal stress is not constrained. Once a crack occurs due to principal stress, say σ_1, this stress will be set to zero and the crack plane must be perpendicular to the direction of this principal stress. In subsequent load cycles, the direction of crack will be fixed and a two-dimensional analysis on the crack plane will be followed to evaluate the values and directions of the other two principal stresses. Section 4.5.6 explains the procedure followed for this purpose.

If the material cracks in two directions, all the principal directions will be fixed , and values of the 'offending' principal stresses will be set to zero.

4.4.5 Modelling of Shear Transfer Across Cracks

After cracking of concrete two main mechanism develop through which shear is transferred from the weak cracked section to the surrounding sound concrete, namely:

a)- aggregate interlocking on the two adjacent surfaces,

b)- dowel action of any reinforcing bars crossing these cracks.

The two mechanism are interrelated and several factors govern their relative contribution towards the total shear transferred. The main known factors are (1)- crack spacing, (2)- presence of reinforcement crossing the cracks, (3)- bar size, (4)- total number of bars crossing, (5)- bar orientation relative to the crack direction, (6)- aggregate size and roughness, (7)- concrete strength, (8)- crack width and (9)- mode of failure.

The mechanisms of shear transfer have been investigated experimentally and several analytical expressions have been suggested. In the finite element modelling, however, these expressions cannot be used directly. In the smeared cracking approach the shear transfer is modelled through the so-called 'shear retention factor',β, which varies between 1 and 0 and is defined as :

$$\beta = G'/G \qquad 4.63$$

where G' is the reduced shear modulus for cracked concrete and G is the shear modulus for the uncracked concrete. Many investigators(61,63,35) have used a constant value for ,β, the value of which was normally determined by trying several reduction factors and finally choosing the value that gave predictions closes to the experimental results of the problem in question. Others[36,37] used a gradually decreasing value for β, following either linear or nonlinear curves. For example, Al-Mahadi[36] proposed the following equations for two-dimensional analysis:

$$\beta = 1 \quad \text{for } \epsilon_1 < \epsilon_{to} \quad \text{(for uncracked concrete)}$$

$$\beta = 0.4\ \epsilon_{to}/\epsilon_m \quad \text{for } \epsilon_1 \geq \epsilon_{to} \qquad 4.64$$

where: ϵ_1 is the maximum principal tensile strain,

ϵ_{to} is the cracking tensile strain which was taken as 0.0002,

ϵ_m is the average of the three principal strains at a cracked point.

In both cases it seems that the shear retention factor has been used more as a numerical device to obtain good results to match experimental data than as a real physical phenomenon. This seems inevitable because of the following reasons:

1)- The actual contribution of the shear transfer mechanisms , i.e., aggregate interlocking and dowel action is not precisely known yet.

2)- More experimental data and also a unification of the existing data is needed.

3)- Even if all that is done ,the treatment of shear transfer with all its components is still uncertain to produce a single finite element model to suit all stress states at one stroke.

4)- Because of the variation of the reinforced concrete behaviour under different loading conditions, the shear transfer is interrelated to other aspects of reinforced concrete behaviour such as tension stiffening and bond-slip behaviour.

5)- In nonlinear finite element analysis, numerical factors such as convergence tolerance, maximum number of iterations, number of increments, etc., also affect results obtained using whatever shear retention model is used[35].

In the present work, irrespective of the number of cracks at the single Gauss point a constant shear retention factor of 0.30 is used for all the cracks at that point.

4.5 Solution of Nonlinear Problems

4.5.1 Introduction

A nonlinear structural problem must obey the basic laws of continuum mechanics. Equilibrium, compatibility and boundary conditions are automatically satisfied in the displacement finite element technique. Common nodes and appropriate interpolation functions ensure continuity and compatibility of displacements along element boundaries, and polynominal shape functions ensure continuity and single valued displacements internally. Therefore it becomes necessary only to enforce that nonlinear constitutive relations are correctly satisfied whilst at the same time preserving the equilibrium of the structure.

There can be several causes of nonlinear behaviour in the structure, which can be divided into three categories:

a) Material nonlinearity

b) Geometric nonlinearity

c) Mixed material and geometric nonlinearity

Stress—strain relations are the major source of nonlinearity. These can vary from short—term nonlinear relationships between stress and strain such as plasticity, cracking, nonlinear elasticity, etc. to time dependent effects such as creep and shrinkage.

Only nonlinearity caused by short—term nonlinear behaviour of concrete and steel is considered in this study. A nonlinear solution is obtained by solving a series of linear problem such that the appropriate nonlinear conditions are satisfied at any stage to a specified degree of accuracy. This technique is required because contrary to linear equations there is no general method which uniquely solves nonlinear equations. In fact it is usually impossible to obtain explicit form of these equations in the first place. One way of achieving this goal is to ensure that at any loading stage, the solution results in stresses consistent which the displacement field and satisfying the given constitutive equations. These stresses will be statically equivalent to the set of internal nodal forces which should be in equilibrium with the externally applied loads. In general, these equivalent nodal forces are not equal to the applied forces and the difference between the external and internal forces are termed "residual forces". These residuals must removed by repeatedly applying them on the structure until an acceptable tolerance on the remaining residual forces is achieved.

4.5.2 Numerical Techniques for Nonlinear Analysis

The solution of nonlinear problems by the finite element method are usually attempted by one of the following basic techniques:

a) Incremental method

b) Iterative method

c) Incremental– Iterative (mixed procedure)

where the nonlinearity occurs in the stiffness matrix [K] which, in the case of short– term behaviour of reinforced concrete, is a function of nonlinear material properties.

The general method of each procedure is similar. For cases where only the material behaviour is nonlinear, the relationship between stress and strain is assumed to be as follows:

$$f(\sigma, \epsilon) = 0 \qquad 4.66$$

The element stiffness matrix is a function of the material properties and can be written as:

$$[K] = K(\sigma, \epsilon) \qquad 4.47$$

The external nodal forces [R] are related to the nodal displacement [δ] through the element stiffness and can be expressed by:

$$[R] = [K][\delta] \qquad 4.68$$

which on inversion becomes:

$$[\,\delta\,] = [\,K\,]^{-1}\,[\,R\,] \qquad 4.69$$

or $$[\,\delta\,] = [\,K(\sigma,\epsilon)\,]^{-1}\,[\,R\,] \qquad 4.70$$

This derivation illustrates the basic nonlinear relationship between $[\,\delta\,]$ and $[\,R\,]$, due to the influence of the material laws on $[\,K\,]$.

Equation 4.70 is solved by successive linear approximations. the three methods mentioned above are now briefly discussed. Further details are given in References (36,57).

4.5.2.1 Incremental Method

The basis of the incremental method is the subdivision of the total applied load vector into smaller increments, which do not usually need to be equal. During each load increment, equation 4.69 is assumed to be linear ,i.e., a fixed value of $[\,K\,]$ is assumed using material data existing at the end of the previous increment. Nodal displacement can be obtained from each increment and these are added to the previous accumulated displacement. The process is repeated until the total load is reached. No account is taken of the force redistribution during the application of the incremental load (i.e., no iteration processes exist to restore equilibrium).

4.5.2.2 Iterative Method

In this method, the full load is applied in one increment. Stresses are evaluated at that load according to the material law. Then the equivalent nodal force are computed These may not be in equilibrium with the externally applied loads. The unbalanced nodal forces $[\,F_u\,]$,i.e., the difference between the external and internal forces, is calculated. These unbalanced forces are then used to compute an additional increment of displacement, and hence new stresses, which give a new set of equivalent nodal forces. This process is repeated until equilibrium is approximated to some acceptable degree.

When this stage is reached the total displacement is taken as the sum of the accumulated displacements from each iteration.

4.5.2.3 Mixed Method (Incremental– Iterative)

The mixed method utilizes a combination of the incremental and iterative schemes. In this case the load is applied in increments but after each increment successive iterations are performed until equilibrium is achieved to the acceptable level of accuracy. Because the mixed method combines the advantage of both the incremental and iterative procedures and tends to minimize the disadvantages of each, the method is widely used. The additional computational effort is justified by the fact that the iterative part of the procedure permits one to assess the quality of the approximate equilibrium at each stage. Further discussions on the merits and demerits of each technique can be found in Reference (34,57).

4.5.2.4 Method Used in This Work

A modified version of mixed procedure is used in the present work. The modified 'Newton– Raphson' approach is used to evaluate the stiffnesses. The stiffnesses are evaluated using a secant rigidity matrix and it was found that varying the stiffness at the second iteration in each increment results in the 'cheapest' solution. For the calculation of the unbalanced nodal forces, a modification of the initial stress method is used, termed the method of 'residual forces'[35,38]. The basic technique is that, at any stage, a load system equivalent to the total stress level is evaluated and checked against the applied loading system. The difference between the two will result in a set of residuals that are a measure of lack of equilibrium. These residuals are then applied to the structure to restore equilibrium. The process is then continued to dissipate the out– of– balance forces (or the residuals) to a sufficiently small value. Thus for equilibrium it is required that:

$$[F_u] = \int_V [B]^T[\sigma]dv - [R] = 0 \tag{4.71}$$

where $[\sigma]$ are the actual stresses depending on the constitutive law being used, $[R]$ is external load vector, $[F_u]$ is the residual forces.

4.5.3 Convergence Criterion

In this study, the convergence process is based on a force convergence criterion because it is a direct measure of equilibrium between the internal and external forces. The convergence is monitored using the following expression:

$$\frac{\left| \sum_{i=1}^{N} (F^r_{u.i})^2 \right|^{0.5}}{\left| \sum_{i=1}^{N} (R_i)^2 \right|^{0.5}} \times 100 \leqslant \text{Toler}(\ 10\%\ ) \tag{4.72}$$

where: N is the total number of nodal points in the system,

r is the iteration number,

F_{ui} is the residual force at node i, and

R is the total external applied load at node i.

4.5.4 Analysis Termination Criterion

The programme must have some means of detecting the collapse of the structure. The failure of the structure takes place when no further loading can be sustained. An allowable maximum deflection can be used as a criterion to stop the analysis at failure. An empirical expression can be used to detect maximum deflection, but obviously this needs great care and no one expression can fit all situations.

The maximum iterations can be used for this purpose. When a specified number of iterations has been performed without achieving convergence, the structure is deemed to have failed and the failure load can then be estimated. It must be mentioned here that this criterion is not always sufficient to indicate the failure of the structure but it can be satisfied when severe discontinuity due to extensive cracking occurs or in the event of large displacement. It may also occur when large load increments are used or very tight convergence tolerances are specified. However, if realistic maximum number of iterations is used and the solution does not converge then this can be realistic indication of failure.

4.5.5 The Frontal Solution Technique

In the nonlinear stress analysis using finite elements, using elements with large number of degrees of freedom improves accuracy. However, this inevitably results in a large set of simultaneous equations to be solved repeatedly, thus creating high demand for computer storage. In this work, a version of the frontal solution modified by Hinton and Owen(53), is used. The main feature of the frontal solution technique is that, it assembles the equations and eliminates the variables at the same time. This means that the total stiffness matrix of the structure is never formed as such, since the reduced equations corresponding to the eliminated variables are stored in core in a temporary array called a buffer area(38). As soon as this array is full, the information is then transferred to disc. This process results in a considerable efficiency in the way core storage is handled.

4.5.6 Computational Procedure

Consider the analysis at a particular iteration i, the displacements are calculated according to equation 4.70 using the appropriate rigidity matrix $[D]_{x,y,z}$.

(1) For every stress sampling point, evaluate the incremental values of strains $[\Delta\epsilon_i]$ and stresses $[\Delta\sigma_i]$ using the appropriate rigidity matrix $[D]_{x,y,z}$.

(2) Check whether the sampling point under consideration has suffered from a compressive crushing situation in any of the previous load cycle, if so step (8) will be executed.

(3) Check whether this sampling point has suffered from a tensile cracking situation in any of the previous load cycles, if so step (7) will be executed.

(4) Using the stress– strain relationships describing the concrete material law, evaluate the total actual stresses in concrete $[\sigma_i]$ which correspond to the calculated total strains.

$$[\ \epsilon_i\ ] = [\ \epsilon_{i-1}\ ] + [\ \Delta\epsilon_i\ ]$$

$$[\ \sigma_i\ ] = [\ \sigma_{i-1}\ ] + [\ D_{x,y,z}\ ]\ [\ \Delta\epsilon_i\ ]$$

(5) Check for concrete compressive failure criteria violation. If violated, all the stress components at this Gauss point will be set to zero in this iteration and in all the subsequent load cycles: $[\sigma_i] = 0$. The components of the rigidity matrix will also be set to zero for stiffness calculations in all the subsequent load cycles.

$$[D]_{x,y,z} = 0.0$$

(6) Check for concrete tensile failure criteria. If violated a crack will occur, thus a new rigidity matrix $[D_c]_{x,y,z}$ will be formulated according to the number and directions of the cracks.

(7) If a crack previously occured in one direction it is necessary to check for further cracking as follows:

a)– For the previous load cycle, the principal stresses σ_1, σ_2, σ_3 had the direction cosines (ℓ_1, m_1, n_1), (ℓ_2, m_2, n_2) and (ℓ_3, m_3, n_3) respectively. These directions are termed here as x', y', z' as shown in Figure 4.12.

b)– In the present load cycle, these direction cosines which were obtained from the previous load cycle were used in stiffness calculation to evaluate the new stress vector $[\sigma]$

with regard to the appropriate rigidity matrix $[D_c]$.

c)- Now for principal stress calculation in cracked material, the new stress vector $[\sigma]$ will be transformed from x, y, z space to $[\sigma']$ in x', y', z' space by:

$$[\sigma'] = [T_\sigma][\sigma] \qquad 4.73$$

where $[T_\sigma]$ is the transformation matrix for stress vector[34] which takes the following form :

$$[T_\sigma] = \begin{bmatrix} \ell_1^2 & m_1^2 & n_1^2 & \ell_1 m_1 & m_1 n_1 & n_1 \ell_1 \\ \ell_2^2 & m_2^2 & n_2^2 & \ell_2 m_2 & m_2 n_2 & n_2 \ell_2 \\ \ell_3^2 & m_3^2 & n_3^2 & \ell_3 m_3 & m_3 n_3 & n_3 \ell_3 \\ \ell_1 \ell_2 & m_1 m_2 & n_1 n_2 & (\ell_1 m_2 + \ell_2 m_1) & (m_1 n_2 + m_2 n_1) & (n_1 \ell_2 + n_2 \ell_1) \\ \ell_1 \ell_3 & m_2 m_3 & n_2 n_3 & (\ell_2 m_3 + \ell_3 m_2) & (m_2 n_3 + m_3 n_2) & (n_2 \ell_3 + n_3 \ell_2) \\ \ell_3 \ell_1 & m_3 m_1 & n_3 n_1 & (\ell_3 m_1 + \ell_1 m_3) & (m_3 n_1 + m_1 n_3) & (n_3 \ell_1 + n_1 \ell_3) \end{bmatrix}$$

The new transformed stress tensor,will be (see figure 4.11)

$$[\sigma'] = [\ \sigma'_x \quad \sigma'_y \quad \sigma'_z \quad \tau'_{xy} \quad \tau'_{yz} \quad \tau'_{zx}\ ]^T \qquad (4.75)$$

and if for instance a crack is caused by σ_1, the value of σ'_x will be set to zero ($\sigma_1 = \sigma'_x$), and to evaluate the new values of σ'_2, and σ'_3 we are dealing with a two dimensional problem of which the active stress components are σ'_y, σ'_z and τ'_{yz}, thus

$$\sigma'_2\ ,\ \sigma'_3 = \frac{\sigma'_y + \sigma'_z}{2} \pm \sqrt{\left[\frac{\sigma'_y - \sigma'_z}{2}\right]^2 + (\tau'_{yz})^2} \qquad (4.76)$$

$$\tan 2\alpha = \frac{2\tau'_{yz}}{\sigma'_y - \sigma'_z} \qquad (4.77)$$

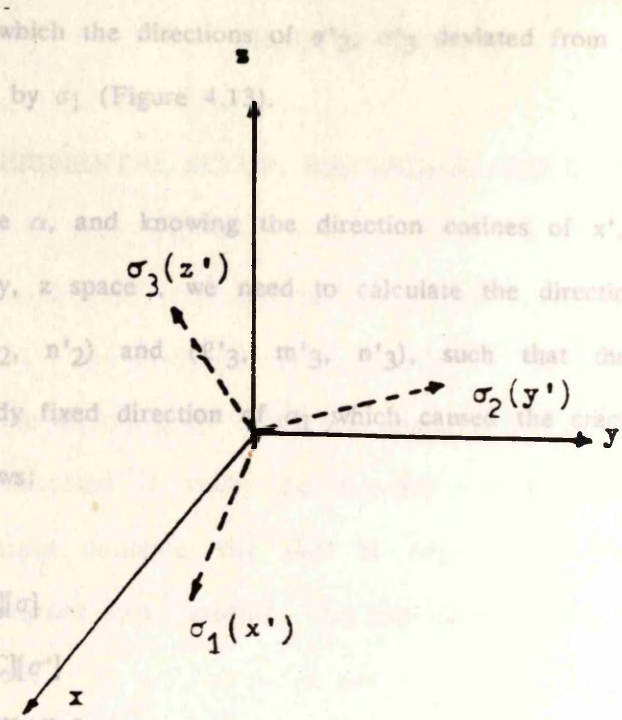

Figure (4.12) : Principal stresses in global axes.

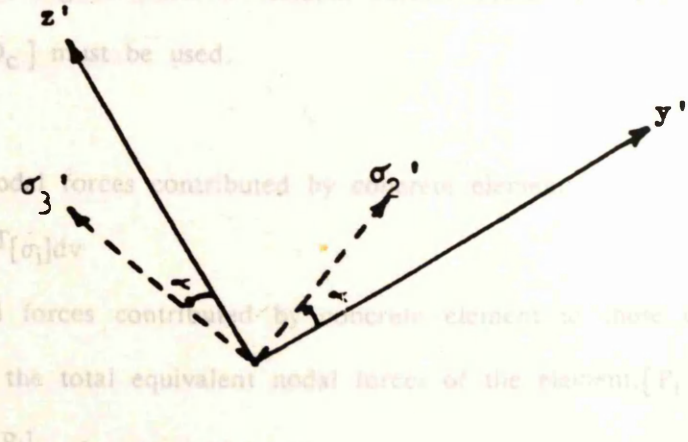

Figure (4.13) : The angle of the new principal stress direction where α is the angle by which the directions of σ'_2, σ'_3 deviated from y', z' axes in the event of the crack caused by σ_1 (Figure 4.13).

d)– Having got the angle α, and knowing the direction cosines of x', y', z' axes with respect to the global x, y, z space , we need to calculate the direction cosines of σ'_2, σ'_3 which are (ℓ'_2, m'_2, n'_2) and (ℓ'_3, m'_3, n'_3), such that their plane remains perpendicular to the already fixed direction of σ_1 which caused the crack in our example. This can be done as follows:

if $[\sigma'] = [A][\sigma]$

and $[\sigma''] = [C][\sigma']$

then $[\sigma''] = [C][A][\sigma]$

where $[A]$ and $[C]$ are the appropriate transformation matrices. The product $[C][A]$ will contain all the required direction cosines of the new principal stresses contained in $[\sigma'']$.

e)– These nine values of direction cosines will be the ones to be used in the next load cycle for stiffness and new stress vector calculation, and values of the principal stresses σ'_2, σ'_3 will be used to check against the cracking criterion because σ_1 was set to zero (in this example). If the cracking criterion is violated further cracks will occur and the appropriate rigidity matrix $[D_c]$ must be used.

(8) Evaluate the equivalent nodal forces contributed by concrete element

$$[P_i]_{conc.} = \int_v [B]^T[\sigma_i]dv$$

(9) Add the equivalent nodal forces contributed by concrete element to those contributed by steel reinforcement to get the total equivalent nodal forces of the element, $[P_i]$

$$[P_i] = [P_i]_{conc.} + [P_i]_{steel}$$

(10) Check the convergence.

CHAPTER FIVE

EXPERIMENTAL SETUP, MATERIALS AND INSTRUMENTATION

5.1 Introduction

This chapter describes in detail the experimental set up which has been designed and constructed to study the strength and behaviour of a series of unbonded prestressed concrete flat slab at edge column junction under the monotonic and reversed cyclic loading. The experimental work is divided into two test series as follows:

a)– Main test series which consists of six models, MS1 to MS6.

b)– Reversed cyclic loading series which consists of two models, RCS7 and RCS8.

The detailed description of these models and their behaviour will be described in Chapters six and seven. In this chapter the materials used for the construction of the models and their properties are described. The instruments employed for measurements of the strains and deflections during the test, as well as the test procedure, are also explained.

5.2 Material Used

5.2.1 Concrete

The concrete mix consisted of rapid hardening portland cement and 10^{mm} uncrushed aggregate. A mix proportion of 1 : 1.6 : 2.0 was used for an average cube strength of 45 N/mm^2 at 7 days. After having mixed these materials for about two minutes in a dry state, water was added such that the water cement ratio was 0.45. Six 100 mm cube and four 150mm × 300mm cylinders were cast with each specimen. The cubes were used to determine the cube strength, two cylinders for the split tensile strength and remaining cylinders to determine the Young's modulus and the compressive strength of the cylinder. For each model about 550 Kg concrete in 7 or 8 batches was used.

5.2.2 Reinforcing Steel

High yield deformed and hot rolled bars of diameter 6, 8 and 10 mm were used as reinforcement. Random samples were cut from the batches of steel bars for all the different diameters and were tested in Tinius Olsen Universal Class A testing machine. Typical stress–strain curves for each diameter obtained from the testing machine are shown in Figures 5.1 to 5.5. Since the yield point for all the bars was not well defined, the yield stress of the bar was taken as the stress at which a line parallel to the initial slope of the curve from 0.2% proof strain intersects the curve. The yield strain was calculated as shown in Figure 5.1. The properties of 'unstressed' and prestressed steel bars are presented in Table 5.1.

5.3 Preparation of Specimens

5.3.1 Strain Gauging on Steel

The first step towards specimen preparation was the fabrication of reinforcement and mounting of the steel strain gauges at selected positions on the reinforcing bar. For fixing strain gauges on steel, the bar surface at the required location was filed and smoothened with sand paper. Care was taken not to

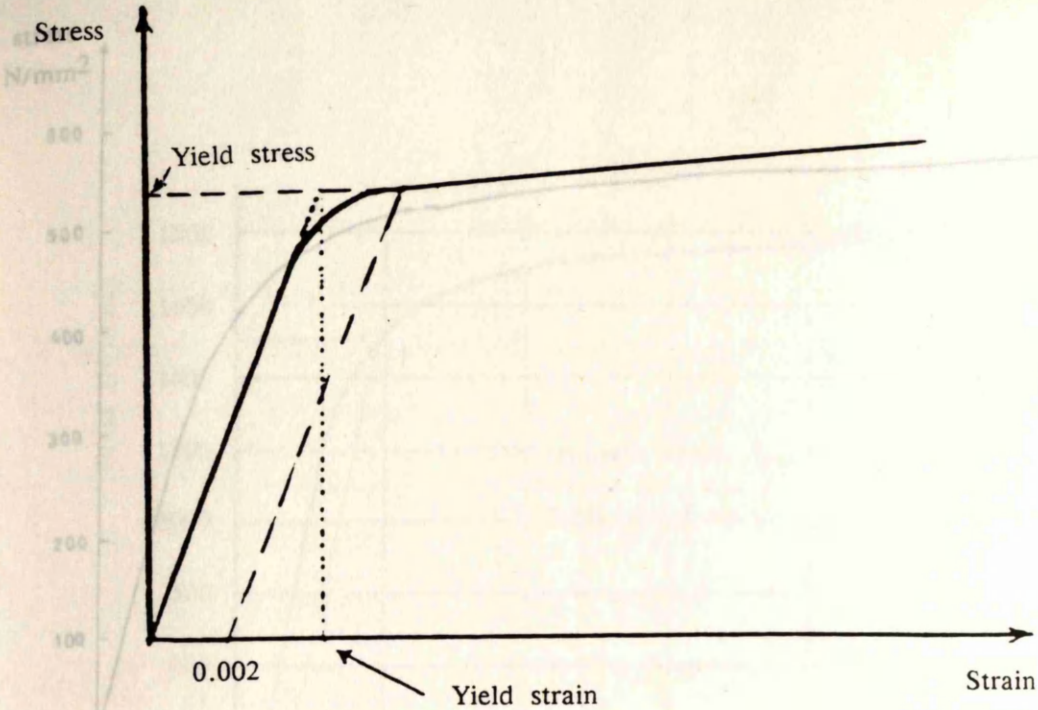

Figure 5.1 : Definitions of yield stress and strain of steel reinforcement.

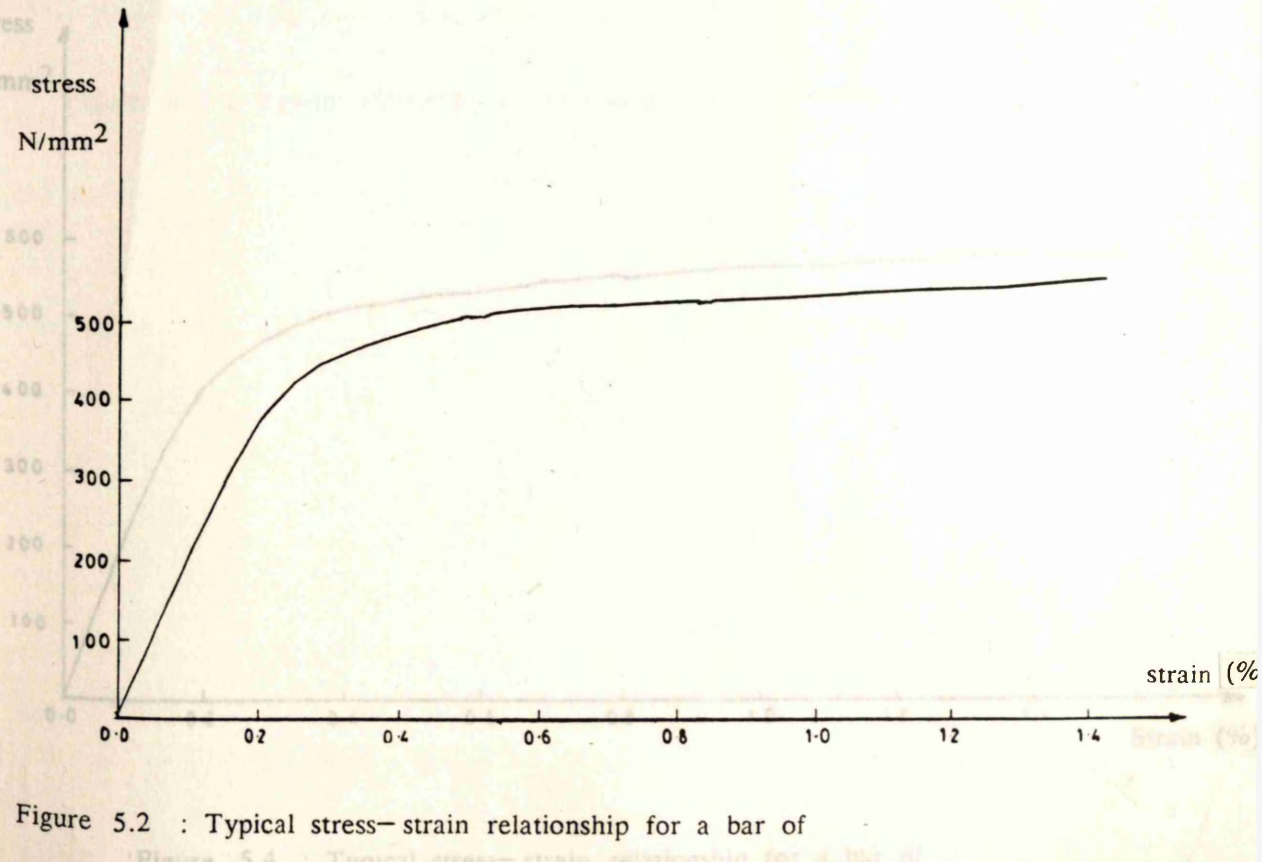

Figure 5.2 : Typical stress– strain relationship for a bar of 6 mm diameter.

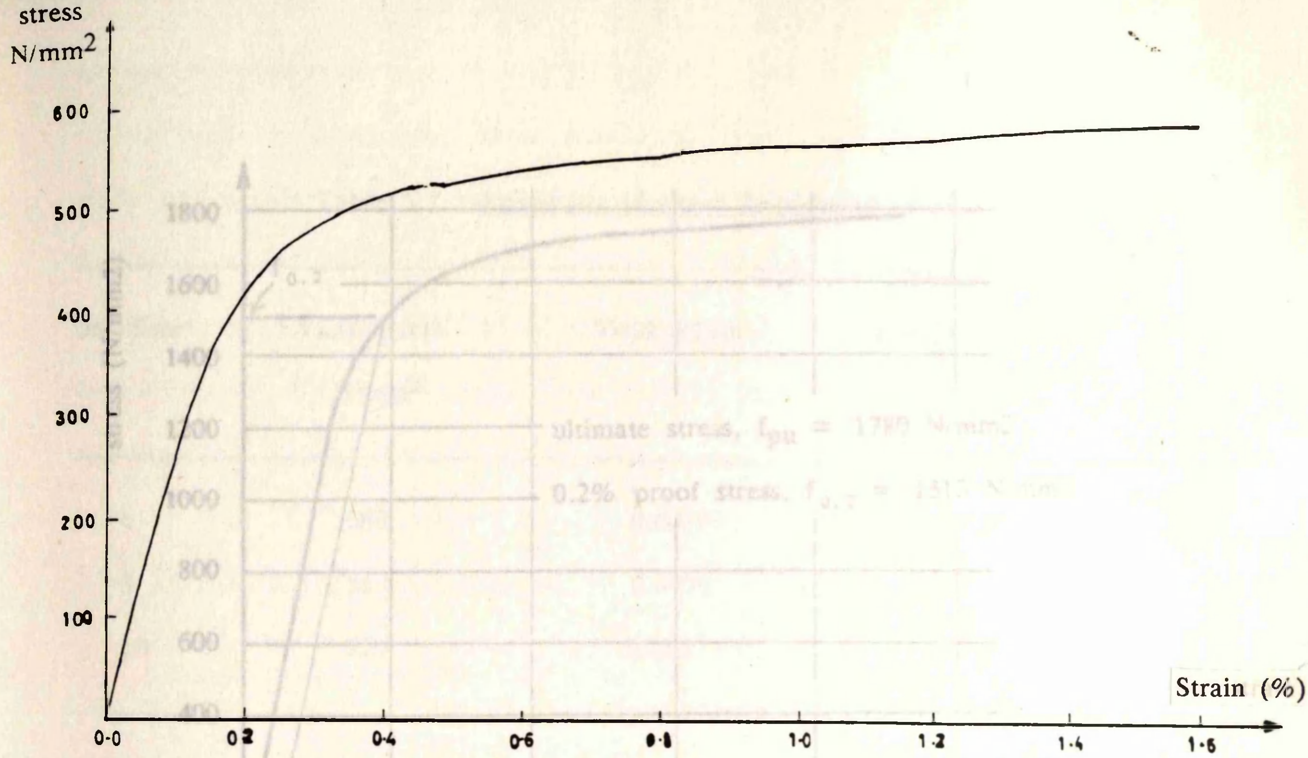

Figure 5.3 : Typical stress– strain relationship for a bar of 8 mm diameter.

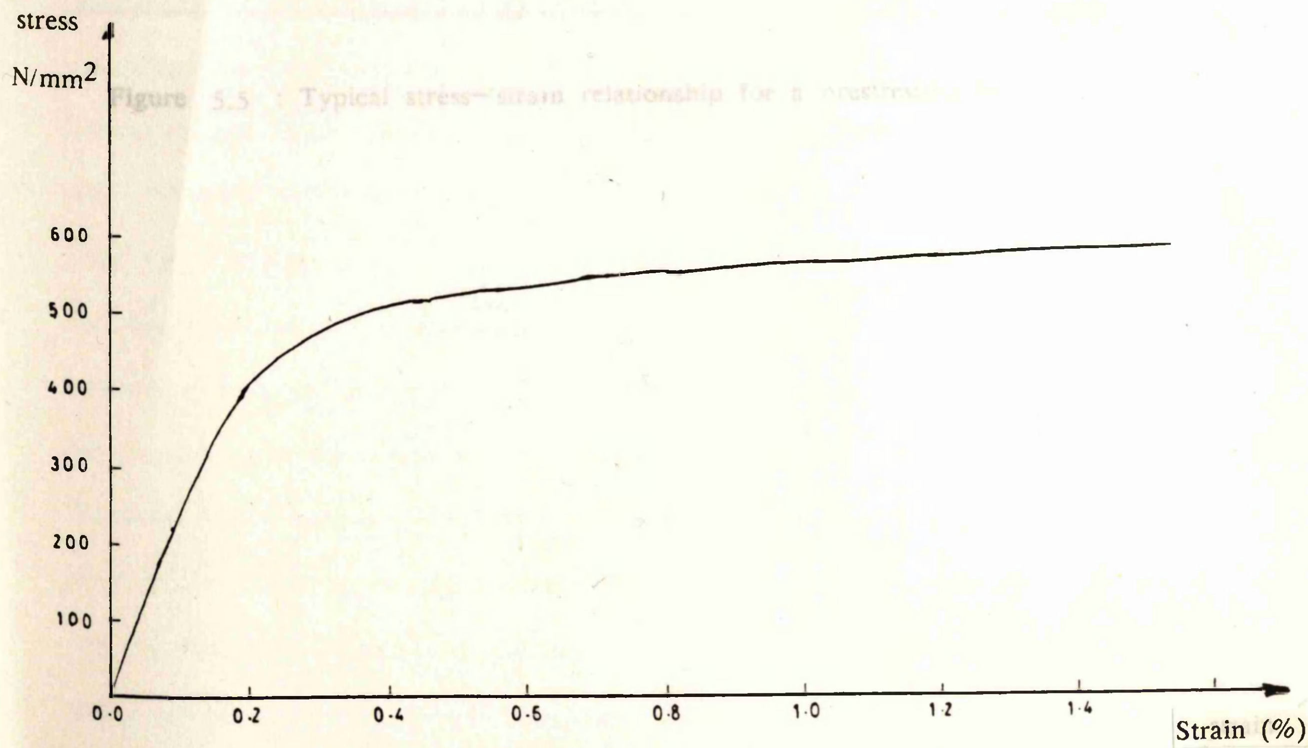

Figure 5.4 : Typical stress– strain relationship for a bar of 10 mm diameter.

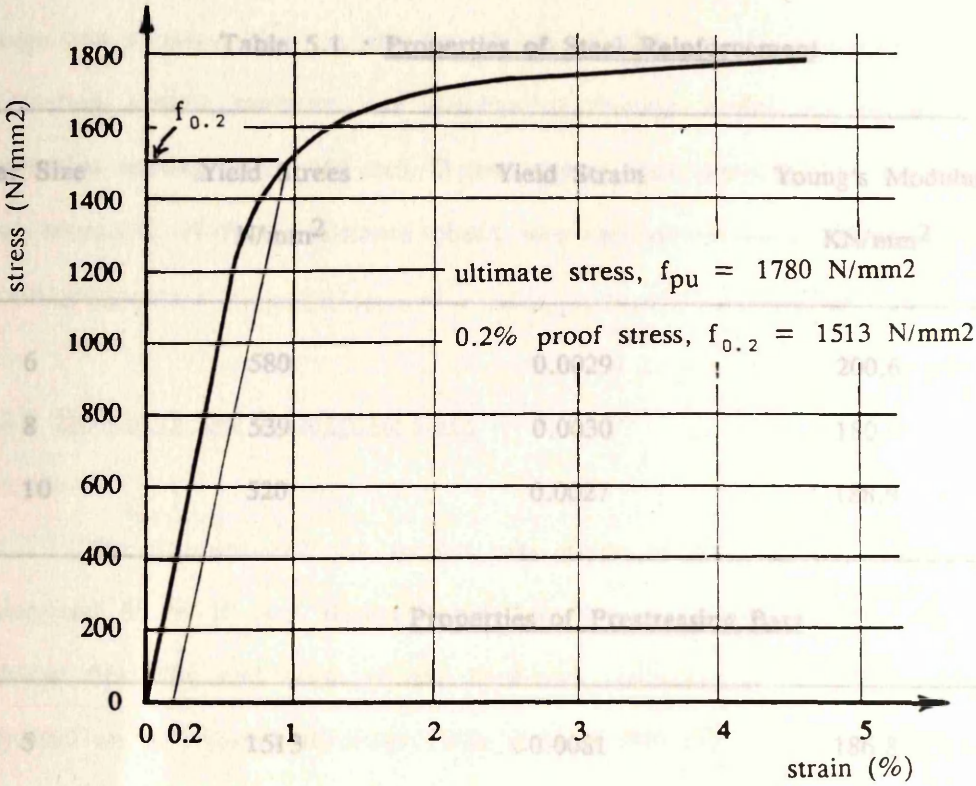

Figure 5.5 : Typical stress– strain relationship for a prestressing bar

Table 5.1 : Properties of Steel Reinforcement

Bar Size	Yield Strees N/mm^2	Yield Strain	Young's Modulus KN/mm^2
6	580	0.0029	200.6
8	539	0.0030	180.0
10	520	0.0027	188.9

Properties of Prestressing Bars

Bar Size	Yield Strees N/mm^2	Yield Strain	Young's Modulus KN/mm^2
5	1513	0.0081	186.8
7	1380	0.0072	191.7

remove a considerable area of steel during this operation. The surface was then cleaned with M- prep neutralizer to remove dirt and grease. To cement the strain gauge and terminal strip on the bar, M- bond 200 adhesive was used. For gauge protection against moisture and mechanical damage during casting and testing, protective coating white M- coat D and epoxy resin were applied on the gauges and terminals. A final resistance check was carried out by a voltmeter for each strain gauge.

5.3.2 Formwork and Reinforcing Cage

The formwork of the models was made of 18^{mm} thick coated plywood sheet and 50 × 50 mm timber battens were used to reinforce the corners. To achieve flexibility and reuse of the formwork, slab and column dimensions were adjusted on a plywood sheet of 1300 × 1300 ^{mm}. All formwork was oiled for easy removal. First the column reinforcement was properly positioned in the formwork and then the slab reinforcing cage was placed. The nylon tubes of 12 mm diameter were threaded through the holes prepared in four sides of the formwork and fixed together to keep them in their positions. Then the tendons were threaded through the nylon tubes. The tendons in the X- direction (Figure 5.6) were straight with the maximum eccentricity of 30 mm at the edge containing the column as shown in Figure 5.6 section A- A. The eccentricity was ensured by position of the holes. Furthermore, these tendons were supported from the column and slab reinforcing cages to remain in a straight line. In the Y- direction the tendons were curved as shown in Figure 5.6 section B- B. These tendons were tied up to the tendons which passed through the column head in the X- direction. Figure 5.7a shows the formwork and reinforcing cage of the slab and column. In Figure 5.7b the model is ready to receive concrete.

5.3.3 Casting and Curing

Casting was normally done in seven to eight batches of concrete, depending on the size of the model. The lower portion of the column was cast first and then the slab was cast and finally the upper portion of column was cast. The specimen was compacted using 25mm internal poker vibrator. The cubes and cylinders mentioned in section 5.2.1 were compacted by means of a vibrating table. A 20mm diameter steel rod was used for providing a hole in the column used for fixing the column to the floor (Figure 5.10). Similar diameter plastic tubes were used to provide holes in the slab for loading purpose (see section 5.4.3.3). At the end of the day all the tubes and the rod were removed from the concrete.

After casting, the model and the control cubes and cylinders were covered in wet hessian and cured under damp environment for the first three days. The specimen was then removed from the formwork for final curing under laboratory conditions until the time of testing. The three cubes and the two cylinders were kept in the curing room in water and the remaining were kept with the model.

5.3.4 Demec Gauges and Strain Gauges on Concrete Surface

The specimen was painted white in order to enable clear tracing of cracks. Demec gauges were glued to the top concrete surface. On the bottom compressive face 30 mm long strain gauges were fixed at marked positions as shown in Figure 5.8. For fixing the strain gauges, the concrete surface was firstly cleaned and smoothened by grinding, using a grinding stone and then smoothened by fine emery paper. Carbon tetrachloride was used to remove the grease and dirt. A thin coating of Adhesive and Hardner mixture was applied to the cleaned surface

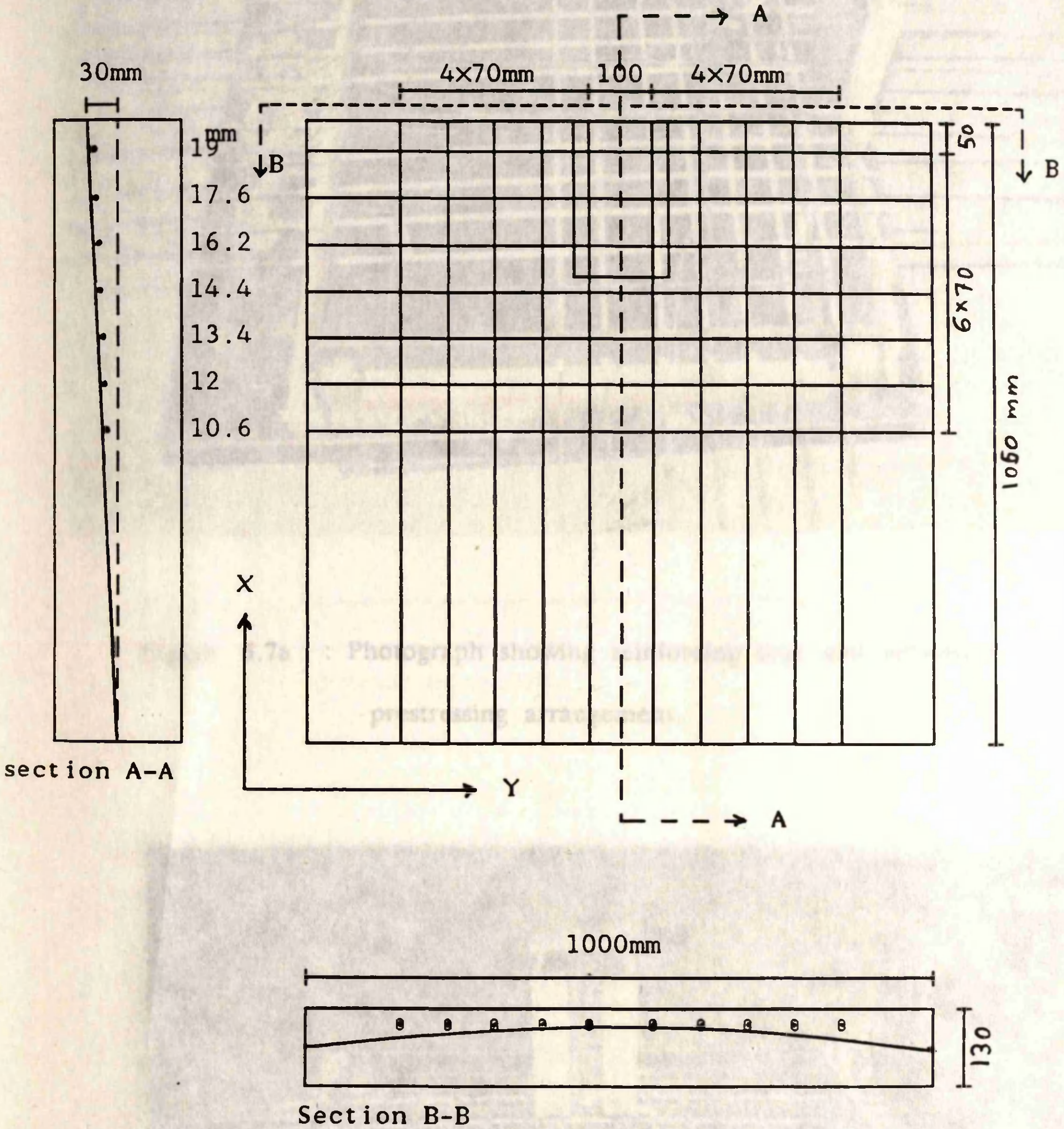

Figure 5.6 : layout of prestressing bars

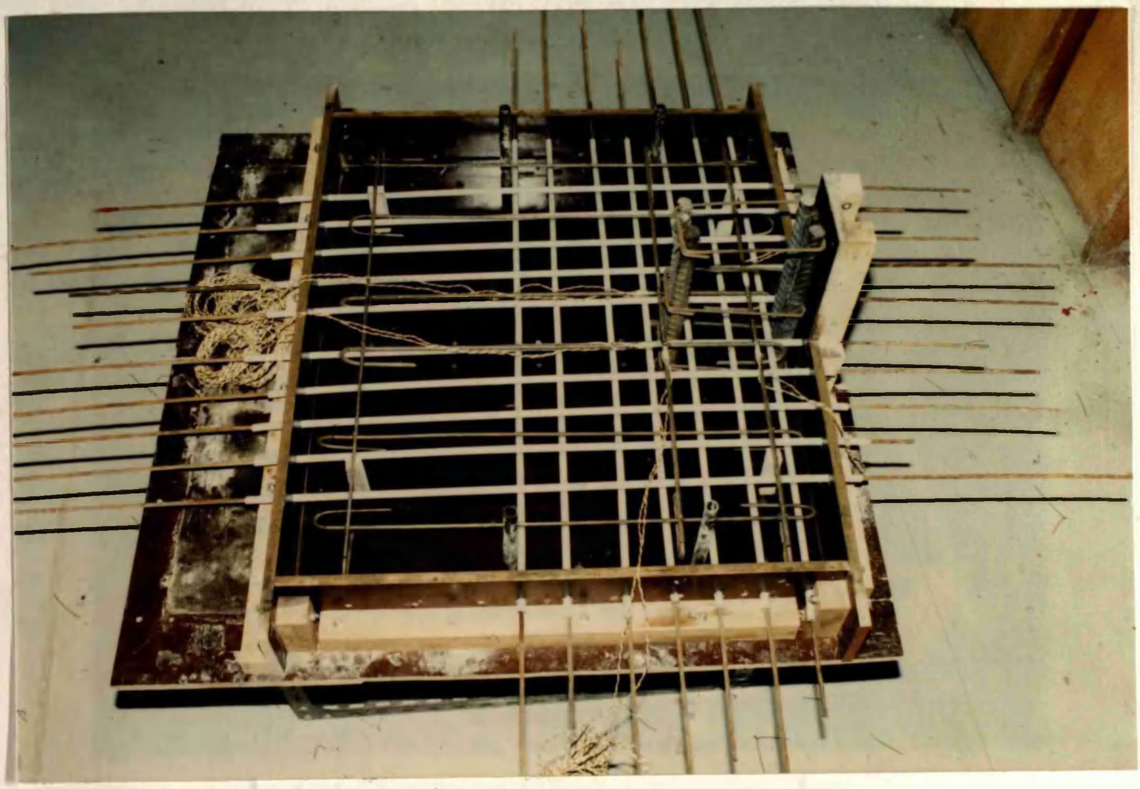

Figure 5.7a : Photograph showing reinforcing cage and unbonded prestressing arrangement.

Figure 5.7b : Photograph showing the bars and tubes for making hole in the column and slab, model is ready to cast.

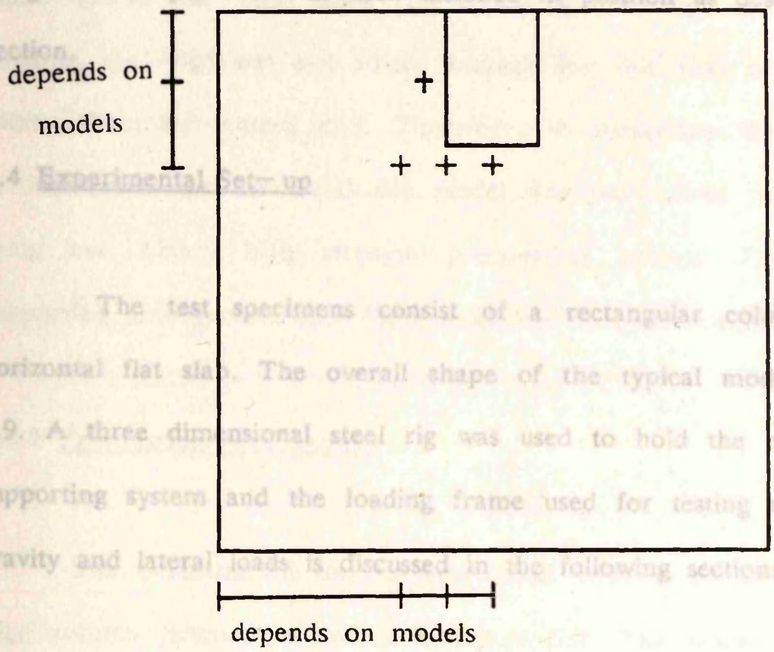

Figure 5.8 : Locations of strain– gauges on the surface of concrete.

and the strain gauge was stuck on it by firmly pressing with the thumb for about two minutes. After a few hours, the wires were soldered to the gauges and terminals. Protective coating (white M–Coat D) was then applied to the strain gauges. The specimen was then installed in position as described in the following section.

5.4 Experimental Set–up

The test specimens consist of a rectangular column stub supporting a horizontal flat slab. The overall shape of the typical model is shown in Figure 5.9. A three dimensional steel rig was used to hold the model in position. The supporting system and the loading frame used for testing the models under both gravity and lateral loads is discussed in the following sections.

5.4.1 Supporting Arrangement

The steel rig was used to support the model against rotation due to application of lateral load as shown in Figures 5.10 and 5.11a. The model had a vertical hole in the column. Through this hole the model was clamped to the "laboratory floor" using a 12mm diameter prestressing strand. To avoid horizontal slipping of column ends, two additional support system were designed to restrain the top and bottom ends of the column against horizontal movement during the application of lateral (wind) load as shown in Figures 5.10, Sections A–A and B–B , and 5.11c.

For the cyclic loading series, when the lateral load was applied in an upward direction, the model started to rotate about the back edge of the column 'GH' (see Figure 5.9) and the previous supporting system was found to be ineffective in resisting the upward rigid body movement of the model. That is, in the case of downward loading the shear force is directly transferred to the rigid floor by column stub, but in the case of upward loading this shear force is transferred to the 'rigid floor' by means of the 'rig' as shown in Figure 5.12. Because the 'rig' was not strong enough for this kind of loading, it started to rotate about its bottom end. Therefore, to strengthen the 'rig', another hollow section beam was used and the model was held down by that transverse beam using two 12mm high strength prestressing strands. Figure 5.11b shows the supporting arrangement used for the models of cyclic loading series.

5.4.2 Prestressing Arrangement

The experimental models were 1050 × 1000 × 130 mm flat slab with an edge column junction as shown in Figure 5.9. The model was prestressed in the longitudinal and transverse directions using unbonded tendons. In each model ten unbonded tendons were used in the longitudinal direction (X− dir.) and seven tendons in transverse direction (Y− dir.). The distance between the tendons was 100 mm centre to centre for model MS1 and 70 mm for the remaining models. Before casting the model, nylon tubes of about 1.5 m in length and 12 mm diameter were threaded through the holes made in formwork at appropriate positions. Then the tendons were threaded through the nylon tubes and connected together and also to formwork to make a firm network against any movement due to vibration of concrete.

5.4.3 Loading Arrangement

5.4.3.1 Prestressing Loads

After the model was fixed by 'rig' and supporting system, and all wires related to strain-gauges were connected to the data logger , all strains, stresses and deflection readings are set to zero. Then both ends of each tendon were fixed on the concrete in the following order:

Stressing End: This consists of a plate, a load cell to monitor prestressing in the tendon, an additional plate and the grip respectively as shown in Figure 5.13a. The load cell used is described in section 5.5.1.

Fixed End: This consists of a plate, a load cell, a ballbearing, a nut-bolt system, an additional plate and the grip respectively as shown in Figure 5.13a.

All the equipment is put together for each type of end condition so that at each side of the model the two types of 'anchorages' alternated as shown in Figure 5.13b. The prestressing load is applied by turning the nut gradually by spanner in increments up to the desired level of prestressing before the application of any gravity or lateral load.

5.4.3.2 Gravity Load

In the first model, the gravity load was applied to each side of the model at three points by tightening the nuts on the three rods as shown in Figure 5.14. One end of the rod was anchored to a beam which had been anchored to the floor of the laboratory and the other end to the top surface of the slab. For each bar, a load cell of 50^{KN} capacity was used to monitor the applied gravity load. But after each increment of lateral loading, the gravity load would be adjusted to maintain its value.

After early stages of lateral loading, due to the deformation caused by application of the lateral load, high tensile force occurred in the bars beside the

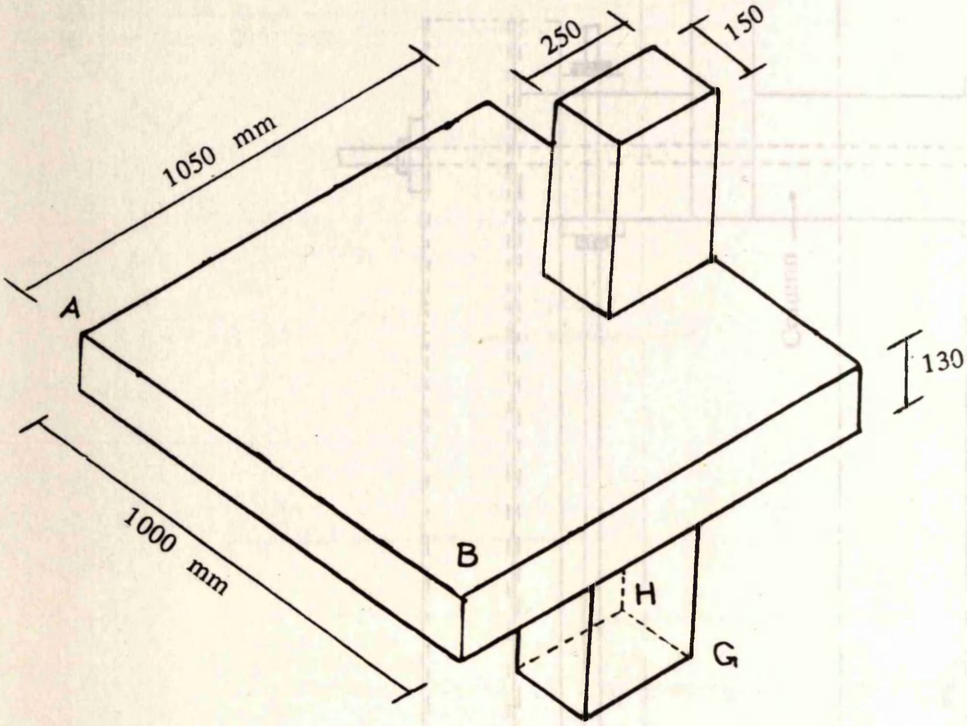

Figure 5.9 : An isometric view of a typical model

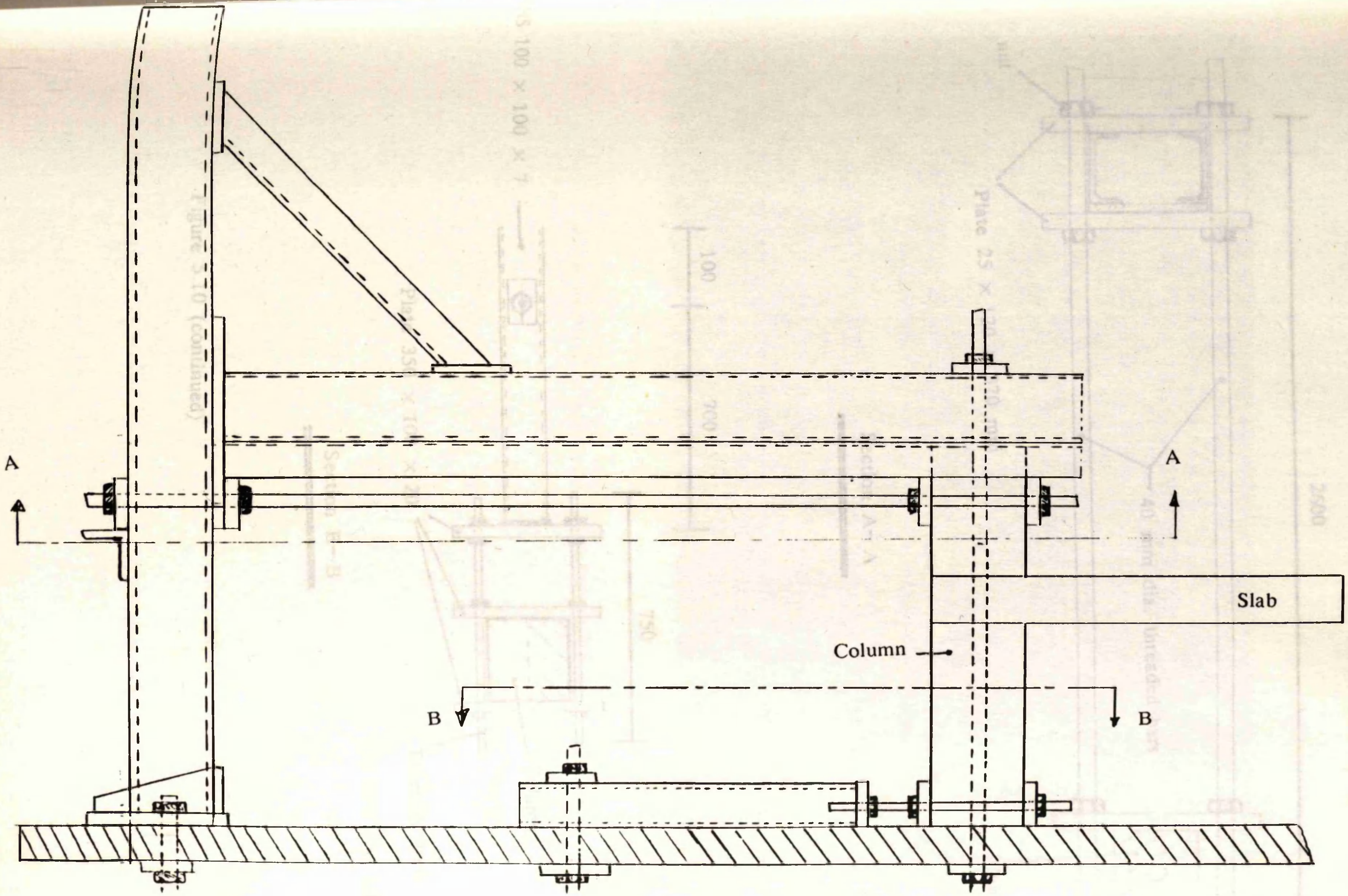

Figure 5.10: Supporting arrangements for models MS1 to MS6.

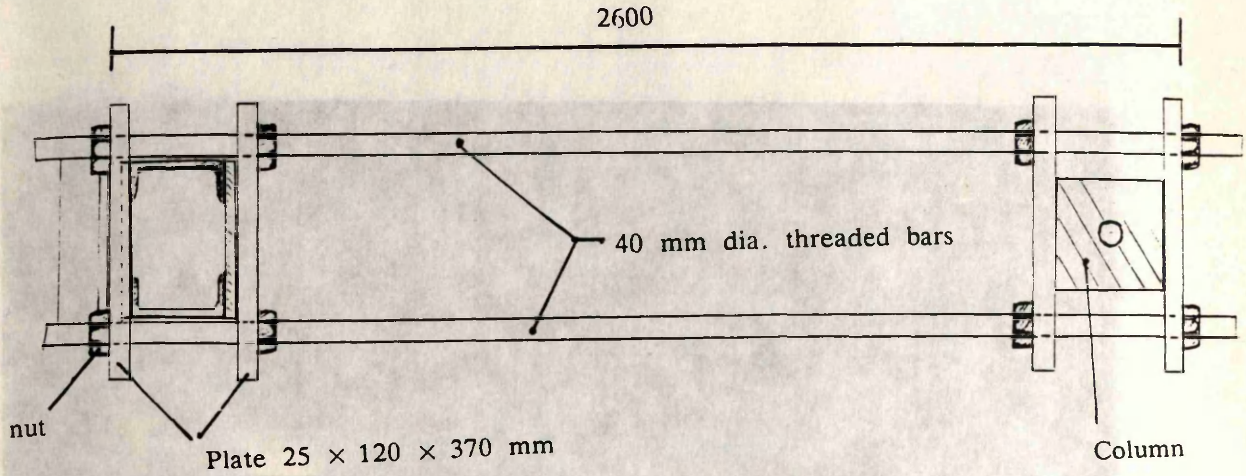

Section A– A

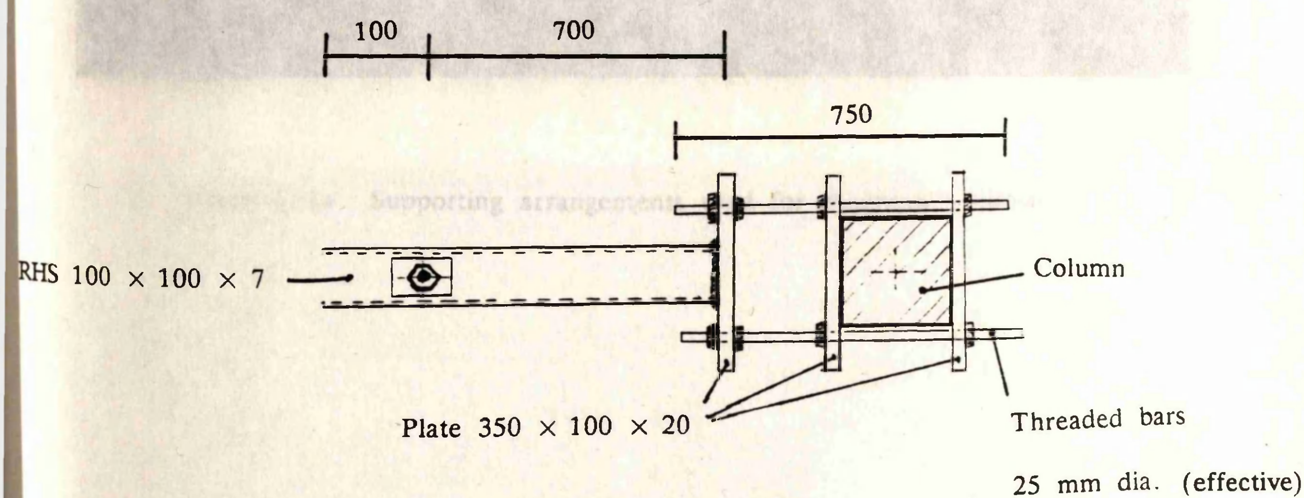

Section B– B

Figure 5.10 (continued)

Figure 5.11a : Supporting arrangements used for monotonic loading

Figure 5.11b: Supporting arrangements used for cyclic loading

Figure 5.11c: Supporting system for column (bottom end) against horizontal movement.

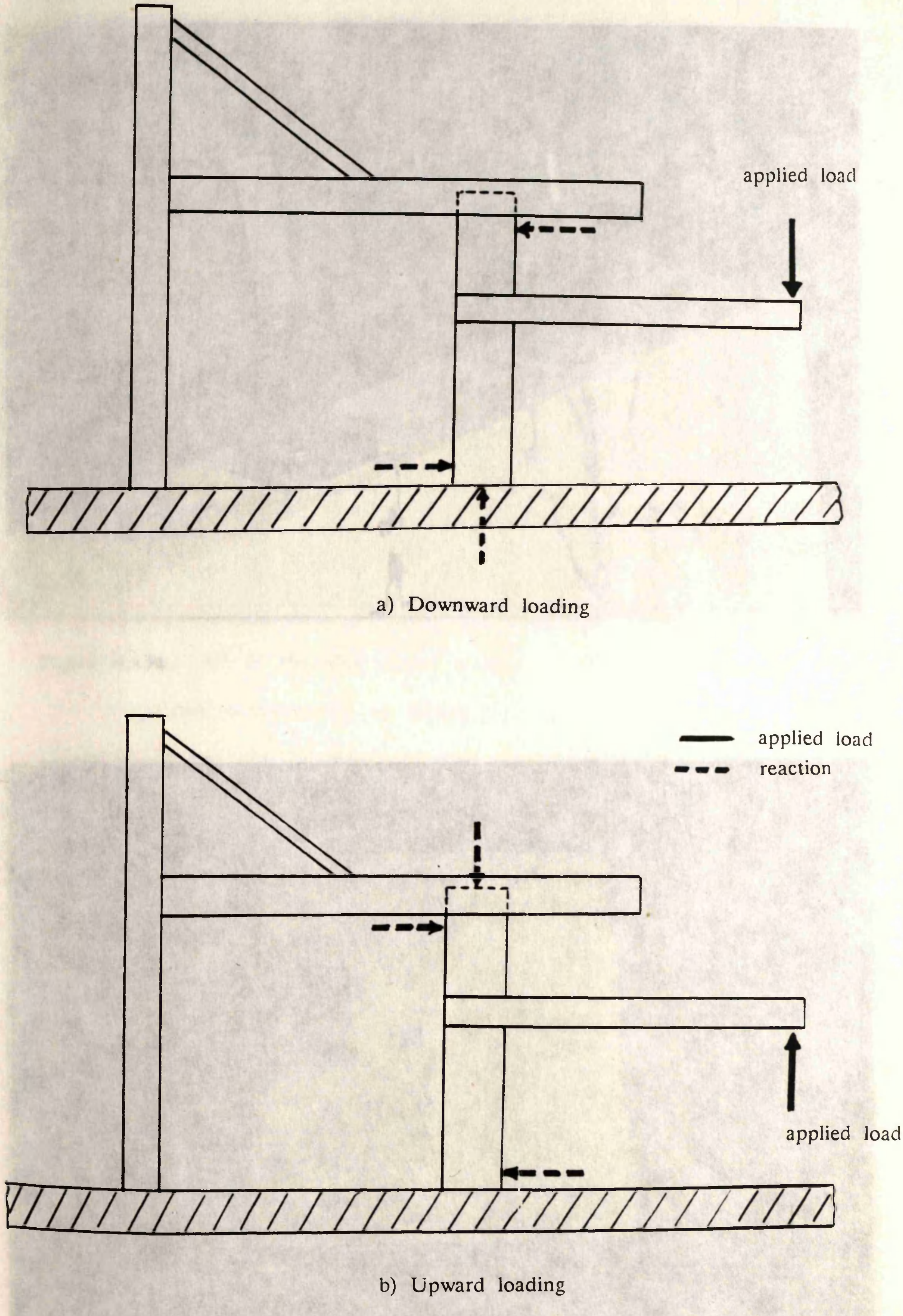

Figure 5.12 : Load transfer from the slab to the 'laboratory' floor.

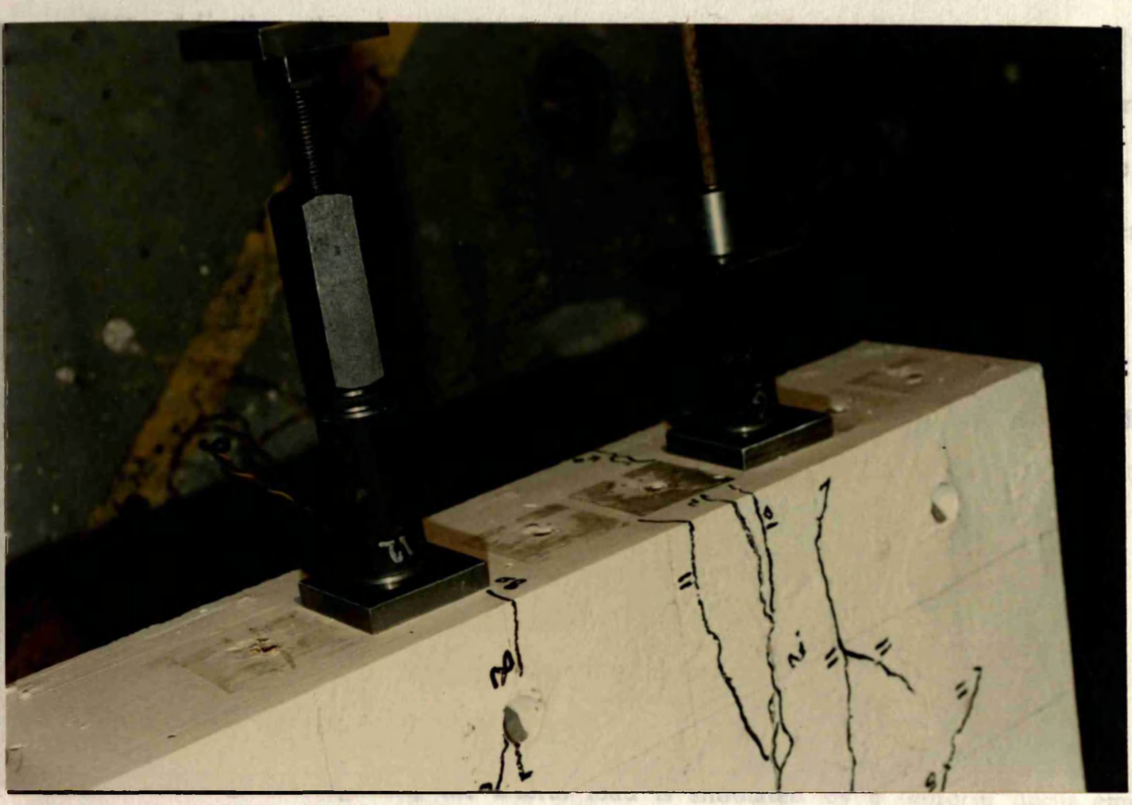

Figure 5.13a

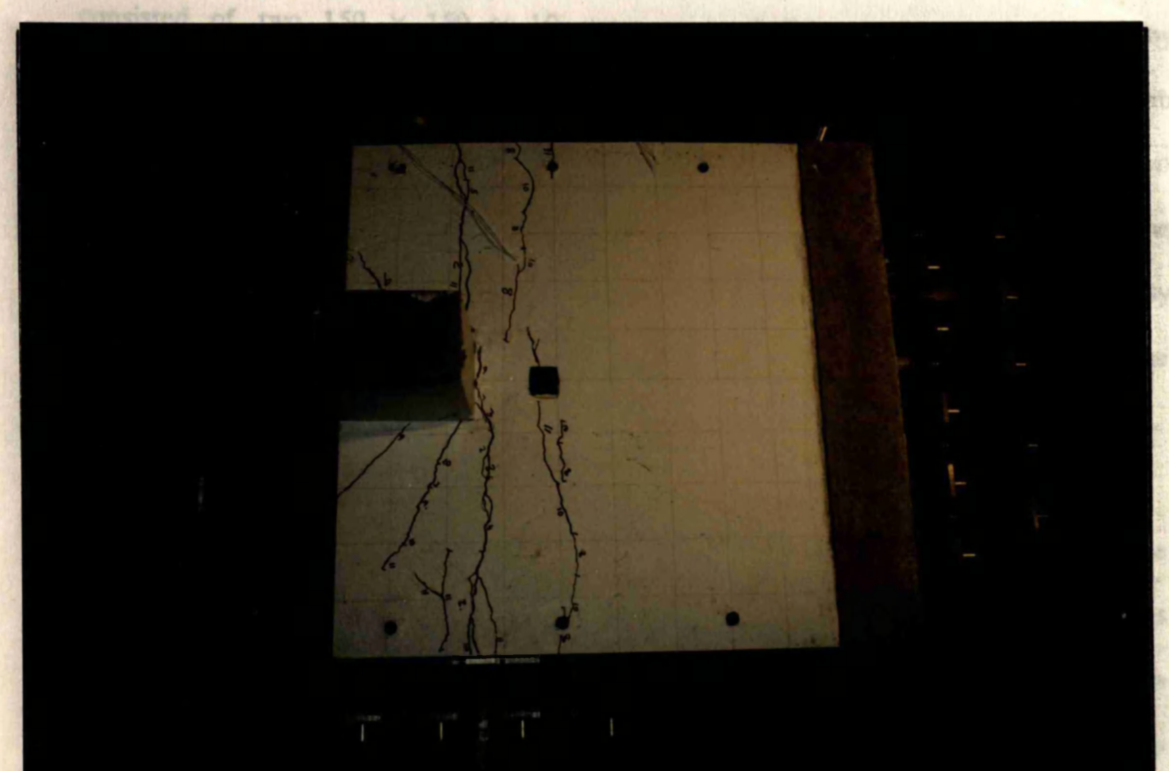

Figure 5.13b

column whereas in the bars near the loaded edge the tensile force dropped to zero. Adjusting the six gravity point loads at each lateral load increment was time–consuming and monitoring of seven loads [6(gravity) + 1(lateral)] simultaneously was not possible. Using the available data logger, it was possible to monitor only four readings simultaneously. In order to solve this problem, each gravity load at one side of the model was connected to its counterpart at the other side by small jacks. In this way instead of applying and adjusting six separate gravity loads by hand, it is done by three jacks which makes it possible to monitor all the jacks [3(gravity) + 1(lateral)] as well. Figure 5.15 shows the gravity loading arrangement for models MS2 to MS6.

5.4.3.3 Lateral Load

In this investigation, the lateral load is simulated by a uniform displacement of the edge AB of the slab shown in Figure 5.9. This was achieved for the models, loaded monotonically to failure, by means of the loading frame which consisted of two 150 × 150 × 10 mm square hollow section, strengthened by welding 12 mm thick plates. The upper beam rested on the edge of the slab while the lower beam was supported by the upper beam by means of two threaded steel rods of 35 mm diameter mild steel, one on each side of the beams, as shown in Figure 5.16. The frame was pulled down by a manually operated hydraulic jack of 500 KN capacity as shown in Photograph 5.17. The load was measured by a load cell.

For the models which where tested for reversed cyclic loading, the downward and upward load was applied by a slightly modified loading frame as shown in Figure 5.18. An additional steel frame was designed and constructed to carry the downward reaction of the hydraulic jack when the frame was pulled up

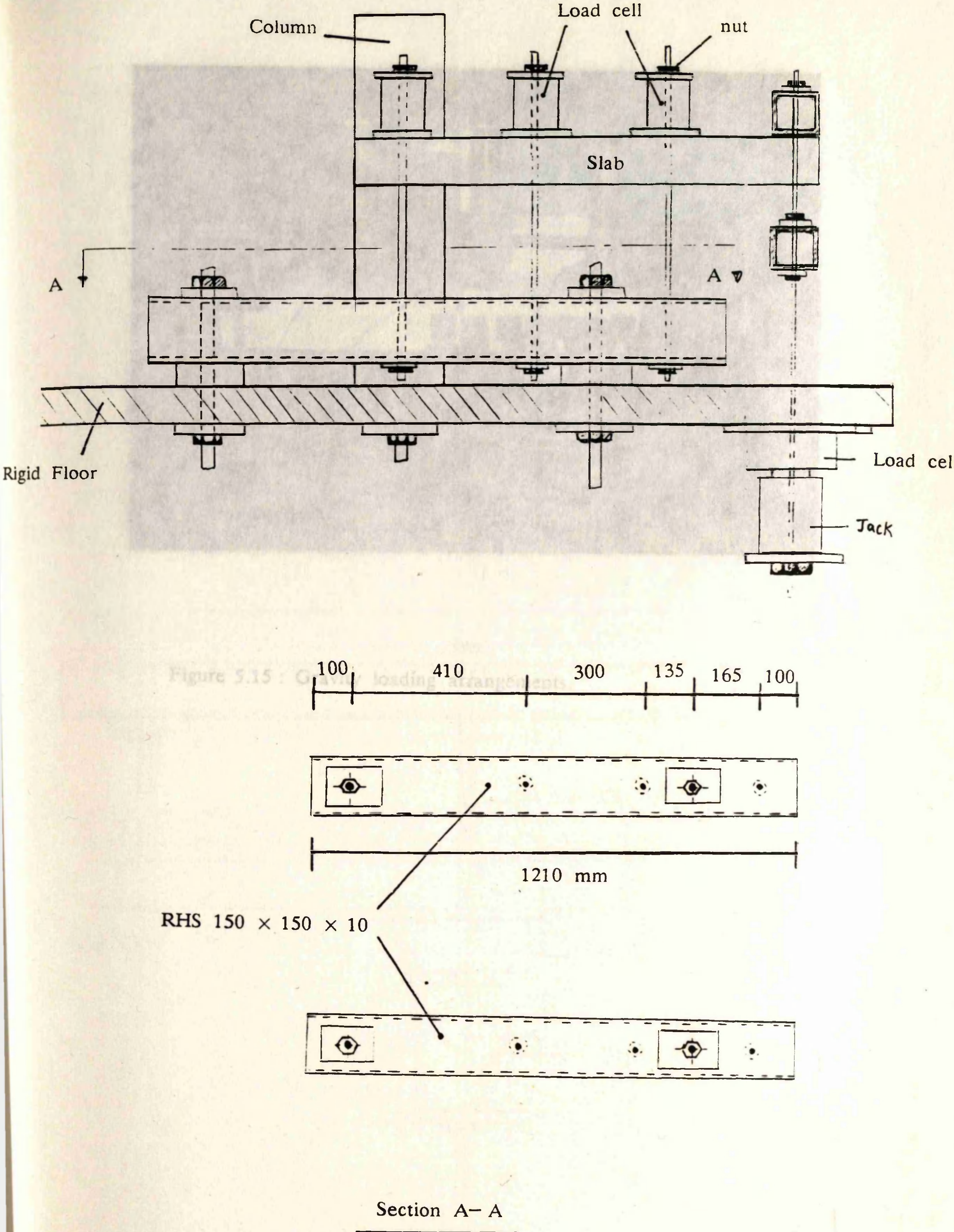

Figure 5.14 : Gravity and lateral loading arrangements.

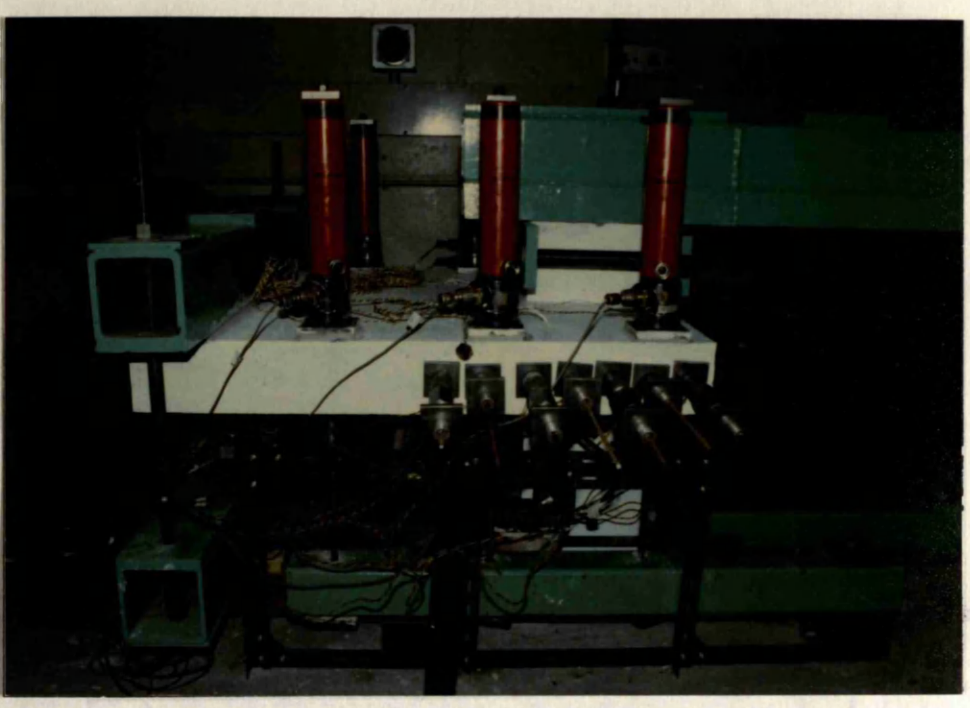

Figure 5.15 : Gravity loading arrangements.

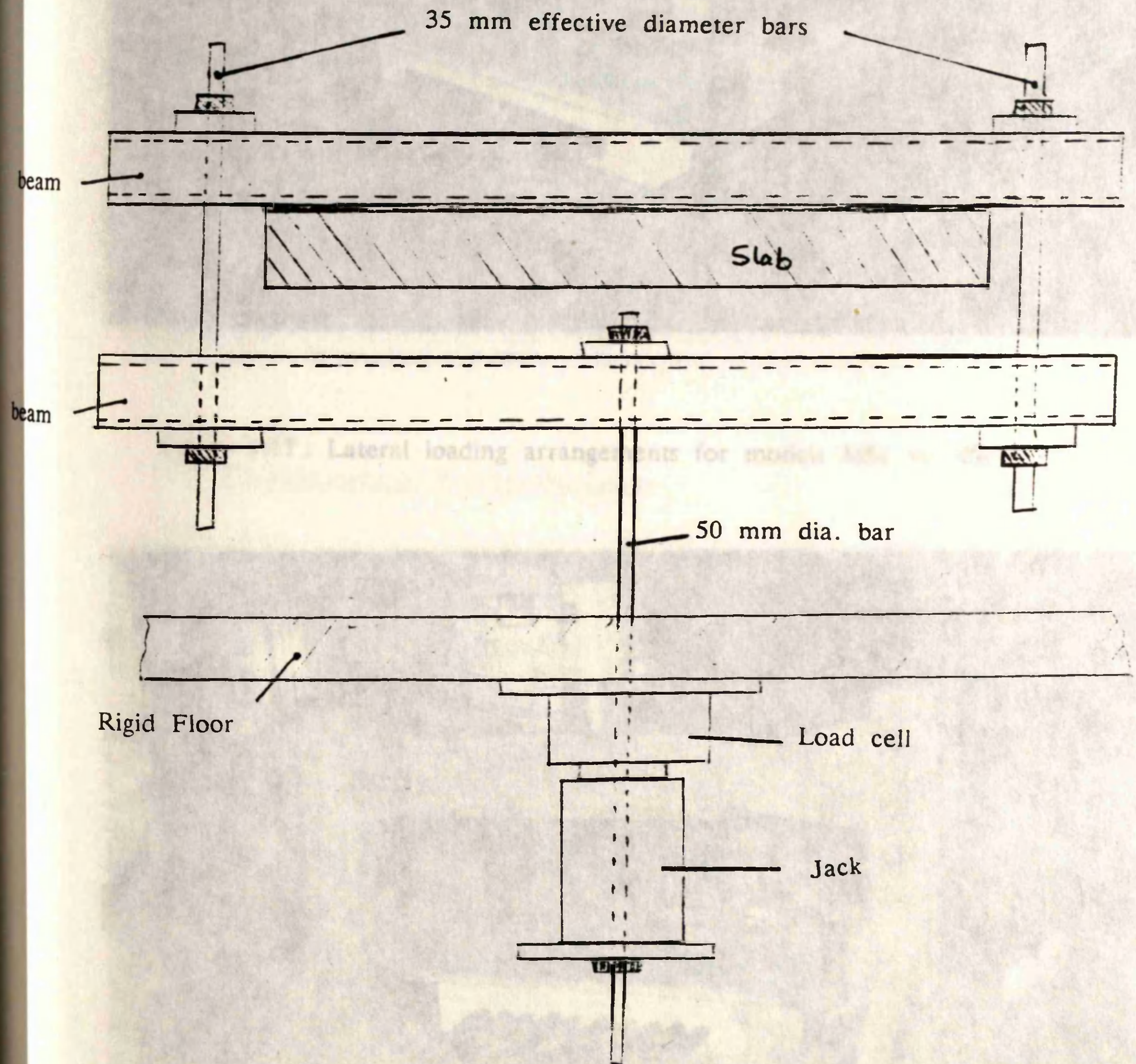

Figure 5.16 : Lateral loading arrangements

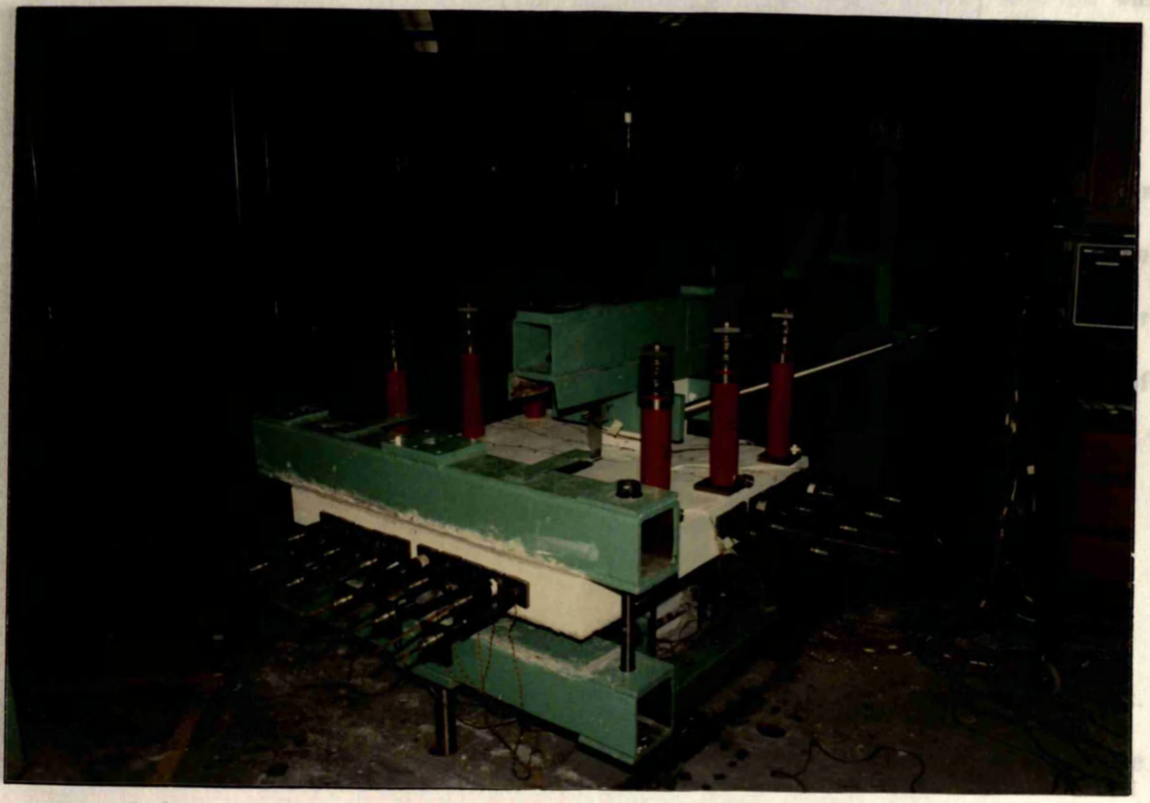

Figure 5.17 : Lateral loading arrangements for models MS1 to MS6.

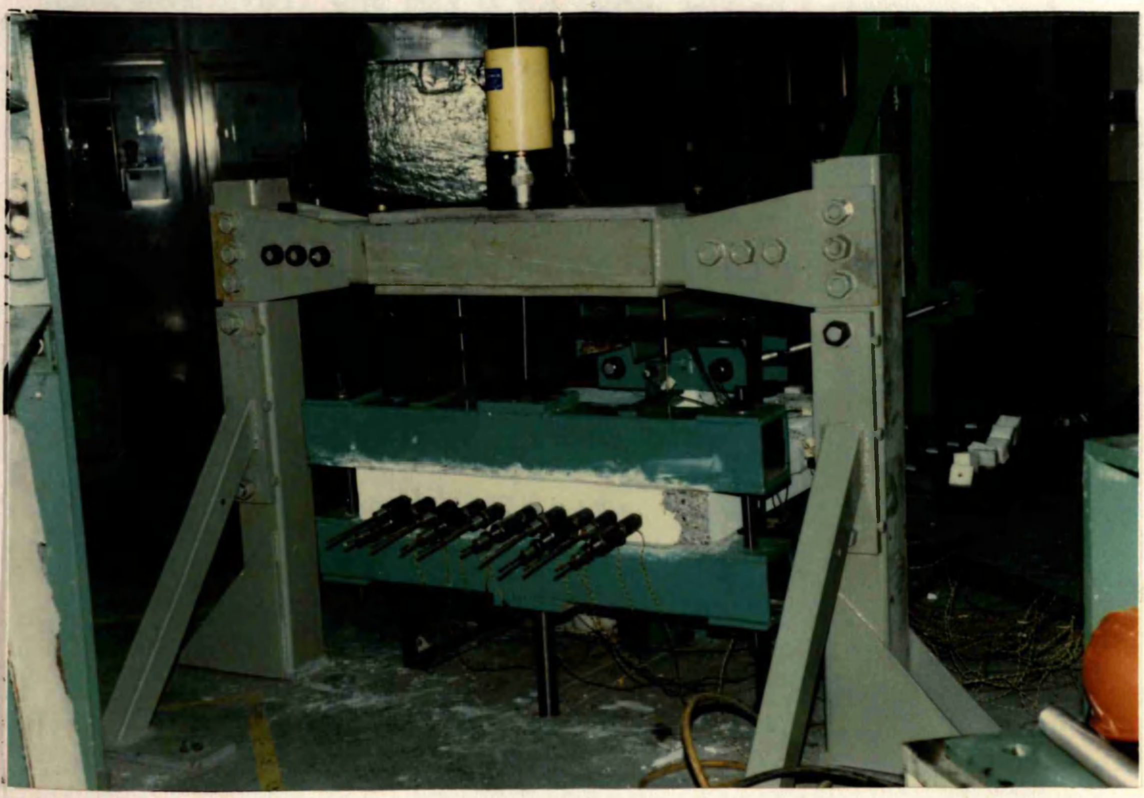

Figure 5.18 : Lateral loading arrangements for cyclic loading models.

by another additional steel rod of 50^{mm} diameter. The lower end of this rod was fixed to the top beam at its centre.

Both the top and bottom beams were placed on the slab edge using plaster for bedding and connected to each other by the same two rods of 35 mm diameter. Two 500 KN load cells, one at the bottom of the 'laboratory' floor and the other at top of the portal frame, were used to measure the amount of lateral load applied to the model.

5.5 Instrumentation

All the models were instrumented to measure loads, deflections and strains. Models of the cyclic loading test series were additionally instrumented to measure the relative rotation of the slab with respect to the column.

5.5.1 Measurement of Prestressing Loads

The prestressing load of each bar was monitored by means of two load cells located at the ends of the bar as shown in Figure 5.13. These load cells were manufactured in the laboratory of The Civil Engineering Department, University of Glasgow using 'Full Poisson Bridge' method(39) for measurement of axial loads. The load cell was manufactured from a cylindrical steel tube of 40mm and 30mm outside and inside diameters respectively and 80mm length. Figure 5.19 shows the arrangement of strain–gauges. There are four strain–gauges, two of them parallel to axis of the cylinder and the other two are perpendicular to the cylinder axis. The parallel strain–gauges must be symmetric about the cylinder axis. This load cell was calibrated by the loading machine from 1 to 40 KN in 1 KN increment. The accuracy of the load cell was within the range of ±1.0%.

5.5.2 Measurement of the Applied Loads

The applied lateral load was monitored by means of a compression load cell of 500 KN capacity for model MS1 to MS6. An additional load cell of the same capacity was used for cyclic loading models RCS7 and RCS8. Gravity loads were monitored by means of six 50 KN capacity load cells attached to each of the six bars used for gravity loading as shown in Figures 5.14 and 5.20.

5.5.3 Measurement of Vertical Displacement

Deflections were measured at various points of the slab as shown in Figure 5.21 by means of electrical displacement transducers. A supporting frame of 'Handy Angles' was made and the transducers were fixed to it at the required points. To facilitate the recording of results, linear voltage displacement transducers (LVDT) were used in conjunction with an automatic data storing and processing data logger, which recorded directly the displacement in mm to an accuracy of 0.01 mm.

In the cyclic loading models, two transducers were installed on the top surface of slab to measure upward / downward deflections. In addition to the deflection , the rotation of the slab relative to the column was also measured. This was done by measuring of horizontal displacement at points A and B which were one slab thickness above and below the slab as shown in Figure 5.22. The transducers one above and one below the slab were mounted on two steel plates attached to the slab as shown in Figures 5.22 and 5.23. Using the notations δ_A and δ_B for horizontal displacements of points A and B, the relative rotation is calculated by:

$$\tan\theta = \frac{\delta_A + \delta_B}{3t}$$

where θ is the relative rotation (Figure 5.19a).

5.5.4 Measurement of Strains

Electrical resistance strain gauges were used to measure the tensile strain in steel and surface compressive strain on concrete. The strain gauges which were used to measure tensile strain of bars were named 'student' EA–06–240LZ–120 and the strain gauges used for concrete were 30 mm long with the elongation capacity of ± 6% and a gauge factor of 2.16 ± 1% at a temperature of 75^{o}F. Their internal resistance was 120 ± 0.3% ^{ohms}. Figure 5.24 shows the positions of steel strain– gauges in the experimental models.

5.5.5 Crack Width

Crack width was measured by means of a hand– held crack width microscope measuring to 0.05^{mm}. For large cracks near the ultimate failure load of the slab, a crack width ruler was also used.

5.6 Installation of The Specimen

The procedure used for installation was as follows:

a)– For monotonic loading models

(1)– Position the model with the help of plaster in marked place on the

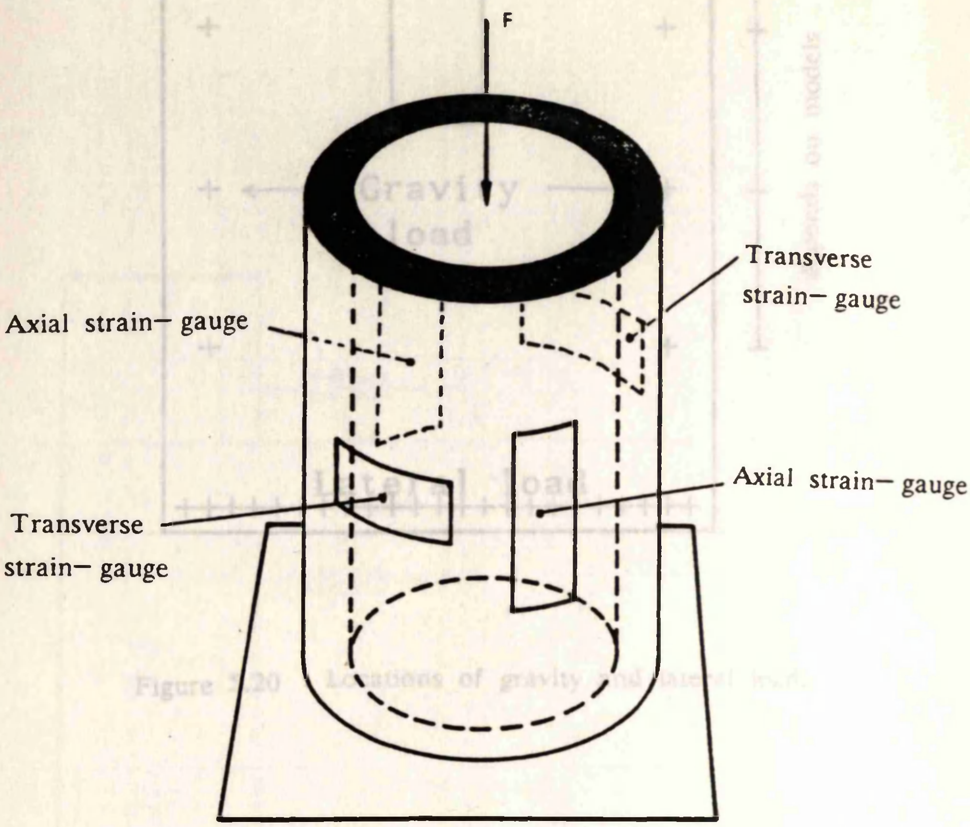

Figure 5.19 : Positions of strain- gauges on cylinderical steel as a load cell.

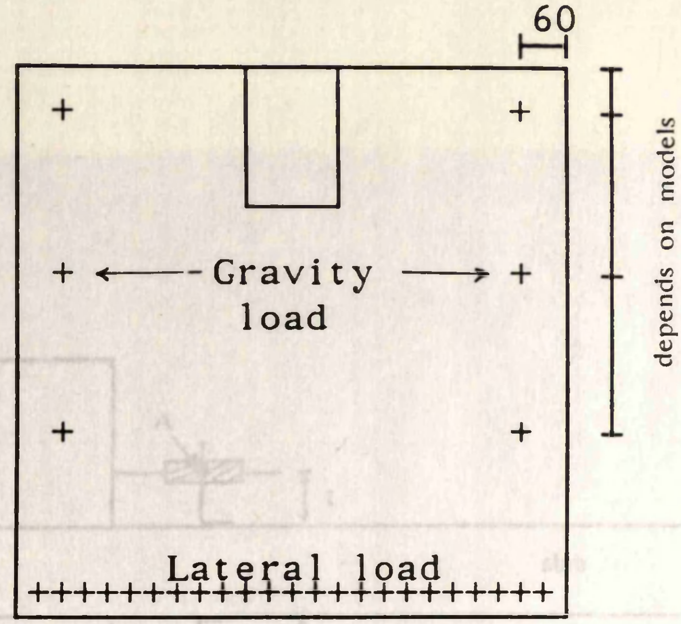

Figure 5.20 : Locations of gravity and lateral loads.

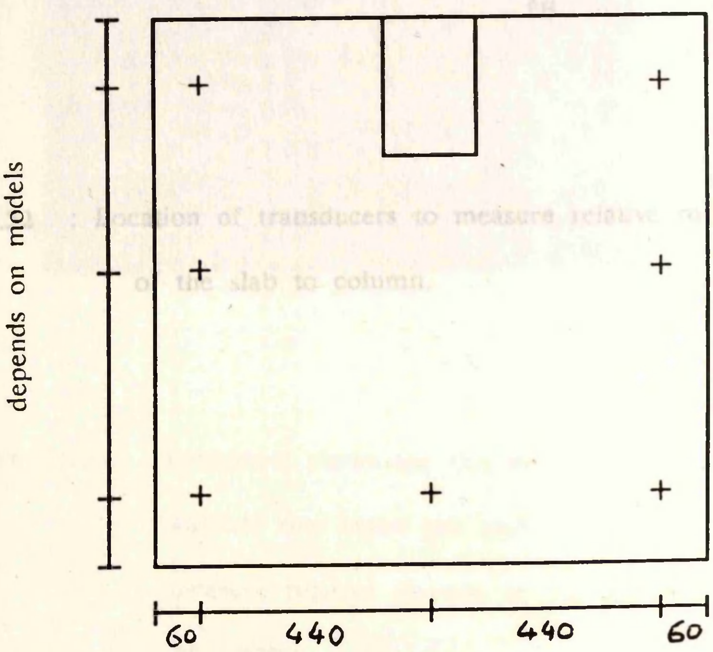

Figure 5.21 : Locations of displacement transducers.

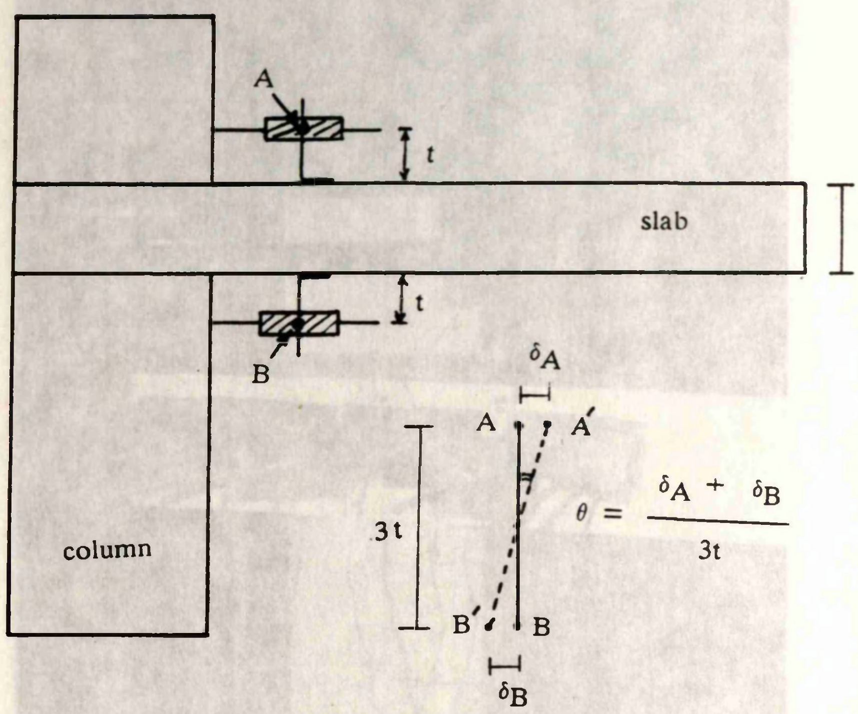

Figure 5.22 : Location of transducers to measure relative rotation of the slab to column.

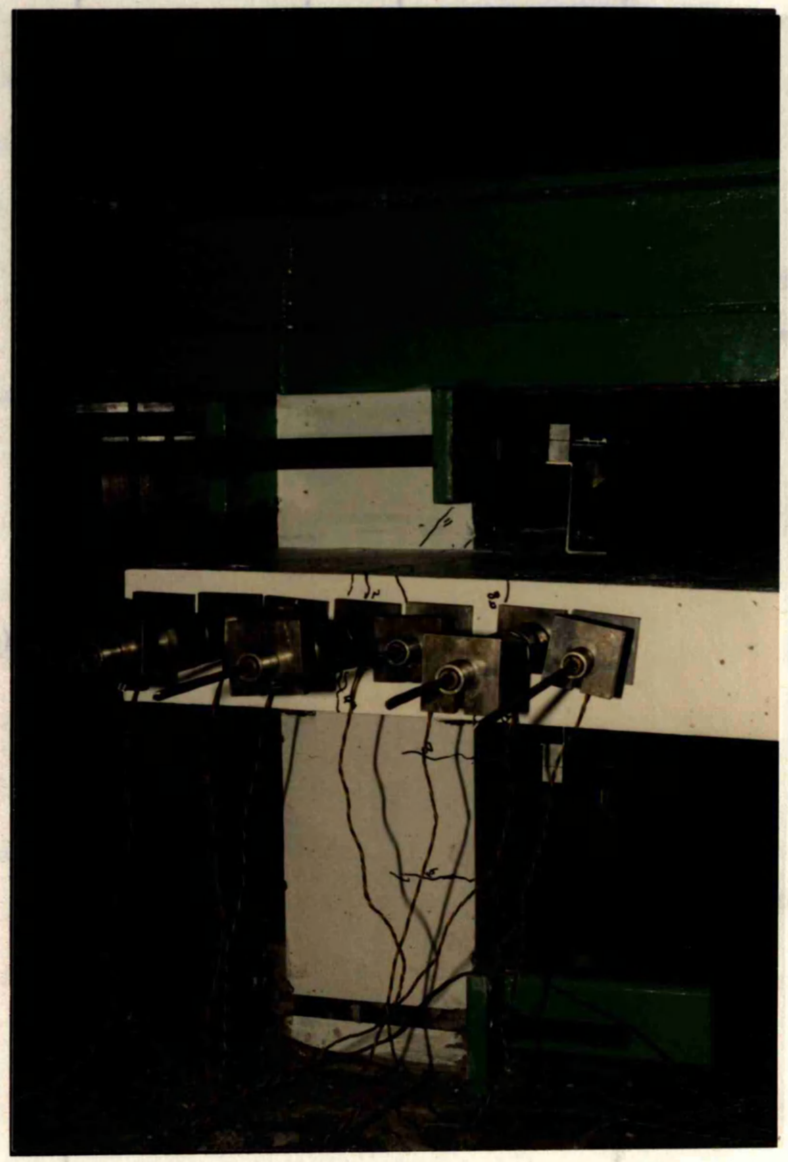

Figure 5.23 : Photograph shows the two transducers, one above and another one below the slab–column connection to measure relative rotation of the slab with respect to the column.

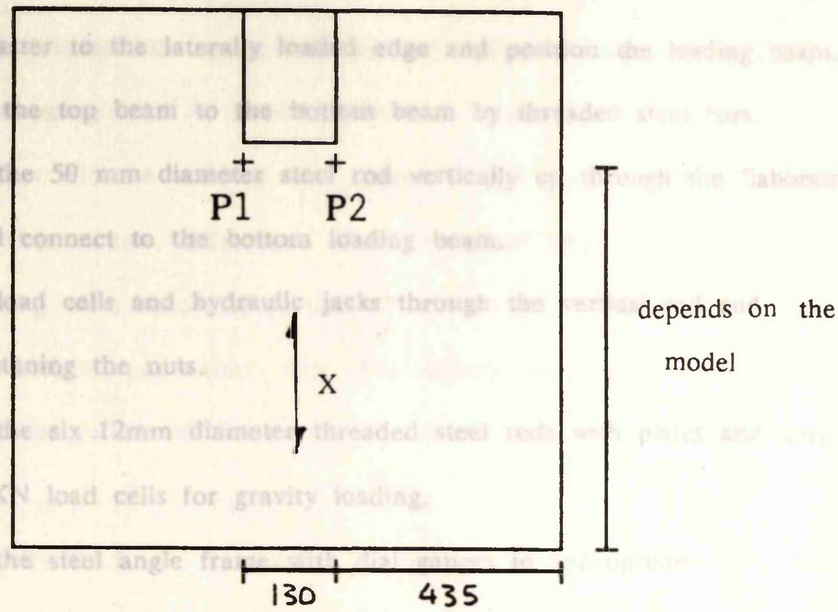

a) On longitudinal steel bars (x– direction).

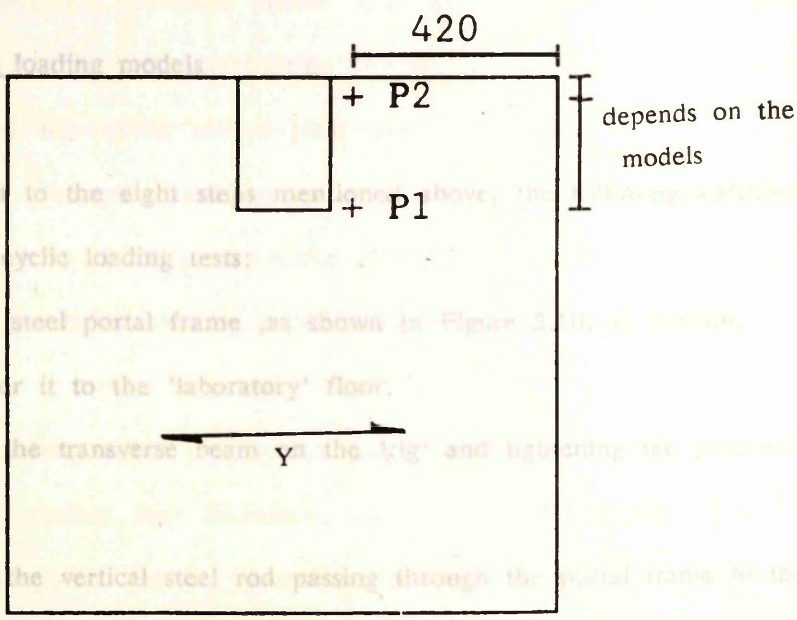

b) On transverse steel bars (y– direction).

Figure 5.24 : Locations of strain– gauges on steel bars.

'laboratory' floor.

(2)– Anchor the column by means of steel strands.

(3)– Apply plaster to the laterally loaded edge and position the loading beam. Connect the top beam to the bottom beam by threaded steel bars.

(4)– Position the 50 mm diameter steel rod vertically up through the 'laboratory' floor and connect to the bottom loading beam.

(5)– Position load cells and hydraulic jacks through the vertical rod and then tightening the nuts.

(6)– Position the six 12mm diameter threaded steel rods with plates and nuts and 50 KN load cells for gravity loading.

(7)– Position the steel angle frame with dial gauges in appropriate position.

(8)– Connect the load cells, transducers and strain– gauges to the data logger for continuous measurements of the various quantities

b)– <u>For cyclic loading models</u>

In addition to the eight steps mentioned above, the following additional steps are specific to cyclic loading tests:

(9)– Place the steel portal frame ,as shown in Figure 5.10, in position and anchor it to the 'laboratory' floor.

(10)– Position the transverse beam on the 'rig' and tightening the prestressing strands.

(11)– Connect the vertical steel rod passing through the portal frame to the top loading beam.

5.7 Test Procedure For Monotonic Loading

Zero readings were taken of all the load cells, transducers and strain gauges before starting the test. First of all the prestressing loads were applied, gradually by turning the nuts against the bolts by means of two spanners. The load was applied in four increments up to the desired value of prestressing level. The amount of prestressing load in each tendon was monitored on the screen of the 'data logger'. For all the tendons the applied load was recorded in each load increments. Further more , deflections of the slab and strains in 'unstressed' steel due to prestressing were recorded as well. Then the gravity loads were applied in two equal increments and after that the lateral load was applied in 5^{KN} increments until the failure of the model.

The gravity load was constantly monitored and maintained at its ultimate value as far as it was practical while lateral load was applied. The reason for the adjustment is that the deflection of the slab due to lateral load alters gravity load. Therefore, the gravity loads were readjusted to the desired value after each lateral load application. In each lateral load increment, all values of deflections, strains, applied loads and prestressing forces in tendons were recorded and monitored. Care was taken to see that the applied load was not causing any eccentricity and consequent twisting of the model. Loading was continued until failure was noted by either a continuous drop of applied load value or a sudden fall of that value accompanied by a physically noticeable failure.

During loading, crack propagation was closely monitored and traced on the slab. The corresponding load increment was recorded at the tip of each crack. The total duration of a test for monotonic loading was at least 8 hours depending on the total number of load increments applied.

5.8 Test Procedure For Cyclic Loading

In cyclic loading models, application of the gravity loads was eliminated because their adjustment needed a lot of time and effort. Especially upward lateral loading proved more difficult to adjust because of the location and proximity of the lateral and gravity loads which by applying the lateral load would release the gravity load.

In this series the procedure of prestressing was the same as that in monotonic loading models. The application of downward lateral load first was started by means of a hydraulic jack of 500 KN capacity up to 50% of the design load. Then the jack was released and upward loading was applied by another hydraulic jack of the same capacity as the previous one until it reached the same level on the downward loading. This process was repeated for all cycles. In each cycle the loading level was increased by 2 KN until failure of the models.

5.9 <u>Precautions Taken</u>

The prestressing bars were unbonded. Therefore if a bar broke during loading, the bars would fly out the model and would be a source of great danger. Therefore, great care was taken to provide a safe area around the slab in order to protect technicians involved in these experimental tests.

CHAPTER SIX

EXPERIMENTAL STUDY

((PART I))

MONOTONIC LOADING BEHAVIOUR OF THE UNBONDED PRESTRESSED FLAT SLAB AT EDGE COLUMN JUNCTION

6.1 Introduction

For load transfer between a flat slab and a column , conditions at the slab–column connection are critical for determining the strength and stiffness of the flat–slab structure. This is particularly true at an edge column junction because of the reduction of the critical perimeter around the column and the presence of twisting moments. Since the punching failure of an edge column–slab junction is a local failure and takes place in the vicinity of an edge column , the region around the column shown hatched in Figure 6.1 is the area of interest in this study. Therefore an isolated edge column–slab joint as shown in Figure 6.2 was selected to investigate strength and overall behaviour of this type of connection.

In this chapter details of six unbonded prestressed reinforced concrete flat slabs at the edge column junction tested under monotonic loading condition are reported. The general plan of these models is shown in figure 6.3.

Since the distribution of shear stress due to lateral loads , as discussed in Chapter Two , is not uniform, this shear will hereafter be called uneven shear and the moment due to lateral loads will be called as unbalanced moment. Unbalanced moment results from unequal consecutive slab spans, edge column and lateral loads.

6.2 Object of Tests

The main object of experimental study are as follows:

i)– Experimental investigation of punching shear strength and overall behaviour of unbonded prestressed flat slabs at an edge column junction.

ii)– Verify the validity of using the direct design method in prestressed flat slab design.

iii)– Verify the validity of the three dimensional finite element analysis modified for prediction of ultimate strength and overall behaviour of flat slab at an edge column junction by comparison the results of analysis and tests.

For this purpose, the following aspects are noted during the experimental investigation.

a) Load– deflection relationship.

b) Load– strain relationship in unstressed steel bar and concrete around the column

c) Stress variation in prestressing bars.

d) Crack pattern and crack propagation.

e) Ultimate load and mode of failure.

6.3 Parameters of Study

The parameters which are involved in the strength of unbonded prestressed flat slab at edge column connections are shown in Table 6.1. Considering the position of the holes in the 'laboratory' floor which determined the dimensions of the models, four parameters which were most appropriate for this study were chosen for investigation as follows:

1) Level of prestress.

2) Column aspect ratio (C_x / C_y).

3) Ratio of wind shear moment to wind shear (M_w / V_w).

4) Resistance of the junction under the reversed cyclic loads.

The explanation of parameters are as follows:

6.3.1 Level of Prestress

Level of prestress is the average compressive stresses of the concrete due to prestressing forces. The maximum value of this level is equal to $0.2f_{cu}$ (f_{cu} is the cube strength of concrete) as shown in Figure 6.4. Three models MS1 , MS2 and MS3 were designed for the level of 1.5 , 2.3 and 4.8 N/mm2 respectively to study the effect of this parameter on the strength of the connection .

6.3.2 Column Aspect Ratio

Transmission of moment M_x between the slab and column takes place by means of bending moment (M_b) at the front face of the column and twisting moment (M_t) at both sides of the column as shown in Figure 6.5. Under the same conditions of prestressing and slab dimensions , the amount of bending and twisting moment depends on the side dimension of the column , C_y and C_x respectively. Therefore any change in the column aspect ratio (C_x/C_y) will change the ratio of bending and twisting moment. As a result, the ultimate load–carrying capacity and the failure mode of the models are affected by this parameter. Consequently three models (MS5 , MS3 and MS6) with the column aspect ratio of 1.33 , 1.67 and 2.0 respectively are considered in order to study the effect of this parameter on behaviour and punching strength of the slab–column connections.

6.4 Dimensions of Models

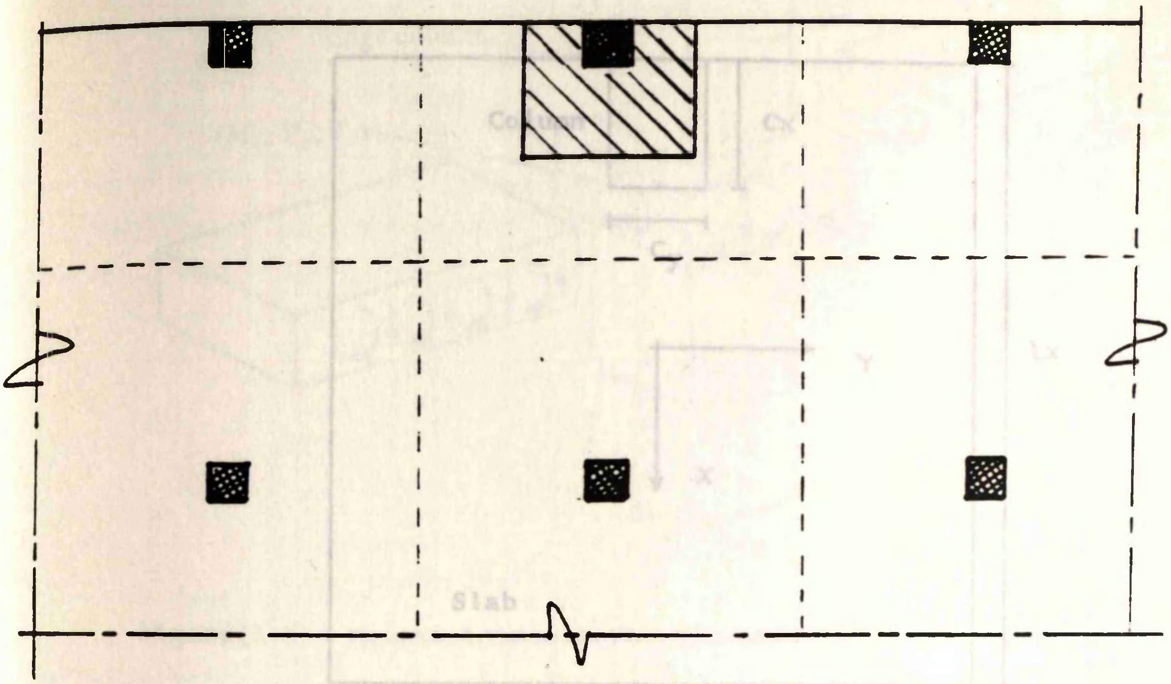

Figure (6.1): Plan of typical flat slab structure.

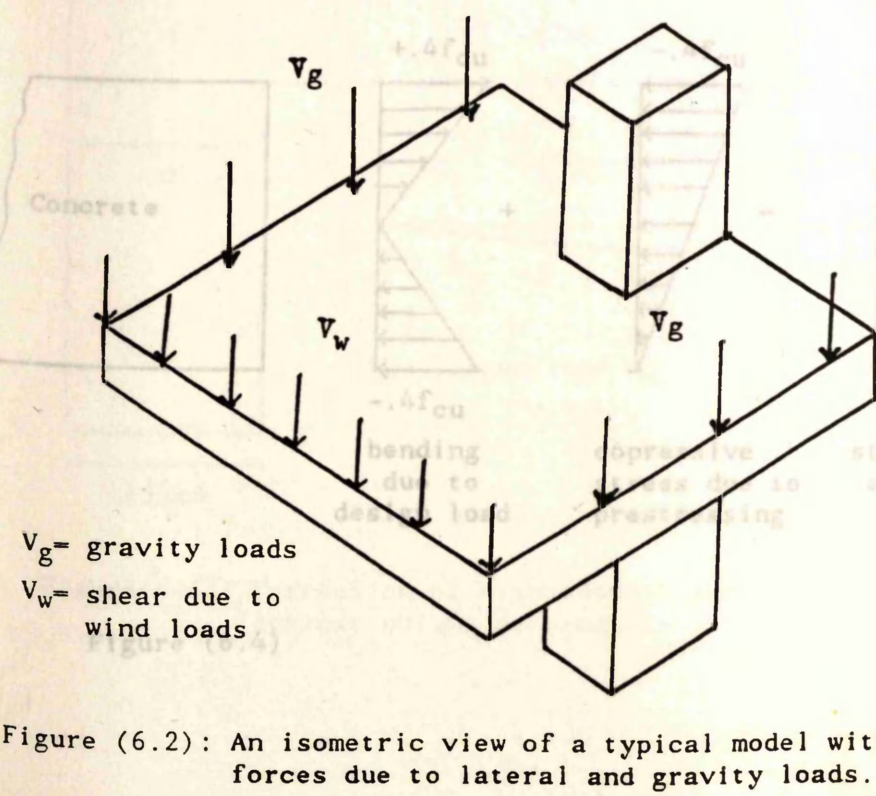

Figure (6.2): An isometric view of a typical model with shear forces due to lateral and gravity loads.

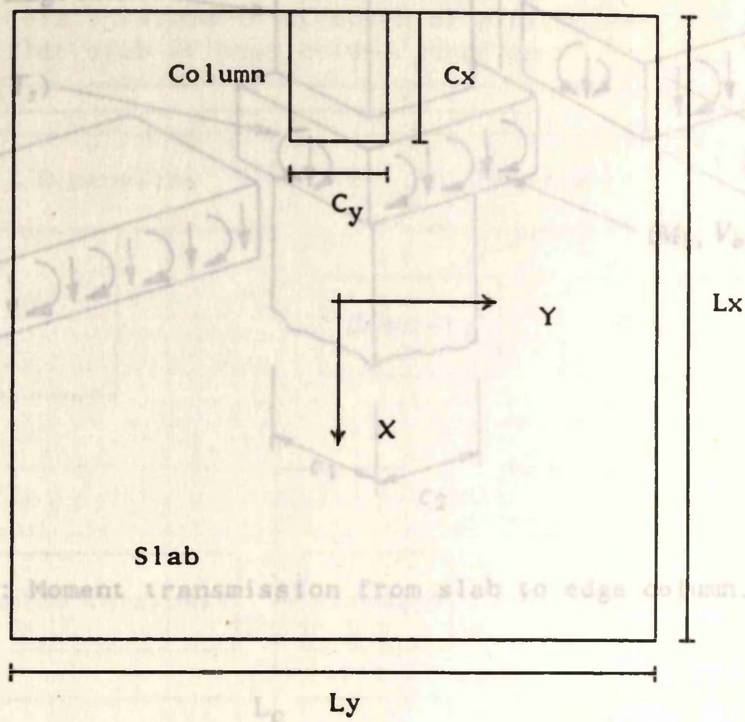

Figure (6.3) : Plan of a typical model.

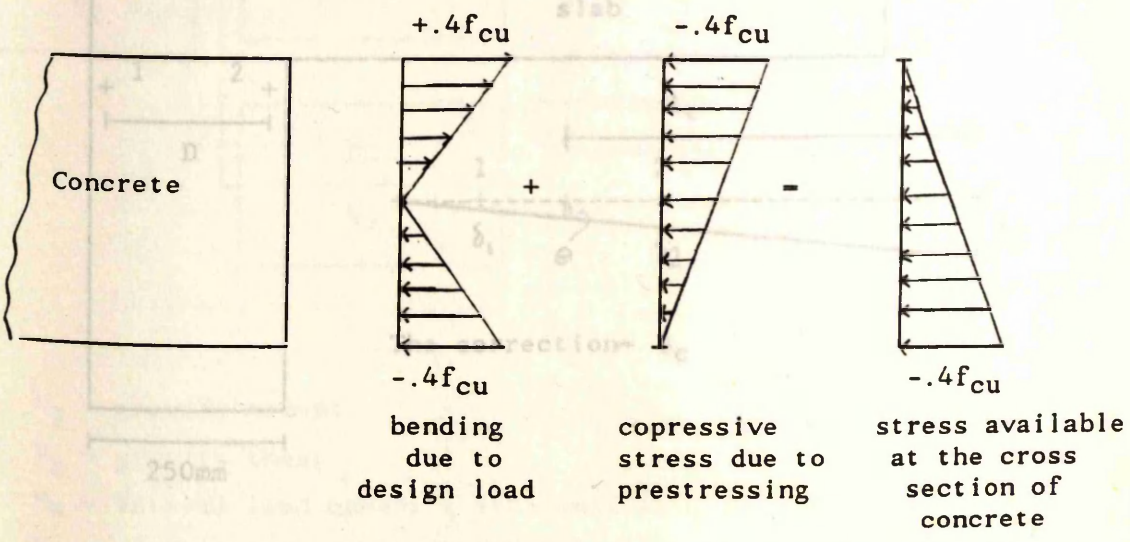

Figure (6.4)

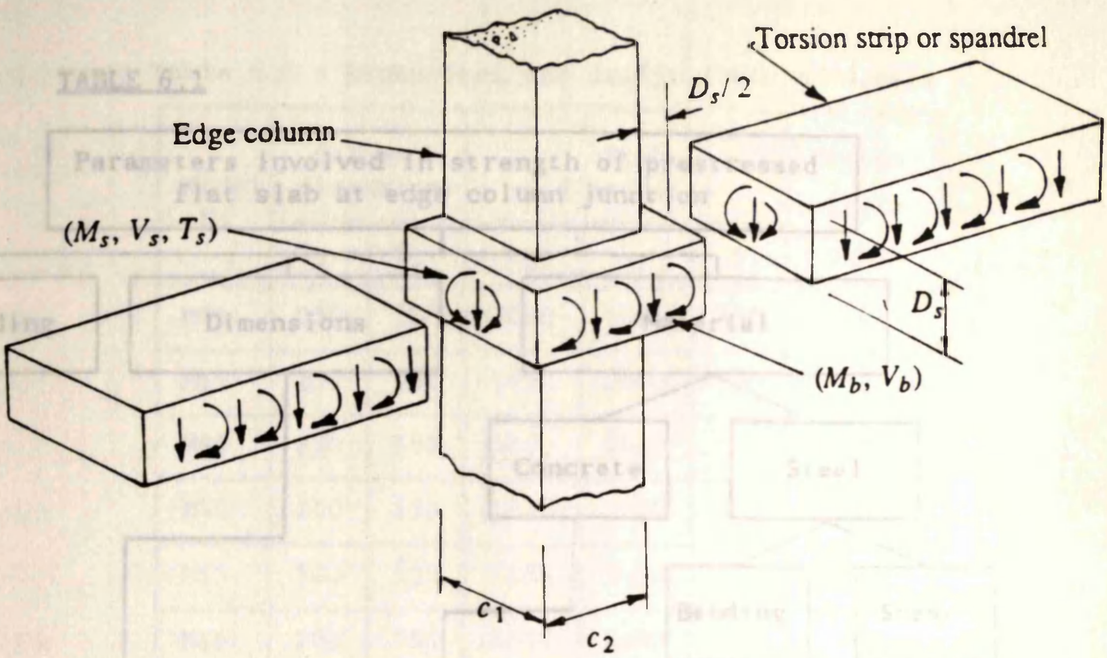

Figure(6-5): Moment transmission from slab to edge column.

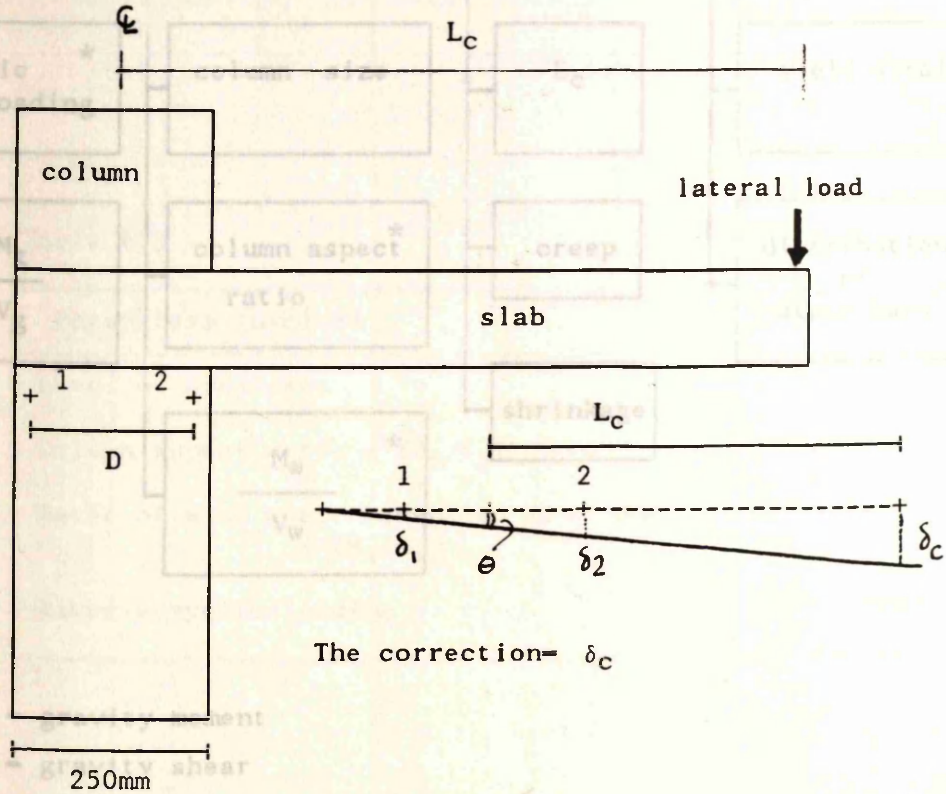

Figure(6-6): Correction of displacement due to lateral load against column deformation.

TABLE 6.1

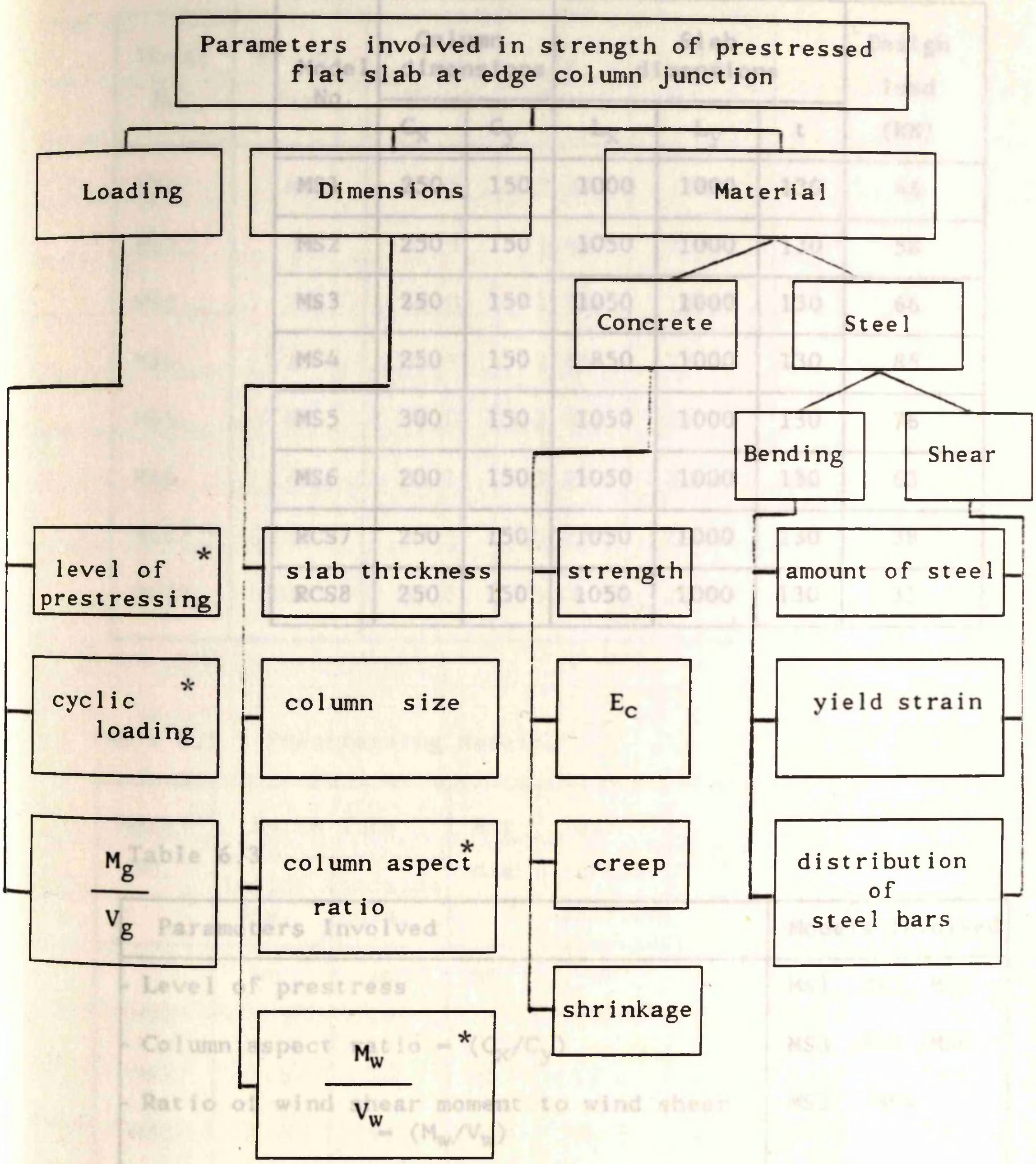

M_g = gravity moment
V_g = gravity shear
M_w = lateral load moment (wind moment)
V_w = " " shear (wind shear)

*) These marked parameters were chosen to investigate in this study.

Table 6.2 : Dimensions and design loads of models

Model No.	Column dimensions		Slab dimensions			Design load
	C_x	C_y	L_x	L_y	t	(KN)
MS1	250	150	1000	1000	130	48
MS2	250	150	1050	1000	130	58
MS3	250	150	1050	1000	130	66
MS4	250	150	850	1000	130	85
MS5	300	150	1050	1000	130	76
MS6	200	150	1050	1000	130	63
RCS7	250	150	1050	1000	130	38
RCS8	250	150	1050	1000	130	31

Table 6.3

Parameters Involved	Models Involved
- Level of prestress	MS1, MS2, MS3
- Column aspect ratio = (C_x/C_y)	MS3 ,MS5 ,MS6
- Ratio of wind shear moment to wind shear = (M_w/V_w)	MS3 , MS4
- Reverse cyclic loading	RCS7 , RCS8

Table 6.4 : Properties of concrete for each model

Model No.	No. of days	f_{cu} N/mm2	f_t N/mm2	E_c N/mm2
MS1	43	67.5	3.38	-
MS2	35	57.5	3.49	21.0
MS3	79	56.0	3.33	18.0
MS4	39	60.7	3.65	18.2
MS5	62	56.0	3.25	22.8
MS6	76	53.1	3.25	21.3
RCS7	186	59.2	3.29	20.5
RCS8	205	60.3	3.01	23.7

Table 6.5 : Prestressing details

Model No.	Nylon Tube		Bar dia.	Bar cross section	f_{pu}*	f_{pe}*	average prestress
	inside dia.	outside dia.					
	mm	mm	mm	mm2	N/mm2	N/mm2	N/mm2
MS1	7.5	10	5	19.6	1780	1020	1.5
MS2	7.5	10	5	19.6	1780	1121	2.3
MS3	7.5	10	7	38.5	1623	1090	4.8
MS4	9	12.5	7	38.5	1623	1090	4.8
MS5	9	12.5	7	38.5	1623	1098	4.8
MS6	9	12.5	7	38.5	1623	1116	4.9
RCS7	9	12.5	7	38.5	1623	1116	4.9
RCS8	9	12.5	7	38.5	1623	779	3.4

*) f_{pu}=Ultimate stress of the prestressing bar

*) f_{pe}=Effective stress in the bar due to prestress

Since the punching failure is a local failure and is related to the stresses adjacent to the column, boundary conditions of the flat slab structure have not been taken into consideration. Therefore, tests were conducted on flat slab specimens which were isolated from a multiple panel flat slab structure with free edges as shown in Figure 6.1. Table 6.2 gives the dimensions of the models. The width (L_y= 1000 mm) and thickness (t = 130 mm) were kept constant but the length (L_x) was varied in model MS4 so as to vary the ratio of wind shear moment to wind shear. All the slabs were cast integrally with a column-slab projecting both above and below the slab as shown in Figure 6.2. The column was rectangular with side dimensions of C_x= 250 mm and C_y = 150 mm. Only in models MS5 and MS6 did C_x change to 300 mm and 200 mm respectively in order to study the column aspect ratio parameter. The column stub was reinforced with four 25 mm and two 12 mm bars.

6.5 Design of Experimental Models

In all the models the steel required was calculated using the 2-dimensional finite element program described in Chapter 3. In this connection, prestressing steel is treated as ordinary steel with an equivalent yield stress equal to the difference between its 0.2% proof stress and effective prestress as shown in Table 6.5. Additional ordinary steel over and above that provided by the prestressing steel was provided as required by subtracting the equivalent steel due to prestress from the total steel required by the design requirements. In addition, according to ACI-ASCE 423 recommendations , the amount of ordinary steel bar passing through the column head should not be less than 0.15 percent of cross sectional area of column strip. Therefore , in all models two 8mm bars passing through the column head in both directions were used. According to design requirements no shear reinforcement was needed.

6.6 Test Programme

The experimental programme is divided into two parts:

I) Main Test Series (or MS).

II) Reverse Cyclic Loading Series (or RCS)

The main test series consists of six models. Three models MS1 ,MS2 and MS3 were tested to study the effect of the prestressing level on the punching strength of the junctions. Models MS3, MS4, MS5 and MS6 were tested to investigate remaining parameter shown in Table 6.3.

The reverse cyclic loading series consists of two models RCS7 and RCS8. They were designed to study the effect of repeated and reversed lateral loads due to wind and earthquake on the behaviour and strength of unbonded prestressed flat slab at edge column junctions. The detailed description of the models of this series will be given in chapter seven.

In model MS3, some cracks developed at the rear face of the column during the application of lateral load especially near the ultimate load. Since the deflection readings of the slab are affected by the deformation of the column, the measured displacements in models MS4 – MS6 were corrected for column deformation from dial gauge readings taken at two positions on the column side as shown in Figure 6.6. The correction for column deformation was calculated as follows.

It is assumed that the variation of strain at a horizontal section of the column is linear. Therefore, referring to Figure 6.6:

$$\text{The correction, } \delta_c = \frac{\delta_1 + \delta_2}{2} + \frac{\delta_2 - \delta_1}{D} \times L_c$$

where : δ_1 and δ_2 = the measured displacements at the column side at points (1) and (2), D = the distance between the two points (1) and (2)

and L_c = shown in Figure 6.6.

The various experimental data and the results on the behaviour of the models are presented for each model in the following order:

a) Sketch showing dimensions and details of the model,
b) Prestressing and 'unstressed' reinforcement details.
c) Load– deflection curve.
d) Load– strain curve for "unstressed" steel bar.
e) Load– strain curve for concrete.
f) Variation of stress in prestressing bars.
g) Crack pattern

6.7 Main Test Series

6.7.1 Model MS1

Figure 6.7 shows the plan of model MS1. It was designed for a gravity load of 18 KN and a lateral load of 30 KN. The model was prestressed in two orthogonal directions by seventeen tendons, ten in the windward direction (called X– direction) and seven tendons in the transverse direction (called Y– direction). The spacing of tendons in both the directions was 100 mm centre to centre as shown in Figure 6.8. The prestressing bar used was of 5mm diameter with the ultimate stress of 1780 N/mm2. The profile in X– direction was linear with 30mm eccentricity at the column side of the slab and it was parabolic in Y– direction with the eccentricity at the centre as shown in the cross section A– A of Figure 6.9. The tendons passed through 10mm diameter plastic tubes which were firmly fixed to the formwork. All tendons were tensioned up to 58% of their ultimate strength in both the directions. Figure 6.10

shows the arrangement of bonded reinforcing bars in the slab and the column of the model. Figure 6.15 shows the locations of strain– gauges on the ordinary steel bars and concrete and shows the positions of transducers.

Behaviour of Model MS1

No hairline cracks were observed after the application of prestressing forces in X and Y directions. At 69% of design load, the first crack was initiated on the top surface of the slab in front of the column as shown in Figure 6.11a. At 77% of design load, cracks extended towards both sides of the slab as shown in Figure 6.11b. At 87% of design load, new cracks appeared on the slab from front corners of the column to the rear side of the slab at various angles in the range of between 0.0 and 45 degrees as shown in figure 6.11d and simultaneously shear cracks initiated at the rear surface of the slab as shown in Figure 6.11c. Finally, failure of the slab took place with large shear cracks at the rear side of the slab at an applied load of 59 KN corresponding to 115% of the design load.

The crack pattern on the tension side of the slab after failure is shown in Figure 6.12. As can be seen, cracking was confined to the region around the junction. The diagonal shear failure cracks on the rear side of the slab are clearly visible in photograph of Figure 6.13. Due to the difficulty in observing cracks on the compressive side of the slab during testing, only the final crack pattern was obtained as shown in Figure 6.14.

Figures 6.16a, 6.16b and 6.16c show the experimental load– deflection curves. Note that, on the vertical axis, the ratio of applied loads to the design load of the slab is plotted. Figures 6.17a and 6.17b show the curves for tensile strains in ordinary reinforcing bars in windward and transverse directions respectively. As can be seen in Figure 6.17a, two bars passing through the column reached 80% of the yield strain and

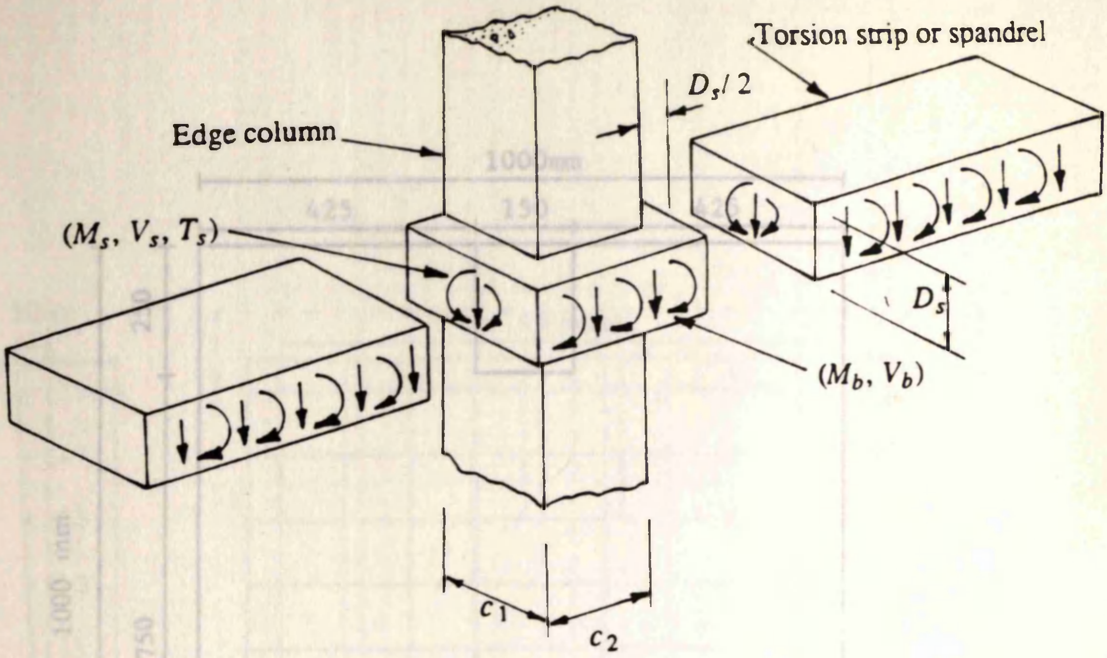

Figure(6-5): Moment transmission from slab to edge column.

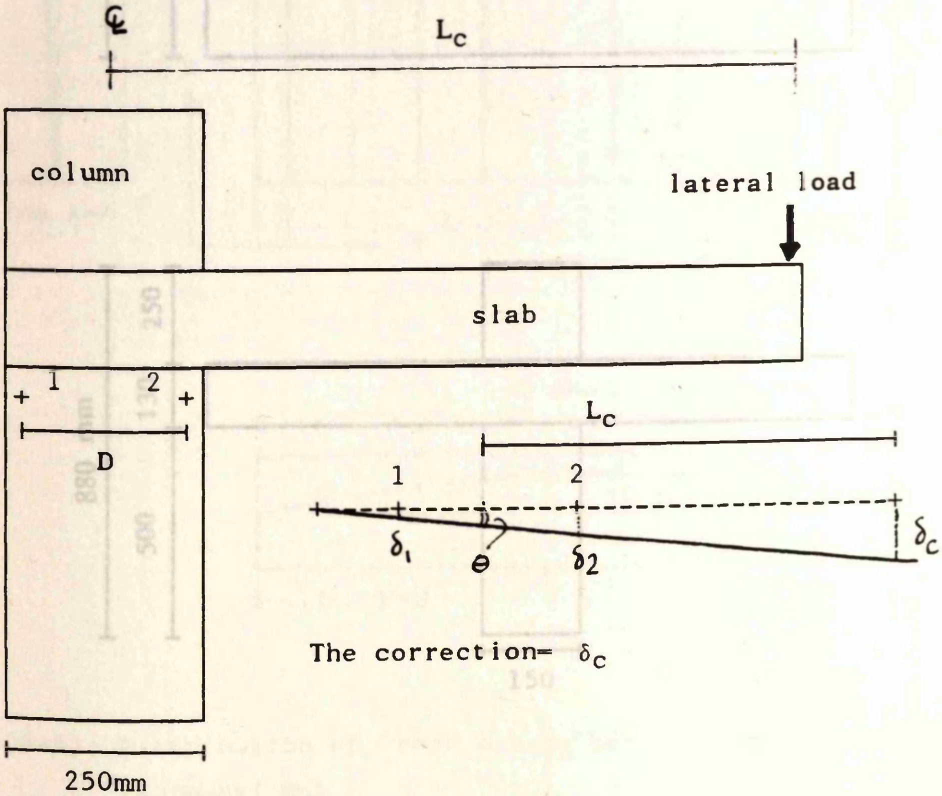

Figure(6-6): Correction of displacement due to lateral load against column deformation.

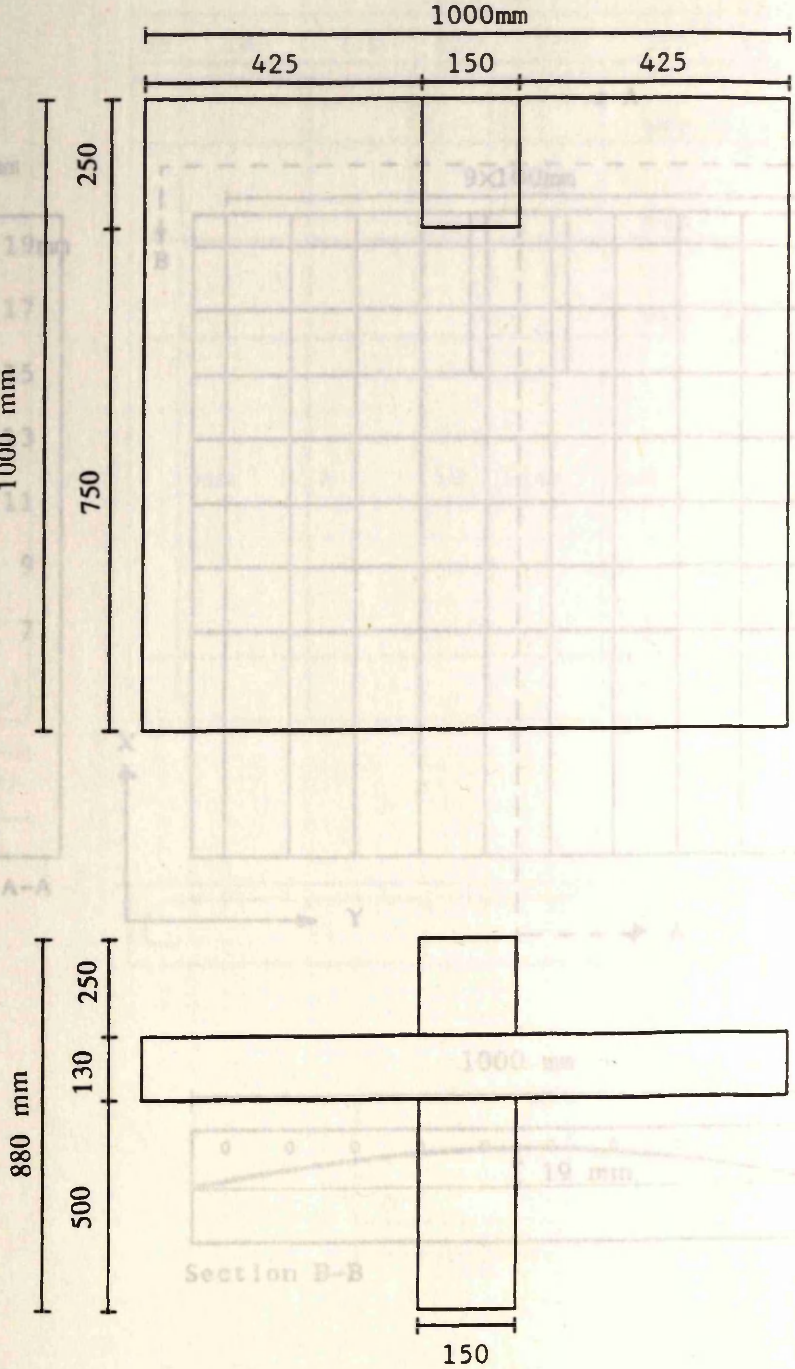

Figure(6-7): Plan and Dimensions of Model MS1.

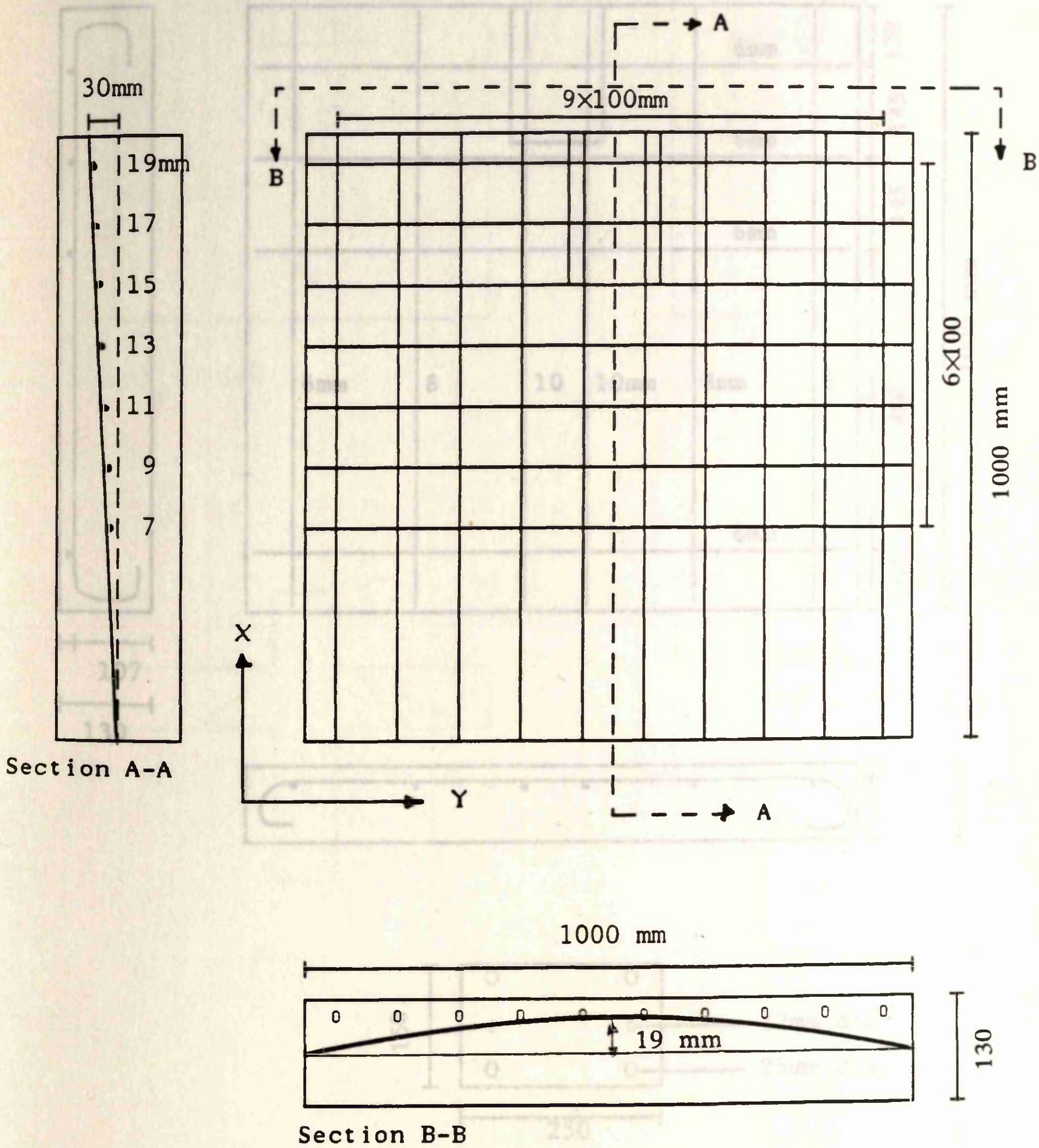

Figure(6-8): Distribution of Prestressing bars in X and Y directions for model MS1.

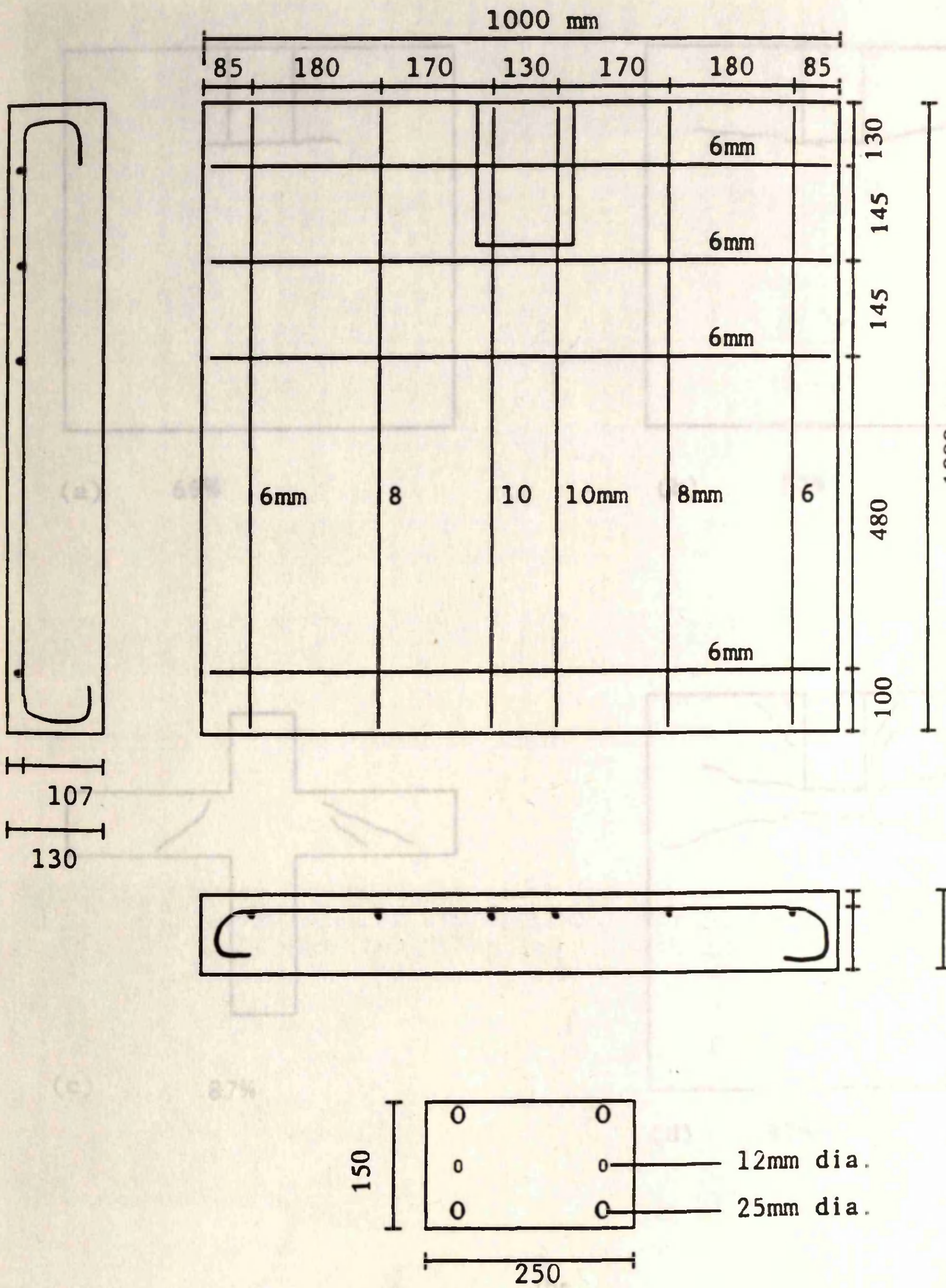

Figure(6-10): Arrangement of ordinary reinforcement bars in the slab and column fir model MS1.

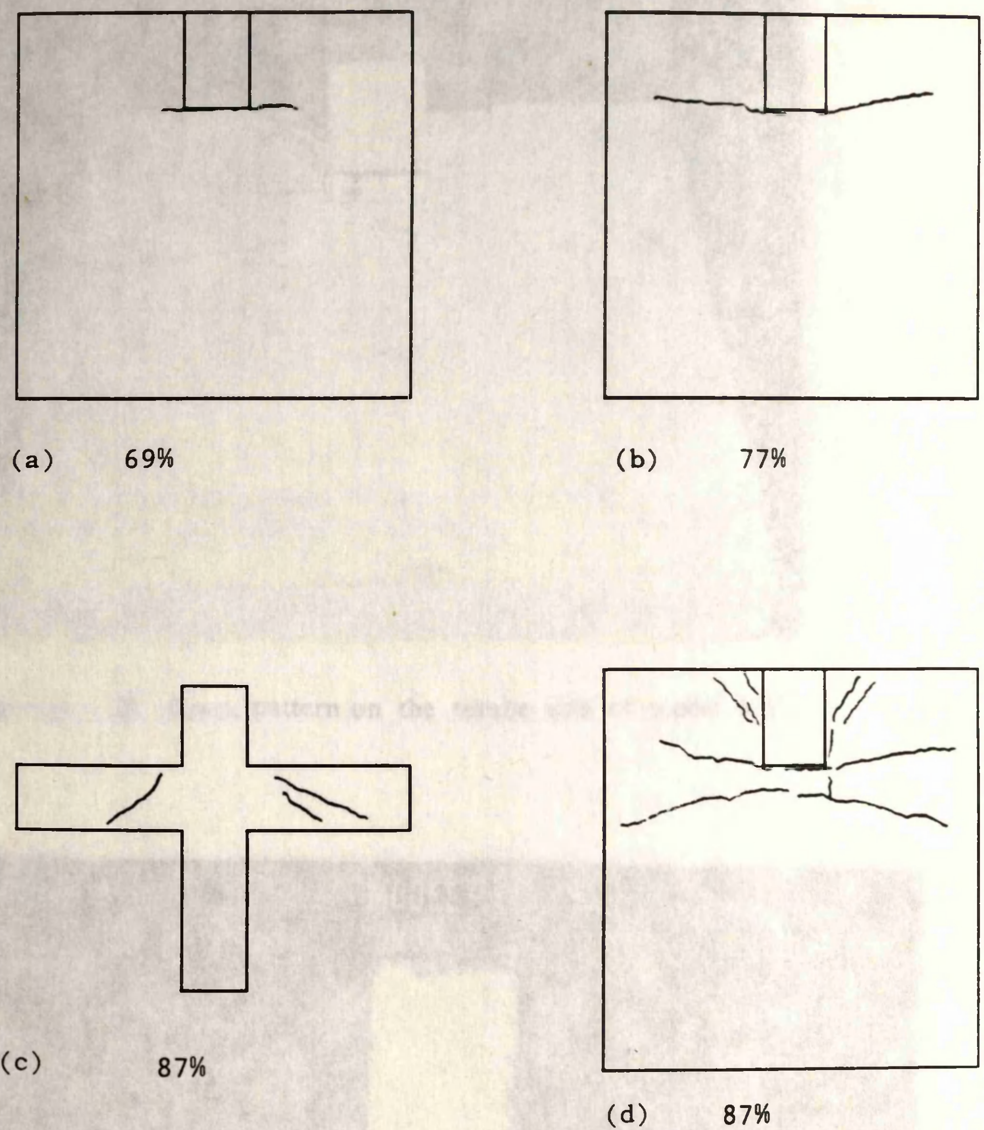

Figure(6-11): Cracks initiation during the testing of model MS1 at different percentages of the design load.

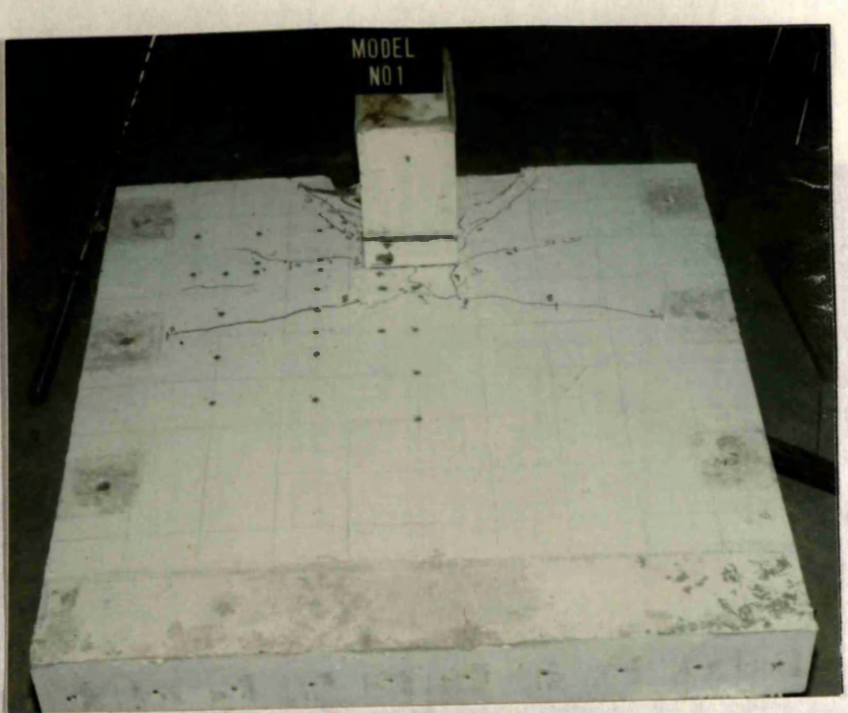

Figure(6-12): Crack pattern on the tensile side of model MS1

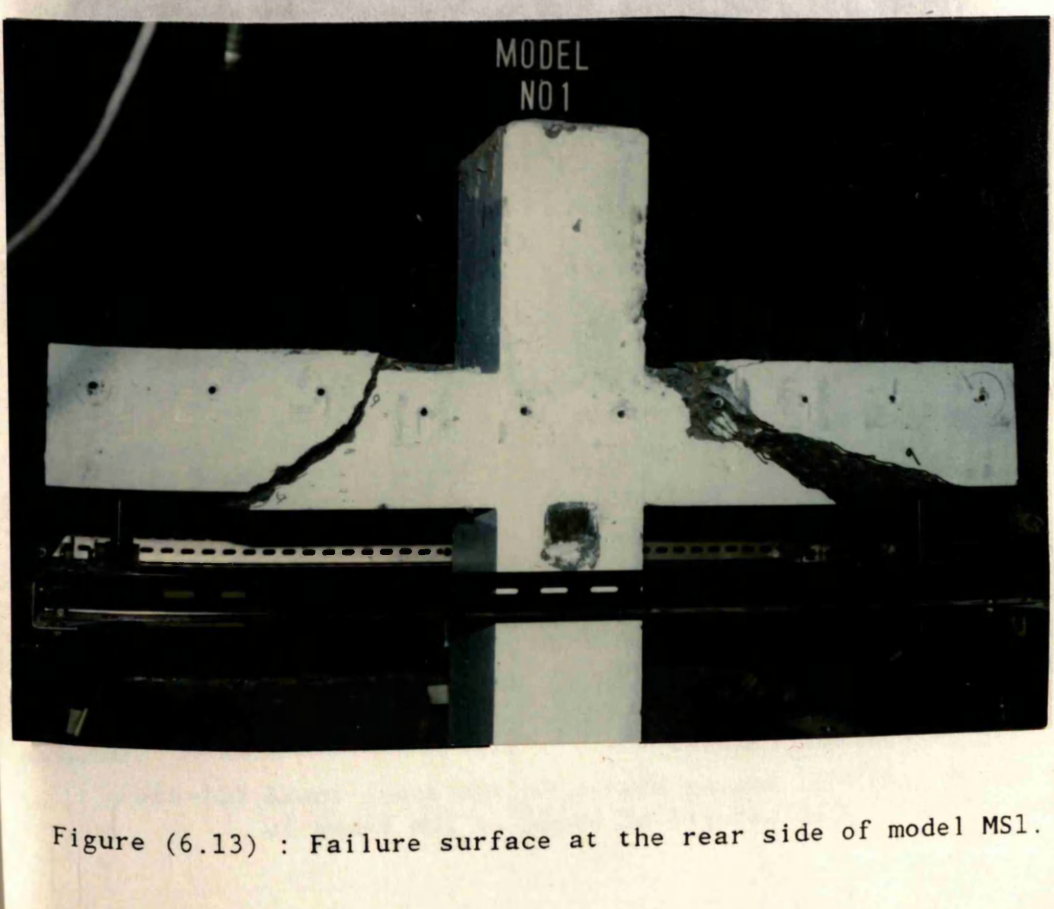

Figure (6.13) : Failure surface at the rear side of model MS1.

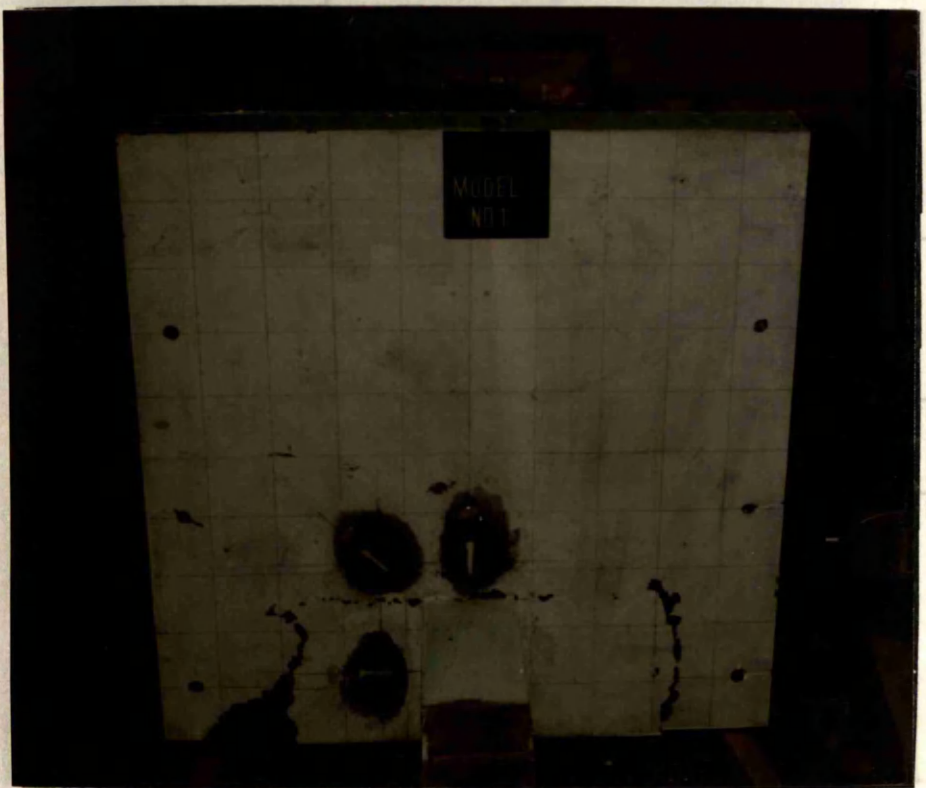

Figure(6−14): Crack pattern on bottom side of model MS1

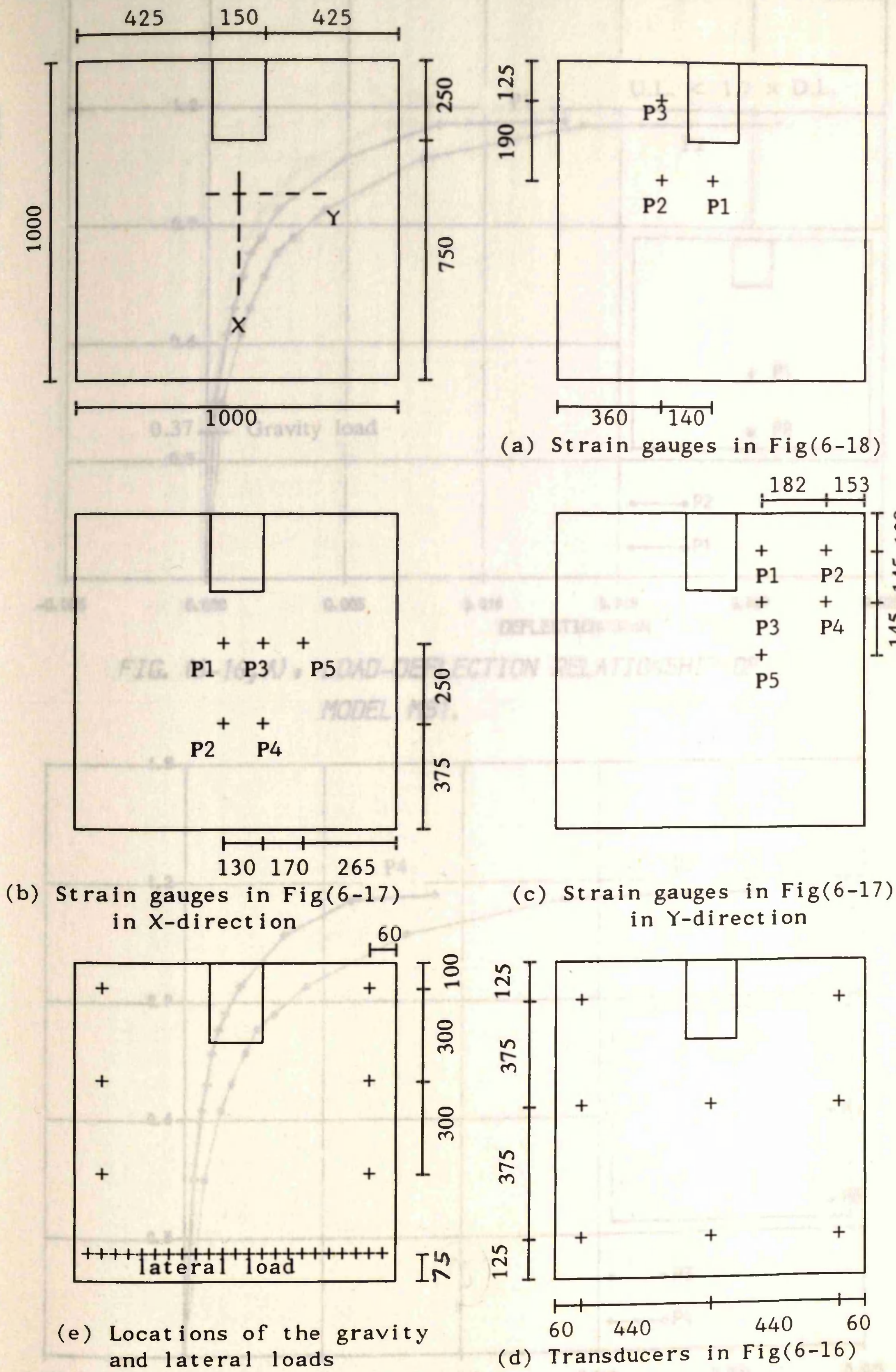

Figure(6-15):Exact locations of strain gauges in the slab and transducers of model MS1 as shown in Figures(6-16), (6-17) and (6-18).

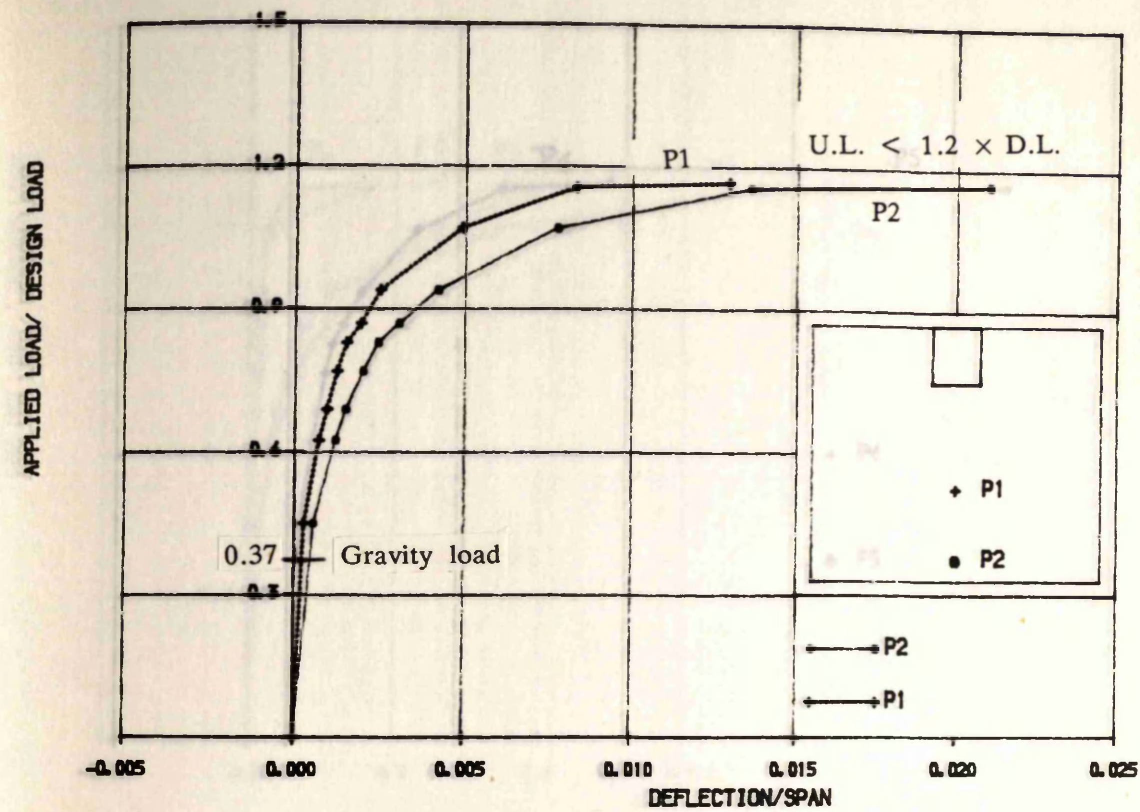

FIG. (6-16,A) : LOAD-DEFLECTION RELATIONSHIP OF MODEL MS1.

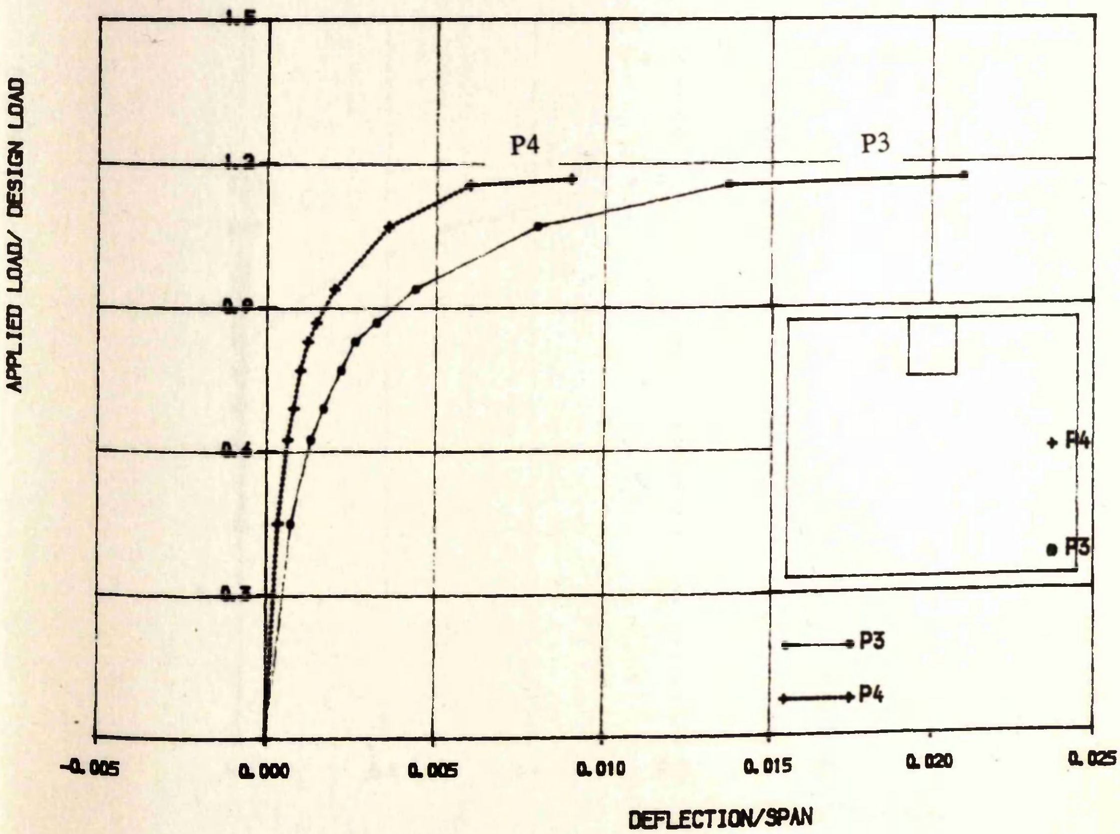

FIG. (6-16,B) : LOAD-DEFLECTION RELATIONSHIP OF MODEL MS1.

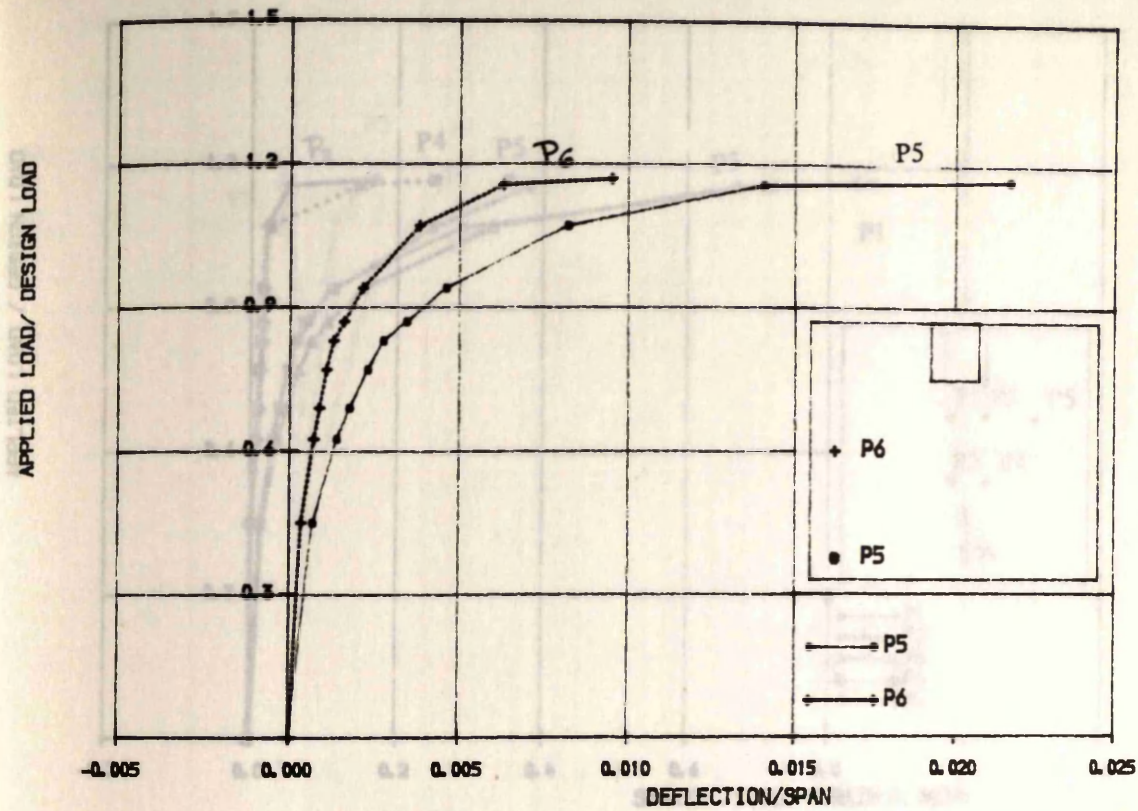

FIG. (6-16,C). LOAD-DEFLECTION RELATIONSHIP OF MODEL MS1.

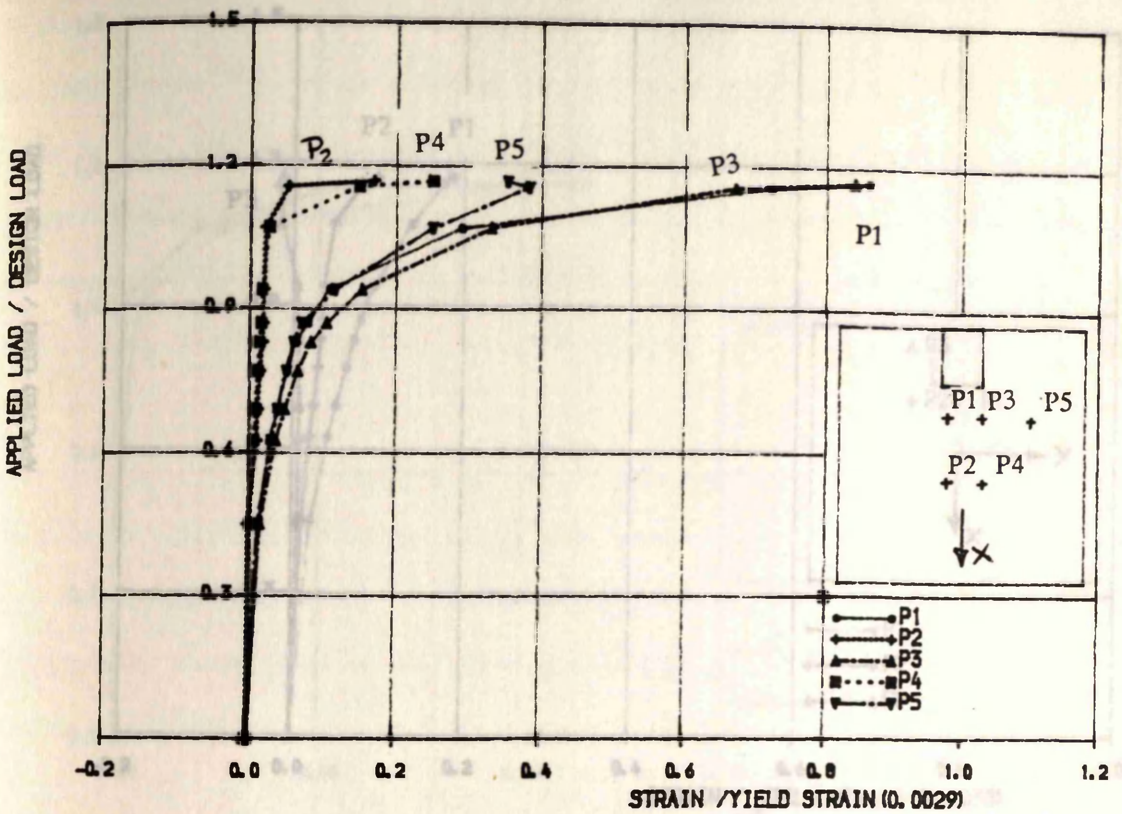

FIG. (6-17, A), LOAD-STRAIN CURVE FOR THE REINFORCING BARS IN X-DIRECTION (MODEL MS1).

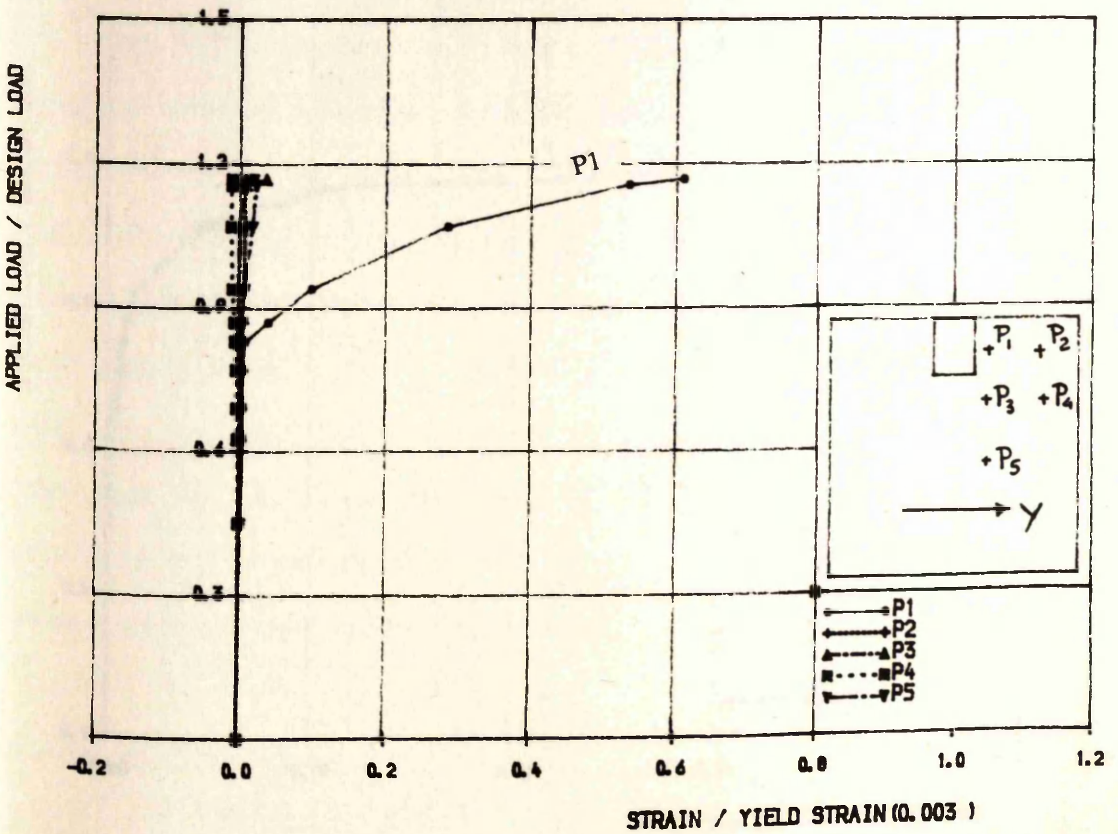

FIG.(6-17B), LOAD-STRAIN CURVE FOR THE REINFORCING BARS IN Y- DIRECTION (MODEL MS1).

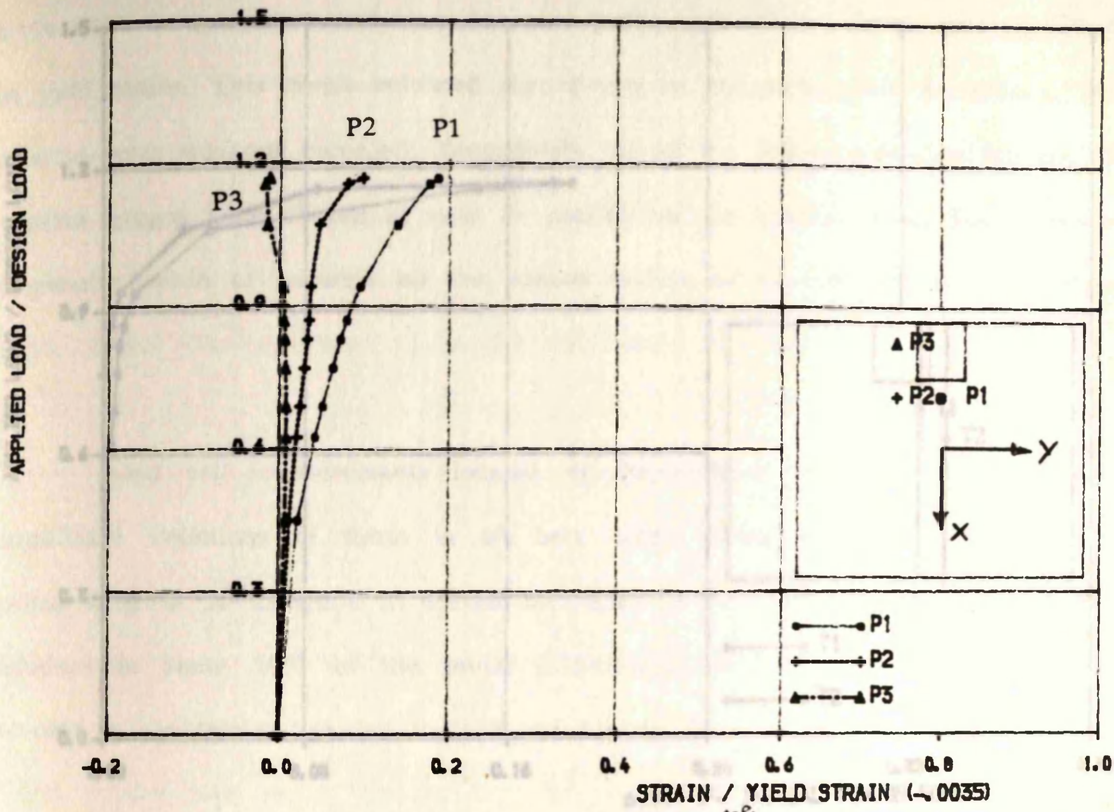

FIG. (6-18) : LOAD-STRAIN CURVE AT the COMPRESSIVE SURFACE OF CONCRETE P1 AND P2 ARE IN X-DIR. AND P3 IN Y-DIR. (MODEL MS1)

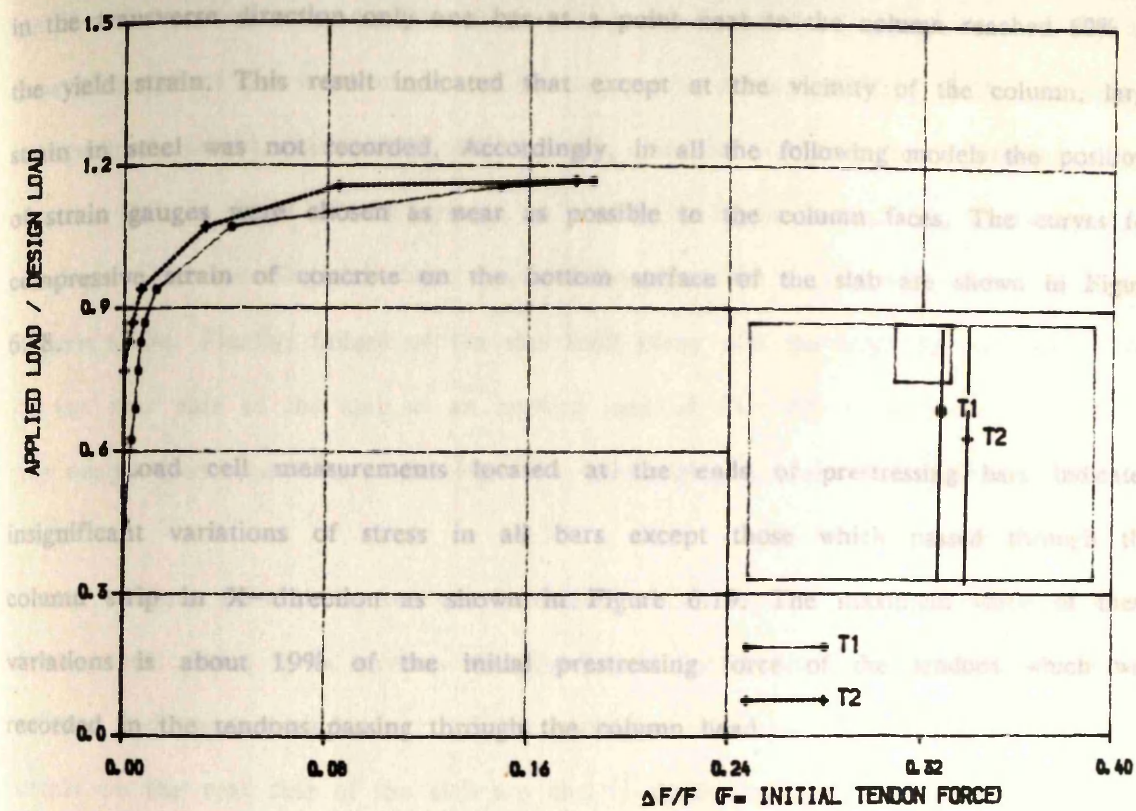

FIG. (6-19, A) : VARIATION IN TENDON FORCE VERSUS APPLIED LOAD FOR MODEL MS1.

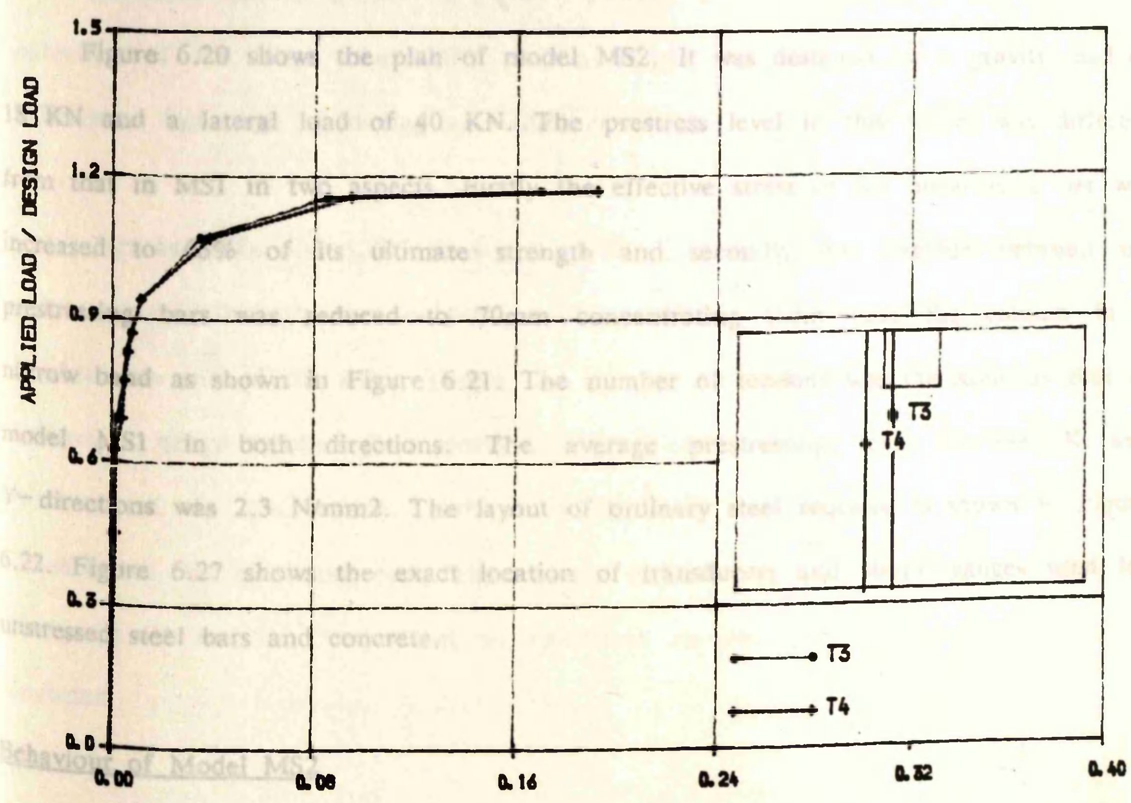

FIG. (6-19, B) : VARIATION IN TENDON FORCE VERSUS APPLIED LOAD FOR MODEL MS1.

in the transverse direction only one bar at a point next to the column reached 60% of the yield strain. This result indicated that except at the vicinity of the column, large strain in steel was not recorded. Accordingly, in all the following models the positions of strain gauges were chosen as near as possible to the column faces. The curves for compressive strain of concrete on the bottom surface of the slab are shown in Figure 6.18.

Load cell measurements located at the ends of prestressing bars indicated insignificant variations of stress in all bars except those which passed through the column strip in X– direction as shown in Figure 6.19. The maximum value of these variations is about 19% of the initial prestressing force of the tendons which was recorded in the tendons passing through the column head.

6.7.2 Model MS2

Figure 6.20 shows the plan of model MS2. It was designed for a gravity load of 18 KN and a lateral load of 40 KN. The prestress level in this model was different from that in MS1 in two aspects. Firstly the effective stress of the prestressing bar was increased to 63% of its ultimate strength and secondly the distance between the prestressing bars was reduced to 70mm concentrating them near the column in a narrow band as shown in Figure 6.21. The number of tendons was the same as that of model MS1 in both directions. The average prestressing level in the X and Y– directions was 2.3 N/mm2. The layout of ordinary steel required is shown in Figure 6.22. Figure 6.27 shows the exact location of transducers and strain– gauges used for unstressed steel bars and concrete.

Behaviour of Model MS2

No hairline cracks were observed after the application of the prestressing forces in X and Y– directions. At 76% of the design load, the first flexural crack on the slab was observed at the front corner of the column as shown in Figure 6.23a. At 93% of design load, cracks extended in the transverse direction and new flexural cracks appeared on the slab in front of the column as shown in Figure 6.23b. Also at this stage of loading a hairline diagonal shear cracks initiated at the rear side of slab as shown in Figure 6.23c. Finally, failure of the slab took place with the large diagonal shear cracks at the rear side of the slab at an applied load of 64.5 KN corresponding to 111% of the design load. Just like model MS1 the failure of this model was punching.

Figure 6.24 shows the crack pattern on the tension side of the slab after the failure took place. It is obvious that there are just a few hairline cracks around the column and the remainder part of the slab was uncracked. The diagonal shear failure cracks on the rear side of the slab are clearly visible in Figure 6.25. The crack pattern on the compressive surface of the slab is shown in Figure 6.26. From the experimental load– deflection curves shown in Figures 6– 28a, 6.28b and 6.28c , the considerable reduction of the slope after 75% of the design load indicates that the first crack initiated at this stage of loading as mentioned above.

Figures 6.29a and 6.29b show the tensile strain curves for the ordinary steel bars which passed through the column head in X and Y– directions respectively. In X– direction one of the strain gauges was damaged at 84% of the design load but the companion gauge reached yield strain at failure load. The curves of compressive strain of concrete on the bottom surface of the slab are shown in Figure 6.30. In X– direction the maximum compressive strain of 77% of the yield strain took place at the point P1 and in Y– direction no significant amount of the compressive strain was recorded.

Figures 6.31a and 6.31b show the variations of stresses in all the prestressing bars in X– direction. The maximum amount of these variations is 14% of the initial force of

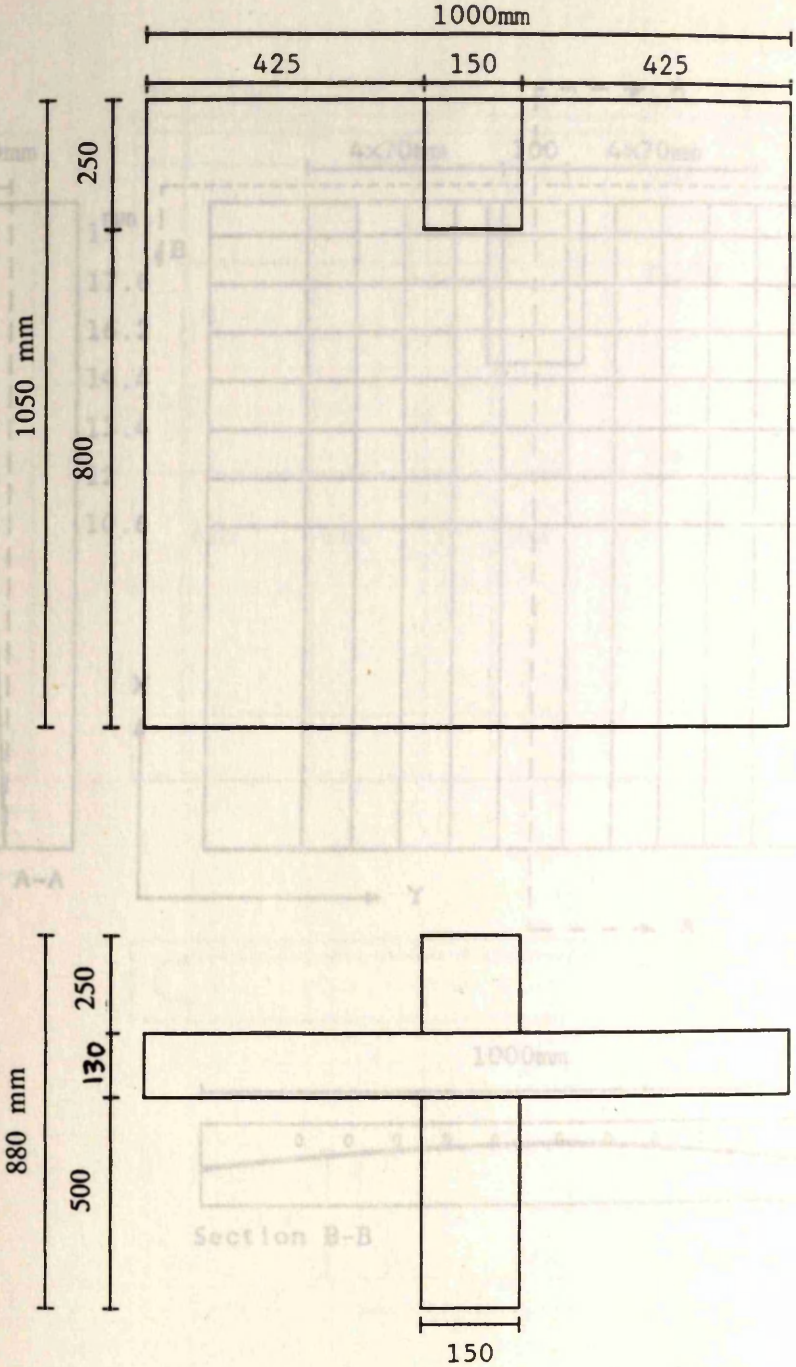

Figure (6.20) : Plane and dimensions of model MS2

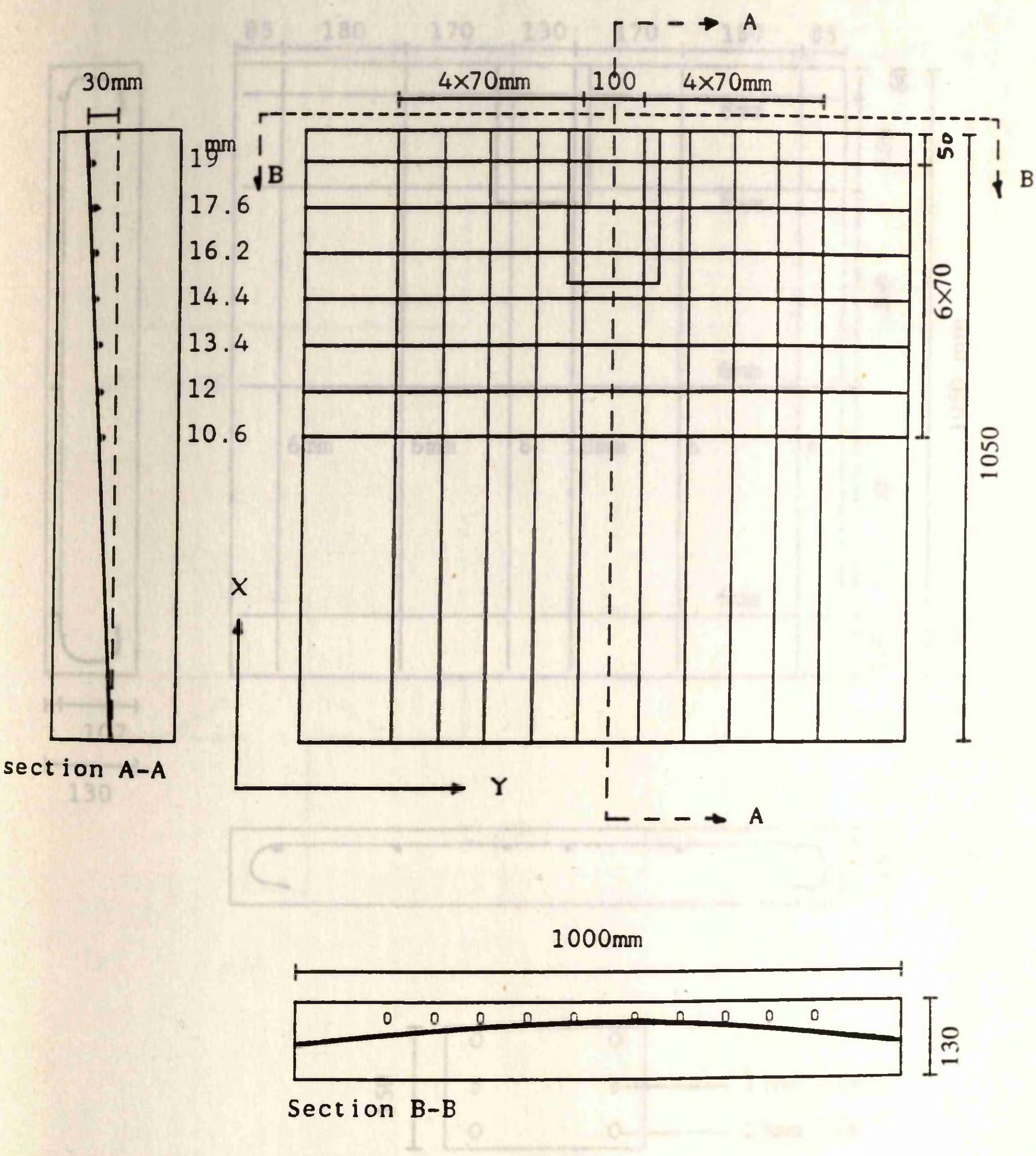

Figure (6.21): Distribution of prestressing bars in X and Y-direction for model MS2.

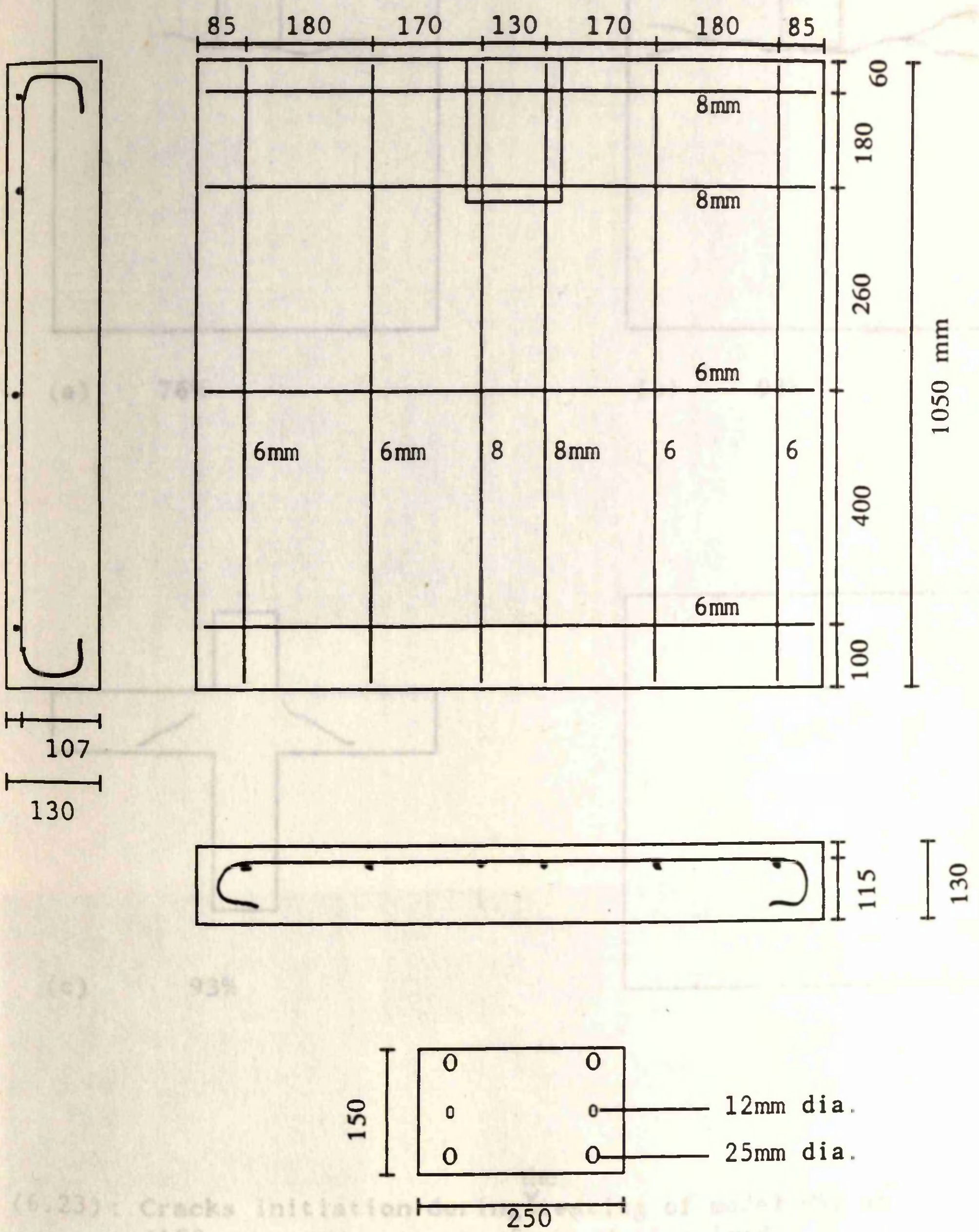

Figure (6.22): Arrangement of ordinary reinforcement bars in the slab and column for model MS2.

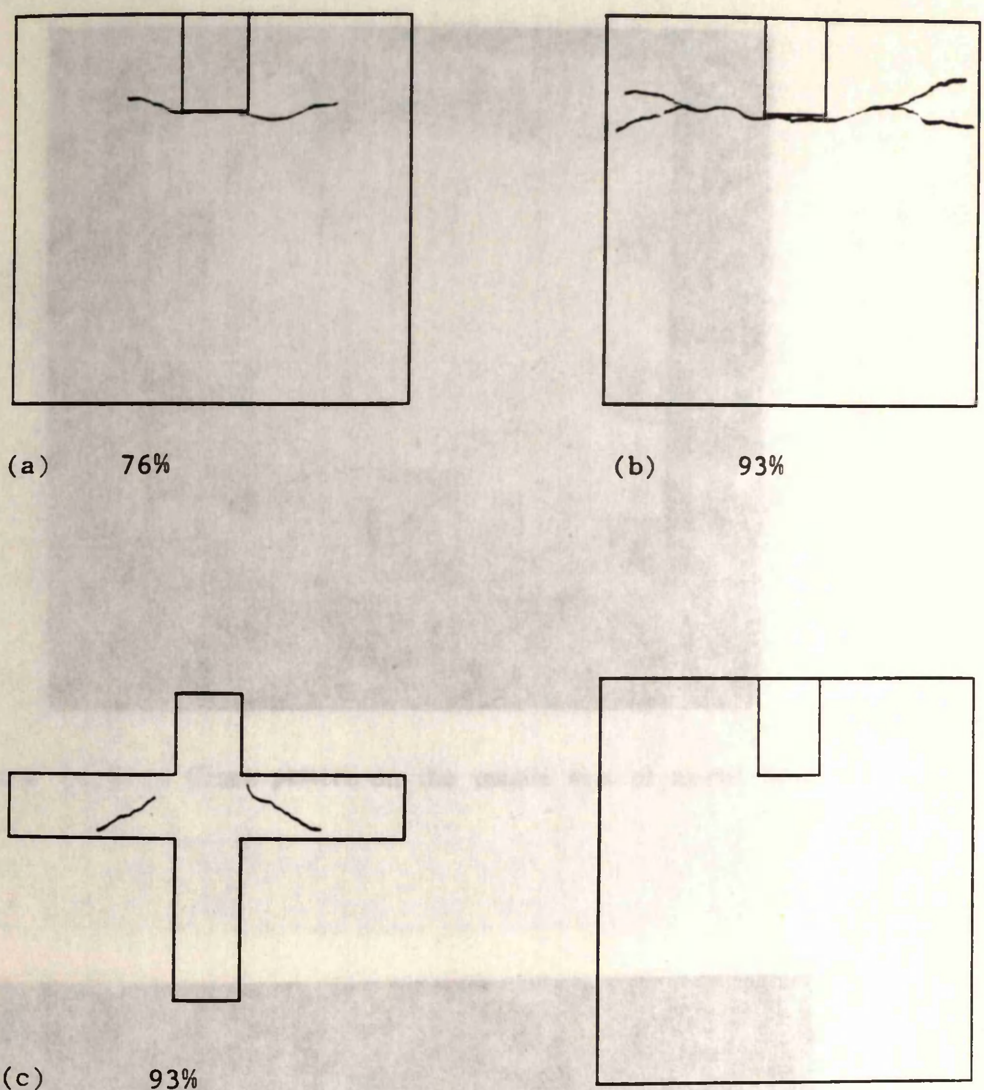

Figure (6.23) : Cracks initiation during the testing of model MS2 at different percentages of the design load.

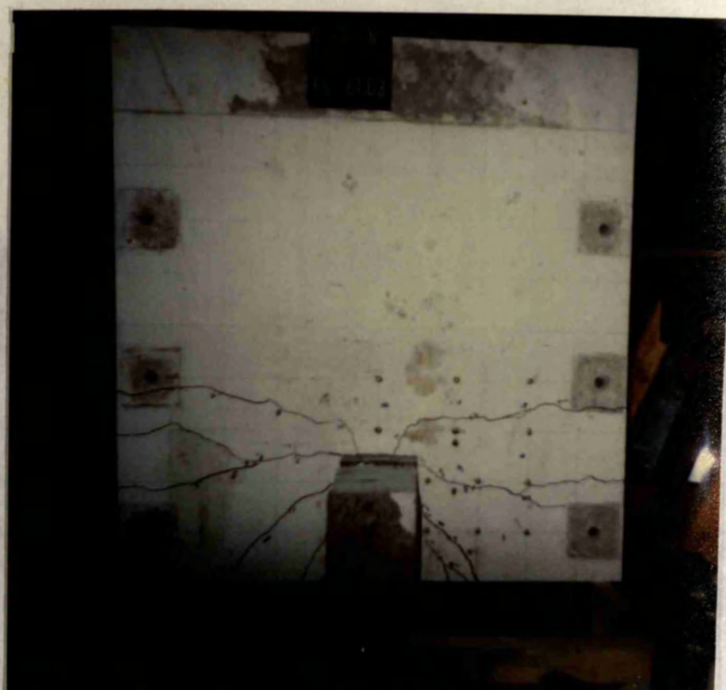

Figure (6.24): Crack pattern on the tensile side of model MS2

Figure (6.25): Failure surface at rear side of model MS2

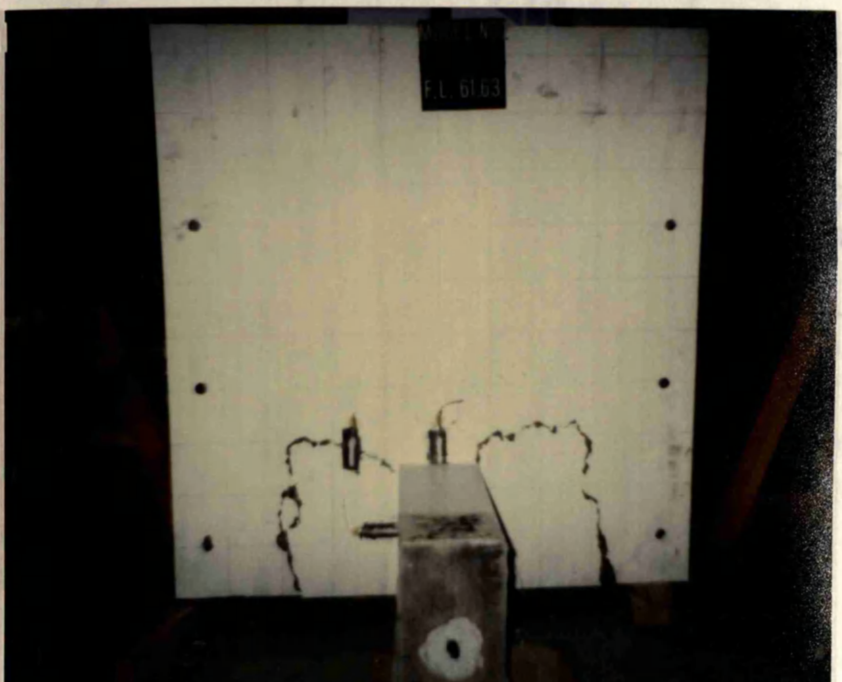

Figure (6.26): Crack pattern on bottom side of model MS2.

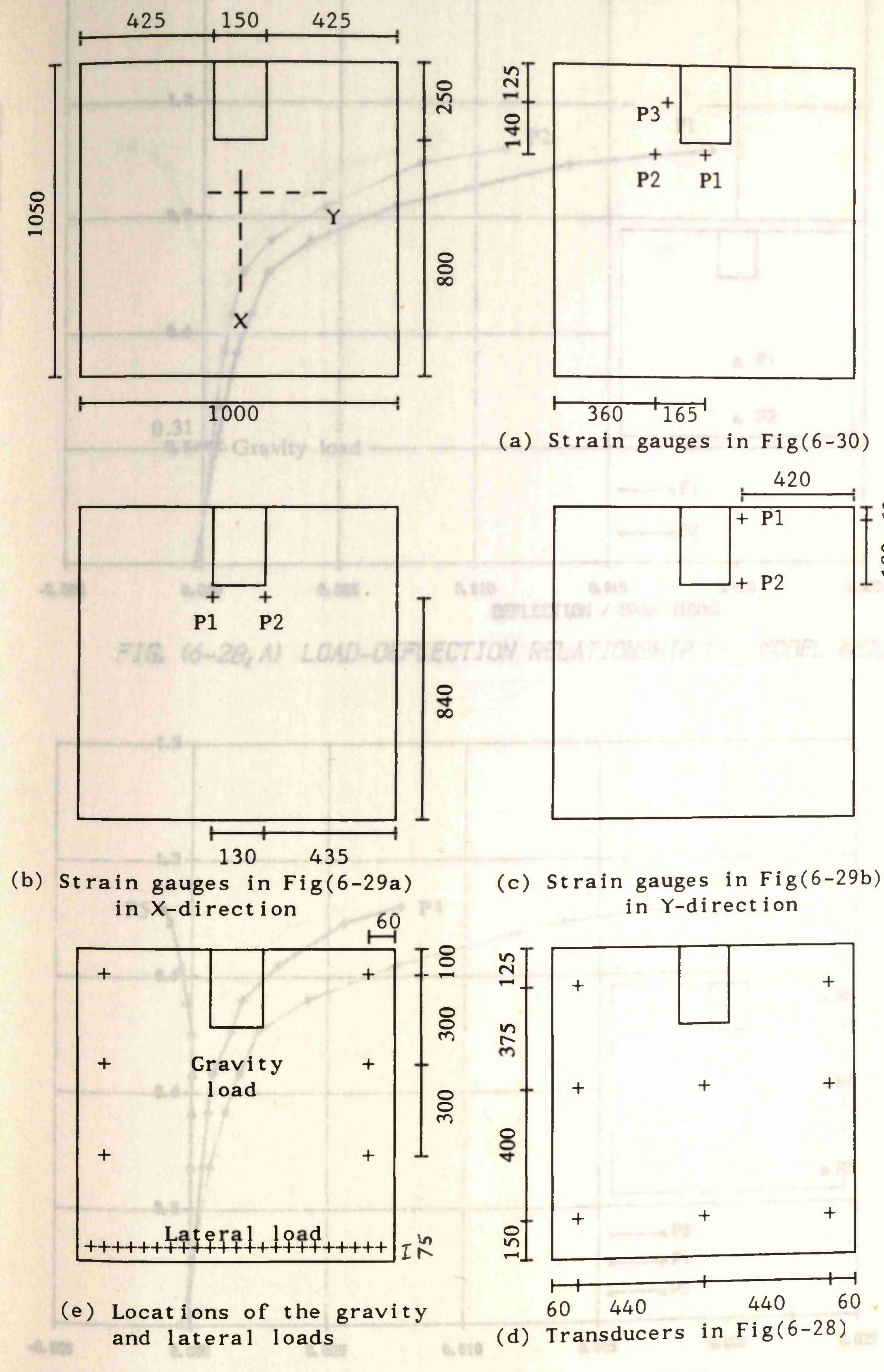

Figure(6-27): Exact locations of strain gauges in the slab and transducers of model MS2 as shown in Figures(6-28), (6-29) and (6-30).

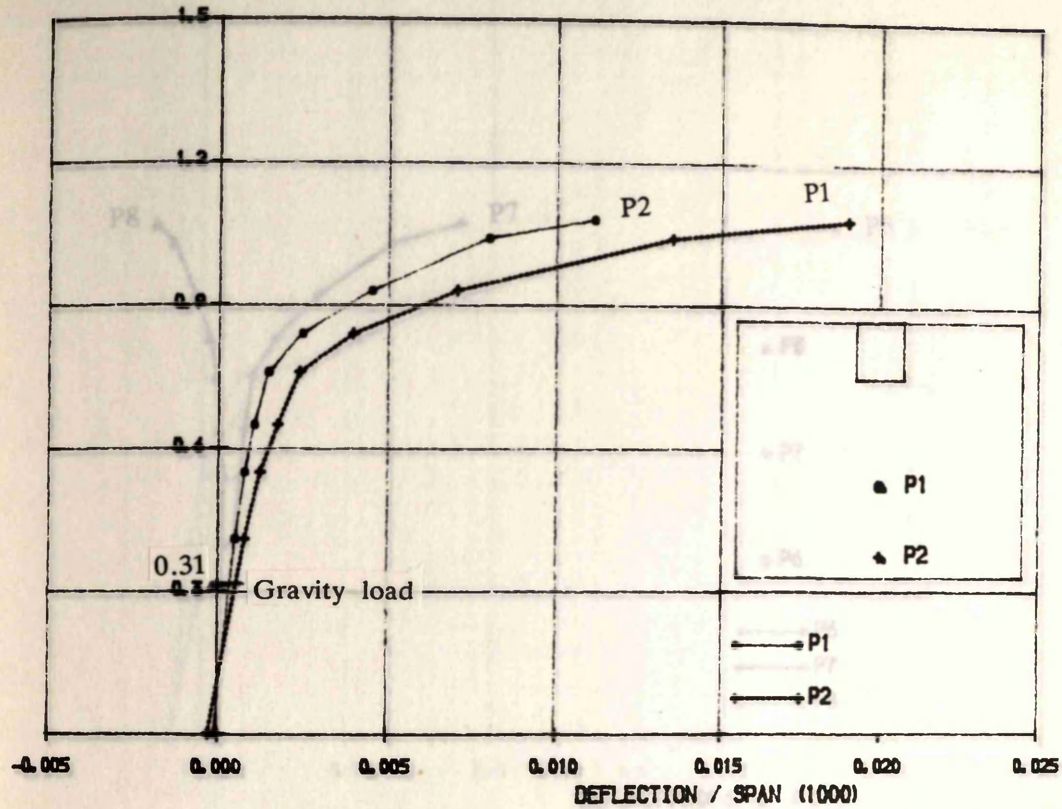

FIG. (6-28,A) LOAD-DEFLECTION RELATIONSHIP OF MODEL MS2.

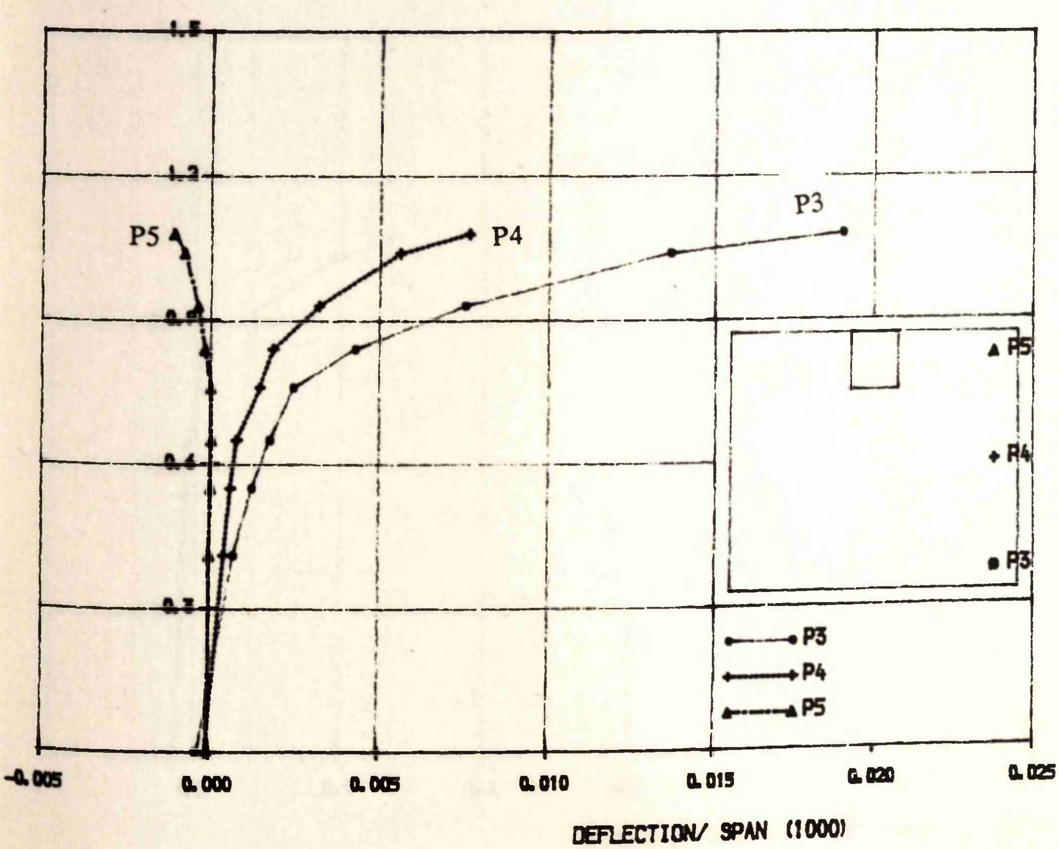

FIG. (6-28,B). LOAD-DEFLECTION RELATIONSHIP OF MODEL MS2.

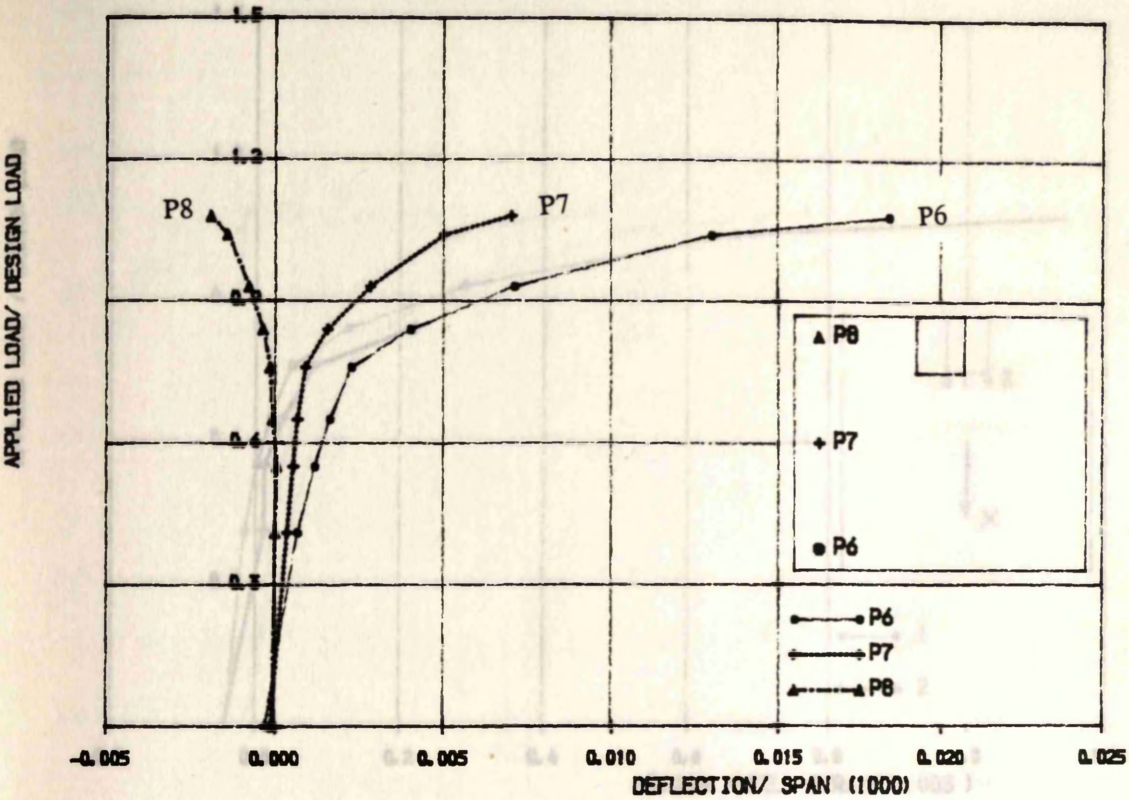

FIG. (6-28,C) . LOAD-DEFLECTION RELATIONSHIP OF MODEL MS2.

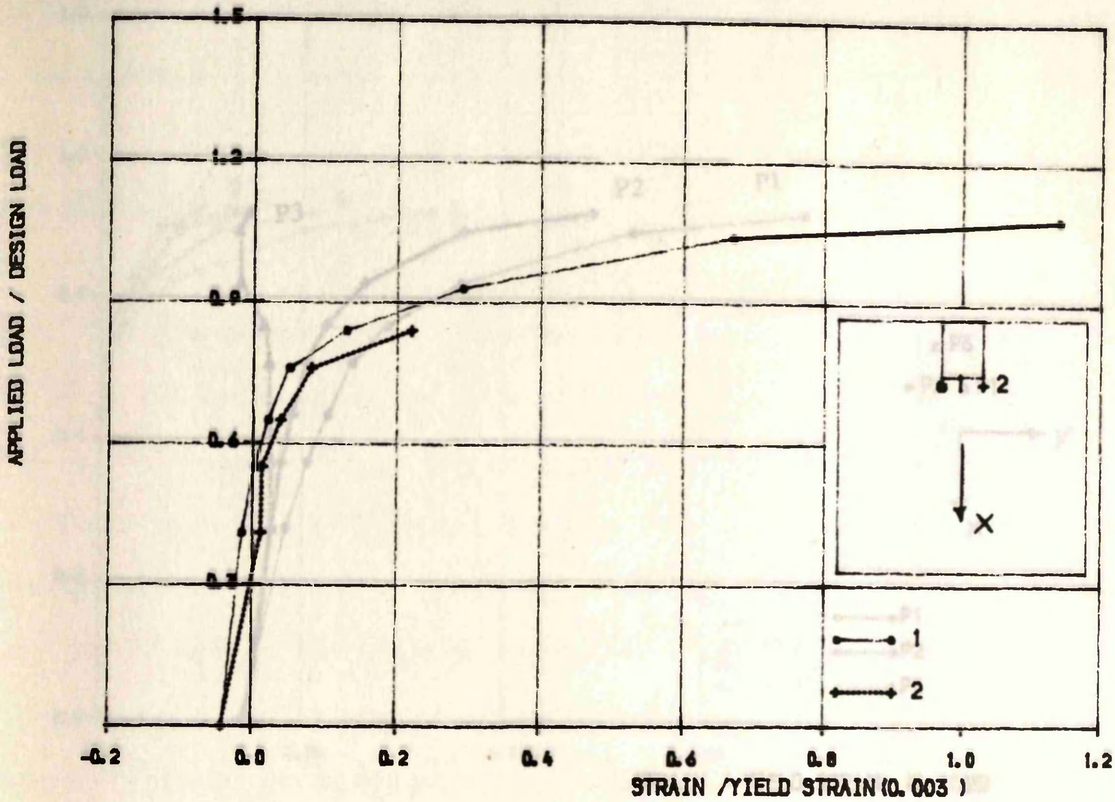

FIG. (6-29,A). LOAD-STRAIN CURVE FOR REINFORCING BAR IN X-DIRECTION (MODEL MS2).

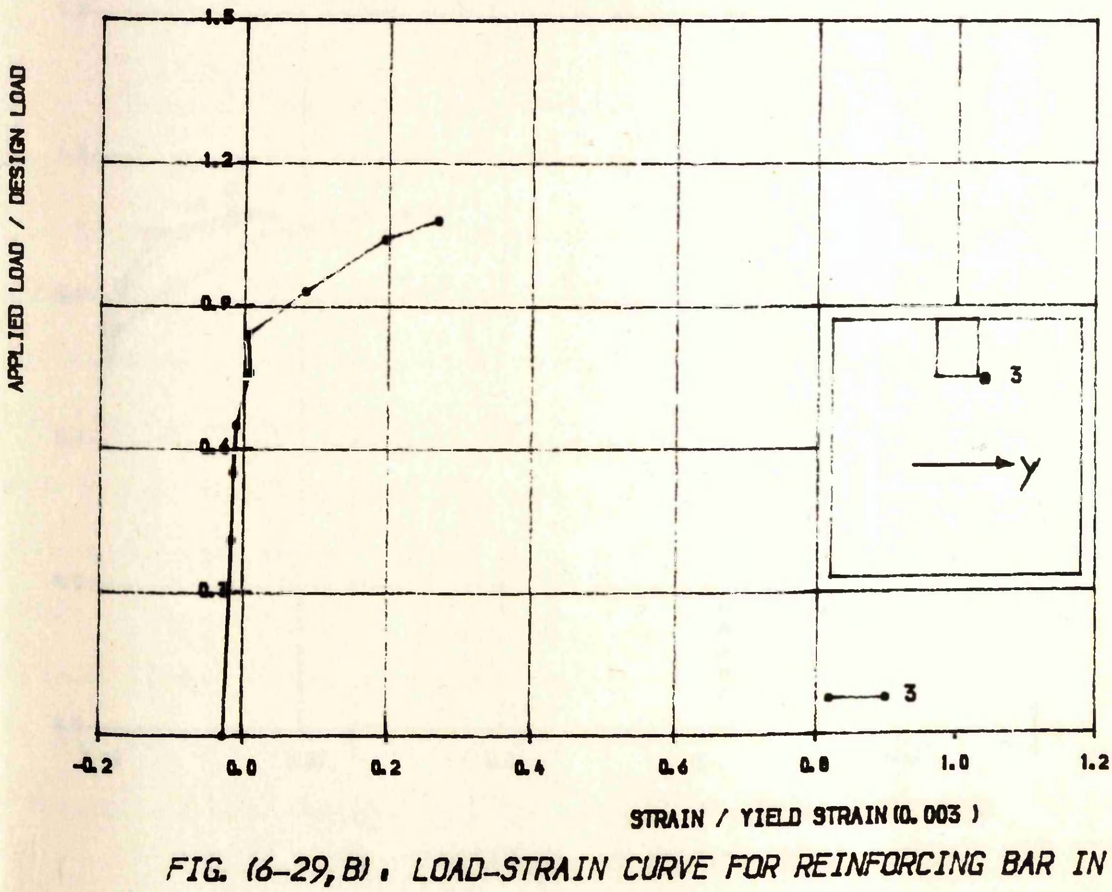

FIG. (6-29,B). LOAD-STRAIN CURVE FOR REINFORCING BAR IN Y-DIRECTION (MODEL MS2).

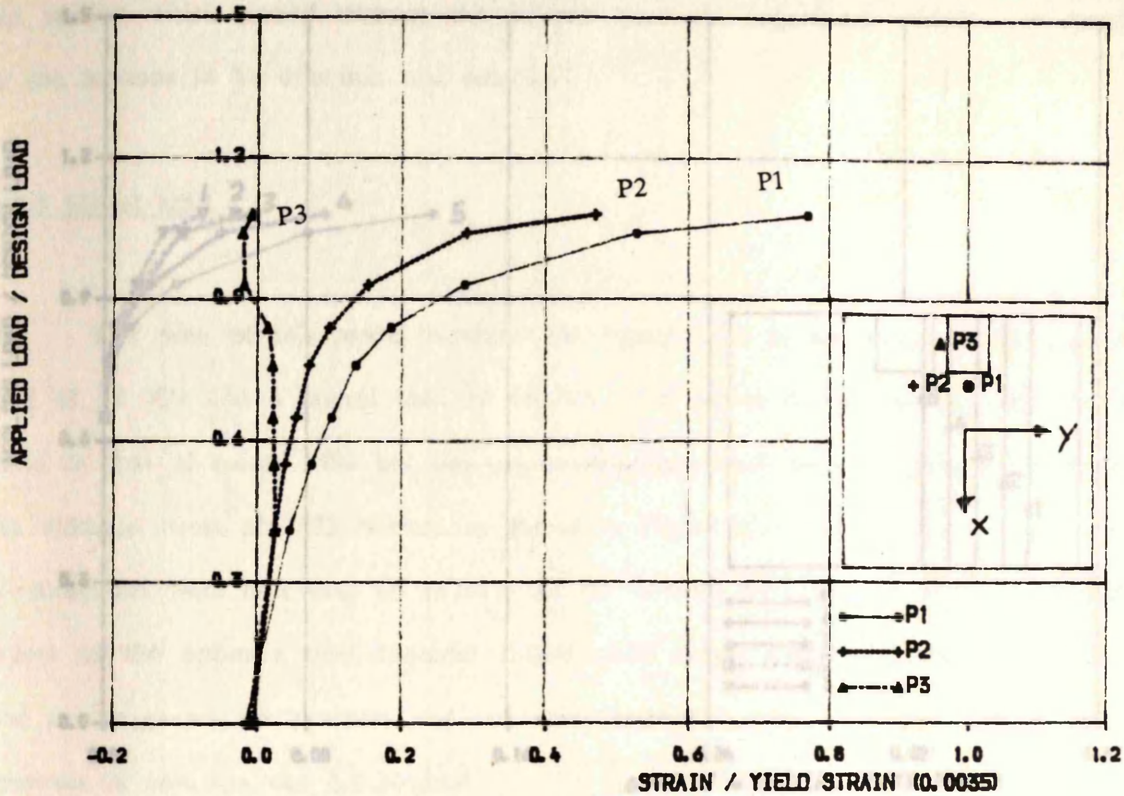

FIG (6-30), LOAD-STRAIN CURVE AT COMPRESSIVE SURFACE OF CONCRE; P1 AND P2 ARE IN X-DIR. AND P3 IN Y-DIR. (MODEL MS:

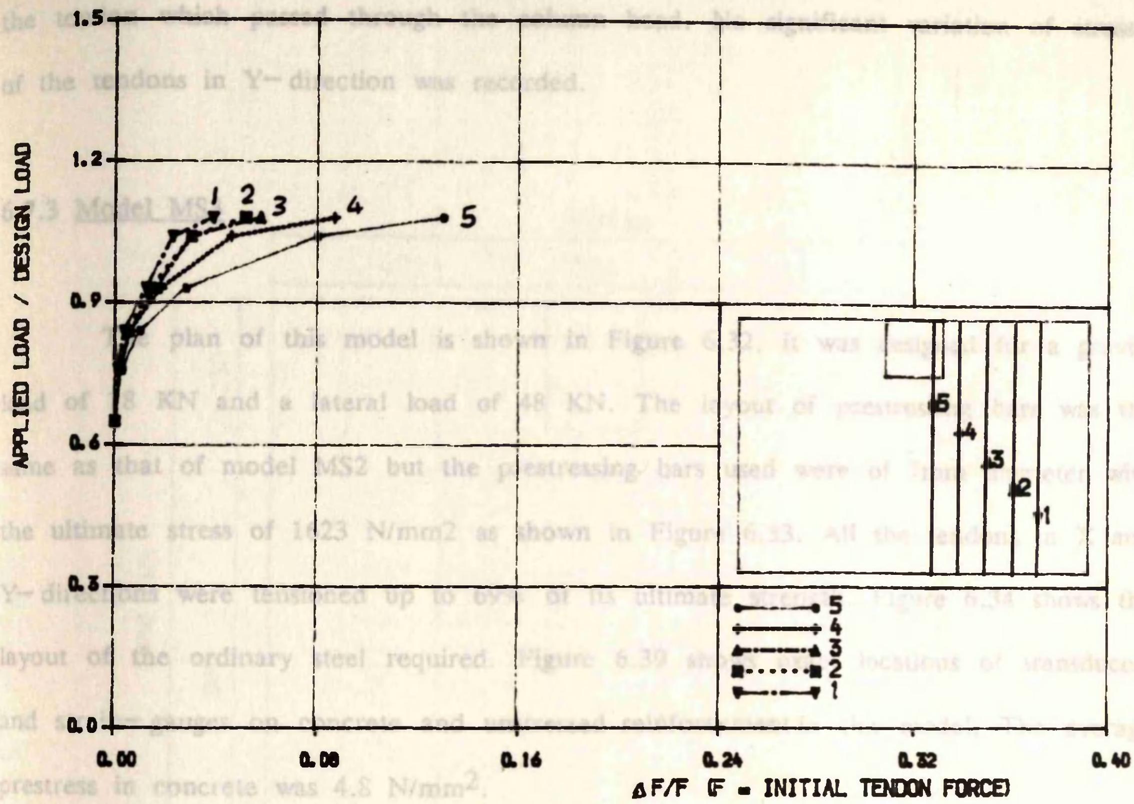

FIG. (6-31,A) : VARIATION IN TENDON FORCE (MODEL MS2).

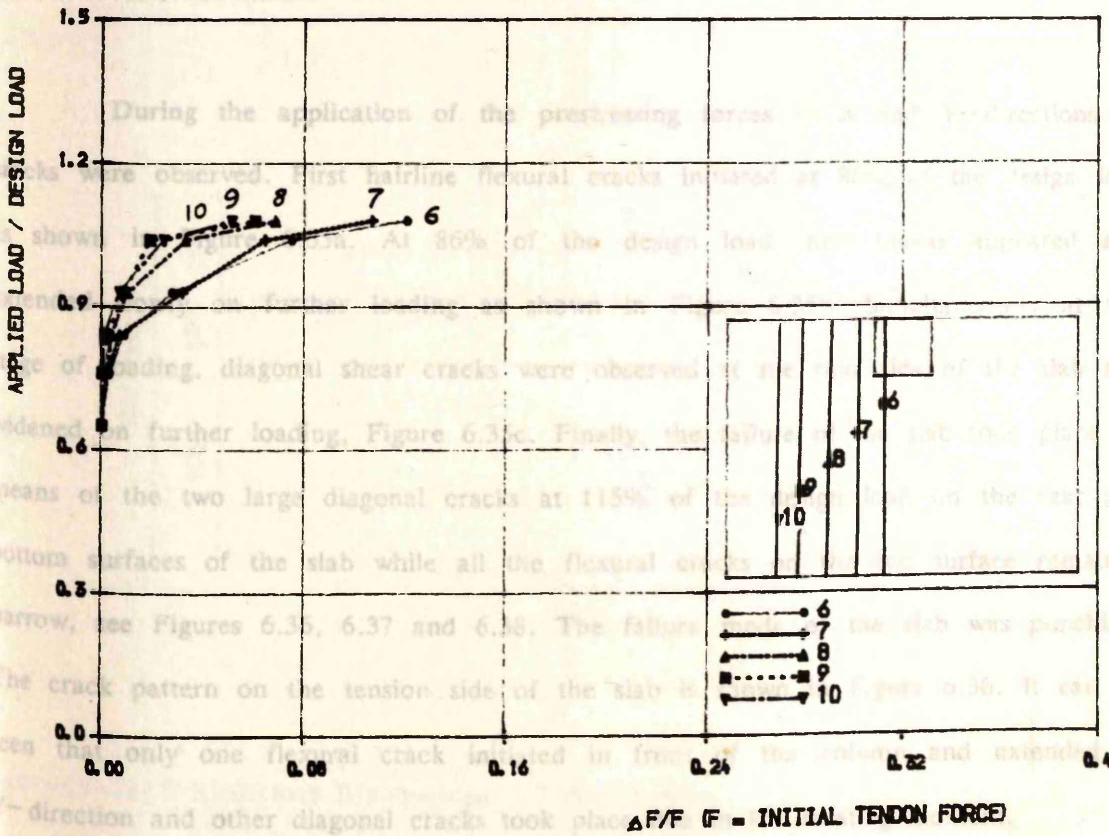

FIG. (6-31,B) : VARIATION IN TENDON FORCE (MODEL MS2).

the tendon which passed through the column head. No significant variation of stresses of the tendons in Y– direction was recorded.

6.7.3 Model MS3

The plan of this model is shown in Figure 6.32. It was designed for a gravity load of 18 KN and a lateral load of 48 KN. The layout of prestressing bars was the same as that of model MS2 but the prestressing bars used were of 7mm diameter with the ultimate stress of 1623 N/mm2 as shown in Figure 6.33. All the tendons in X and Y– directions were tensioned up to 69% of its ultimate strength. Figure 6.34 shows the layout of the ordinary steel required. Figure 6.39 shows exact locations of transducers and strain– gauges on concrete and unstressed reinforcement in this model. The average prestress in concrete was 4.8 N/mm^2.

Behaviour of Model MS3

During the application of the prestressing forces in X and Y– directions no cracks were observed. First hairline flexural cracks initiated at 80% of the design load as shown in Figure 6.35a. At 86% of the design load, new cracks appeared and extended slowly on further loading as shown in Figure 6.35b. Simultaneously at this stage of loading, diagonal shear cracks were observed at the rear side of the slab and widened on further loading, Figure 6.35c. Finally, the failure of the slab took place by means of the two large diagonal cracks at 115% of the design load on the rear and bottom surfaces of the slab while all the flexural cracks on the top surface remained narrow, see Figures 6.36, 6.37 and 6.38. The failure mode of the slab was punching. The crack pattern on the tension side of the slab is shown in Figure 6.36. It can be seen that only one flexural crack initiated in front of the column and extended in Y– direction and other diagonal cracks took place due to the twisting moment.

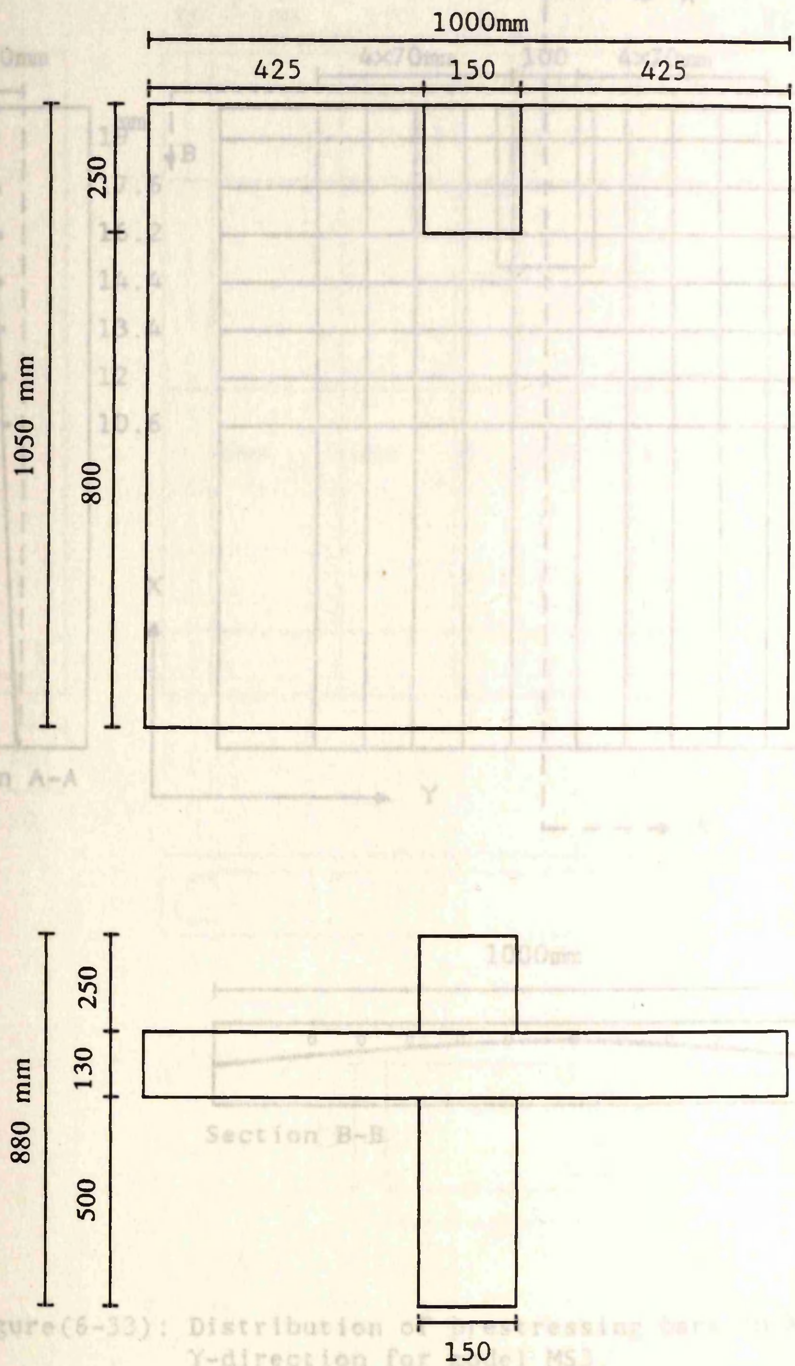

Figure(6-32): Plan and Dimensions of Model MS3.

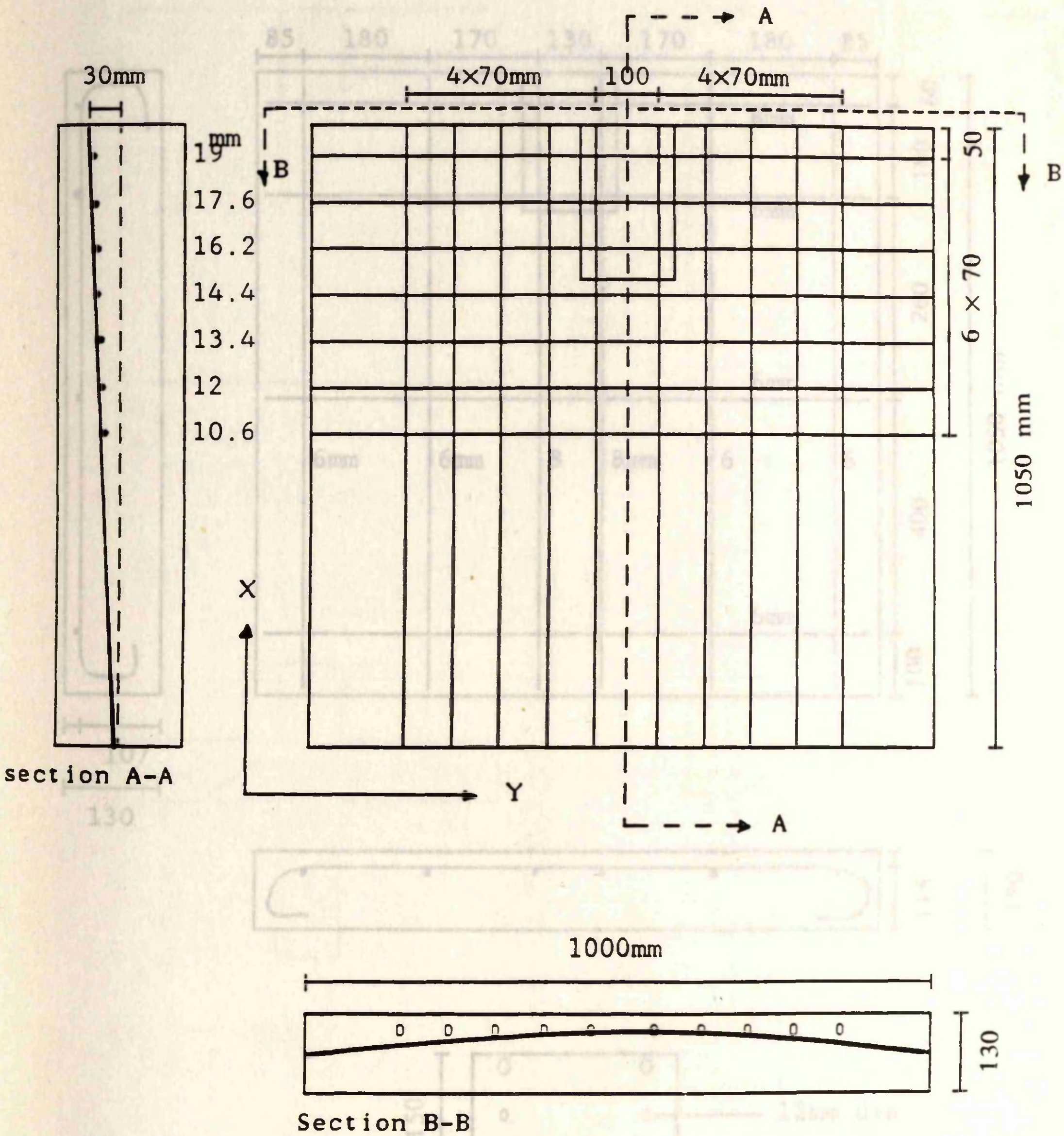

Figure(6-33): Distribution of prestressing bars in X and Y-direction for model MS3.

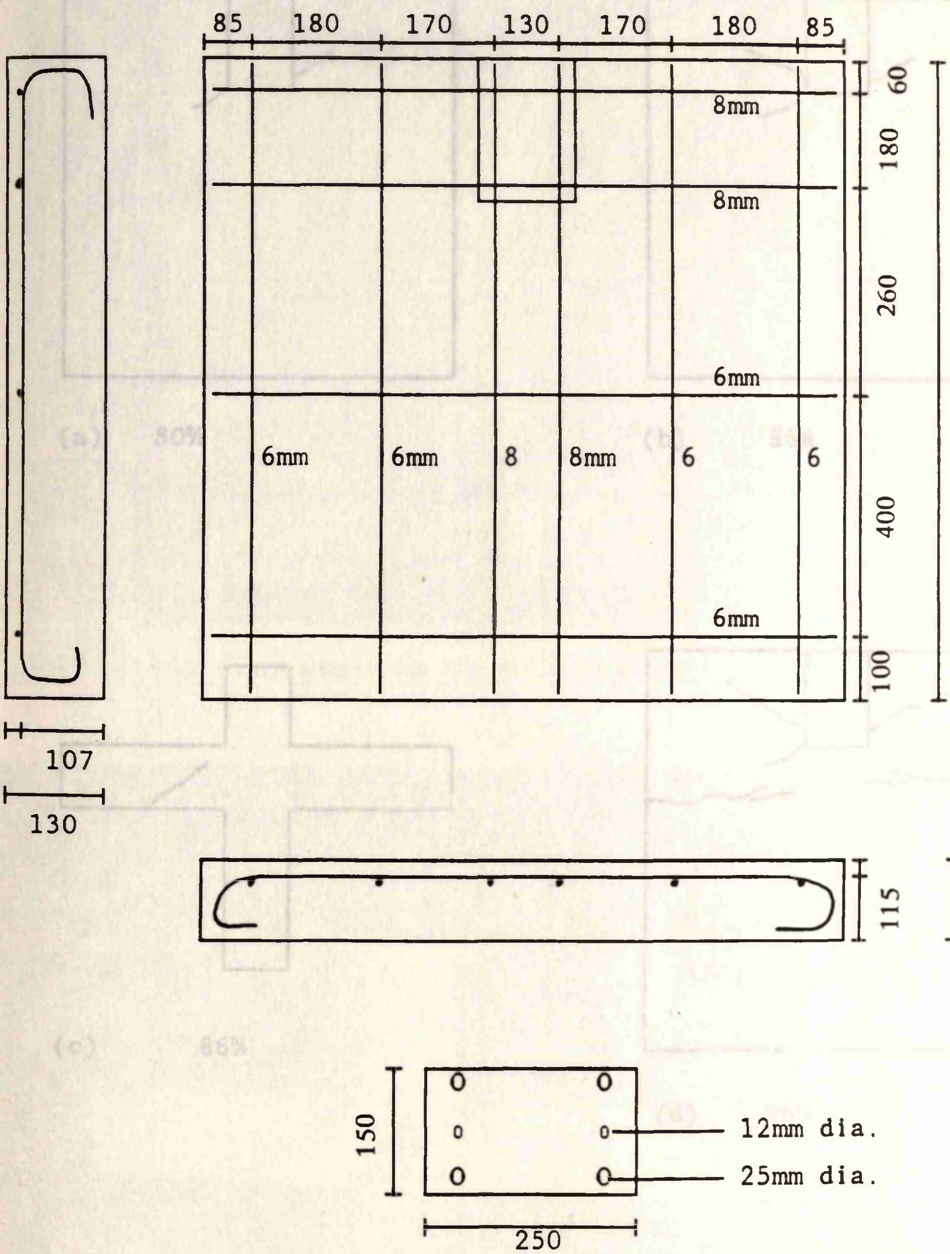

Figure(6-34): Arrangement of ordinary reinforcement bars in the slab and column for model MS3.

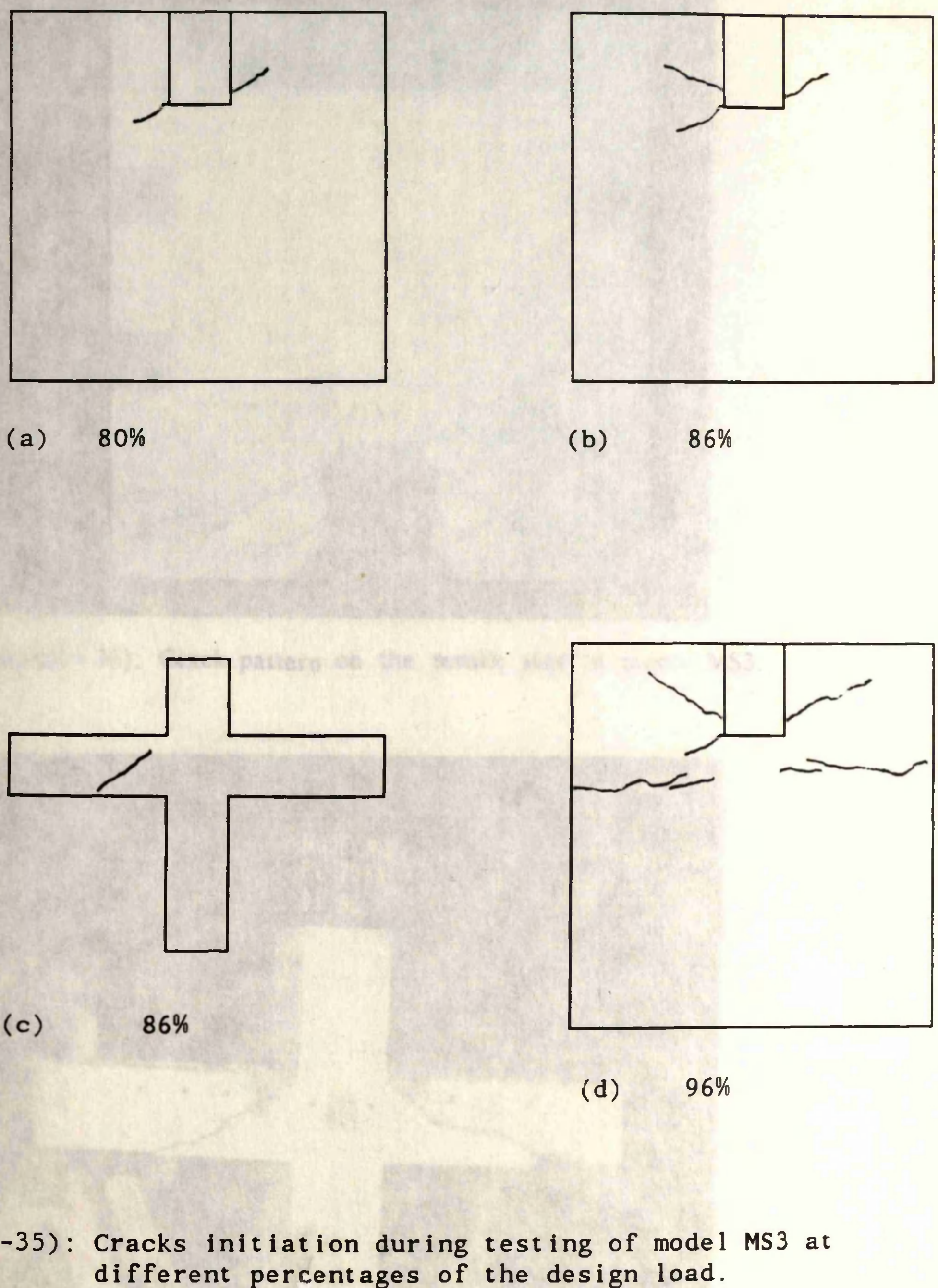

Figure(6-35): Cracks initiation during testing of model MS3 at different percentages of the design load.

Figure(6– 36): Crack pattern on the tensile side of model MS3.

Figure (6.37): Failure surface at rear side of model MS3

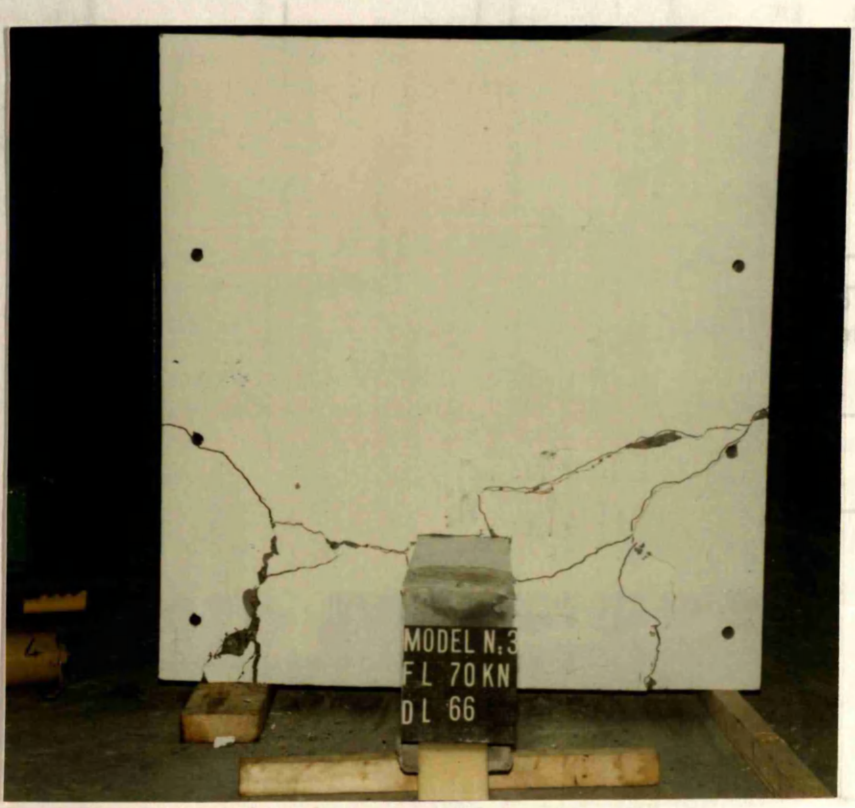

Figure(6– 38): Crack pattern on bottom side of model MS3.

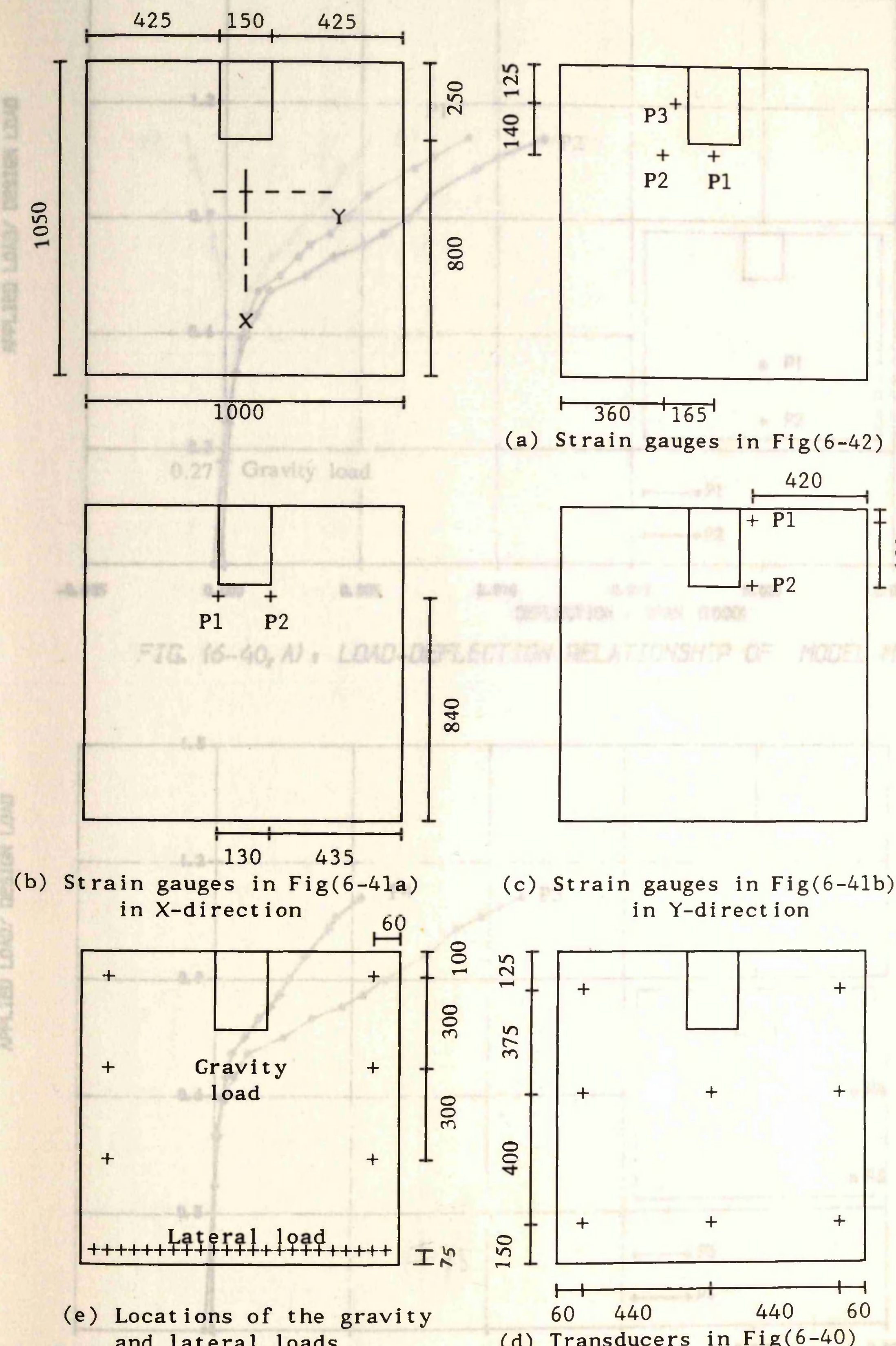

Figure(6-39): Exact locations of strain gauges in the slab and transducers of model MS3 as shown in Figures(6-40), (6-41) and (6-42).

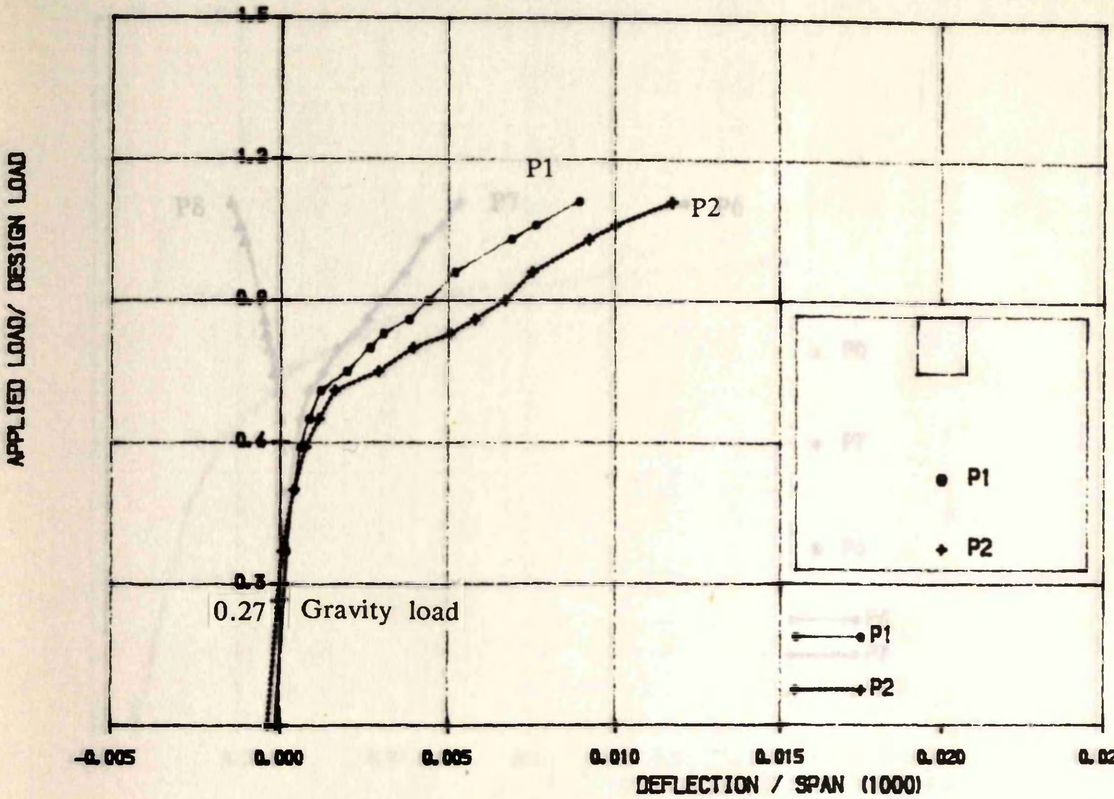

FIG. (6-40,A) . LOAD-DEFLECTION RELATIONSHIP OF MODEL MS3.

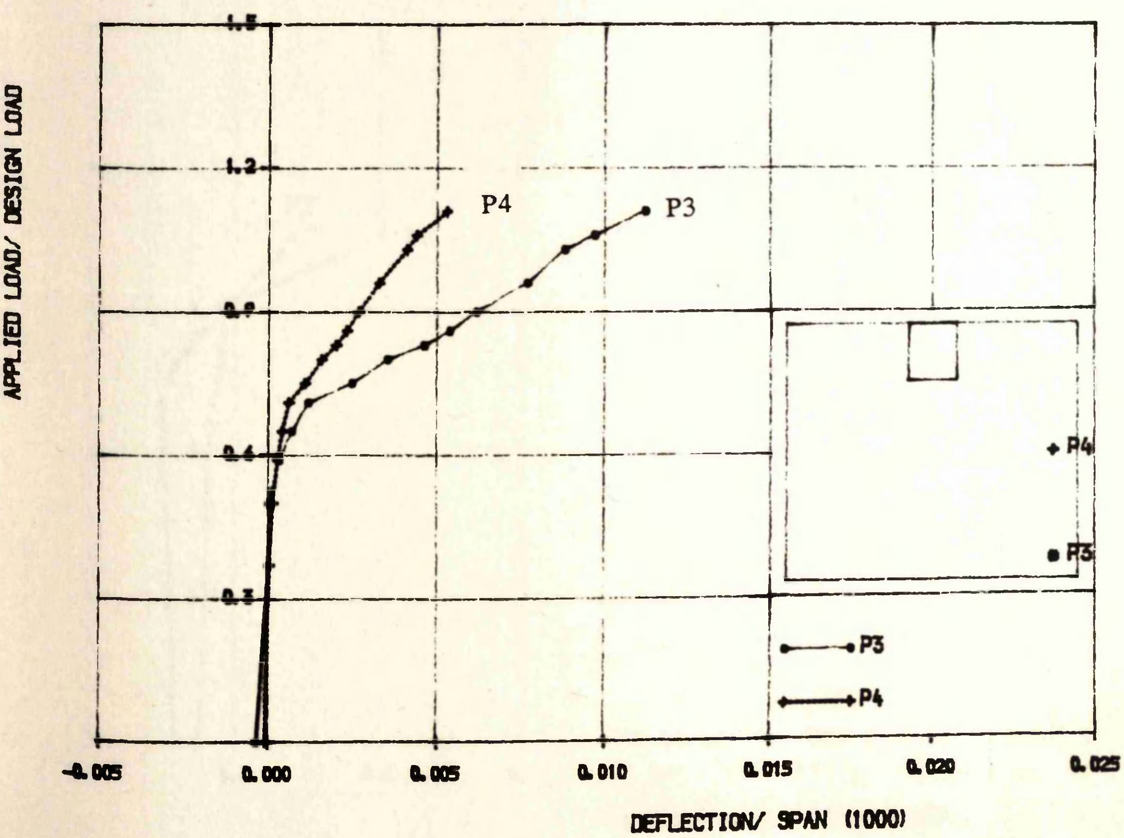

FIG. (6-40,B) . LOAD-DEFLECTION RELATIONSHIP OF MODEL MS3.

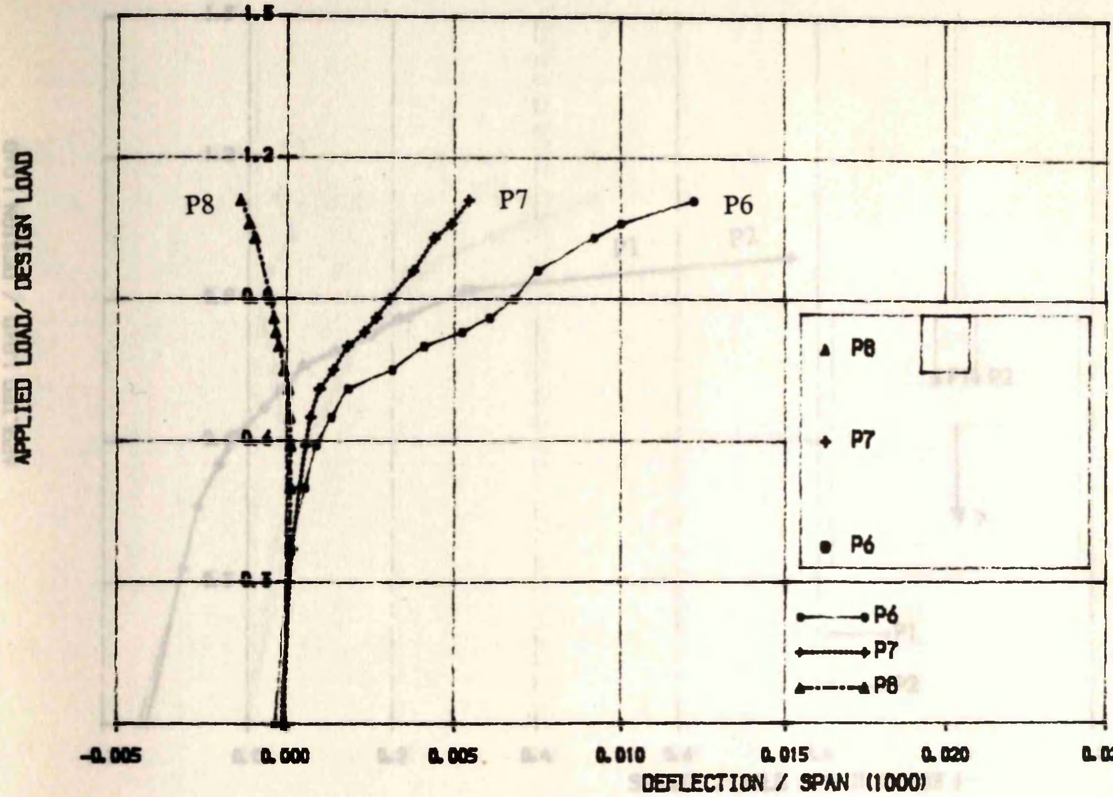

FIG. (6-40,C) : LOAD-DEFLECTION RELATIONSHIP OF MODEL MS3.

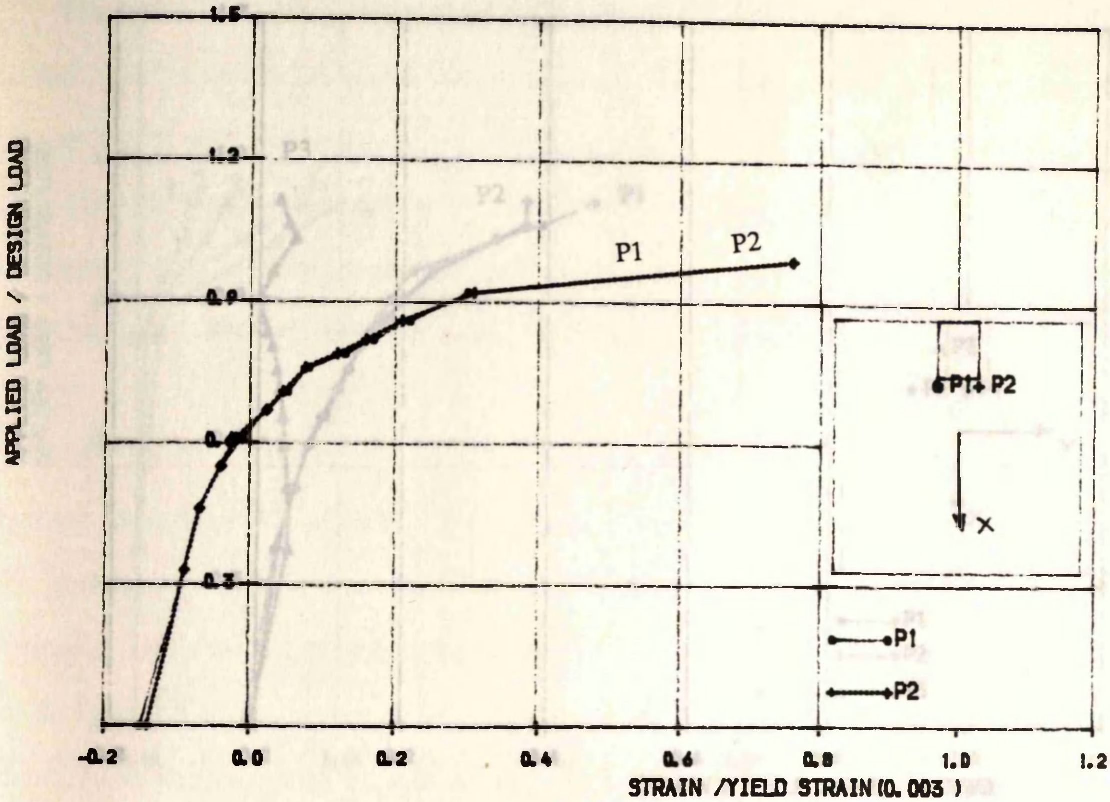

FIG. (6-41,A). LOAD-STRAIN CURVE FOR REINFORCING BAR IN X- DIRECTION (MODEL MS3).

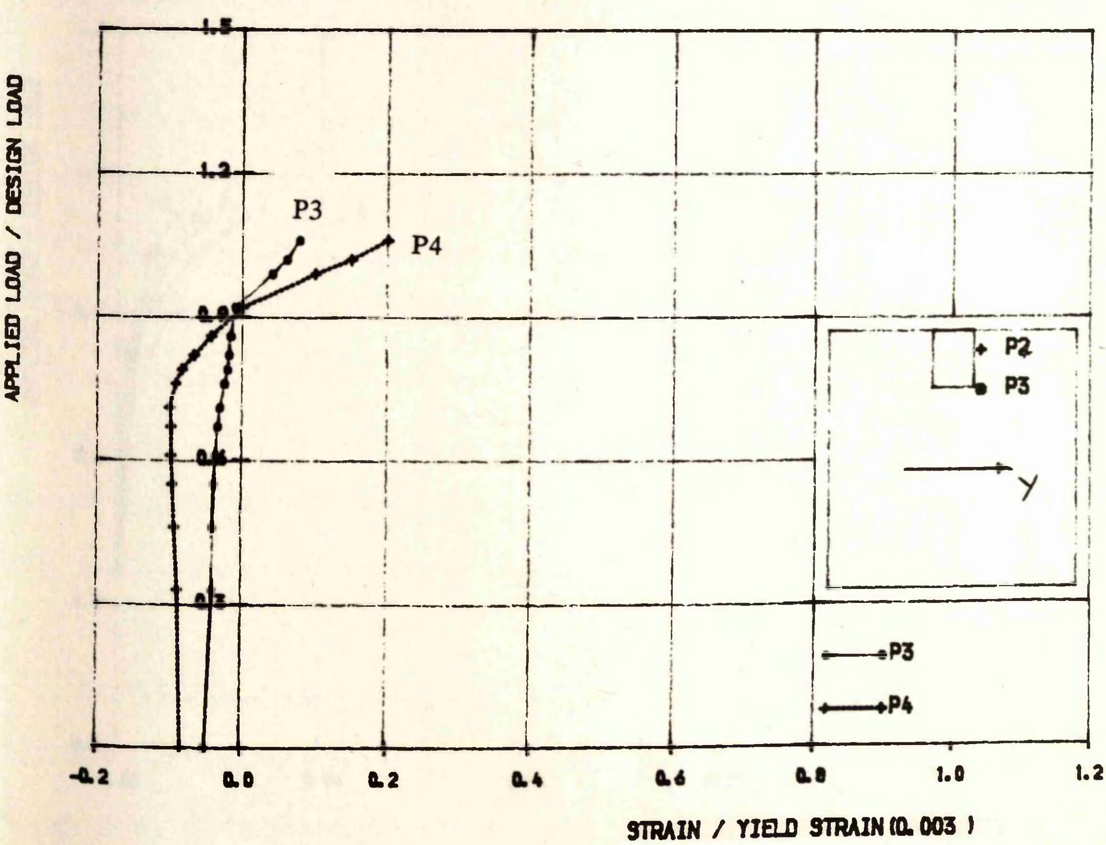

FIG. (6-41,B). LOAD-STRAIN CURVE FOR REINFORCING BAR IN Y- DIRECTION (MODEL MS3).

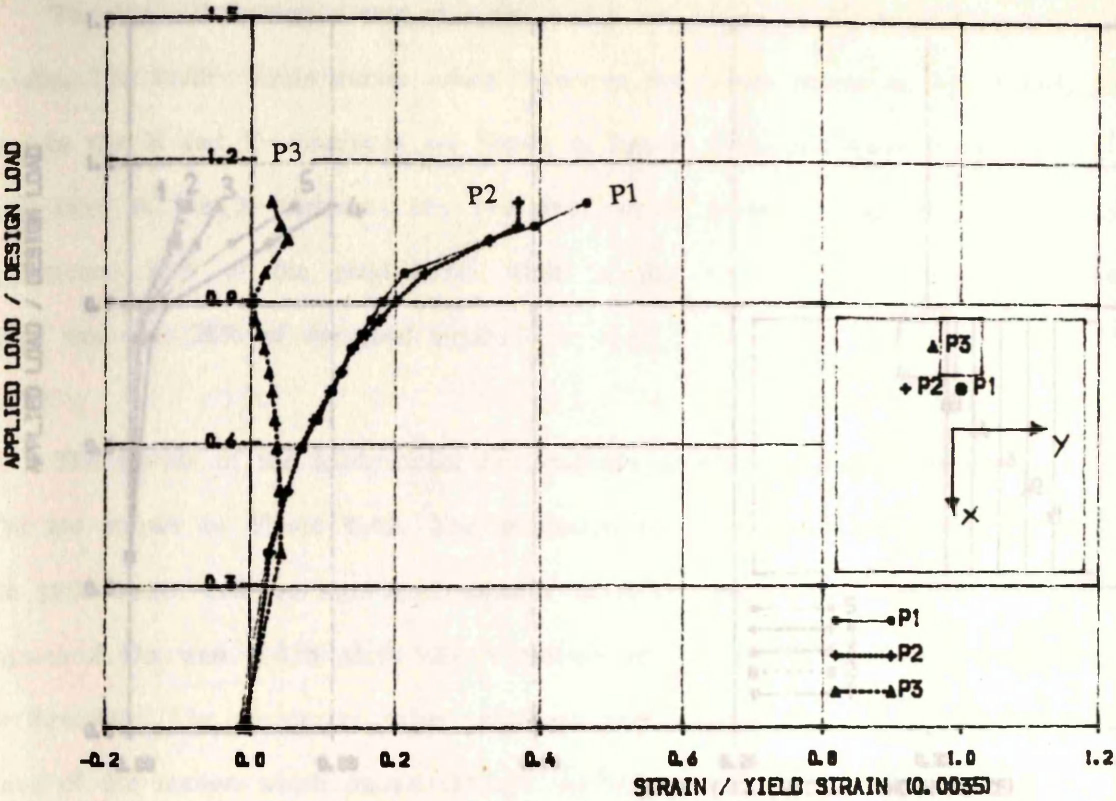

FIG. (6-42). LOAD-STRAIN CURVE AT COMPRESSIVE SURFACE OF CONCRE
P1 AND P2 ARE IN X-DIR. AND P3 IN Y-DIR. (MODEL MS

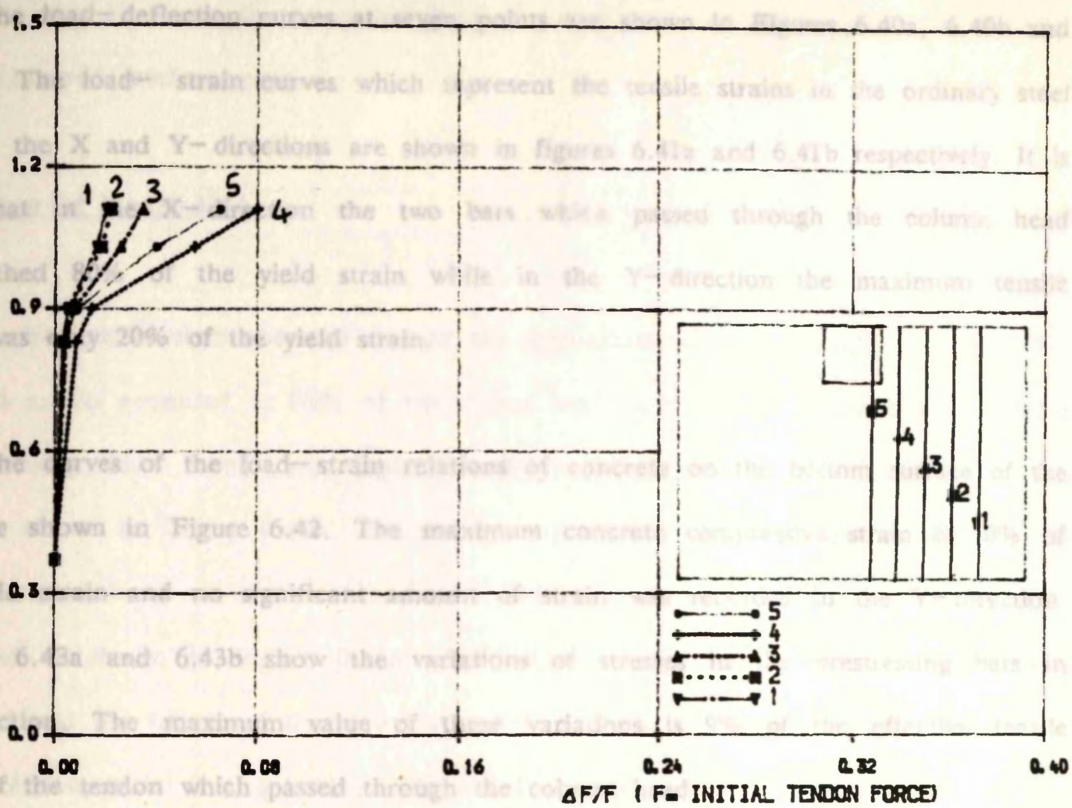

FIG. (6-43,A) . VARIATION IN TENDON FORCE VERSUS APPLIED LOAD (MODEL MS3).

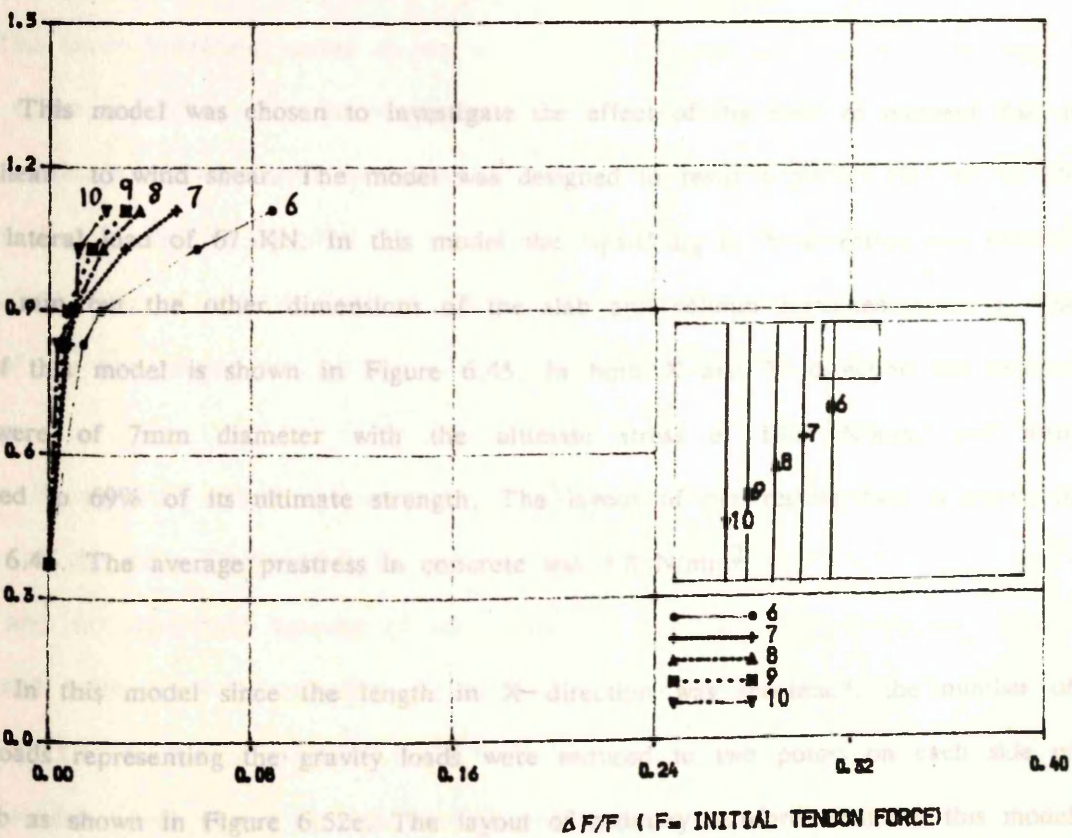

FIG. (6-43,B) . VARIATION IN TENDON FORCE VERSUS APPLIED LOAD (MODEL MS3).

The load–deflection curves at seven points are shown in Figures 6.40a, 6.40b and 6–40c. The load– strain curves which represent the tensile strains in the ordinary steel bars in the X and Y–directions are shown in figures 6.41a and 6.41b respectively. It is seen that in the X–direction the two bars which passed through the column head approached 80% of the yield strain while in the Y–direction the maximum tensile stress was only 20% of the yield strain.

The curves of the load–strain relations of concrete on the bottom surface of the slab are shown in Figure 6.42. The maximum concrete compressive strain is 50% of the yield strain and no significant amount of strain was recorded in the Y–direction. Figures 6.43a and 6.43b show the variations of stresses in the prestressing bars in X–direction. The maximum value of these variations is 9% of the effective tensile force of the tendon which passed through the column head.

6.7.4 Model MS4

This model was chosen to investigate the effect of the ratio of moment due to wind shear to wind shear. The model was designed to resist a gravity load of 18 KN and a lateral load of 67 KN. In this model the 'span' L_x in X–direction was reduced to 850 mm but the other dimensions of the slab and column remained constant. The plan of this model is shown in Figure 6.45. In both X and Y–direction the tendons used were of 7mm diameter with the ultimate stress of 1623 N/mm2 and were tensioned to 69% of its ultimate strength. The layout of prestressing bars is shown in Figure 6.46. The average prestress in concrete was 4.8 N/mm^2.

In this model since the length in X–direction was shortened, the number of point loads representing the gravity loads were reduced to two points on each side of the slab as shown in Figure 6.52e. The layout of ordinary reinforcement for this model is shown in Figure 6.47.

Figure 6.52 shows the exact locations of transducers and strain–gauges on concrete and unstressed reinforcement.

Behaviour of Model MS4

No cracks were observed due to the application of prestressing forces. The first hairline cracks appeared at 80% of the design load as shown in Figure 6.48a. At 85% of the design load, some new diagonal cracks were observed at the top surface of the slab as shown in Figure 6.48b. At this stage of loading, hairline diagonal shear cracks on the rear side of the slab and horizontal cracks on the rear face of the column were observed as shown in Figure 6.48c. On further loading, these diagonal shear cracks widened and the failure of the slab took place at 111% of the design load. The failure mode of the model was punching. The crack patterns on tensile, compressive and rear surfaces of the slab are shown respectively in Figures 6.49, 6.50 and 6.51.

The load–deflection curves at the seven points on the slab are shown in Figures 6.53a, 6.53b and 6.53c. The load–strain curves, Figures 6.54a and 6.54b, represent the tensile strain in ordinary steel reinforcement in the X and Y–directions respectively. It is seen that in the X–direction the two bars which passed through the column head approached 80% of the yield strain while in the Y–direction the maximum tensile stress of the bar passing through the column head is 35% of the yield strain.

Figure 6.55 shows the compressive strain curves of concrete on the bottom surface of the slab, from which the maximum compressive strain is 50% of the yield strain and no significant amount of the strain was recorded in Y–direction. Figures 6.56a and 6.56b show the variations of forces in the prestressing bars in the windward direction. The maximum value of these variations is 8% of the effective tensile force of the tendon which passed through the column head.

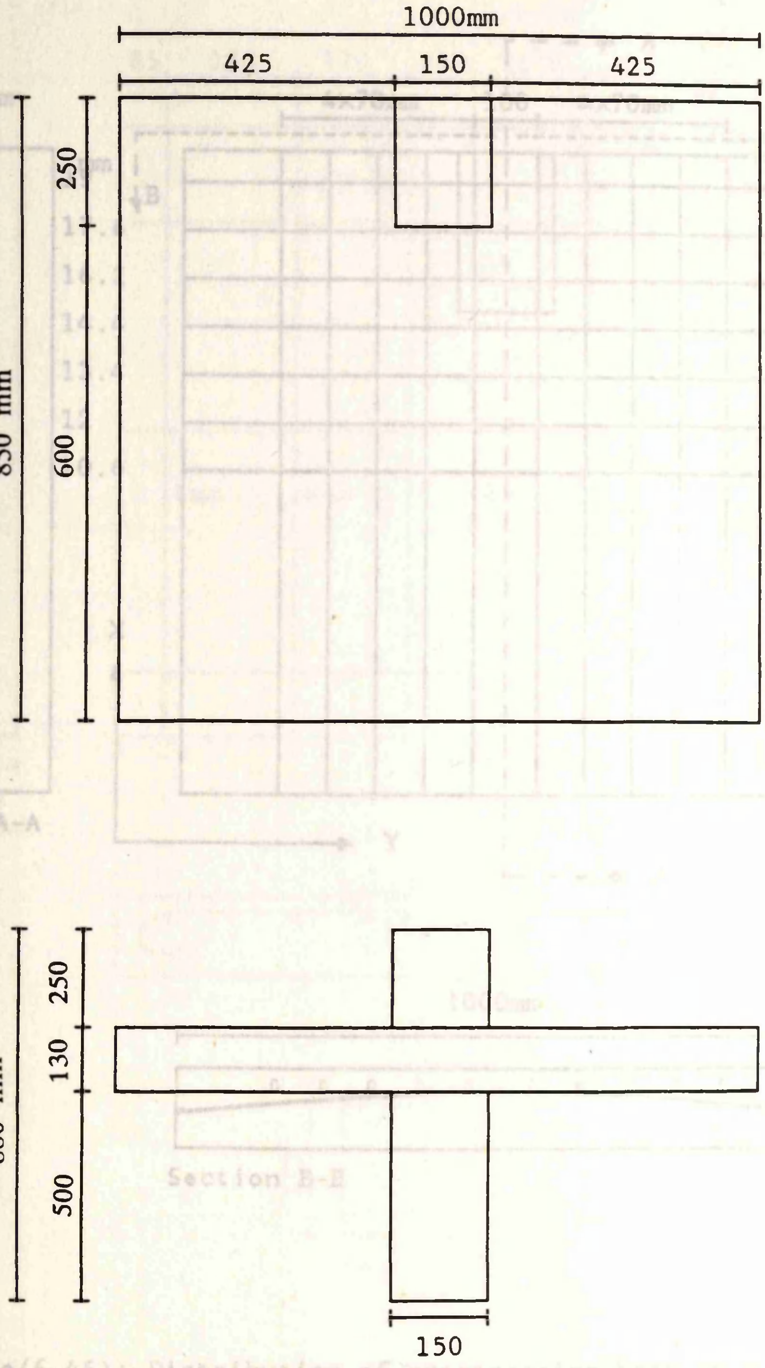

Figure(6-45): Plan and Dimensions of Model MS4.

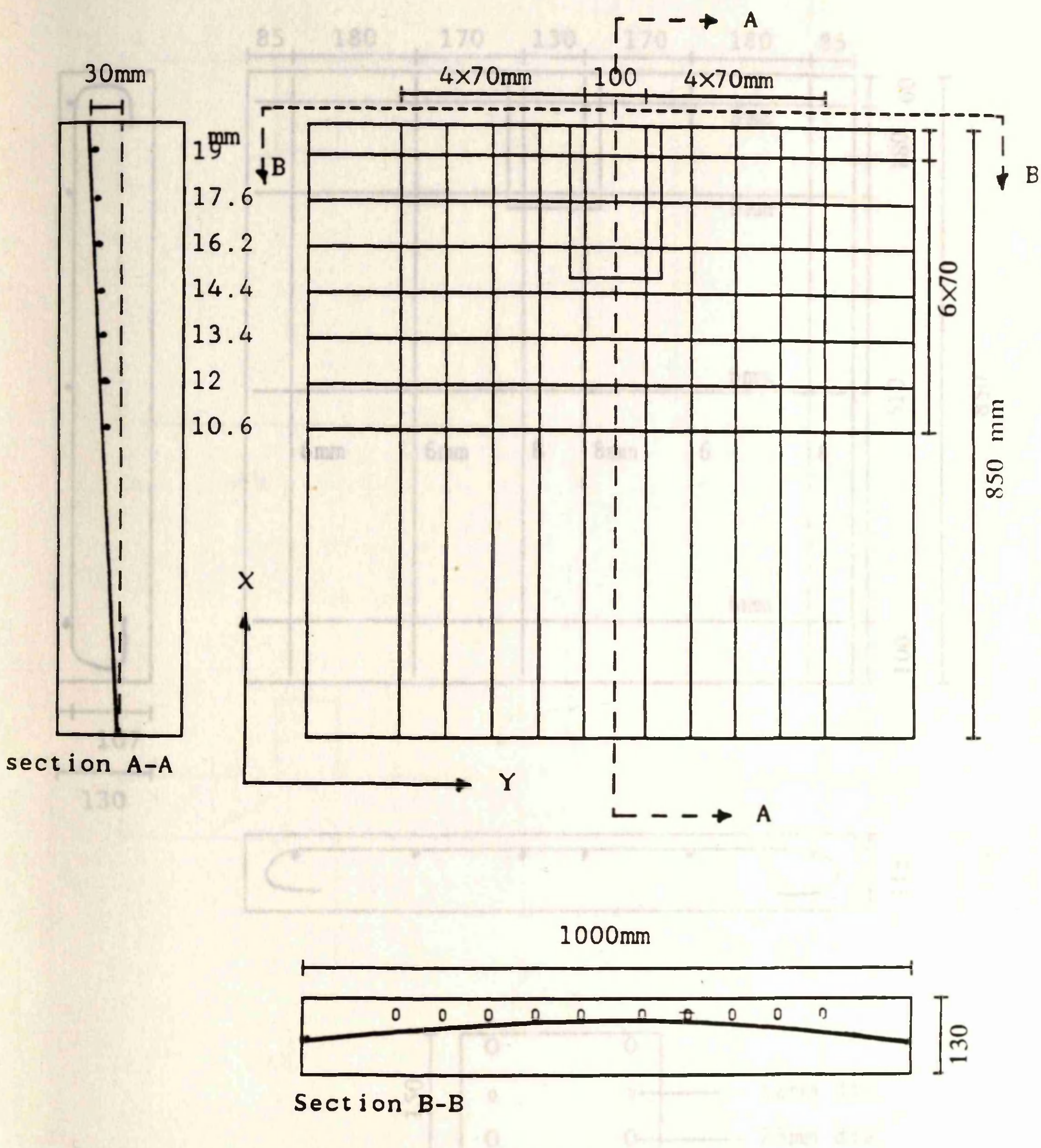

Figure(6-46): Distribution of prestressing bars in X and Y-direction for model MS4.

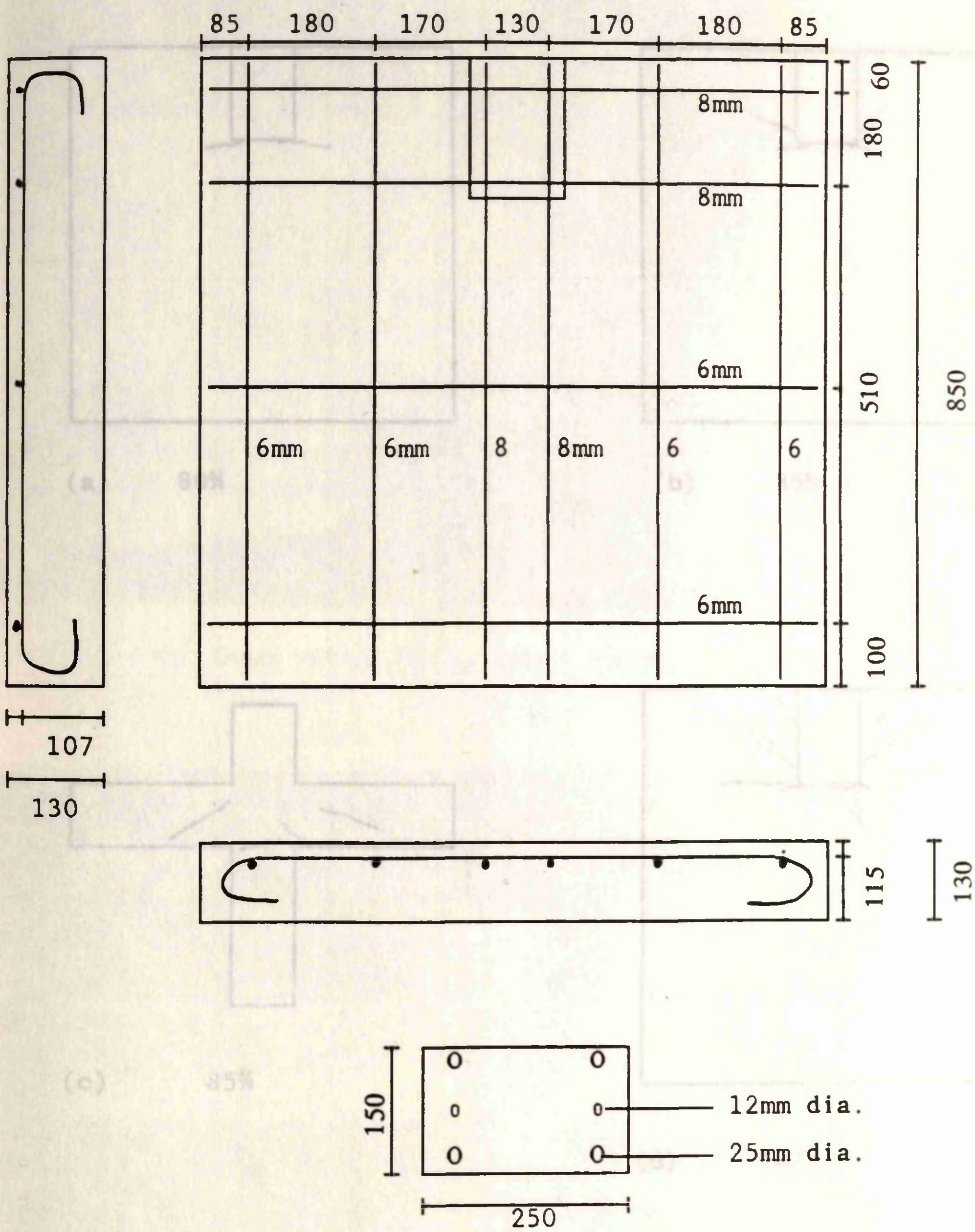

Figure(6-47): Arrangement of ordinary reinforcement bars in the slab and column for model MS4.

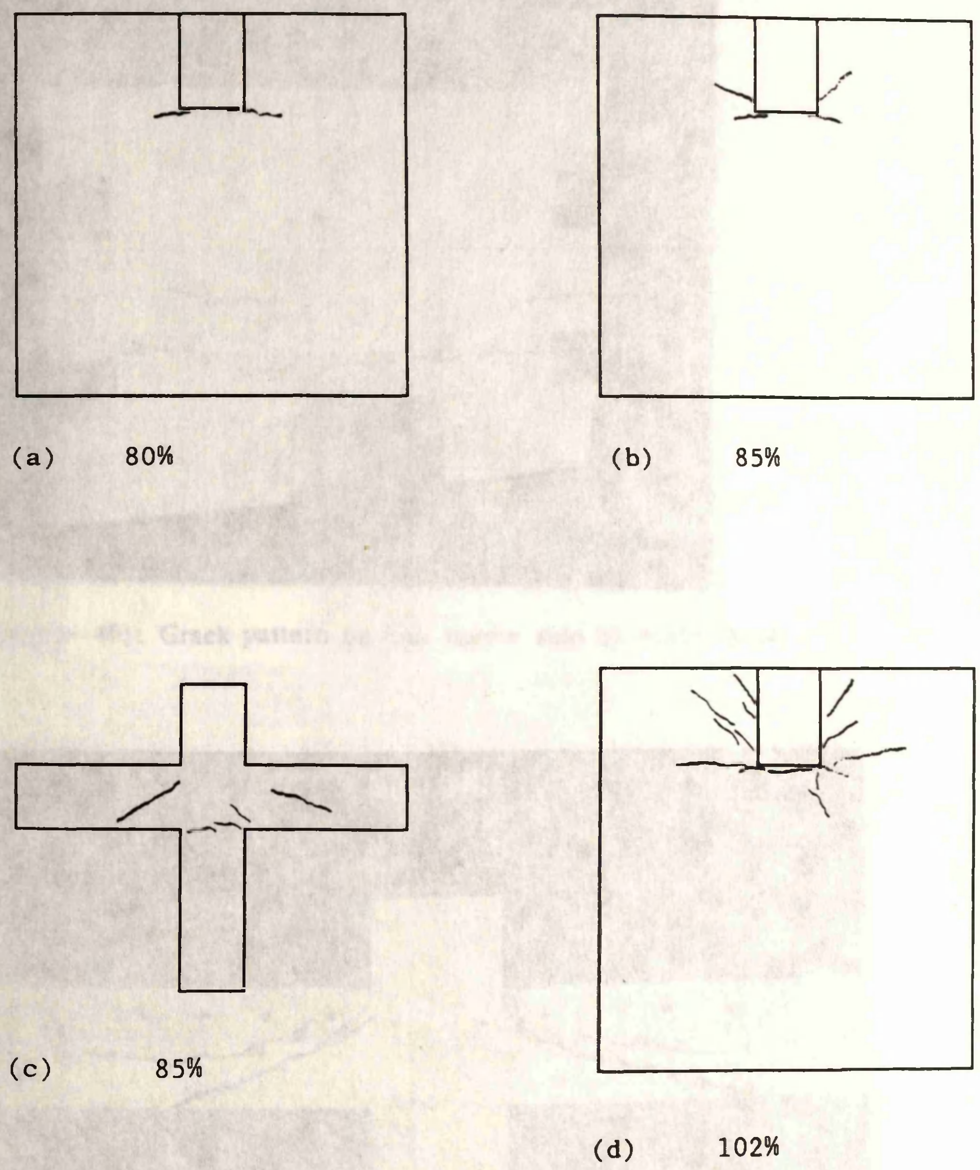

Figure(6-48): Cracks initiation during testing of model MS4 at different percentages of the design load.

Figure(6– 49): Crack pattern on the tensile side of model MS4.

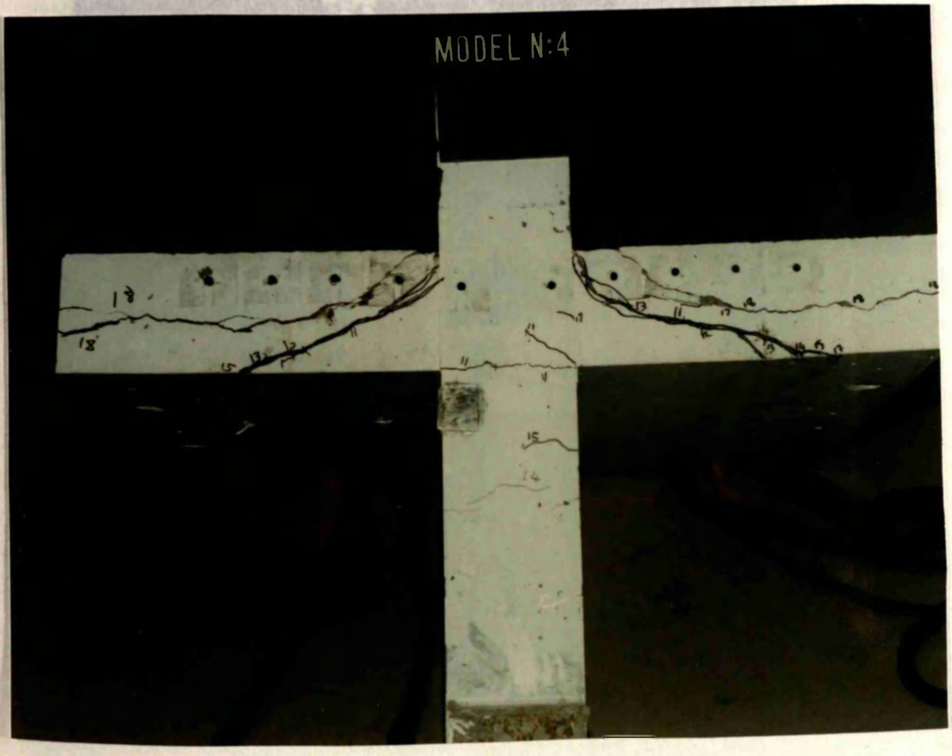

Figure (6.50): Failure surface at rear side of model MS4

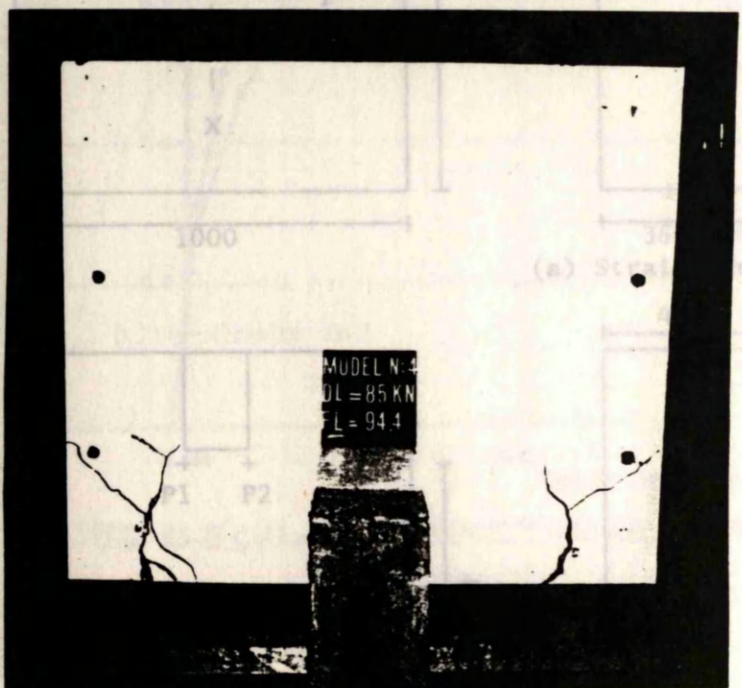

Figure(6– 51): Crack pattern on bottom side of model MS4.

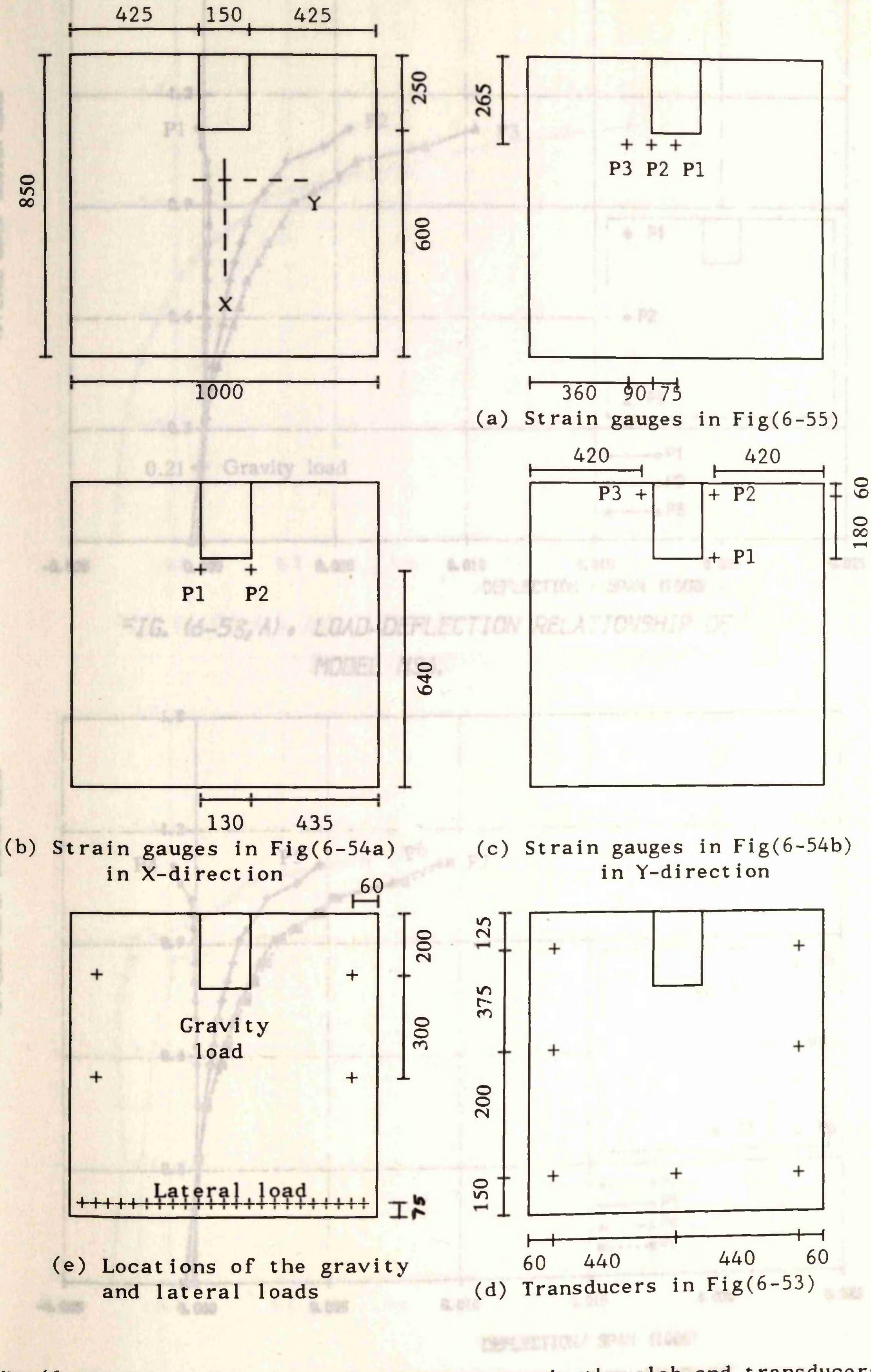

Figure(6-52):Exact locations of strain gauges in the slab and transducers of model MS4 as shown in Figures(6-53), (6-54) and (6-55).

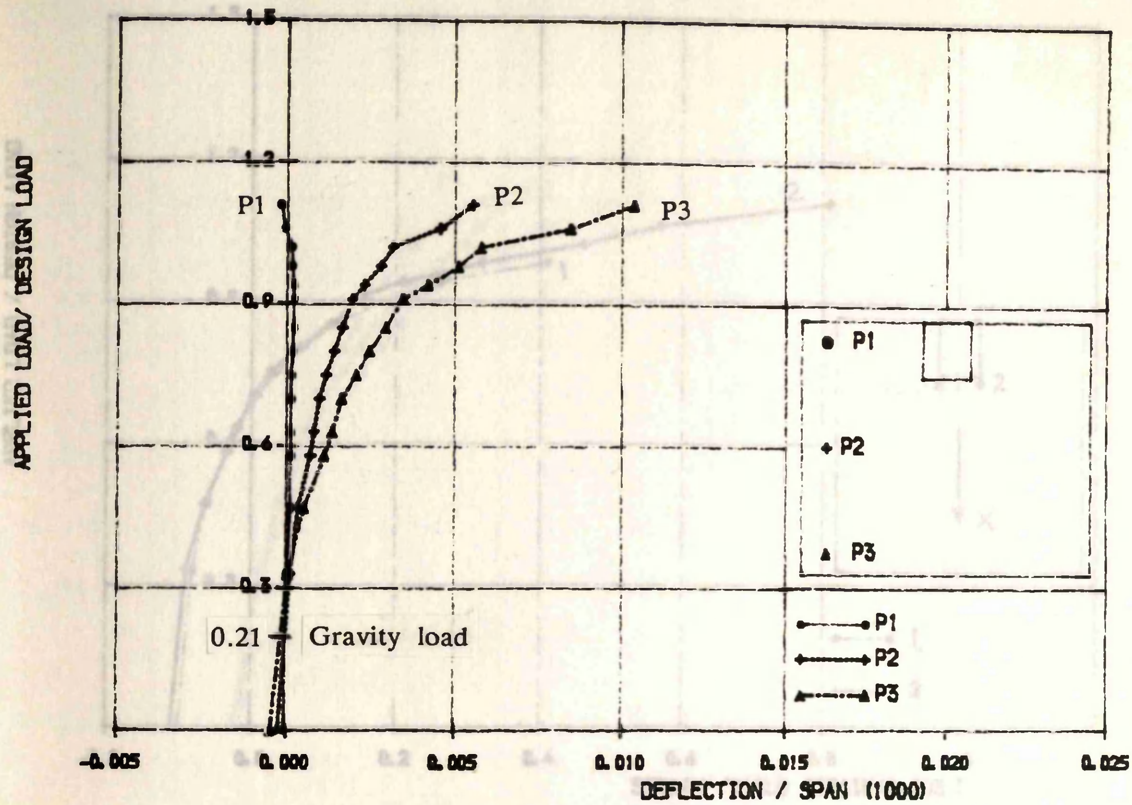

FIG. (6-53,A) : LOAD-DEFLECTION RELATIONSHIP OF MODEL MS4.

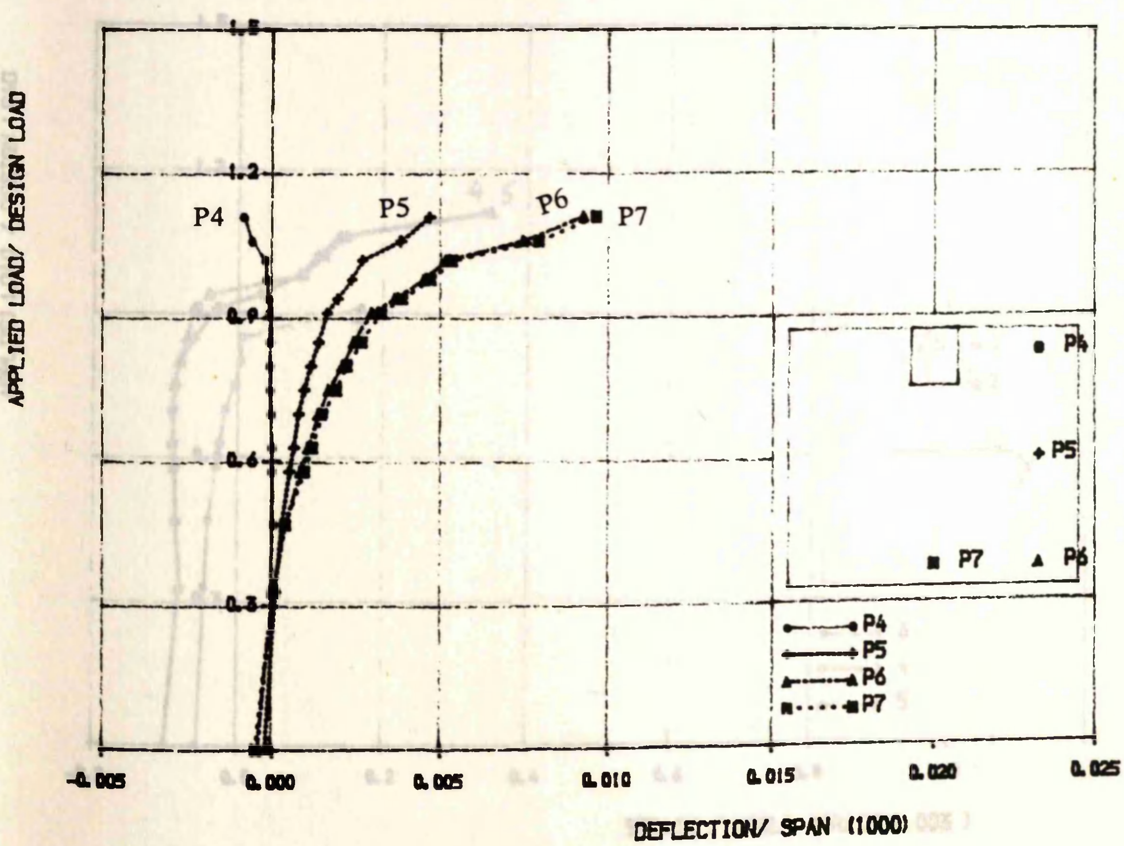

FIG. (6-53,B) : LOAD-DEFLECTION RELATIONSHIP OF MODEL MS4.

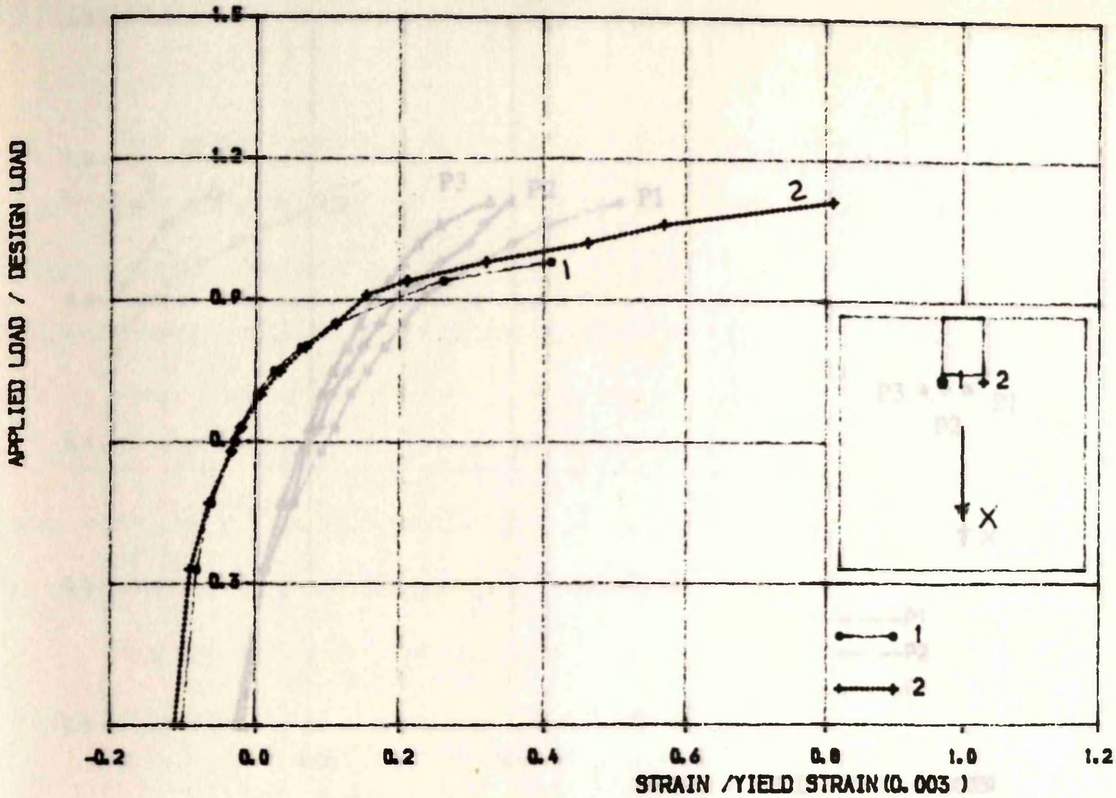

FIG. (6-54,A) . LOAD-STRAIN CURVE FOR REINFORCING BAR IN X- DIRECTION (MODEL MS4).

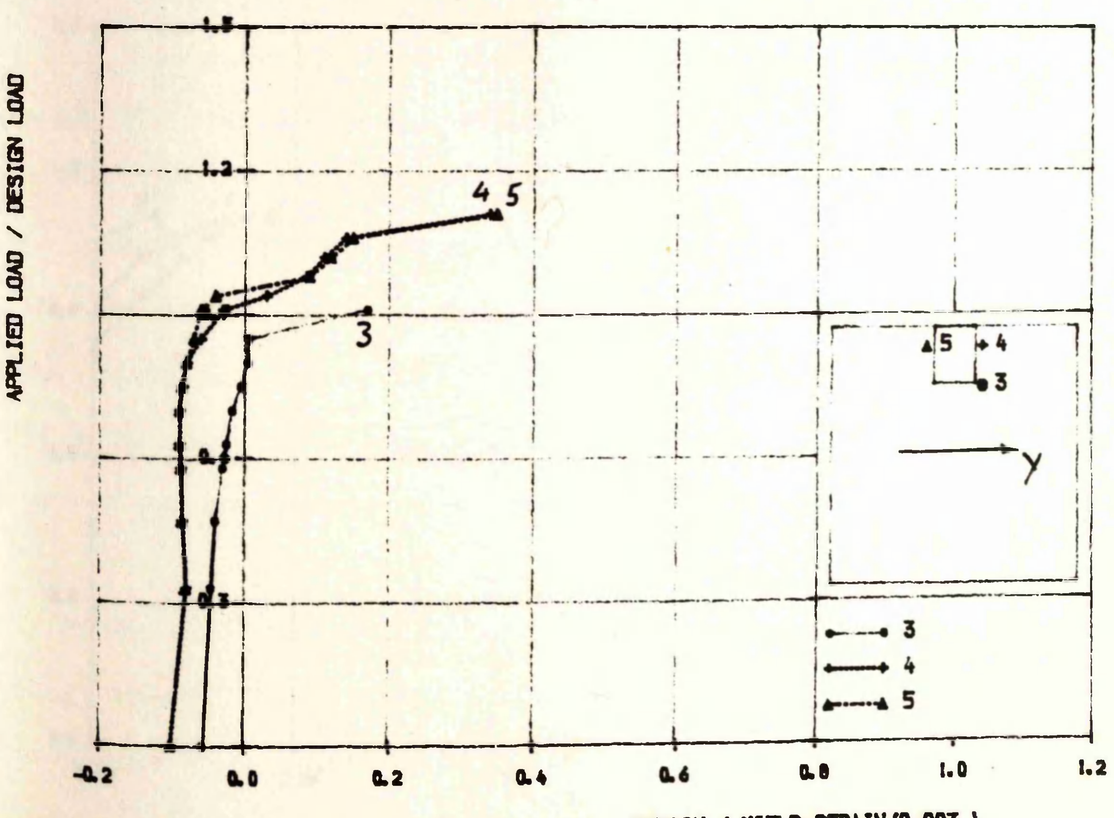

FIG. (6-54,B) . LOAD-STRAIN CURVE FOR REINFORCING BAR IN Y- DIRECTION (MODEL MS4).

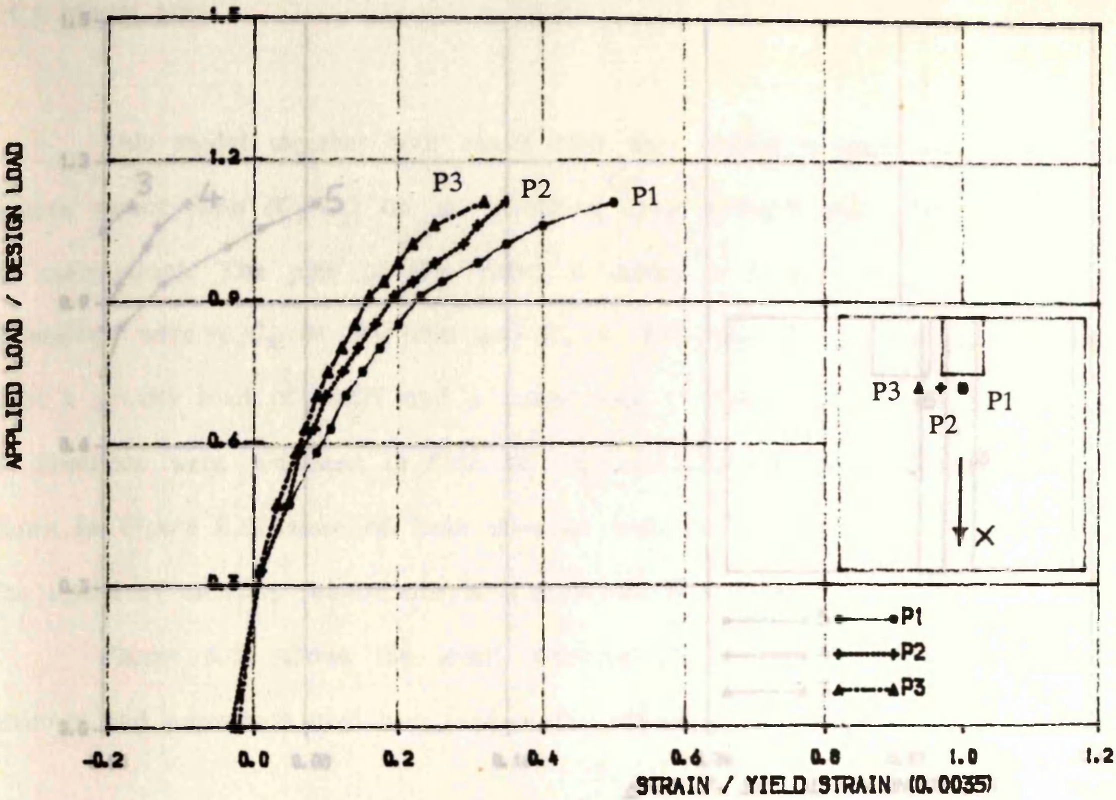

FIG. (6-55). LOAD-STRAIN CURVE AT COMPRESSIVE SURFACE OF CONCRETE FOR MODEL MS4.

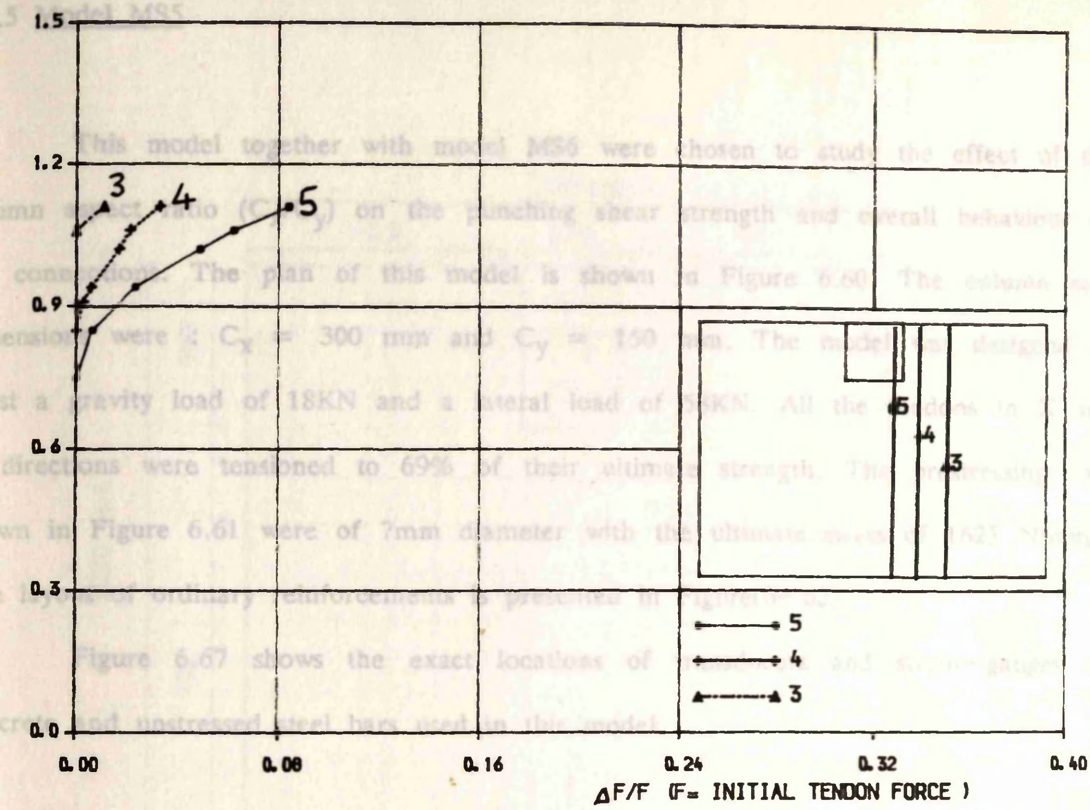

FIG. (6-56, A) . VARIATION IN TENDON FORCE (MODEL MS4).

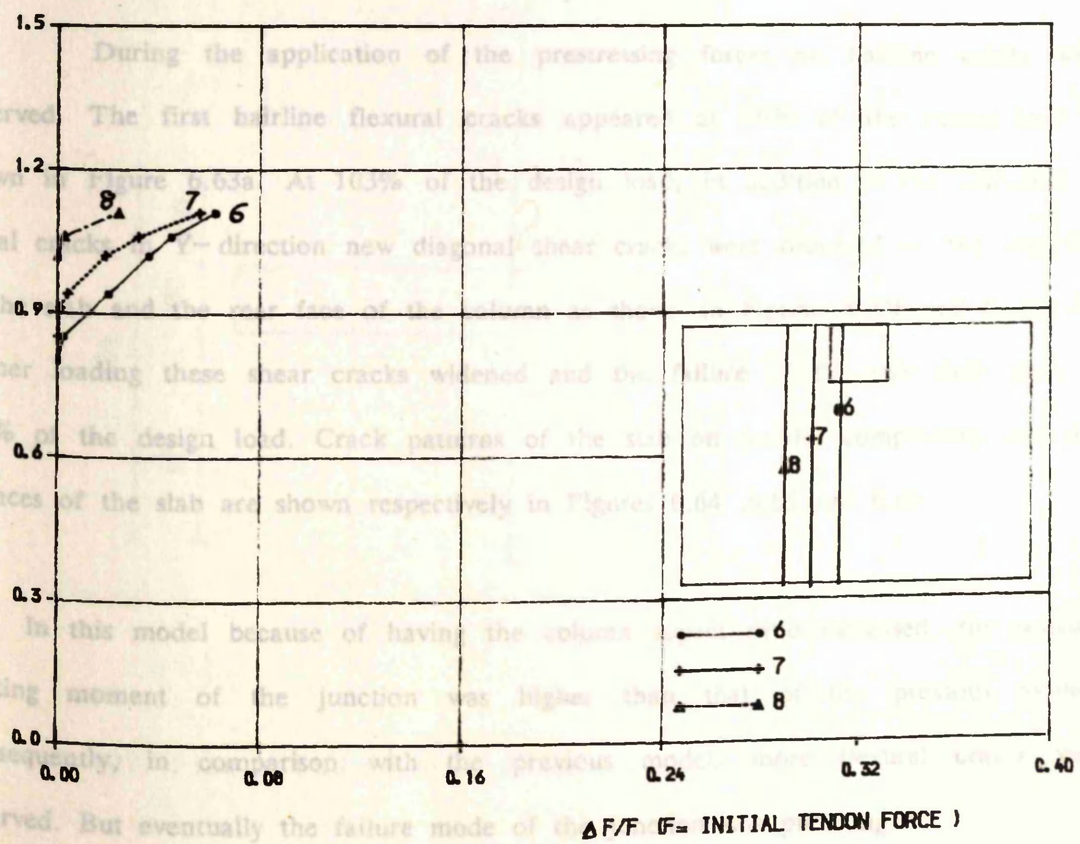

FIG. (6-56, A) . VARIATION IN TENDON FORCE (MODEL MS4).

6.7.5 Model MS5

This model together with model MS6 were chosen to study the effect of the column aspect ratio (C_x/C_y) on the punching shear strength and overall behaviour of the connections. The plan of this model is shown in Figure 6.60. The column side dimensions were : C_x = 300 mm and C_y = 150 mm. The model was designed to resist a gravity load of 18KN and a lateral load of 58KN. All the tendons in X and Y–directions were tensioned to 69% of their ultimate strength. The prestressing bars shown in Figure 6.61 were of 7mm diameter with the ultimate stress of 1623 N/mm2. The layout of ordinary reinforcements is presented in Figure(6–62).

Figure 6.67 shows the exact locations of transducers and strain–gauges on concrete and unstressed steel bars used in this model.

Behaviour of Model MS5

During the application of the prestressing forces no hairline cracks were observed. The first hairline flexural cracks appeared at 86% of the design load as shown in Figure 6.63a. At 103% of the design load, in addition to the extension of initial cracks in Y–direction new diagonal shear cracks were observed on the rear side of the slab and the rear face of the column as shown in Figures 6.63b and 6.63c. On further loading these shear cracks widened and the failure of the slab took place at 118% of the design load. Crack patterns of the slab on tensile, compressive and rear surfaces of the slab are shown respectively in Figures 6.64 ,6.65 and 6.66.

In this model because of having the column aspect ratio increased, the resistant twisting moment of the junction was higher than that of the previous models. Consequently, in comparison with the previous models more flexural cracks were observed. But eventually the failure mode of the junction was punching.

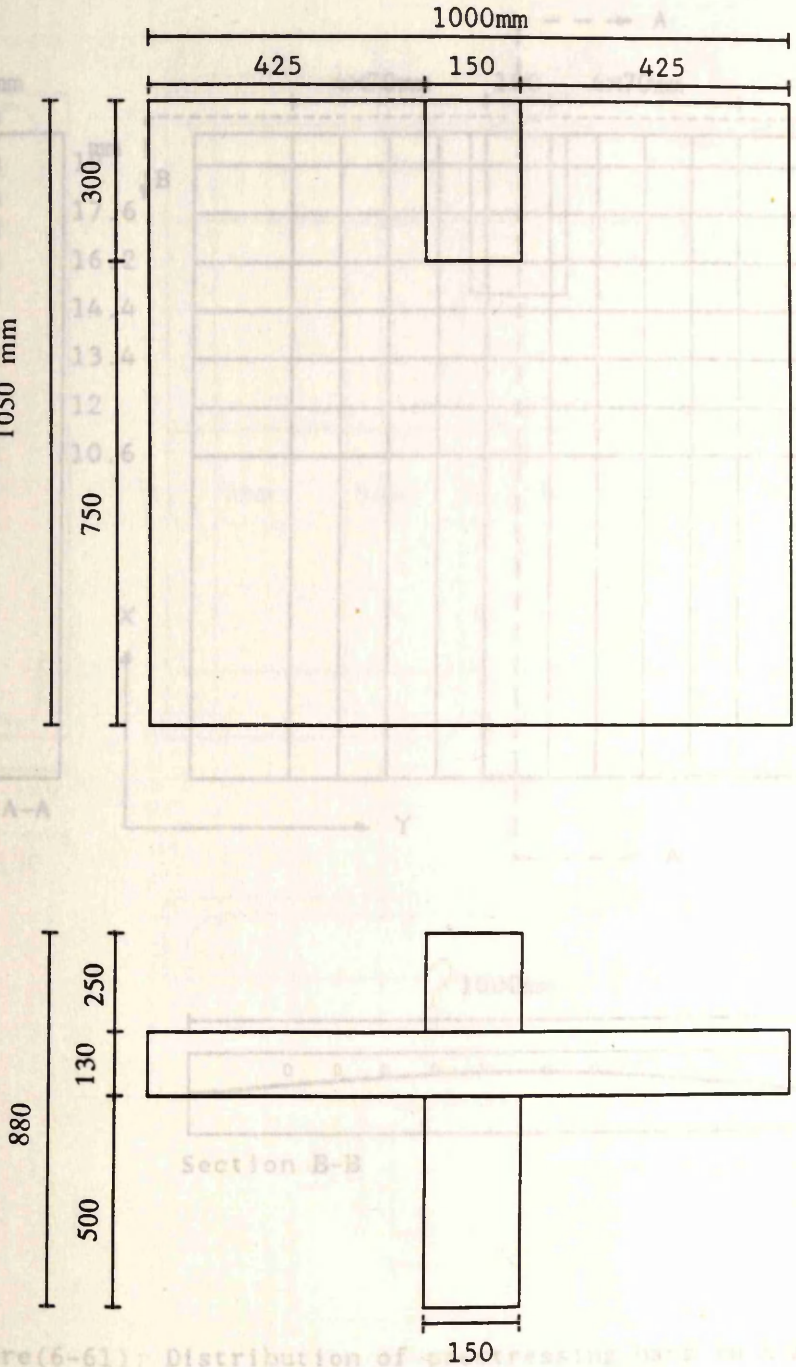

Figure(6-60): Plan and Dimensions of Model MS5.

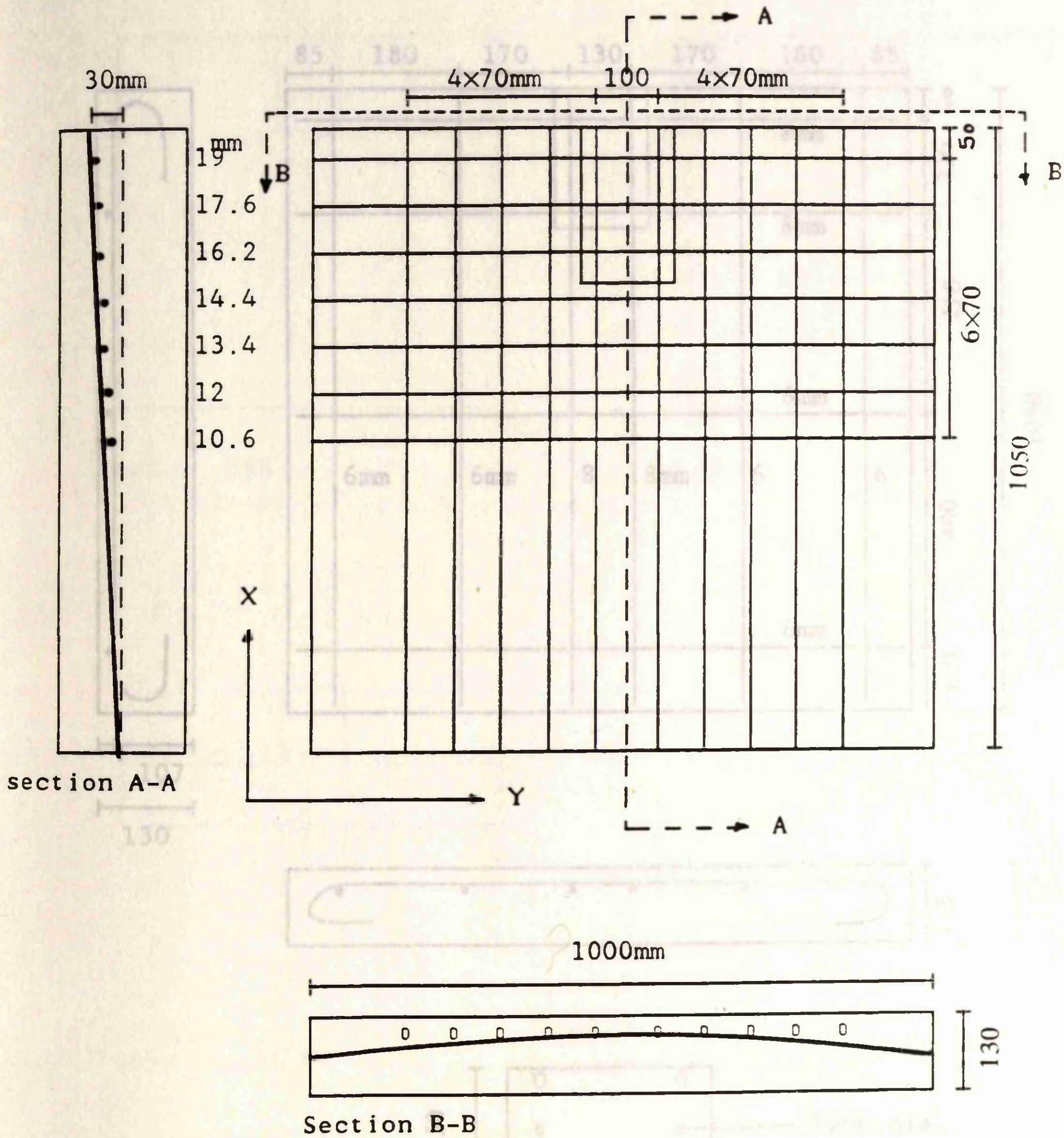

Figure(6-61): Distribution of prestressing bars in X and Y-direction for model MS5.

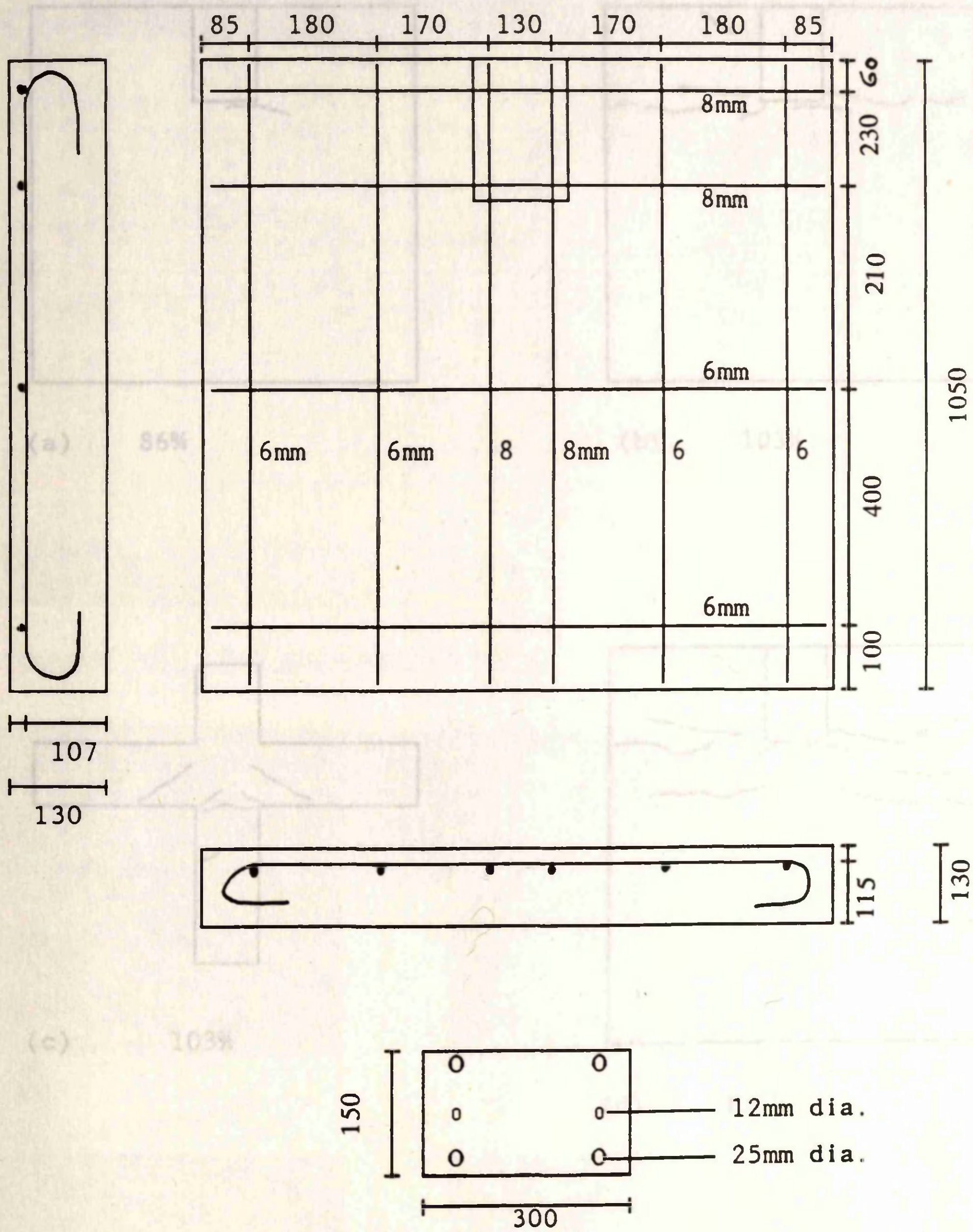

Figure(6-62): Arrangement of ordinary reinforcement bars in the slab and column for model MS5.

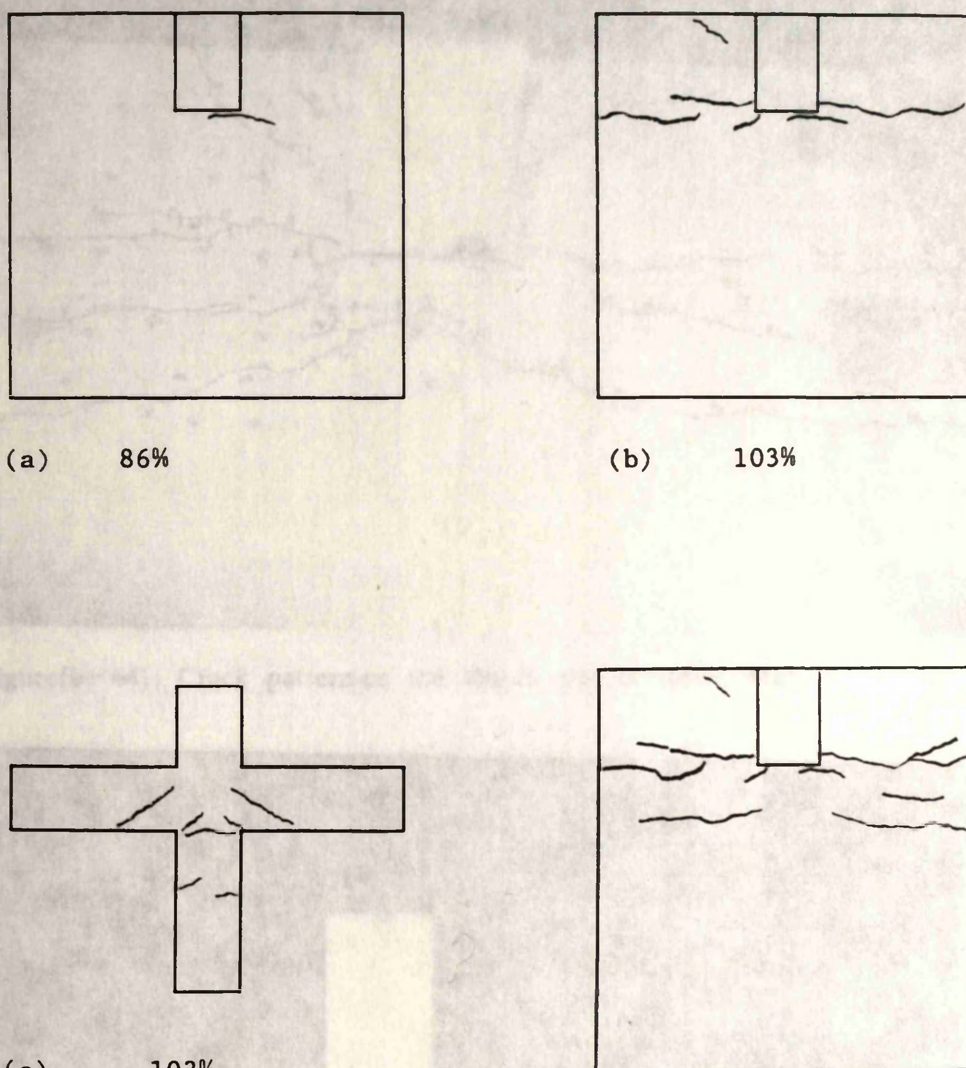

(a) 86%

(b) 103%

(c) 103%

(d) 114%

Figure(6-63): Cracks initiation during testing of model MS5 at different percentages of the design load.

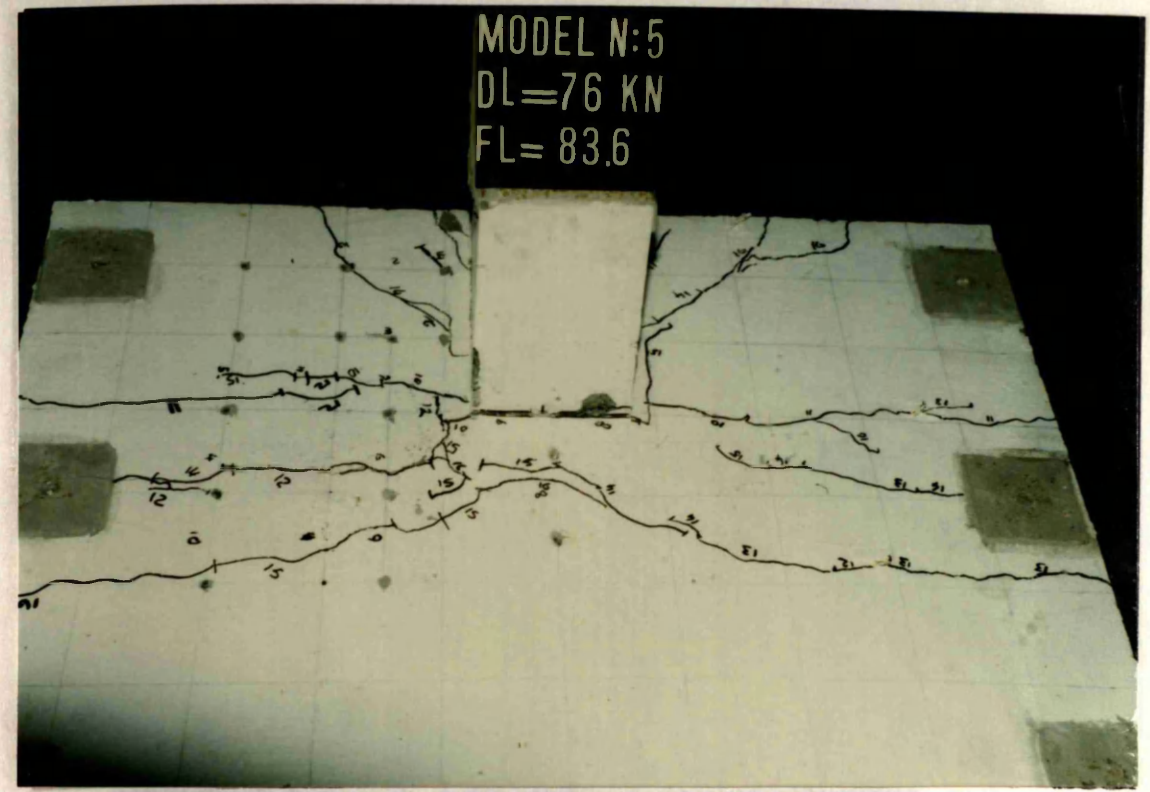

Figure(6- 64): Crack pattern on the tensile side of model MS5.

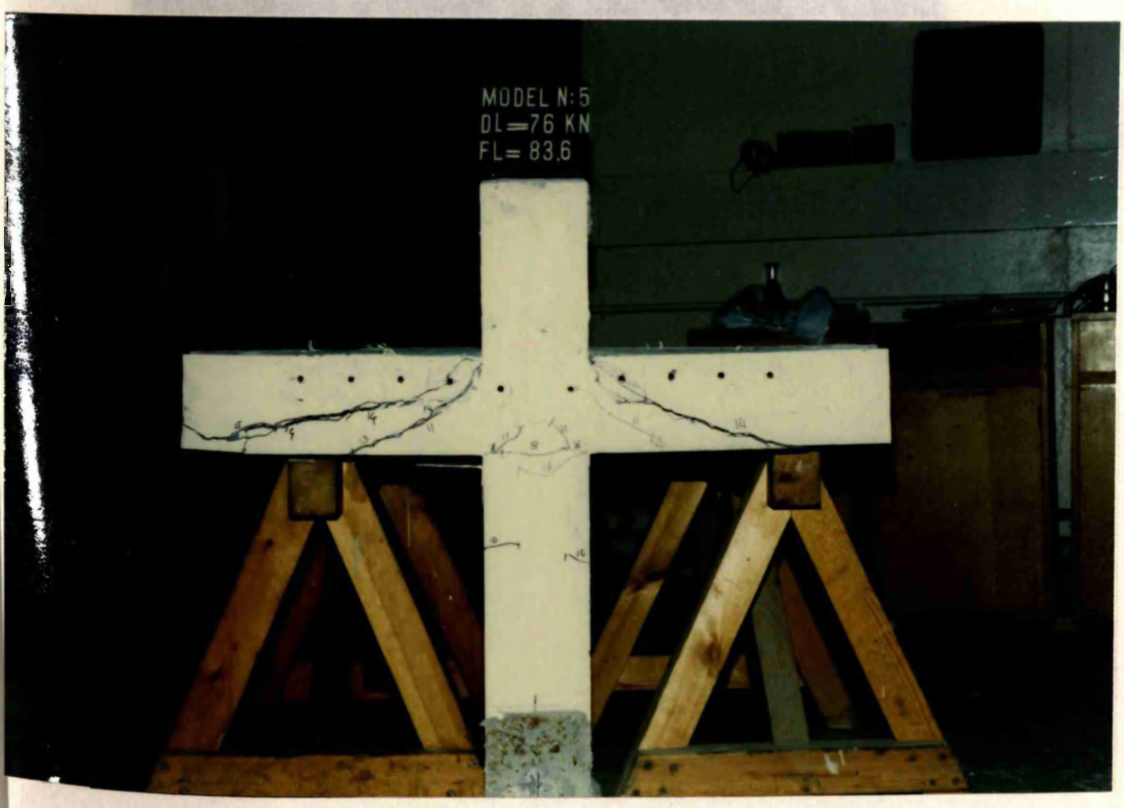

Figure (6.65): Failure surface at rear side of model MS5

Figure(6– 66): Crack pattern on bottom side of model MS5.

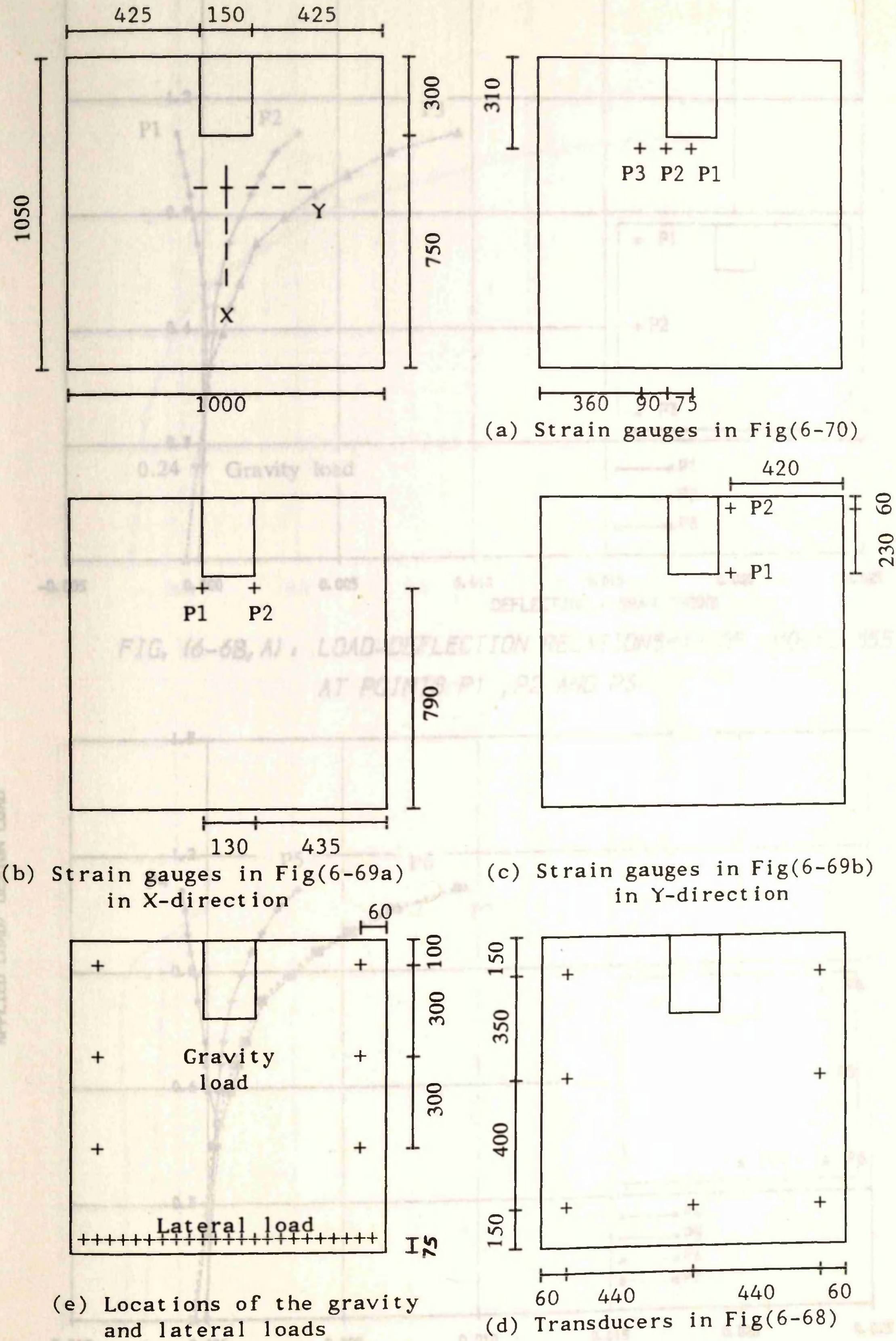

Figure(6-67):Exact locations of strain gauges in the slab and transducers of model MS5 as shown in Figures(6-68), (6-69) and (6-70).

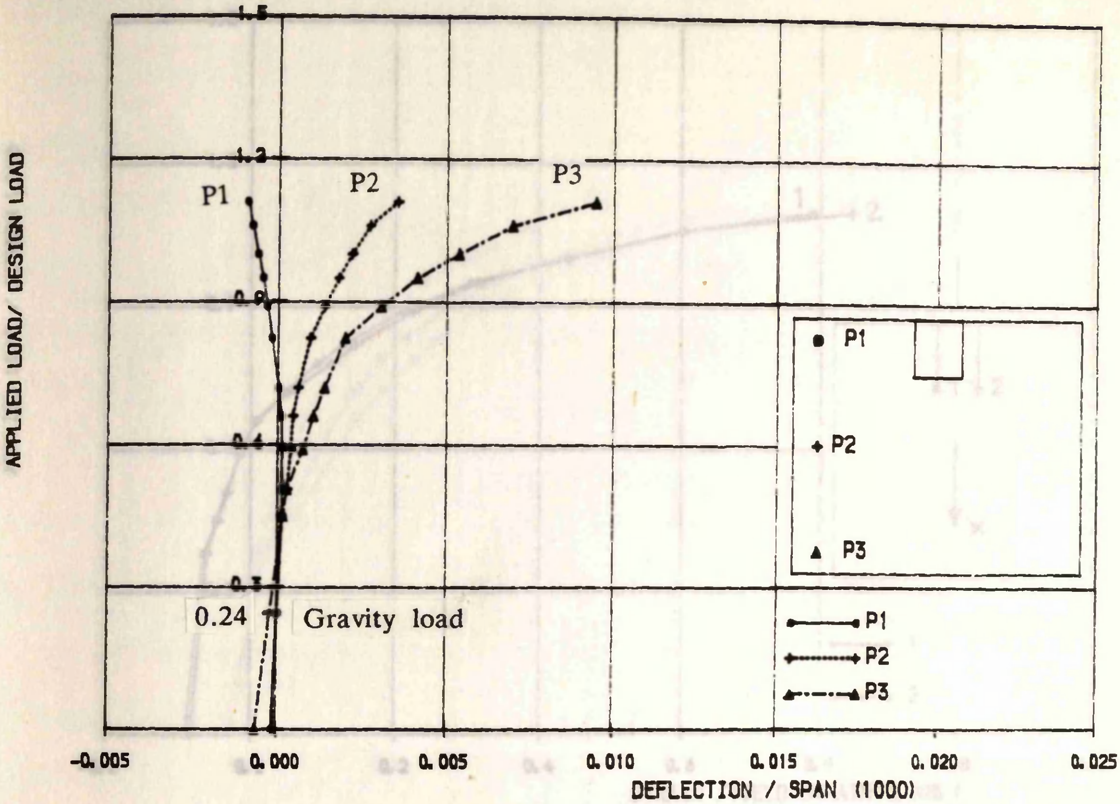

FIG. (6-68, A) . LOAD-DEFLECTION RELATIONSHIP OF MODEL MS5 AT POINTS P1 , P2 AND P3 .

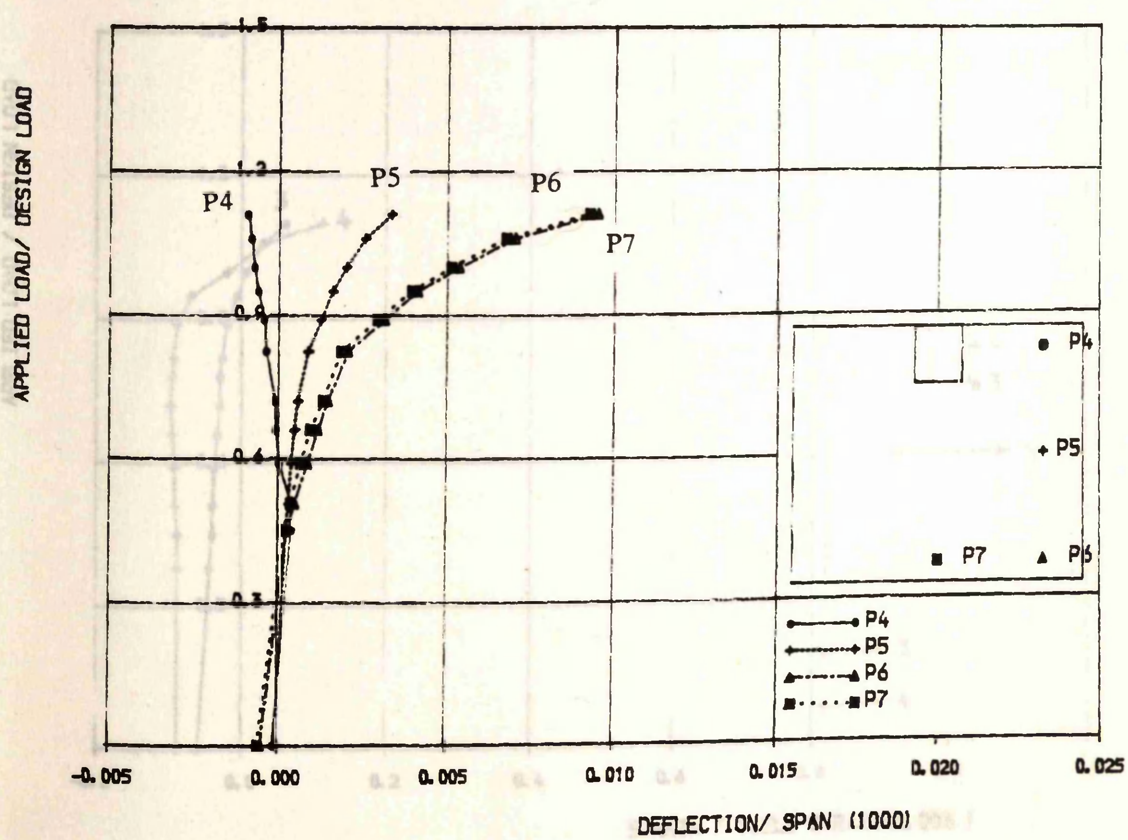

FIG. (6-68, B) . LOAD-DEFLECTION RELATIONSHIP OF MODEL MS5 AT POINTS P4 - P7 .

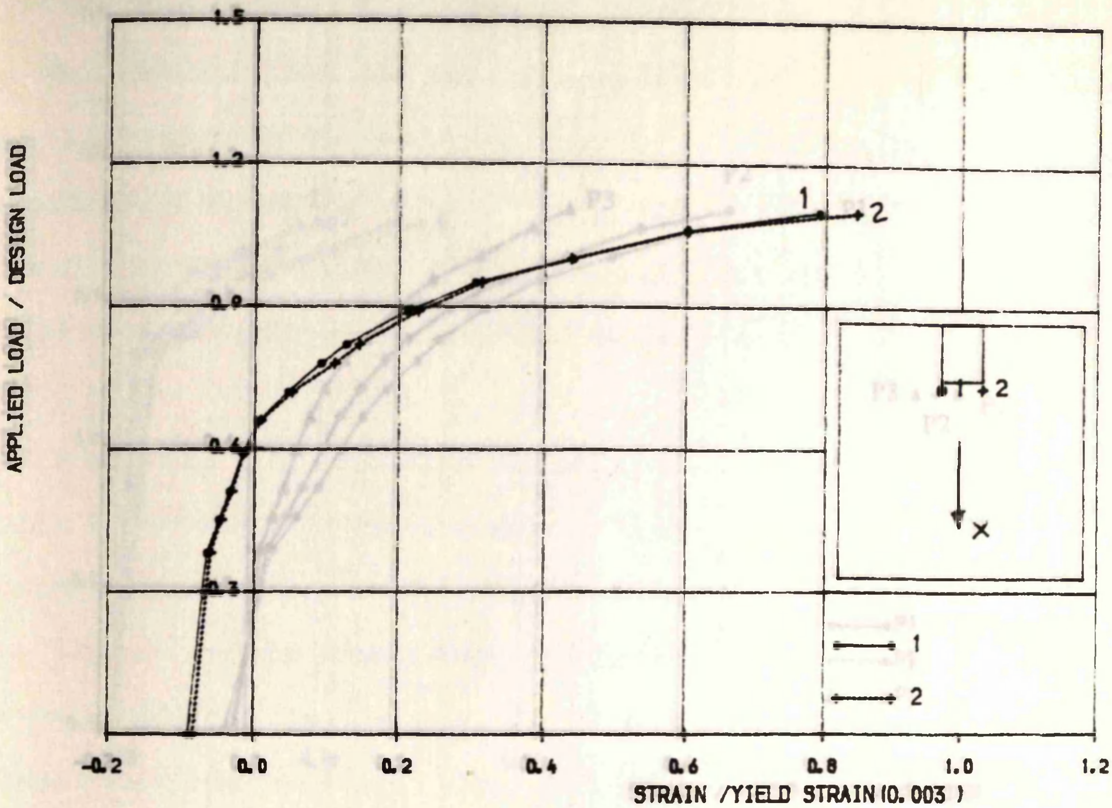

FIG. (6-69,A), LOAD-STRAIN CURVE FOR REINFORCING BAR IN X- DIRECTION (MODEL MS5).

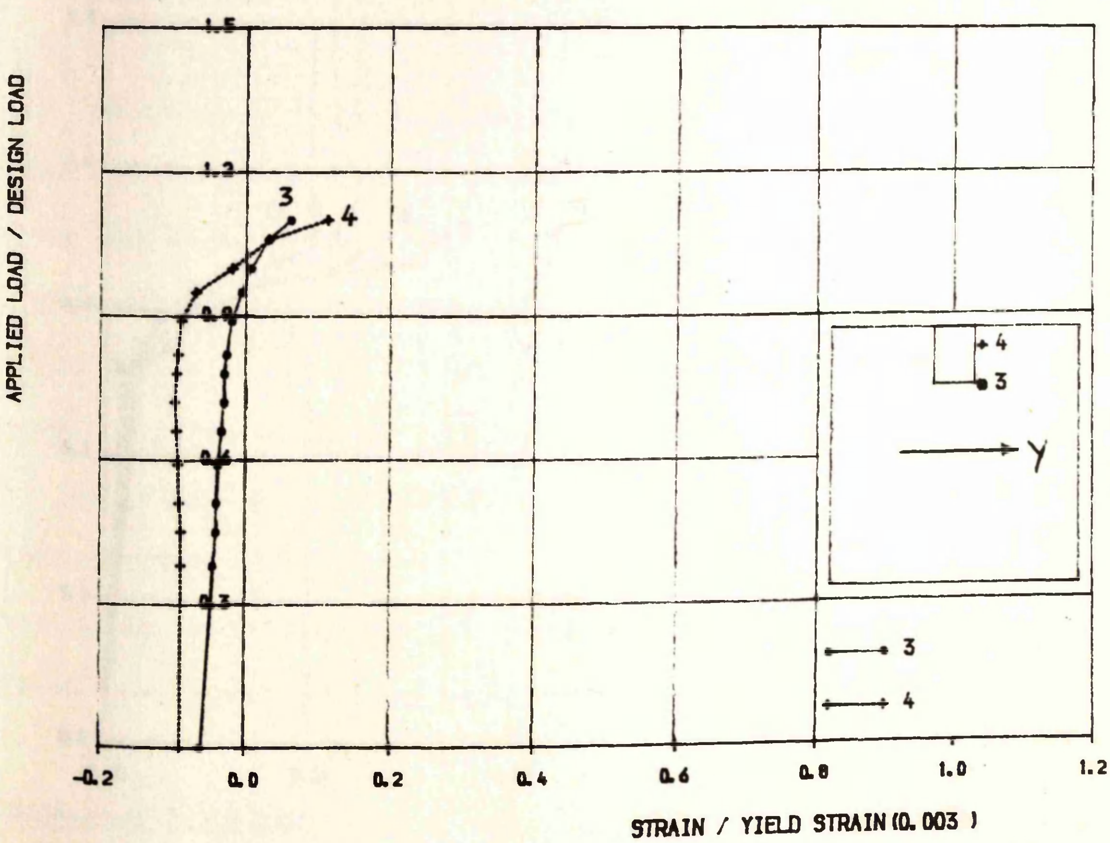

FIG. (6-69,B), LOAD-STRAIN CURVE FOR REINFORCING BAR IN Y- DIRECTION (MODEL MS5).

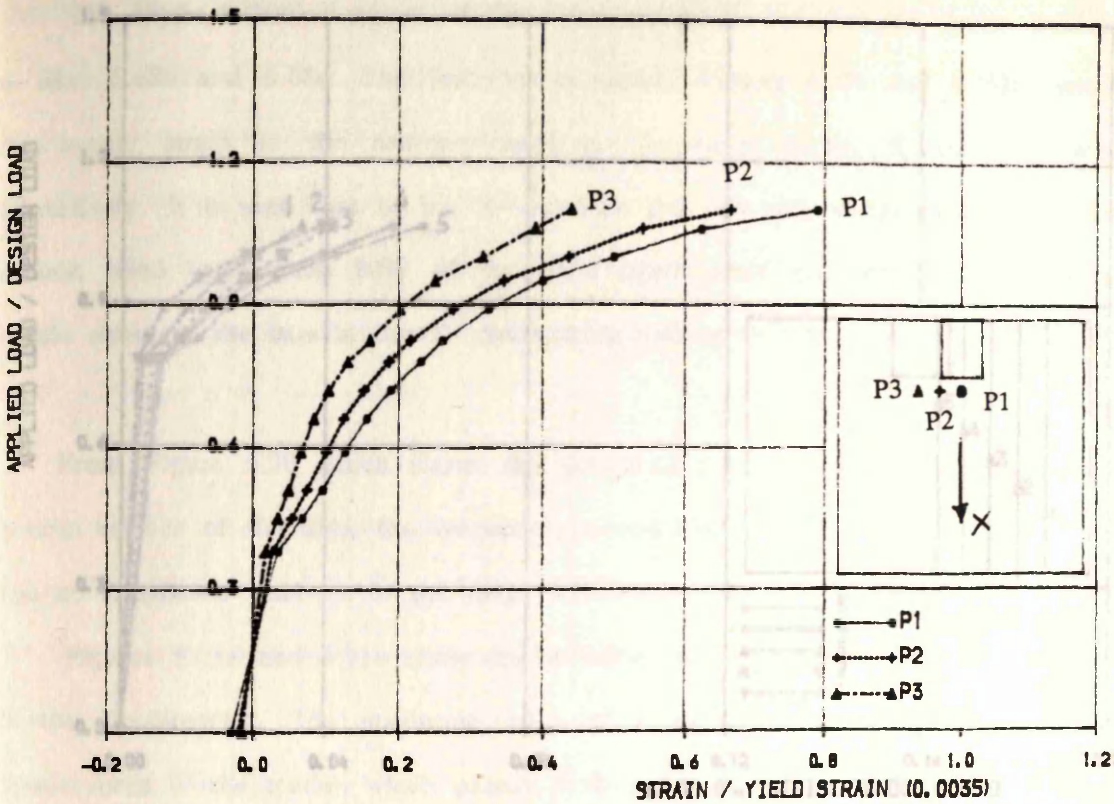

FIG. (6-70) . LOAD-STRAIN CURVE AT COMPRESSIVE SURFACE OF CONCRETE AT P1 , P2 AND P3 FOR MODEL MS5.

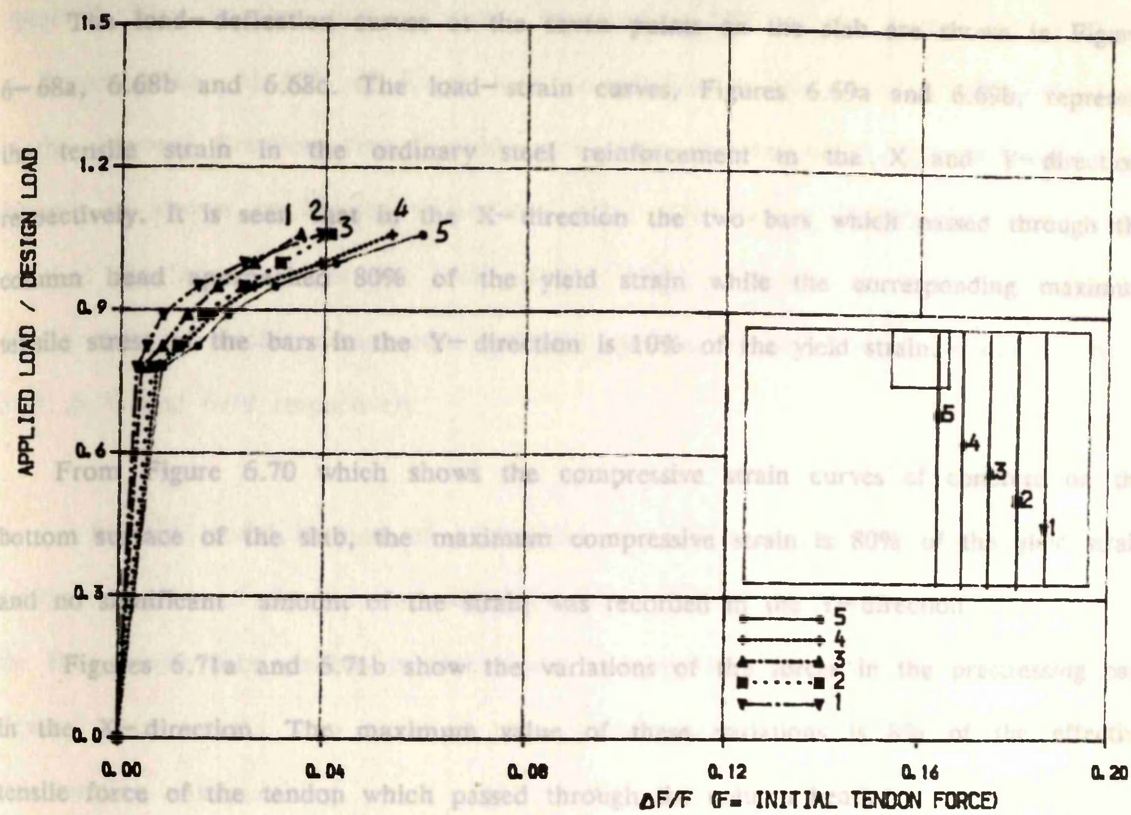

FIG. (6-71,A) , VARIATION IN TENDON FORCE (MODEL MS5).

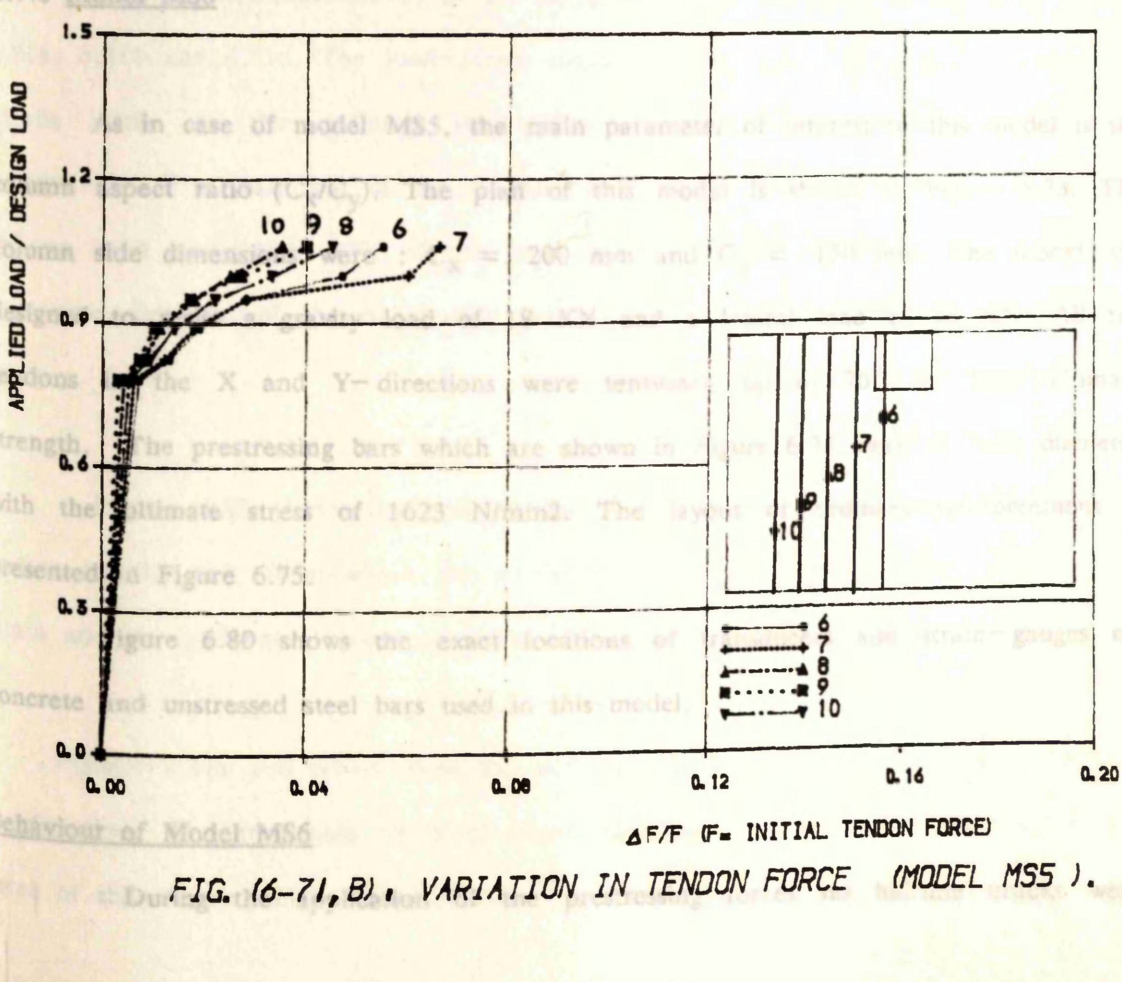

FIG. (6-71,B) , VARIATION IN TENDON FORCE (MODEL MS5).

The load–deflection curves at the seven points on the slab are shown in Figures 6–68a, 6.68b and 6.68c. The load–strain curves, Figures 6.69a and 6.69b, represent the tensile strain in the ordinary steel reinforcement in the X and Y–directions respectively. It is seen that in the X–direction the two bars which passed through the column head approached 80% of the yield strain while the corresponding maximum tensile stress of the bars in the Y–direction is 10% of the yield strain.

From Figure 6.70 which shows the compressive strain curves of concrete on the bottom surface of the slab, the maximum compressive strain is 80% of the yield strain and no significant amount of the strain was recorded in the Y–direction.

Figures 6.71a and 6.71b show the variations of the forces in the prestressing bars in the X–direction. The maximum value of these variations is 8% of the effective tensile force of the tendon which passed through the column head.

6.7.6 Model MS6

As in case of model MS5, the main parameter of interest in this model is the column aspect ratio (C_x/C_y). The plan of this model is shown in Figure 6.73. The column side dimensions were : C_x = 200 mm and C_y = 150 mm. The model was designed to resist a gravity load of 18 KN and a lateral load of 42 KN. All the tendons in the X and Y–directions were tensioned up to 70% of their ultimate strength. The prestressing bars which are shown in Figure 6.74 were of 7mm diameter with the ultimate stress of 1623 N/mm2. The layout of ordinary reinforcement is presented in Figure 6.75.

Figure 6.80 shows the exact locations of transducers and strain–gauges on concrete and unstressed steel bars used in this model.

Behaviour of Model MS6

During the application of the prestressing forces no hairline cracks were observed. First hairline diagonal cracks appeared at 81% of the design load as shown in Figure 6.76a. At 85% of design load, in addition to the extension of initial cracks in the diagonal direction, first flexural cracks were observed on the slab in front of the column as shown in Figures 6.76b and 6.76c. On further loading the shear cracks widened the failure of the slab took place at 103% of the design load. Crack patterns of the slab on tensile, compressive and rear surfaces of the slab are shown in Figures 6.77 ,6.78 and 6.79 respectively.

In this model because of having the column aspect ratio reduced, the resistant twisting moment of the junction was lower than that of previous models. Consequently, the first cracks that occurred in this model were twisting moment shear cracks and less flexural shear cracks were observed than in the previous models and failure mode of the junction was punching.

The load−deflection curves at the seven points of the slab are shown in Figures 6.81a, 6.81b and 6.81c. The load−strain curves, Figures 6.82a and 6.82b, represent the tensile strain in the ordinary steel reinforcements in the X and Y−directions respectively. It is seen that in the X−direction the two bars which passed through the column head approached 88% of the yield strain while the corresponding strain in the transverse direction of the bar passed through the column head is 13% of the yield strain.

Figure 6.83 shows the compressive strain curves of concrete on the bottom surface of the slab, from which the maximum compressive strain is 60% of the yield strain and no significant amount of strain was recorded in the transverse direction.

Figures 6.84a and 6.84b show the variations of forces in the prestressing bars in X−direction. The maximum value of these variations is 7% of the effective tensile force of the tendon which passed through the column head.

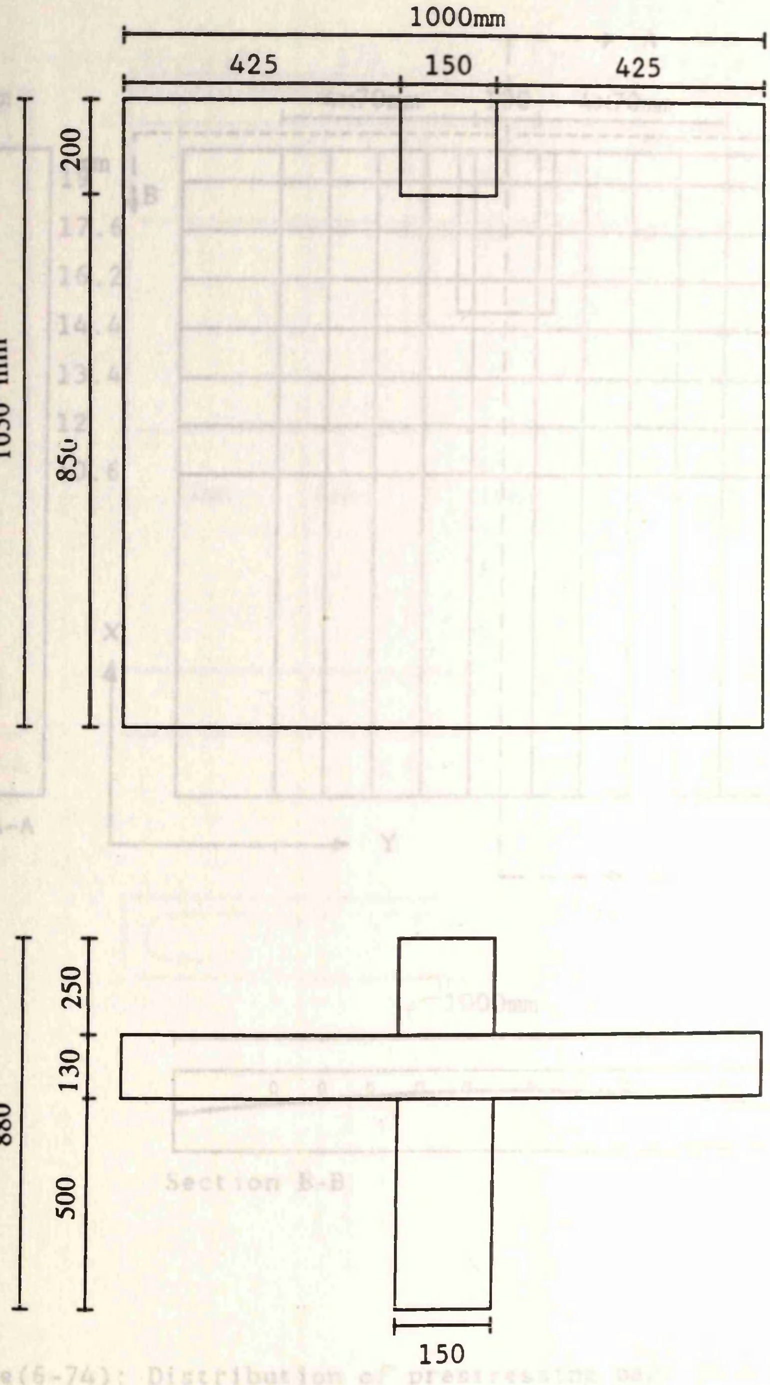

Figure(6-73): Plan and Dimensions of Model MS6.

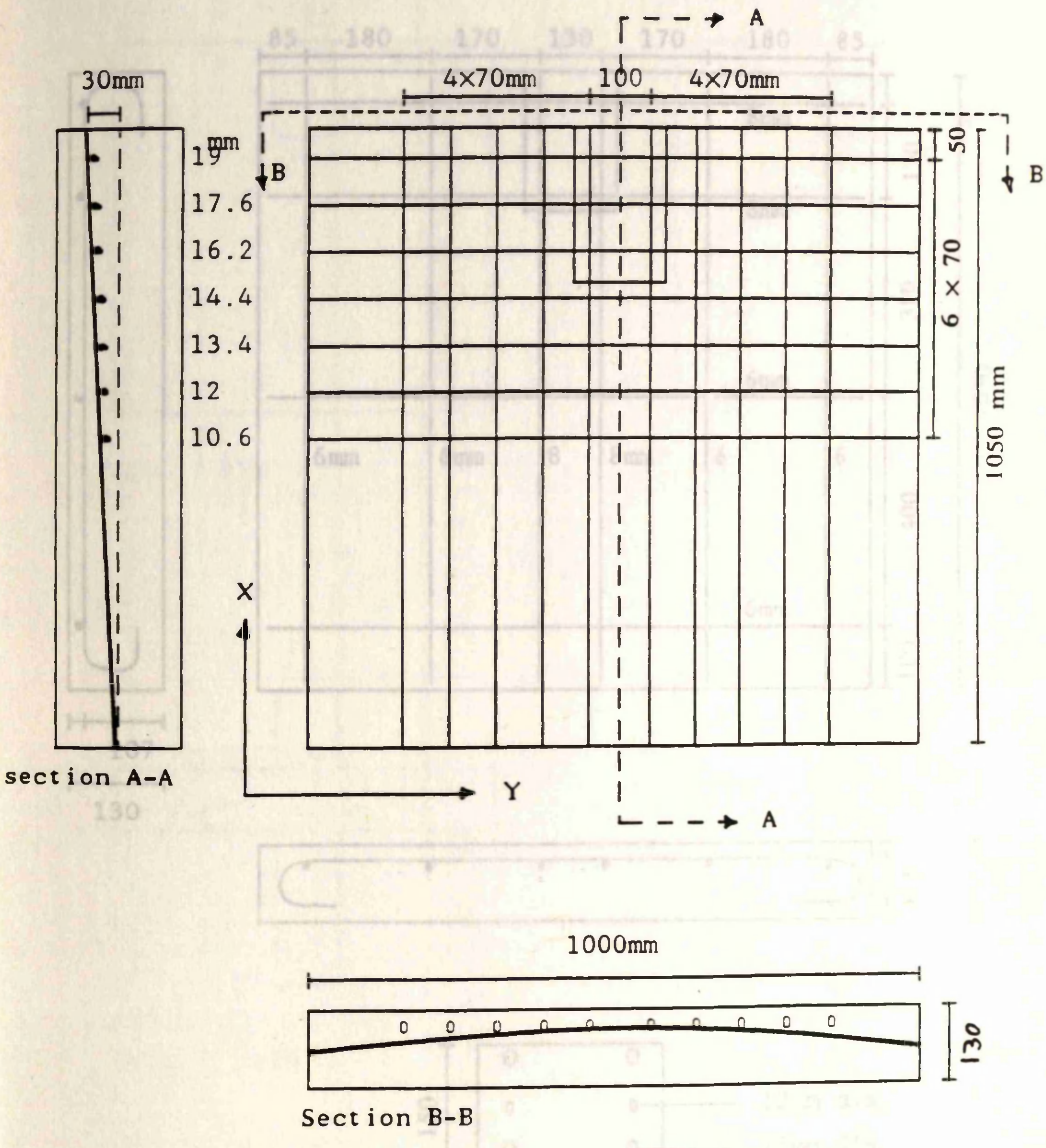

Figure(6-74): Distribution of prestressing bars in X and Y-direction for model MS6.

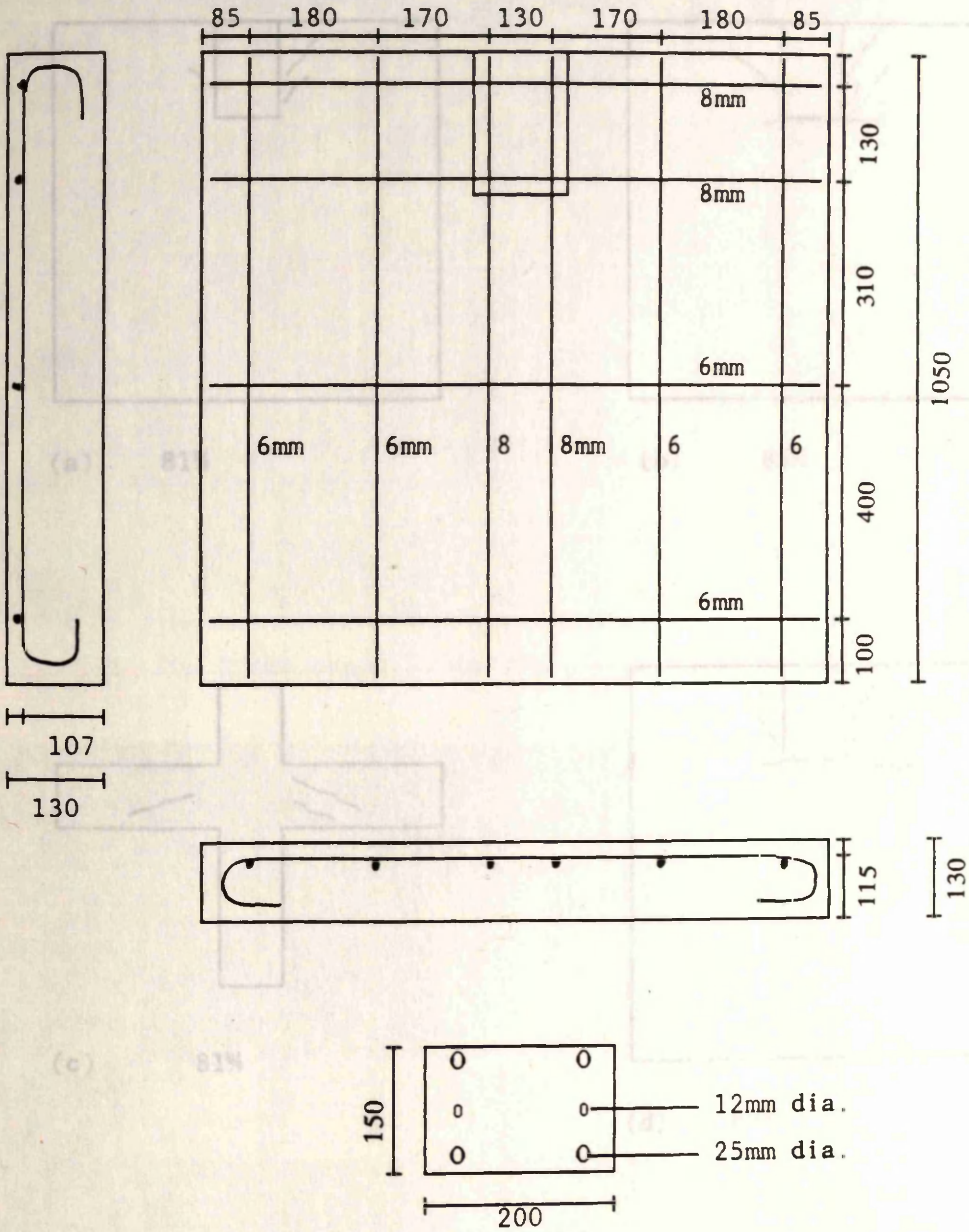

Figure(6-75): Arrangement of ordinary reinforcement bars in the slab and column for model MS6.

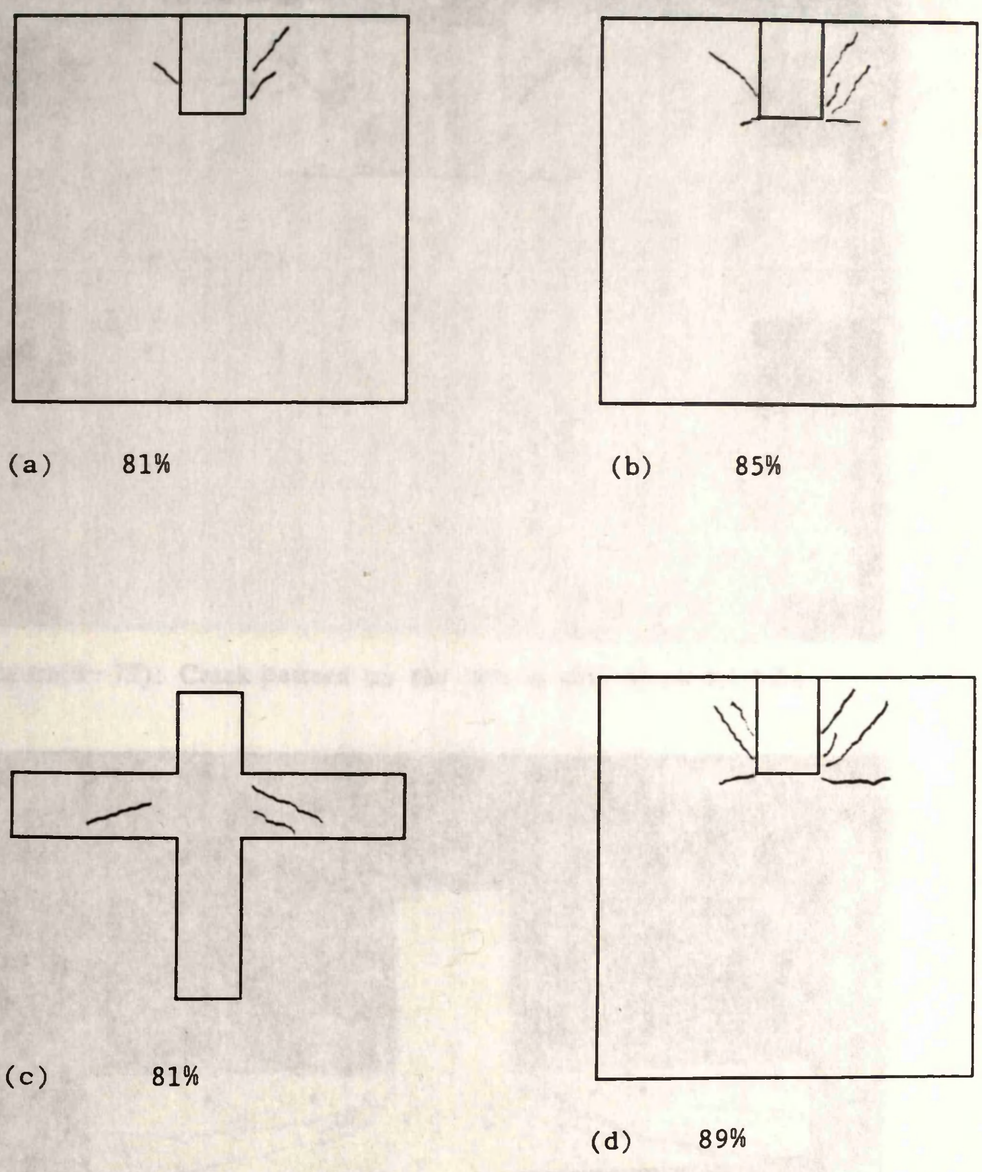

Figure(6-76): Cracks initiation during testing of model MS6 at different percentages of the design load.

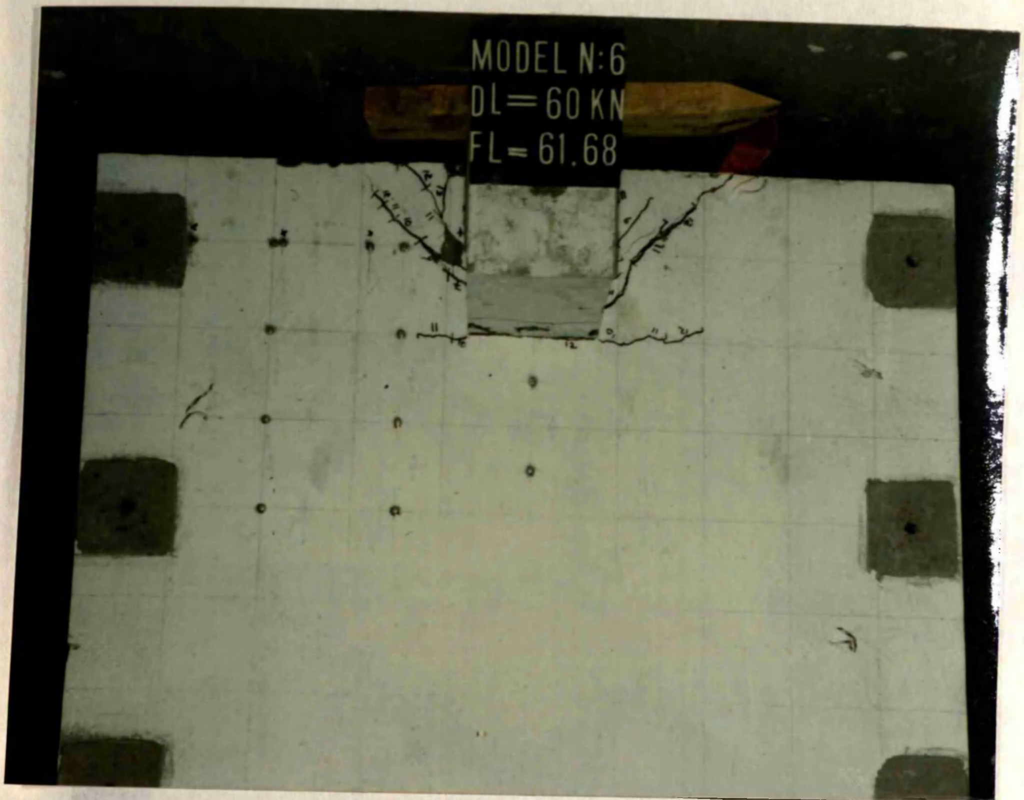

Figure(6-77): Crack pattern on the tensile side of model MS6.

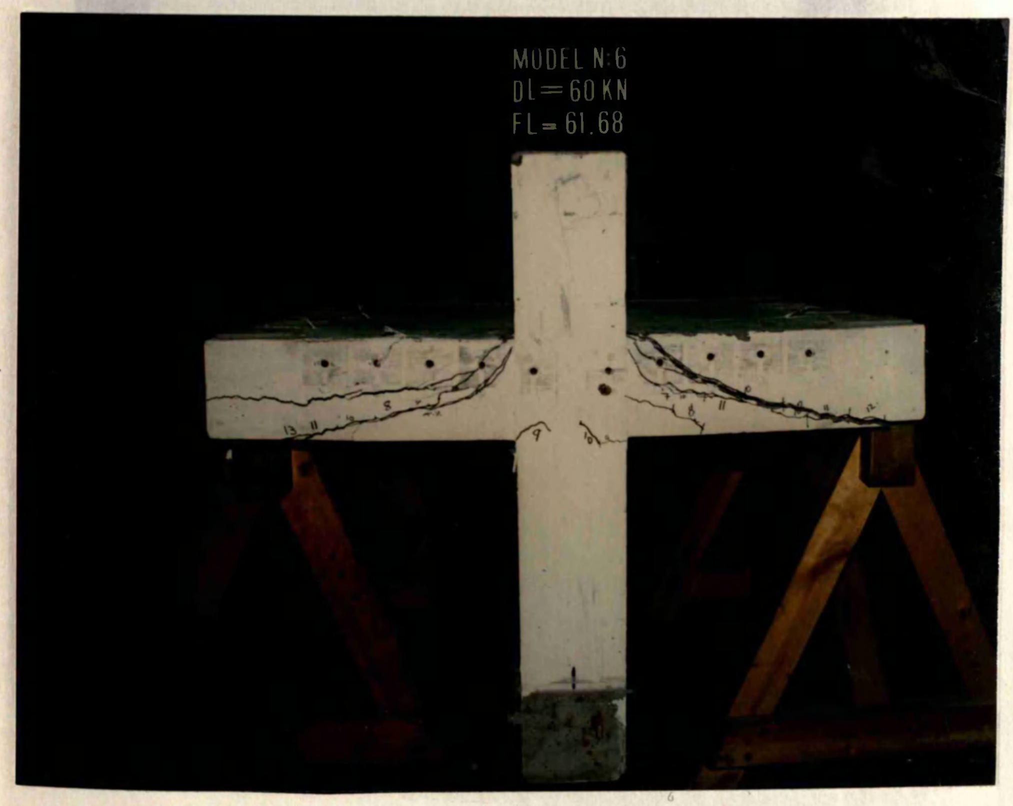

Figure (6.78): Failure surface at rear side of model MS6

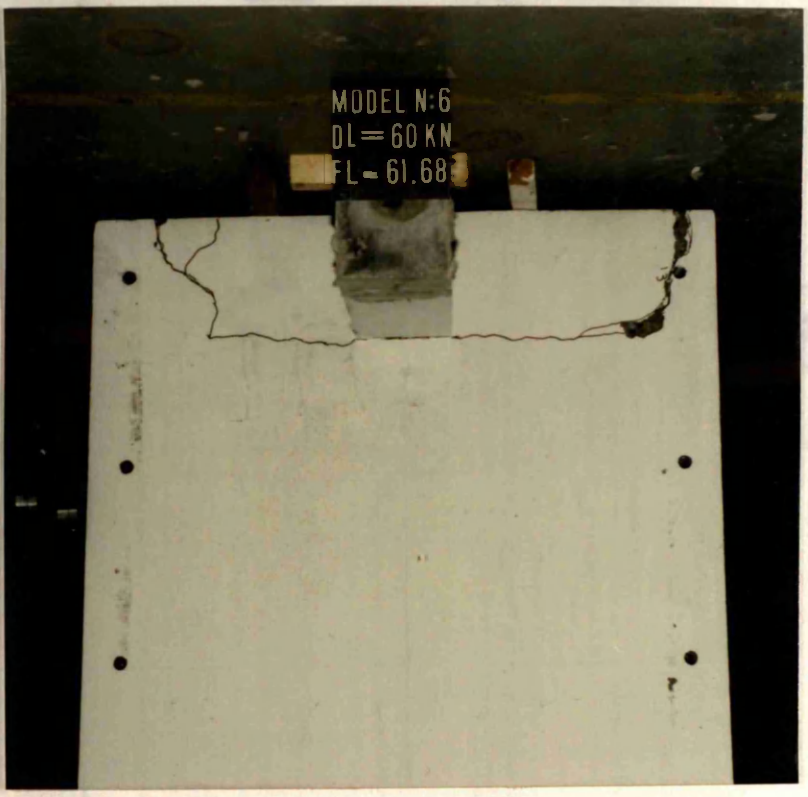

Figure(6–79): Crack pattern on bottom side of model MS6.

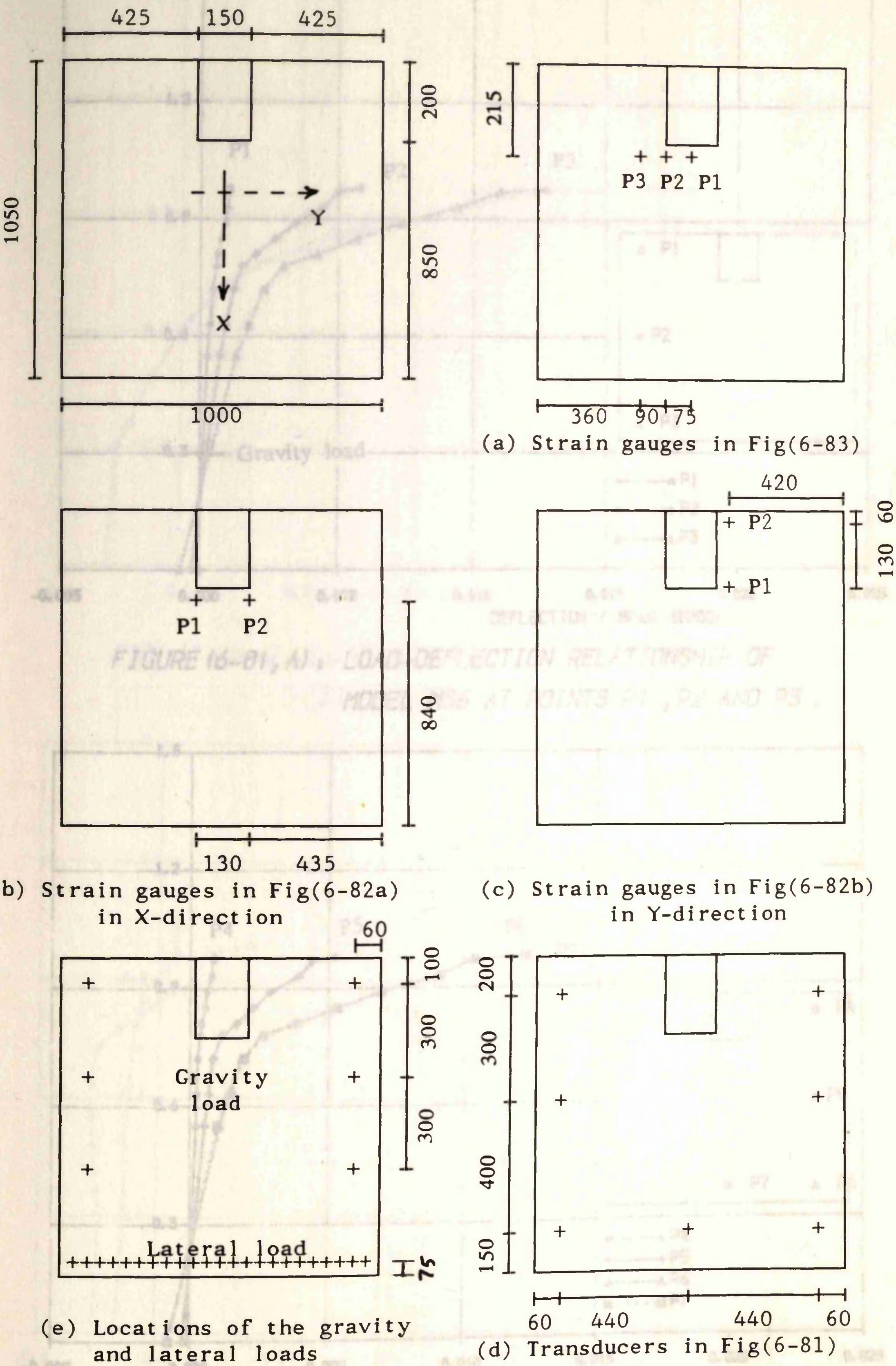

Figure(6-80): Exact locations of strain gauges in the slab and transducers of model MS6 as shown in Figures(6-81), (6-82) and (6-83).

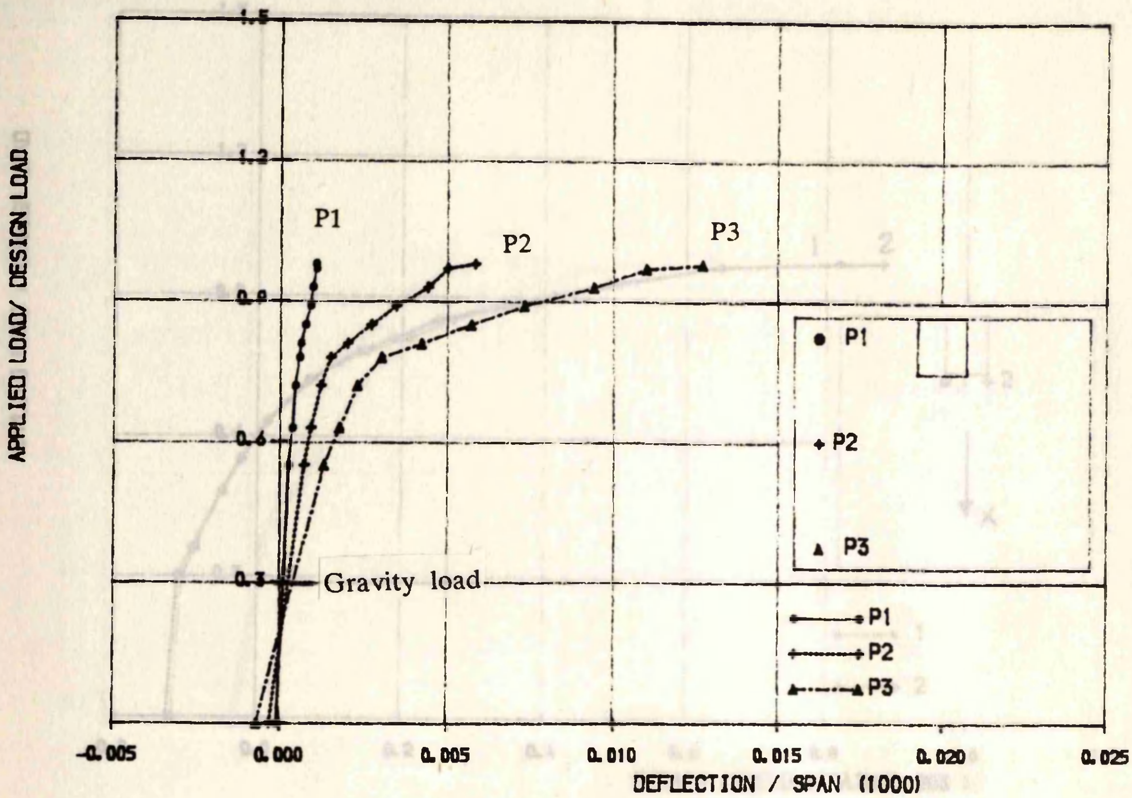

FIGURE (6-81, A) : LOAD-DEFLECTION RELATIONSHIP OF MODEL MS6 AT POINTS P1 ,P2 AND P3 .

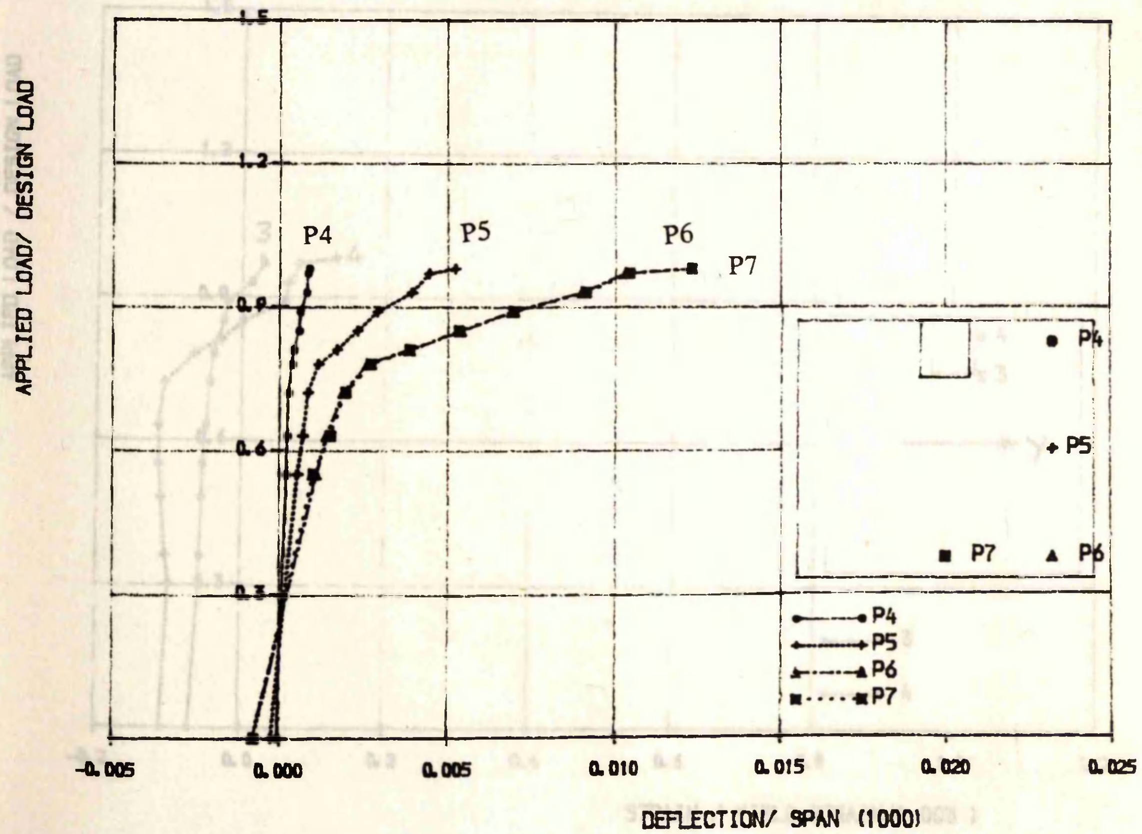

FIGURE (6-81, B) : LOAD-DEFLECTION RELATIONSHIP OF MODEL MS6 AT POINTS P1 TO P7 .

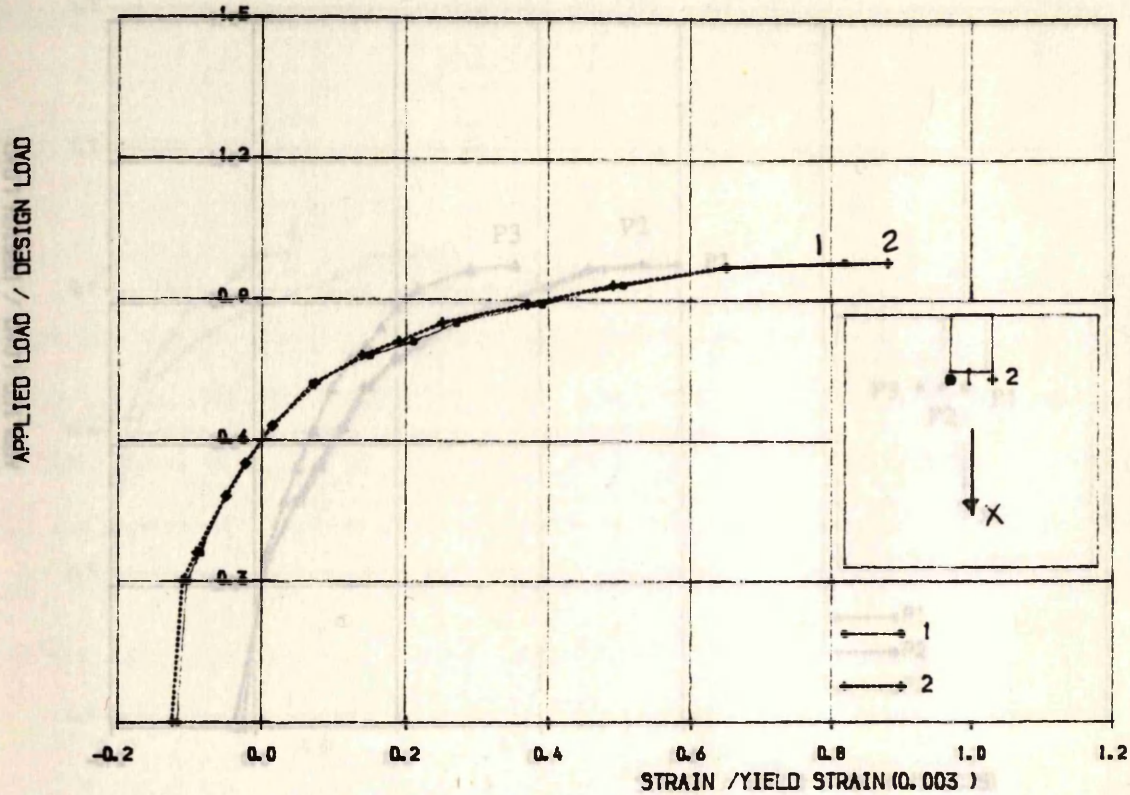

FIG. (6-82,A). LOAD-STRAIN CURVE FOR REINFORCING BAR IN X- DIRECTION (MODEL MS6).

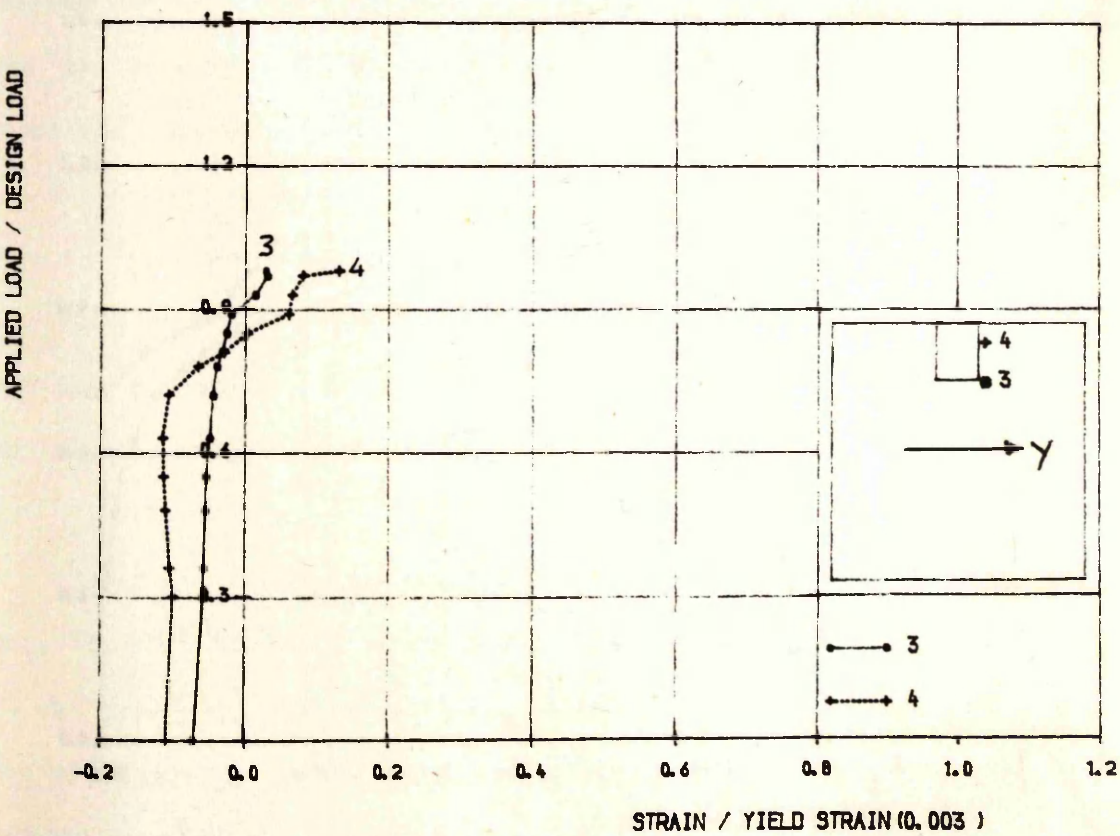

FIG. (6-82,B). LOAD-STRAIN CURVE FOR REINFORCING BAR IN Y- DIRECTION (MODEL MS6).

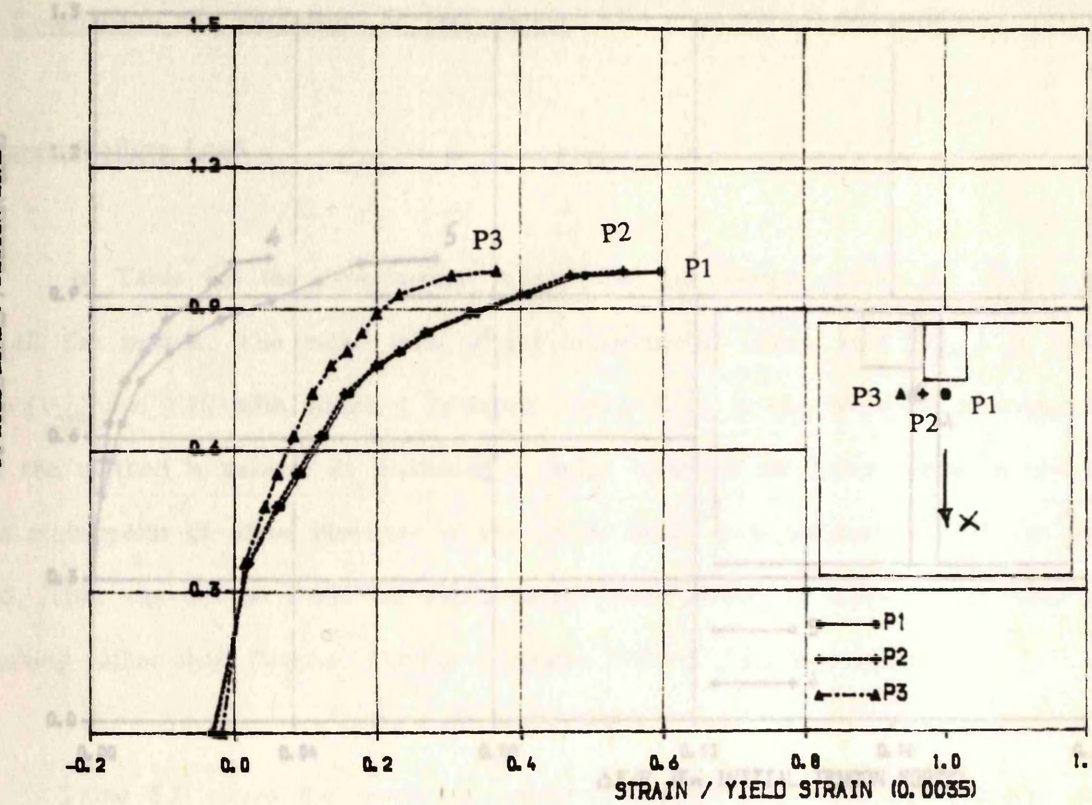

FIG. (6-83). LOAD-STRAIN CURVE AT COMPRESSIVE SURFACE OF CONCRETE AT P1 , P2 AND P3 FOR MODEL MS6.

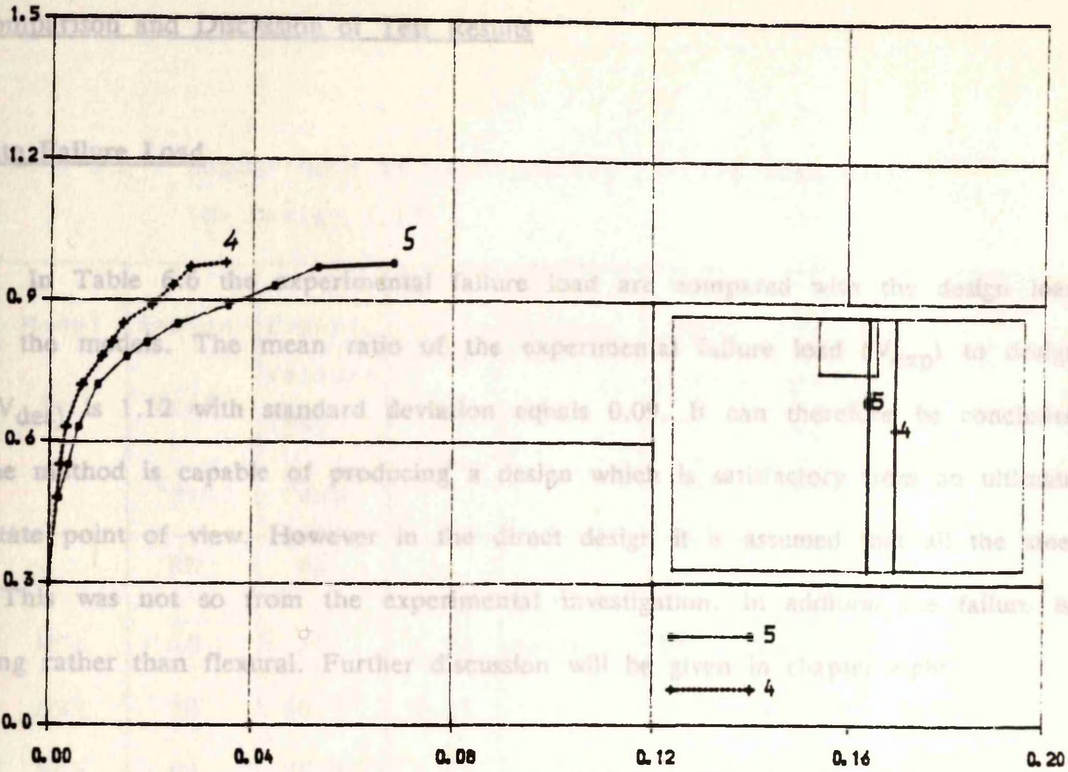

FIGURE (6-84,A), VARIATION IN TENDON FORCE FOR MODEL MS6 .

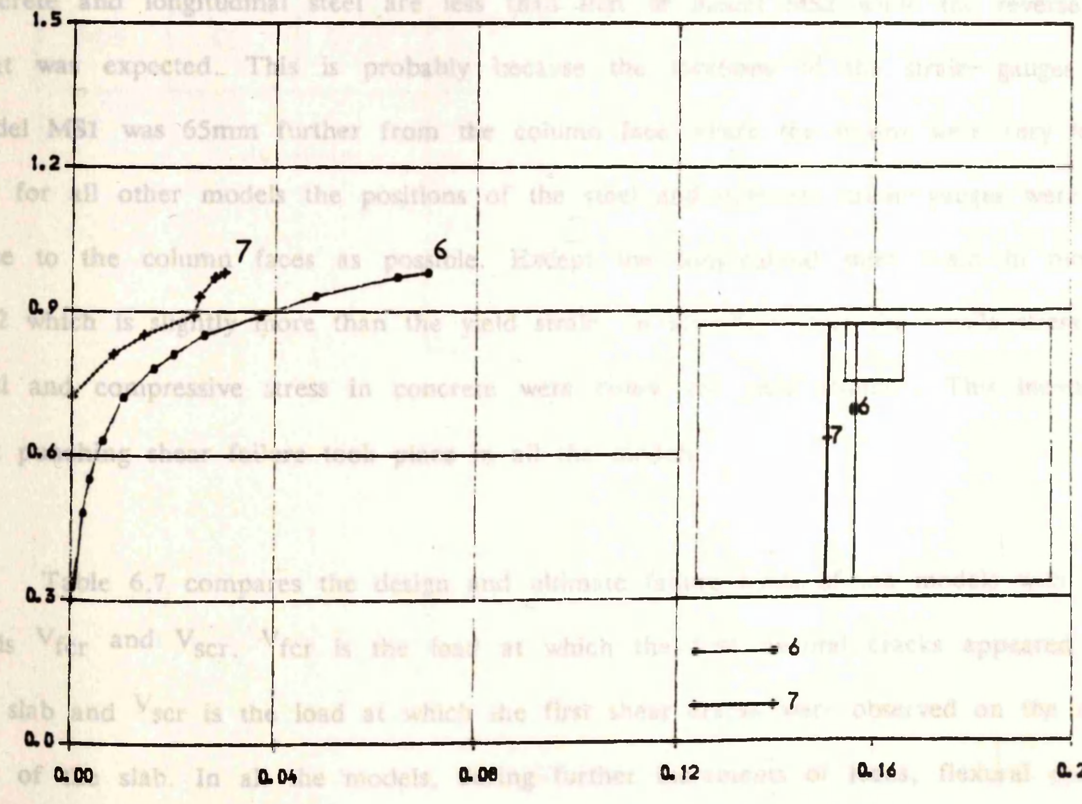

FIGURE (6-84,B), VARIATION IN TENDON FORCE FOR MODEL MS6 .

6.8 Comparison and Discussion of Test Results

Ultimate Failure Load

In Table 6.6 the experimental failure load are compared with the design load for all the models. The mean ratio of the experimental failure load (V_{exp}) to design load (V_{des}) is 1.12 with standard deviation equals 0.09. It can therefore be concluded that the method is capable of producing a design which is satisfactory from an ultimate limit state point of view. However in the direct design it is assumed that all the steel yield. This was not so from the experimental investigation. In addition the failure is punching rather than flexural. Further discussion will be given in chapter eight.

Table 6.8 shows the maximum strain of concrete and steel and the maximum variations of the tendon forces for all the six models. In model MS1 the strain of concrete and longitudinal steel are less than that of model MS2 while the reverse is what was expected. This is probably because the locations of the strain–gauges in model MS1 was 65mm further from the column face where the strains were very low. But for all other models the positions of the steel and concrete strain–gauges were as close to the column faces as possible. Except the longitudinal steel strain in model MS2 which is slightly more than the yield strain, in all other cases the tensile stress in steel and compressive stress in concrete were below the yield strains . This indicates that punching shear failure took place in all the models.

Table 6.7 compares the design and ultimate failure loads of the models with the loads V_{fcr} and V_{scr}. V_{fcr} is the load at which the first flexural cracks appeared on the slab and V_{scr} is the load at which the first shear cracks were observed on the rear side of the slab. In all the models, during further increments of loads, flexural cracks remained narrow and insignificant while the shear cracks widened and caused the punching shear failure of the slabs.

Table 6.6 : Comparisons of experimental failure load with the design load.

Model No.	design load $V_{des.}$	Experi. failure load $V_{exp.}$	$\frac{V_{exp}}{V_{des}}$	Failure mode	Parameters of study		
					$\frac{M_w}{V_w}$	$\frac{C_x}{C_y}$	prestress level
	KN	KN					N/mm2
MS1	48	59	1.16	punching	925	1.67	1.5
MS2	58	64.5	1.11	=	925	1.67	2.3
MS3	66	76.3	1.15	=	925	1.67	4.8
MS4	85	94.8	1.11	=	775	1.67	4.8
MS5	76	89.5	1.18	=	925	2.0	4.8
MS6	63	64.7	1.03	=	925	1.33	4.9
		average =	1.12				
		S. D. =	0.09				

Table 6.7 : Comparisons of the design loads with the experimental loads at which first flexural cracks (V_{fcr}) and first shear cracks (V_{scr}) were observed.

Model No.	design load $V_{des.}$ KN	$\frac{V_{exp}}{V_{des}}$	$\frac{V_{fcr}}{V_{des}}$	$\frac{V_{scr}}{V_{des}}$	Parameters of study		
					$\frac{M_w}{V_w}$	$\frac{C_x}{C_y}$	prestress level N/mm2
MS1	48	1.16	0.69	0.89	925	1.67	1.5
MS2	58	1.11	0.76	0.93	925	1.67	2.3
MS3	66	1.15	0.76	0.82	925	1.67	4.8
MS4	85	1.11	0.80	0.85	775	1.67	4.8
MS5	76	1.18	0.78	0.95	925	2.0	4.8
MS6	63	1.03	0.89	0.79	925	1.33	4.9
average =		1.12	0.78	0.87			

Table 6.8 :

Model No.	design load (V_{des})	$\frac{V_{exp}}{V_{des}}$ *	$\frac{\epsilon_{cmax}}{\epsilon_{cy}}$ * (X_{dir})	$\frac{\epsilon_{smax}}{\epsilon_{sy}}$ * X_{dir}	Y_{dir}	$\frac{\Delta F}{F}$ *
	KN					
MS1	48	1.16	0.20	0.86	0.6	0.18
MS2	58	1.11	0.76	1.14	0.26	0.10
MS3	66	1.15	0.46	0.76	0.20	0.06
MS4	85	1.11	0.50	0.81	0.35	0.08
MS5	76	1.18	0.79	0.84	0.11	0.06
MS6	63	1.03	0.6	0.85	0.13	0.07
average =		1.12	0.55	0.88	0.28	0.09

*) V_{exp} = Experimental failure load,

ϵ_{cmax} = Maximum compressive strain of concrete at experimental failure load,

ϵ_{smax} = Maximum tensile stress of the steel bar at experimental failure load,

ϵ_{cy} = Compressive yield strain of concrete,

ϵ_{sy} = Yield strain of the steel bar,

F = Initial prestressing force of the tendon,

ΔF = Variations of the tendon force due to applied loads.

6.9 Effect of The Parameters on The Behaviour of The Models

In this section, it is intended to compare the behaviour of the models for each parameter of study mentioned in section 6.3. Therefore, the experimental models were divided into three groups as follows:

- Group(1) consists of the models MS1, MS2 and MS3 in order to study the parameter of Prestressing Level.
- Group(2) consists of the models MS3 and MS4 in order to study the parameter of the ratio of wind shear moment to wind shear.
- Group(3) consists of the models MS3, MS5 and MS6 in order to study the parameter of the column aspect ratio.

In the design of all the models care was taken to keep all the parameters constant except the parameter in question. Therefore any change in the behaviour of the model can be related to the effect of the parameter involved. So a comparison of the behaviour of models within each group for a specific parameter will be useful.

6.9.1 Group(1)

The models of this group have level of prestress of 1.5, 2.3 and 4.8 N/mm2 respectively for MS1 ,MS2 and MS3. Figure 6.86 shows the load-deflection curves for the model of this group. These curves indicate that by increasing the prestressing level; firstly the load-carrying capacity of the junction increases and secondly, the deflection of the slab decreases.

Figure 6.87 shows the load-strain curves for ordinary reinforcement which passed through the column head. It is seen that for model MS3 with the maximum prestressing level in this group, the maximum tensile strain of the bar is 75% of the yield strain while for model MS2 is 115% of the yield strain. The maximum tensile strain recorded in model MS1 was 85% of the yield strain ,however, it is not shown in Figure 6.87 because the strain– gauge was in different position from MS2 and MS3.

Figure 6.88 shows the variation of tendon force versus applied load for all the models of this group. The maximum variation of force in the tendon for models MS1, MS2 and MS3 is respectively, 18% ,10% and 6% of the initial prestressing force of the tendon. Therefore it can be concluded that when the prestressing level increases the increase in the tensile stress in steel bars(tendons and unstressed bars) decreases.

Figure 6.89 shows the load– strain curves on the compressive surface of concrete from which the maximum compressive strain of concrete for models MS2 and MS3 are 75% and 43% of the yield strain respectively. Data for model MS1 was not entered in the figures 6.87 and 6.89 because of its different position of steel and concrete strain gauges and maximum value of compressive strain of concrete recorded in this model was 19% of the yield strain.

6.9.2 <u>Group(2)</u>

The models of this group have different length in the windward direction to vary the ratio of wind shear moment to wind shear. The cantilever 'span' of model MS4 is 78% of that in model MS3. The behaviour of these models are compared in Figures 6.90, 6.91, 6.92 and 6.93. In spite of the fact that the failure load of model MS4 is 124% of that of MS3, the maximum deflection of model MS4 is 83% of that of model MS3 (Figure 6.90). It is concluded that the reduction of 22% of the ratio causes the increase of 24% of the ultimate load.

6.9.3 Group(3)

The models of this group MS6, MS3 and MS5 have the column aspect ratios of 1.33 ,1.67 and 2.0 respectively. The behaviour of these models are compared in Figures 6.94, 6.95, 6.96 and 6.97. The model MS5 with the high column aspect ratio had a maximum ultimate load (89.5 KN) amongst these models and model MS6 with the lowest aspect ratio had the minimum ultimate load (64.68 KN) in this group. Therefore, the ultimate failure load of the connection increased in proportion to the aspect ratio of the column.

A study of Figures related to this group of models, indicates that increasing the aspect ratio of the column in moment transfer direction increases the strength and stiffness of the junction. The reason for this behaviour is the mechanism of moment transfer between the slab and edge column of the junction. The wind shear moment is transferred from the slab to the column by means of bending moment at the front face of the column and twisting moment at two side faces of the column. On the other hand the failure mode of the models were punching failure due to the twisting moment shear. It can be therefore said that in the case of edge column connection, the twisting moment resisting capacity has a significant contribution to the punching strength of the connection and it increases when the column aspect ratio increases. Further discussion on these parameters is prescribed in Chapter 8.

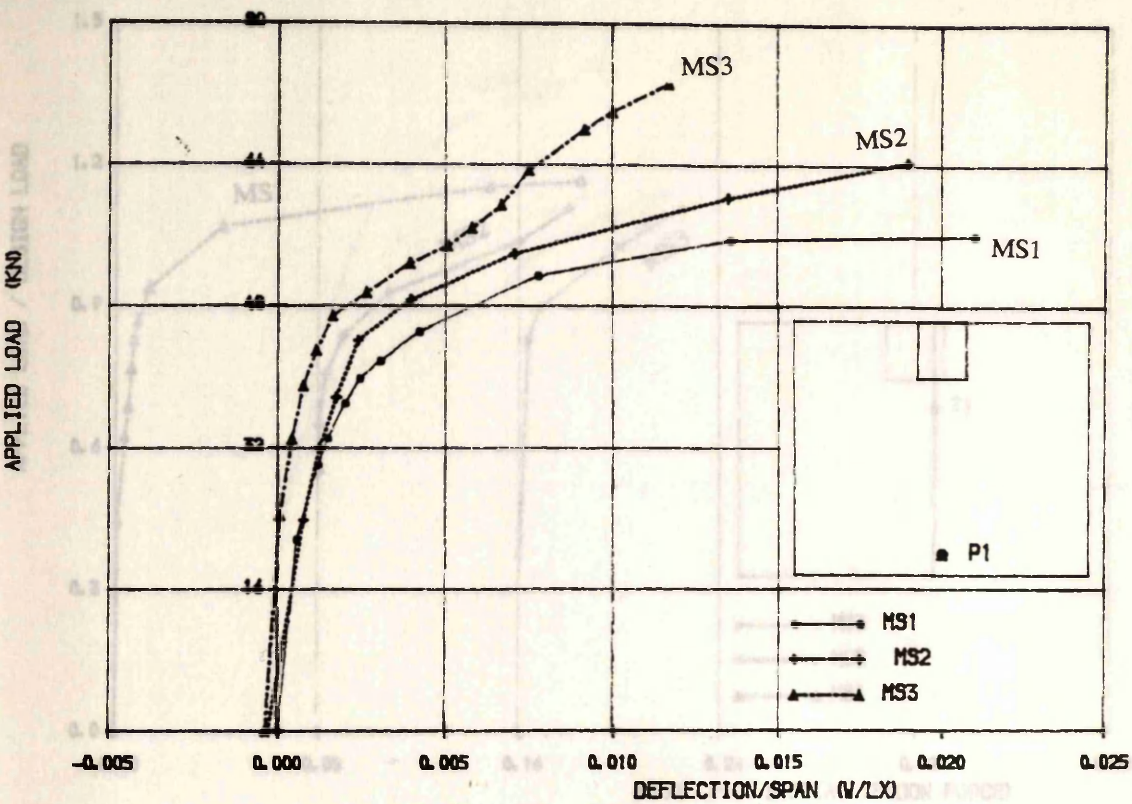

FIG. (6-86), LOAD-DEFLECTION RELATIONSHIP OF MODELS MS1 ,MS2 AND MS3 AT POINT P1.

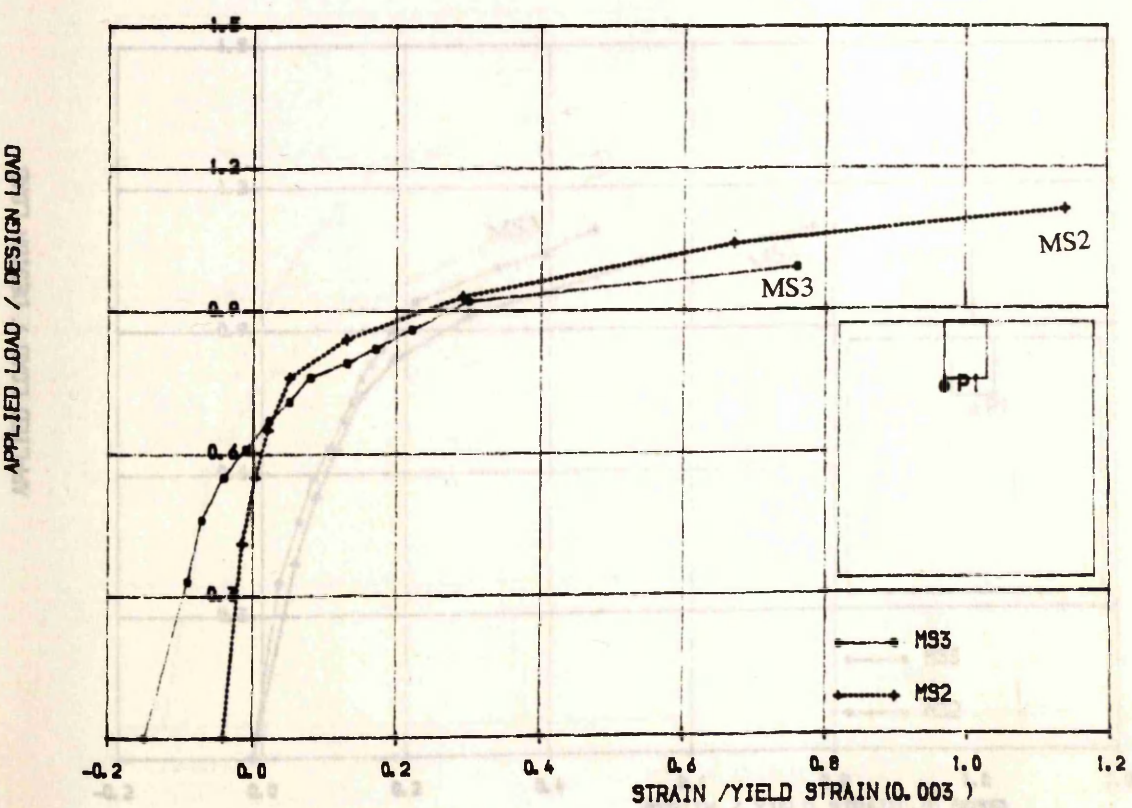

FIG. (6-87), LOAD-STRAIN CURVE FOR REINFORCING BAR IN X-DIRECTION FOR MODELS MS2 AND MS3.

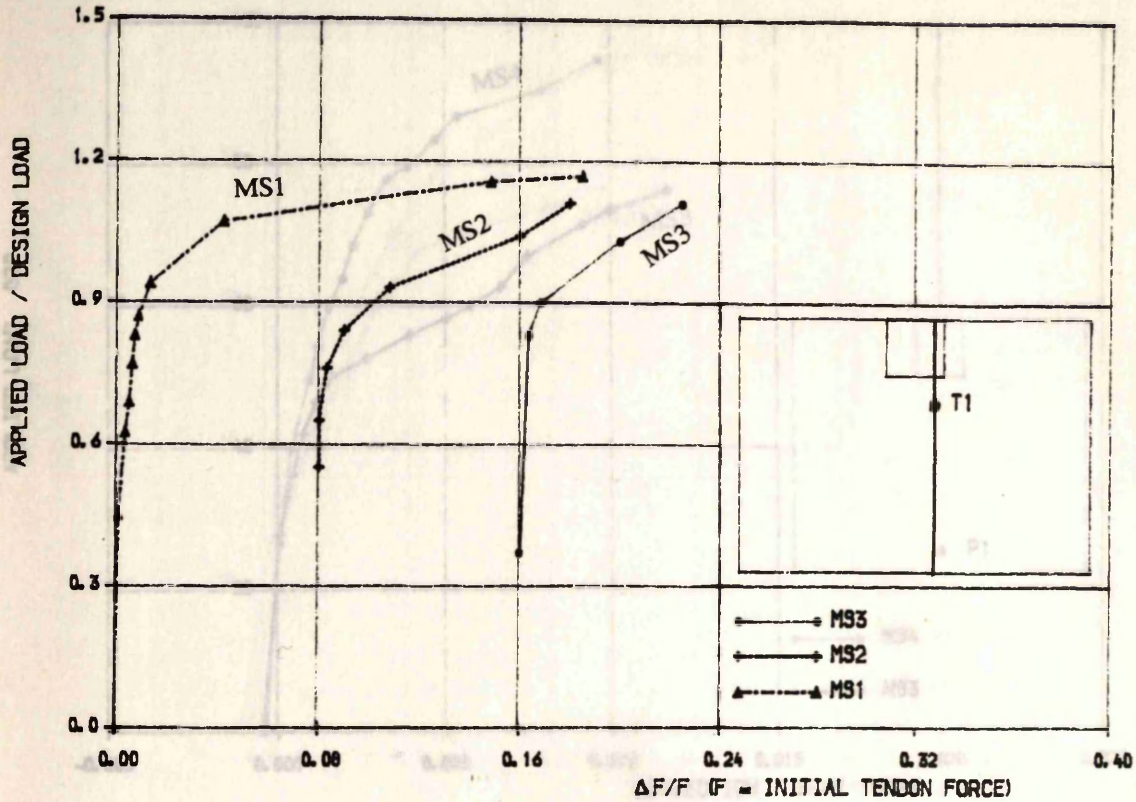

FIG. (6-88), VARIATION IN THE TENDON FORCE VERSUS APPLIED LOAD FOR MODELS MS2 AND MS3.

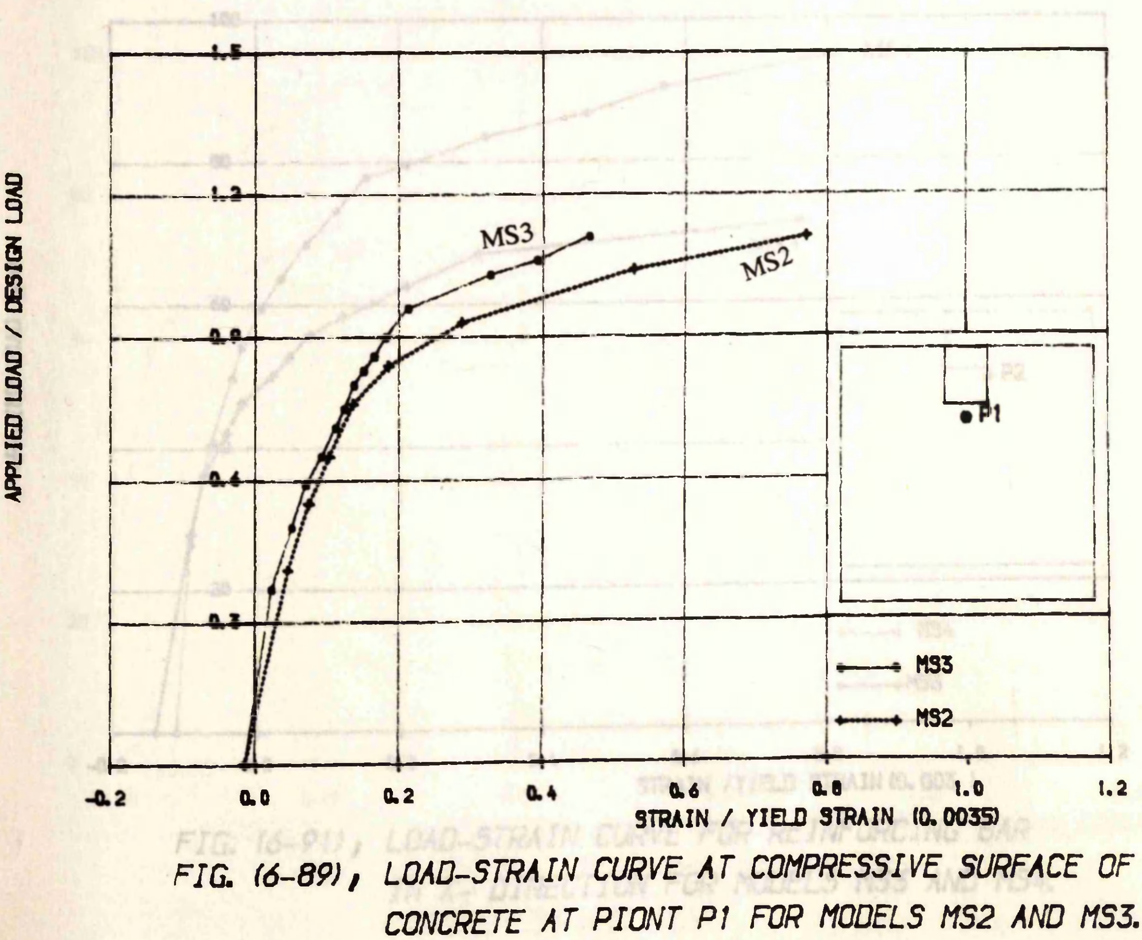

FIG. (6-89), LOAD-STRAIN CURVE AT COMPRESSIVE SURFACE OF CONCRETE AT PIONT P1 FOR MODELS MS2 AND MS3.

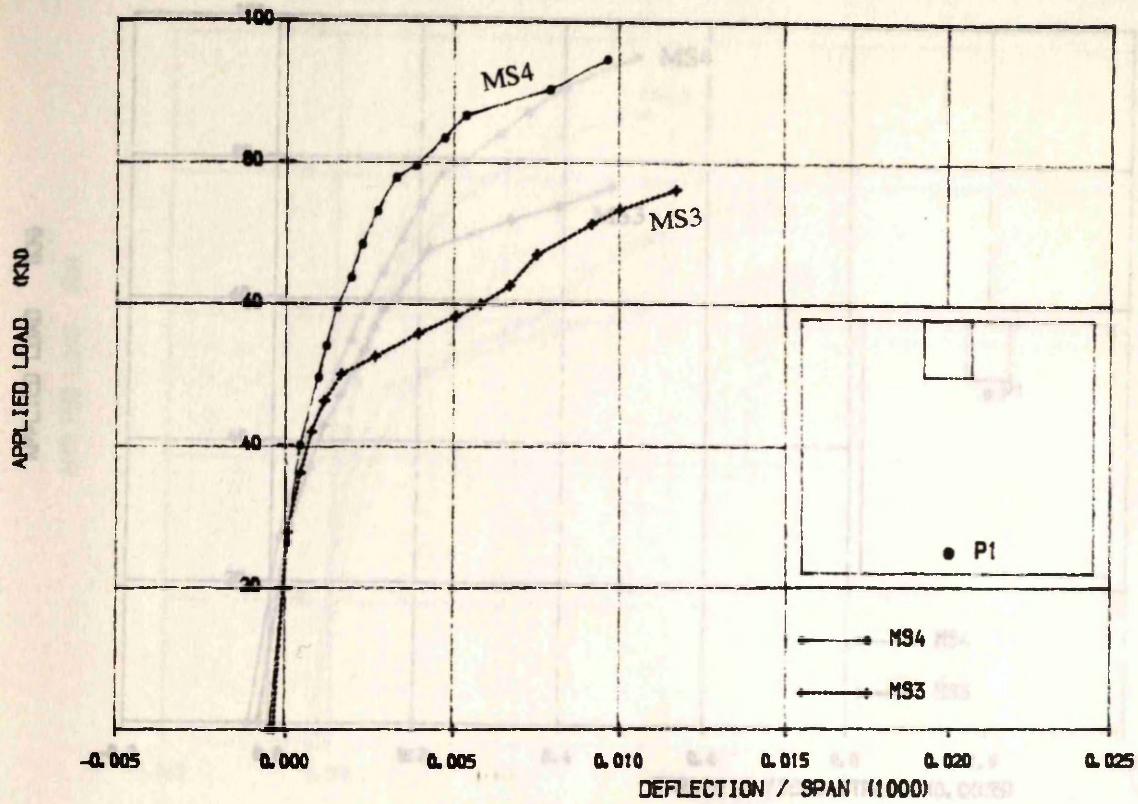

FIG. (6-90), LOAD-DEFLECTION RELATIONSHIP OF MODELS MS3 AND MS4.

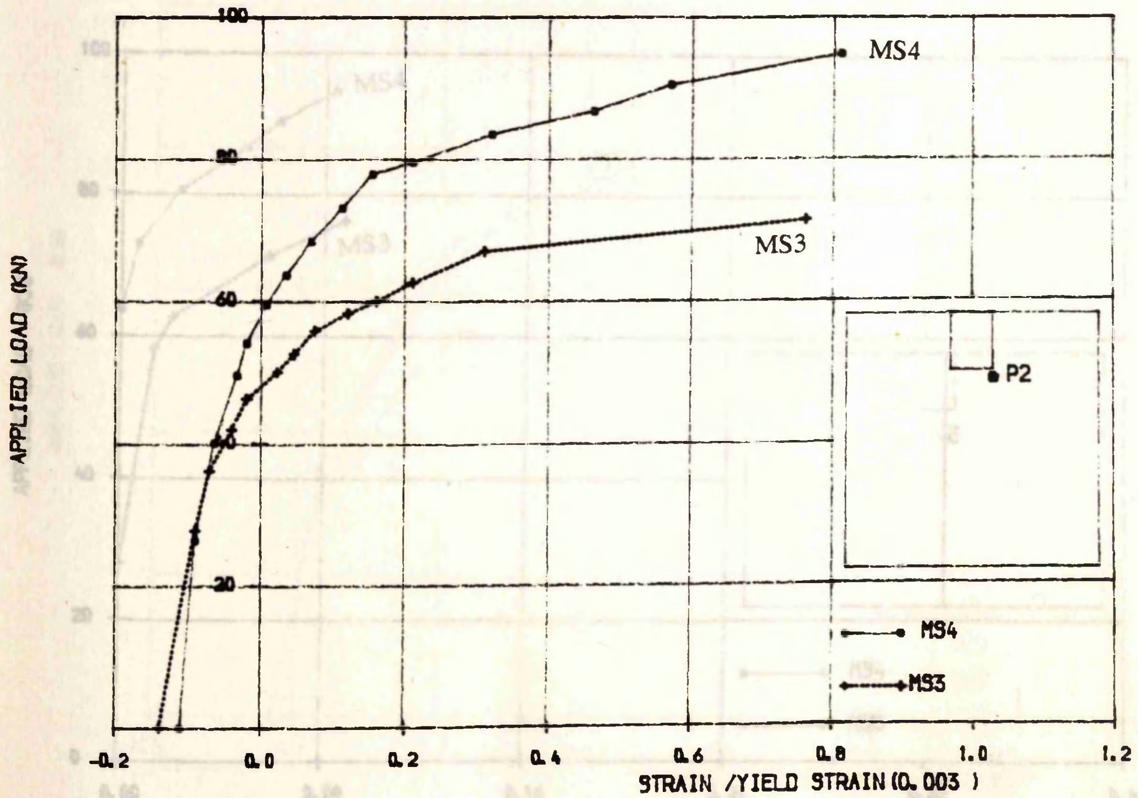

FIG. (6-91), LOAD-STRAIN CURVE FOR REINFORCING BAR IN X- DIRECTION FOR MODELS MS3 AND MS4.

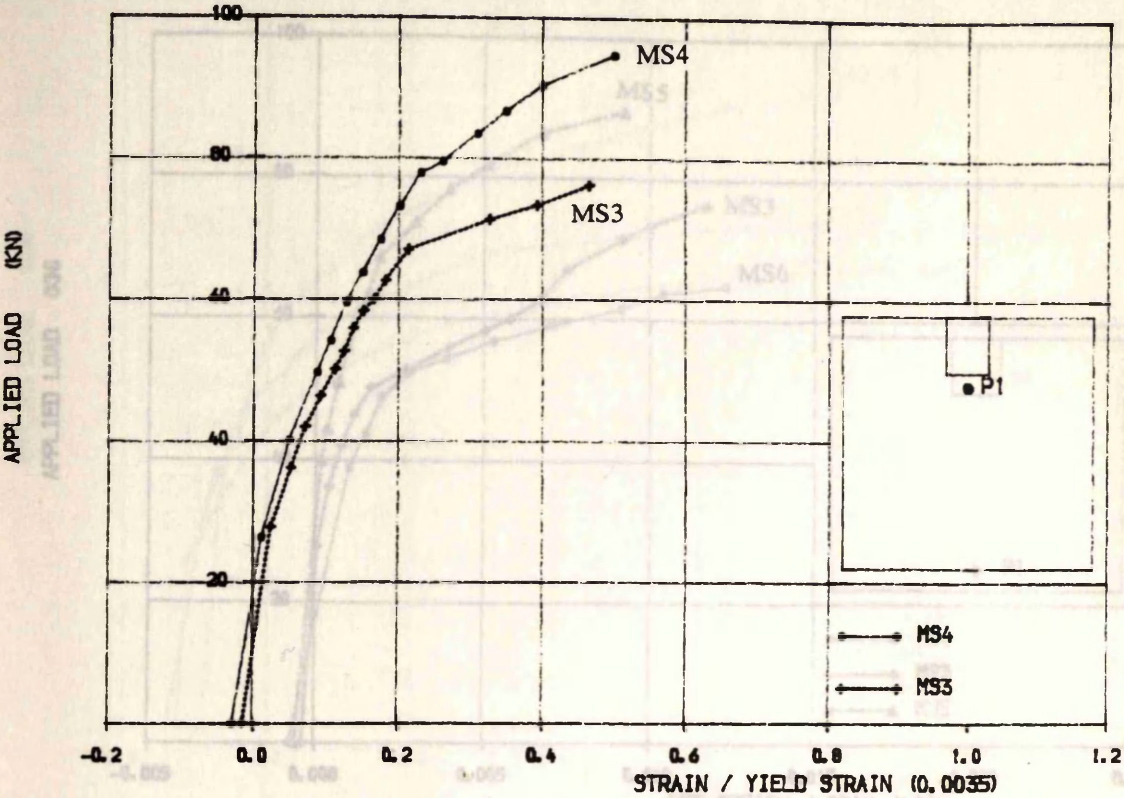

FIG. (6-92), LOAD-STRAIN CURVE AT COMPRESSIVE SURFACE OF CONCRETE FOR MODELS MS3 AND MS4.

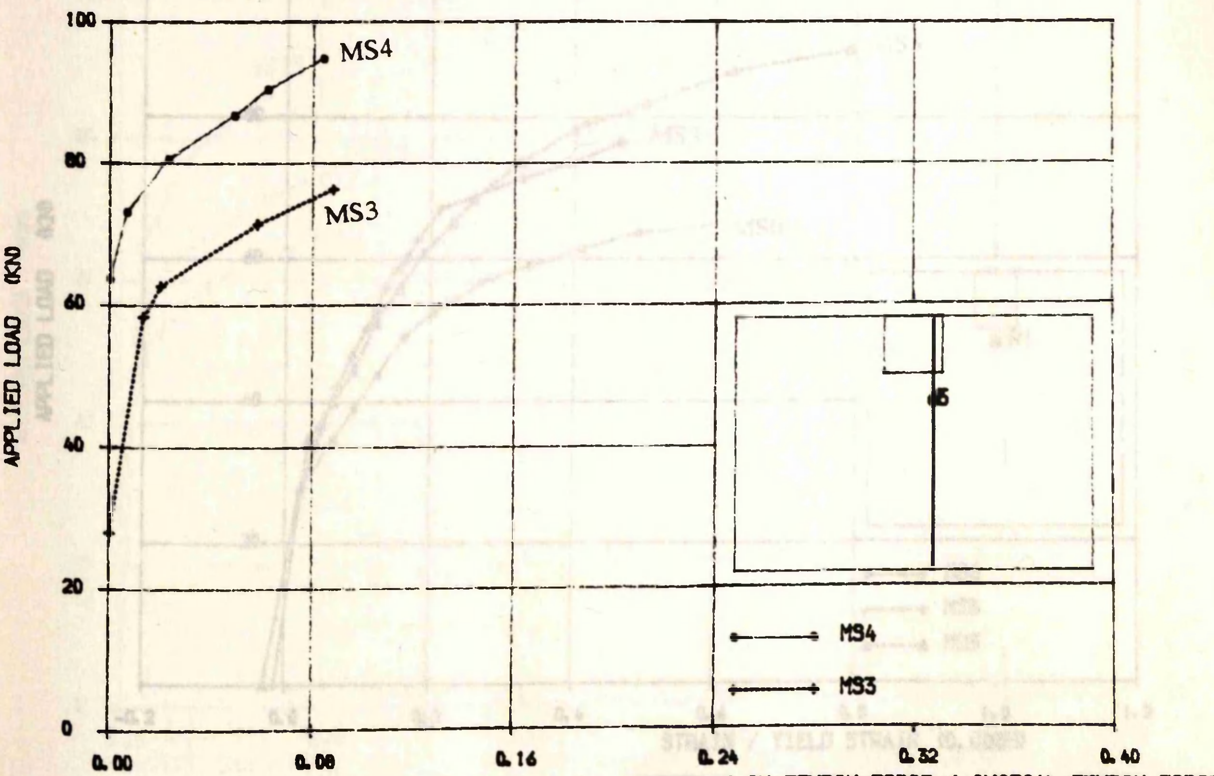

FIG. (6-93), VARIATION IN TENDON FORCE FOR MODELS MS3 AND MS4.

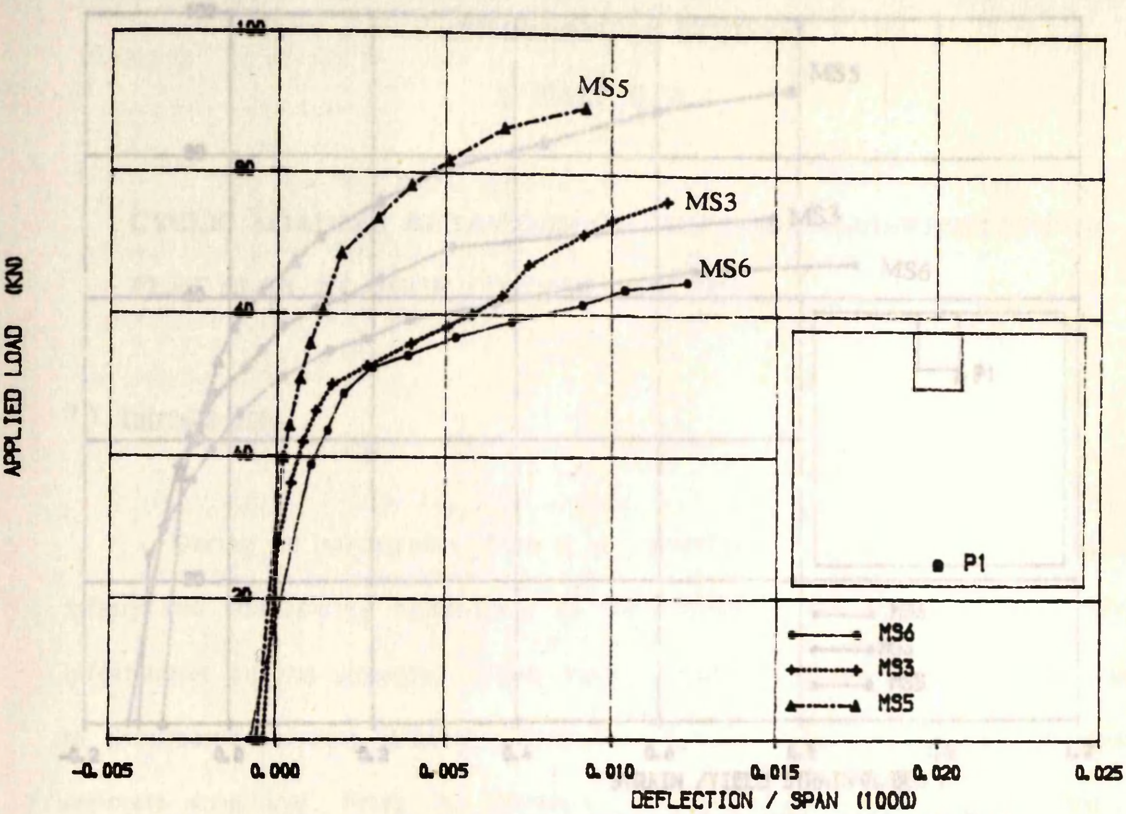

FIG. (6-94), LOAD-DEFLECTION RELATIONSHIP OF MODELS MS3 MS5 AND MS6.

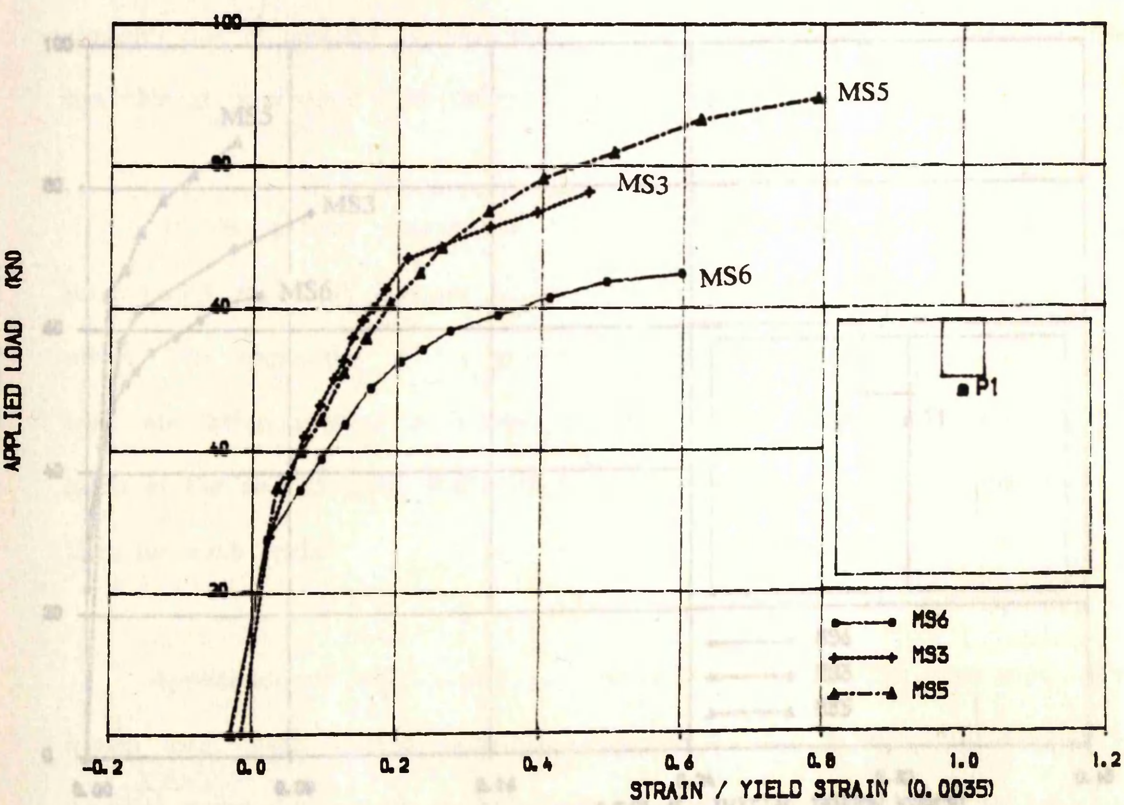

FIG. (6-95), LOAD-STRAIN CURVE AT COMPRESSIVE SURFACE OF CONCRETE, MODELS MS3, MS5 AND MS6.

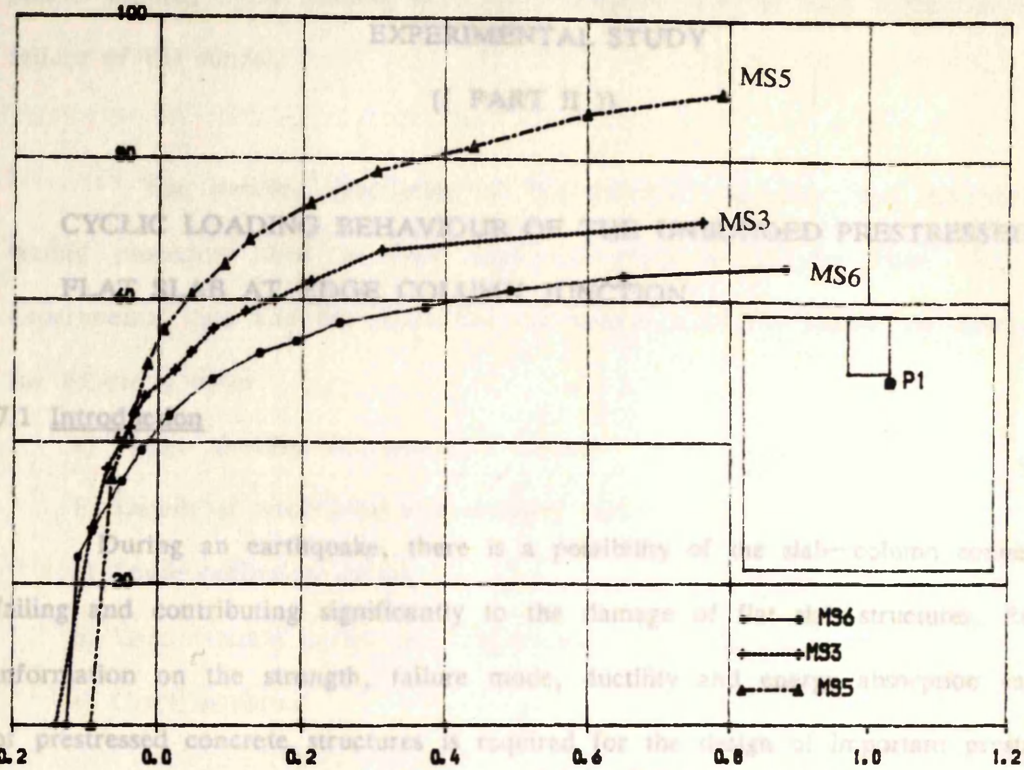

FIG. (6-96), LOAD-STRAIN CURVE FOR REINFORCING BAR IN X-DIRECTION FOR MODELS MS3 , MS5 AND MS6 .

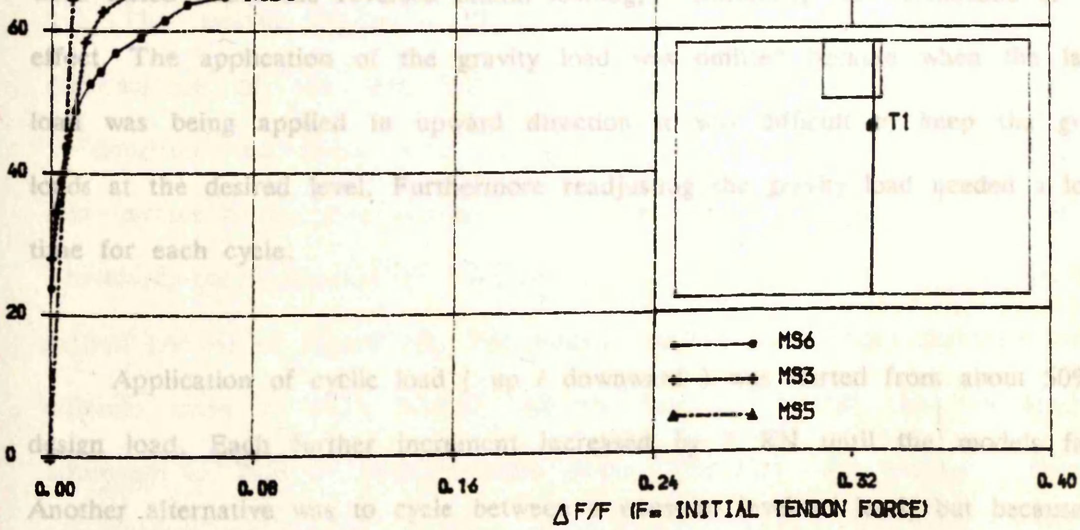

FIG. (6-97), VARIATION IN TENDON FORCE FOR MODELS MS3 , MS5 AND MS6.

CHAPTER SEVEN

EXPERIMENTAL STUDY

((PART II))

CYCLIC LOADING BEHAVIOUR OF THE UNBONDED PRESTRESSED FLAT SLAB AT EDGE COLUMN JUNCTION

7.1 Introduction

During an earthquake, there is a possibility of the slab–column connections failing and contributing significantly to the damage of flat slab structures. Reliable information on the strength, failure mode, ductility and energy absorption capacity of prestressed concrete structures is required for the design of important prestressed concrete structures. From the literature survey reported in chapter two, there is very little information about the seismic resistance of slab column connections especially when the slab is prestressed. The deterioration of the load carrying capacity due to reversal of loads and the ductility and the energy absorption that is available at prestressed slab–column junctions require close examination.

In this chapter results are reported on two models RCS7 and RCS8 which were tested under the reversed lateral loading, " simulating" an earthquake or wind effect. The application of the gravity load was omitted because when the lateral load was being applied in upward direction it was difficult to keep the gravity loads at the desired level. Furthermore readjusting the gravity load needed a lot of time for each cycle.

Application of cyclic load (up / downward) was started from about 50% of design load. Each further increment increased by 2 KN until the models failed. Another alternative was to cycle between a constant level of load, but because the behaviour of the prestressed concrete slabs until about 90% of design load was elastic keeping cyclic loading between a constant level of load might not lead to failure of the model.

The detailed description of the material properties, test equipment and testing procedure used in these tests was given in Chapter Five. The various experimental data and the results on the behaviour of the models are presented in the following order:

a) Sketch showing dimensions of models

b) Details of prestressing and ordinary bars.

c) Load– deflection curves .

d) Load – strain curves for " unstressed " steel bar.

e) Crack pattern.

7.2 Experimental Programme on Cyclic Loading

7.2.1 Model RCS7 (Reversed Cyclic Series)

The design lateral load of this model was 38 KN acting in downward direction. The plan and dimensions of this model are shown in figure 7.1. The top and bottom unstressed reinforcement of the slab were identical as shown in Figure 7.2. The tendon profile in X– direction was linear and passed through the mid– surface of the slab without any eccentricity. The tendon profile in Y– direction was linear too, but it was not possible to pass through the mid– surface of the slab because of coincidence with the tendons in X– direction. Therefore, the tendons in Y– direction had an eccentricity of 12.5 mm as shown in section (A– A) of Figure 7.2. The tendons used were of 7mm diameter with the ultimate stress of 1623 N/mm2. All the tendons in both the directions were tensioned to 70% of their ultimate stress. Therefore, the average prestress in concrete was 4.8 N/mm2.

At the first cycle of loading, a downward load of 50% of the design lateral load was applied in increments to the model by means of a hydraulic jack of 500(KN) capacity. Then the jack was released and an upward load was applied in increments by another hydraulic jack of the same capacity as the previous one. This jack, which was installed on the rigid frame, was loaded up to the same level of load as it was for the downward loading. From the second cycle, the applied load (downward and upward) was increased by 2 (KN) at each cycle of loading until failure occurred.

The two transducers were mounted on the top and bottom surfaces of the slab to measure the rotation of the cantilever slab relative to the column as shown in Figures 5—19a and 5.19b. The relative rotation of the slab at the onset of steel yielding is termed as " the yield rotation = θ_y " as shown in Figures 7.4 and 7.5. The loading cycles sequence used in testing the model is shown versus relative rotation and tensile strain of the ordinary reinforcement in Figures 7.6 and 7.7 respectively.

Behaviour of the Model

During the application of the prestressing forces, no cracks were observed on the top and bottom surfaces of the slab. The first cycle of loading (downward and upward) comprised a load of 50% of the design lateral load and on further loading up to 85% of the design load no crack was observed. In cycle number seven corresponding to 85% of the design load, first hairline cracks were initiated from the front corners of the column on top surface of the slab as shown in Figure 7.8a. At 92% of the design load (8^{th} cycle of loading) first hairline cracks were observed on the bottom surface similar to that on the top surface. At this stage the flexural cracks on the top surface of the slab extended in the Y—direction of the slab as shown in Figure 7.8b. At 118% of the design load corresponding to the 13^{th} cycle, torsional cracks developed simultaneously on the top and bottom surfaces of the slab as shown in Figure 7.8c. Finally, at 137% of

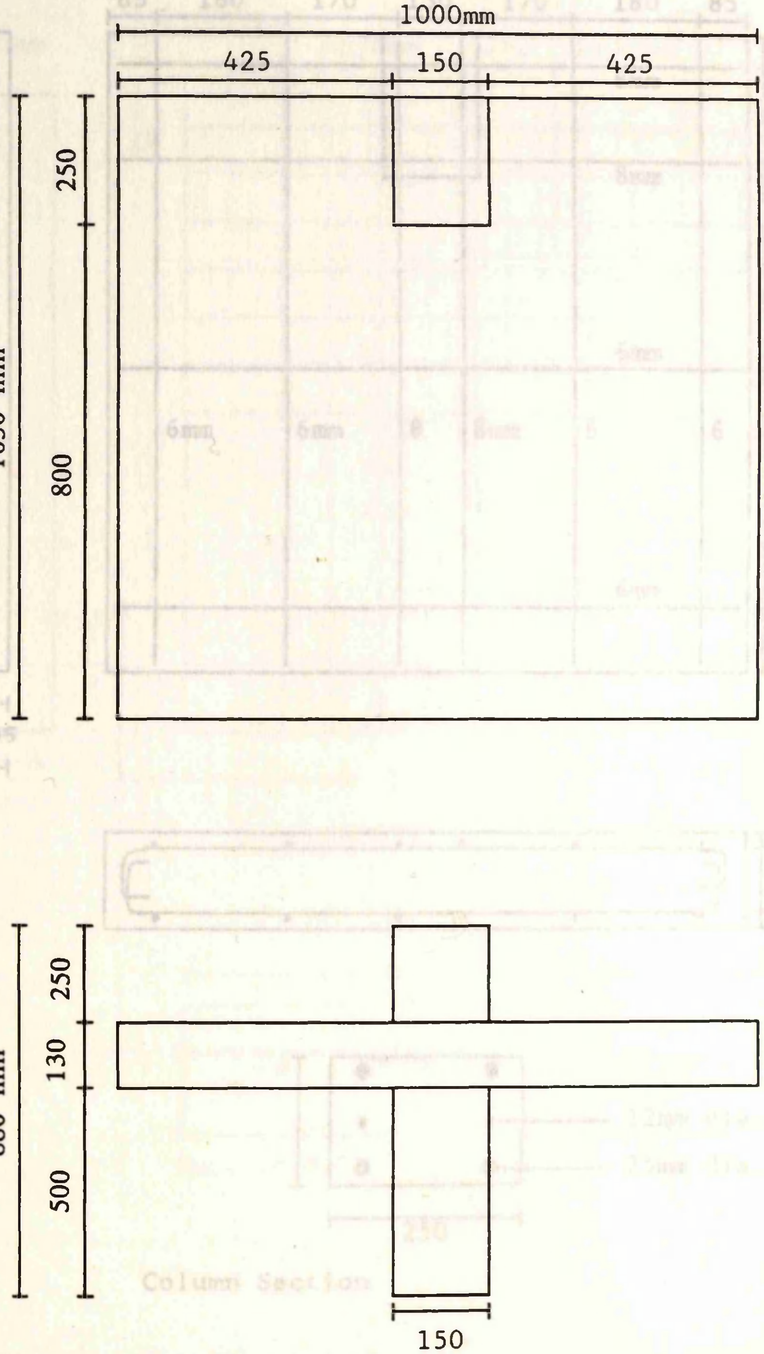

Figure(7-1): Plan and Dimensions of Models RCS7 and RCS8.

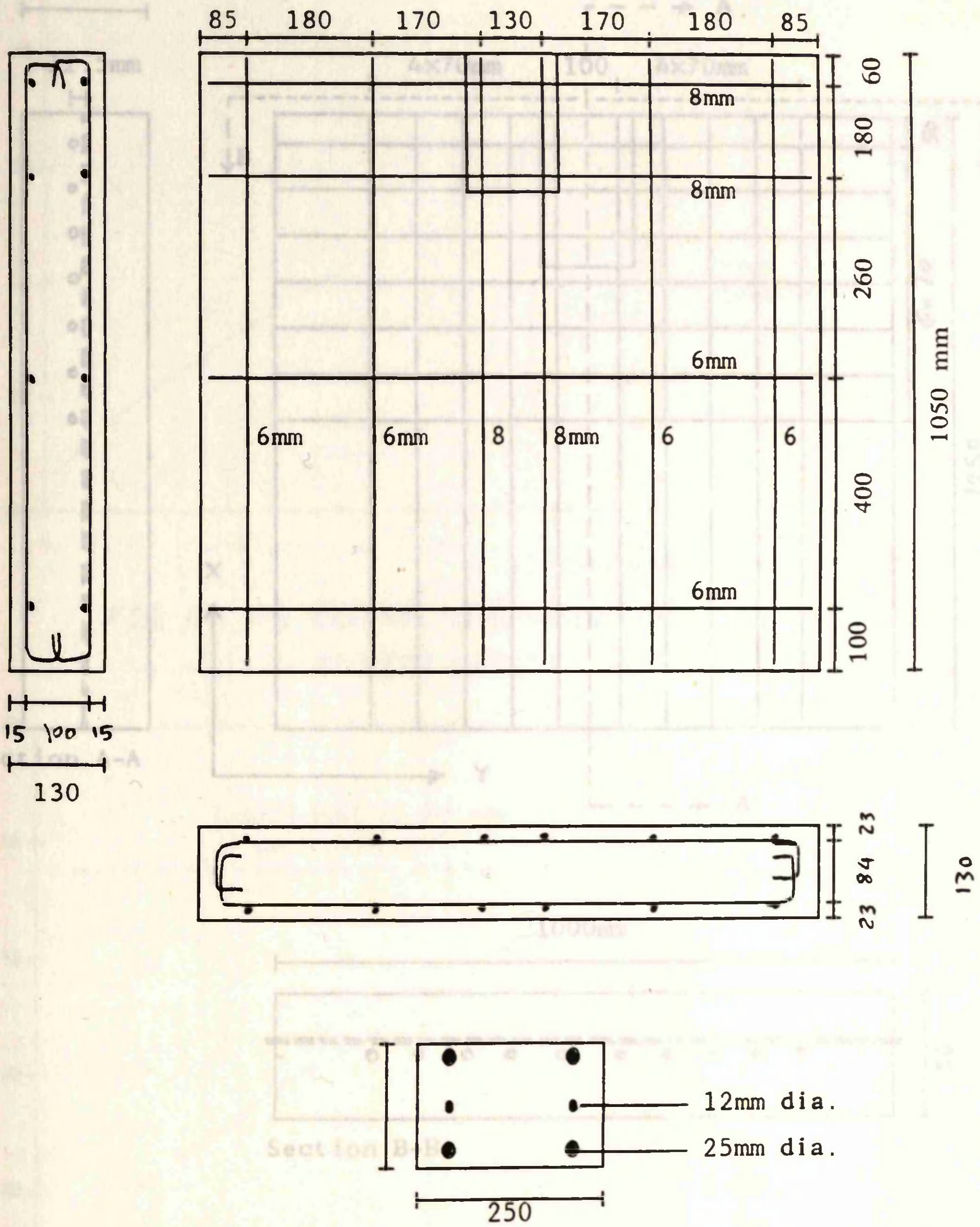

Column Section

Figure(7-2): Arrangement of top and bottom ordinary reinforcing bars in the slab for models RCS7 and RCS8.

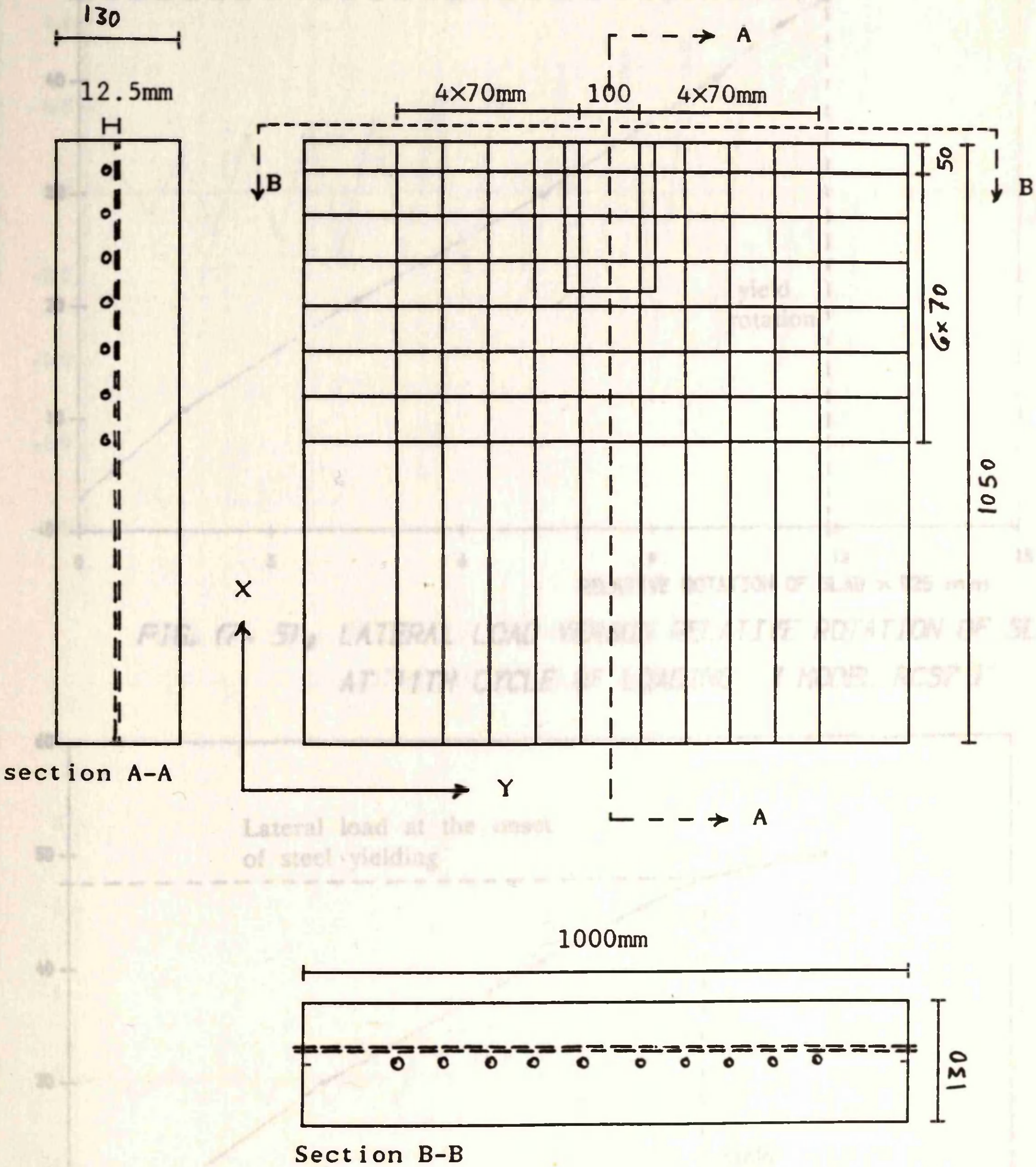

Figure(7-3): Distribution of prestressing bars in X and Y-directions for models RCS7 and RCS8.

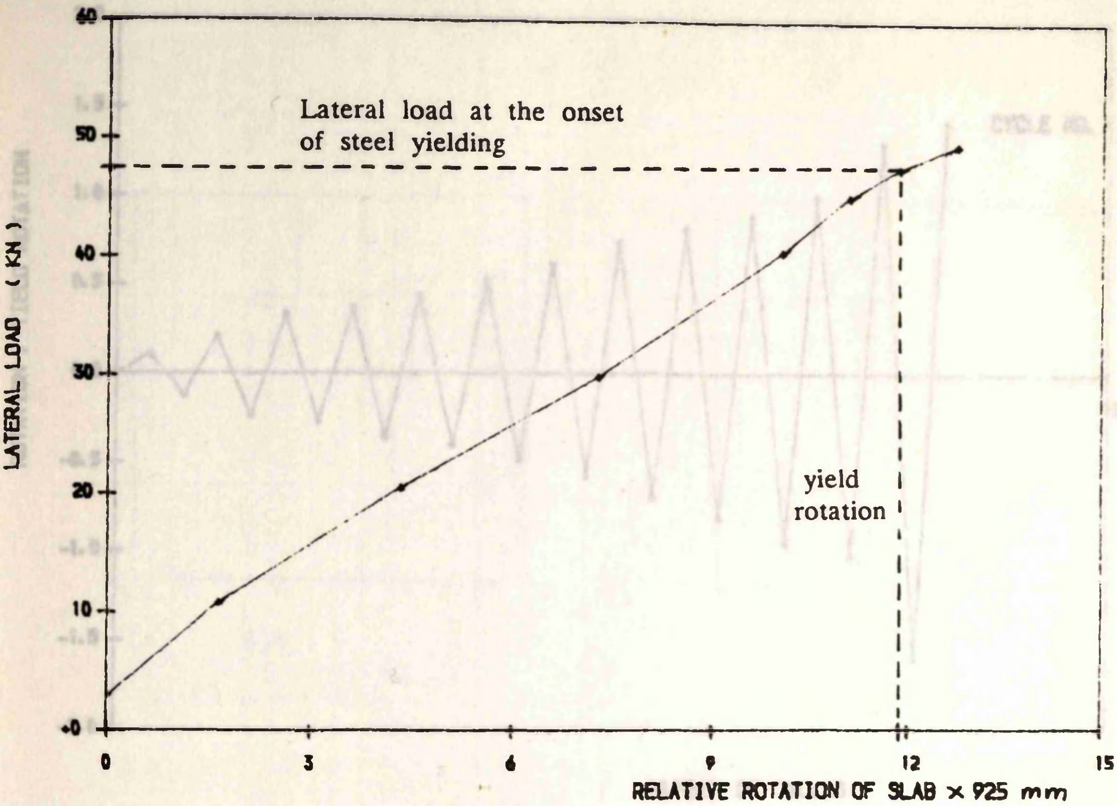

FIG. (7- 5), LATERAL LOAD VERSUS RELATIVE ROTATION OF SLAB AT 11TH CYCLE OF LOADING (MODEL RCS7)

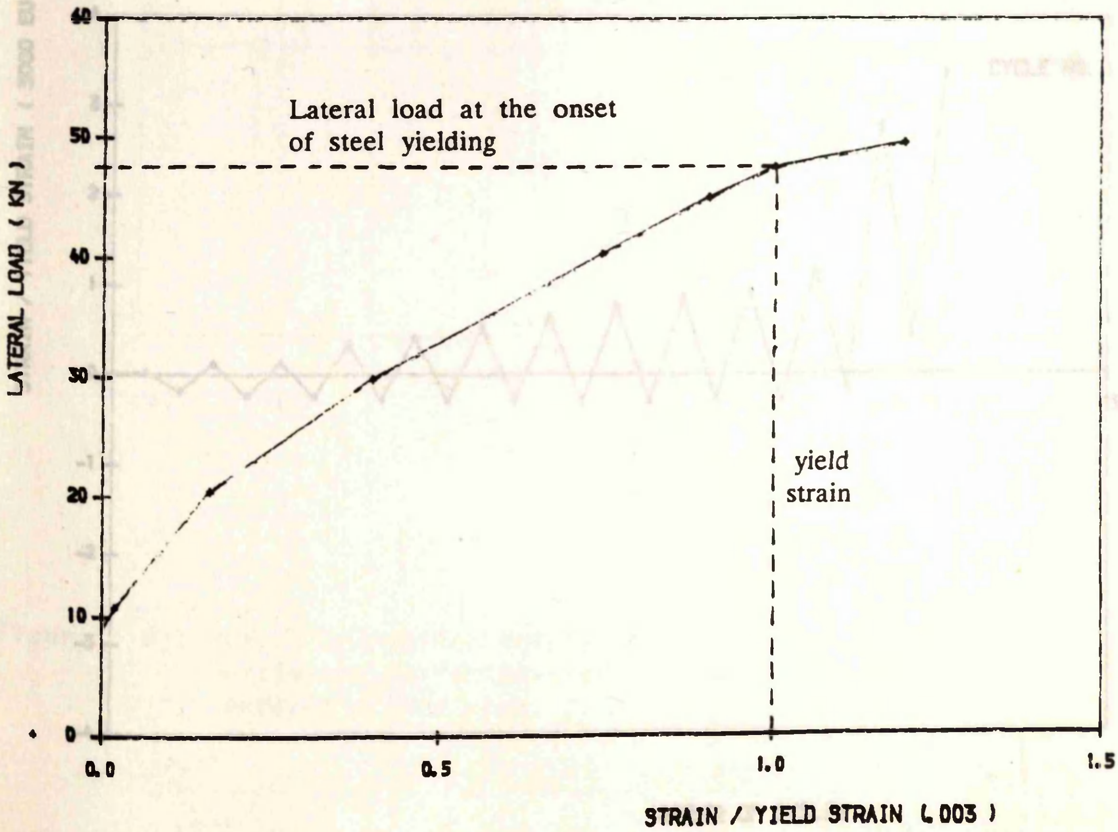

FIG. (7- 4), LATERAL LOAD VERSUS STEEL STRAIN MEASURED AT 11TH CYCLE OF LOADING (MODEL RCS7)

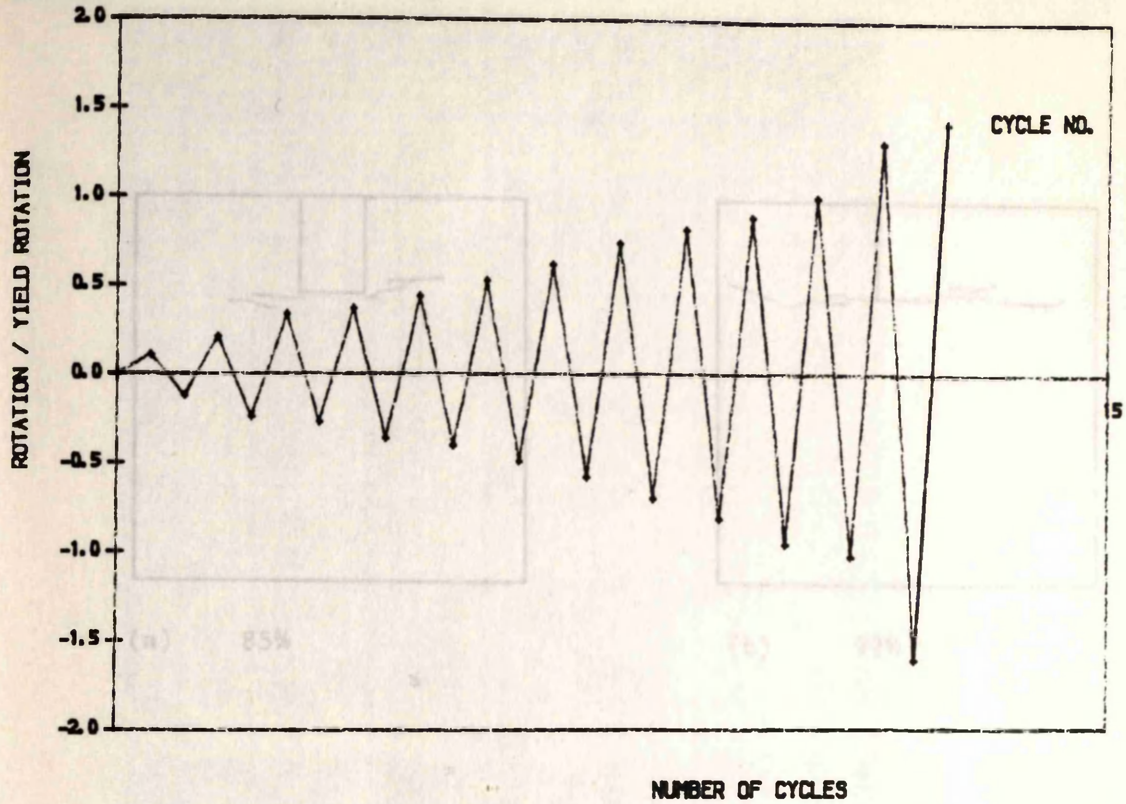

FIG. (7- 6), RELATION BETWEEN LOADING CYCLES AND ROTATION OF SLAB TO COLUMN IN MODEL RCS7.

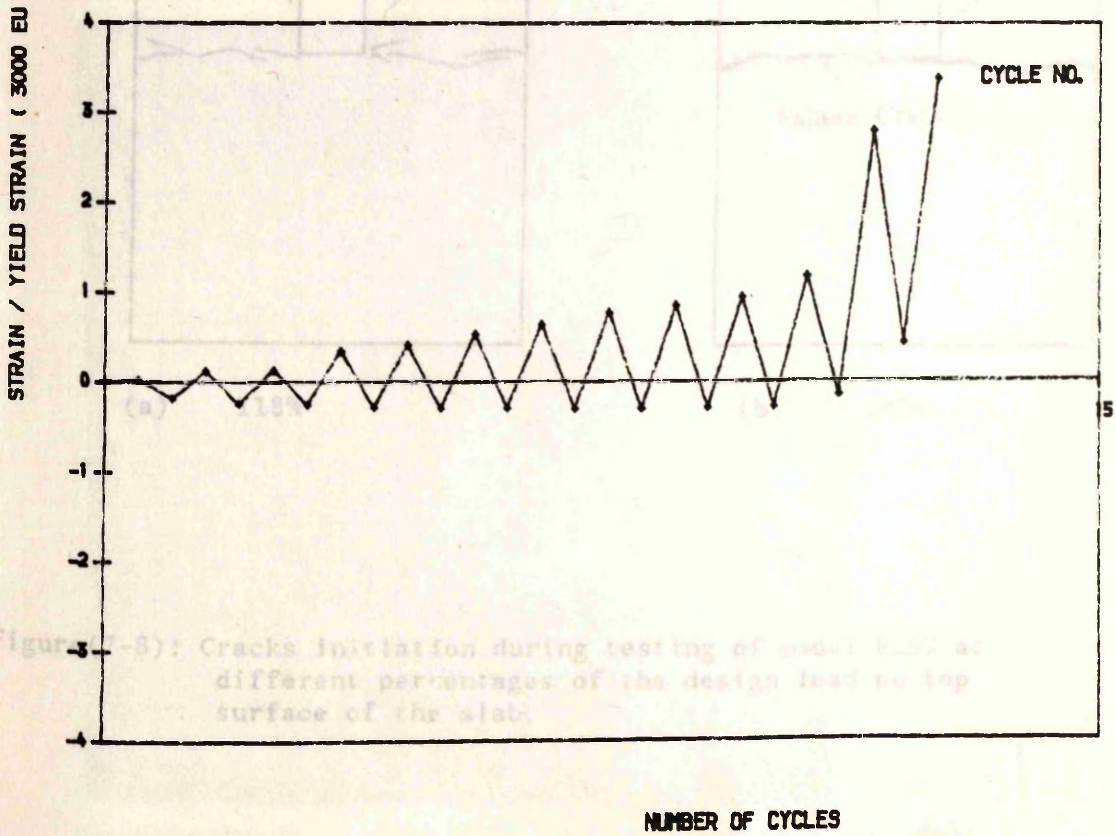

FIG. (7- 7), RELATION BETWEEN STRAIN IN ORDINARY BAR AND LOADING CYCLES IN MODEL RCS7.

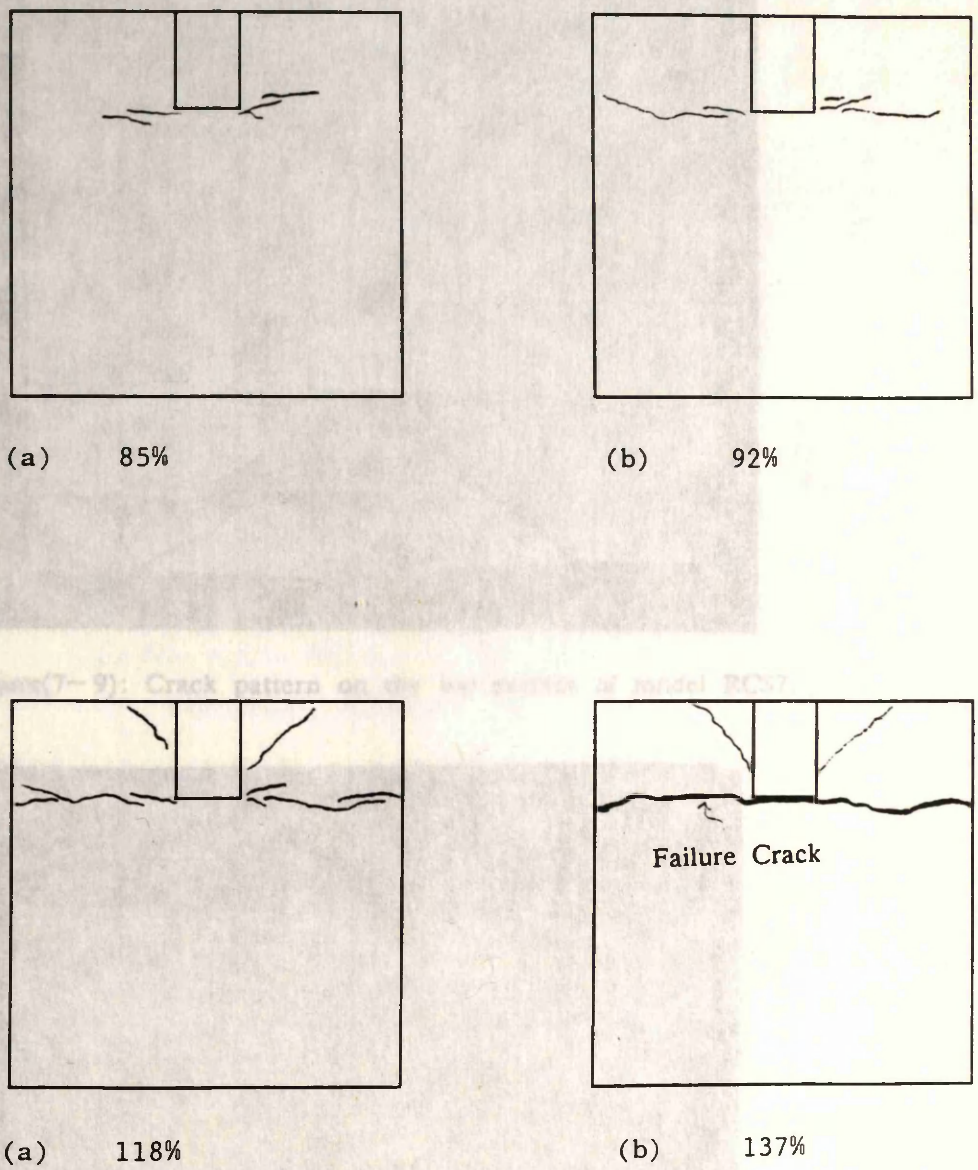

Figure(7-8): Cracks initiation during testing of model RCS7 at different percentages of the design load on top surface of the slab.

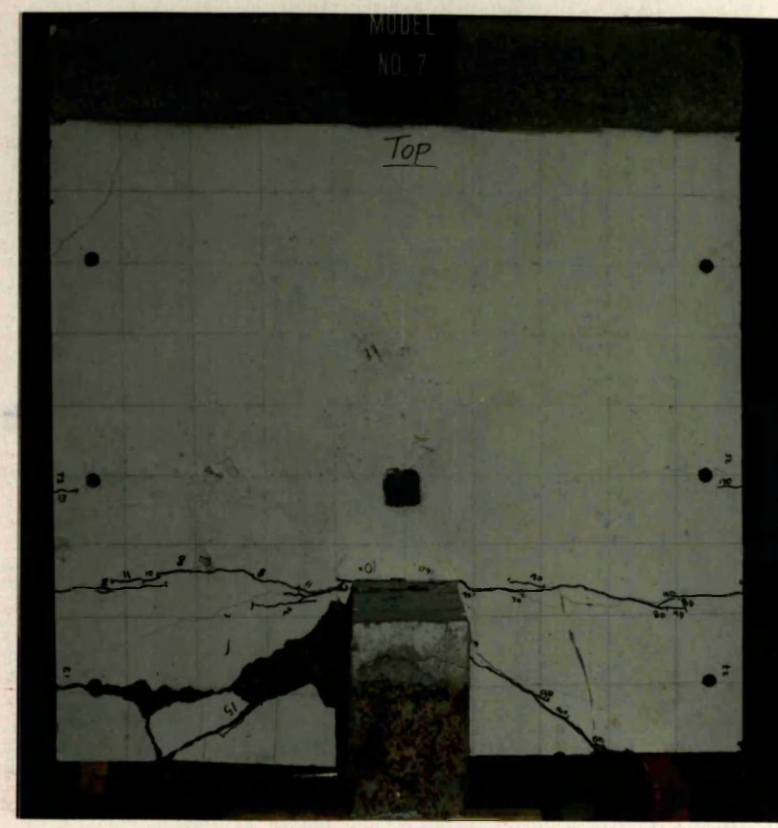

Figure(7– 9): Crack pattern on the top surface of model RCS7.

Figure(7– 10): Crack pattern on the bottom surface of Model RCS7.

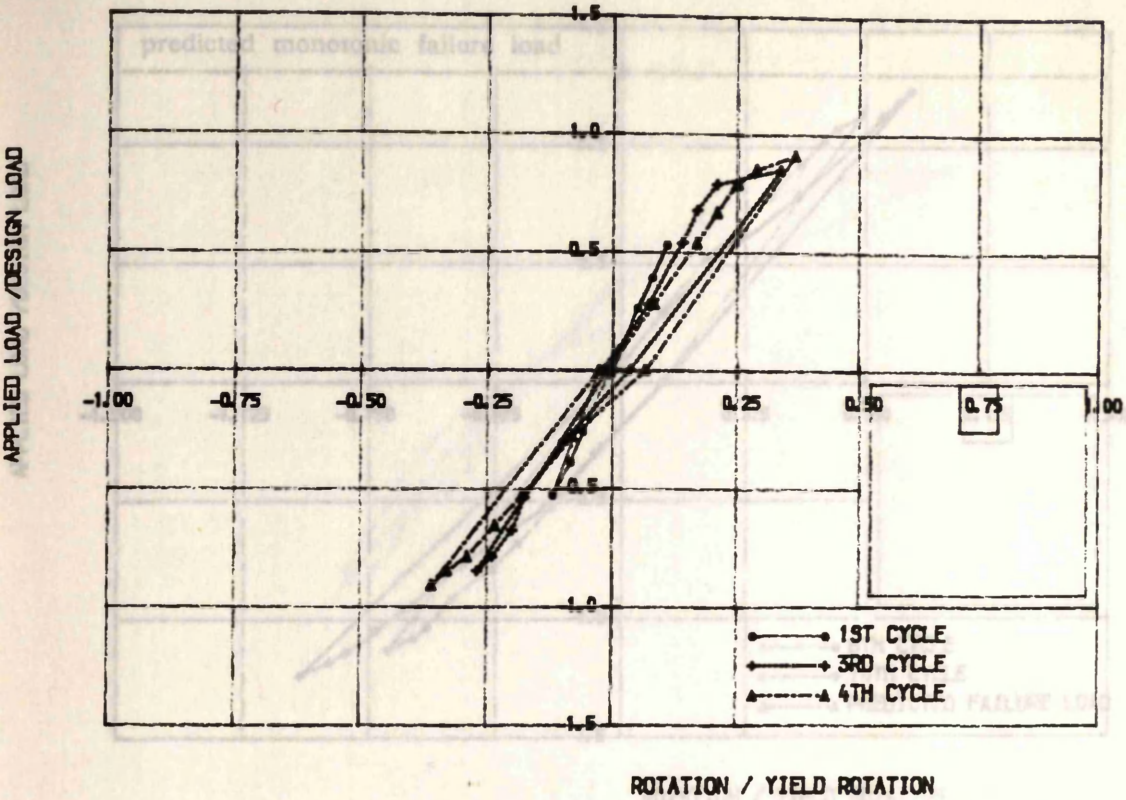

FIG. (7-11,A). RELATIVE ROTATION OF THE SLAB TO COLUMN FOR MODEL RCS7 AT EARLY STAGES OF LOADING CYCLE.

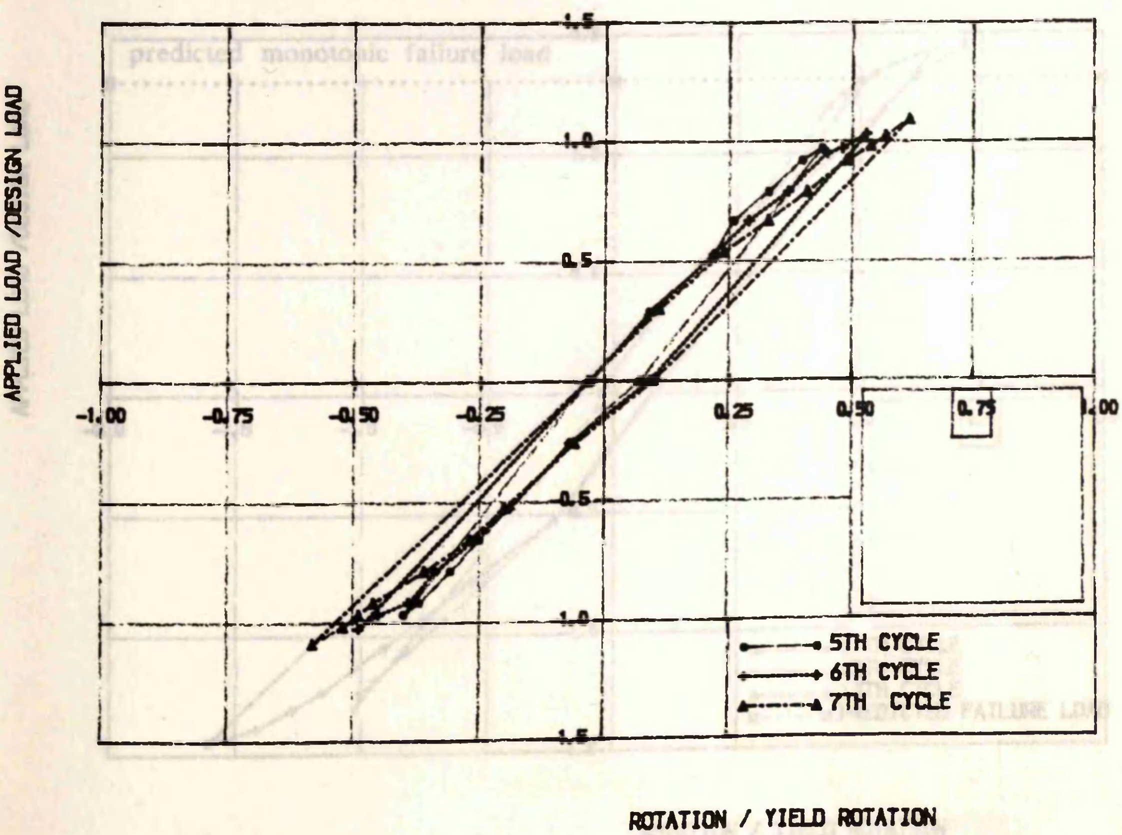

FIG. (7-11,B). RELATIVE ROTATION OF THE SLAB TO COLUMN FOR MODEL RCS7

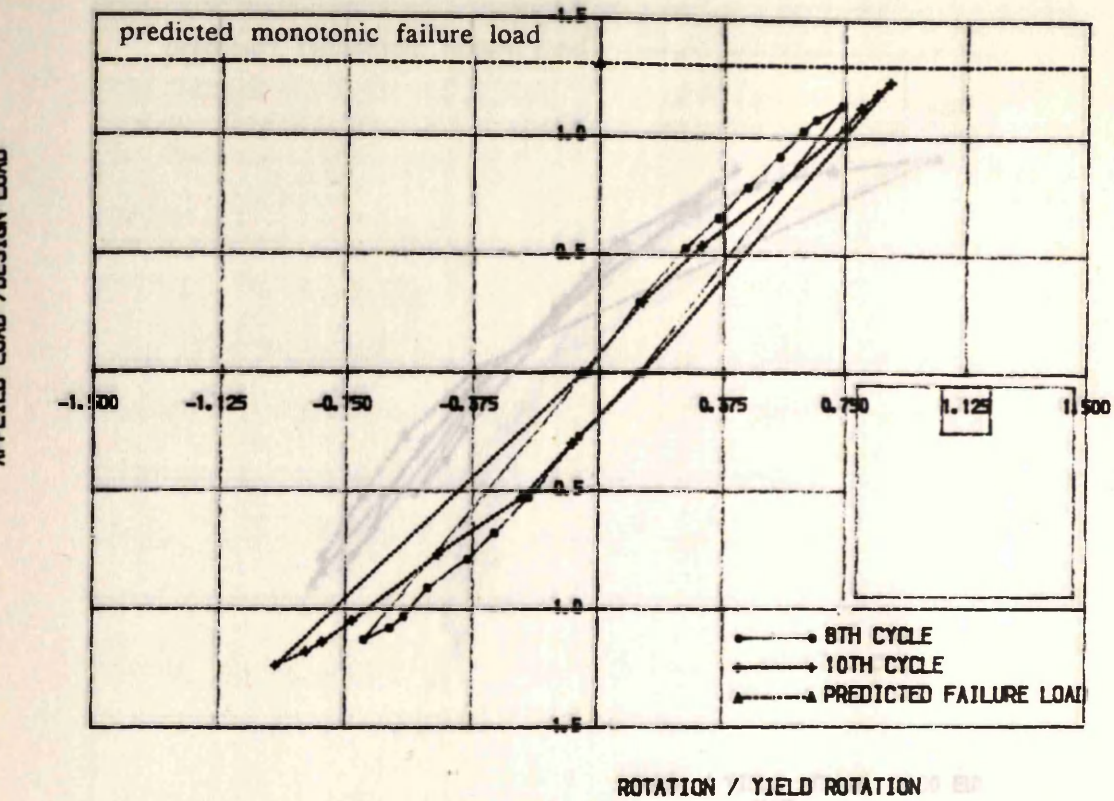

FIG. (7-11,C). RELATIVE ROTATION OF THE SLAB TO COLUMN FOR MODEL RCS7.

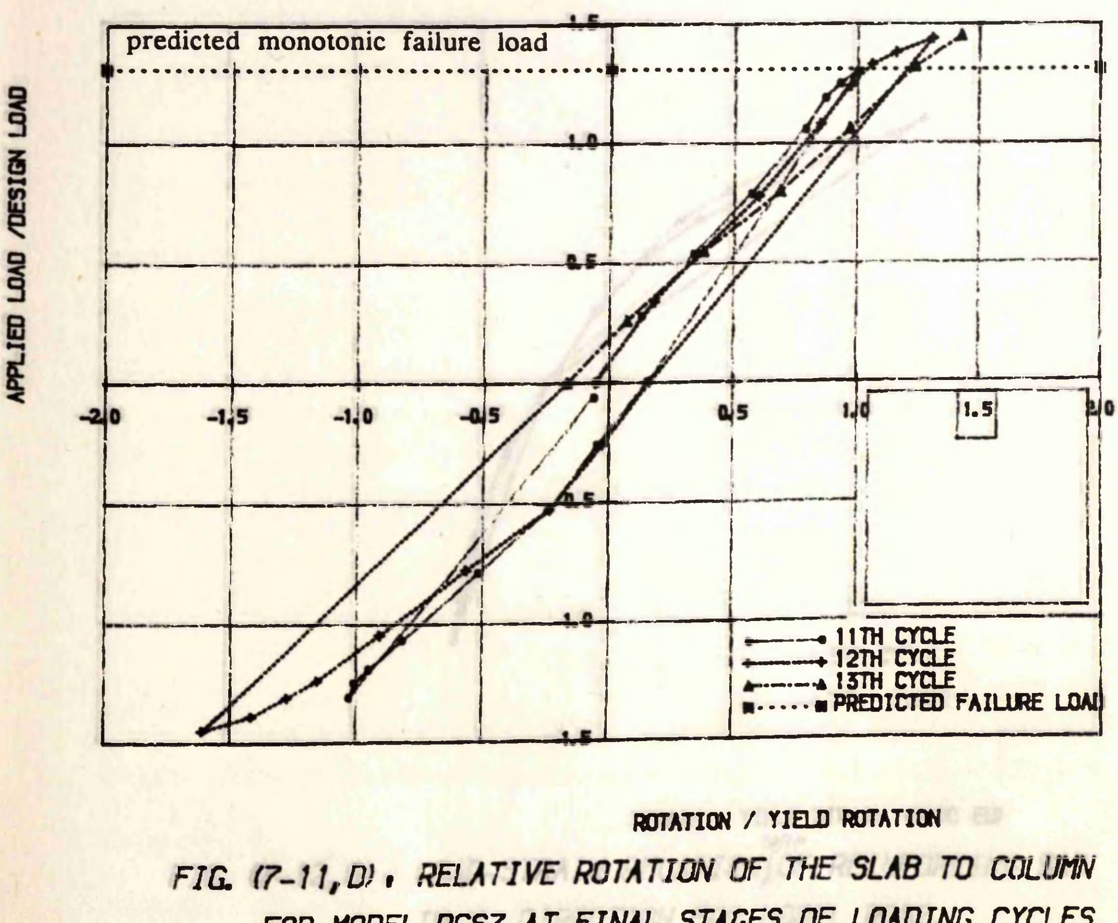

FIG. (7-11,D). RELATIVE ROTATION OF THE SLAB TO COLUMN FOR MODEL RCS7 AT FINAL STAGES OF LOADING CYCLES.

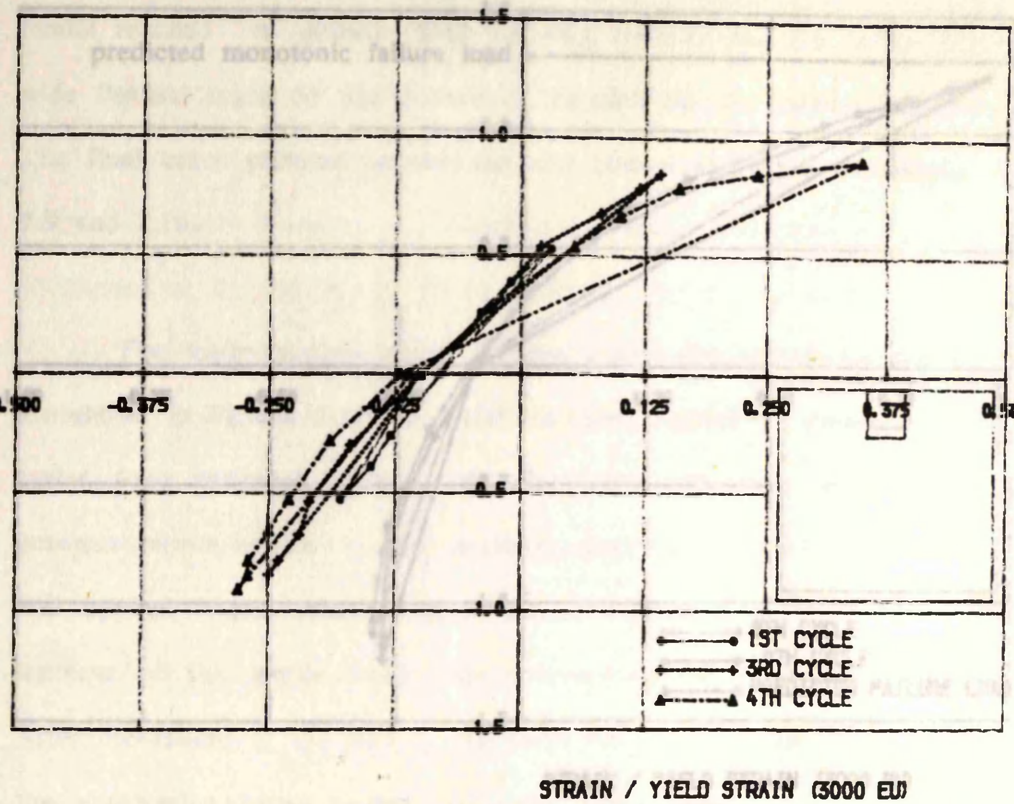

FIG. (7-12,A). LOAD-STRAIN RELATIONSHIP OF REINFORCING BAR IN X- DIRECTION FOR MODEL RCS7.

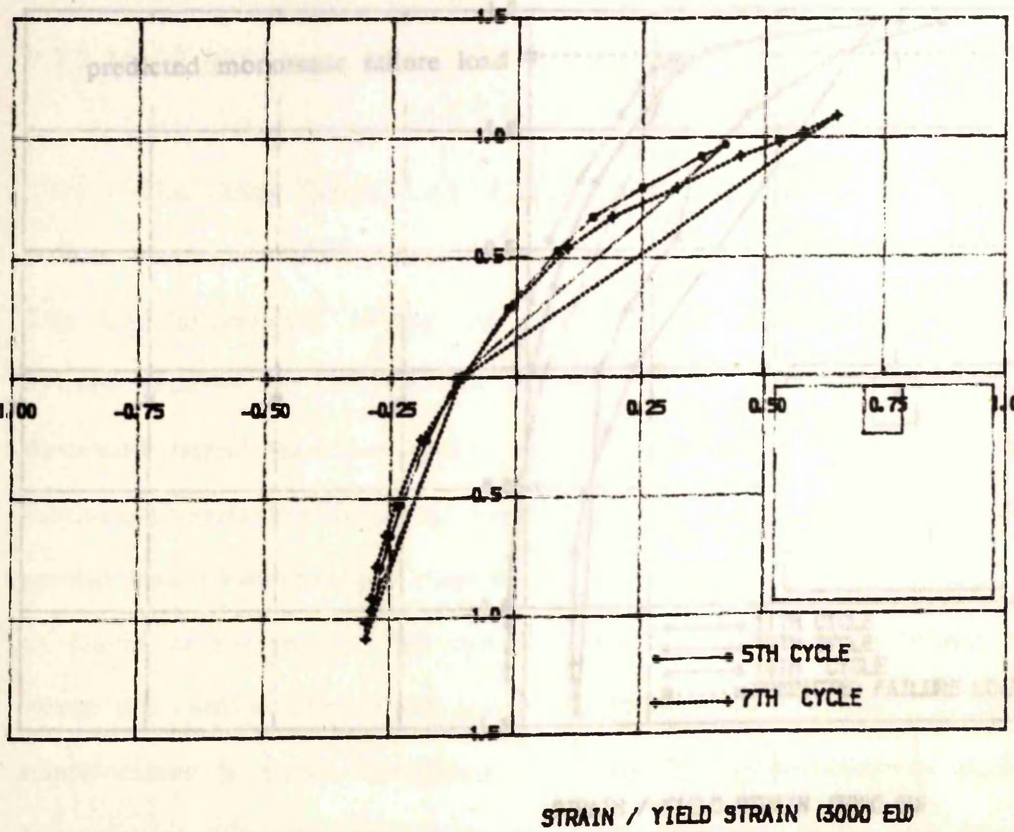

FIG. (7-12,B). LOAD-STRAIN RELATIONSHIP OF REINFORCING BAR IN X- DIRECTION FOR MODEL RCS7.

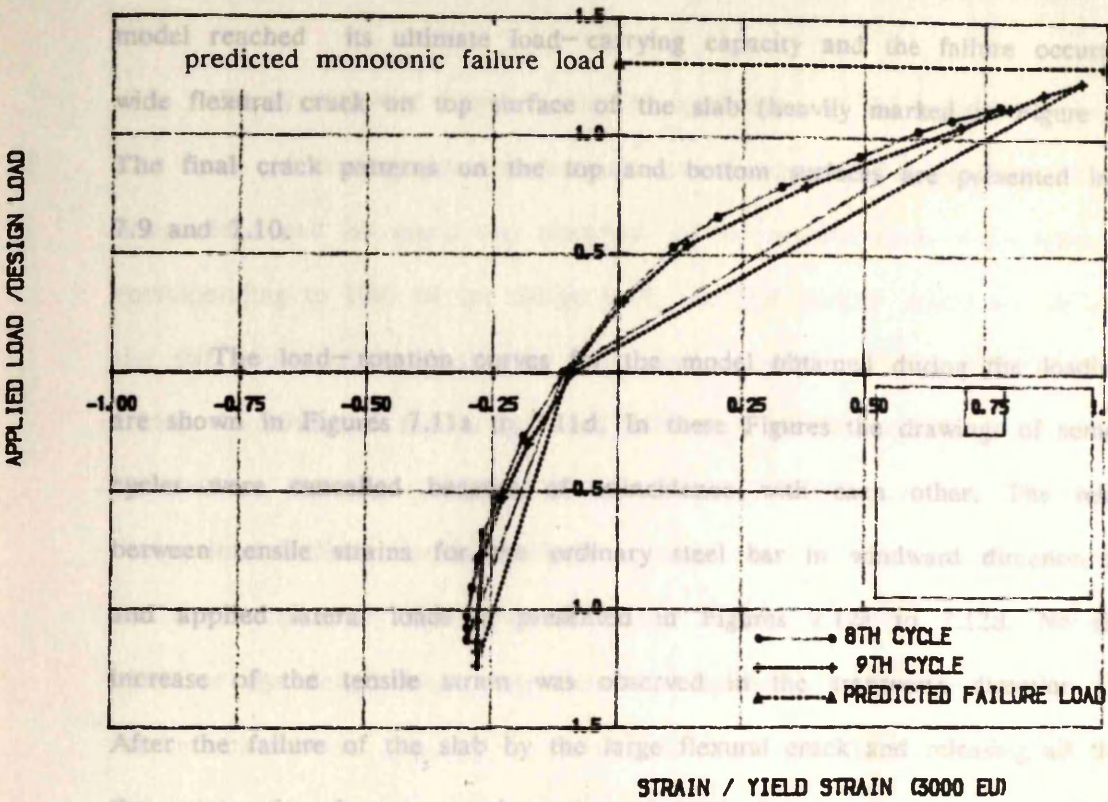

FIG. (7-12,C). LOAD-STRAIN RELATION IN REINFORCING BAR IN X-DIRECTION FOR MODEL RCS7.

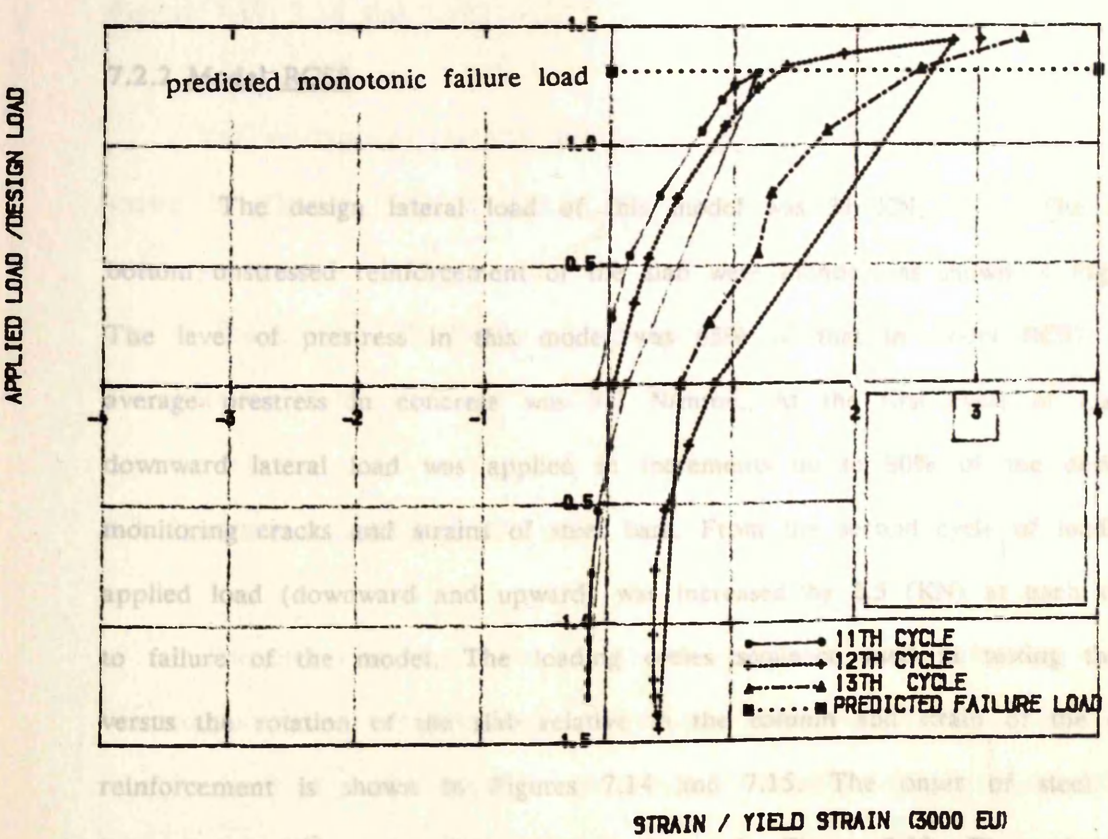

FIG. (7-12,D). LOAD-STRAIN RELATION IN REINFORCING BAR IN X-DIRECTION FOR MODEL RCS7.

the design lateral load (17^{th} cycle) while the load was being applied downward, the model reached its ultimate load–carrying capacity and the failure occurred by a wide flexural crack on top surface of the slab (heavily marked in Figure 7.8d). The final crack patterns on the top and bottom surfaces are presented in Figures 7.9 and 7.10.

The load–rotation curves for the model obtained during the loading cycles are shown in Figures 7.11a to 7.11d. In these Figures the drawings of some of the cycles were cancelled because of coincidence with each other. The relationship between tensile strains for the ordinary steel bar in windward direction (X–dir.) and applied lateral loads is presented in Figures 7.12a to 7.12d. No significant increase of the tensile strain was observed in the transverse direction (Y–dir.). After the failure of the slab by the large flexural crack and releasing all the jacks, the prestressing forces caused crush and local damage at the corners of the slab which is shown in Figure 7.9.

7.2.2 Model RCS8

The design lateral load of this model was 31 KN. The top and bottom unstressed reinforcement of the slab were identical as shown in Figure 7.2. The level of prestress in this model was 65% of that in model RCS7 and the average prestress in concrete was 3.2 N/mm^2. At the first cycle of loading, a downward lateral load was applied in increments up to 80% of the design load monitoring cracks and strains of steel bars. From the second cycle of loading, the applied load (downward and upward) was increased by 2.5 (KN) at each cycle up to failure of the model. The loading cycles sequence used in testing the model versus the rotation of the slab relative to the column and strain of the ordinary reinforcement is shown in Figures 7.14 and 7.15. The onset of steel yielding happened at 7^{th} cycle of loading as shown in Figure 7.20. The relative yield rotation of the model (θ_y) is obtained from Figure 7.21.

Behaviour of the Model

No cracks were found during the application of the prestressing forces. The first cycle of loading (downward and upward) comprised a load of 80% of the design load and no crack was observed. At the second cycle in downward loading corresponding to 89% of the design load, the first hairline cracks on top surface of the slab were initiated from the front corners of the column as shown in Figure 7.16a. At 104% of the design load (4^{th} cycle of loading) the first cracks were observed on the bottom surface similar to that on the top surface. At 144% of the design load inclined torsional cracks appeared on the top and bottom surfaces of the slab respectively as shown in Figure 7.16b. At 12^{th} cycle corresponding to 161% of the design load while the load was being applied downward, the model reached its ultimate capacity of carrying load and the failure occurred by the wide flexural cracks on top surface of the slab (heavily marked in Figure 7.16d). The final crack patterns of the top, back and bottom surfaces of the slab are shown in Figures 7.17, 7.18 and 7.19.

The rotations of the slab relative to column versus applied lateral loads are shown in Figures 7.22a to 7.22d. The relation between tensile strain of the ordinary steel bar in X— direction and the applied lateral load is shown in Figures 7.23a to 7.23d. No significant increases were observed in steel strain in Y— direction of the slab.

7.3 Discussion of Test Results

The object of these tests was to study the strength and overall behaviour of the models under the cyclic loading condition. The main parameter which changed was the level of prestressing. Therefore, the prestressing level in model RCS8 was 65% of that in model RCS7. This 35% reduction of prestressing level caused a 9% reduction in ultimate failure load of model RCS8. Secondly, the maximum

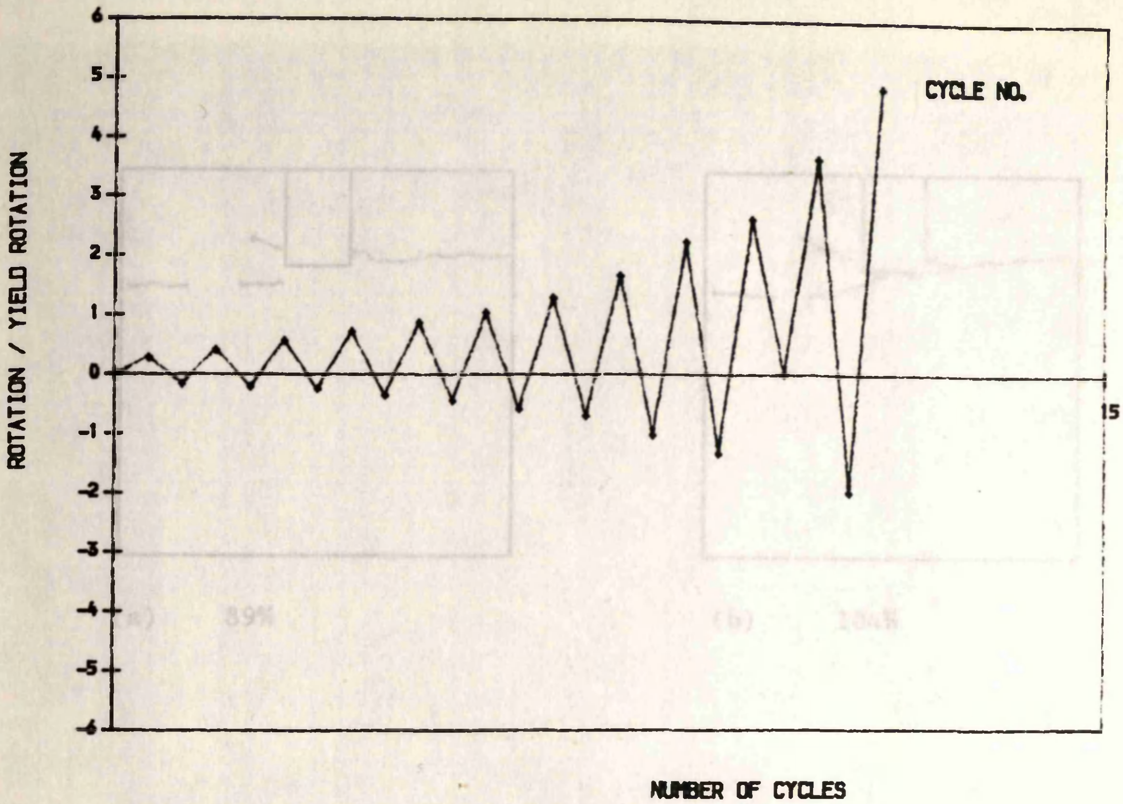

FIG. (7-14), RELATION BETWEEN LOADING CYCLES AND ROTATION OF SLAB TO COLUMN IN MODEL RCS8.

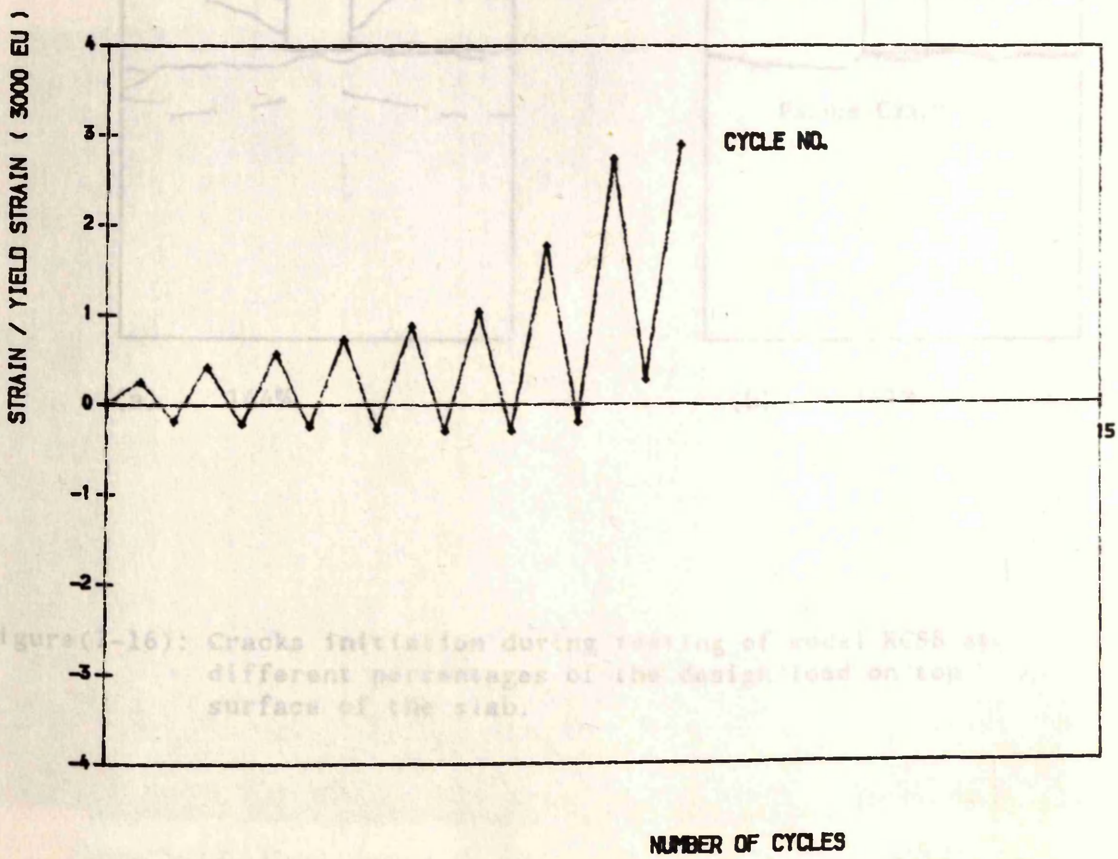

FIG. (7-15), RELATION BETWEEN STRAIN IN ORDINARY BAR AND LOADING CYCLES IN MODEL RCS8.

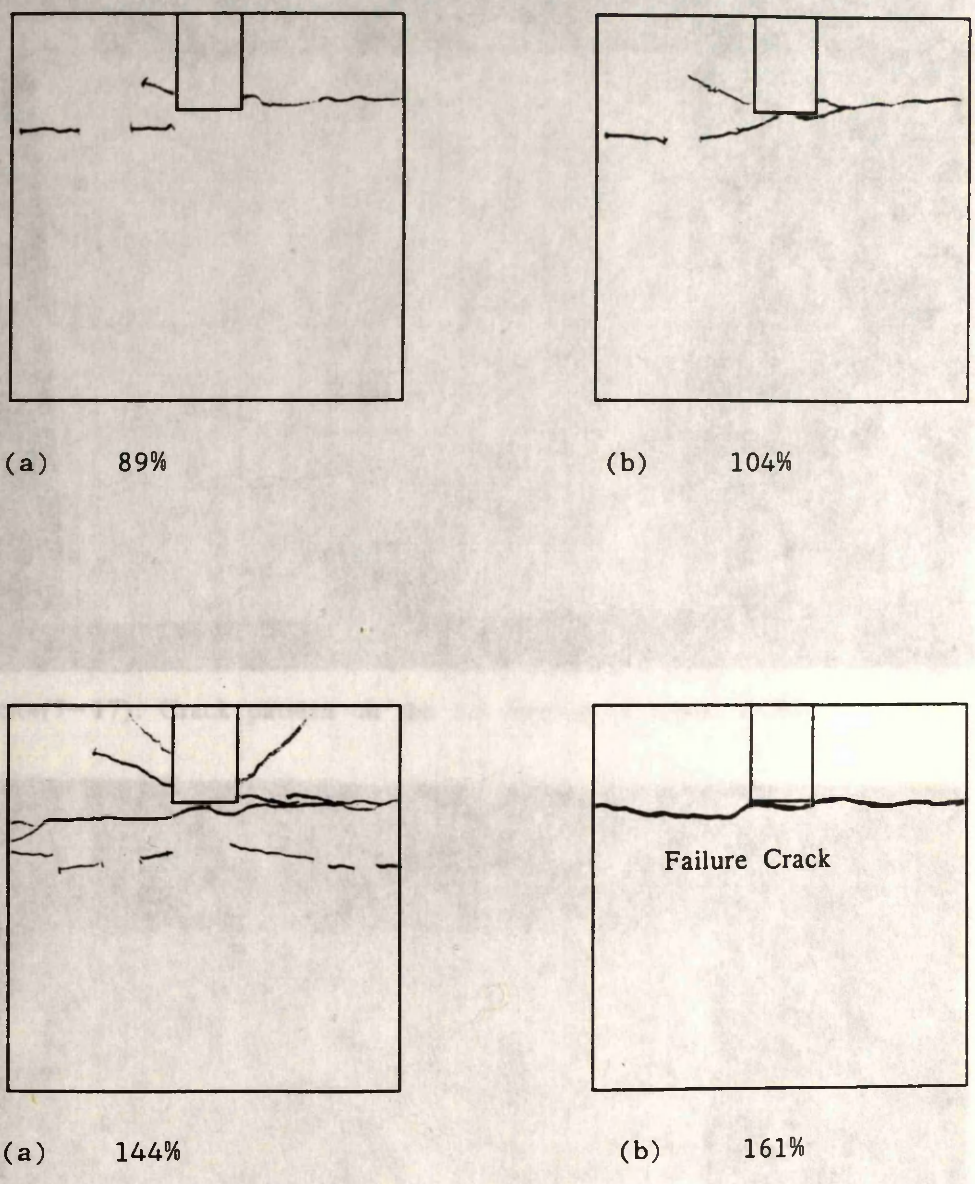

Figure(7-16): Cracks initiation during testing of model RCS8 at different percentages of the design load on top surface of the slab.

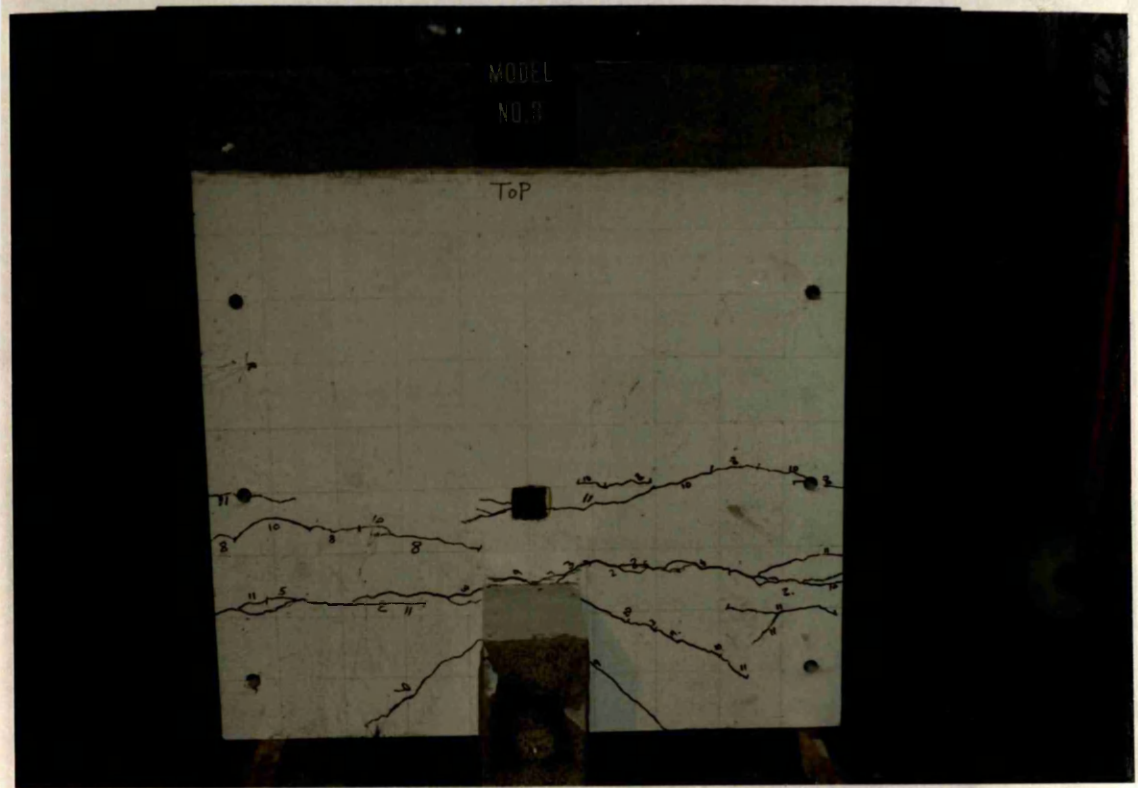

Figure(7– 17): Crack pattern on the top surface of model RCS8.

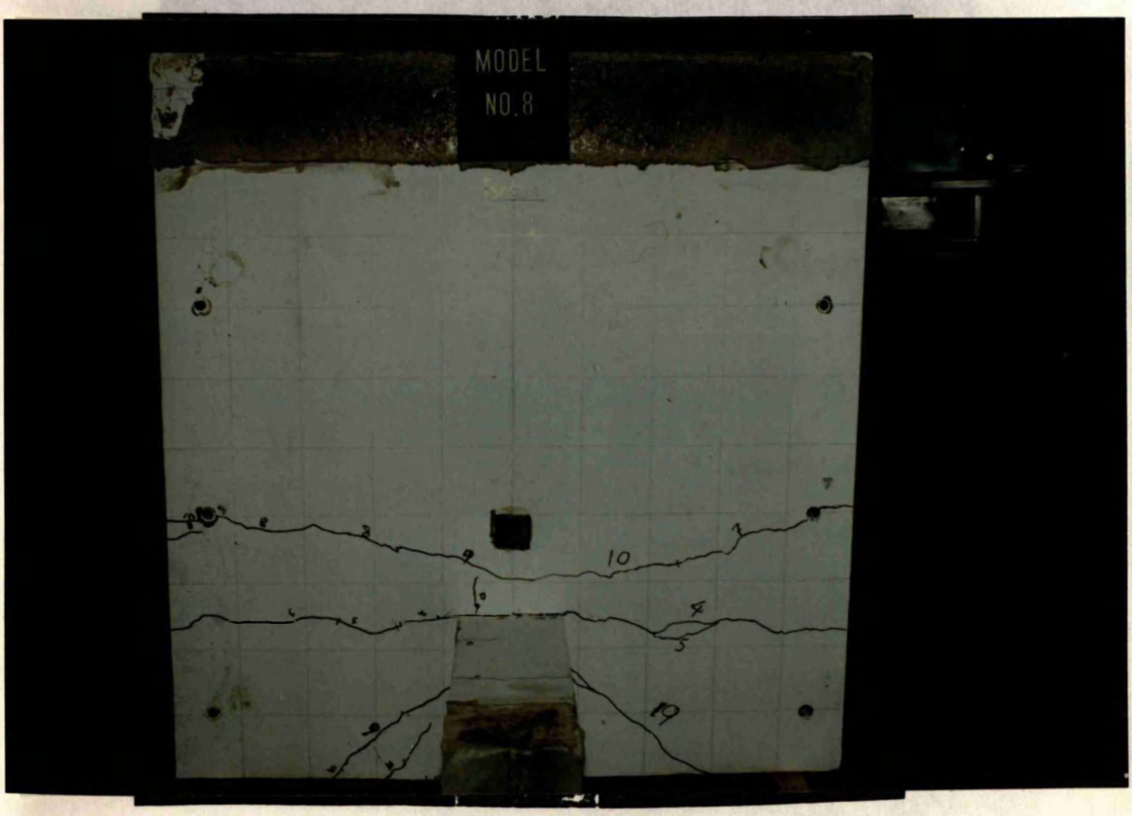

Figure(7– 18): Crack pattern on the bottom surface of Model RCS8.

Figure(7–19): Crack pattern on the rear side of model RCS8.

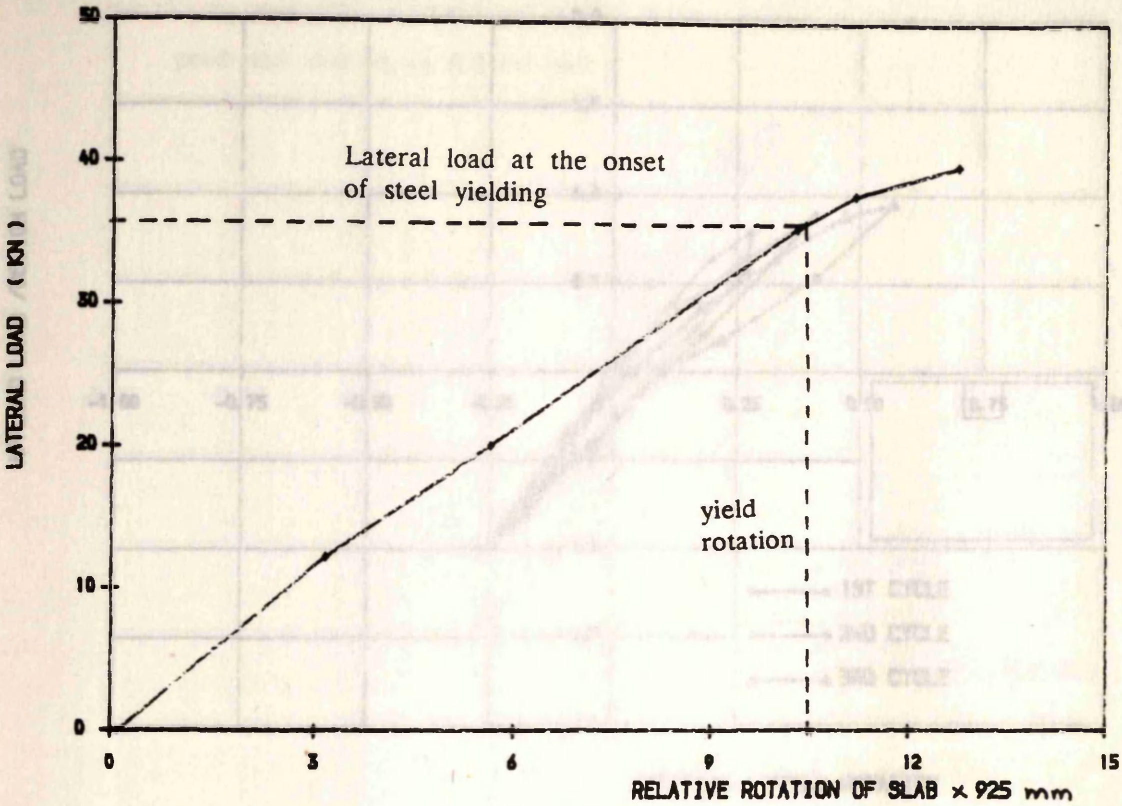

FIG. (7-21), LATERAL LOAD VERSUS RELATIVE ROTATION OF SLAB AT 7TH CYCLE OF LOADING (MODEL RCS8)

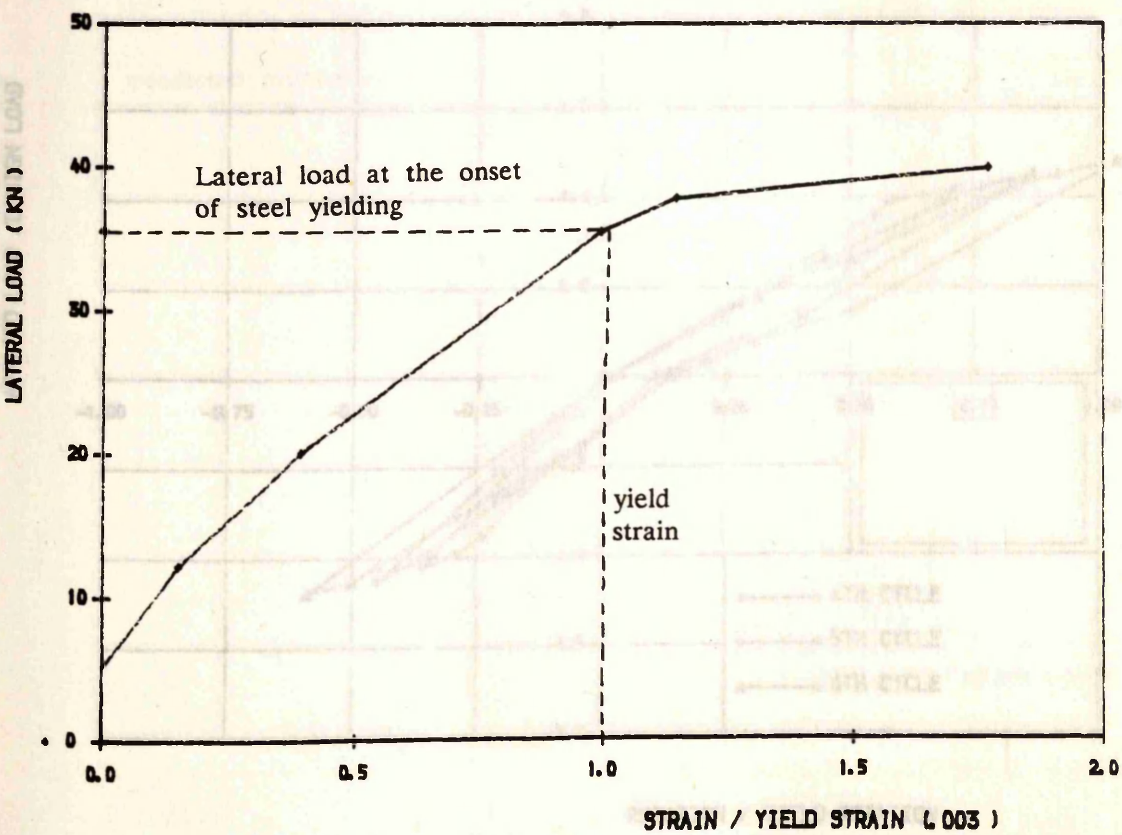

FIG. (7-20), LATERAL LOAD VERSUS STEEL STRAIN MEASURED AT 7TH CYCLE OF LOADING (MODEL RCS8)

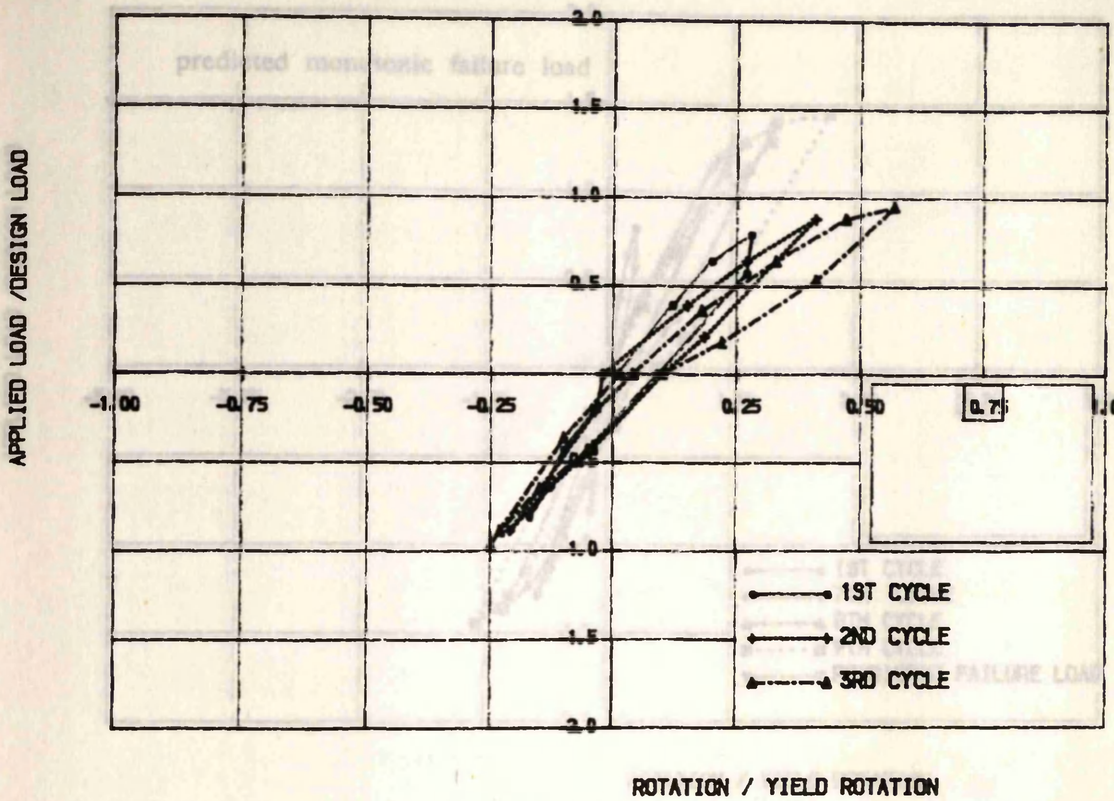

FIG. (8-22,A), RELATIVE ROTATION OF THE SLAB TO THE COLUMN FOR MODEL RCS8 AT INITIAL STAGE OF LOADING CYCLE.

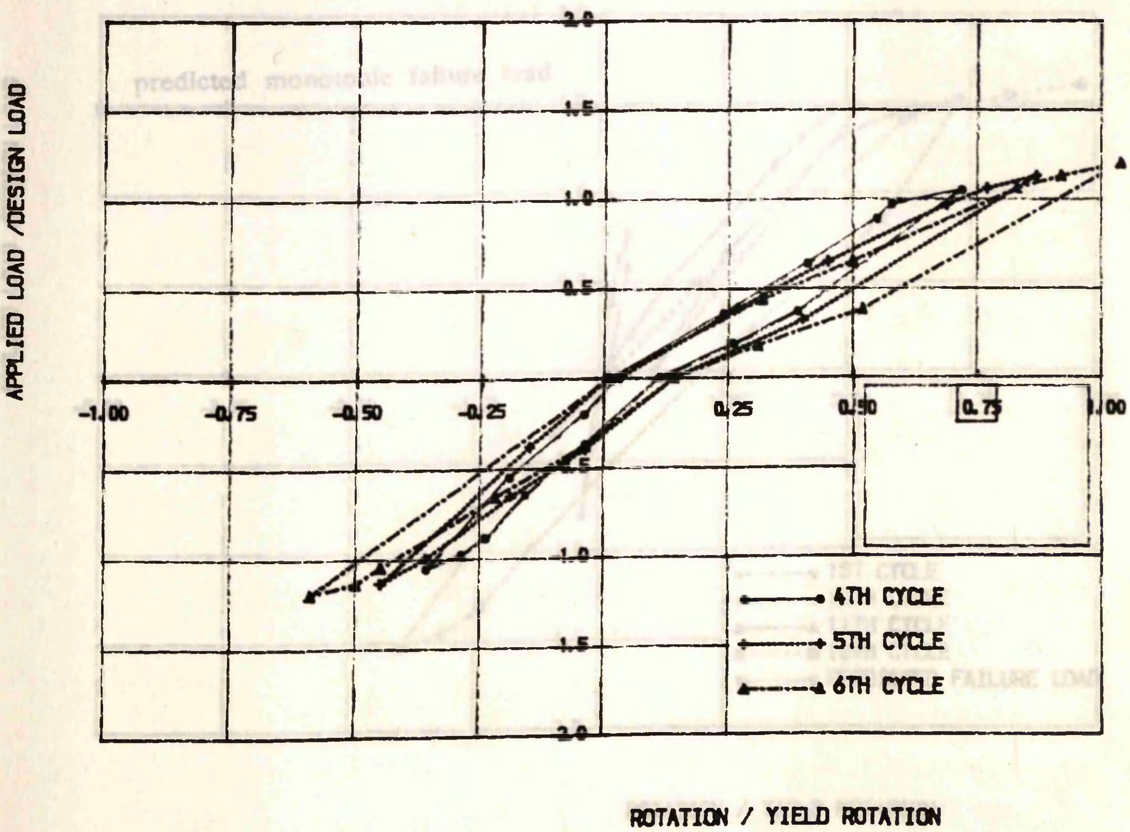

FIG. (8- 22,B), RELATIVE ROTATION OF THE SLAB TO COLUMN FOR MODEL RCS8.

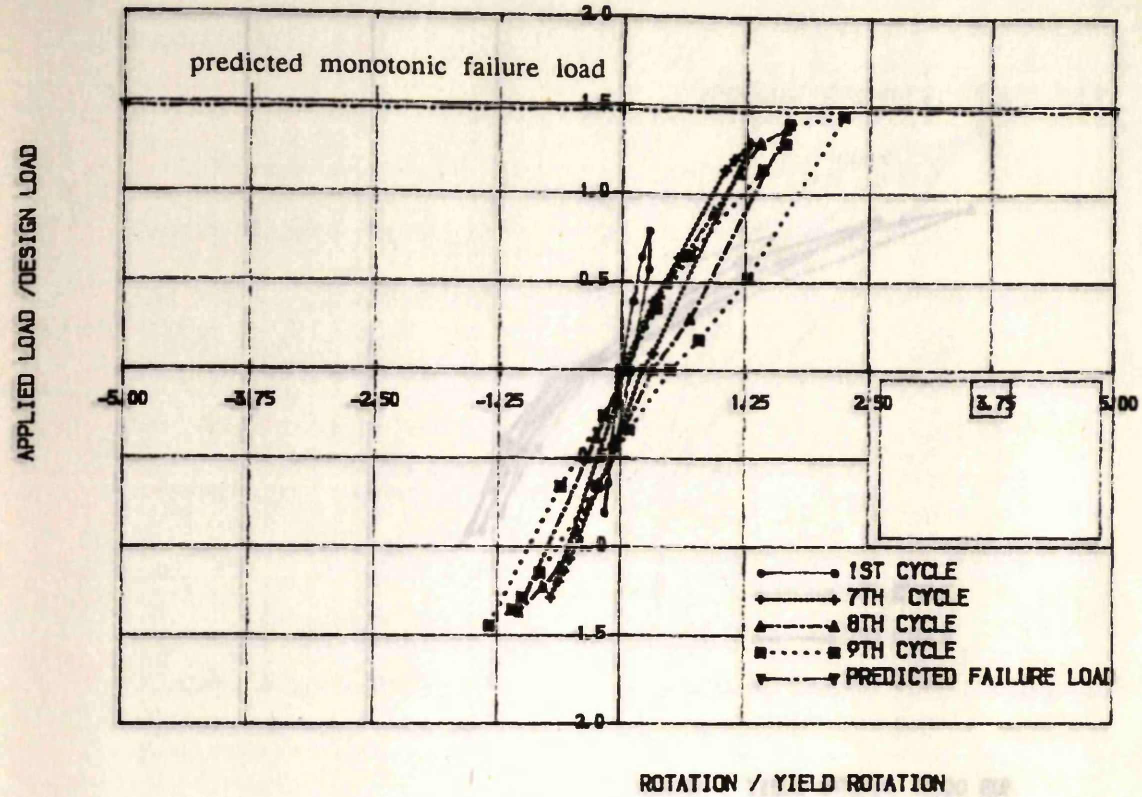

FIG. (8-22,C). RELATIVE ROTATION OF THE SLAB TO THE COLUMN FOR MODEL RCS8.

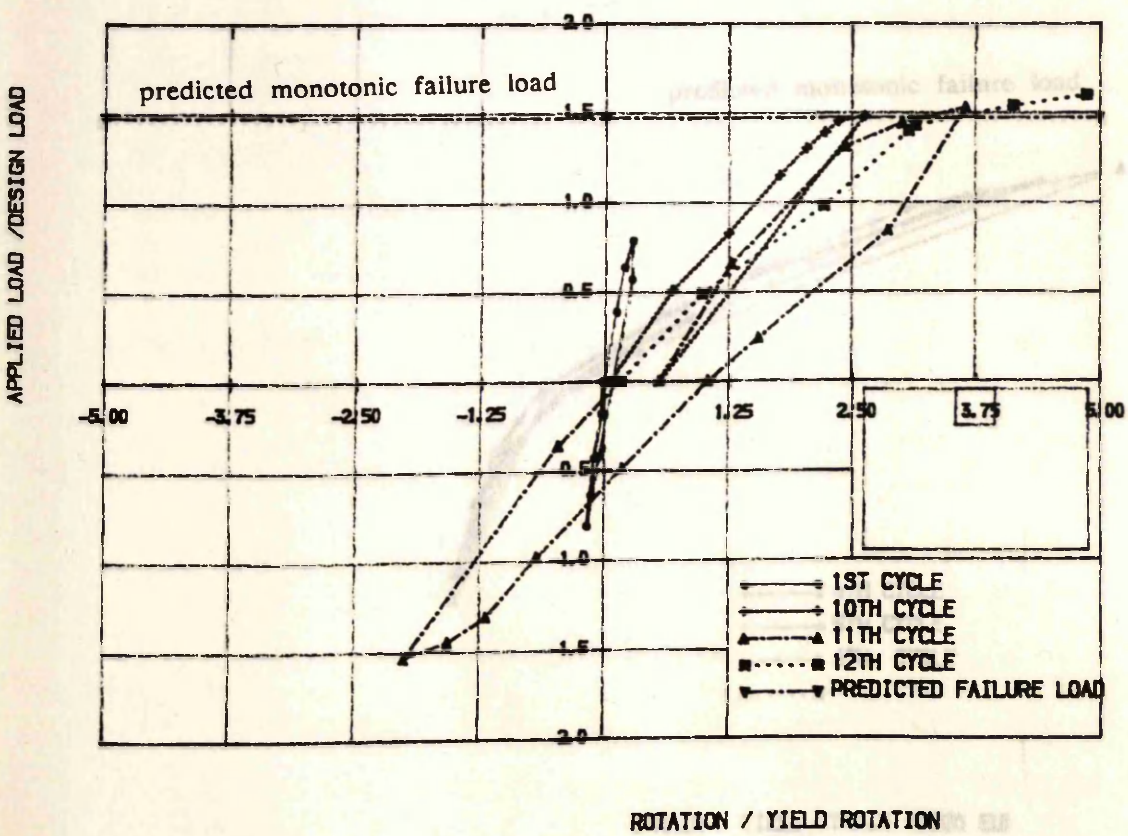

FIG. (8-22,D). RELATIVE ROTATION OF THE SLAB TO COLUMN FOR MODEL RCS8 AT FINAL STAGES OF LOADING CYCLE.

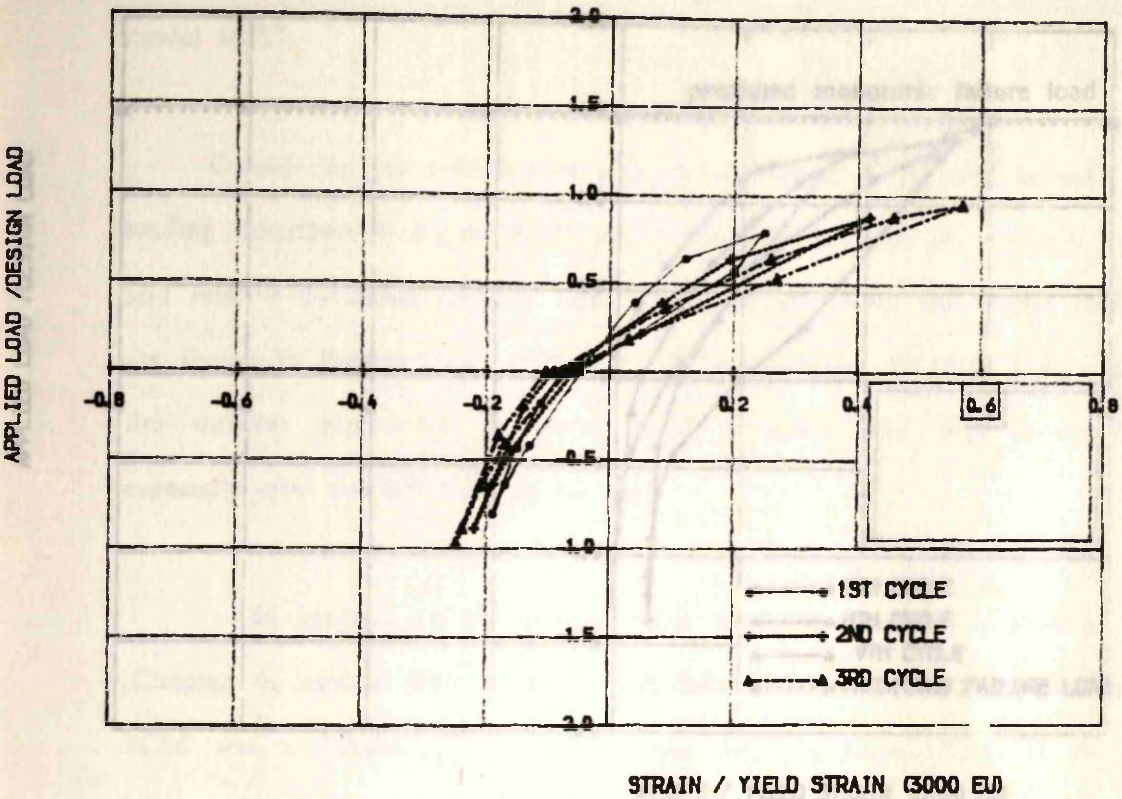

FIG. (8-23,A). LOAD-STRAIN RELATIONSHIP OF REINFORCING BAR IN X- DIRECTION FOR MODEL RCS8.

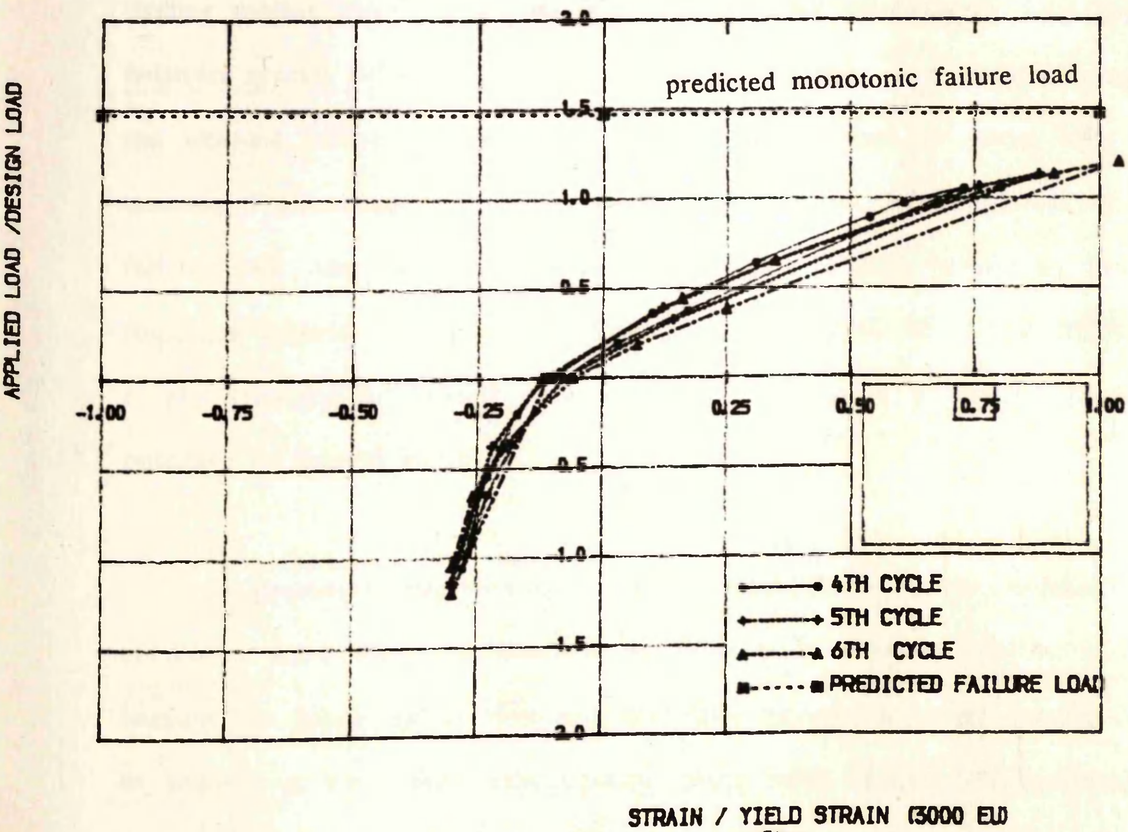

FIG. (8-23,B). LOAD-STRAIN RELATIONSHIP OF REINFORCING BAR IN X- DIRECTION FOR MODEL RCS8.

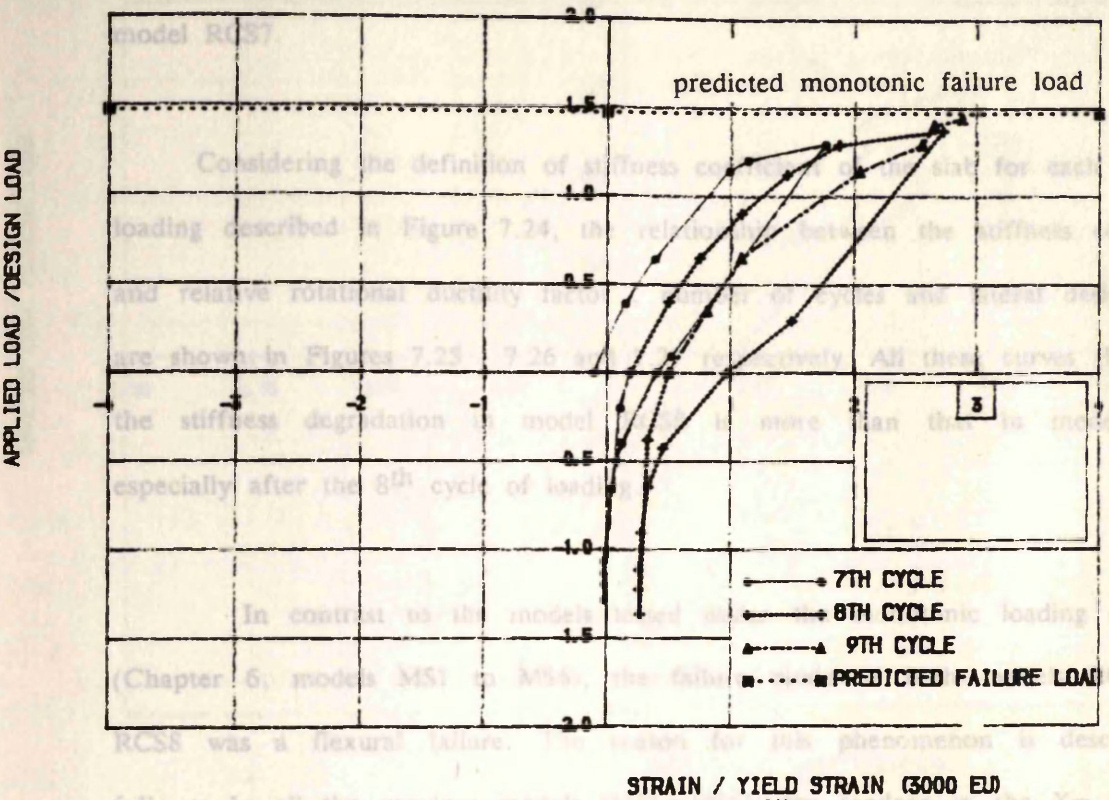

FIG. (8-23,C). LOAD-STRAIN RELATIONSHIP OF REINFORCING BAR IN X-DIRECTION FOR MODEL RCS8.

rotational ductility factor (θ/θ_y) of model RCS8 increased up to 3 times of that of model RCS7.

Considering the definition of stiffness coefficient of the slab for each cycle of loading described in Figure 7.24, the relationship between the stiffness coefficient and relative rotational ductility factor , number of cycles and lateral design loads are shown in Figures 7.25 , 7.26 and 7.27 respectively. All these curves show that the stiffness degradation in model RCS8 is more than that in model RCS7 especially after the 8^{th} cycle of loading.

In contrast to the models tested under the monotonic loading condition (Chapter 6, models MS1 to MS6), the failure mode of both models RCS7 and RCS8 was a flexural failure. The reason for this phenomenon is described as follows: In all the previous models (MS1 – MS6), the tendons in the X– direction had an eccentricity of 27mm at the front face of the column while in the cyclic loading models there was not any eccentricity in the X– direction. In a comparison between models MS3 and RCS7, which both have the same level of prestressing, the ultimate failure load of model RCS7 is 72% of that of model MS3, that is, omitting 27mm eccentricity in model RCS7 resulted in 28% reduction of ultimate failure load. Also, this omission of eccentricity is directly related to the flexural resistance capacity of the model. As a result, in models RCS7 and RCS8 because of the reduction of flexural resisting capacity, the mode of failure changed from punching to flexural mode.

In prestressed flat slabs at an edge column junction , for monotonic loading conditions using shear reinforcement would help to improve ductility of the slab because the failure modes were punching. But for reverse cyclic loading conditions in addition to using shear reinforcement using extra flexural reinforcement in the counterside of tendons eccentricity is recommended.

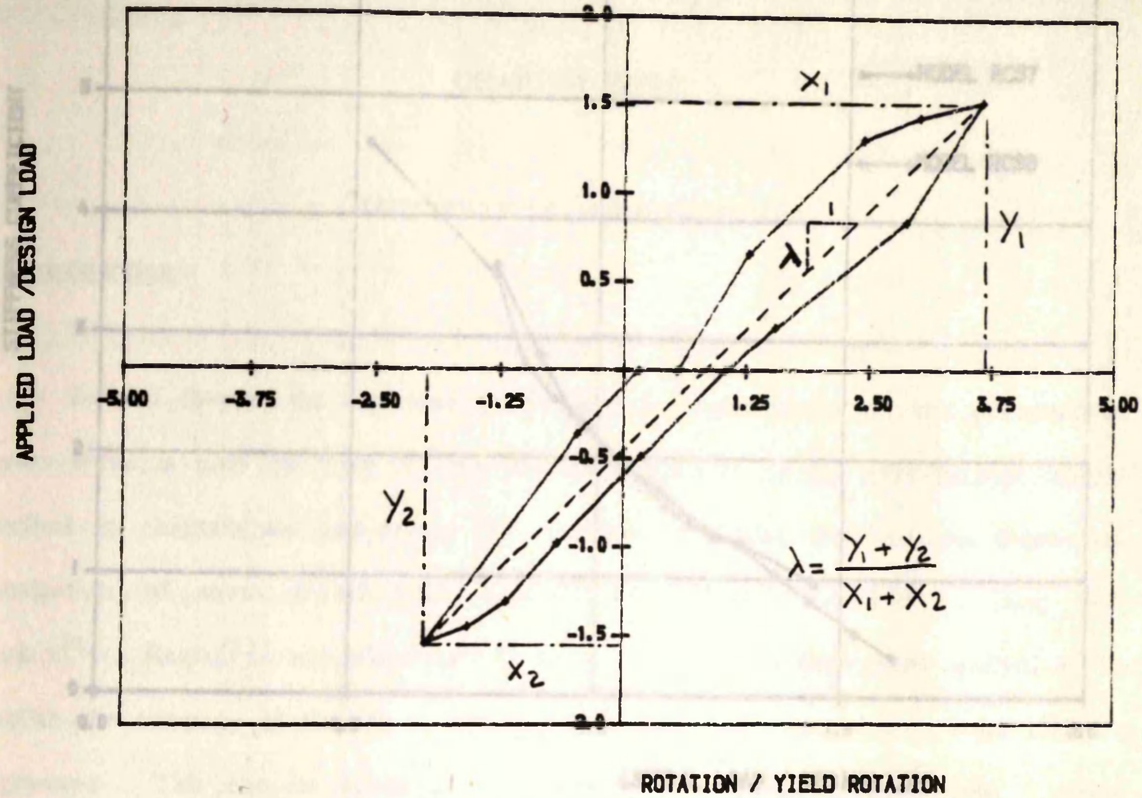

FIGURE (7-24), CALCULATION OF STIFFNESS COEFFICIENT

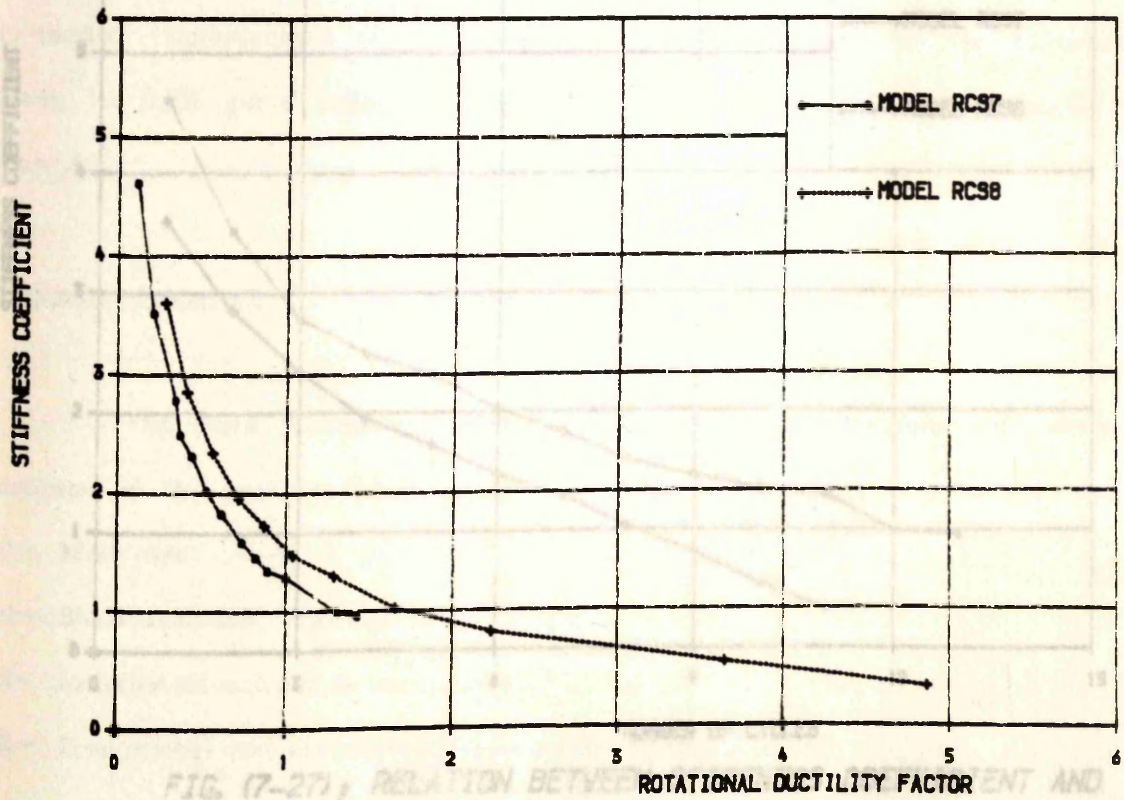

FIG. (7-25), RELATION BETWEEN STIFFNESS COEFFICIENT AND ROTATIONAL DUCTILITY FACTOR (RCS7 AND RCS8).

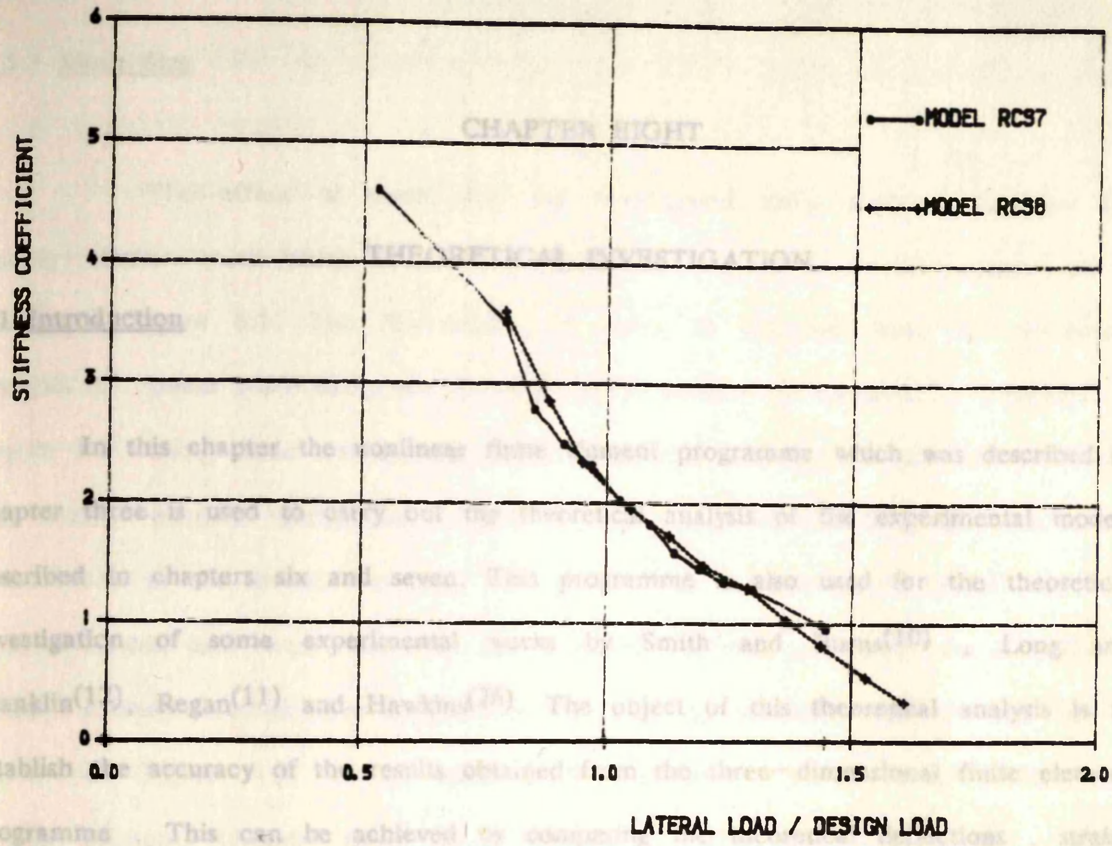

FIG. (7-26), RELATION BETWEEN STIFFNESS COEFFICIENT AND APPLIED LATERAL LOAD (MODELS RCS7 AND RCS8)

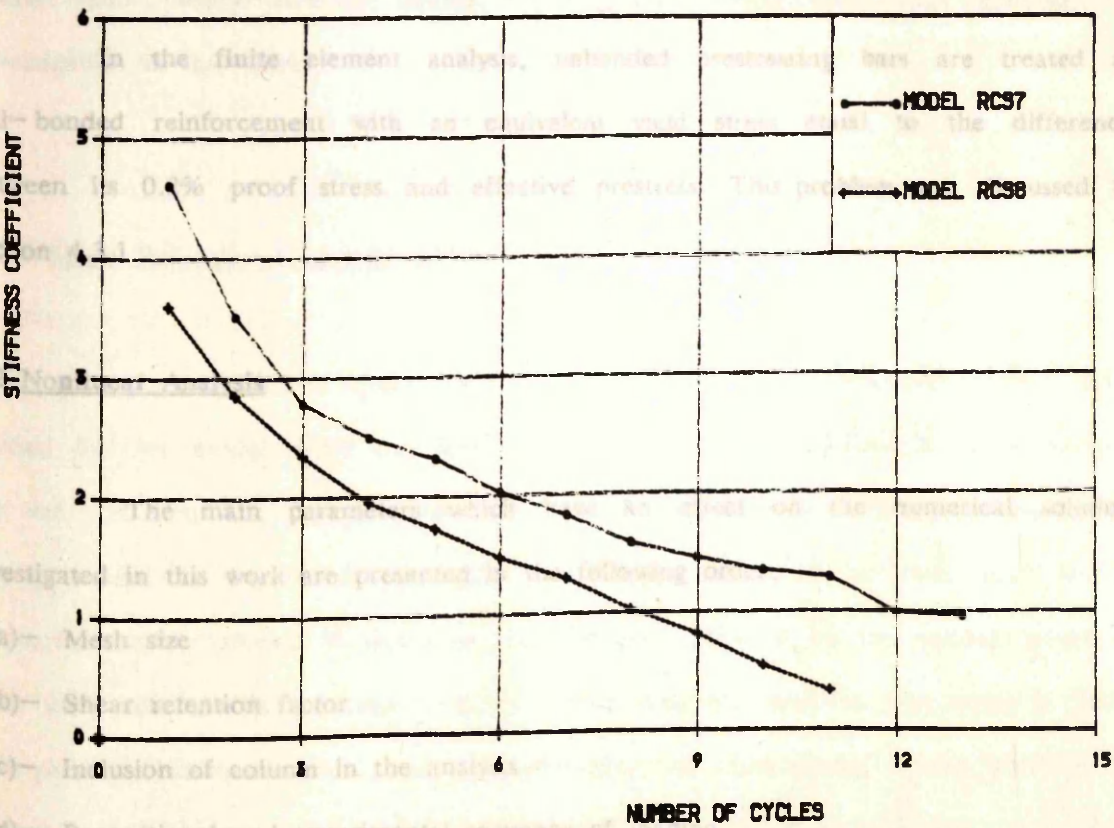

FIG. (7-27), RELATION BETWEEN STIFFNESS COEFFICIENT AND CYCLIC LOADING SEQUENCE FOR MODELS RCS7 AND RCS8.

CHAPTER EIGHT

THEORETICAL INVESTIGATION

8.1 Introduction

In this chapter the nonlinear finite element programme which was described in chapter three is used to carry out the theoretical analysis of the experimental models described in chapters six and seven. This programme is also used for the theoretical investigation of some experimental works by Smith and Burns(10) , Long and Franklin(12), Regan(11) and Hawkins(26). The object of this theoretical analysis is to establish the accuracy of the results obtained from the three-dimensional finite element programme . This can be achieved by comparing the theoretical deflections , strains and failure loads with their counterpart values in the experimental models.

In the finite element analysis, unbonded prestressing bars are treated as full-bonded reinforcement with an equivalent yield stress equal to the difference between its 0.2% proof stress and effective prestress. This problem was discussed in section 4.3.1.

8.2 Nonlinear Analysis

The main parameters which have an effect on the numerical solution investigated in this work are presented in the following order;

a)- Mesh size

b)- Shear retention factor

c)- Inclusion of column in the analysis

d)- Proportional and experimental sequence of loading.

8.2.1 Mesh Size

The effect of mesh size was investigated using twelve , sixteen and twenty– element mesh which have 366 , 468 and 564 degrees of freedom respectively as shown in Figure 8.1. The displacement at point P1 obtained from the theoretical analysis of model MS5 using the three different meshes of elements is presented in Figure 8.2. Using these meshes, the predicted ultimate failure loads for twelve, sixteen and twenty– element meshes were respectively 86% , 102% and 89% of experimental failure load of the model. Nonlinear analysis was also carried out on model MS3 with twelve, sixteen and twenty elements and it was found that the results for sixteen and twenty– element meshes have insignificant difference in behaviour and ultimate load as shown in Figure 8.3. It is apparent from Figure 8.3 that the sixteen and twenty– element meshes have better agreement with the experimental results. Considering the importance of computational cost and insignificant difference between sixteen and twenty– element meshes, the sixteen– element mesh was adopted for investigation in this work.

8.2.2 Shear Retention Factor *(Beta)*

For investigation of shear retention factor effect, several nonlinear analysis were carried out for models MS3 and MS5 using different values of Beta(β). In each case the value of Beta was kept constant in all the increments of load. Some of the results are presented in Figures 8.4 to 8.8. From these figures it is clear that neither displacements nor strains of steel and concrete were affected by the various values of Beta until near the failure load. But the failure load increased in proportion to Beta. The predicted ultimate failure load as a percentage of experimental failure load due to variation of Beta for model MS5 was 89% and 113% for $\beta = 0.05$ and $\beta > 0.45$ as shown in Table 8.1a.

For model MS3 the prediction varies between 82% and 107% as shown in Table 8.1b. From this investigation, the results of the analysis with $\beta = 0.25$ and $\beta = 0.35$ have good agreement with the experimental results. Therefore, $\beta = 0.3$ was used in the analysis of all the models presented in this chapter.

8.2.3 Proportional and Experimental Sequence of Loading

In nonlinear analysis, the following methods were used for loading sequence of the models:

a)– Proportional loading.

b)– Experimental sequence of loading.

In proportional loading, gravity and lateral load were incremented such that they reached their ultimate values simultaneously. But in the experimental sequence , gravity load was applied during the first two increments in which no lateral load was applied. Then holding the ultimate gravity load constant , the lateral load was applied in increments up to failure of the model.

In this study both proportional and experimental sequence of loading were duplicated in the theoretical analysis for all the models. Some of the results are shown in Figures 8.9 to 8.12 and Table 8.2 for comparison between the two methods. It is clear from these figures that there is no significant difference between the two results except in the ultimate failure loads. Table 8.2 shows a comparison of ultimate load for all the models. The ultimate lateral load in experimental sequence of loading is 10% less than in the proportional sequence of loading. Since most of the numerical work had been carried out using proportional loading and as the difference between proportional and experimental sequence was small, the results are presented for proportional loading only.

8.2.4 Analysis of Junctions including the column stub

Two methods were used to simulate the column support of the slab. In the first method the column stub was eliminated and the foot print of the column was considered as a single element. In this element, deflection of the nodes at the front edge of the bottom face (a, b, c) and back edge of the top face (d, e, f) were restrained as shown in Figure 8.1e. In the second method , the column stub at the top and bottom were included as two additional elements . The bottom face of the column was considered fully restrained while the top face of column was restrained only in the x- direction as shown in Figure 8.1f. Results of the analysis and the comparison between these two methods are shown in Figures 8.13 to 8.15 and in Table 8.3. It is evident from these figures , that there is insignificant difference between the methods in predicting of displacement and strains of steel and concrete. But in the prediction of ultimate failure load , analysis with column elements has better agreement with experimental results. Therefore , this method was used for theoretical study of all the models.

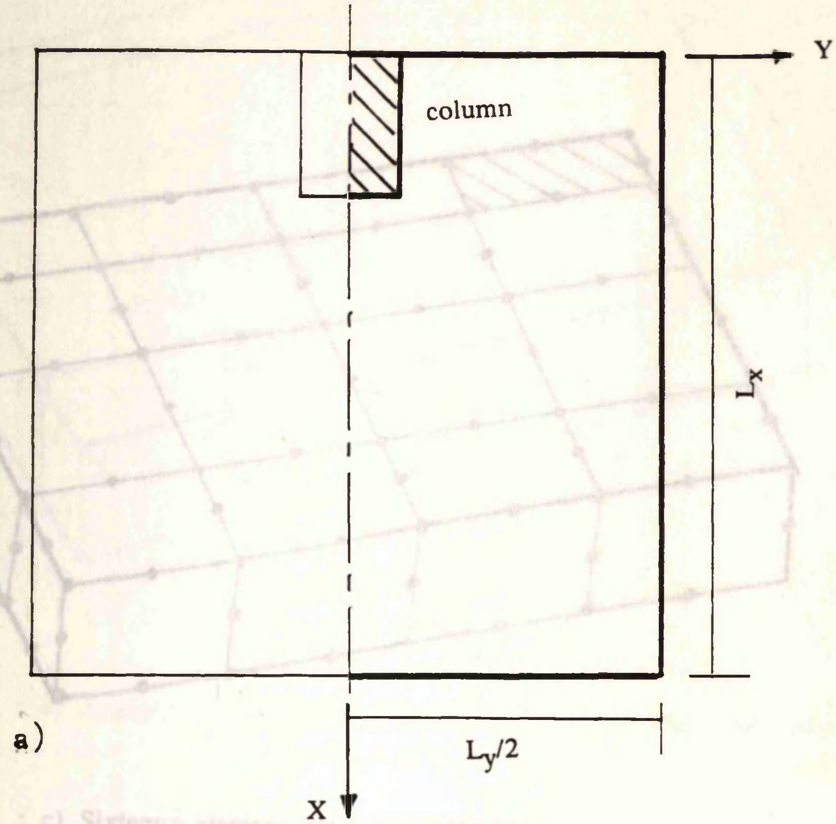

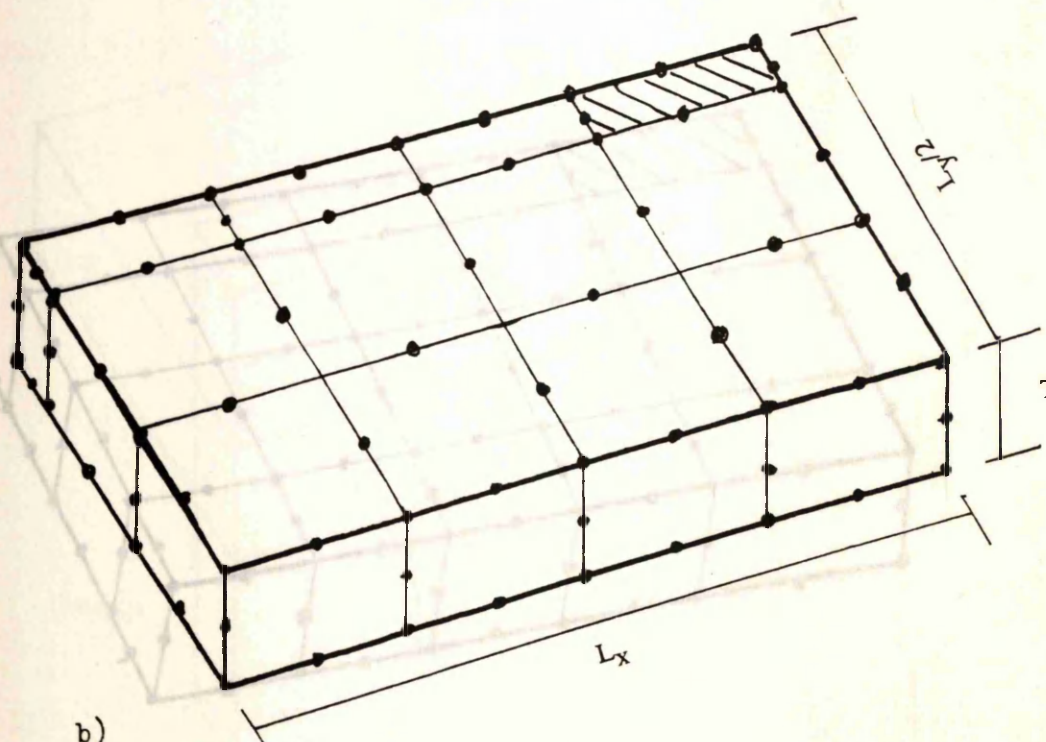

Figure 8.1: a) Symmetrical half of model used for analysis

b) Twelve – element mesh arrangement

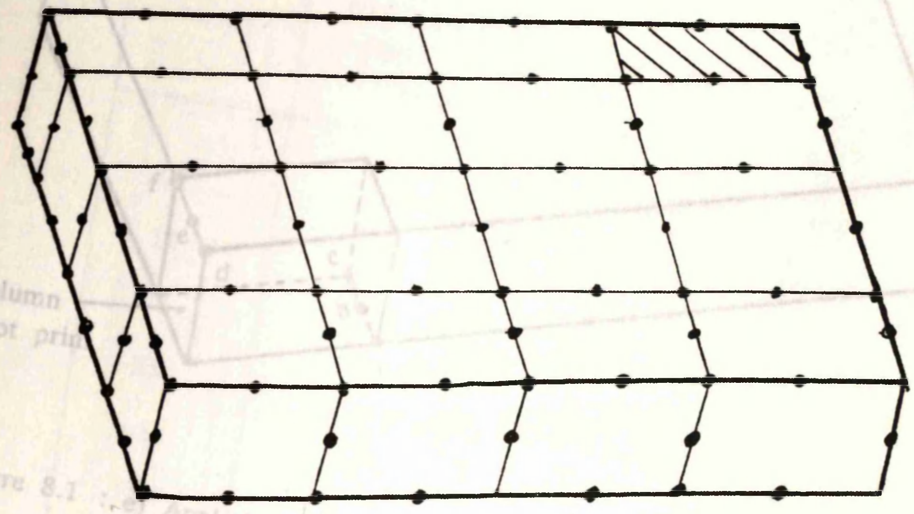

Figure 8.1 : c) Sixteen-element mesh arrangement

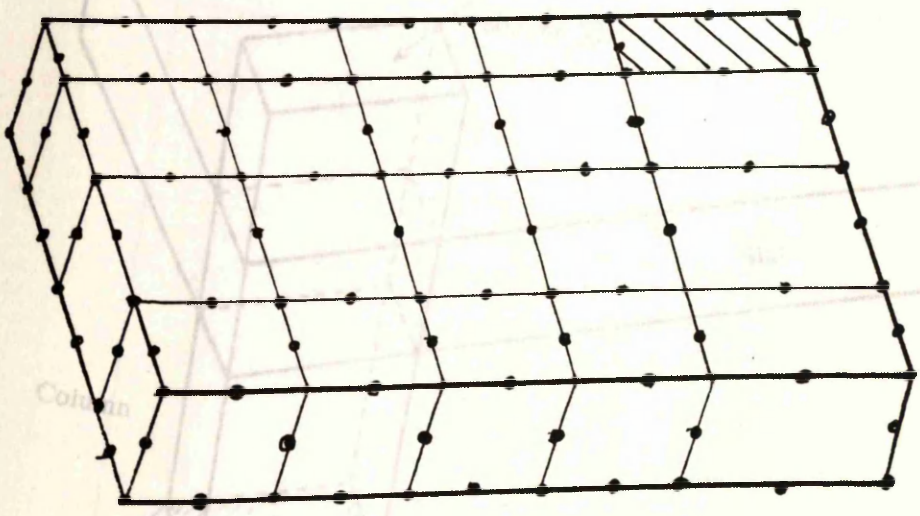

Figure 8.1 : d) Twenty-element mesh arrangement

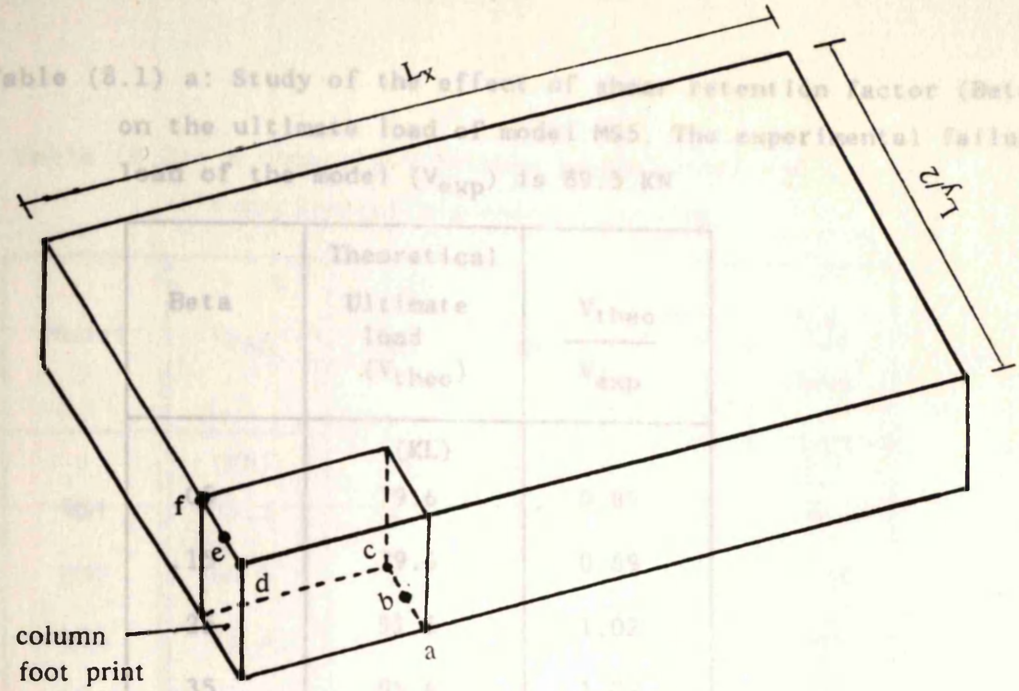

Figure 8.1 : e) Analytical model without column stub(symmetrical half shown)

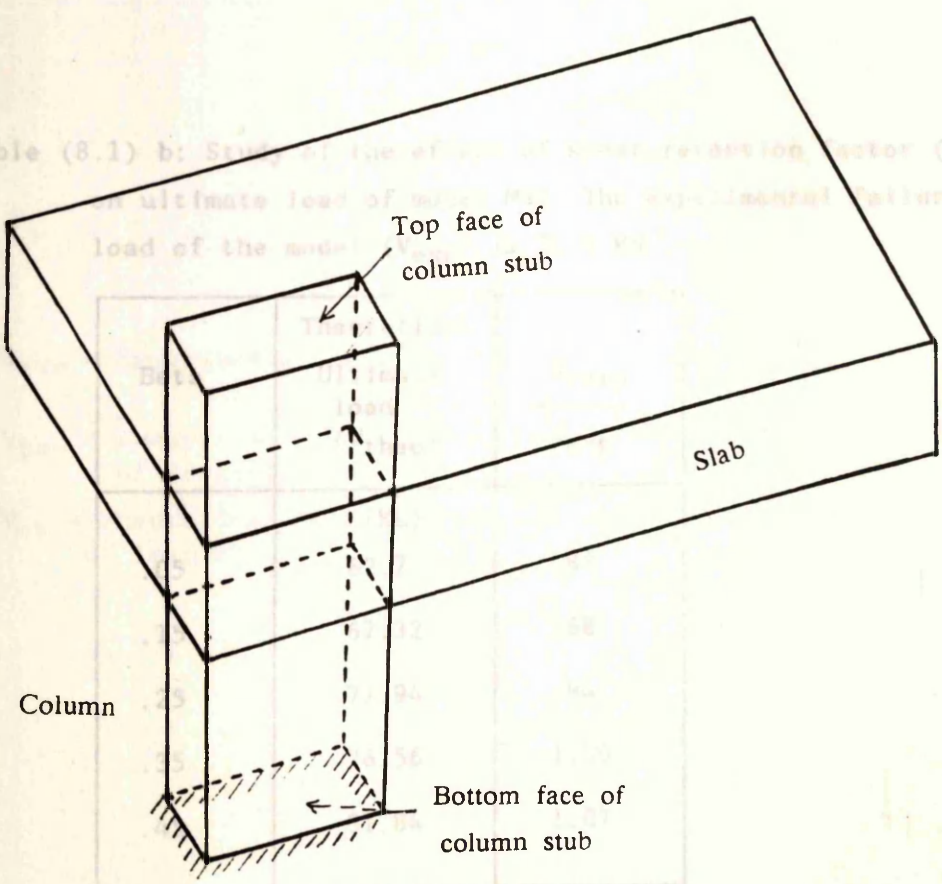

Figure 8.1 : f) Analytical model including column stub (symmetrical half shown)

Table (8.1) a: Study of the effect of shear retention factor (Beta) on the ultimate load of model MS5. The experimental failure load of the model (V_{exp}) is 89.5 KN

Beta	Theoretical Ultimate load (V_{theo}) (KL)	$\frac{V_{theo}}{V_{exp}}$
.05	79.6	0.89
.15	79.6	0.89
.25	91.6	1.02
.35	91.6	1.02
.45	98.9	1.13
.75	101	1.13

Table (8.1) b: Study of the effect of shear retention factor (Beta) on ultimate load of model MS3. The experimental failure load of the model (V_{exp}) is 76.5 KN

Beta	Theoretical Ultimate load (V_{theo}) (KL)	$\frac{V_{theo}}{V_{exp}}$
.05	62.7	.82
.15	67.32	.88
.25	71.94	.94
.35	76.56	1.00
.45	81.84	1.07

Table (8.2): A comparison between proportional and experimental sequence of loading.

Model	V_{exp} *	V_{es} *	V_{ps} *	$\frac{V_{es}}{V_{exp}}$	$\frac{V_{ps}}{V_{exp}}$
	(KN)	(KN)	(KN)		
MS1	55.5	48.0	53.1	1.0	.96
MS2	64.5	54.9	67.5	.85	1.04
MS3	76.3	71.5	74.7	.94	.98
MS4	94.8	91.1	96.9	.96	1.02
MS5	89.5	79.3	91.6	.89	1.02
MS6	64.7	69.8	72.3	1.07	1.12
			Average =	.95	1.03
			S. D. =	.07	.05

V_{exp} = Experimental failure load

V_{ps} = Theoretical failure load with proportional sequence of loading.

V_{es} = Theoretical failure load with experimental sequence of loading.

Table (8.3): Study of the effect of including/excluding the column in the analysis.

Model	V_{exp}^{*} (KN)	V_{t}^{*} (KN)	V_{t-c}^{*} (KN)	$\frac{V_t}{V_{exp}}$	$\frac{V_{t-c}}{V_{exp}}$
MS1	55.5	55.5	53.1	1.0	.96
MS2	64.5	62.2	67.5	.96	1.05
MS3	76.3	69.9	74.7	.92	.98
MS4	94.8	76.5	96.9	.81	1.02
MS5	89.5	82	91.6	.92	1.02
MS6	64.7	53.5	72.3	.83	1.12
		Average =		.91	1.03
		S. D. =		0.04	0.05

V_{exp} = Experimental failure load

V_t = Theoretical failure load without column elements

V_{t-c} = Theoretical failure load considering column elements

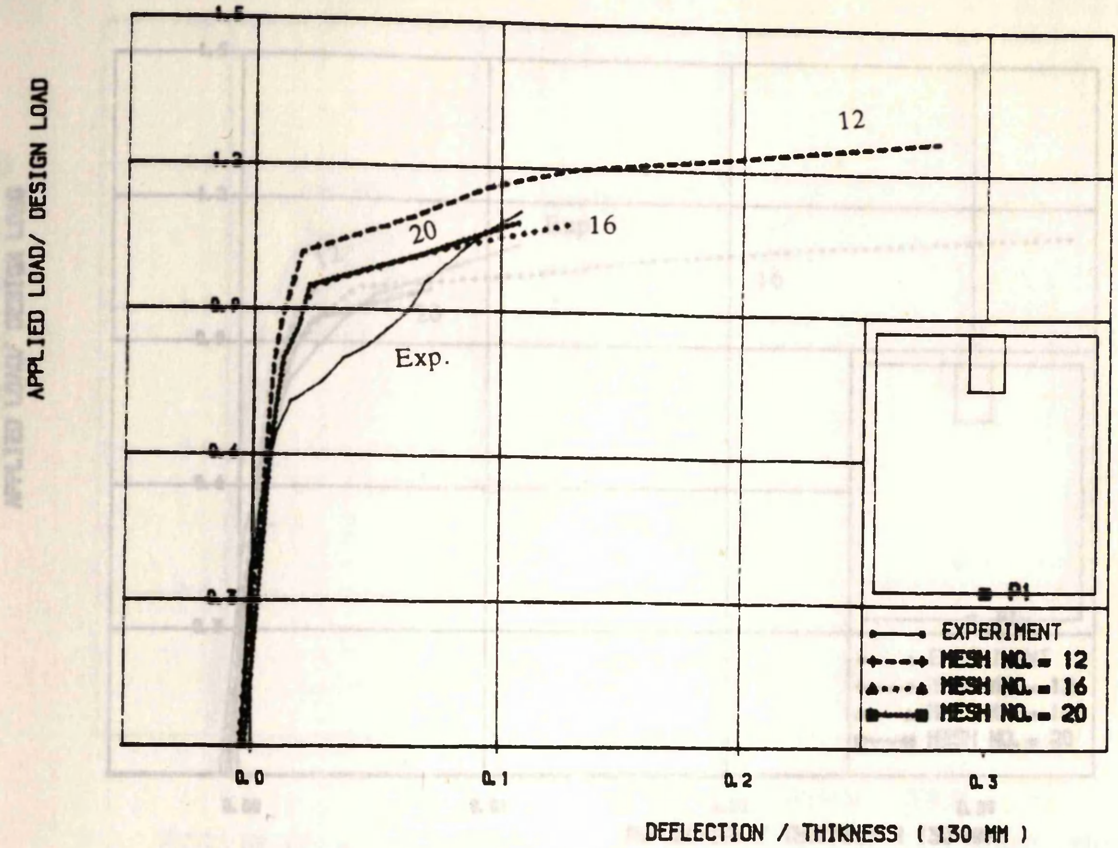

FIG. (8.2) A. LOAD-DEFLECTION RELATIONSHIP OF MODEL MS3 AT POINT P1 FOR VARIOUS MESH SIZES

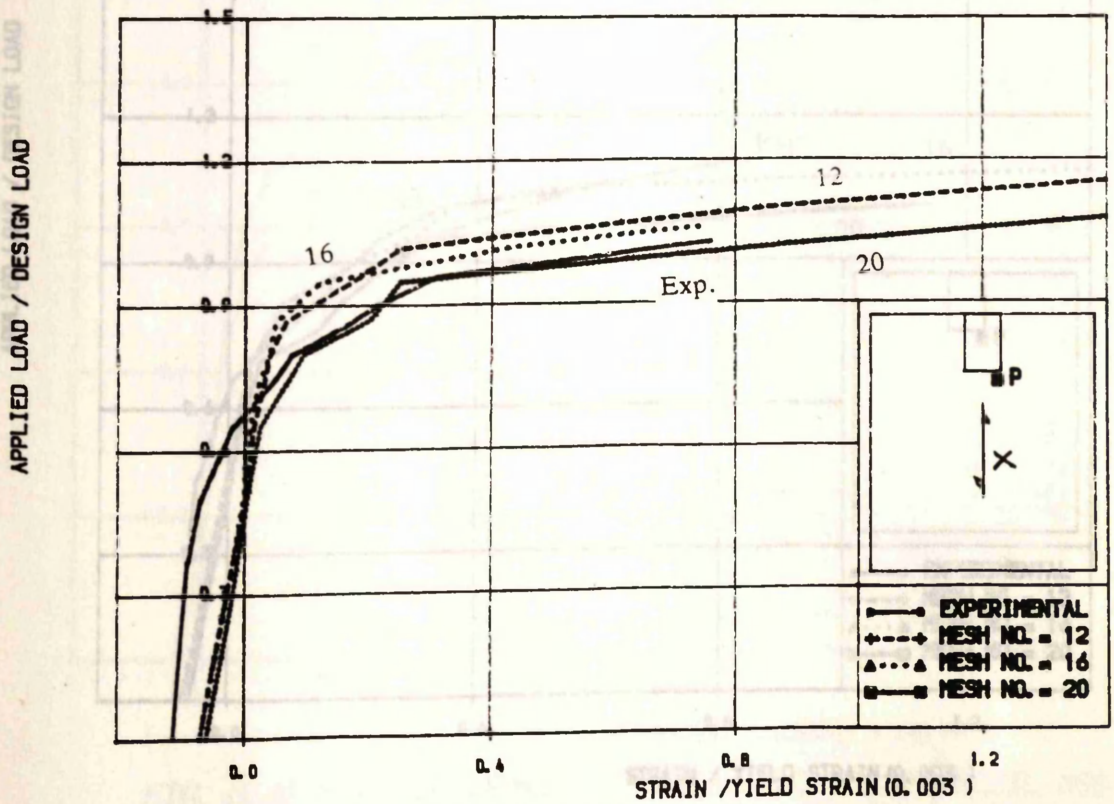

FIG. (8.2) B. LOAD-STRAIN CURVES OF STEEL IN AT P IN X-DIR. FOR VARIOUS MESH SIZES (MODEL MS3)

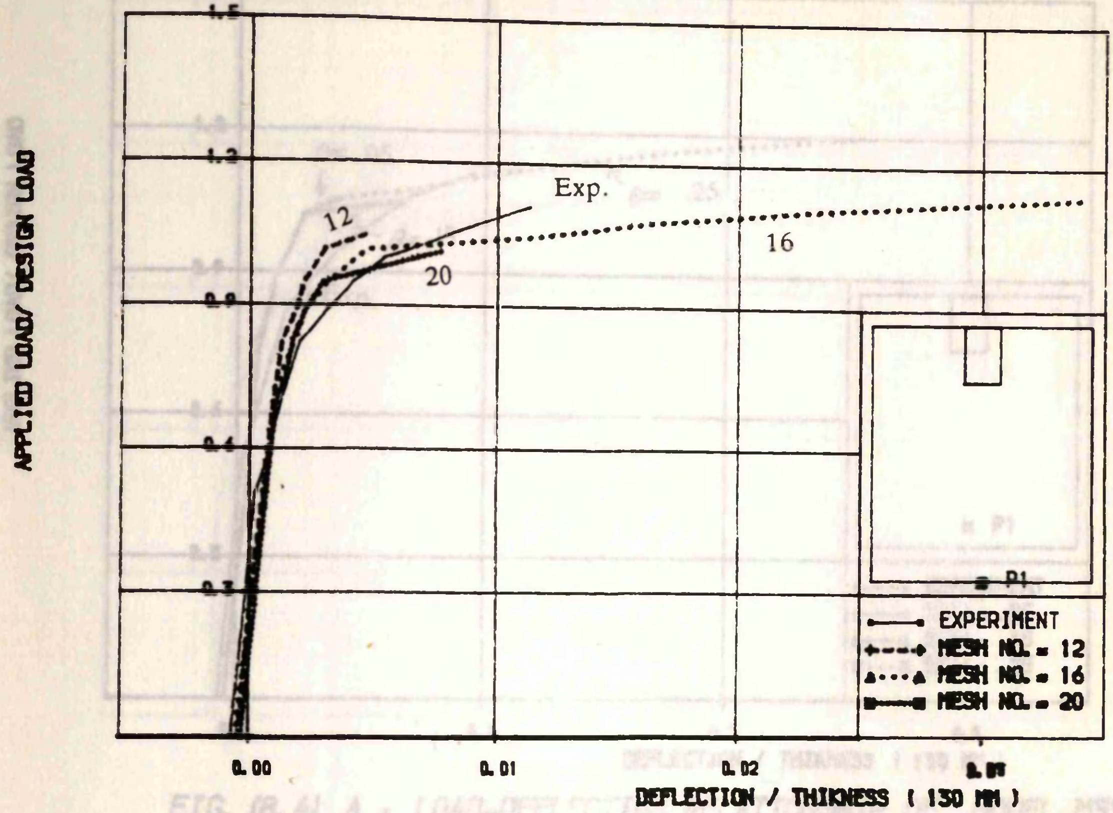

FIG. (8. 3) A. LOAD-DEFLECTION RELATIONSHIP OF MODEL MS5 AT POINT P1 FOR VARIOUS MESH SIZES

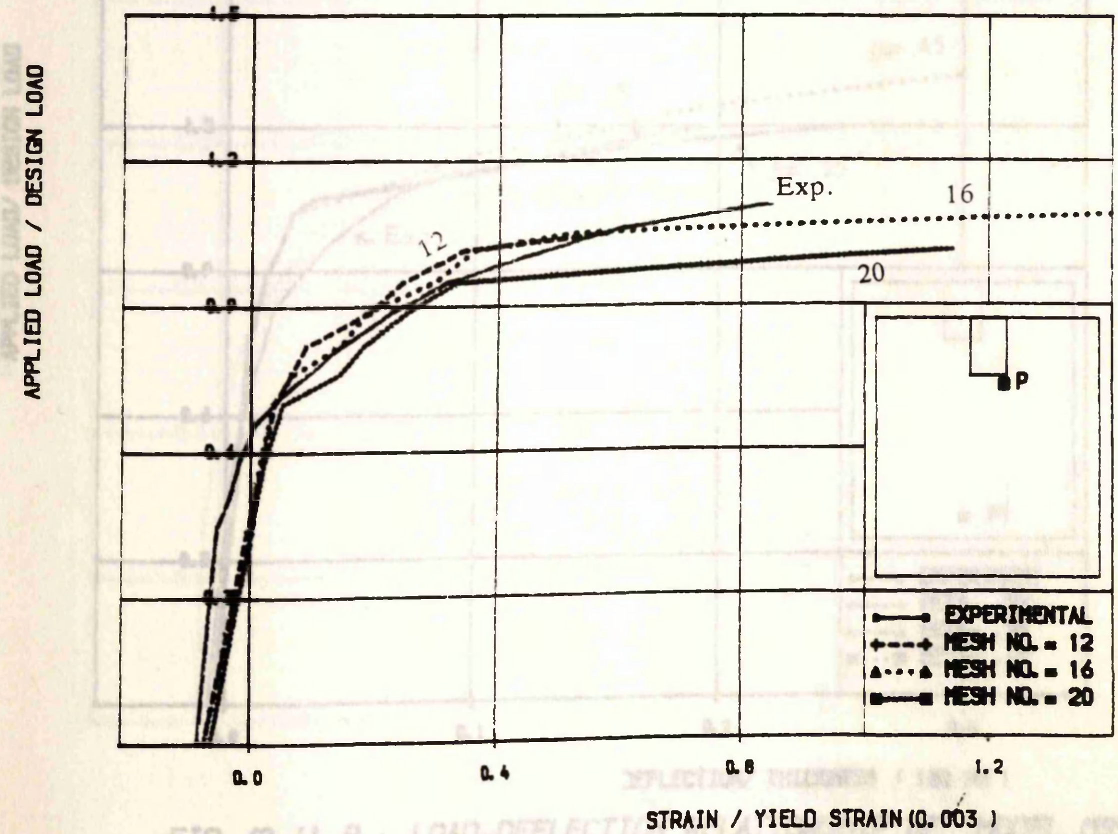

FIG. (8. 3) B. LOAD-STRAIN CURVES OF STEEL AT P IN X-DIR. FOR VARIOUS MESH SIZES (MODEL MS5)

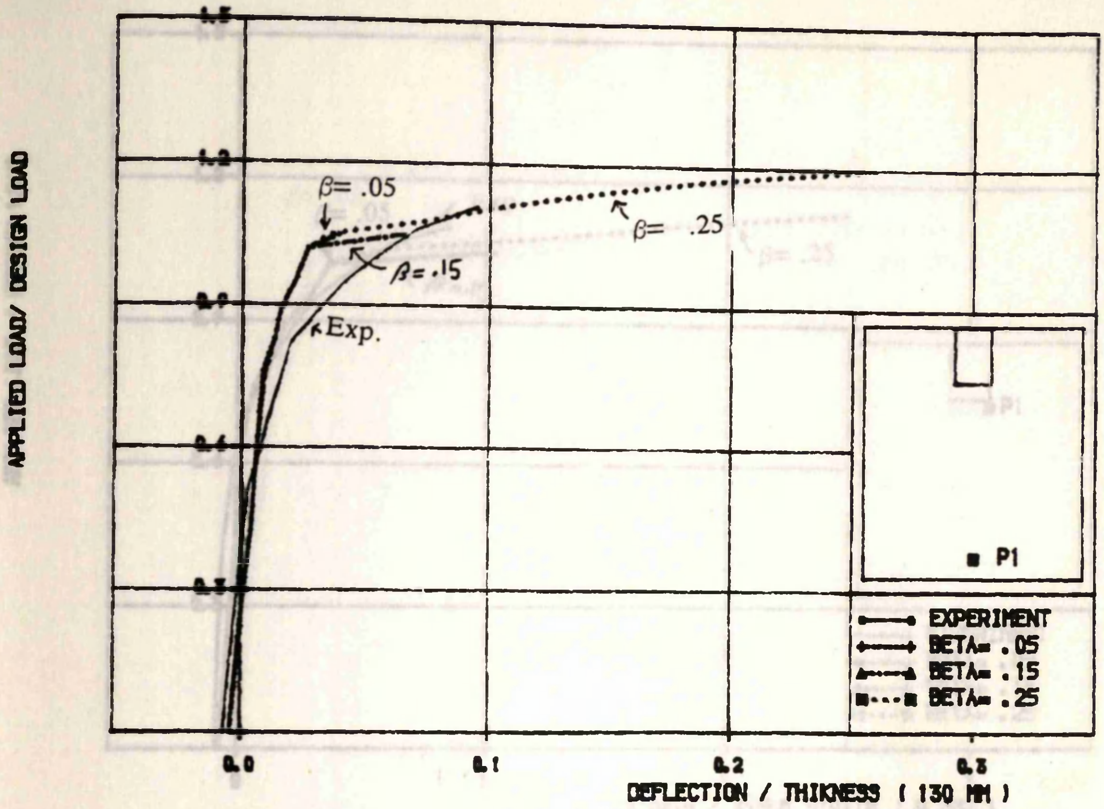

FIG. (8.4) A : LOAD-DEFLECTION RELATIONSHIP OF MODEL MS5 AT POINT P1 FOR VARIOUS VALUES OF BETA

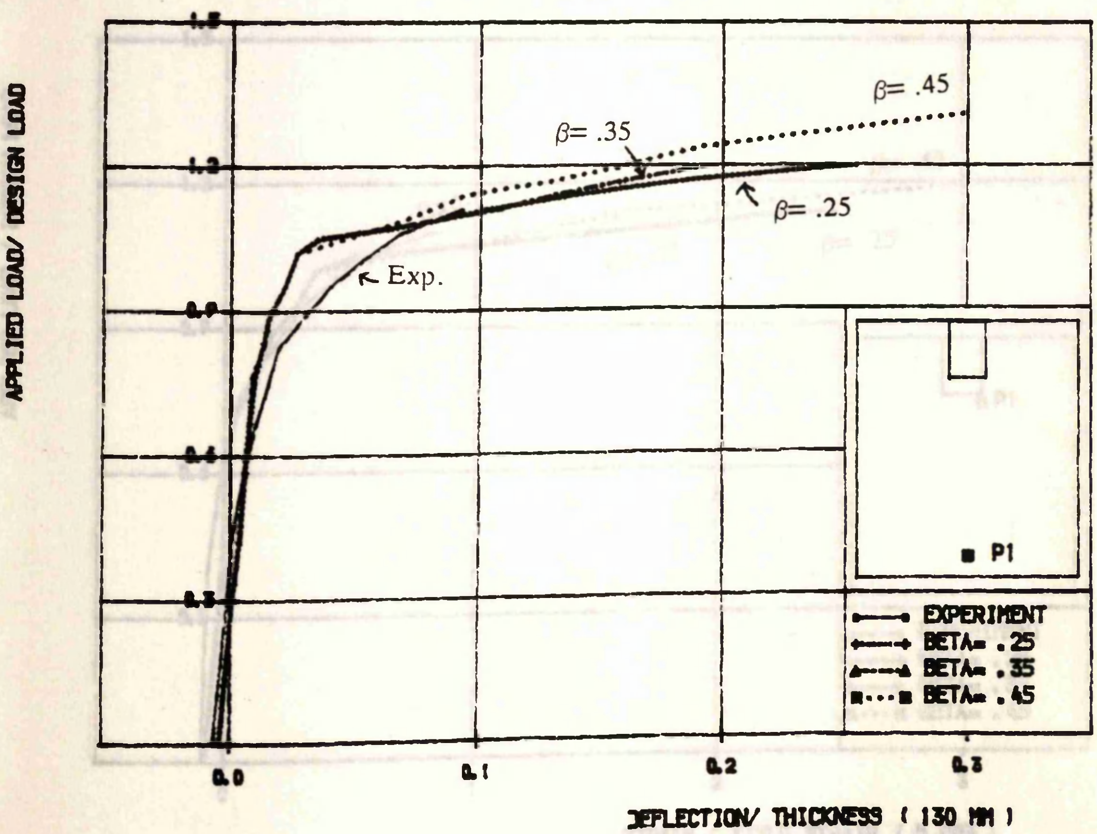

FIG. (8.4) B : LOAD-DEFLECTION RELATIONSHIP OF MODEL MS5 AT POINT P1 FOR VARIOUS VALUES OF BETA.

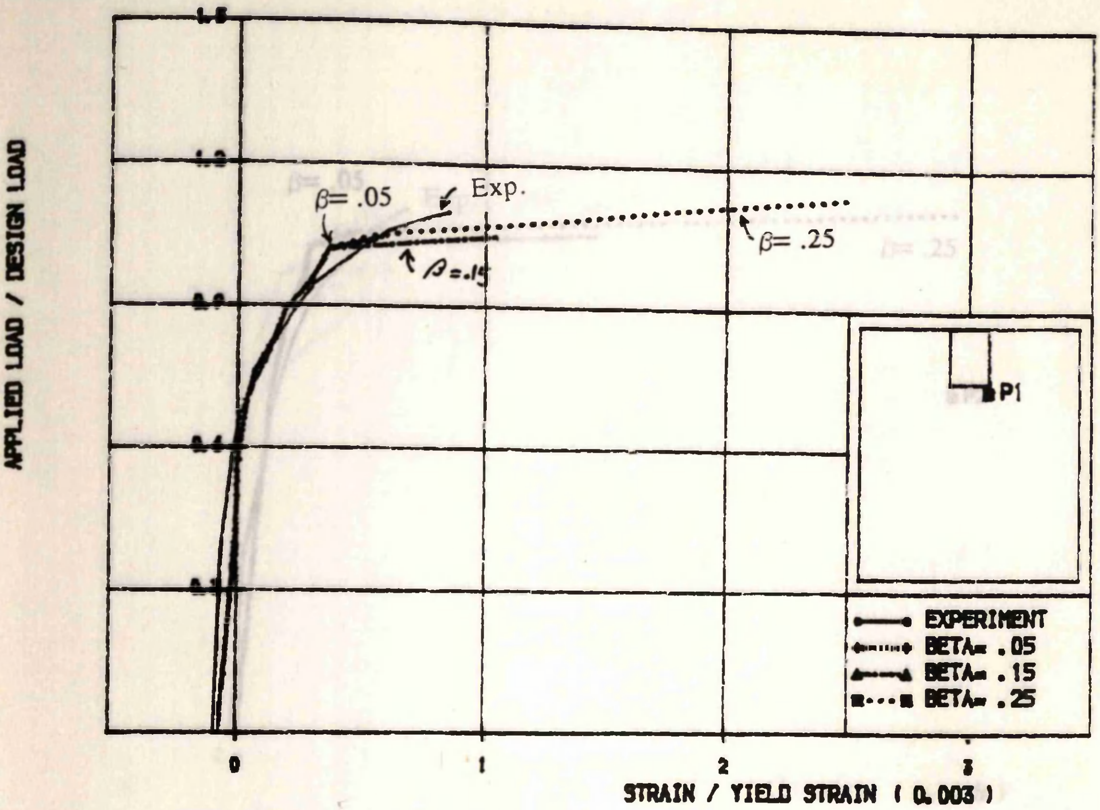

FIG. (8.5) A . LOAD-STRAIN CURVE FOR REINFORCING BAR AT P1 IN X- DIRECTION (MODEL MS5).

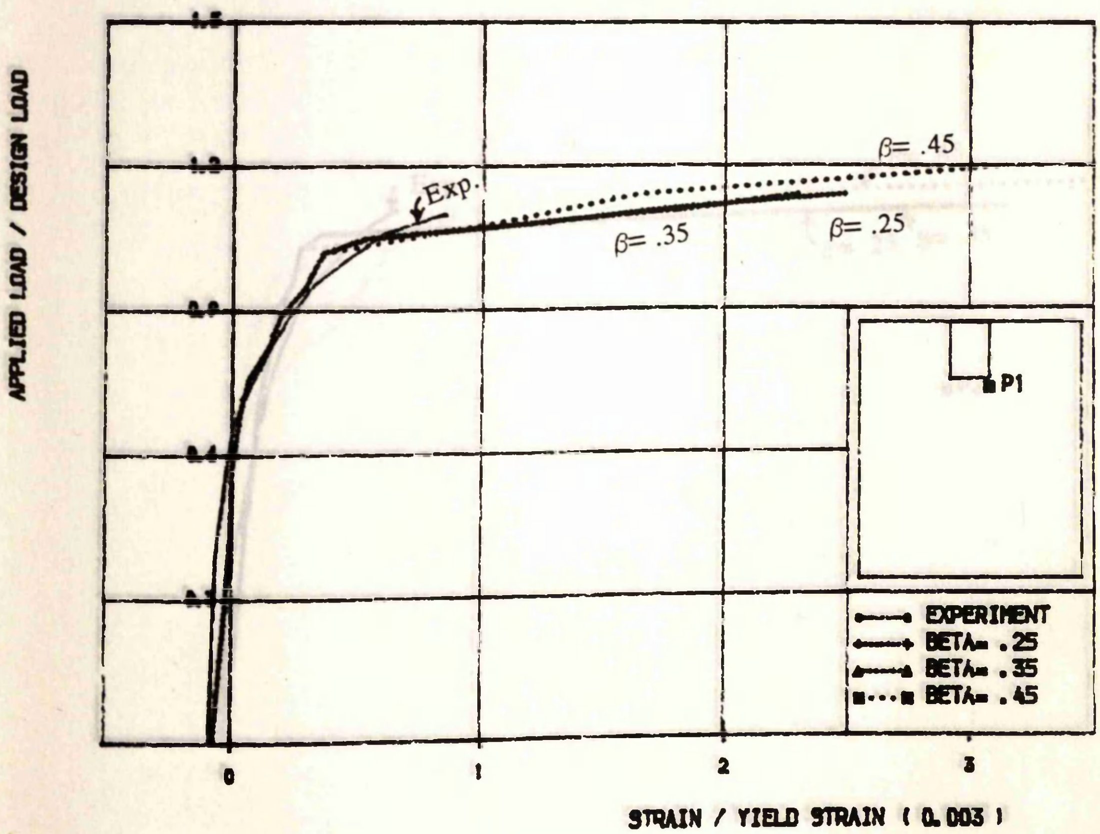

FIG. (8.5) B . LOAD-STRAIN CURVE FOR REINFORCING BAR AT P1 IN X- DIRECTION (MODEL MS5).

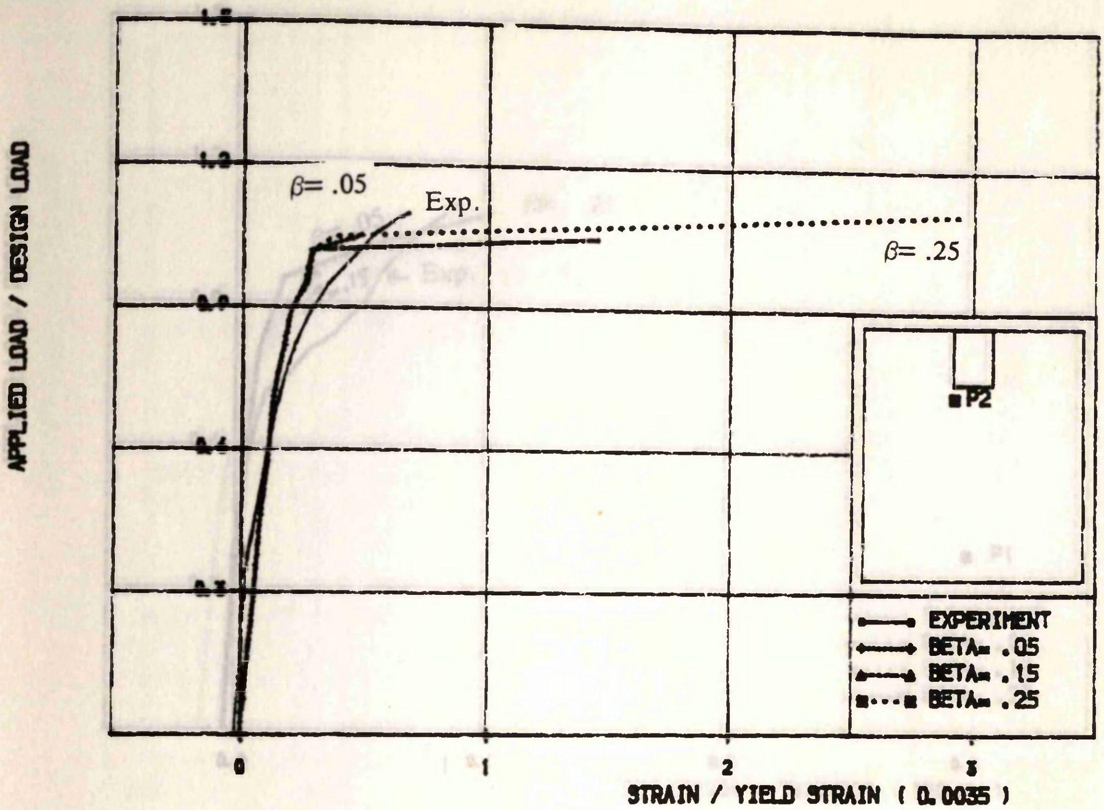

FIG. (8.6) A. LOAD-STRAIN CURVE ON COMPRESSIVE SURFACE OF CONCRETE AT P2 FOR BETA= .05 , .15 AND .25

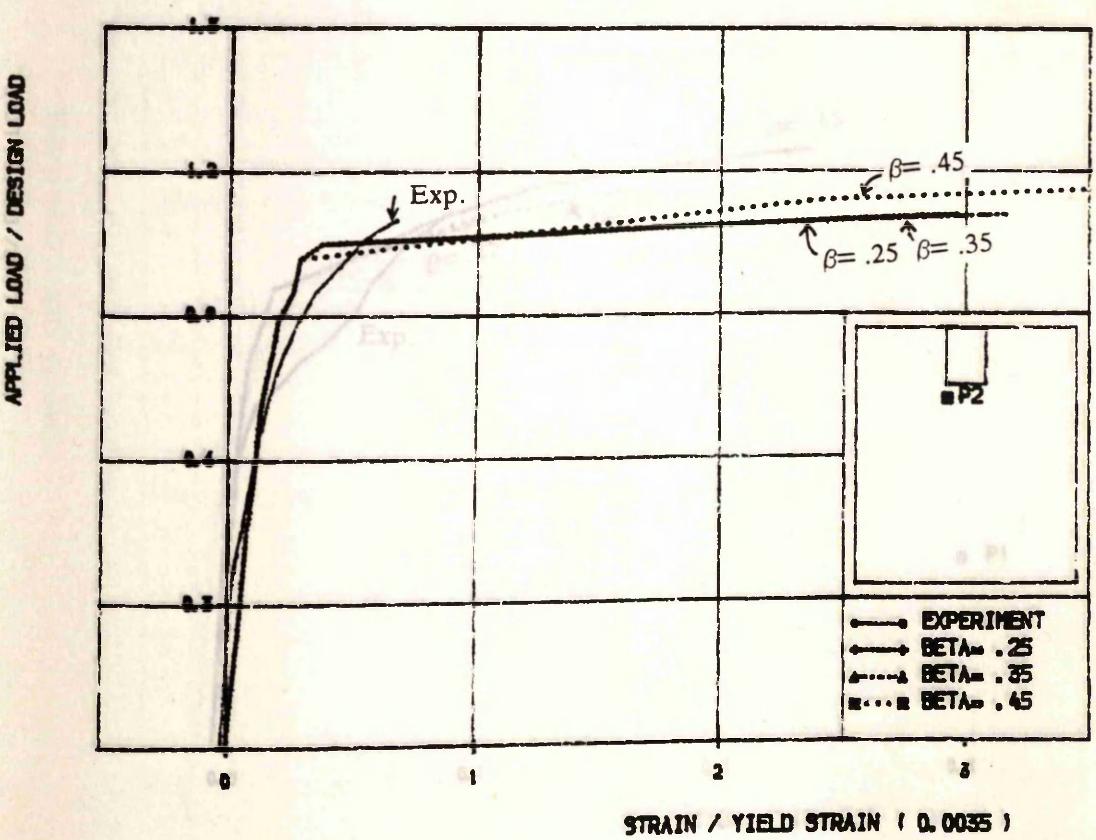

FIG. (8.6) B. LOAD-STRAIN CURVE ON COMPRESSIVE SURFACE OF CONCRETE AT P2 FOR BETA= .25 , .35 AND .45

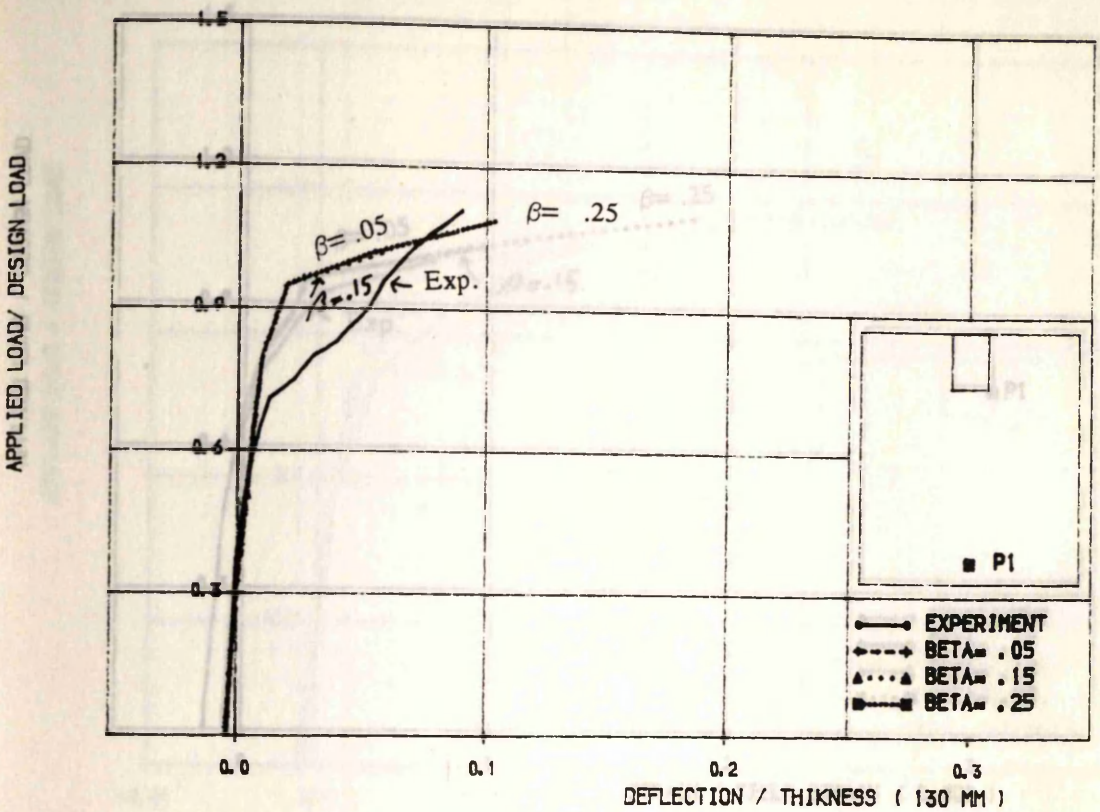

FIG. (8.7) A. LOAD-DEFLECTION RELATIONSHIP OF MODEL MS3 AT POINT P1 FOR VARIOUS VALUES OF BETA

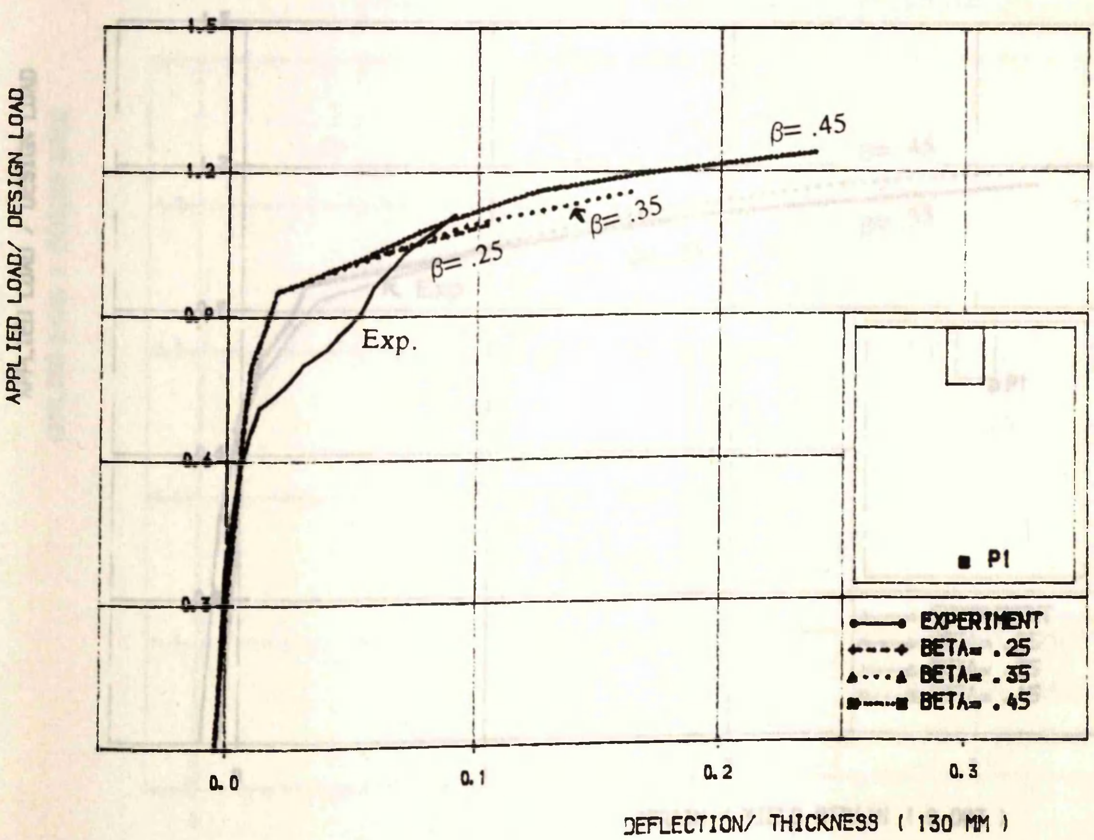

FIG. (8.7) B. LOAD-DEFLECTION RELATIONSHIP OF MODEL MS3 AT POINT P1 FOR VARIOUS VALUES OF BETA.

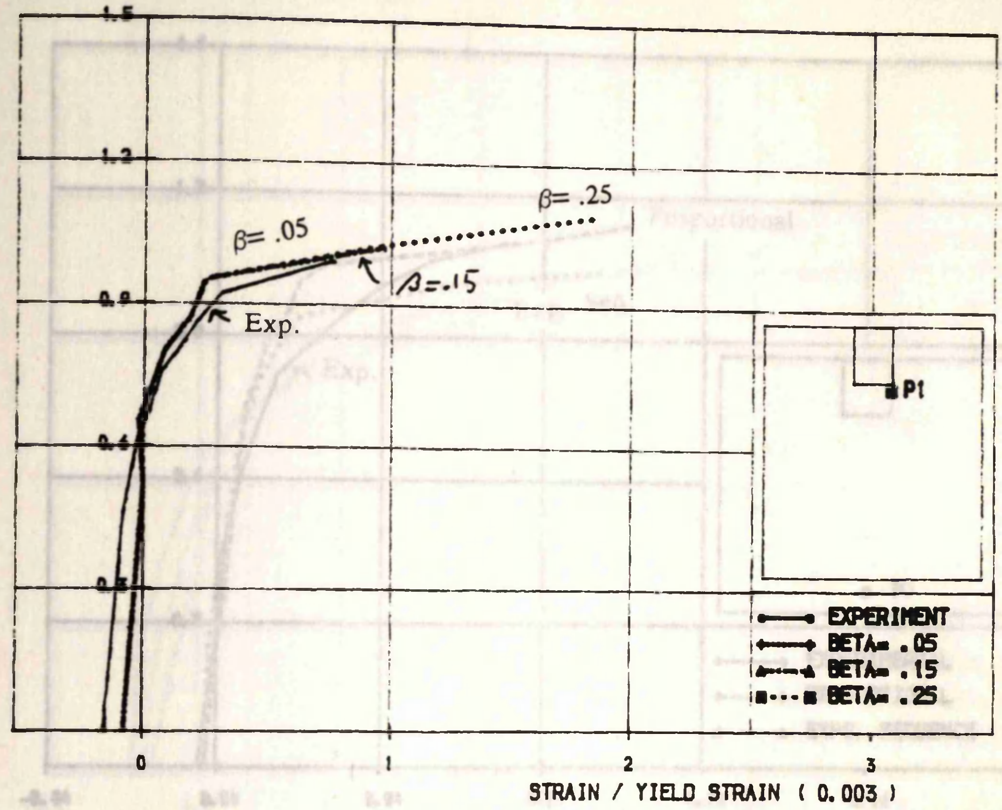

FIG. (8.8) A , LOAD-STRAIN CURVE FOR REINFORCING BAR AT P1 IN X- DIRECTION (MODEL MS3).

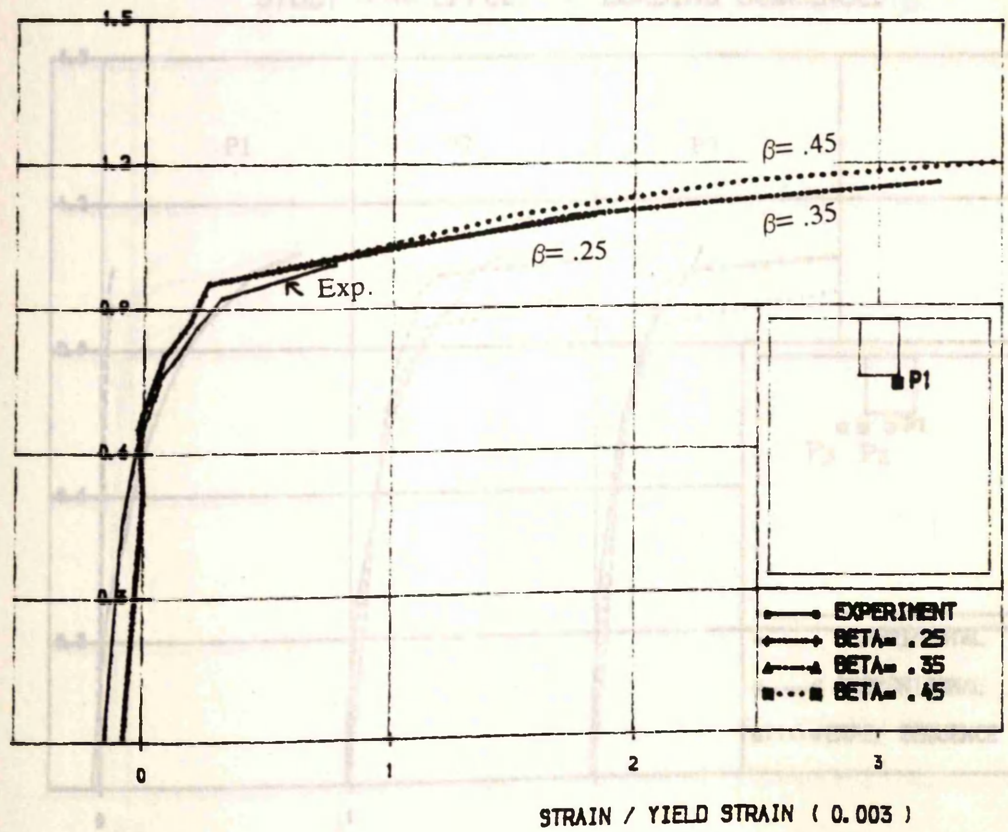

FIG. (8.8) B, LOAD-STRAIN CURVE FOR REINFORCING BAR AT P1 IN X- DIRECTION (MODEL MS3).

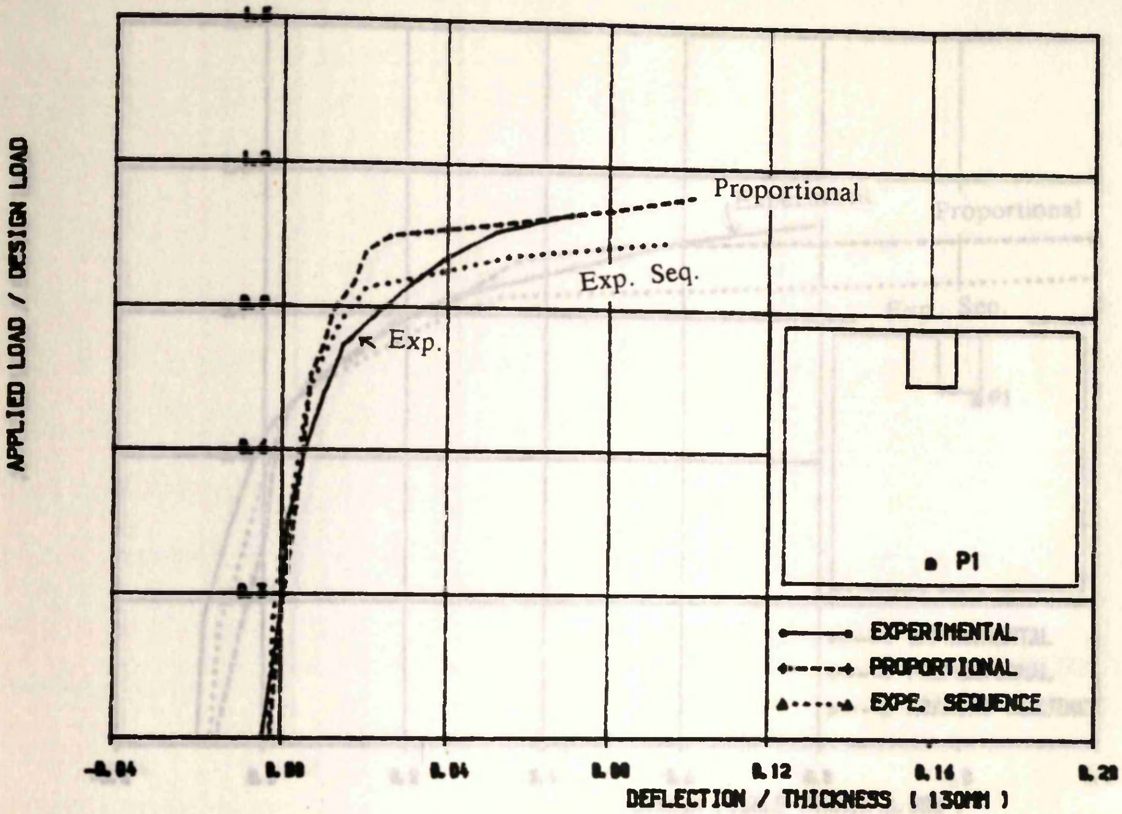

FIG. (8. 9). LOAD-DEFLECTION CURVES OF MODEL MS5 TO STUDY THE EFFECT OF LOADING SEQUENCE.

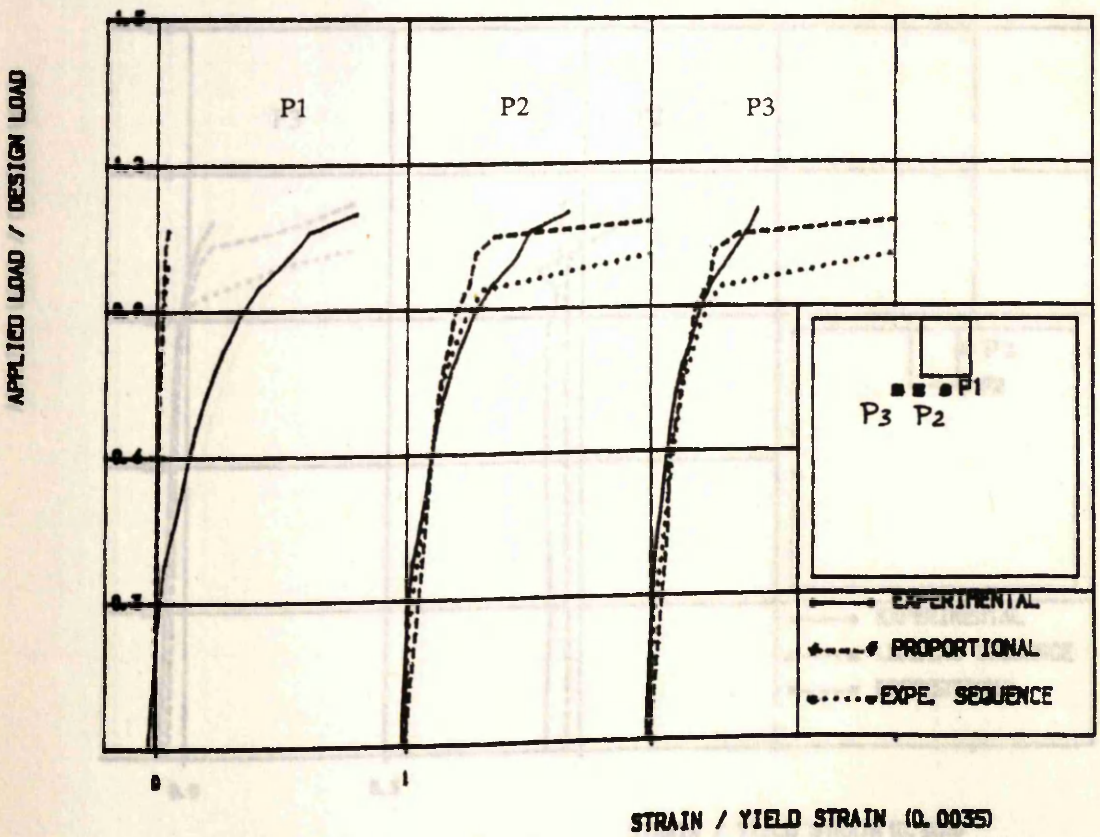

FIG. (8. 10). LOAD-STRAIN CURVE ON COMPRESSIVE SURFACE OF MS5 TO STUDY EFFECT OF LOADING SEQUENCE

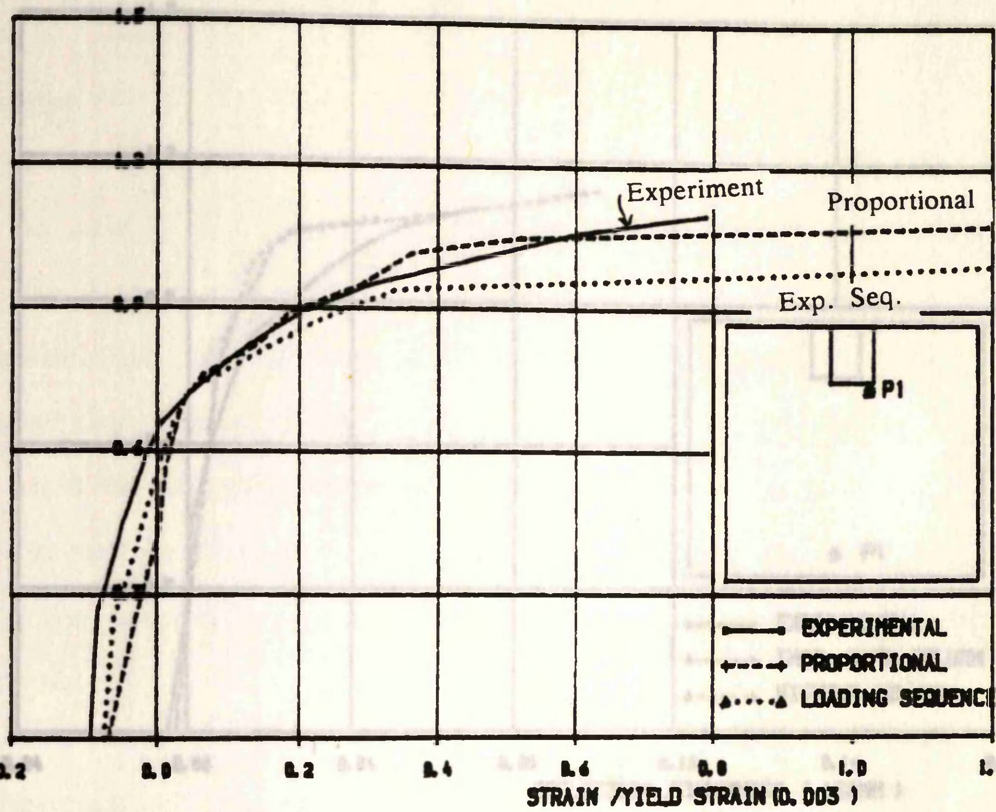

FIG. (8.11). EFFECT OF LOADING SEQUENCE ON TENSILE STRAIN AT P1, IN STEEL, IN X-DIR. FOR MODEL MS5.

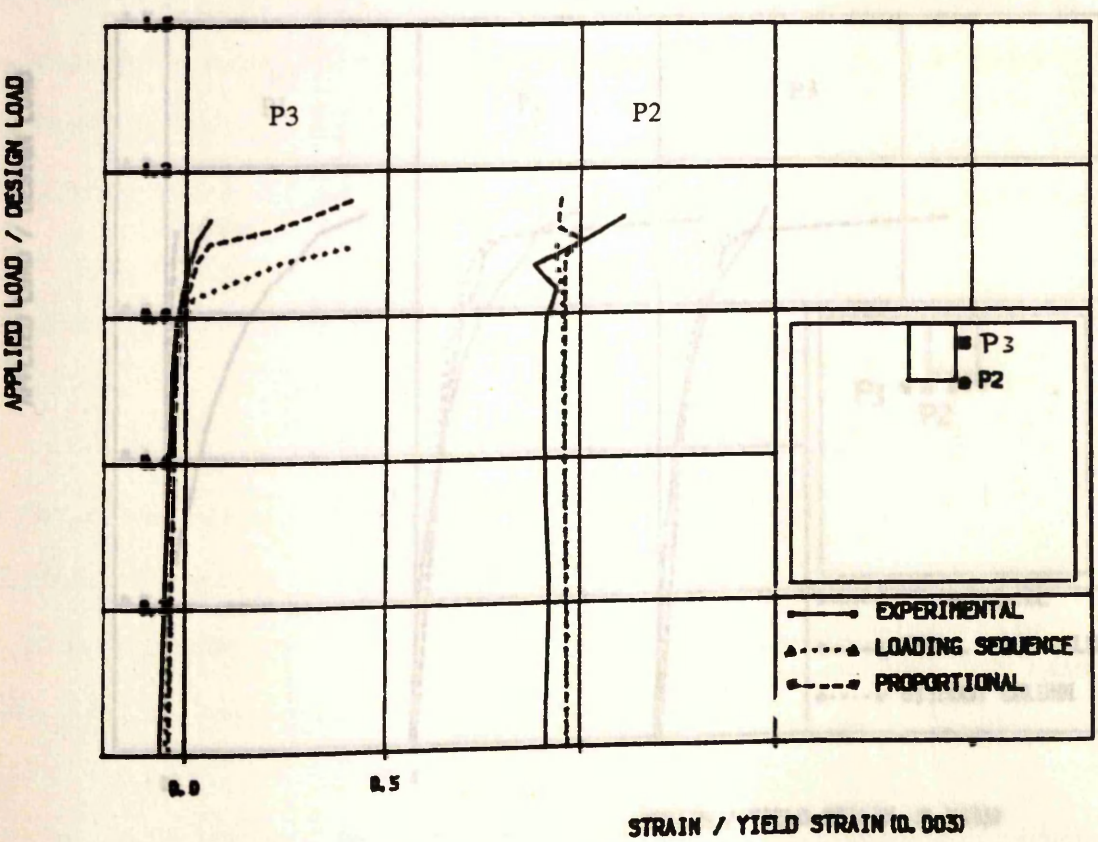

FIG. (8.12). EFFECT OF COLUMN ELEMENTS ON TENSILE STRAIN IN STEEL IN X-DIR. FOR MODEL MS5.

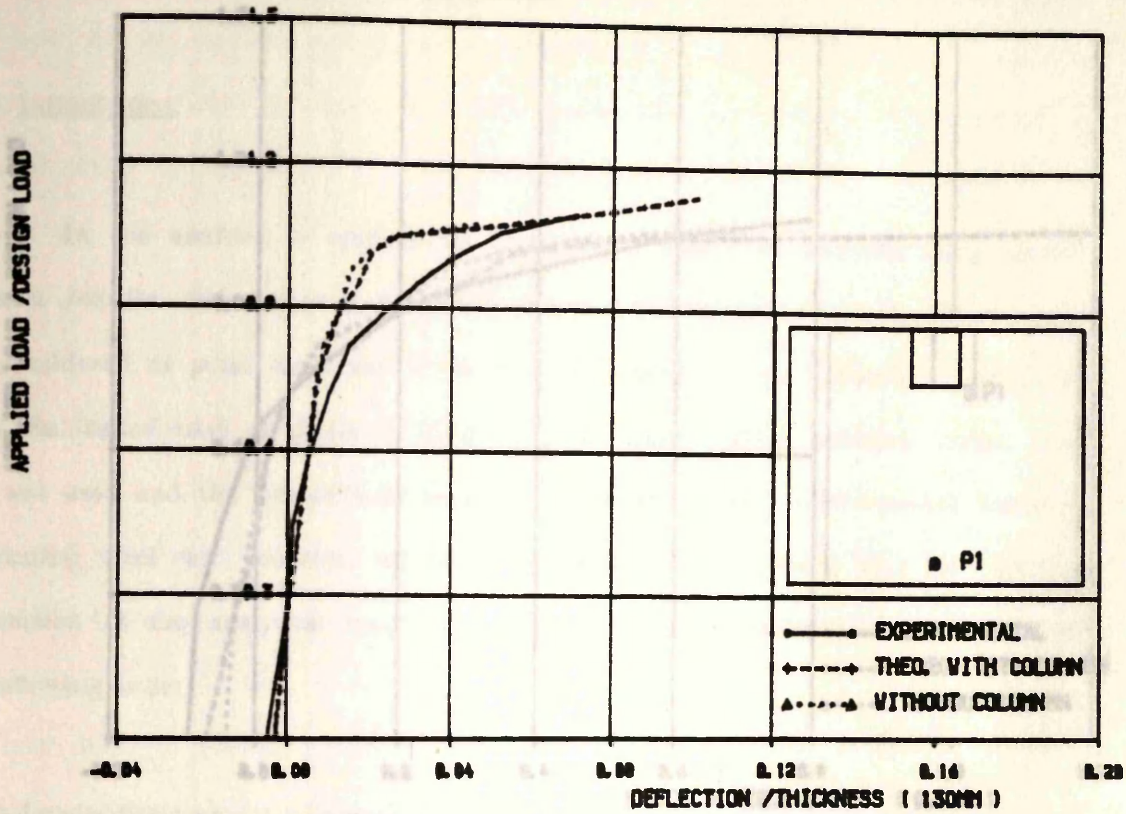

FIG. (8.13). LOAD-DEFLECTION CURVES OF MODEL MS5 TO STUDY EFFECT OF THE COLUMN ELEMENTS.

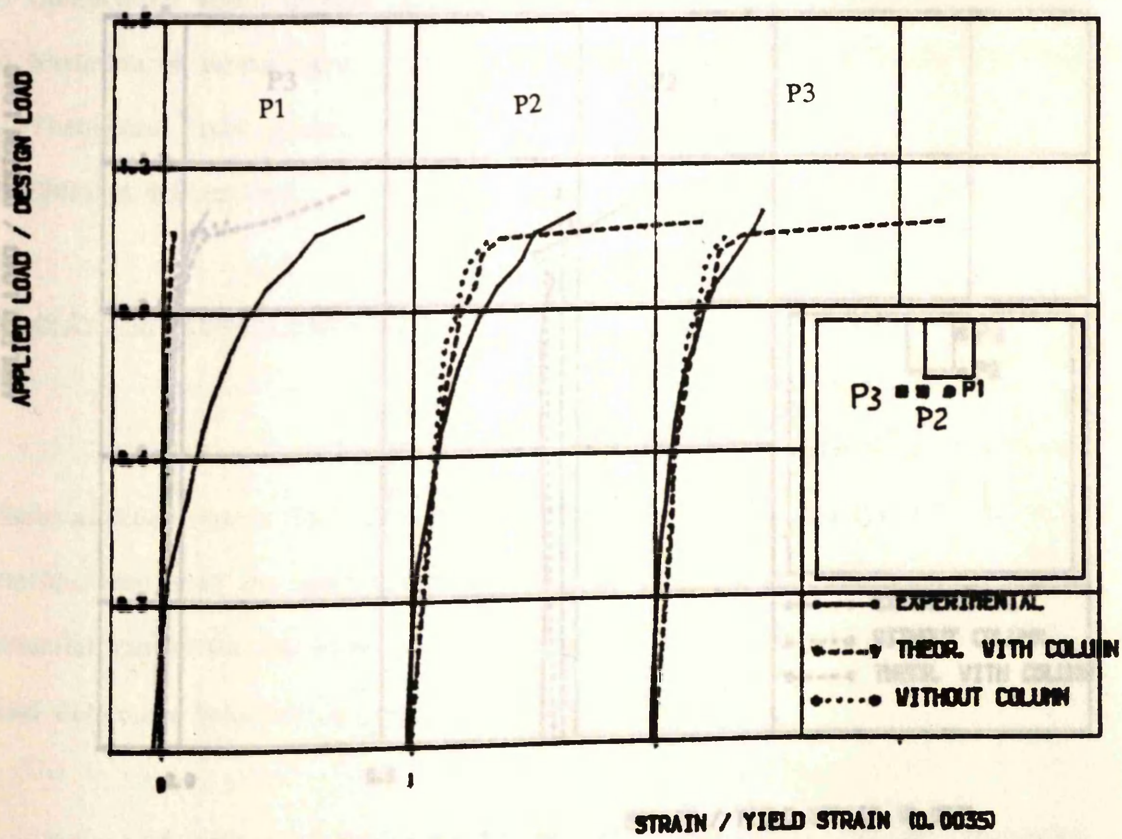

FIG. (8.14). LOAD-STRAIN CURVE AT COMPRESSIVE SURFACE OF MS5 TO STUDY EFFECT OF COLUMN ELEMENTS.

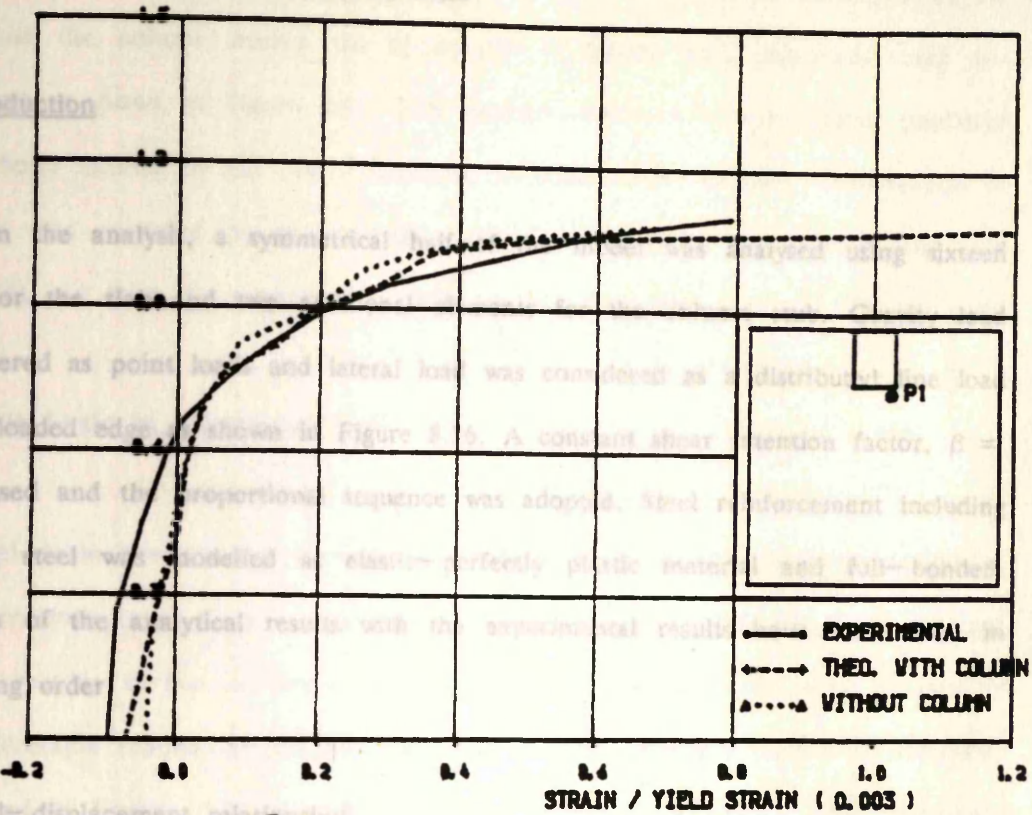

a

FIG. (8. 15) . EFFECT OF COLUMN ELEMENTS ON TENSILE STRAIN IN STEEL IN X-DIR. FOR MODEL MS5.

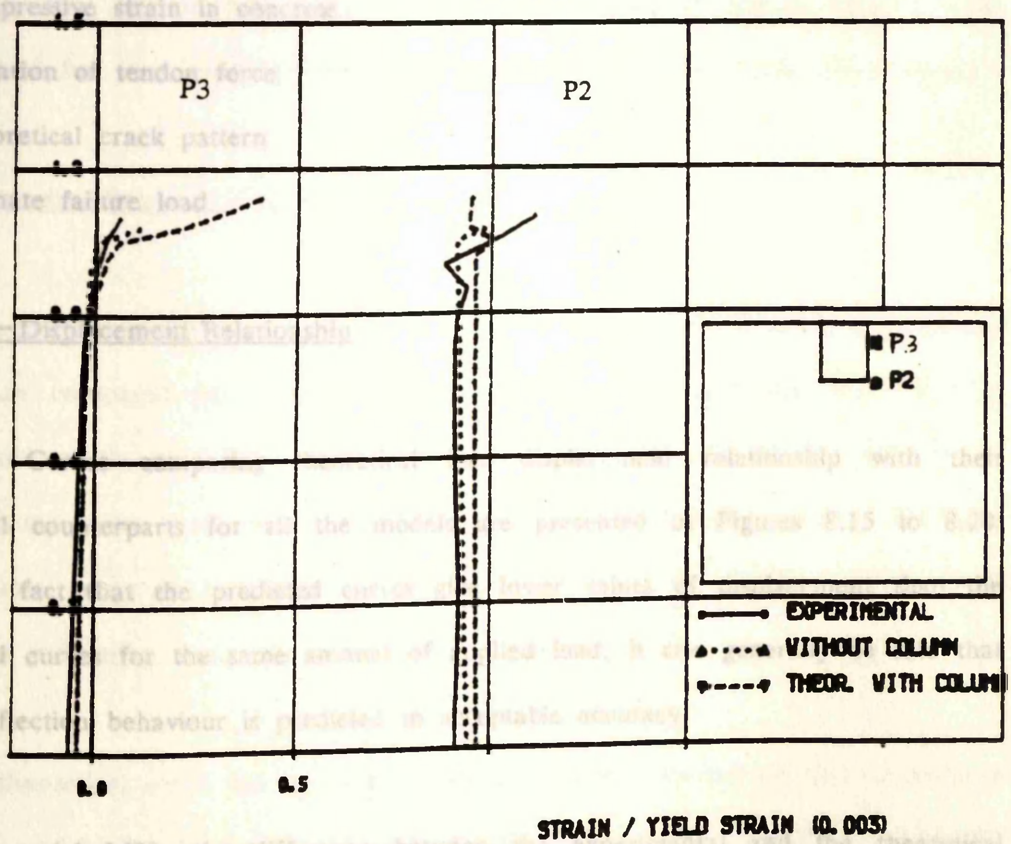

b

FIG. (8. 15) . EFFECT OF COLUMN ELEMENTS ON TENSILE STRAIN IN STEEL IN X-DIR. FOR MODEL MS5.

8.3 Analysis of Slab– Edge Column Junctions

8.3.1 Introduction

In the analysis, a symmetrical half of the model was analysed using sixteen elements for the slab and two additional elements for the column stub. Gravity load was considered as point loads and lateral load was considered as a distributed line load along the loaded edge as shown in Figure 8.16. A constant shear retention factor, β = 0.3, was used and the proportional sequence was adopted. Steel reinforcement including prestressing steel was modelled as elastic– perfectly plastic material and full– bonded. Comparison of the analytical results with the experimental results have been done in the following order:

a) Load– displacement relationship
b) Tensile strain in 'unstressed' steel
c) Compressive strain in concrete
d) Variation of tendon force
e) Theoretical crack pattern
f) Ultimate failure load

8.3.2 Load– Displacement Relationship

Curves comparing theoretical load– displacement relationship with their experimental counterparts for all the models are presented in Figures 8.15 to 8.20. Despite the fact that the predicted curves give lower values of displacement than the experimental curves for the same amount of applied load, it can generally be said that the load deflection behaviour is predicted to acceptable accuracy.

In model MS3, the difference between the experimental and the theoretical values above 80% of design load (corresponding to the start of flexural and shear cracks in the experimental model) is probably due to fact that some cracks developed at the rear face of the column during the application of lateral load, especially near the ultimate load as shown in Figure 8.17. This flexural behaviour of the column produced the rigid– body motion of the slab. Therefore, in models MS4 to MS6, deformation of the column was recorded by the two dial– gauges mounted on the column side face (Figure 8.17) and then the experimental deflection was corrected.

8.3.3 Tensile Strain in 'unstressed' Steel

Steel strain prediction is carried out for both the longitudinal and the transverse unstressed reinforcement. Care was taken to choose the Gauss points for strain readings as near as possible to the location of strain gauges in the experiment. Strain in steel in windward direction (called X– direction) and in transverse direction (called Y– direction) are presented in Figures 8.23 to 8.34 for all the models. In general , good agreement is shown at all points for all the models. In most of the models, at above 65% of design load, the experimental strain at point P_1 is slightly higher than that in theoretical one but very good agreement is found at point P_2 and P_3 in Y– direction.

8.3.4 Compressive Strain in Concrete

Theoretical compressive strain in concrete in both the windward and transverse directions are compared with their experimental counterparts in Figures 8.35 to 8.43. The behaviour of the first three models MS1 , MS2 and MS3 showed that there is no significant compressive strain in the transverse direction. So in models MS4 , MS5 and MS6 the strain gauge in that direction was omitted. Instead an additional strain gauge was used for measuring strains in the windward direction.

The theoretical strain are measured at sampling points located on the compressive face of the model. But in the experimental models strain gauges were mounted on the extreme compressive surface of the concrete. The distance between these two locations

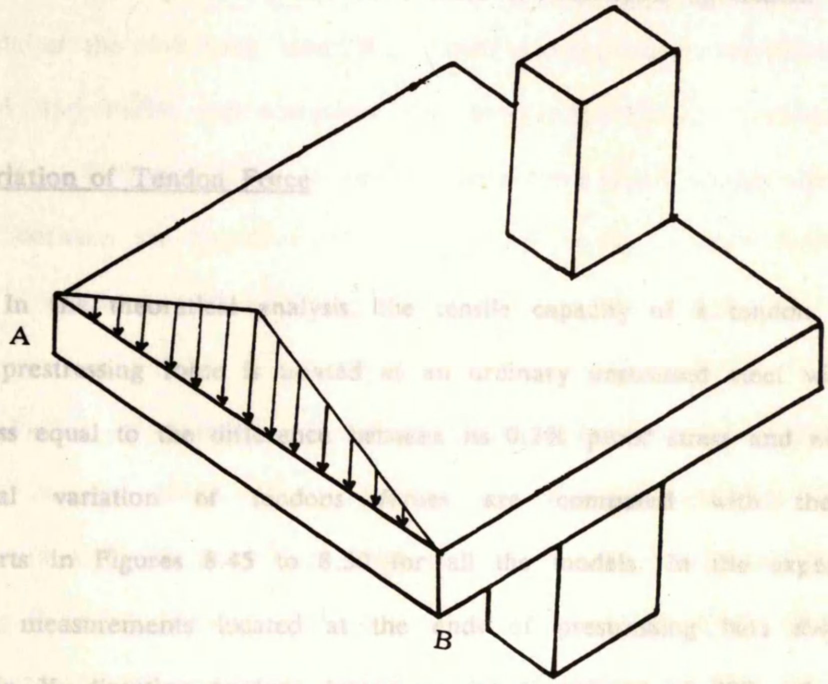

Figure 8.16 : Distribution of lateral load to simulate uniform displacement along the line 'AB'

for a slab of 130 mm thickness is 15 mm as shown in Figure 8.44. Therefore , it was expected that the values of experimental compressive strains will be slightly higher than that of theoretical value calculated at the nearest Gauss points. This is evident in most of the curves presented in Figures 8.35 to 8.43. In general , these curves show elastic behaviour of the slab up to the first cracking which took place at an average of 78% of the design load. At point P1, experimental curves show higher values of strain than theoretical curves. This is because of the stress concentration near the point due to column reaction. At point P2 and P3 , there is reasonable agreement between the two results.

8.3.5 Variation of Tendon Force

In the theoretical analysis, the tensile capacity of a tendon in excess of its effective prestressing force is treated as an ordinary unstressed steel with an equivalent yield stress equal to the difference between its 0.2% proof stress and effective prestress. Theoretical variation of tendons forces are compared with their experimental counterparts in Figures 8.45 to 8.50 for all the models. In the experimental models, load–cell measurements located at the ends of prestressing bars showed very small increase in X–direction tendons forces up to an average of 90% of the design load. The theoretical curves showed the same behaviour as experimental ones. For example, for the tendon which passed through the column head, the average increase in the tendon force as a percentage of the initial load is 4% at 90% of the design load and 13% at ultimate failure load. The experimental counterparts of these figures are 2% and 10% respectively.

It should be noted that while in the experimental models the tendon was unbonded , in the finite element analysis it was treated as bonded 'unstressed' steel. Therefore, the theoretical results were averaged over the whole tendon length before comparing with the experimental results. Figure 8.51 shows the typical variation of a tendon force over its length in model MS6 at 70% , 93% and 100% of theoretical failure load of the model. In general , good agreement is obtained between the experimental and the theoretical results. In all the models, load cell measurements and theoretical calculations indicated that no significant changes were observed in the tendon forces in the Y– direction.

8.3.6 Theoretical Crack Pattern

In order to compare the crack patterns obtained by theoretical analysis with the experimental ones, cracks which occurred at those sampling points located on the tension side of the slab were used. Such crack patterns were obtained for models MS1, MS3, MS5 and RCS8 and compared with their experimental counterparts in Figures 8.53 , 8.55 , 8.57 and 8.59. It can be seen from these figures that there is good agreement between the experimental and analytical results at crack initiating points and spreading of cracks throughout the slab.

Failure of concrete was extracted from theoretical analysis to observe the progress of compressive failure of concrete. On the compressive side of the slab , the region around a Gauss Point fails when the concrete at that Gauss Point crushes. As the loading increases, crushing spreads to other Gauss points in the slab. The sequence of this spreading presented in Figures 8.54 , 8.56 and 8.58 , indicate the progressive failure of concrete respectively for models MS1, MS3 and MS5. From these figures it is clear that on the bottom face of the slab, crushing of concrete starts from the area near the column front corners and spreads towards the loaded edge. On the tension face, crushing takes place in the area beside the column rear corners. This leads to the punching failure of the column– slab connection which corresponds to that from experimental observations as well.

The monotonic analysis of the cyclic loading models showed that crushing of concrete is limited to the area in front of the column on the compressive side of slab only. On the other hand, considering extensively spread flexural cracks on the tensile side of the model RCS8 (see Figure 8.59) , it can be concluded that the theoretical failure mode of the cyclic loading models is flexural. It is interesting to note that not only the punching type of failure was successfully predicted but also of the flexural type as well.

8.3.7 Ultimate Failure Load

In the experiment, failure of the slab–column connections took place when a major diagonal cracks took place on the rear side of slab or excessive deflection of the slab was observed (in cyclic loading models) accompanied by rapid decrease in lateral load. On the other hand, in the theoretical analysis failure of the connections is assumed to have taken place when the termination criterion described in section 3.5.5 was fulfilled

For all the models tested, the theoretical ultimate load (V_{theo}) is compared with the experimental ultimate load (V_{exp}) in Table 8.4. In the monotonic loading series , MS1 to MS6 , all the models failed in punching mode but in cyclic loading series failure mode of both models , RCS7 and RCS8 , was flexural. The ratio of (V_{theo}/V_{exp}) is equal to 1.01 with standard deviation of 0.08. Therefore, from this it can be said that the proposed finite element analysis predicts failure load of the connections satisfactorily.

In Table 8.5, the experimental punching failure load is compared with punching shear strength predicted by BS8110 (chapter 2, equation 2.10) and ACI 318–83 (equation 2.8). It is clear from the results in Table 8.5 that, shear strength predicted by ACI–83 is an underestimation. The reason may be that the ACI design equation is dominated by the parameter of (M/V) whereas in the British Code the effect of this parameter is considered as a constant at 0.8. The calculations are shown in Appendix 'A'.

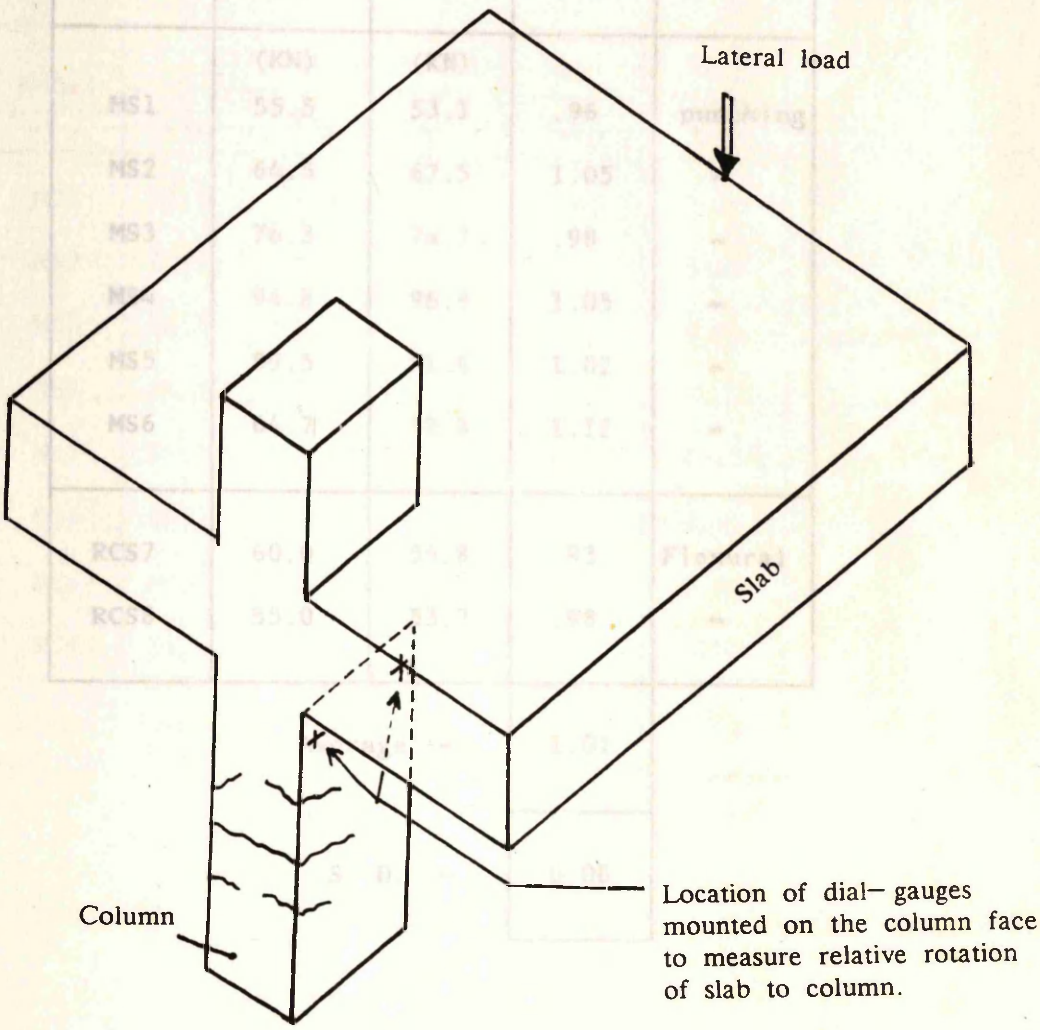

Figure 8.17 : Cracks on the rear face of the column

Table (8.4): Comparison between theoretical and experimental ultimate loads.

Model	V_{exp}^{*}	V_{theo}^{*}	$\frac{V_{theo}}{V_{exp}}$	Failure mode
	(KN)	(KN)		
MS1	55.5	53.1	.96	punching
MS2	64.5	67.5	1.05	=
MS3	76.3	74.7	.98	=
MS4	94.8	96.9	1.05	=
MS5	89.5	91.6	1.02	=
MS6	64.7	72.3	1.12	=
RCS7	60.0	55.8	.93	Flexural
RCS8	55.0	53.7	.98	=
		Average =	1.01	
		S. D. =	0.08	

V_{exp} = Experimental failure load

V_{theo} = Theoretical failure load

Table 8.5 – Comparison of the experimental failure load in this study with shear failure load predicted by BS8110 and American Code (ACI– 83).

Model	Failure Loads (KN)			V_{BS} / V_{exp}	V_{ACI} / V_{exp}
	V_{exp}	V_{BS}	V_{ACI}		
MS1	55.5	89.0	39.9	1.60	0.72
MS2	64.5	98.8	41.2	1.53	0.64
MS3	76.3	112.0	51.1	1.45	0.68
MS4	94.8	112.0	66.4	1.16	0.70
MS5	89.5	118.0	54.9	1.32	0.61
MS6	64.7	104.3	42.2	1.61	0.65
RCS7	60.0	82.4	53.2	1.37	0.89
RCS8	55.0	82.4	46.8	1.49	0.85
		Average =		1.44	0.72

V_{exp}= Experimental Ultimate Failure Load in this study.

V_{BS} = Predicted Failure Load by BS8110 code.

V_{ACI}= Predicted Failure Load by ACI code.

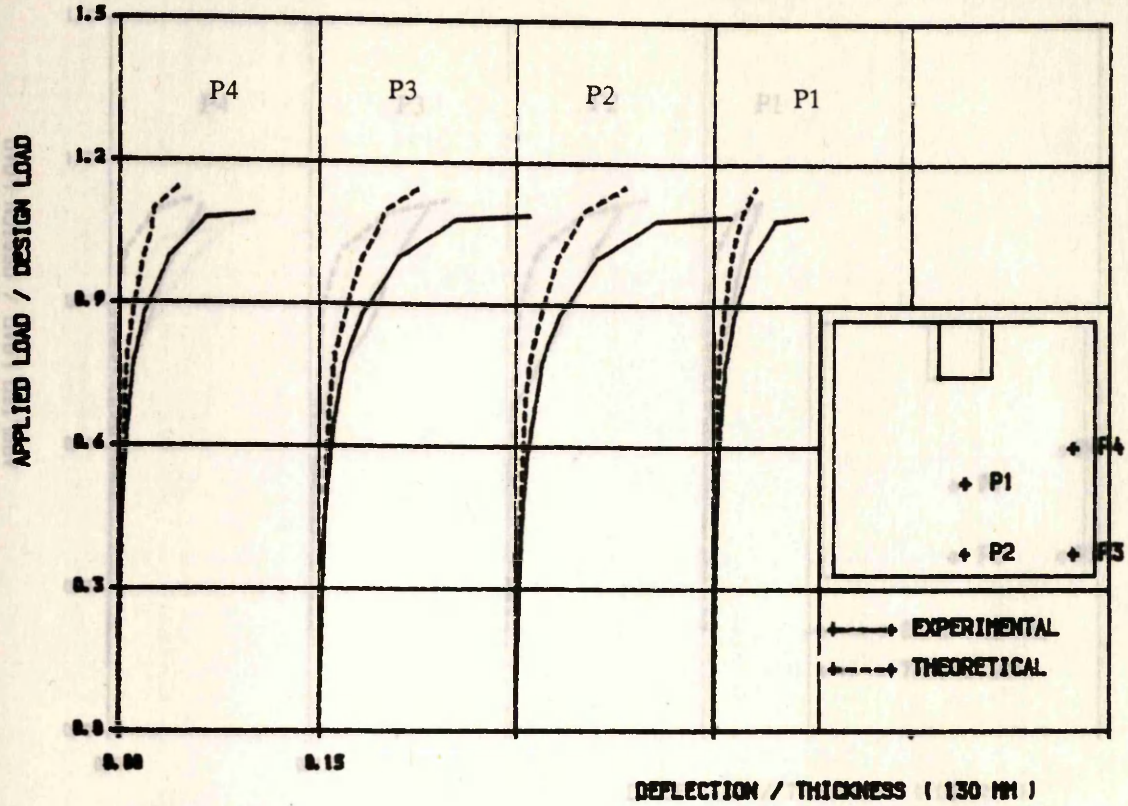

FIG. (8. 18) A : LOAD-DEFLECTION CURVES OF MODEL MS1.

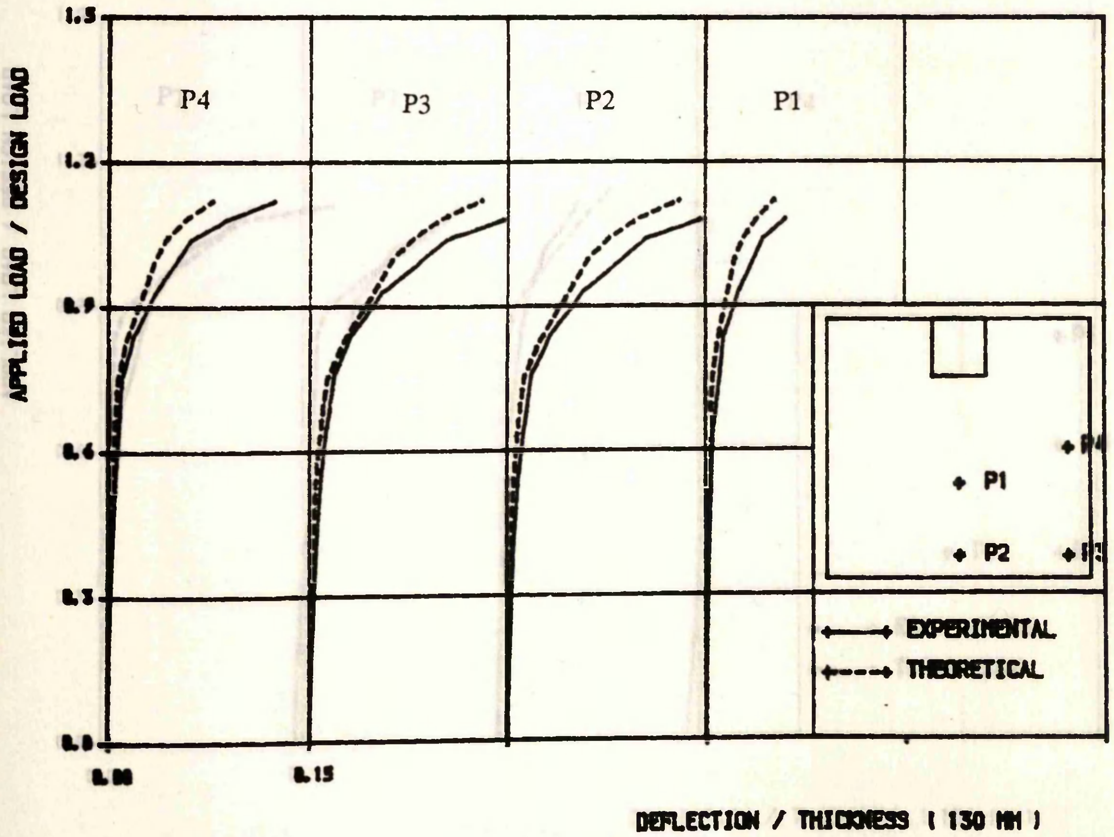

FIG. (8. 18) B : LOAD-DEFLECTION CURVES OF MODEL MS2.

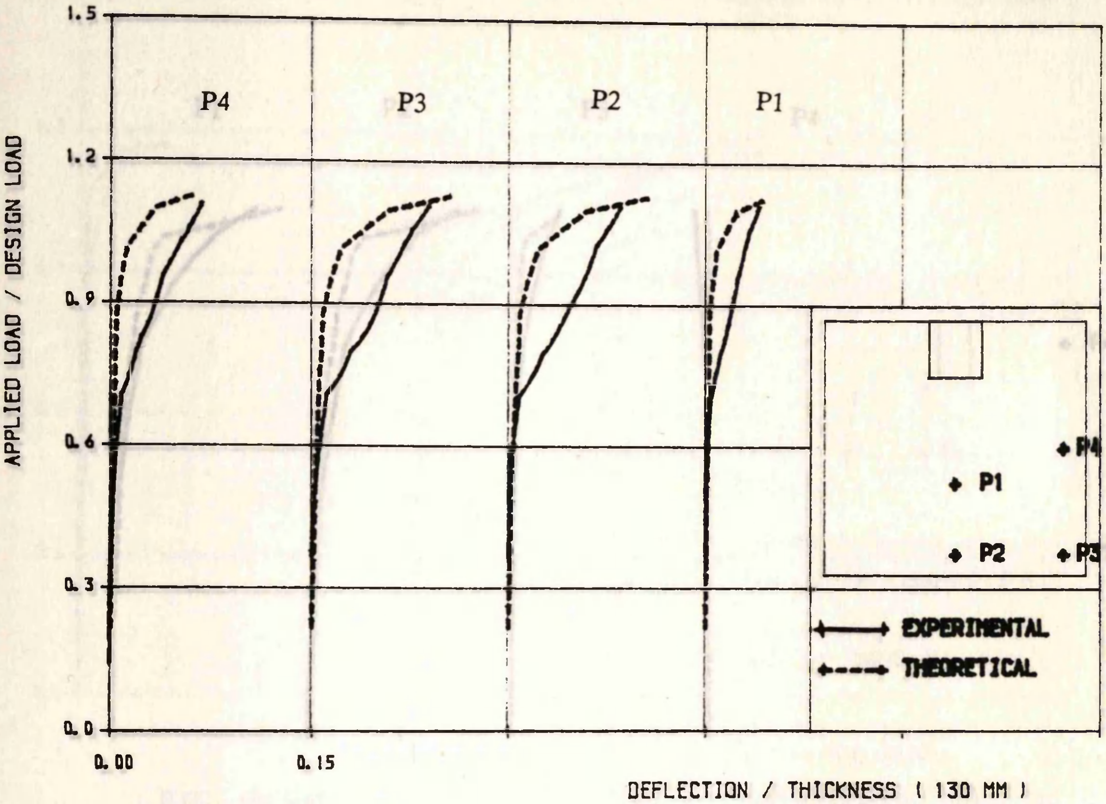

FIG. (8.19). LOAD-DEFLECTION CURVES OF MODEL MS3.

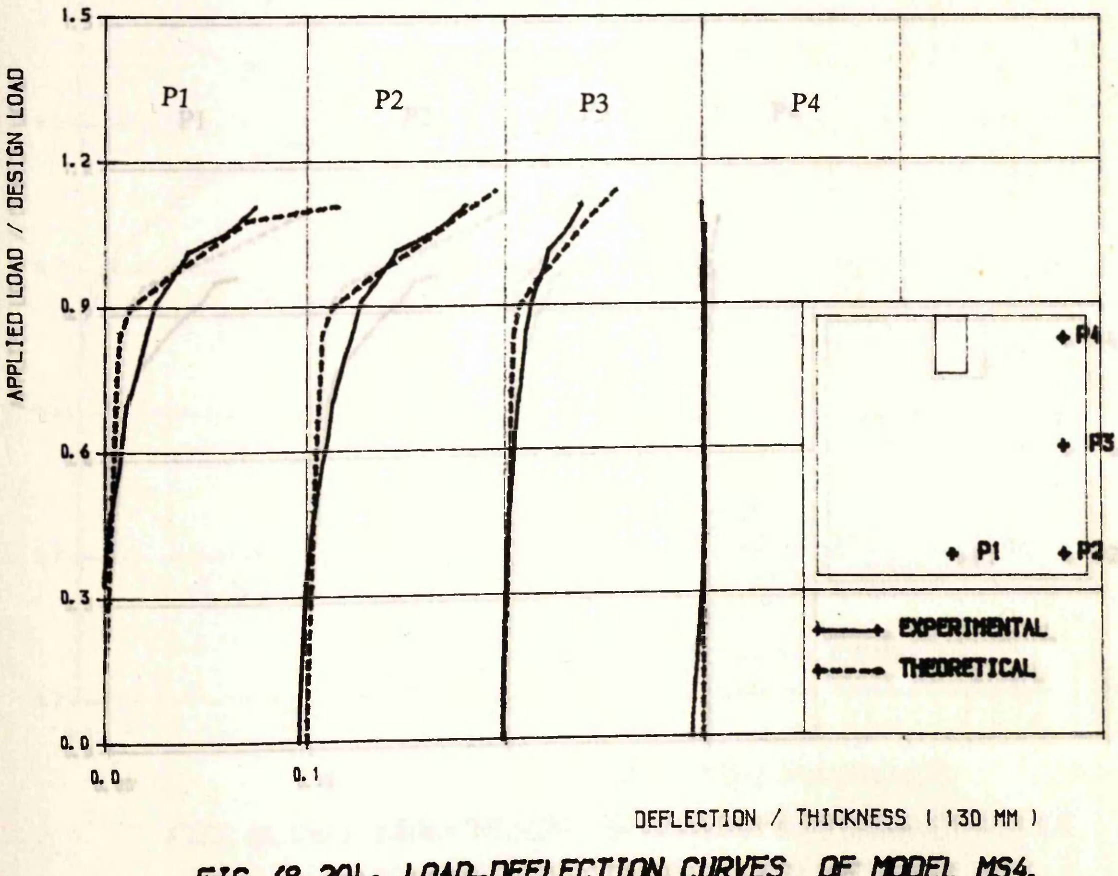

FIG. (8.20). LOAD-DEFLECTION CURVES OF MODEL MS4.

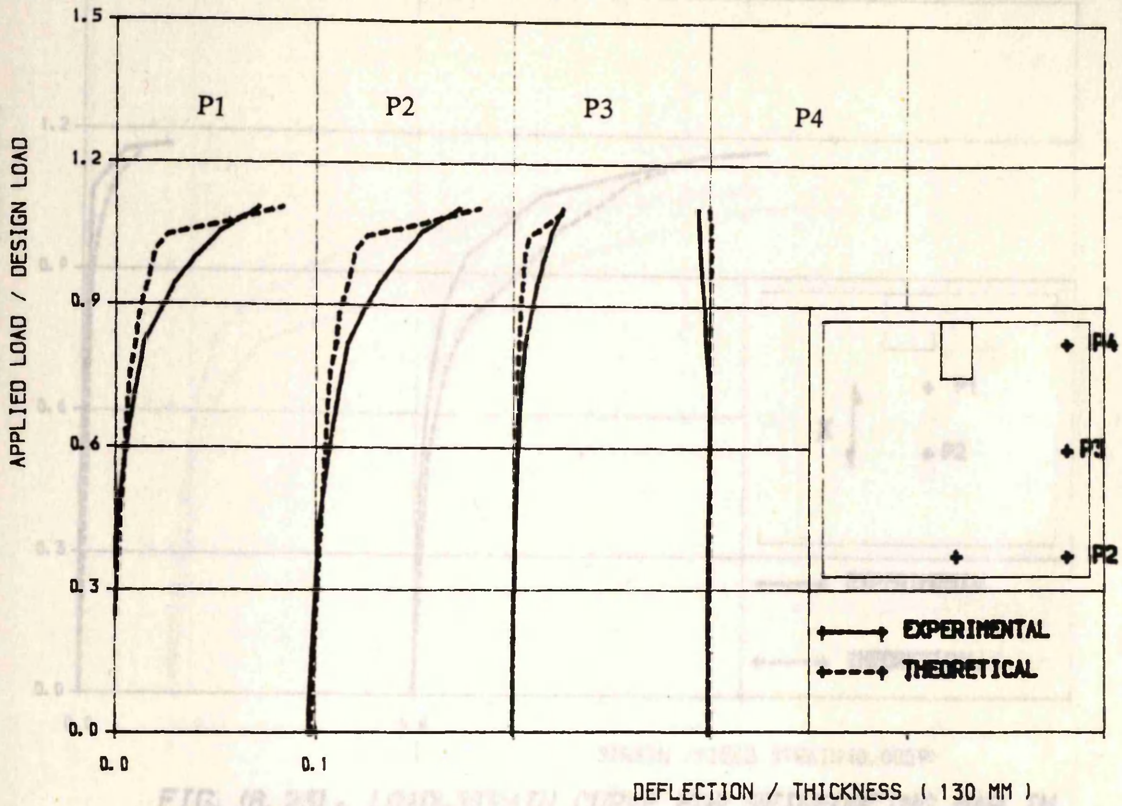

FIG. (8.21) : LOAD-DEFLECTION CURVES OF MODEL MS5.

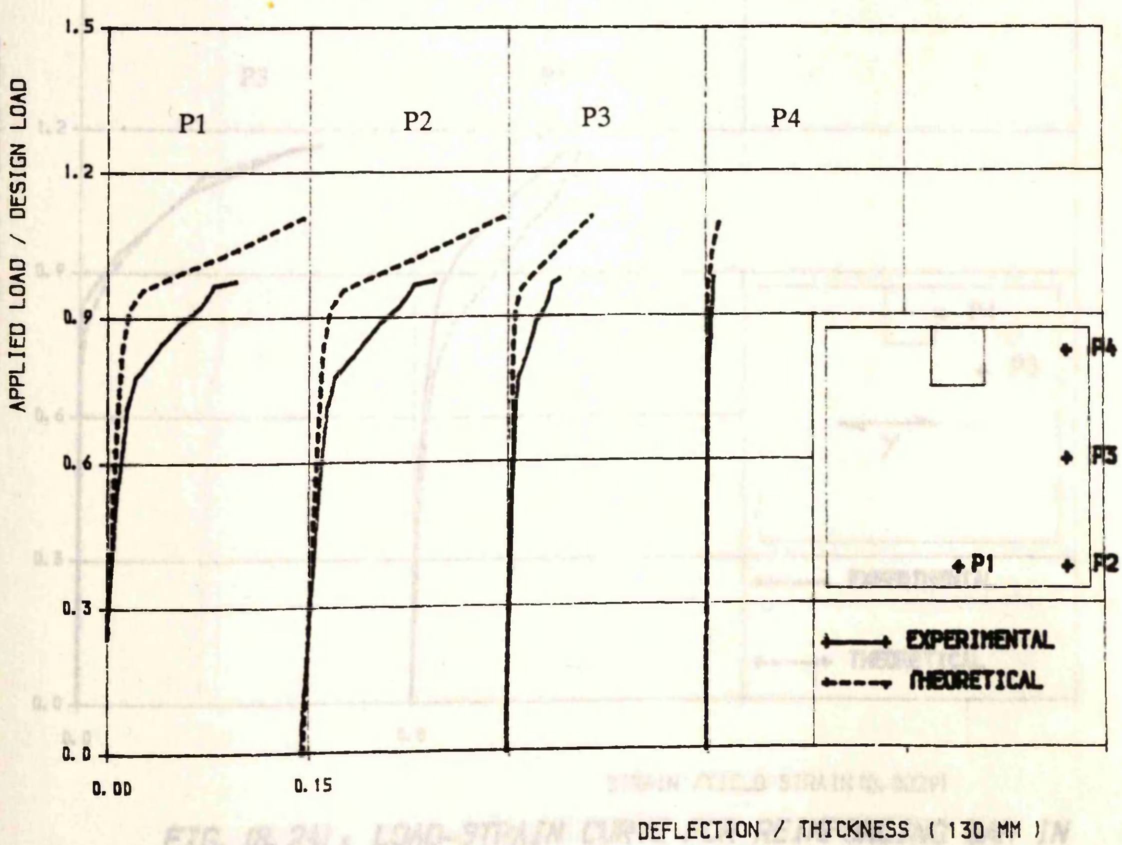

FIG. (8.22) : LOAD-DEFLECTION CURVES OF MODEL MS6.

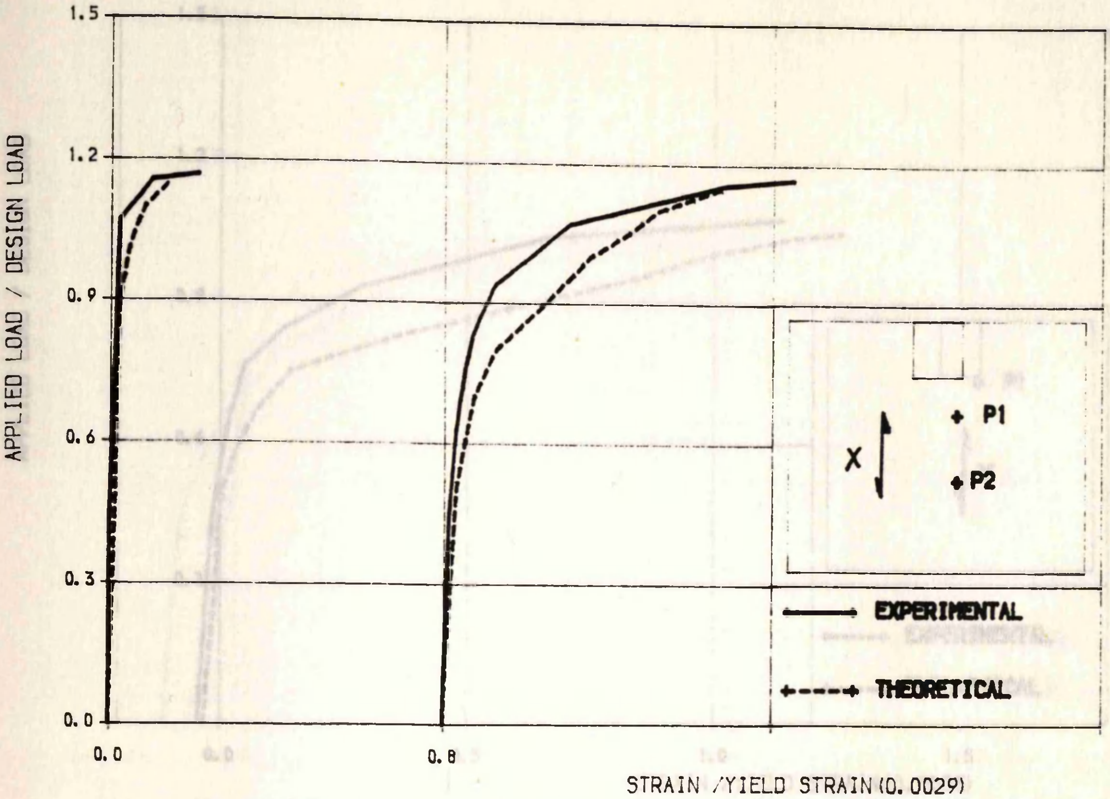

FIG. (8.23). LOAD-STRAIN CURVE FOR REINFORCING BAR IN X-DIRECTION FOR MODEL MS1.

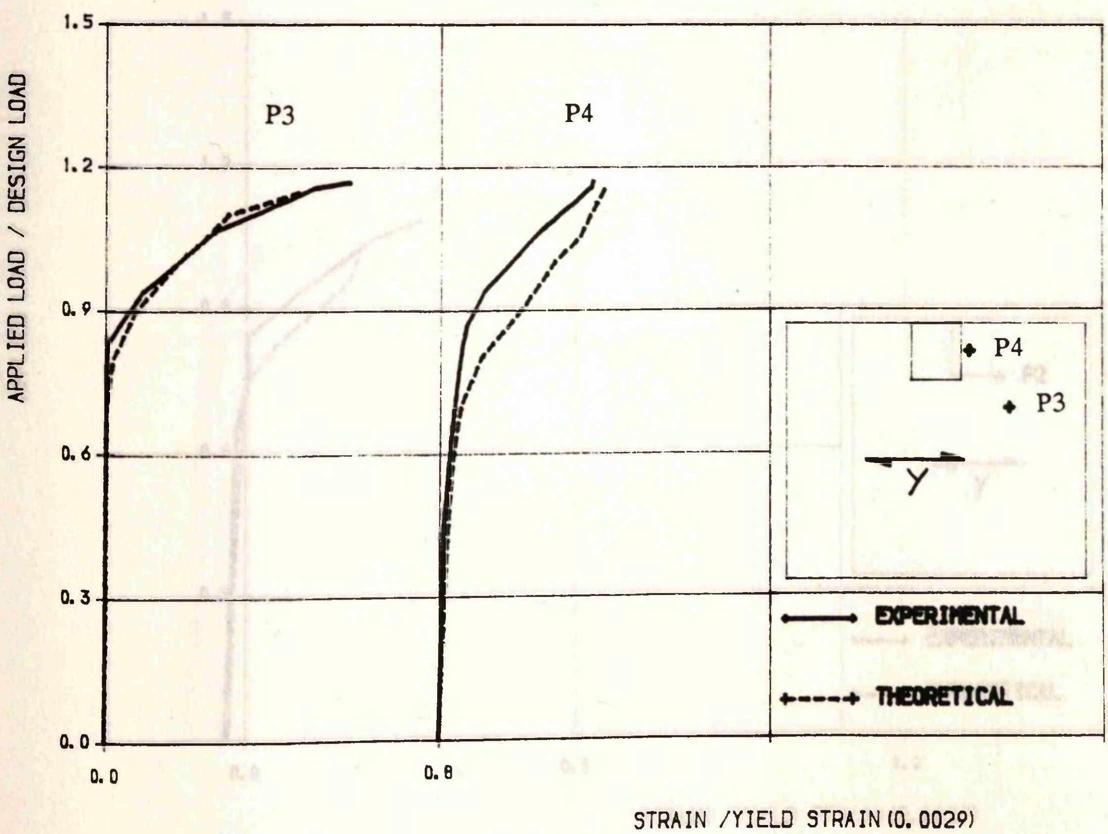

FIG. (8.24). LOAD-STRAIN CURVE FOR REINFORCING BAR IN Y-DIRECTION FOR MODEL MS1.

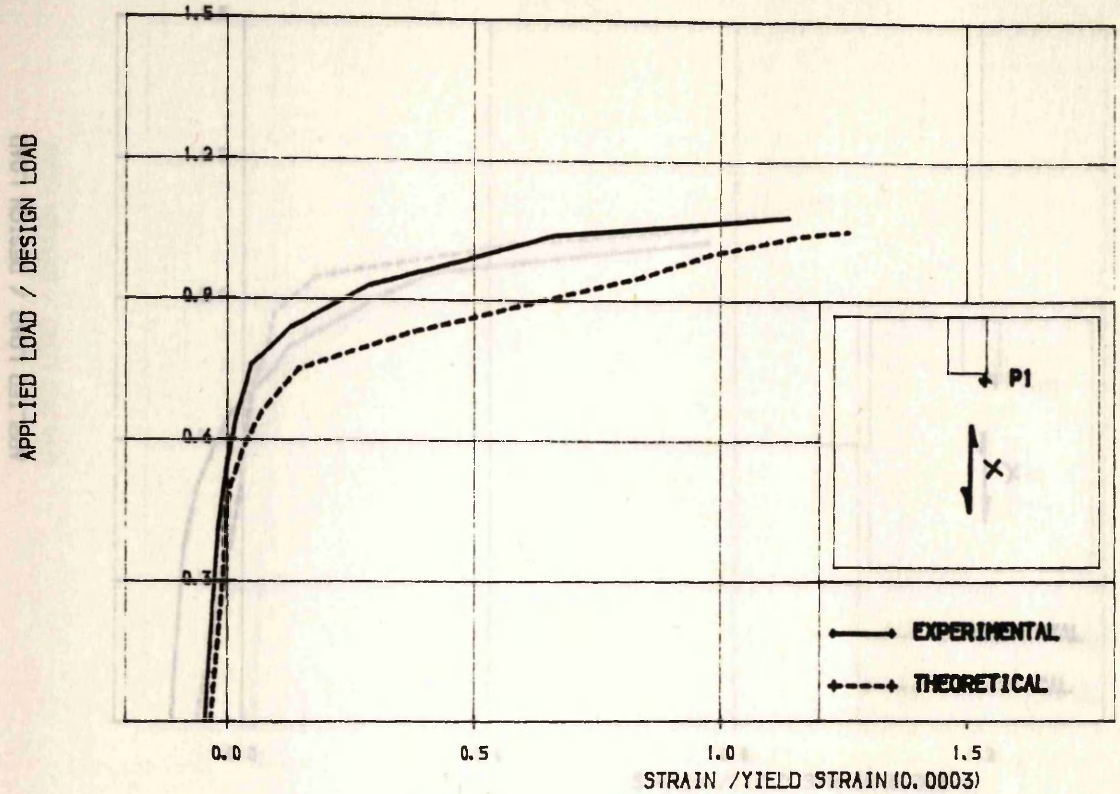

FIG. (8.25) : LOAD-STRAIN CURVE FOR REINFORCING BAR IN X-DIRECTION FOR MODEL MS2.

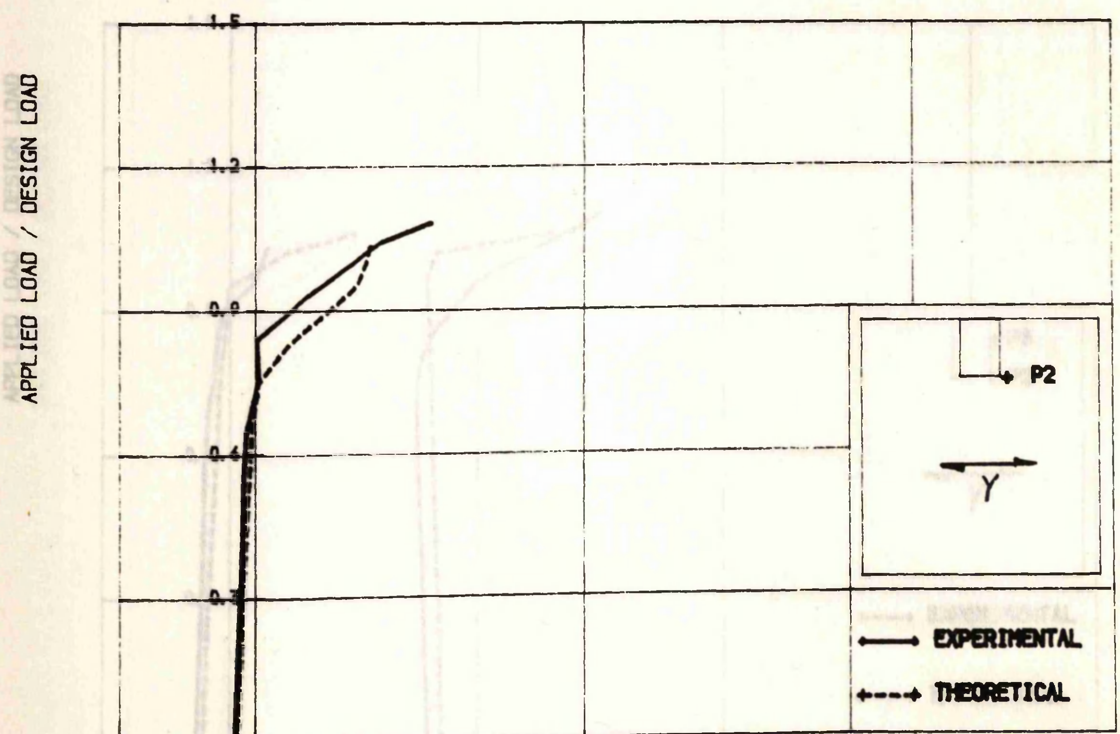

FIG. (8.26) : LOAD-STRAIN CURVE FOR REINFORCING BAR IN Y-DIRECTION FOR MODEL MS2.

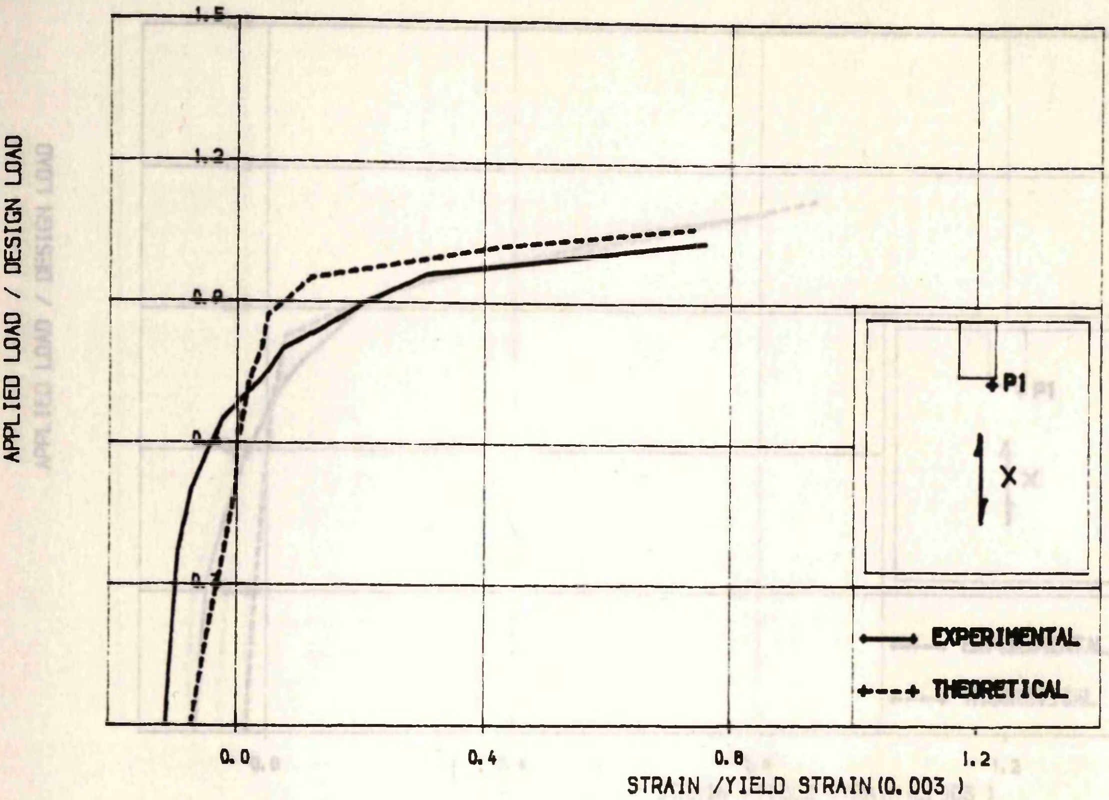

FIG. (8.27) : LOAD-STRAIN CURVES OF REINFORCING BAR IN X- DIRECTION FOR MODEL MS3.

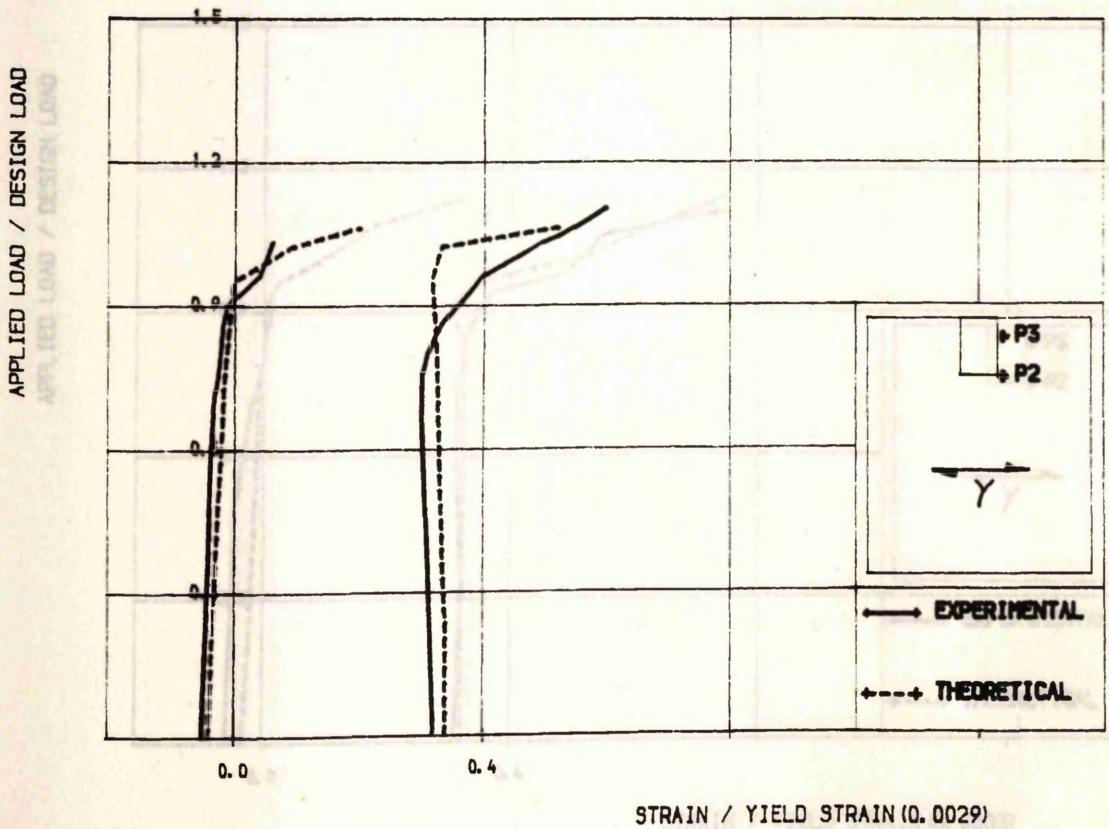

FIG. (8.28) : LOAD-STRAIN CURVES OF REINFORCING BAR IN Y- DIRECTION FOR MODEL MS3.

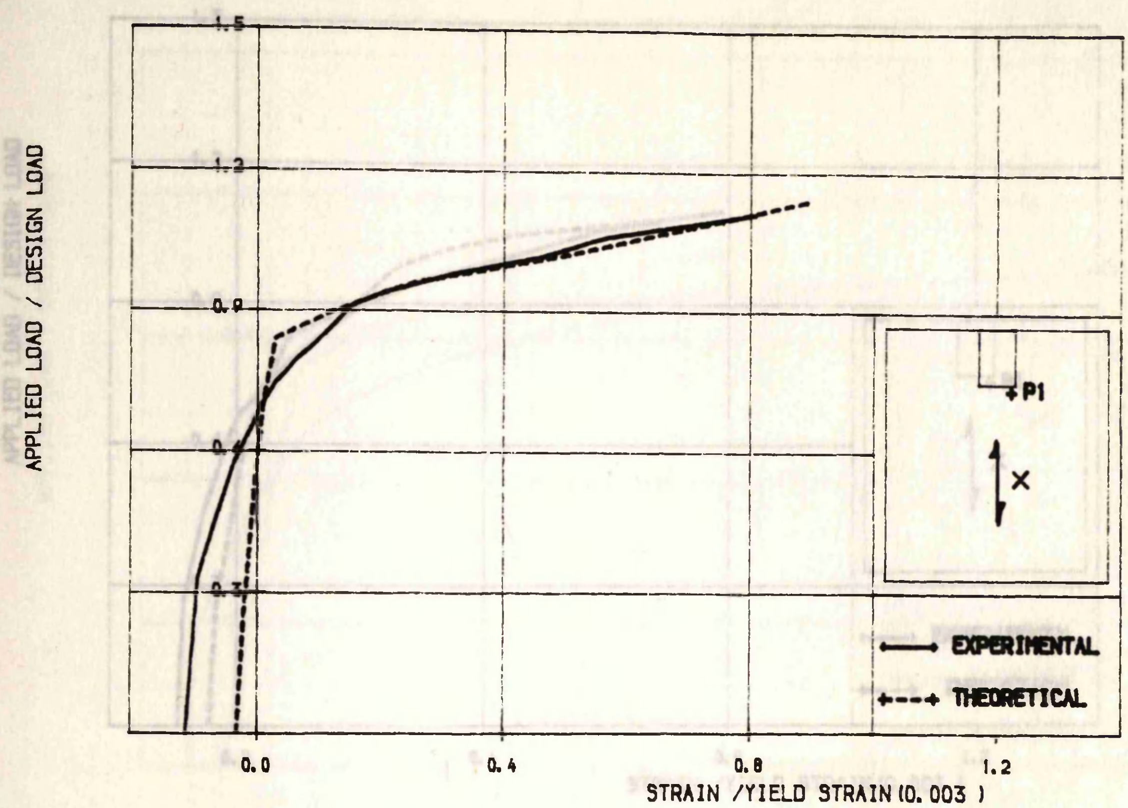

FIG. (8.29) . LOAD-STRAIN CURVES OF REINFORCING BAR IN X- DIRECTION FOR MODEL MS4.

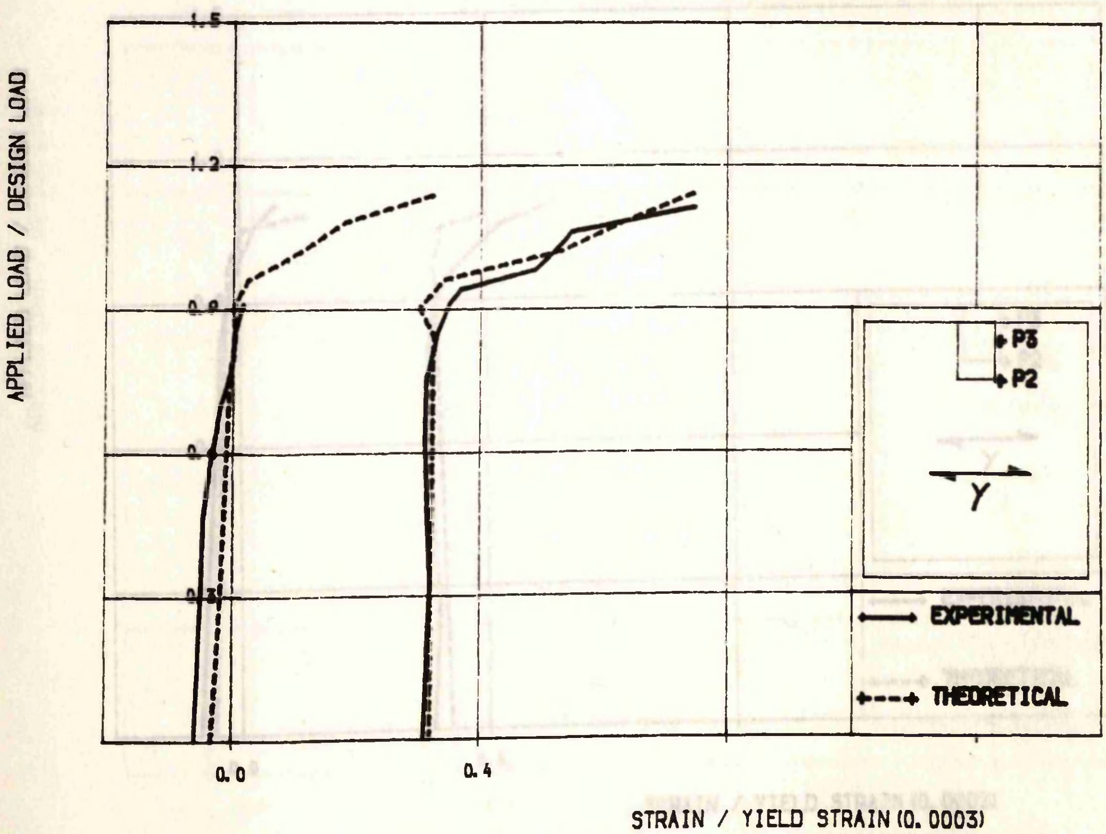

FIG. (8.30) . LOAD-STRAIN CURVES OF REINFORCING BAR IN Y- DIRECTION FOR MODEL MS4.

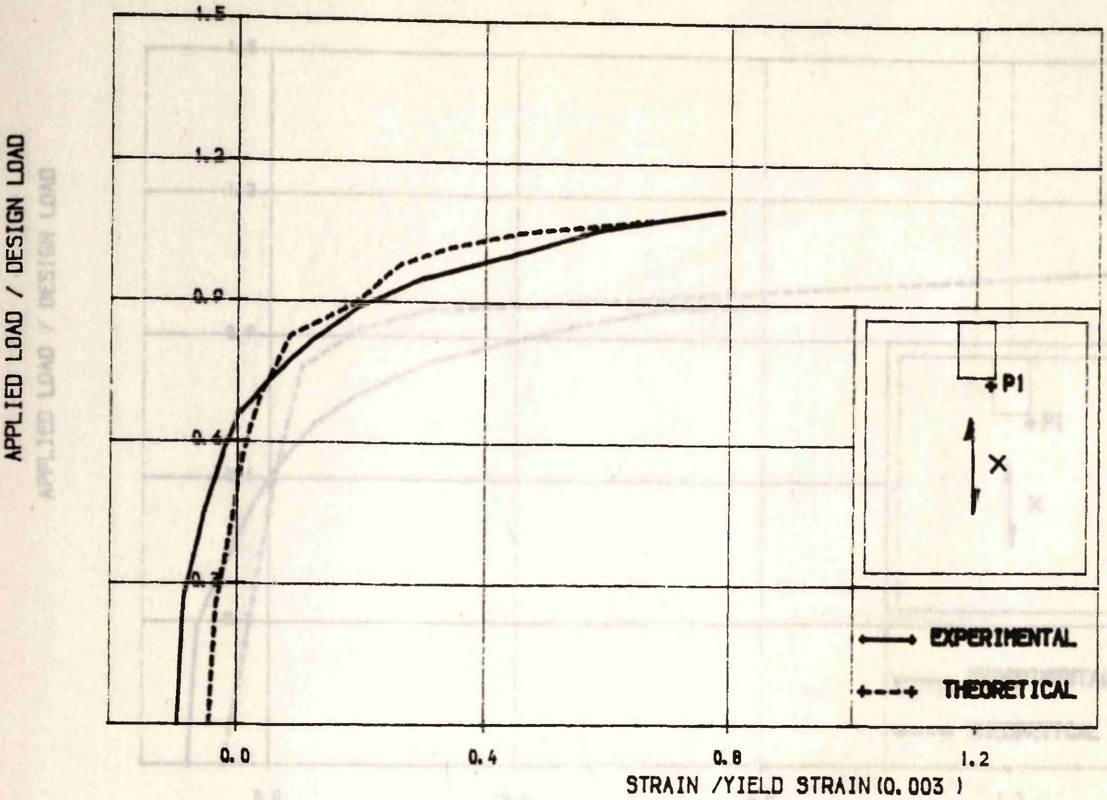

FIG. (8. 31) . LOAD-STRAIN CURVES OF REINFORCING BAR IN X- DIRECTION FOR MODEL MS5.

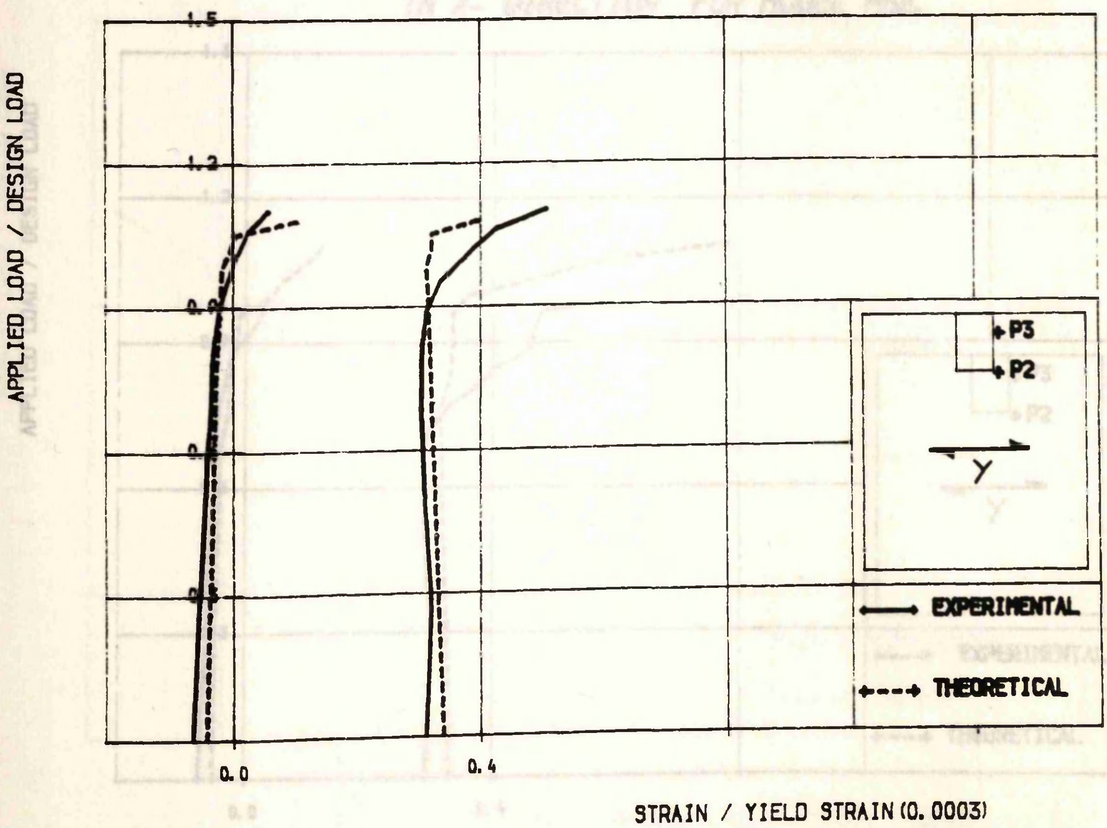

FIG. (8. 32) . LOAD-STRAIN CURVES OF REINFORCING BAR IN Y- DIRECTION FOR MODEL MS5.

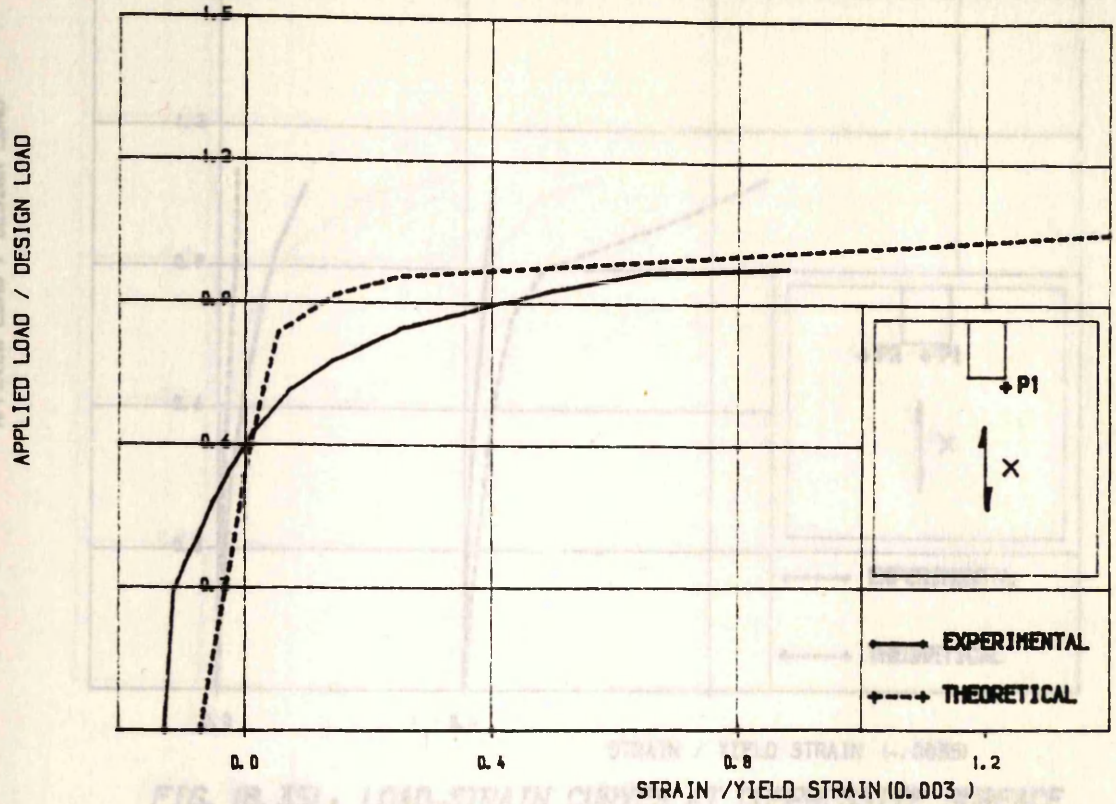

FIG. (8.33) , LOAD-STRAIN CURVES OF REINFORCING BAR IN X- DIRECTION FOR MODEL MS6.

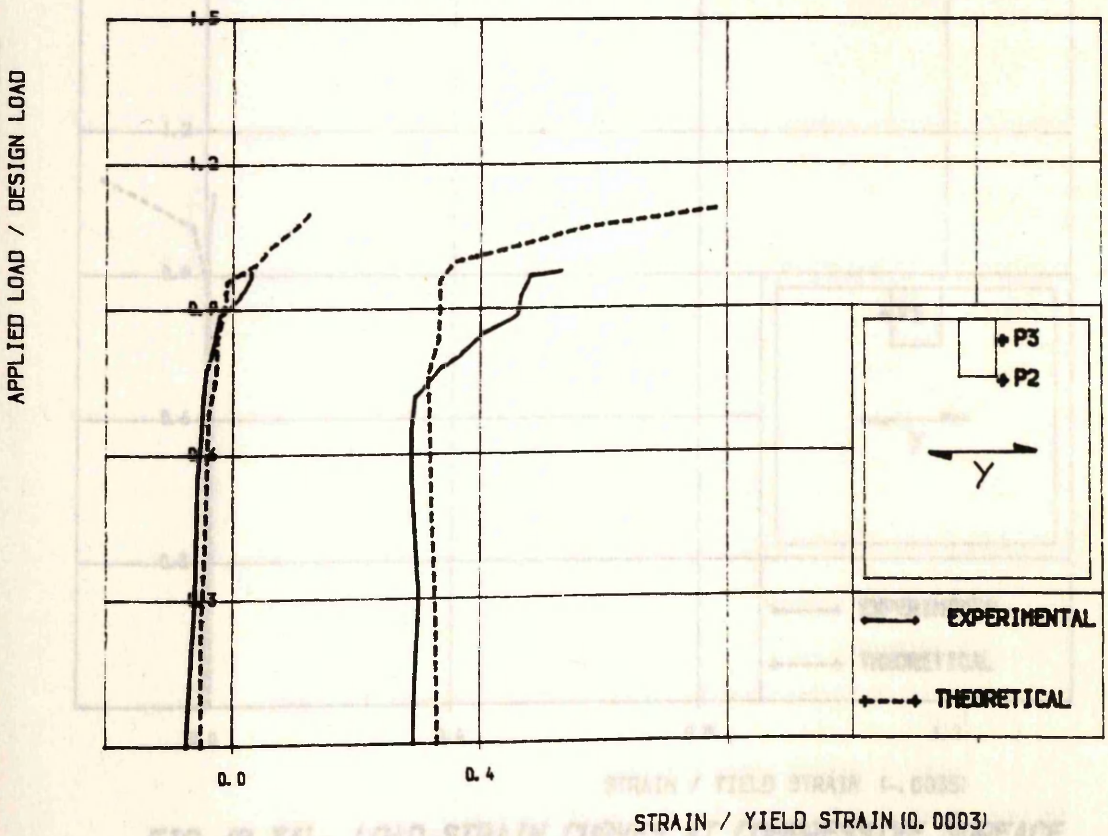

FIG. (8.34) , LOAD-STRAIN CURVES OF REINFORCING BAR IN Y- DIRECTION FOR MODEL MS6.

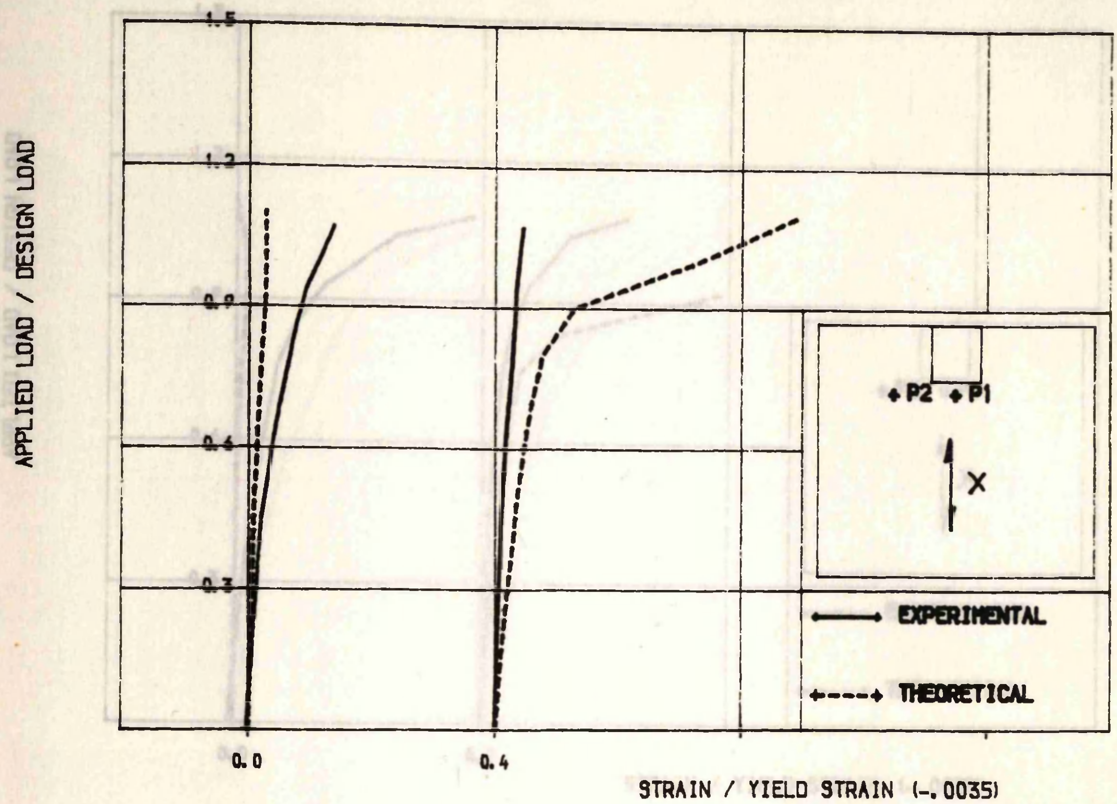

FIG. (8.35) : LOAD-STRAIN CURVES AT COMPRESSIVE SURFACE OF CONCRETE IN X-DIR. FOR MODEL MS1.

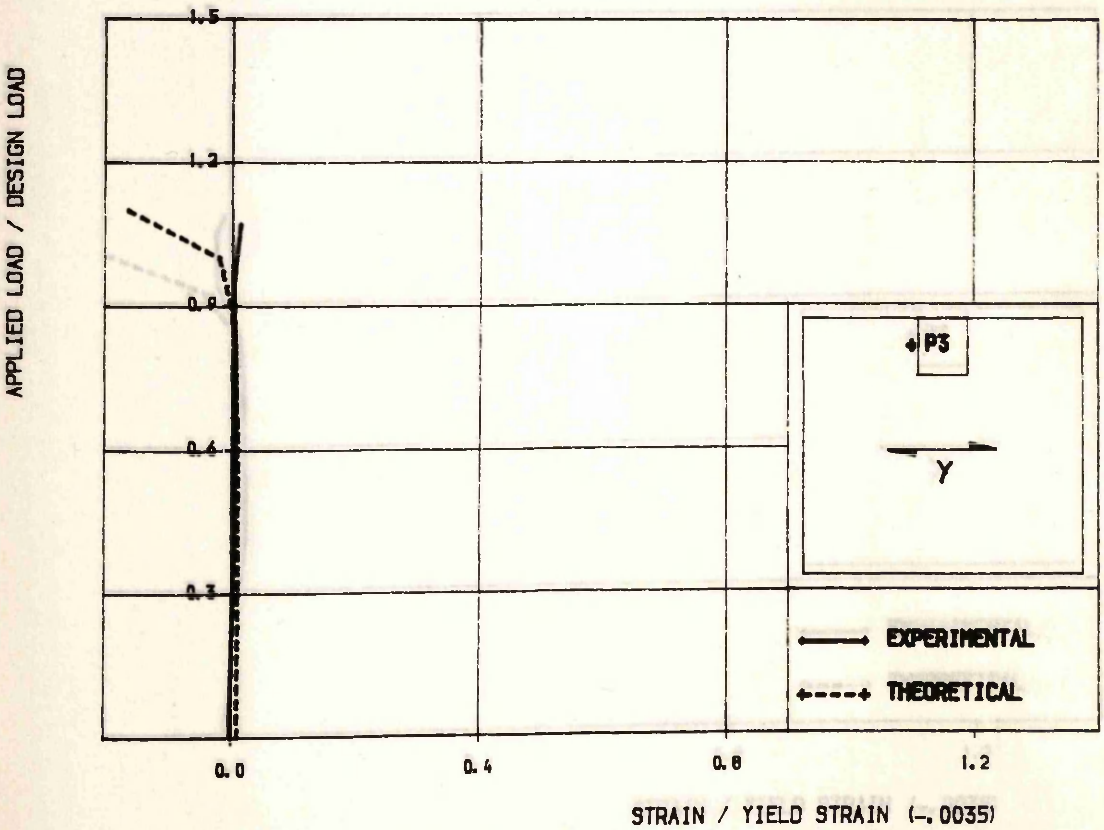

FIG. (8.36) : LOAD-STRAIN CURVES AT COMPRESSIVE SURFACE OF CONCRETE IN Y-DIR. FOR MODEL MS1.

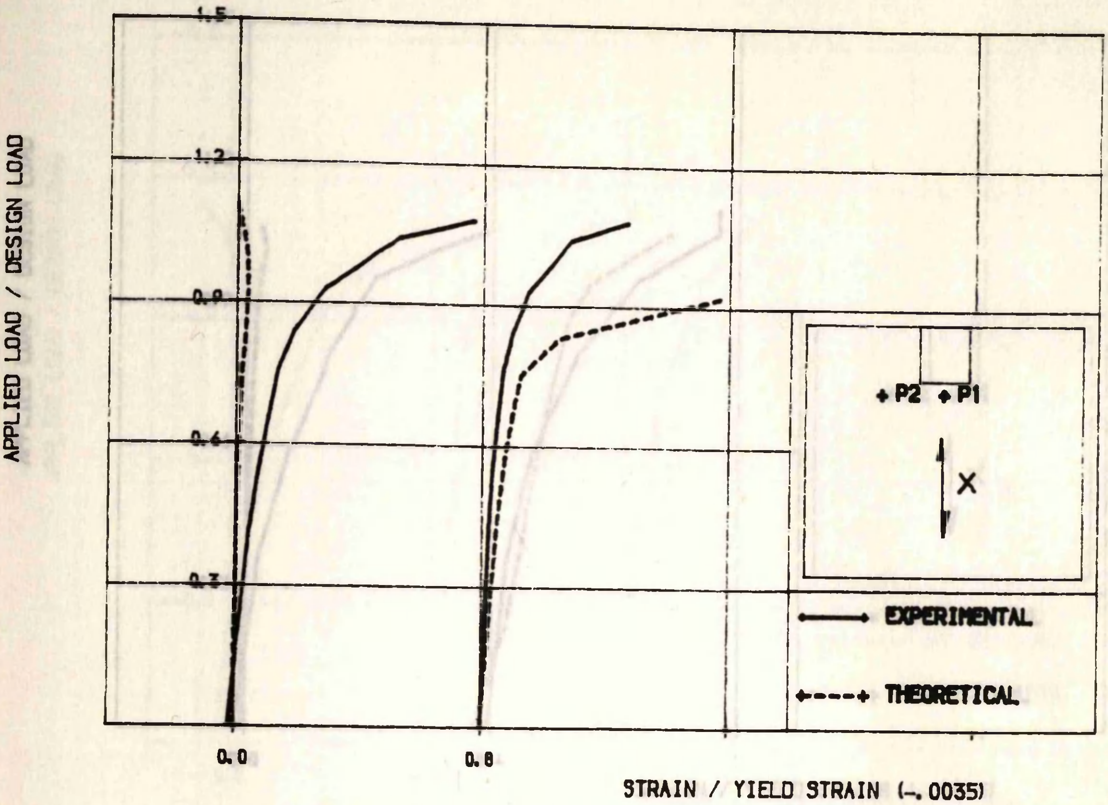

FIG. (8.37): LOAD-STRAIN CURVES AT COMPRESSIVE SURFACE OF CONCRETE IN X-DIR. FOR MODEL MS2.

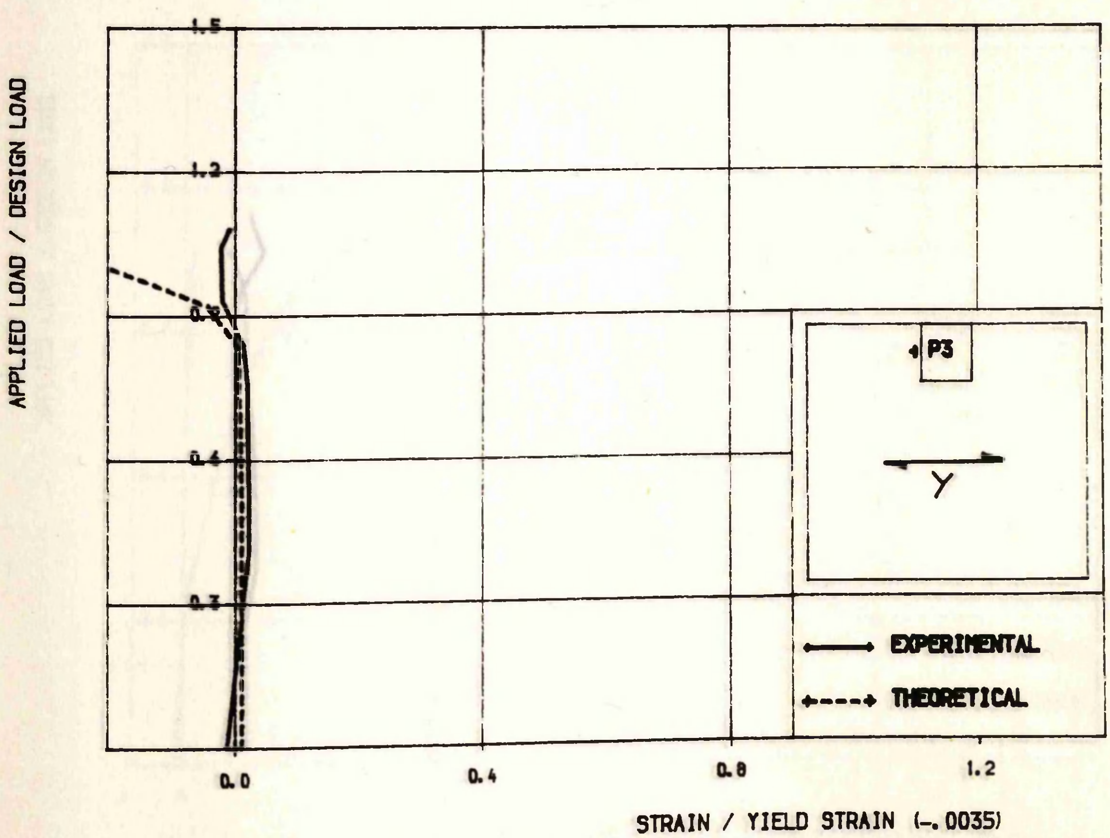

FIG. (8.38): LOAD-STRAIN CURVES AT COMPRESSIVE SURFACE OF CONCRETE IN Y-DIR. FOR MODEL MS2.

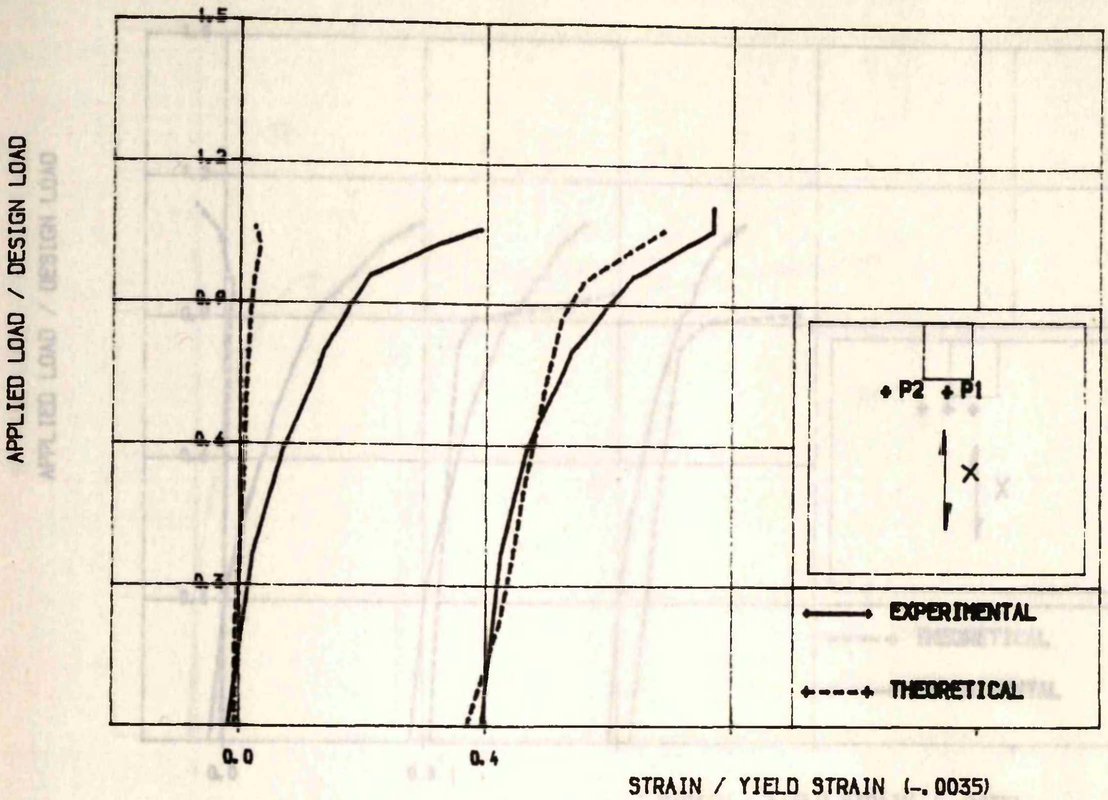

FIG. (8.39) . LOAD-STRAIN CURVES AT COMPRESSIVE SURFACE OF CONCRETE IN X-DIR. FOR MODEL MS3.

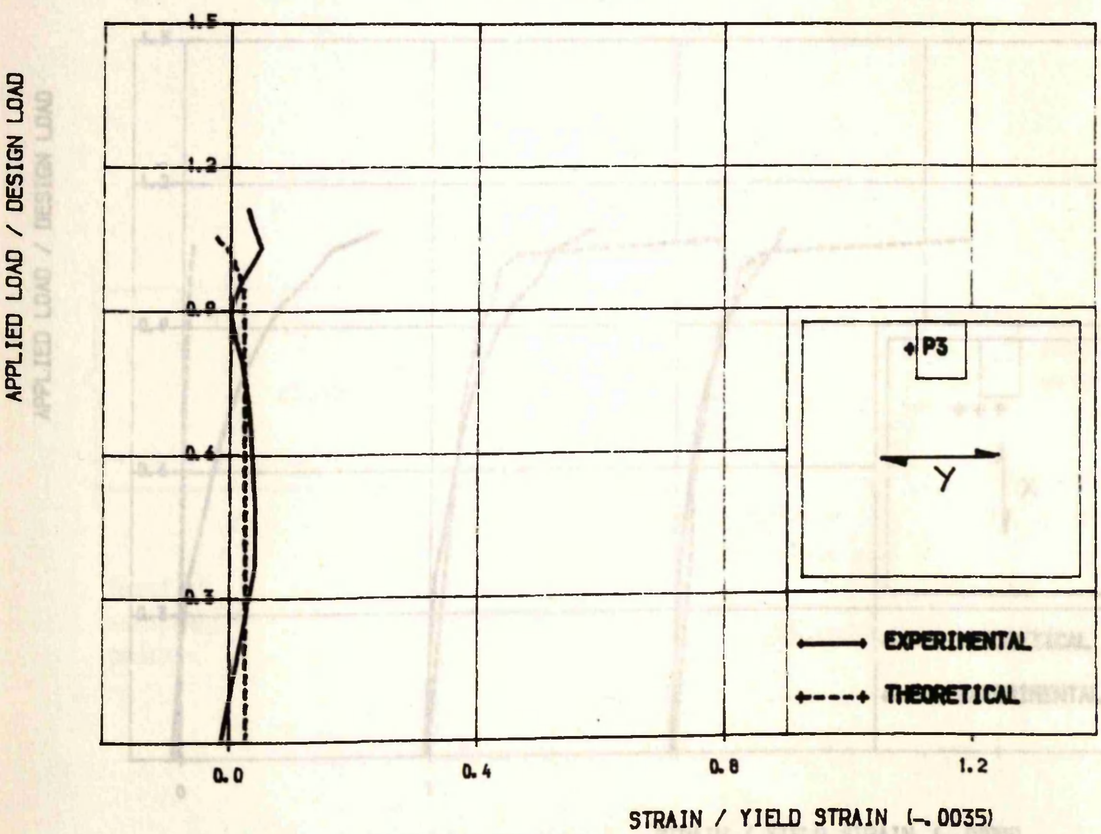

FIG. (8.40) . LOAD-STRAIN CURVES AT COMPRESSIVE SURFACE OF CONCRETE IN Y-DIR. FOR MODEL MS3.

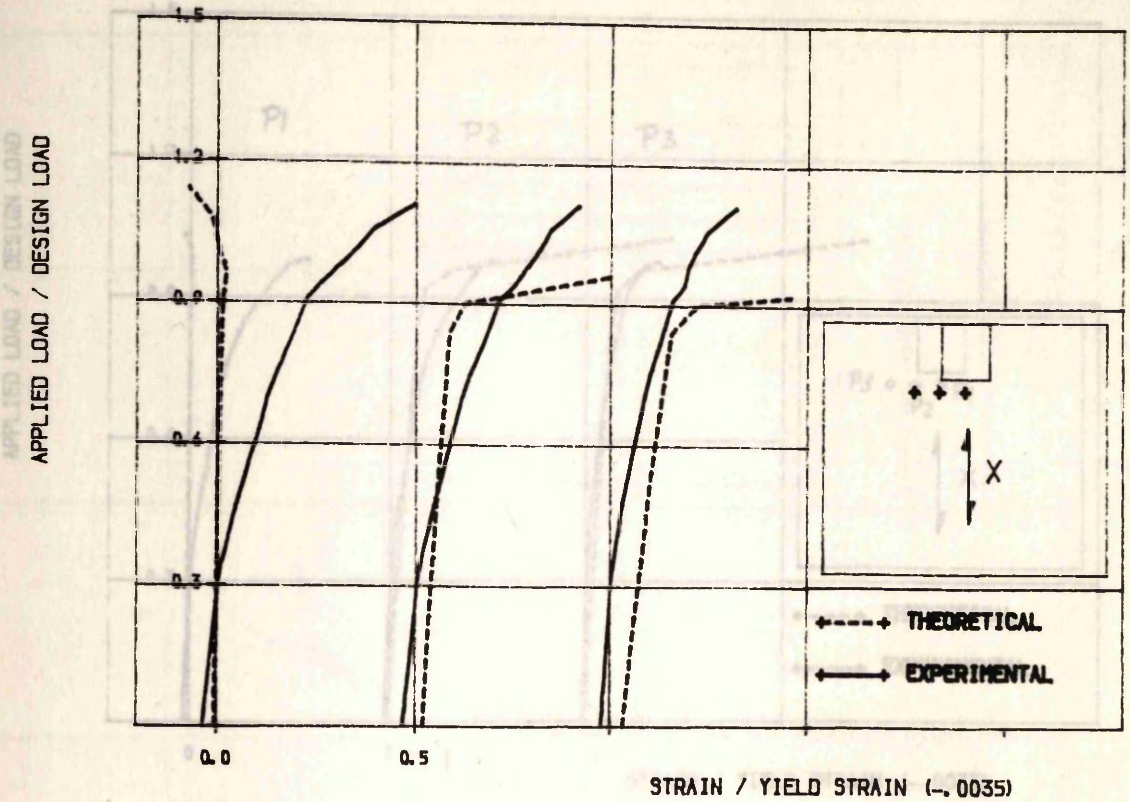

FIG. (8. 41) : LOAD-STRAIN CURVES AT COMPRESSIVE SURFACE OF CONCRETE IN X-DIR. FOR MODEL MS4.

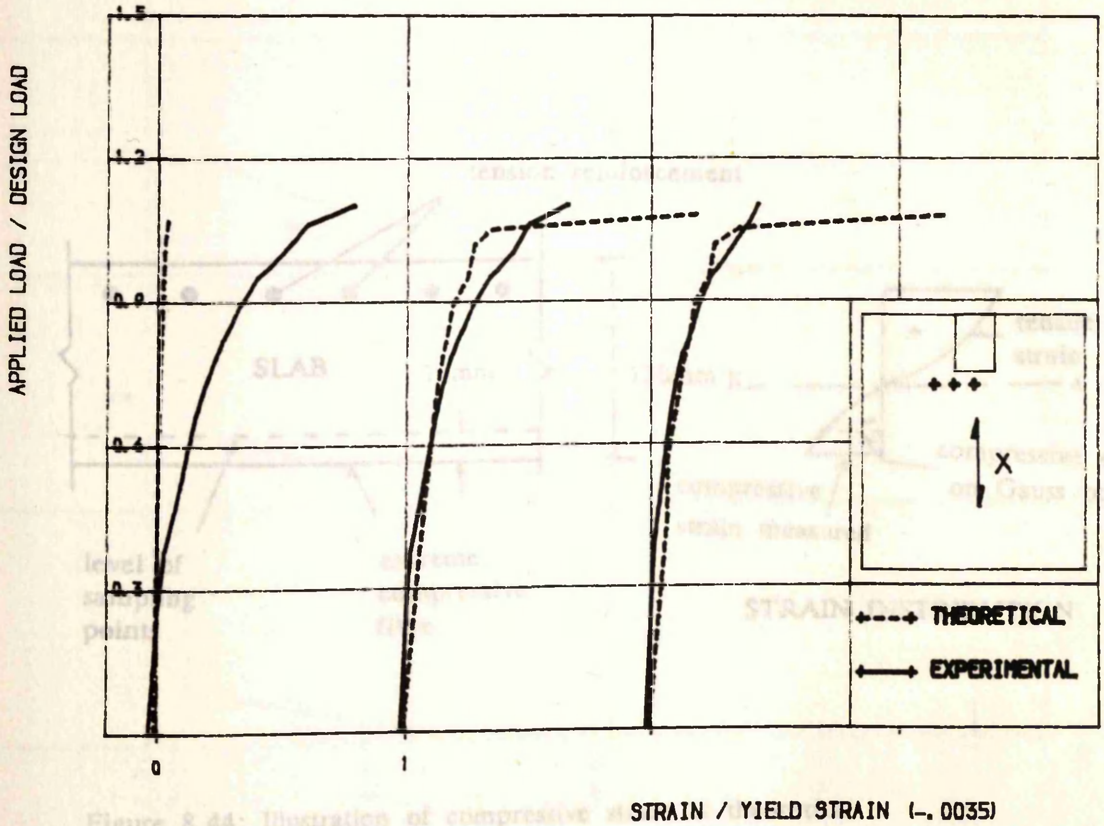

FIG. (8. 42) : LOAD-STRAIN CURVES AT COMPRESSIVE SURFACE OF CONCRETE IN X-DIR. FOR MODEL MS5.

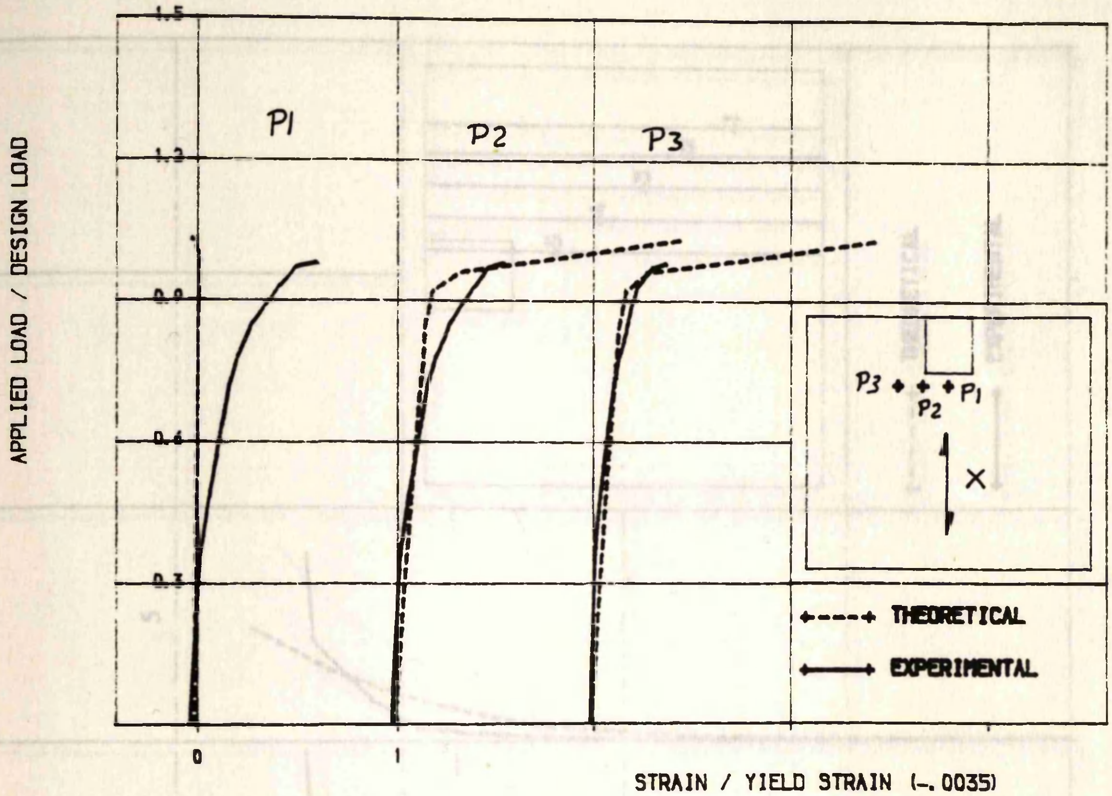

FIG. (8.43): LOAD-STRAIN CURVES AT COMPRESSIVE SURFACE OF CONCRETE IN X-DIR. FOR MODEL MS6.

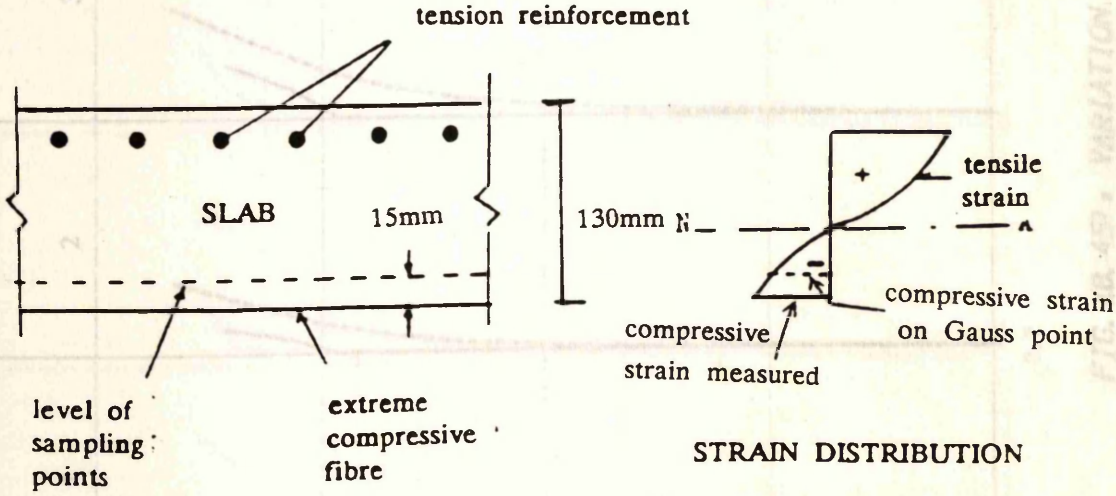

Figure 8.44: Illustration of compressive strain at theoretical sampling points.

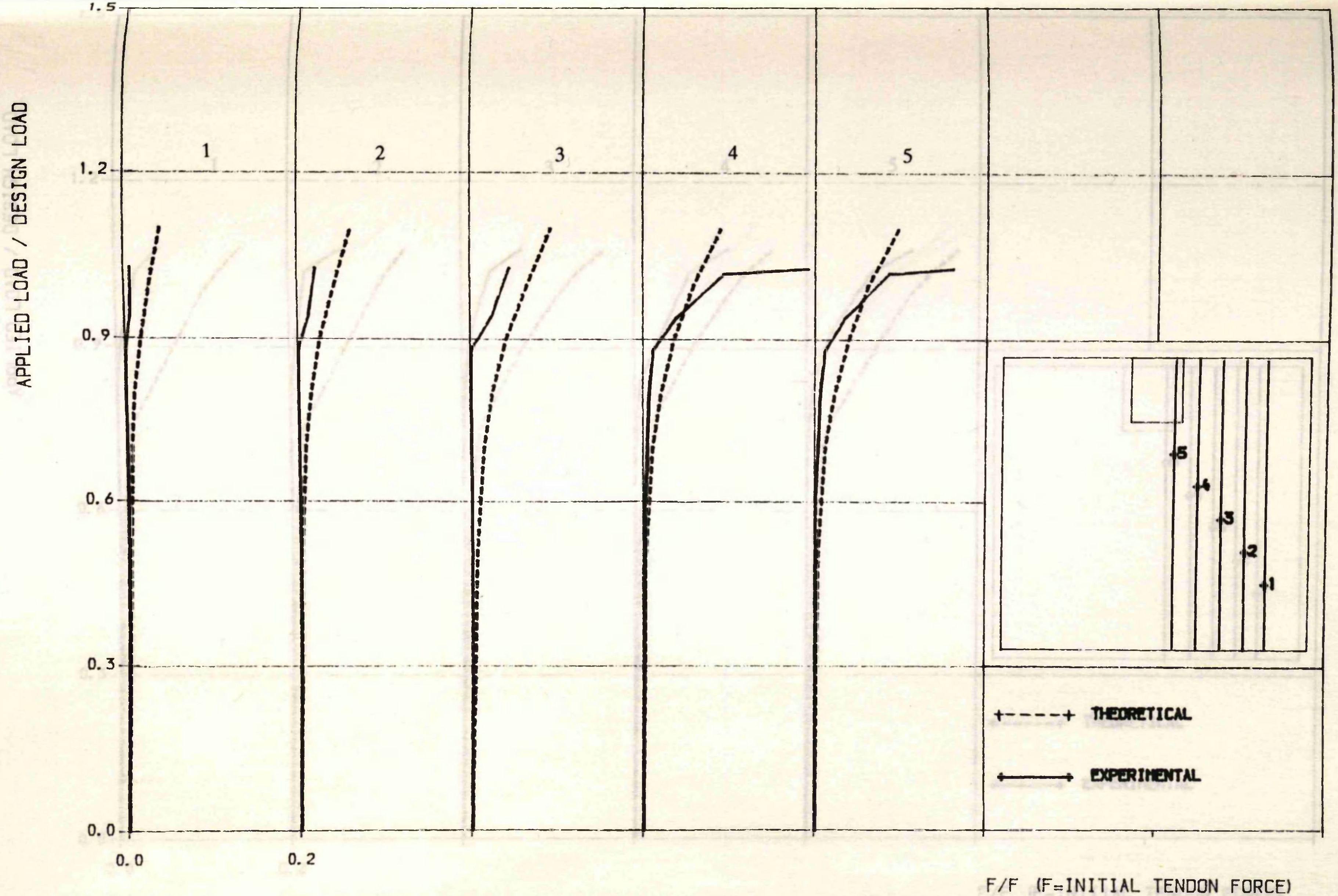

FIG. (8.45). VARIATION IN TENDON FORCE IN X-DIRECTION VERSUS APPLIED LOAD FOR MODEL MS1.

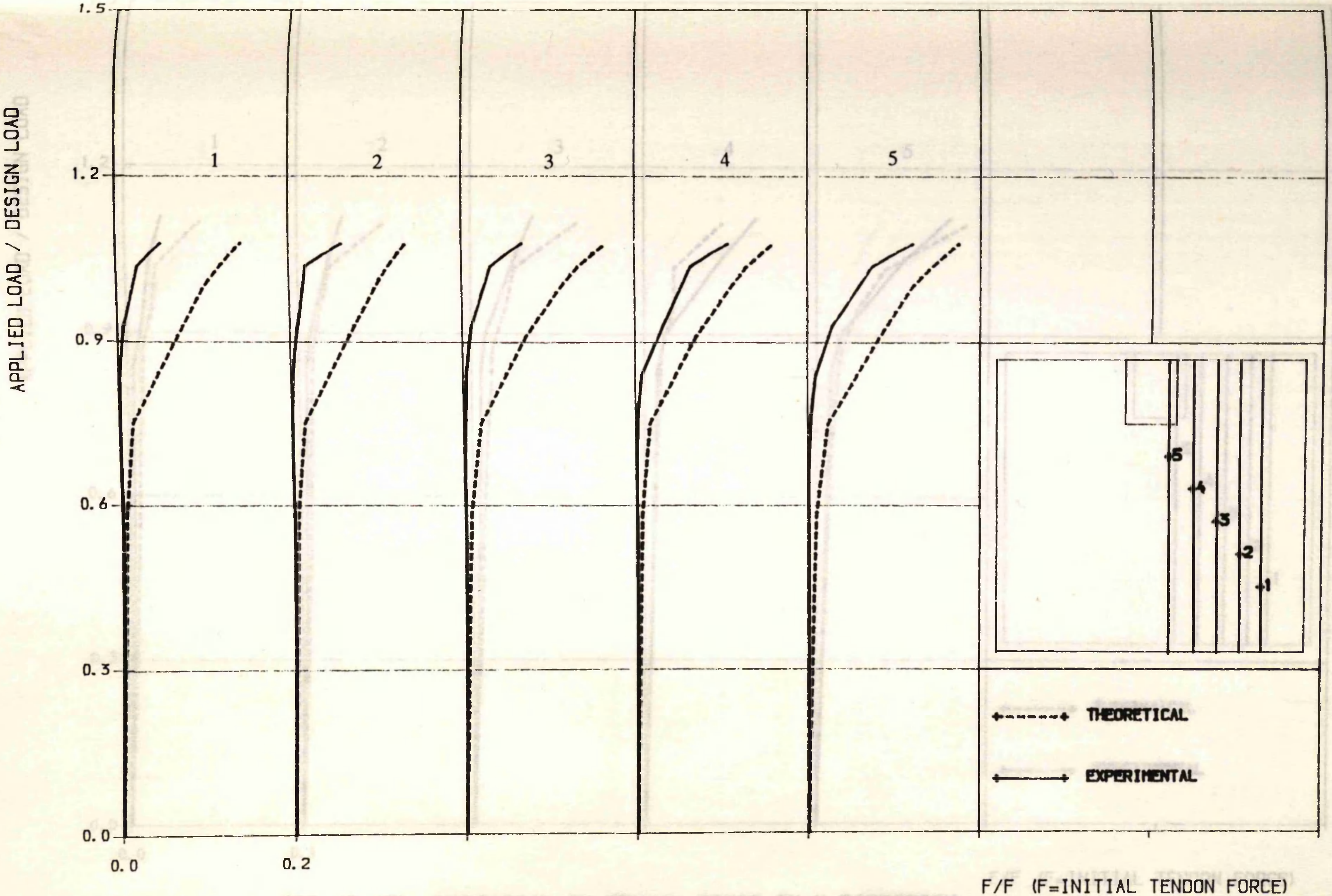

FIG. (8.46). VARIATION IN TENDON FORCE IN X-DIRECTION VERSUS APPLIED LOAD FOR MODEL MS2.

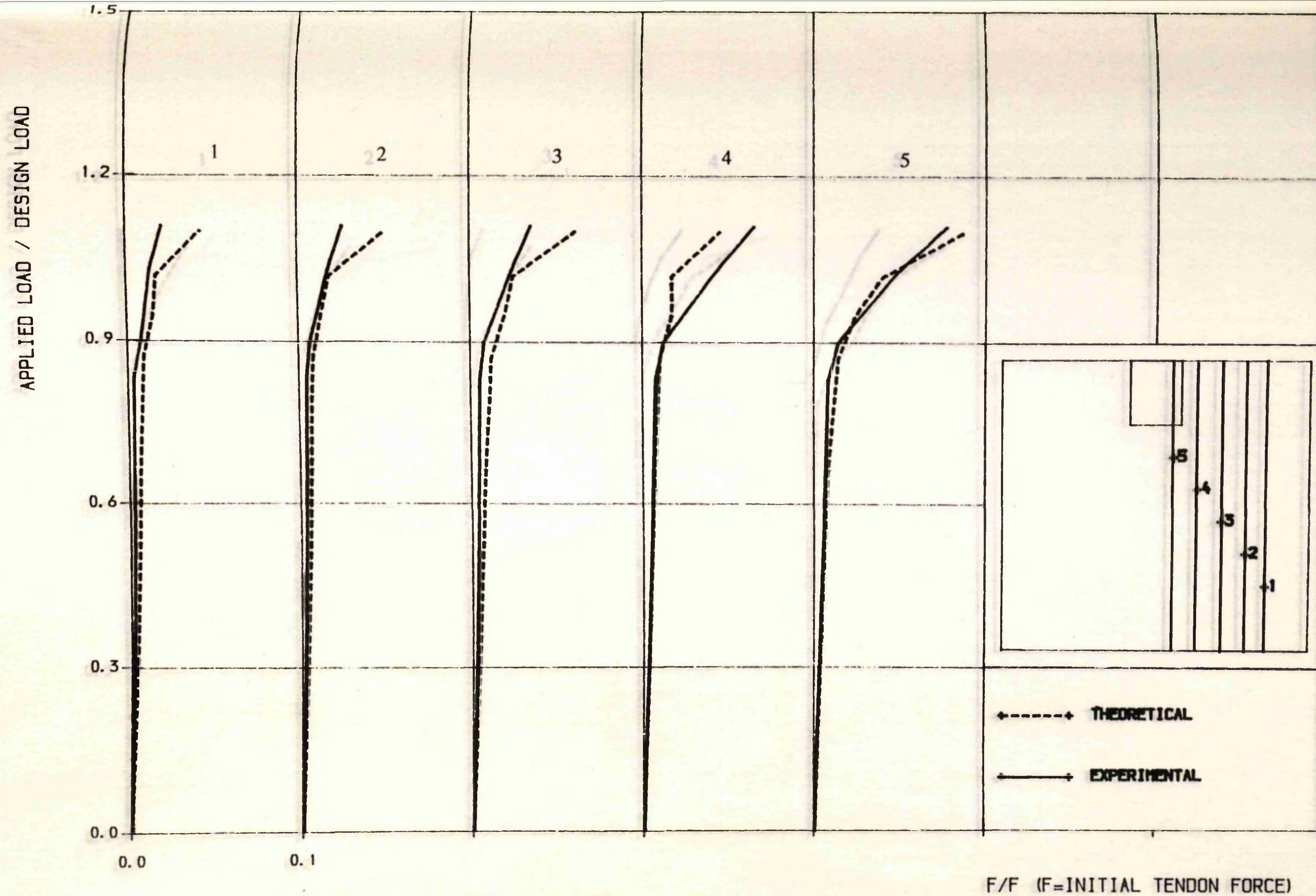

FIG. (8.47). VARIATION IN TENDON FORCE IN X-DIRECTION VERSUS APPLIED LOAD FOR MODEL MS3.

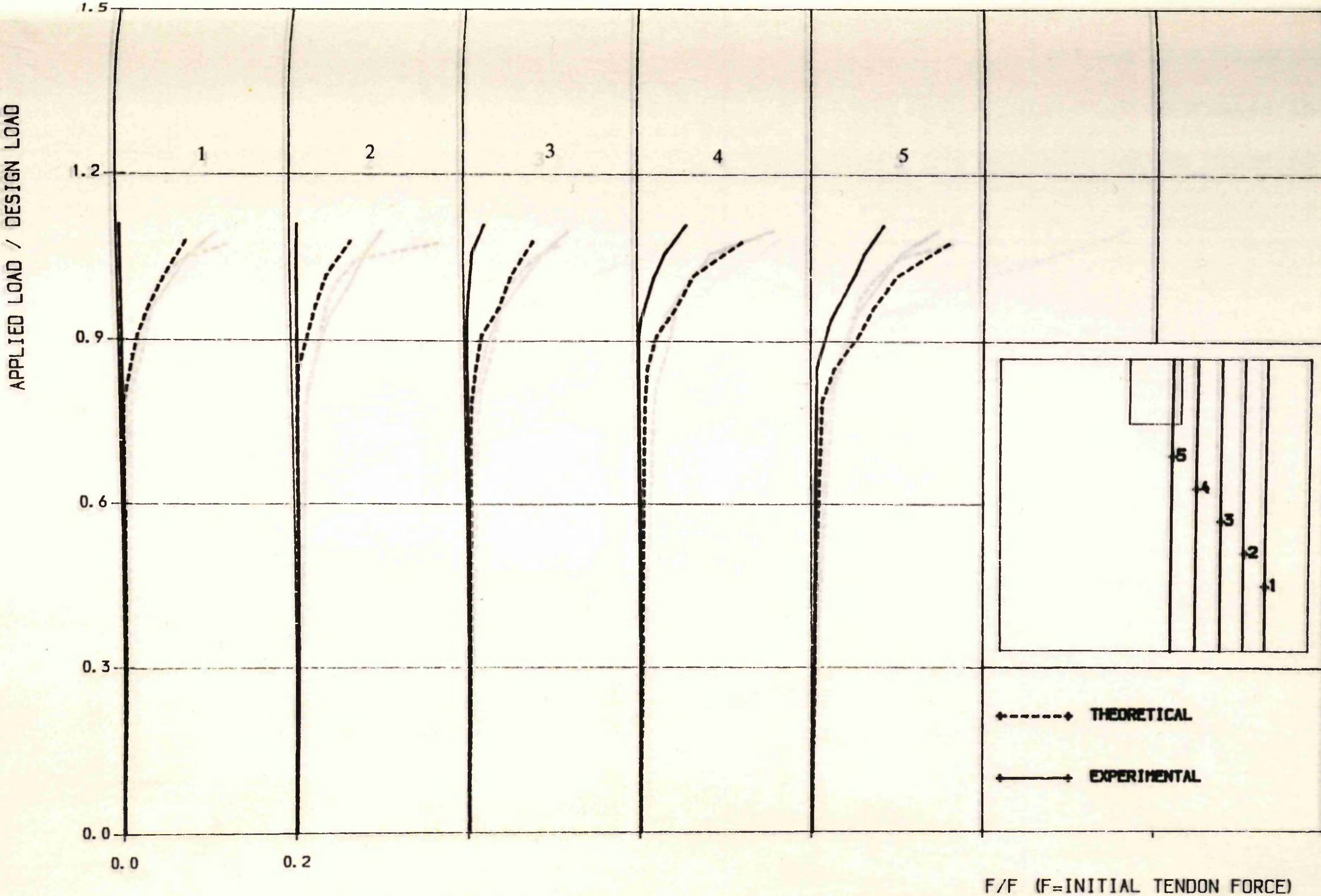

FIG. (8.48). VARIATION IN TENDON FORCE IN X-DIRECTION VERSUS APPLIED LOAD FOR MODEL MS4

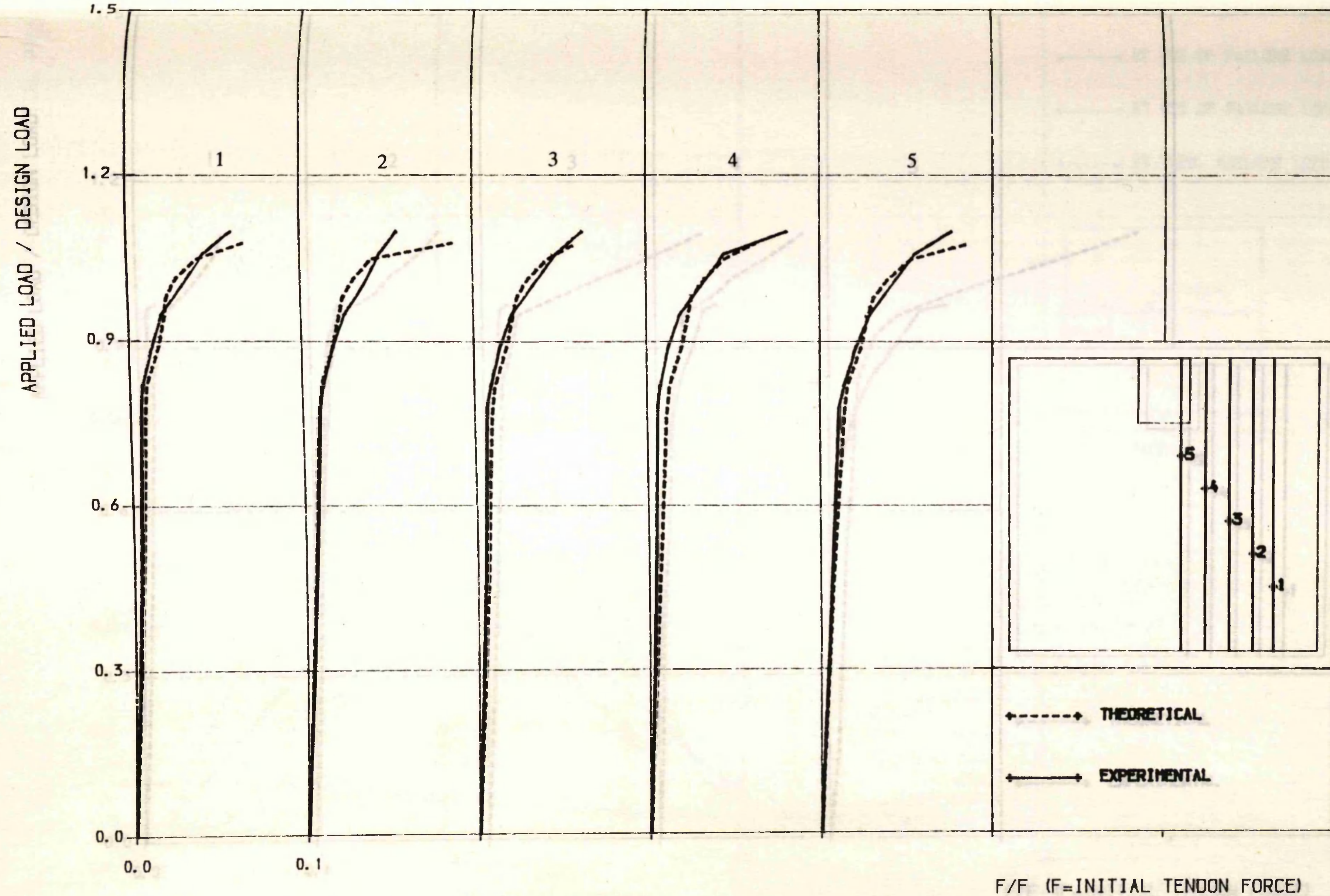

FIG. (8.49). VARIATION IN TENDON FORCE IN X-DIRECTION VERSUS APPLIED LOAD FOR MODEL MS5.

FIG. (8.50). VARIATION IN TENDON FORCE IN X-DIRECTION VERSUS APPLIED LOAD FOR MODEL MS6.

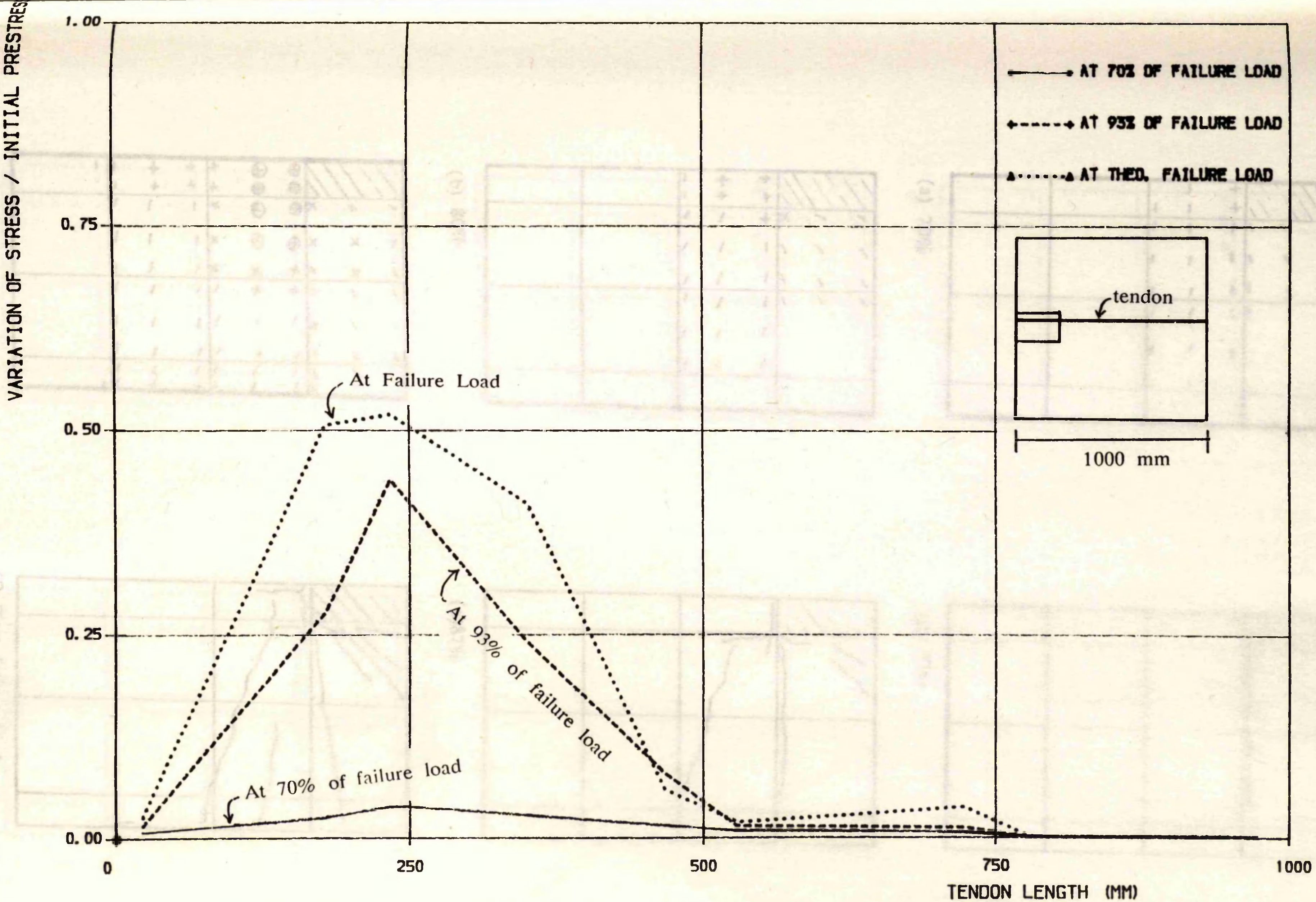

Figure 8.51 : Variation of stress in tendon passed through the column head, in X– direction at different load stages in model MS6.

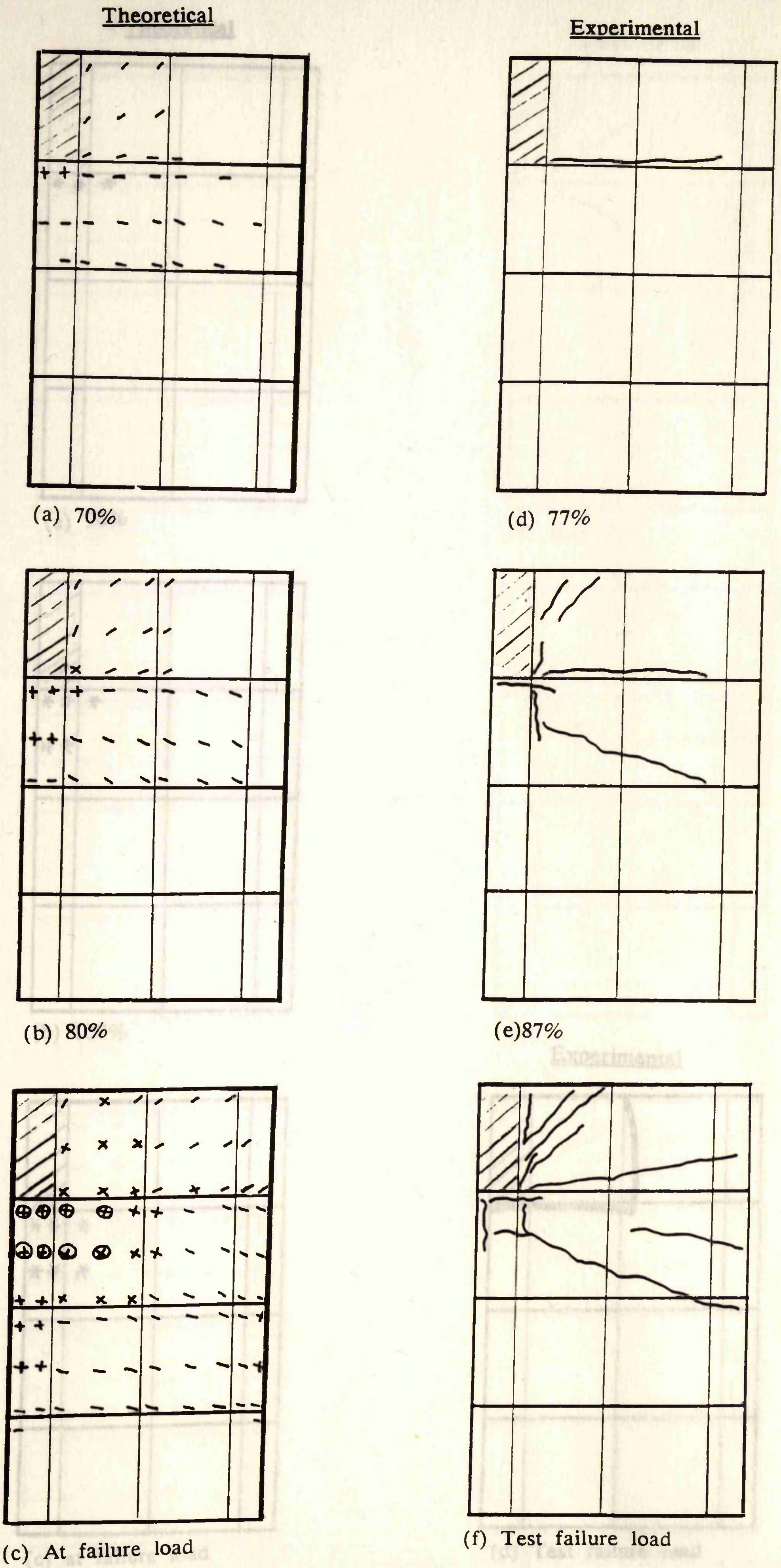

Figure 8.53 : Comparison between theoretical and experimental crack pattern in model MS1 at different percentage of design load.
(−) Single crack, (+) Double crack, (⊕) Triple crack
(*) Crush point

Theoretical

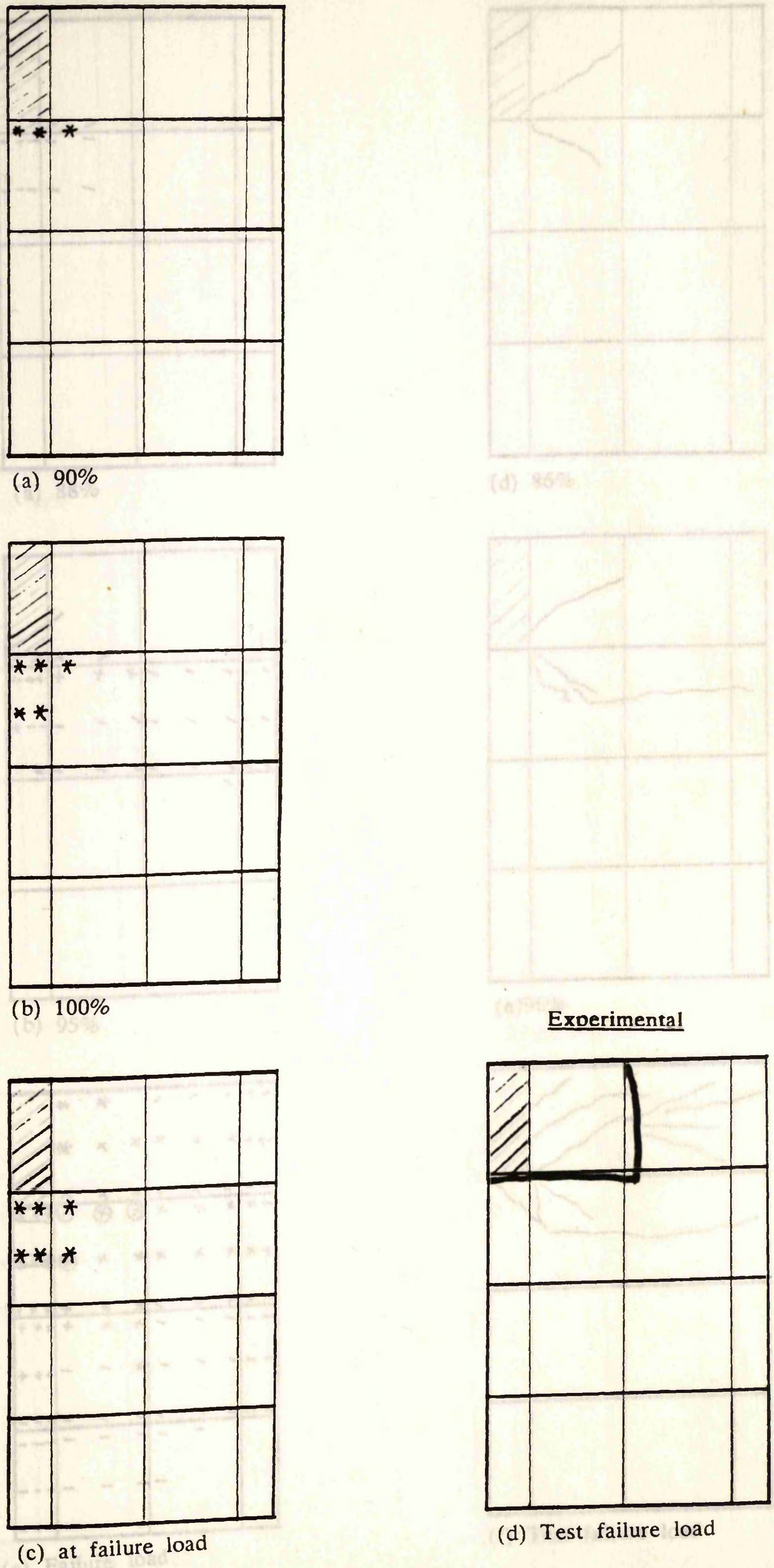

Figure 8.54 : Failure in concrete in the compressive side of model MS1 at different percentage of design load.

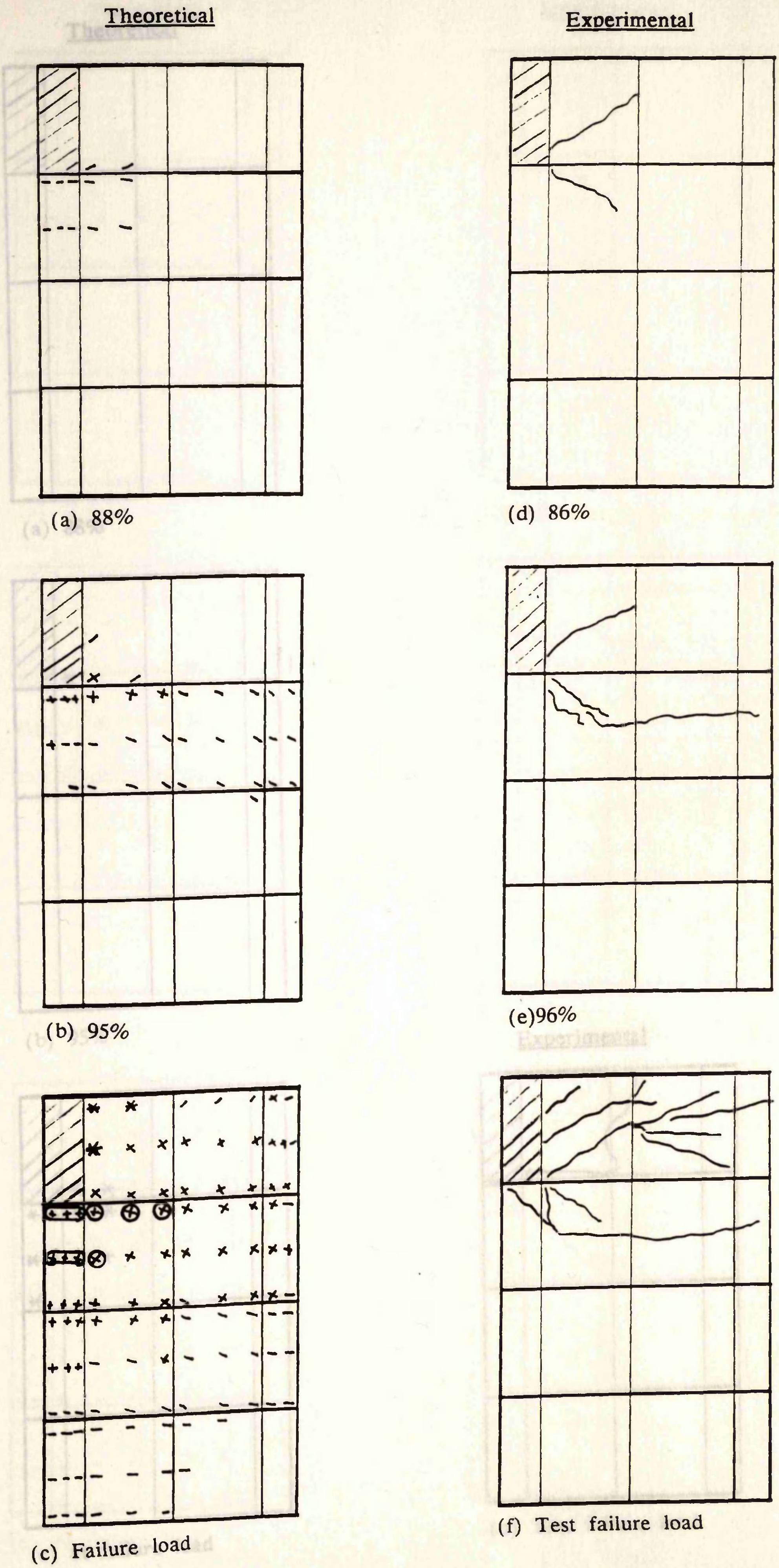

Figure 8.55 : Comparison between theoretical and experimental crack pattern in model MS3 at different percentage of design load.
(−) Single crack, (+) Double crack, (⊕) Triple crack
(*) Crush point

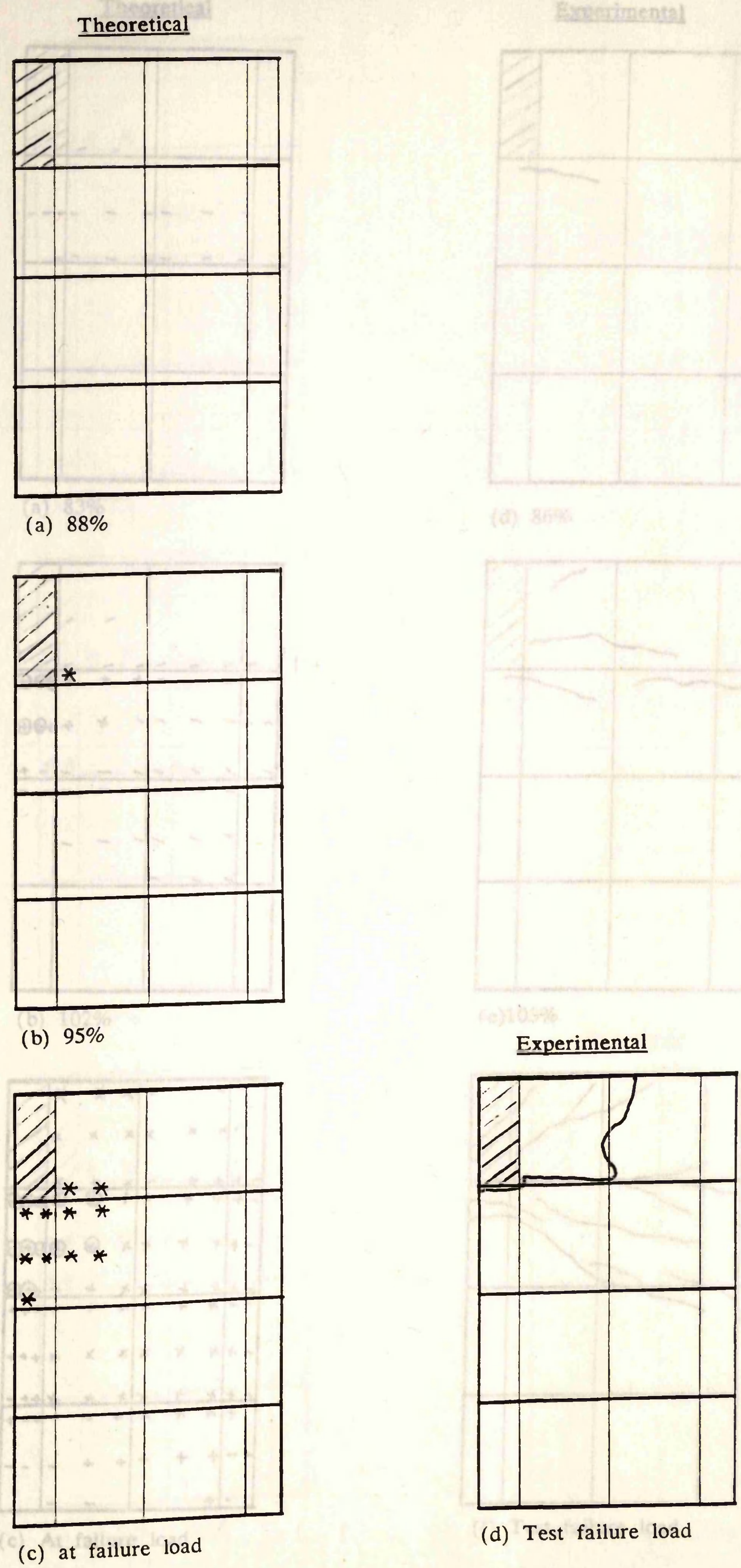

Figure 8.56 : Failure in concrete in the compressive side of model MS3 at different percentage of design load.

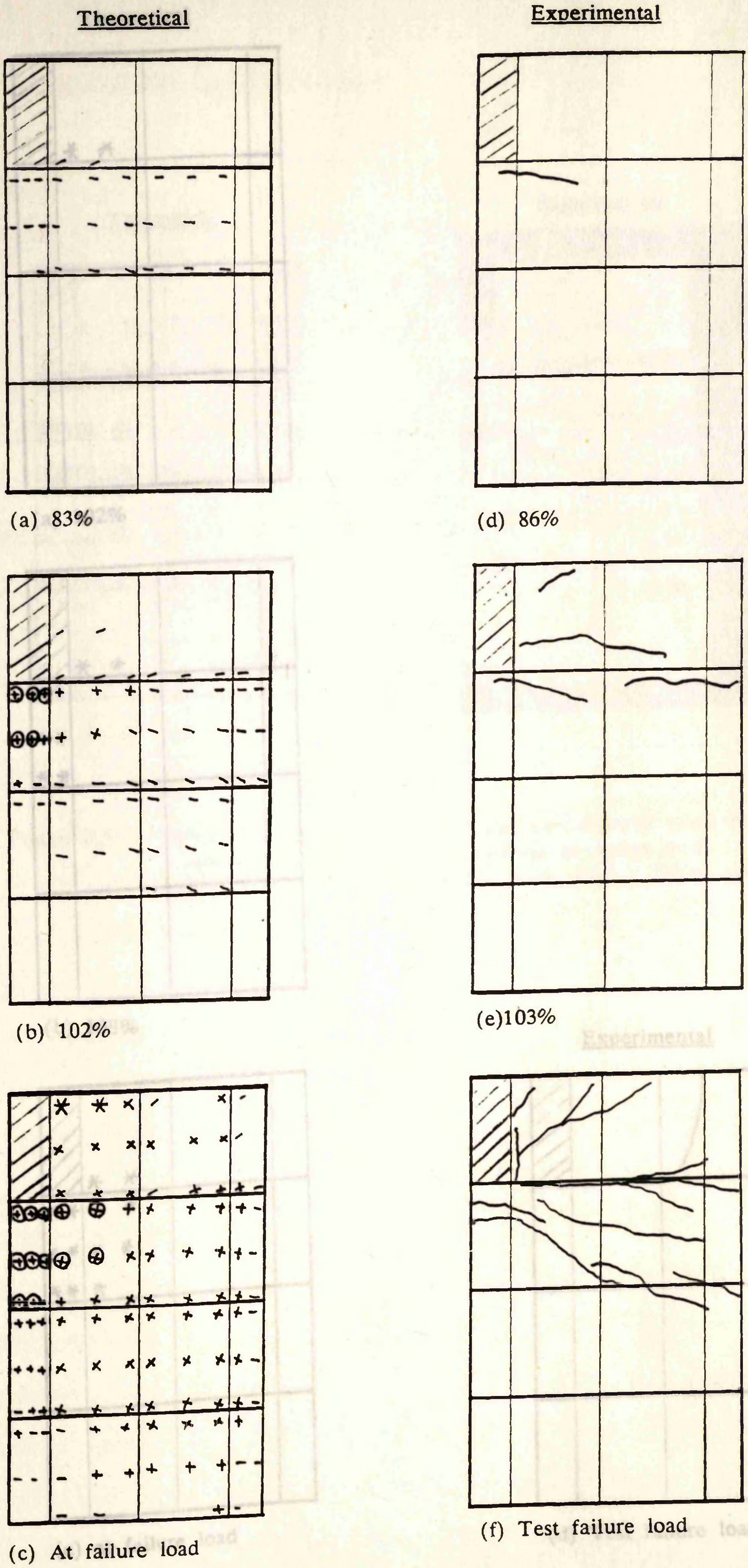

Figure 8.57 : Comparison between theoretical and experimental crack pattern in model MS5 at different percentage of design load.
(–) Single crack, (+) Double crack, (⊕) Triple crack
(*) Crush point

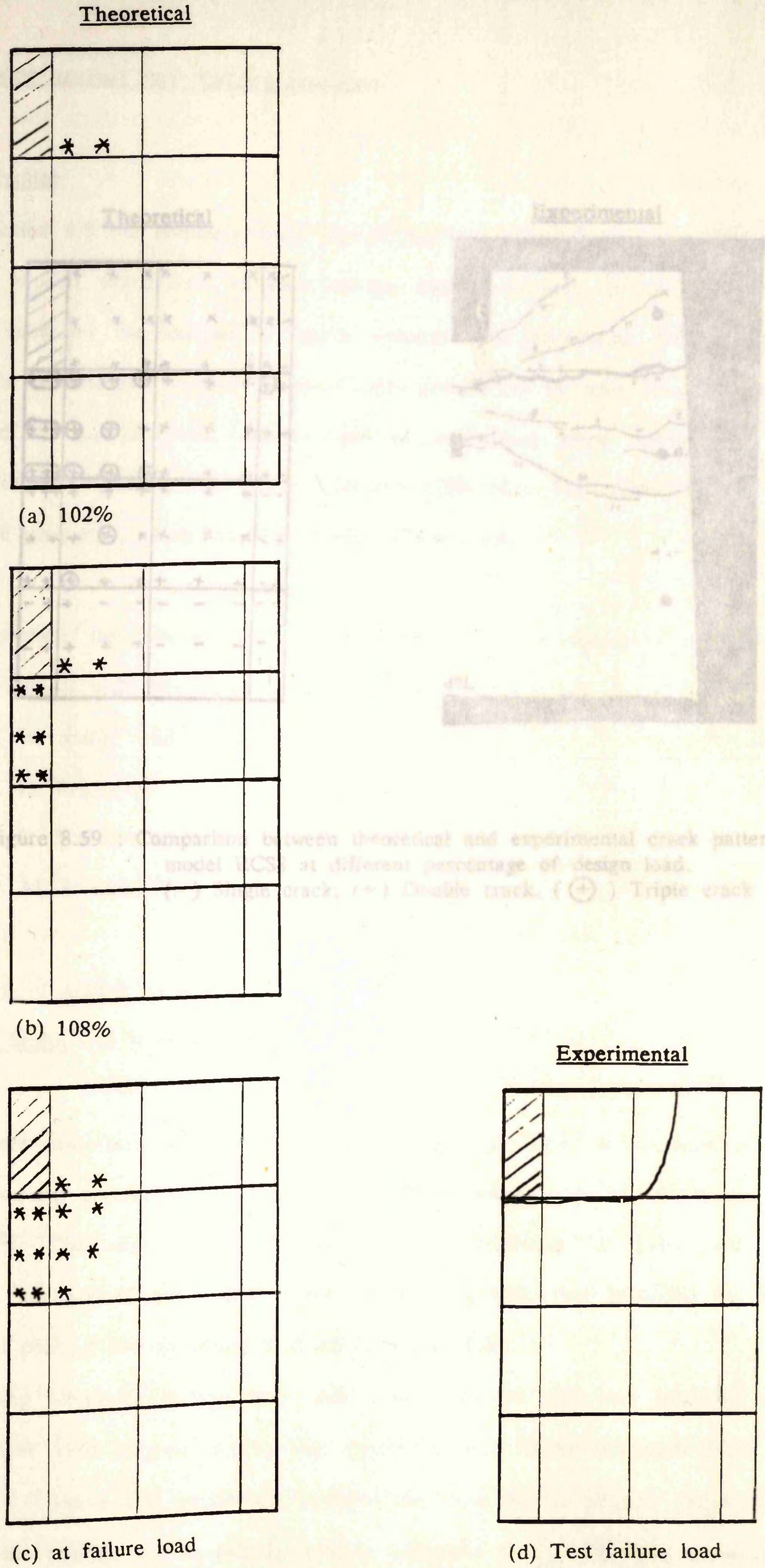

Figure 8.58 : Failure in concrete in the compressive side of model MS5 at different percentage of design load.

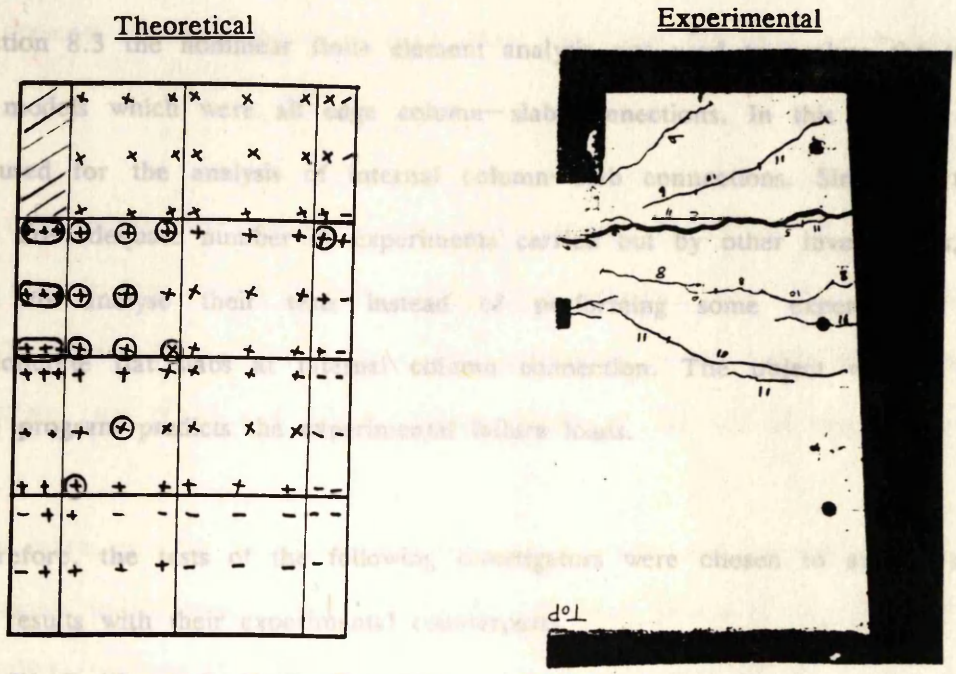

Figure 8.59 : Comparison between theoretical and experimental crack pattern in model RCS8 at different percentage of design load.
(−) Single crack, (+) Double crack, (⊕) Triple crack

8.4 Analysis of Internal Slab– Column Junctions

8.4.1 Introduction

In section 8.3 the nonlinear finite element analysis was used to analyse the tests on author's models which were all edge column– slab connections. In this section the program is used for the analysis of internal column– slab connections. Since on this subject there are adequate number of experiments carried out by other investigators, it was decided to analyse their tests instead of performing some experiments on prestressed concrete flat slabs at internal column connection. The object was to see how well the program predicts the experimental failure loads.

Therefore, the tests of the following investigators were chosen to analyse and compare the results with their experimental counterparts.

a– S. W. Smith and N. H. Burns(10)

b– P. E. Regan(11)

c– S. O. Franklin and A. E. Long(12).

d– N. M. Hawkins[26]

8.4.2 Analysis of Models Tested by: S W Smith and N H Burns(10)

Three post– tensioned flat plate specimens with a single column stub in the centre and various amount of reinforcement have been tested by S. W. Smith and N. H. Burns[10]. The object was to investigate the behaviour of prestressed flat slab– column connections and compare the tests results with that predicted by ACI code. Typical plan of the specimens is shown in Figure 8.61a.

Taking advantage of symmetry, one– quarter of the slab was modelled and sixteen– element mesh (Figure 8.61b) was employed using shear retention factor of 0.30. Table 8.6 shows the comparison between the experimental ultimate failure load and that of the analysis and as calculated using American code (ACI). The mean ratio of (V_{exp}/V_{theo}) is 1.05 and that of (V_{exp}/V_{ACI}) is 1.05 as well. Figures 8.62 to 8.64 present the load–deflection curves of experimental tests comparing with their theoretical counterparts. Figure 8.65 shows the positions of additional bonded reinforcing bars and Figure 8.66 presents the load–strain curves of these bars from the tests and theoretical analysis.

In the analysis, the maximum increase in tendons forces for all the models occurred in the tendons which passed through the column head. The theoretical (experimental) increase in the tendon force as a percentage of the initial tendon force were 17% (N/A), 16% (12%) and 14% (13%) for models S1, S2 and S3 respectively.

The crack patterns and crush points at top, middle and bottom surfaces of theoretical models which coincide with the Gauss points are shown in Figures 8.67 to 8.69 respectively for models S1 , S2 and S3. The results show that all the models have failed by a combination of flexural and punching failure but the final mode of failure predicted by the analysis is punching failure. In the distribution of cracks and directions of main cracks there is good agreement between the tests and theoretical results. In model S1, because there was no bonded reinforcement , main cracks happened in both X and Y–directions but in model S2 and S3 bonded reinforcement caused the main cracks to occur in Y–direction (the north–south direction in the tests) only. Comparison of the experimental failure surface and crack patterns with their theoretical counterparts (Figures 8.67 to 8.69) indicates very good agreement between the two.

In models S2 and S3 , bonded reinforcements passing through the column in X–direction yielded first. Then the other bars yielded prior to the ultimate failure load. As a result, comparison between experimental behaviour of the models and theoretical behaviour predicted by the 3–dimensional finite element analysis through this section indicates that there is good agreement between them. It can therefore be concluded that the theoretical method is capable of predicting the ultimate failure load of models accurately.

Table 8.6– Comparison of experimental failure load with theoretical failure load and that predicted by American Code (ACI) in Reference (10).

Model	Failure Loads			$\frac{V_{exp}}{V_{theo}}$	$\frac{V_{exp}}{V_{ACI}}$
	V_{exp}	V_{theo}	V_{ACI}		
S1	112.5	106.7	108.0	1.05	1.04
S2	121.4	119.0	120.4	1.02	1.01
S3	134.8	124.5	122.1	1.08	1.10
		Average =		1.05	1.05

V_{exp}= Experimental Ultimate Failure Load

V_{theo}= Theoretical = = =

V_{ACI}= Predicted Failure Load by ACI code.

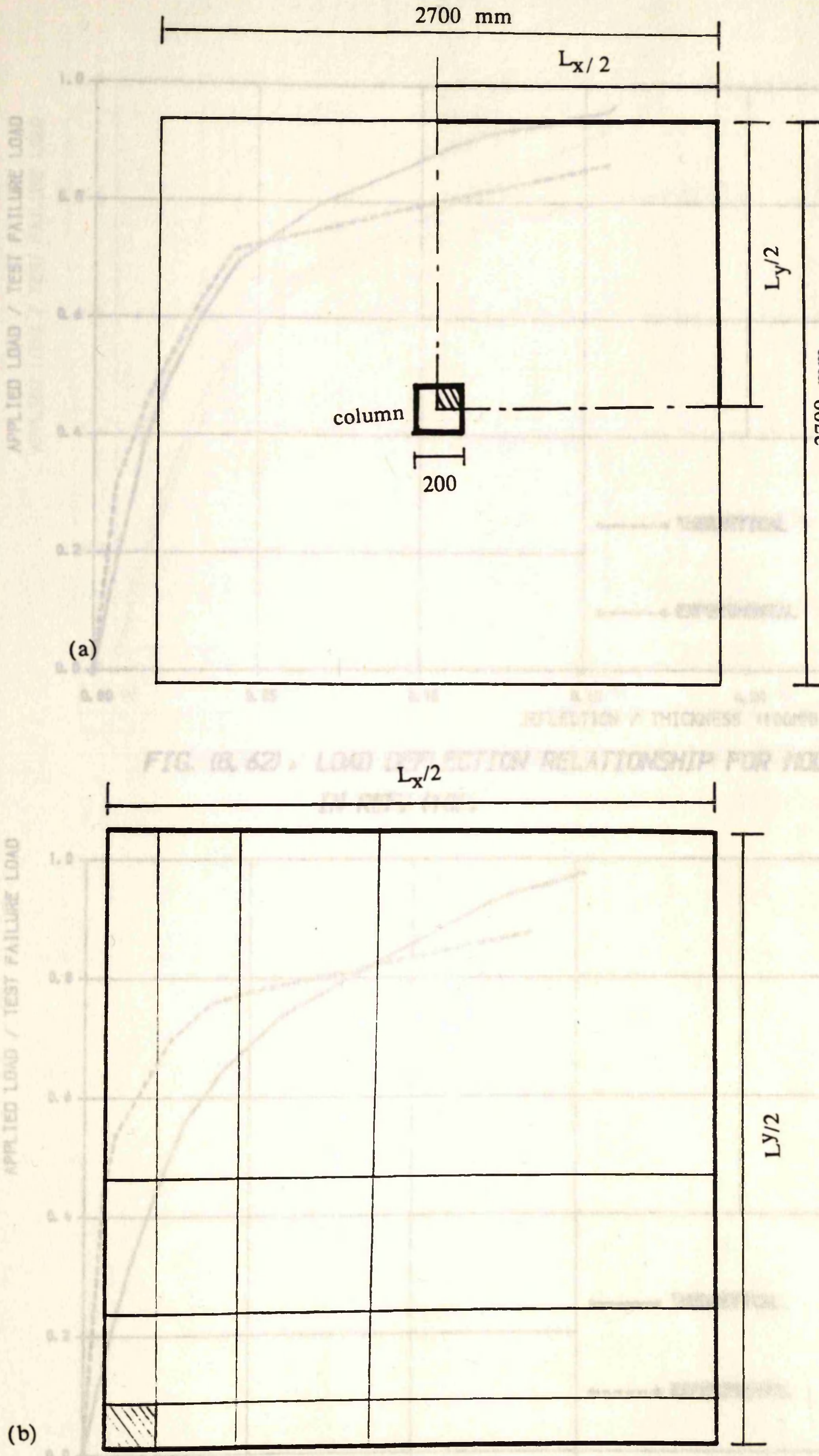

Figure 8.61 : a) Plan of the models
b) Typical sixteen– element mesh for analysis of the models.

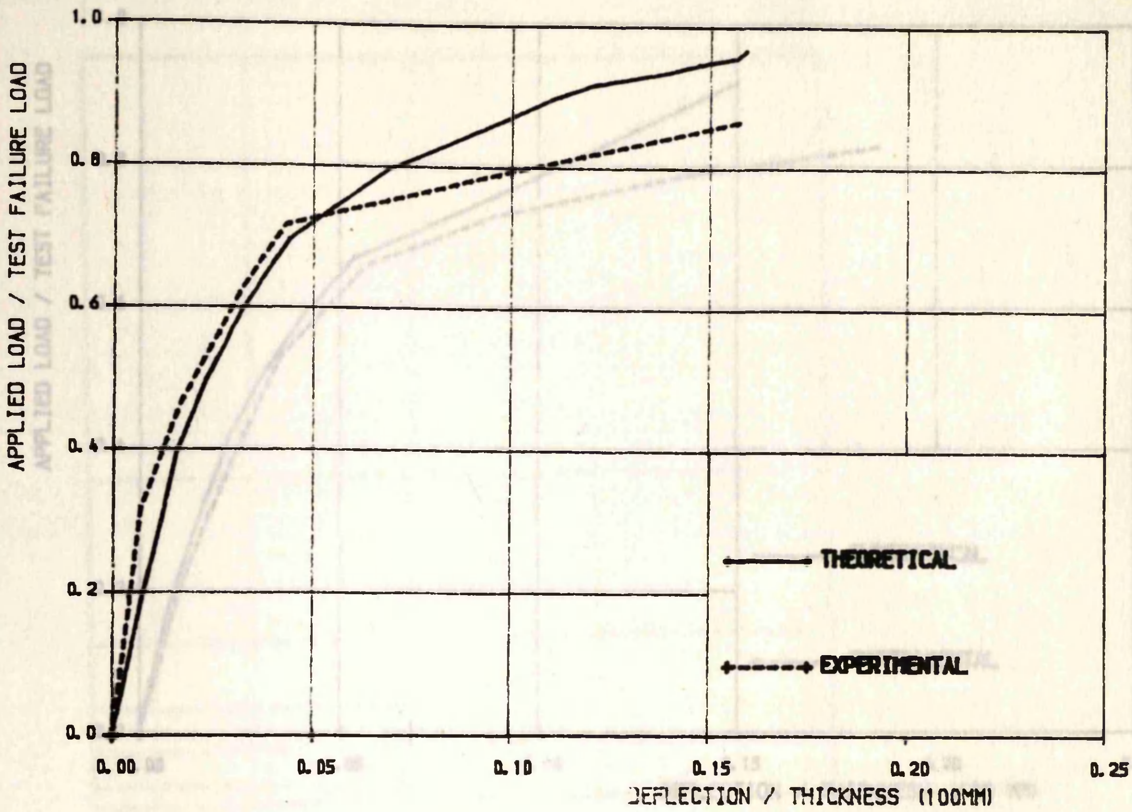

FIG. (8.62). LOAD DEFLECTION RELATIONSHIP FOR MODEL S-1 IN REF. (10).

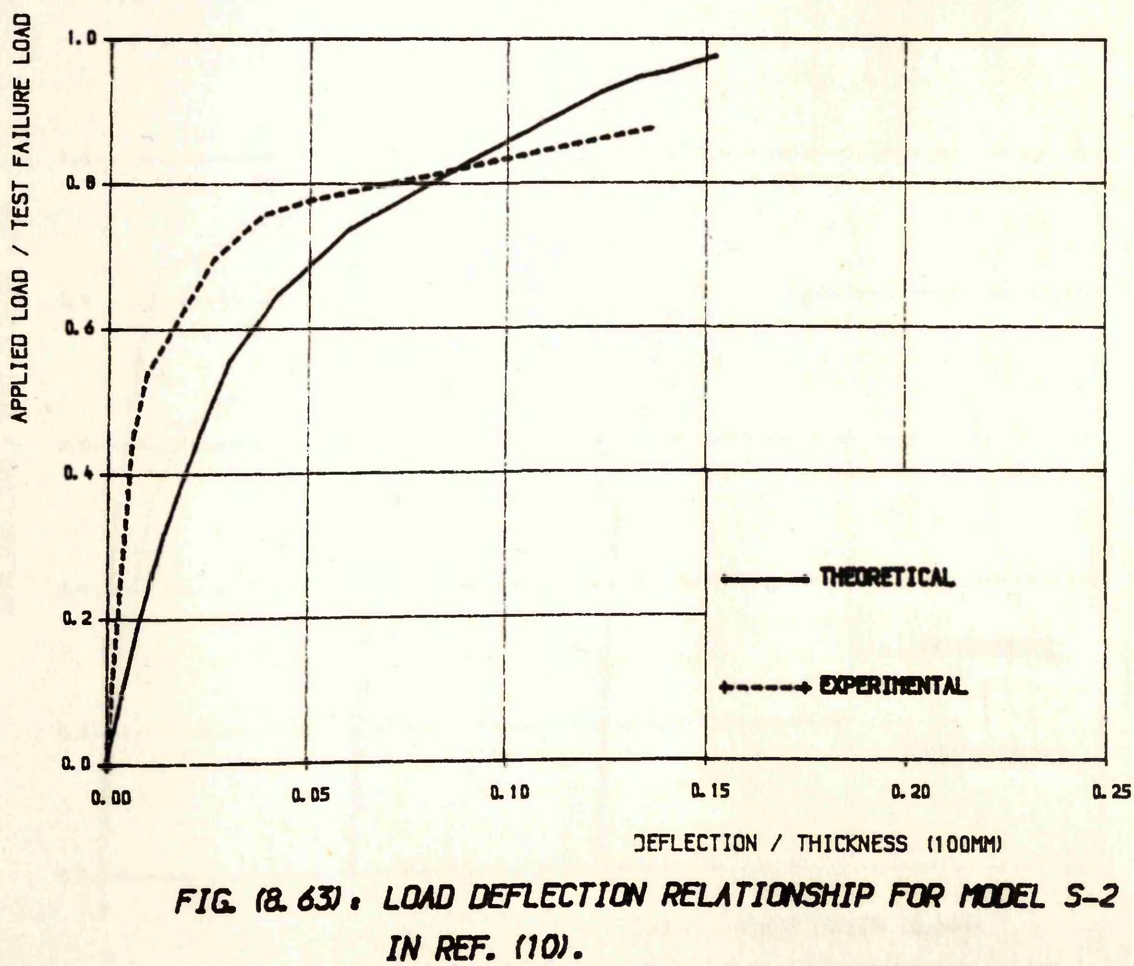

FIG. (8.63). LOAD DEFLECTION RELATIONSHIP FOR MODEL S-2 IN REF. (10).

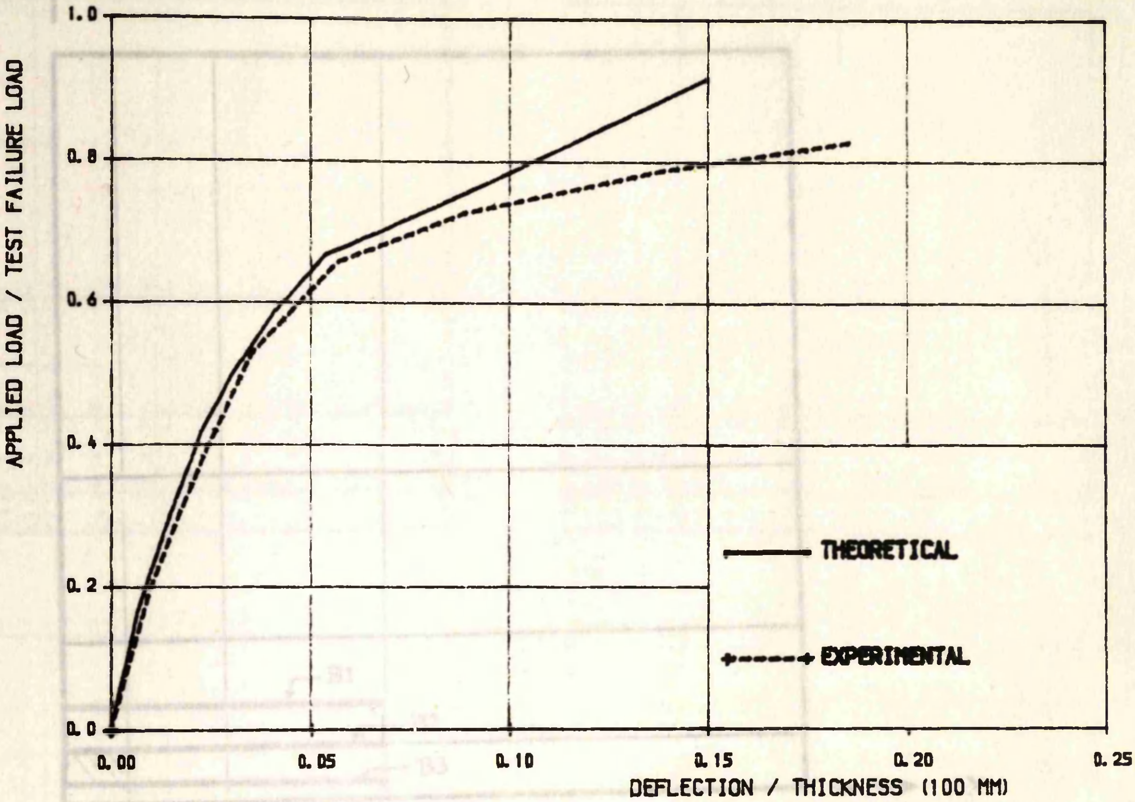

FIG. (8.64). LOAD-DEFLECTION RELATIONSHIP FOR MODEL S-3 IN REF. (10).

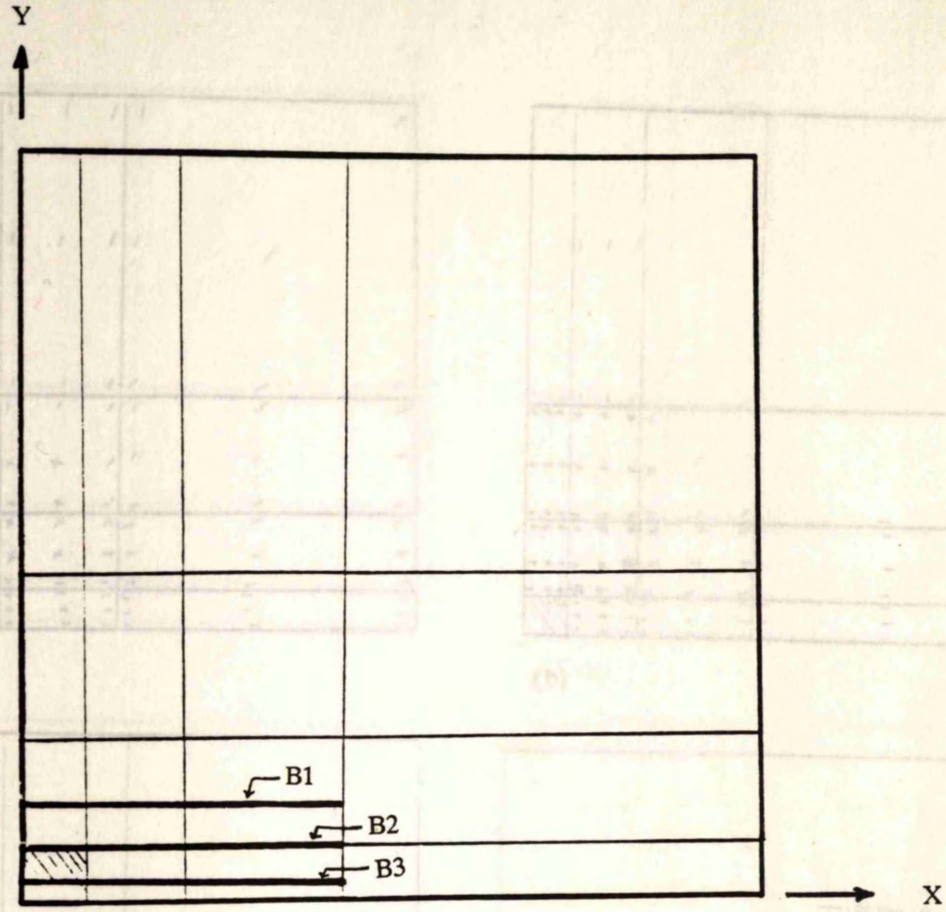

Figure 8.65 : Bonded unstressed bars in X– direction in model S– 3.

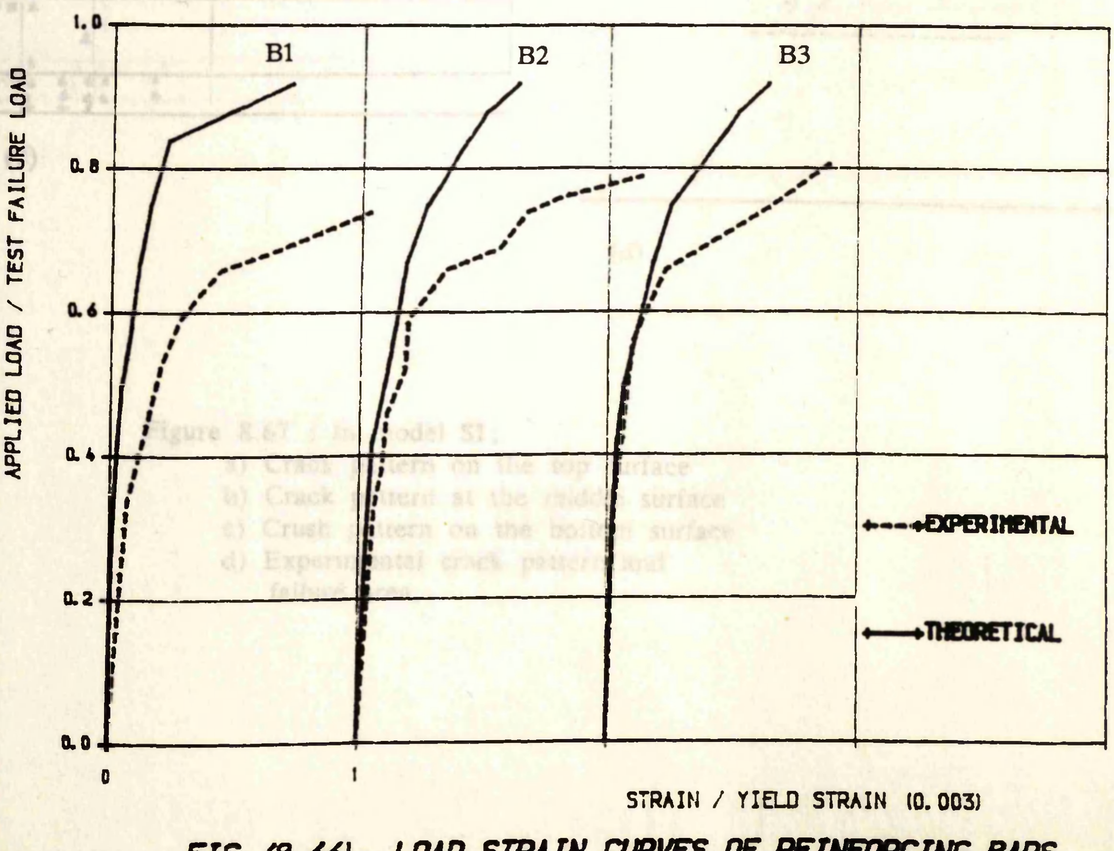

FIG. (8.66) : LOAD-STRAIN CURVES OF REINFORCING BARS IN X-DIRECTION IN MODEL S-3 (REF. (10)).

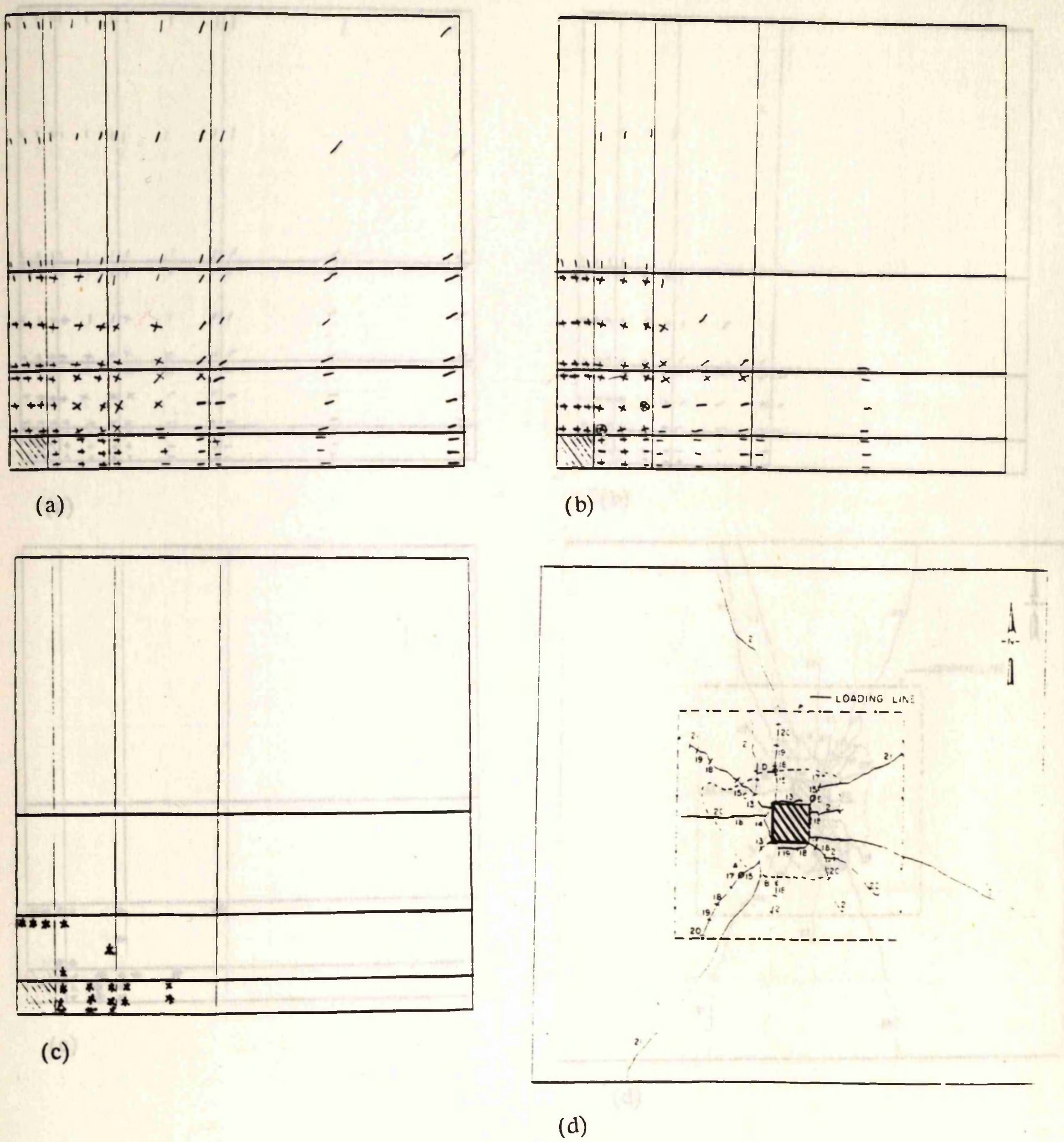

Figure 8.67 : In model S1;

a) Crack pattern on the top surface
b) Crack pattern at the middle surface
c) Crush pattern on the bottom surface
d) Experimental crack pattern and failure area.

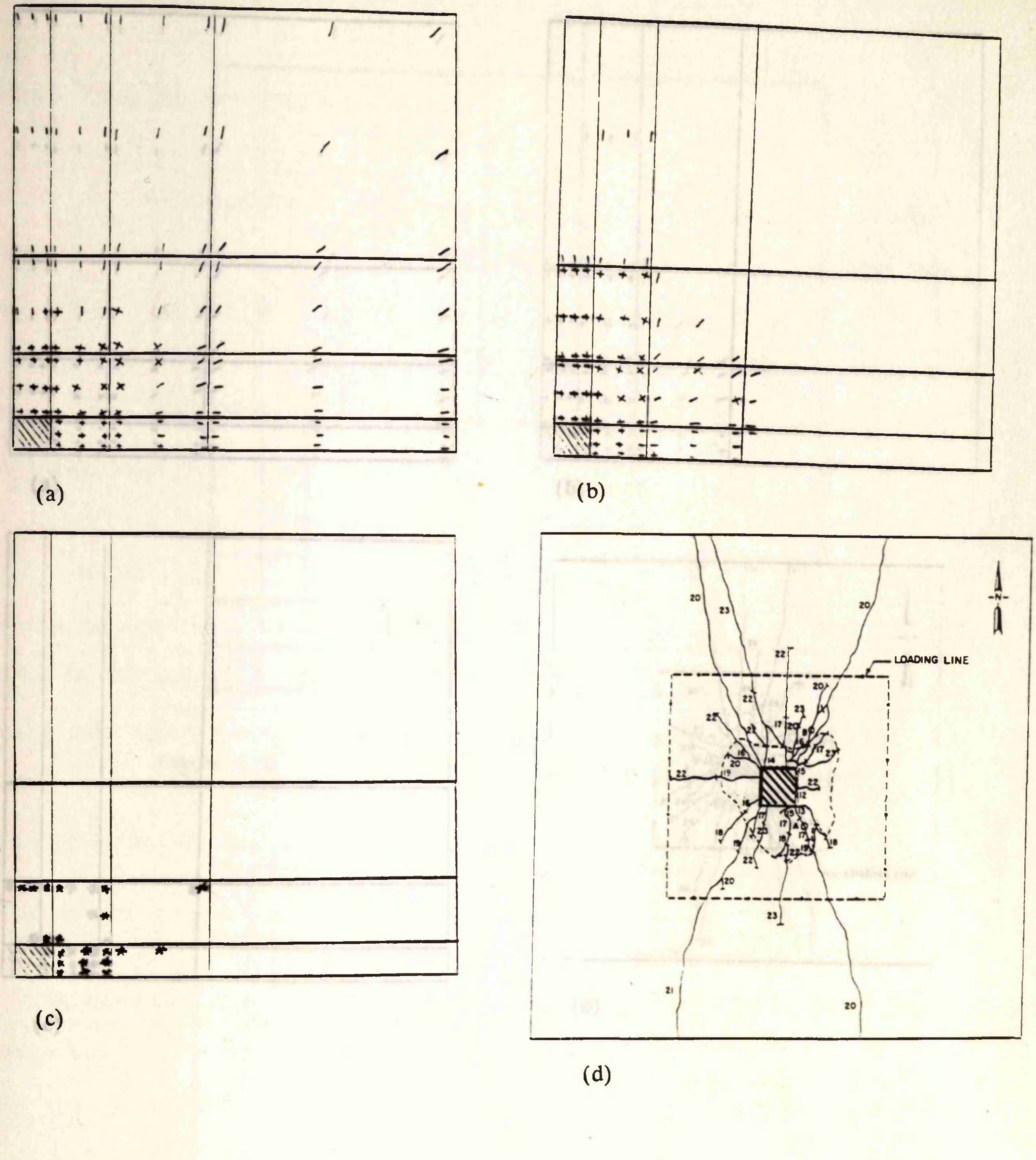

Figure 8.68 : In model S2;
a) Crack pattern on the top surface
b) Crack pattern at the middle surface
c) Crush pattern on the bottom surface
d) Experimental crack pattern and failure area.

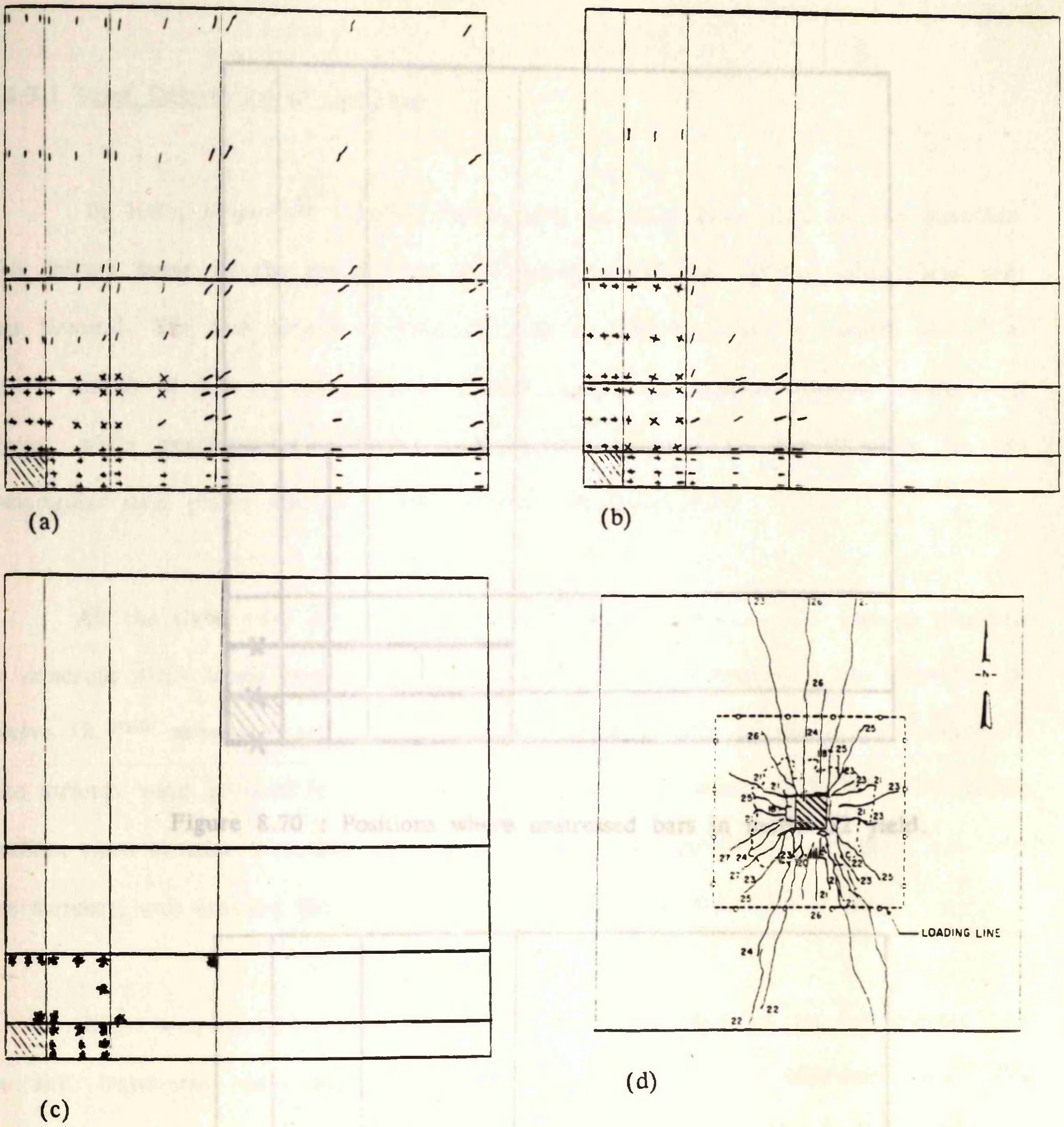

Figure 8.69 : In model S3;
a) Crack pattern on the top surface
b) Crack pattern at the middle surface
c) Crush pattern on the bottom surface
d) Experimental crack pattern and failure area.

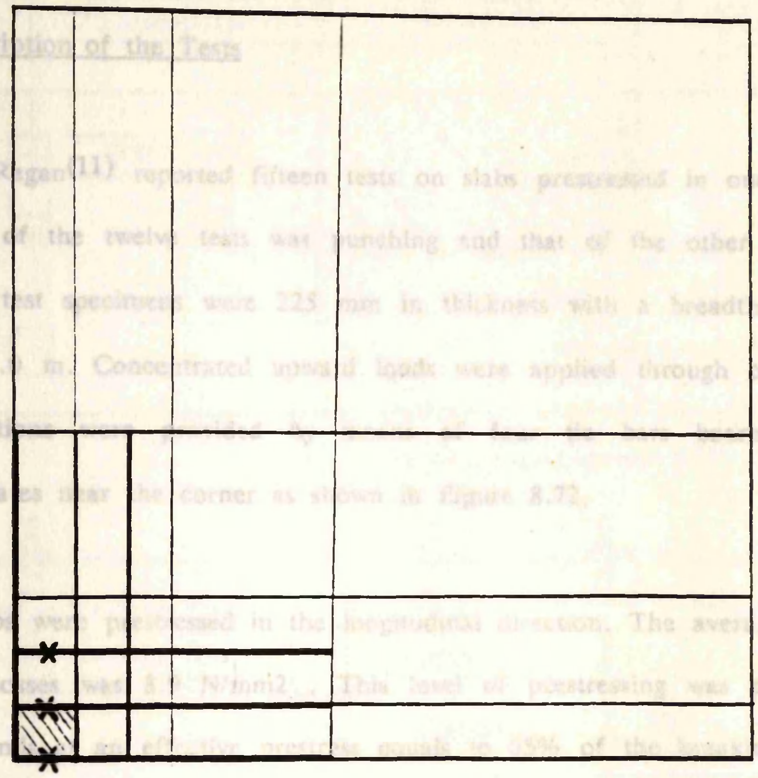

Figure 8.70 : Positions where unstressed bars in model S2 yield.

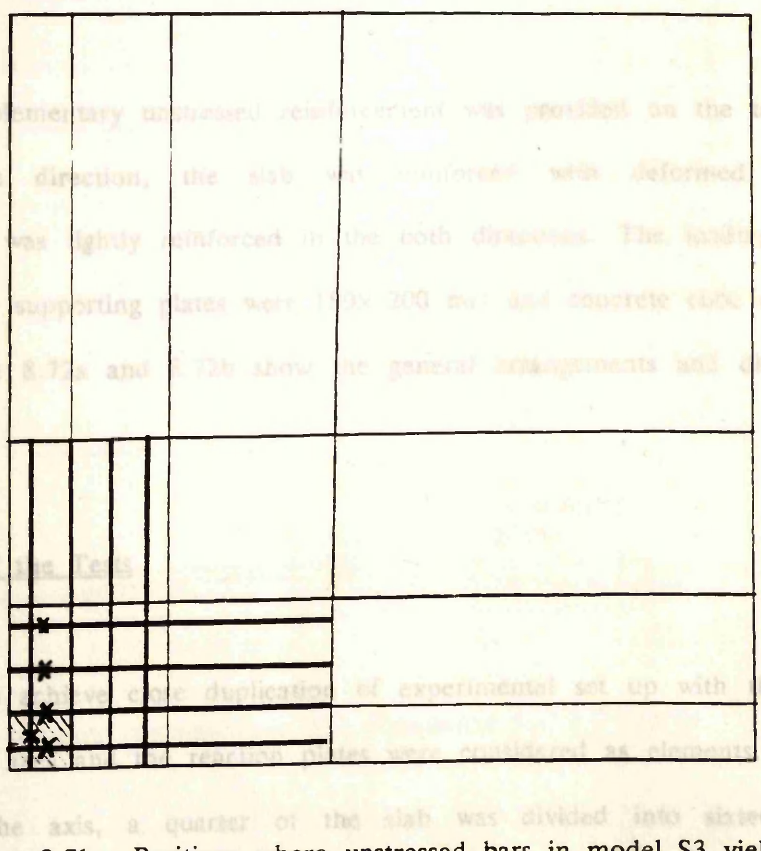

Figure 8.71 : Positions where unstressed bars in model S3 yield.

8.4.3 Analysis of Regan's Tests

8.4.3.1 Brief Description of the Tests

In 1985, Regan(11) reported fifteen tests on slabs prestressed in one direction. The failure mode of the twelve tests was punching and that of the other three tests was flexural. The test specimens were 225 mm in thickness with a breadth of 1.5 m and a length of 3.0 m. Concentrated upward loads were applied through central steel plates, while reactions were provided by means of four tie bars bearing on the rectangular steel plates near the corner as shown in Figure 8.72.

All the slabs were prestressed in the longitudinal direction. The average prestress in concrete after losses was 8.9 N/mm2 . This level of prestressing was provided by twelve 18 mm strands at an effective prestress equals to 65% of the breaking strength. The strands were grouted in metal ducts with internal diameters of 30mm. The tendon profiles were circular arcs with the strands reaching high points at mid–span, i.e. over the support, and crossing the middle surface of the slab at the reaction lines.

Light supplementary unstressed reinforcement was provided on the tension face. In the transverse direction, the slab was reinforced with deformed bars. The compression zone was lightly reinforced in the both directions. The loading plate was 150× 150 mm and supporting plates were 180× 200 mm and concrete cube strength was 50 N/mm2. Figure 8.72a and 8.72b show the general arrangements and dimensions of all the models.

8.4.3.2 Analysis of the Tests

In order to achieve close duplication of experimental set up with the analytical model, the loaded area and the reaction plates were considered as elements. Because of symmetry about the axis, a quarter of the slab was divided into sixteen elements

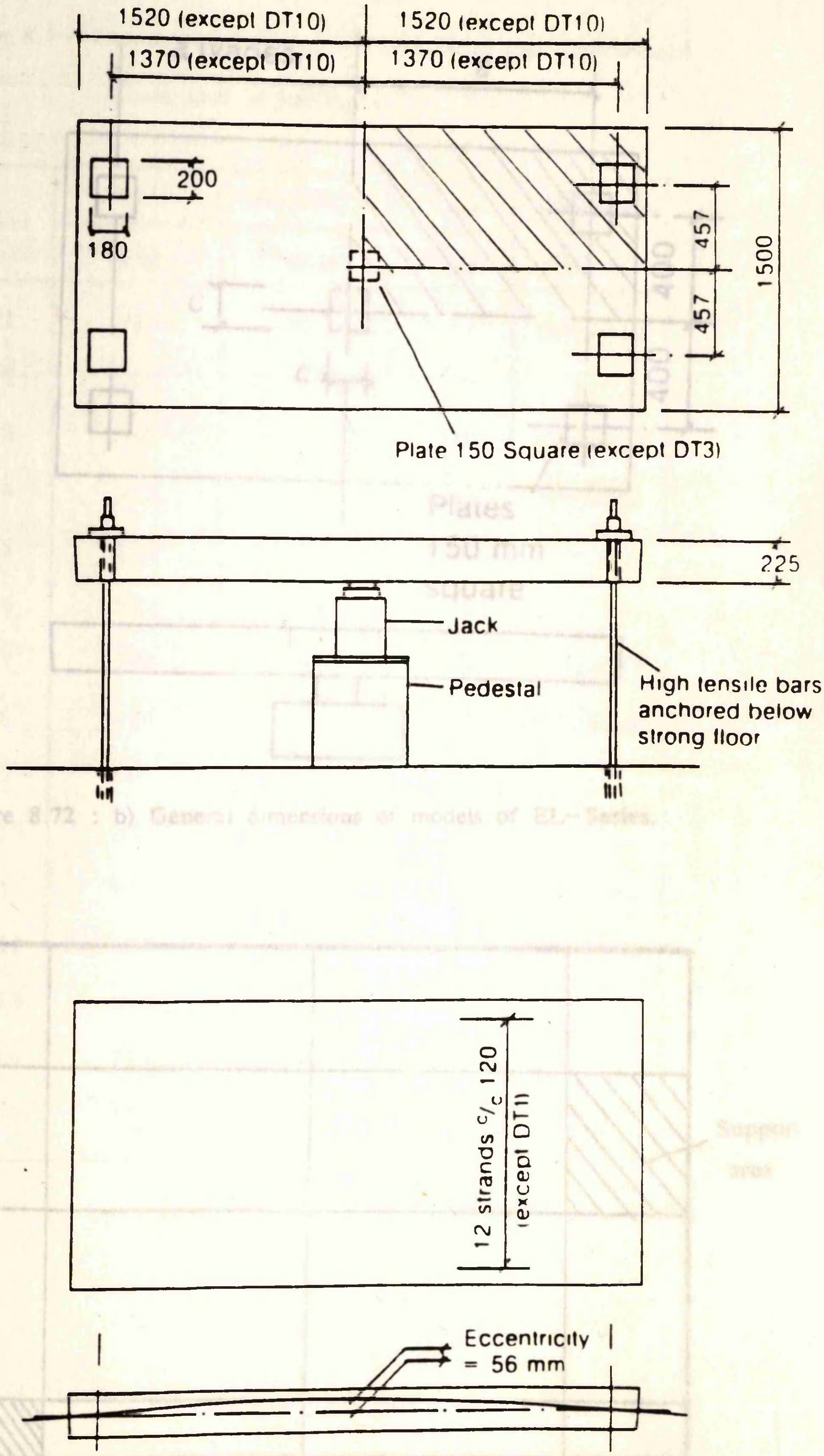

Figure 8.72 : a) General arrangements and dimensions for DT– Series.

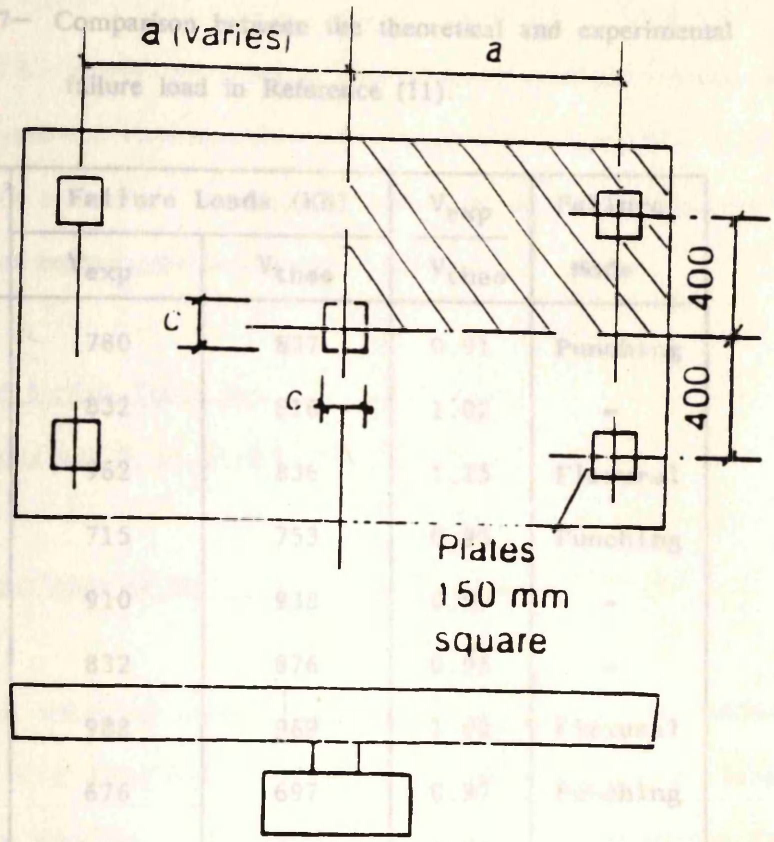

Figure 8.72 : b) General dimensions of models of EL– Series.

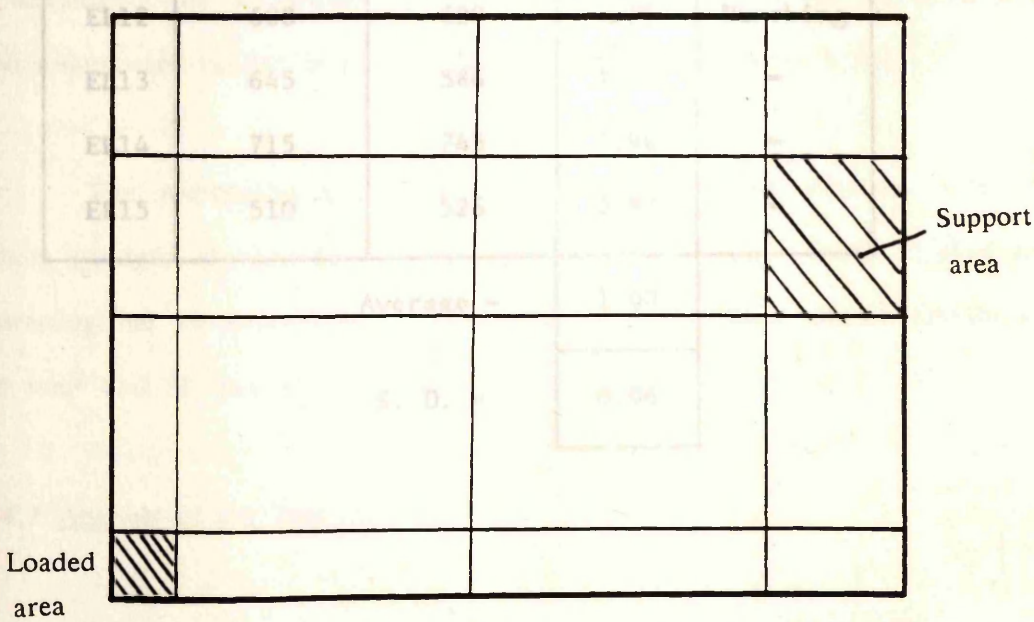

Figure 8.72 : c) Typical sixteen– element mesh for analysis of all the models (1/4 of the slab)

Table 8.7– Comparison between the theoretical and experimental failure load in Reference (11).

Model	Failure Loads (KN)		$\frac{V_{exp}}{V_{theo}}$	Failure Mode
	V_{exp}	V_{theo}		
DT1	780	857	0.91	Punching
DT2	832	816	1.02	=
DT3	962	836	1.15	Flexural
DT4	715	753	0.95	Punching
DT5	910	938	0.97	=
DT6	832	876	0.95	=
DT7	988	969	1.02	Flexural
DT8	676	697	0.97	Punching
DT9	806	790	1.02	=
DT10	832	824	1.01	=
EL11	475	466	1.02	Flexural
EL12	608	620	0.98	Punching
EL13	645	586	1.10	=
EL14	715	745	0.96	=
EL15	510	526	0.97	=
		Average =	1.00	
		S. D. =	0.06	

(Figure 8.72c) and analysed using a shear retention factor of 0.30.

Table 8.7 shows the ultimate failure loads predicted by the finite element method (V_{theo}) and the experimental results (V_{exp}). The mean ratio of (V_{exp}/V_{theo}) is equal to 1.0 with a Standard Deviation of 0.06 This comparison indicates that there is a good agreement between the two results.

8.4.4 Analysis of Models Tested by:

A. E. Long and S. O. Franklin[12]

8.4.4.1 Brief Description of the Tests

Seven unbonded post-tensioned flat slabs with internal column connections were tested by A E Long and S O Franklin[12] to investigate the behaviour of the slabs. The main variables of the slabs were the level of eccentricity and boundary conditions. Three of the seven tests (type M) had controlled boundary conditions while the remaining tests (type B) had free edges similar to Smith[10]. In all the specimens, the tendons in the Y-direction were distributed uniformly while the tendons in the X-direction were banded in the column strip as shown in Figure 8.73a.

The prestressing steel used in the tests was 5 mm diameter wire with an ultimate strength of 1580 N/mm^2. An effective force of 20 KN was applied to each prestressing bar in both X and Y-directions. The dimensions of the specimens were 2536 mm^2 and 58 mm in thickness.

8.4.4.2 Analysis of the Test Data

Taking advantage of symmetry about X-axis, half of the slab was analysed using twenty-eight element mesh for all the models. The finite element meshes were chosen so that the column foot print was considered as an element and column stubs (above and below the slab) were included as two additional elements. Figures 8.74a and 8.74b. show the typical element mesh arrangements for the models. The shear retention factor used in the analysis was 0.30. As previously mentioned, in models 2M, 3M and 4M the boundary conditions of slab were controlled. The boundary conditions were:

i) Along the edges parallel to X− axis: $dW/dY = 0$

ii) Along the edge parallel to Y− axis : $dW/dX = 0$ (8.1)

These boundary conditions cause moment reactions along the restrained edges. If we know the resulting moment reactions, then instead of imposing the slope restrictions, these reactions together with the applied load can be used to analyse the slab.

Since in the three−dimensional finite element analysis it is difficult to apply slope boundary conditions, the following approach was adopted. First a two−dimensional finite element programme based on elastic plate analysis under the combination of bending and inplane loads was used to analyse the given tests with the prescribed boundary conditions of equation (8.1). This analysis resulted in all the reactions including the boundary reactions along the edges. These moments reactions were used in the three−dimensional analysis as external loads imposed to the model along with the applied loads.

The ultimate failure loads obtained from this procedure are compared with the tests results in Table 8.8. The mean ratio of (V_{exp}/V_{theo}) is 1.10 with Standard Deviation of 0.05. In Table 8.8 comparisons are also made between the tests results and the failure loads predicted by the American Code (ACI) and the Concrete Society[13].

These comparisons for the ultimate loads together with the results for deflections in Figures 8.75 to 8.78 indicate that there is good agreement between the experimental and the theoretical results while the ACI− ASCE design method and the Concrete

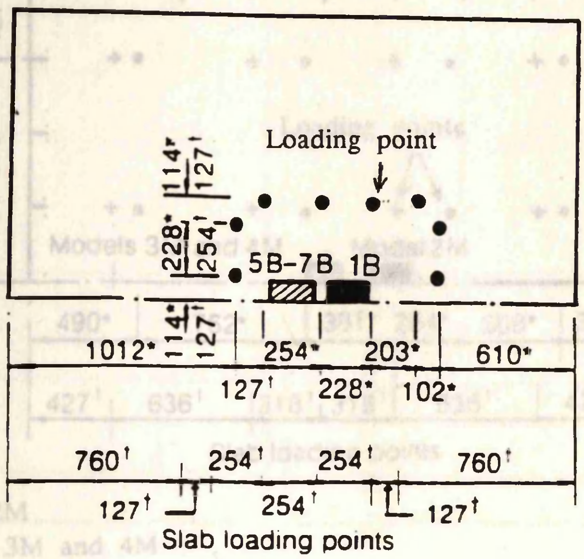

* For model 1B
† For models 5B– 7B

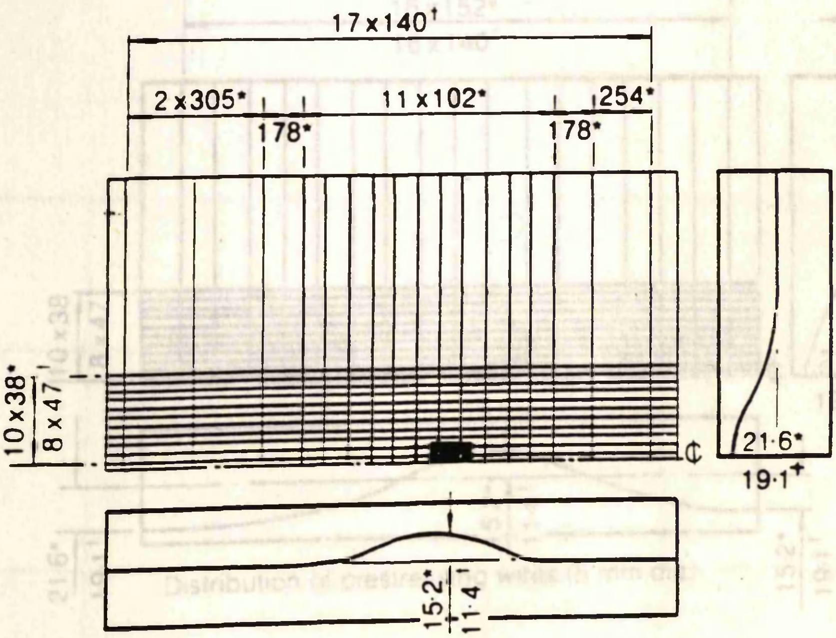

Distribution of prestressing wires (5 mm dia.)

* For model 1B
† For models 5B– 7B

Figure 8.73 : a) Dimensions and distribution of prestressing wires and loading points for models 1B, 5B, 6B and 7B. More details in Reference (12).

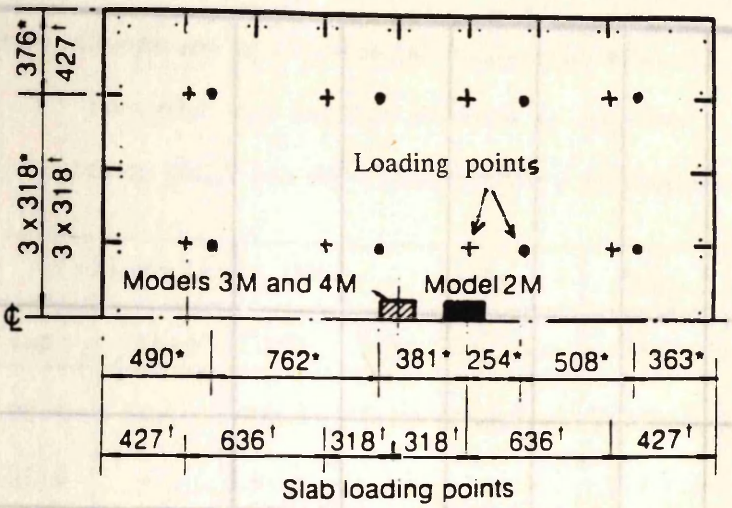

* For model 2M

† For models 3M and 4M

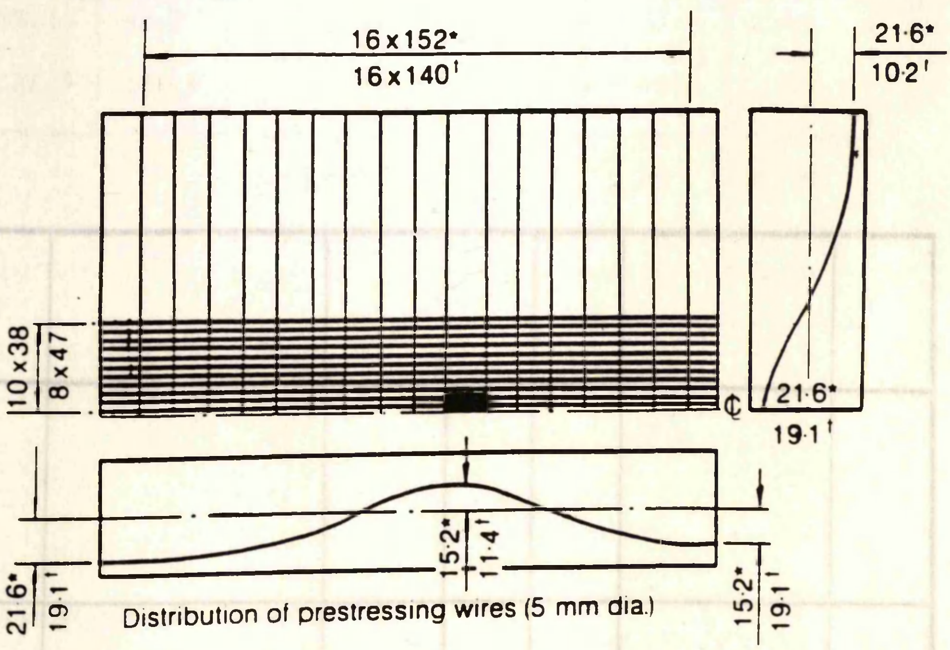

* For model 2M

† For models 3M and 4M

Figure 8.73 : b) Dimensions and distribution of prestressing wires and loading points for models 2M, 3M and 4M. More details in Reference (12).

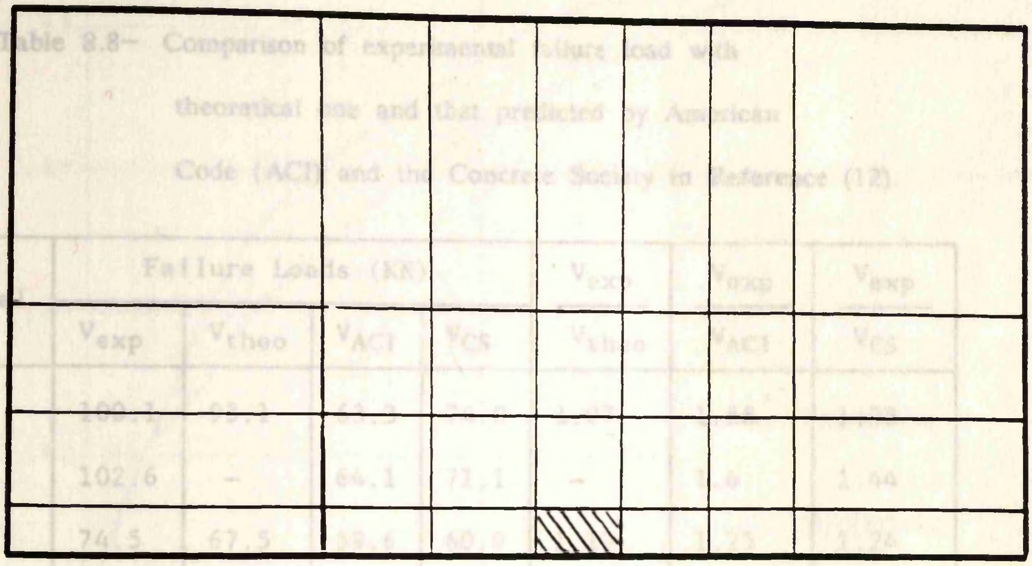

a) Element mesh arrangement for analysis of models 1B, 5B, 6B and 7B.

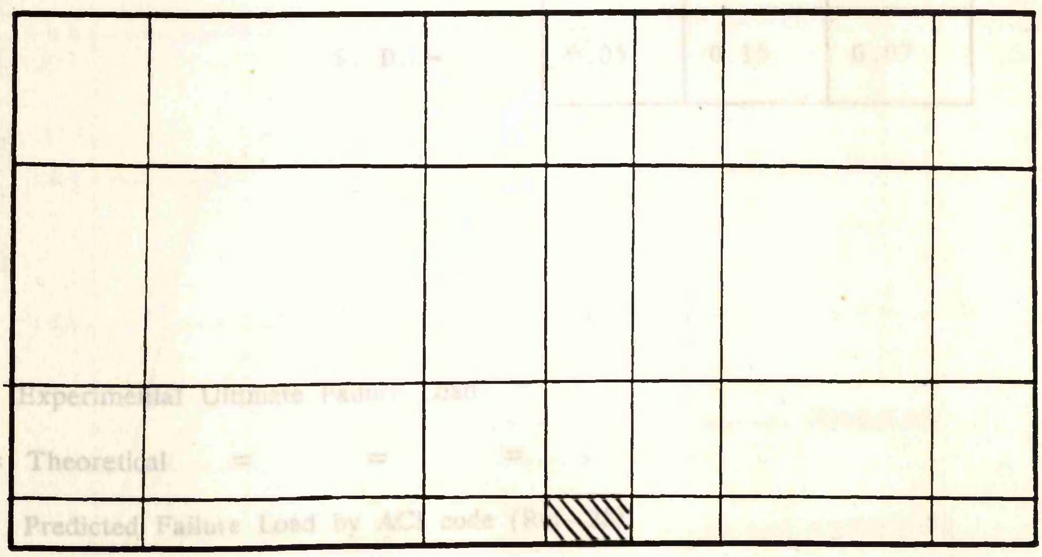

b) Element mesh arrangement for analysis of models 2M, 3M and 4M.

Figure 8.74 :

Table 8.8— Comparison of experimental failure load with theoretical one and that predicted by American Code (ACI) and the Concrete Society in Reference (12).

Model	Failure Loads (KN)				$\frac{V_{exp}}{V_{theo}}$	$\frac{V_{exp}}{V_{ACI}}$	$\frac{V_{exp}}{V_{CS}}$
	V_{exp}	V_{theo}	V_{ACI}	V_{CS}			
1B	100.1	93.1	63.3	74.0	1.07	1.58	1.35
2M	102.6	–	64.1	71.1	–	1.6	1.44
3M	74.5	67.5	59.6	60.0	1.10	1.25	1.24
4M	79.4	67.5	53.1	52.7	1.17	1.5	1.51
5B	57.6	53.0	46.4	46.5	1.09	1.24	1.24
6B	55.2	49.7	37.5	38.6	1.11	1.47	1.43
7B	127.9	122.8	101.6	98.2	1.04	1.26	1.30
			Average =		1.10	1.41	1.36
			S. D. =		0.05	0.15	0.07

V_{exp}= Experimental Ultimate Failure Load

V_{theo}= Theoretical = = =

V_{ACI}= Predicted Failure Load by ACI code (Ref. 28)

V_{CS} = Predicted Failure Load by the Concrete Society recommendations (Ref. 29)

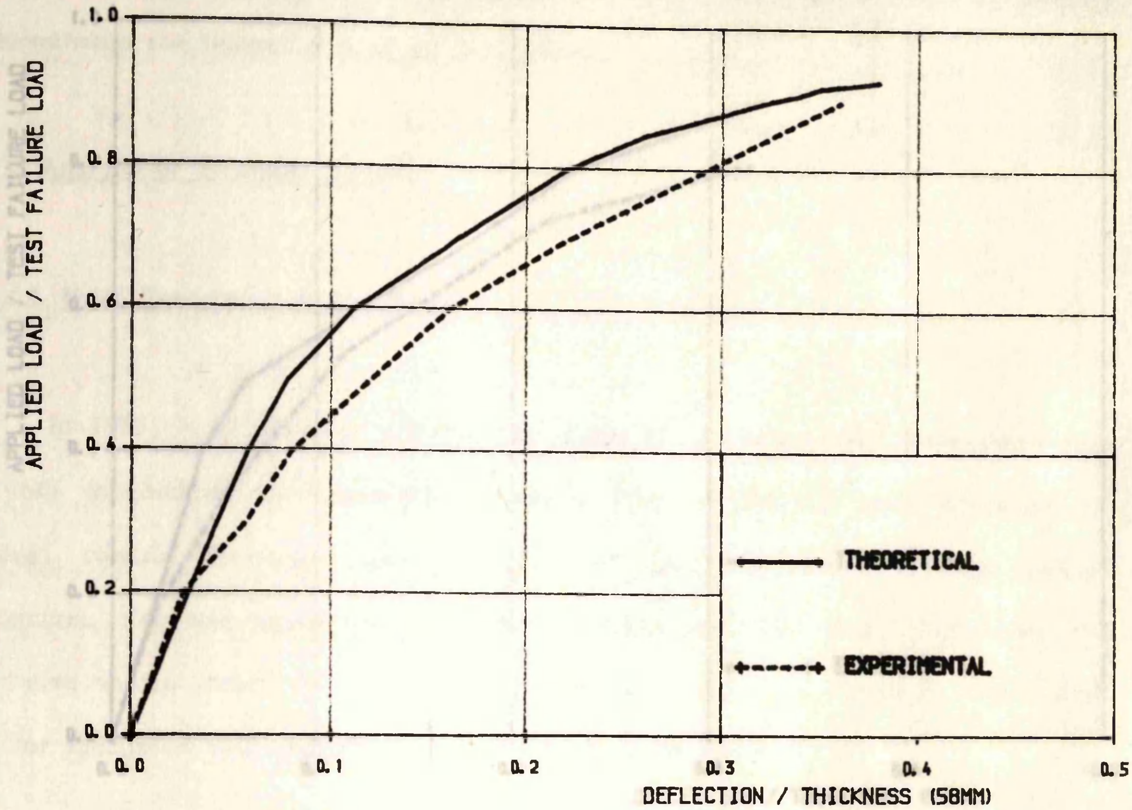

FIG. (8.75). LOAD-DEFLECTION RELATIONSHIP FOR MODEL (1B) IN REF. (12).

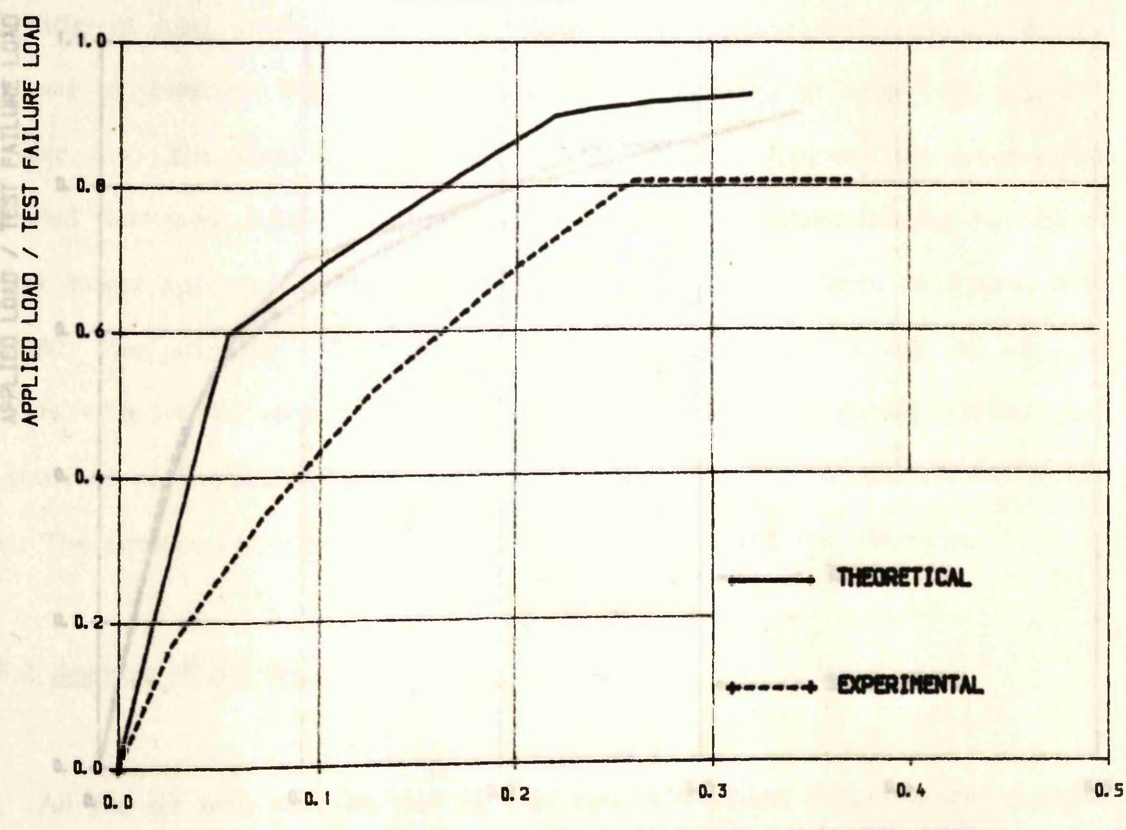

FIG. (8.76). LOAD-DEFLECTION RELATIONSHIP FOR MODEL (5B) IN REF. (12).

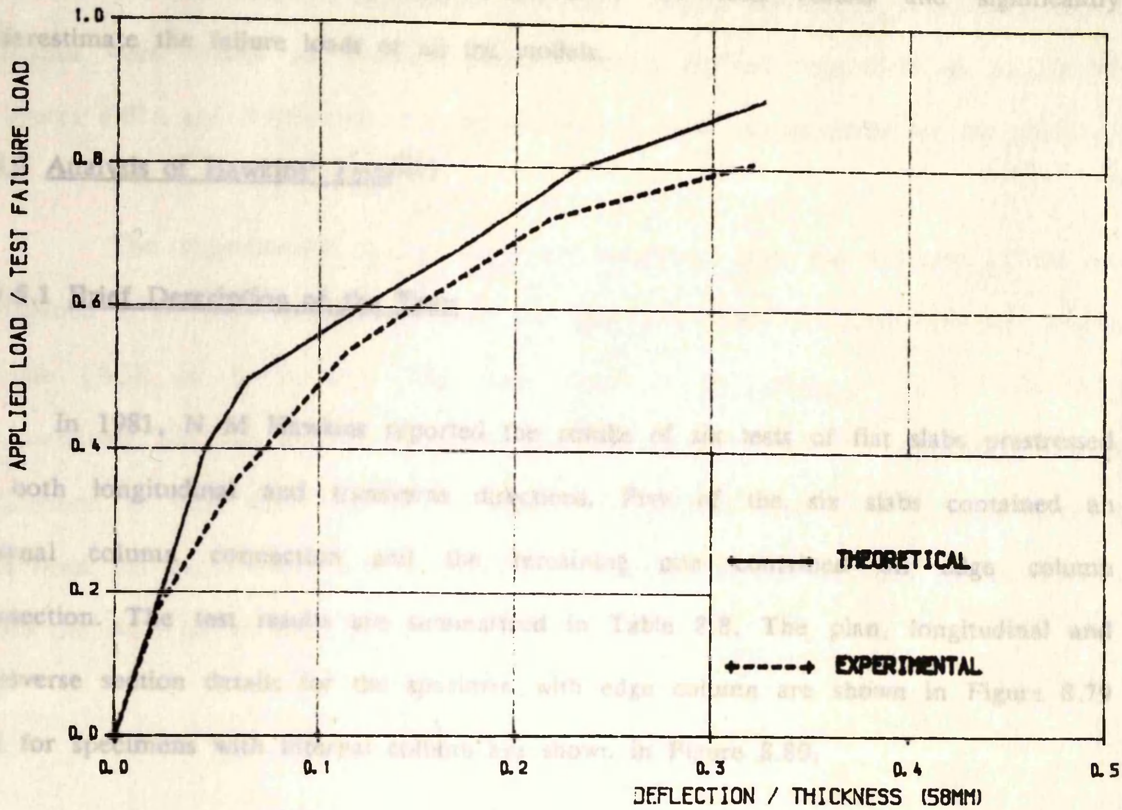

FIG. (8.77) : LOAD-DEFLECTION RELATIONSHIP FOR MODEL (6B) IN REF. (12).

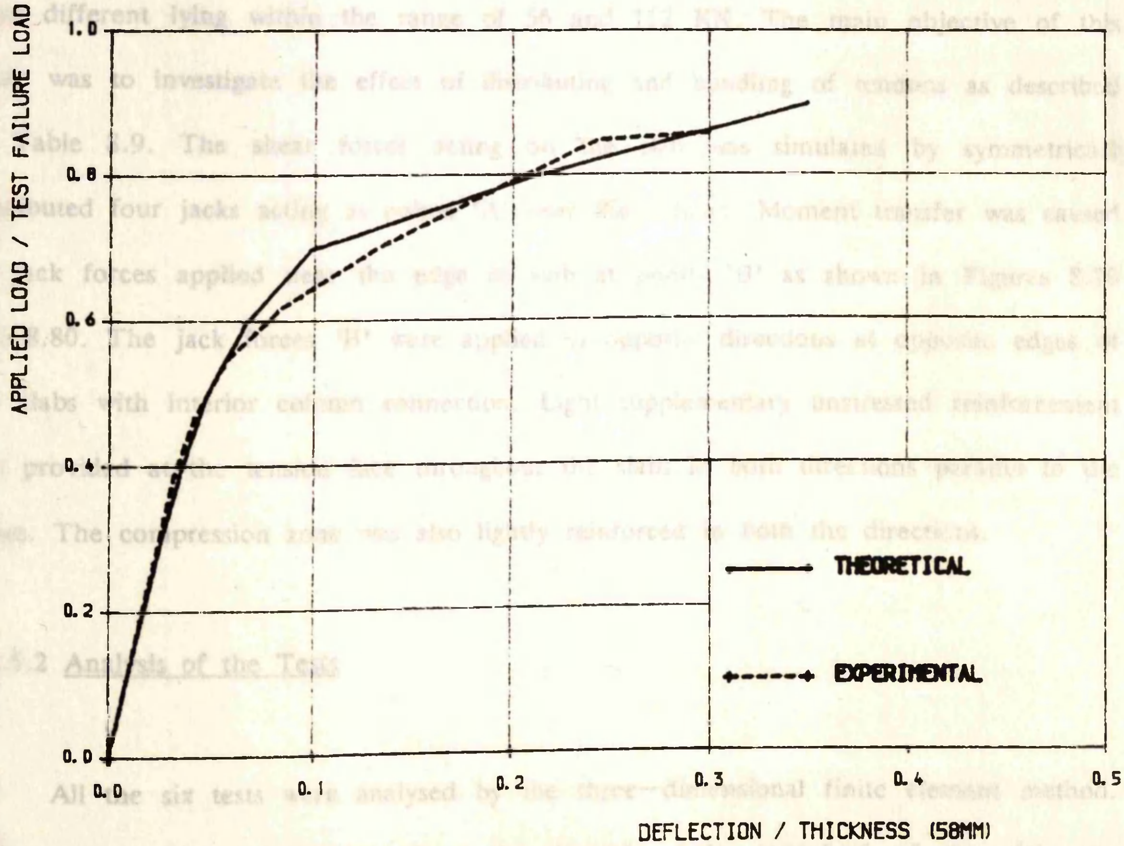

FIG. (8.78) : LOAD-DEFLECTION RELATIONSHIP FOR MODEL (7B) IN REF. (12).

Society approach is in poor agreement with the tests results and significantly underestimate the failure loads of all the models.

8.4.5 Analysis of Hawkins' Tests[26]

8.4.5.1 Brief Description of the Tests

In 1981, N M Hawkins reported the results of six tests of flat slabs prestressed in both longitudinal and transverse directions. Five of the six slabs contained an internal column connection and the remaining one contained an edge column connection. The test results are summarized in Table 8.8. The plan, longitudinal and transverse section details for the specimen with edge column are shown in Figure 8.79 and for specimens with internal column are shown in Figure 8.80.

In all the specimens, tendons of 13 mm diameter were used. Their prestresses were different lying within the range of 56 and 112 KN. The main objective of this study was to investigate the effect of distributing and bundling of tendons as described in Table 8.9. The shear forces acting on the slab was simulated by symmetrically distributed four jacks acting at points 'A' near the column. Moment transfer was caused by jack forces applied near the edge of slab at points 'B' as shown in Figures 8.79 and 8.80. The jack forces 'B' were applied in opposite directions at opposite edges of the slabs with interior column connection. Light supplementary unstressed reinforcement was provided at the tension face throughout the slabs in both directions parallel to the edges. The compression zone was also lightly reinforced in both the directions.

8.4.5.2 Analysis of the Tests

All the six tests were analysed by the three-dimensional finite element method. Taking advantage of symmetry about the X-axis, only one-half of the slab was analysed using twenty-eight element mesh for the models with interior column and sixteen– element mesh for the model with edge column connection. The finite element meshes were chosen so that the column foot print was considered as an element. Figures 8.81a and 8.81b show the typical element mesh arrangements for the models.

The experimental failure loads are compared with the ultimate failure loads obtained from the numerical analysis and also with those predicted by the American Code (ACI) in Table 8.10. The main ratios of (V_{exp}/V_{theo}) are 1.03 and 1.06 respectively for the numerical analysis and the ACI– 83 with corresponding Standard deviation of 0.04 and 0.16. These comparisons indicate that there is good agreement between the experimental and the theoretical results and also between the experimental and the ACI– 83 as well.

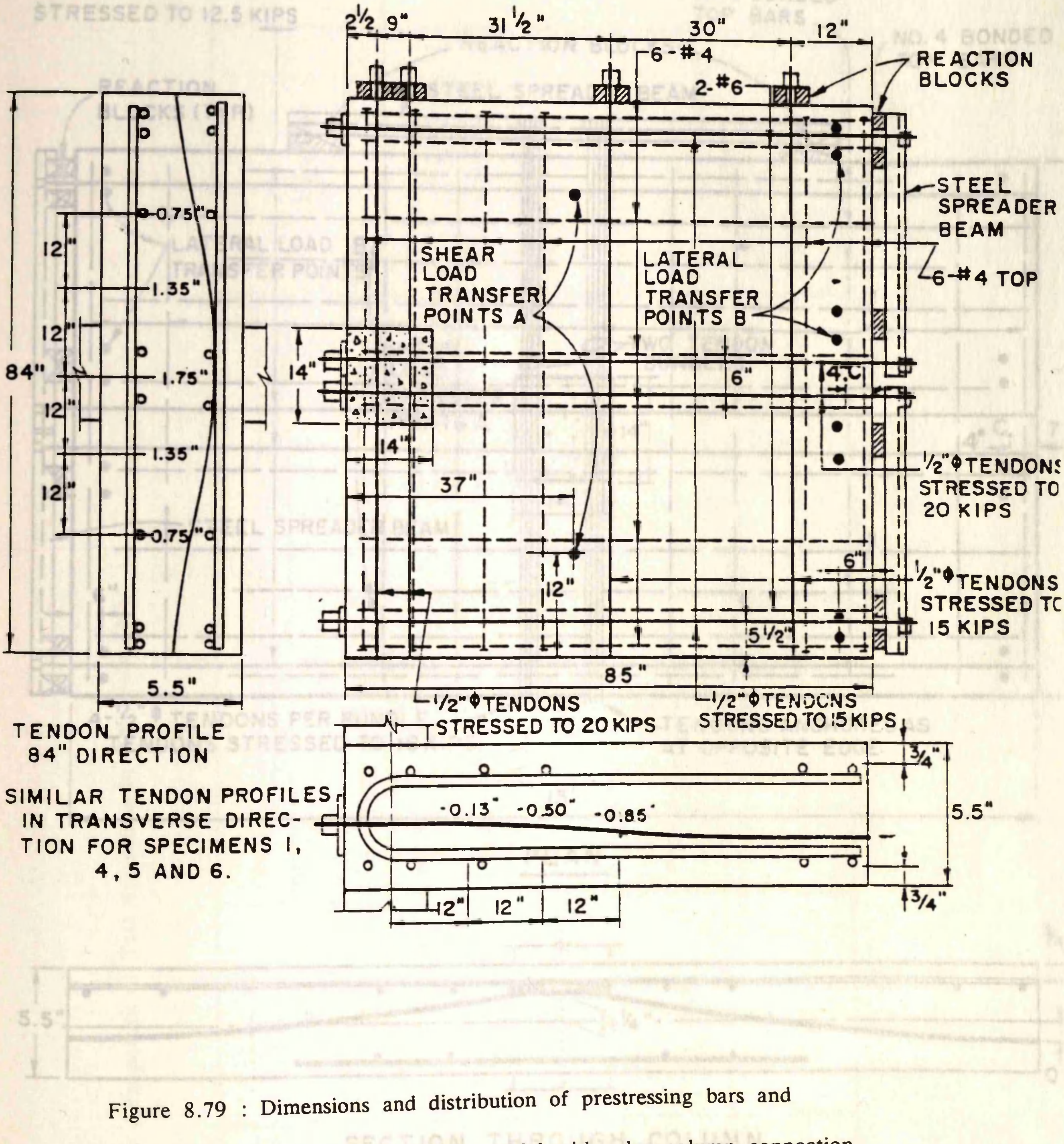

Figure 8.79 : Dimensions and distribution of prestressing bars and loading points for the model with edge column connection. More details in Reference (26).

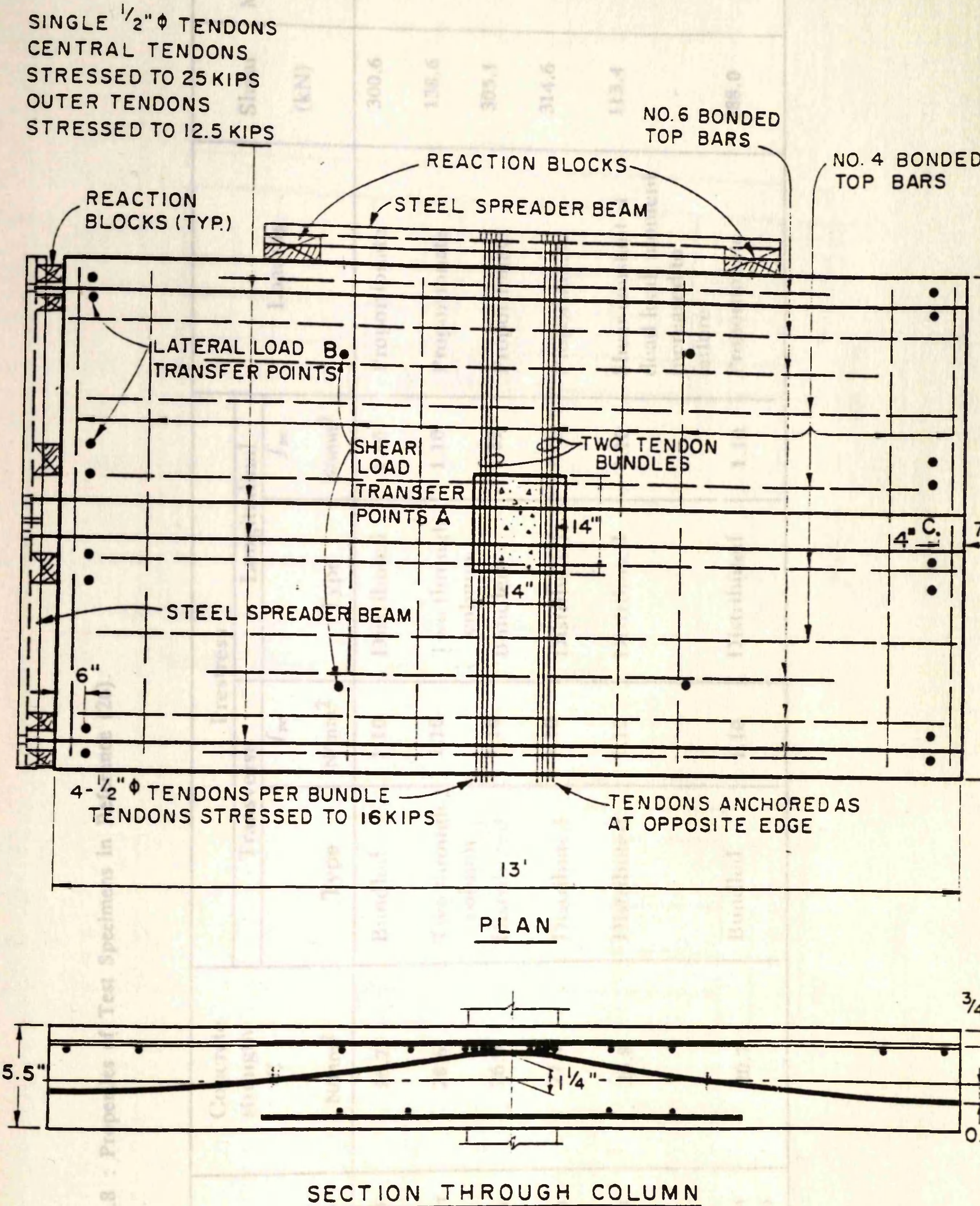

Figure 8.80 : Dimensions and distribution of prestressing bars and loading points for the models with internal column connection. More details in Reference (26).

Table 8.8 : Properties of Test Specimens in Reference (26).

Slab No.	Type	Concrete strength f'_c	Prestress				Loading	Shear	Moment
			Transverse		Longitudinal				
		N/mm2	Type	f_{pc} N/mm2	Type	f_{pc} N/mm2		(kN)	KN– m
1	Interior	26.75	Bundled	1.10	Distributed	1.10	Proportionate	300.6	707
2	Exterior	28.6	Two through column	1.10	Two through column	1.10	Proportionate	138.6	50.8
3	Interior	26.0	Distributed	1.10	Bundled	1.89	Proportionate	305.1	87.0
4	Interior	27.4	Distributed	1.10	Distributed	1.10	Proportionate	314.6	41.1
5	Interior	26.8	Distributed	1.10	Distributed	1.10	Shear constant at dead load, moment increased to failure	113.4	135.9
6	Interior lift slab	20.7	Bundled	1.10	Distributed	1.10	Proportionate	288.0	107.1

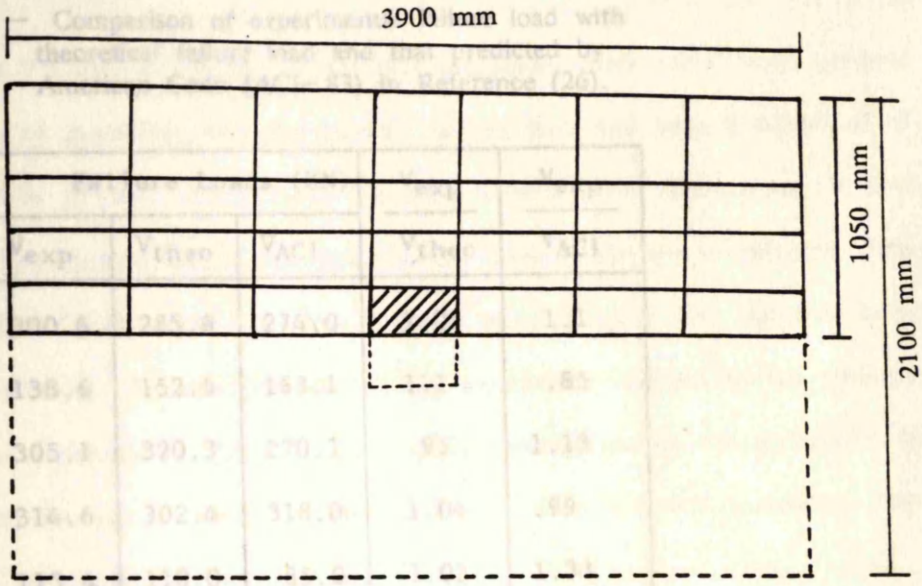

a)– Twenty– eight element mesh for models with internal column connection (for half of slab).

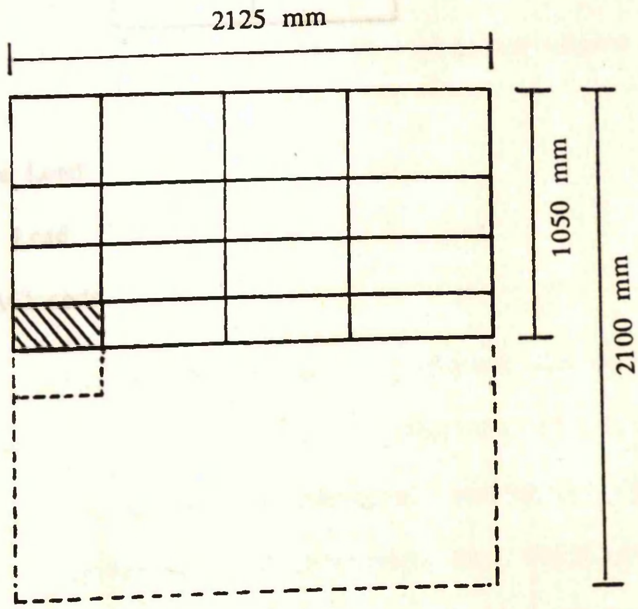

b)– Sixteen element mesh for model with edge collumn connection (for half of slab).

Figure 8.81 : Mesh arrangements for analysis of the models in Reference (26).

Table 8.10 – Comparison of experimental failure load with theoretical failure load and that predicted by American Code (ACI–83) in Reference (26).

Model	Failure Loads (KN)			$\frac{V_{exp}}{V_{theo}}$	$\frac{V_{exp}}{V_{ACI}}$
	V_{exp}	V_{theo}	V_{ACI}		
S1	300.6	285.6	274.0	1.05	1.1
S2	138.6	152.5	163.1	1.1	.85
S3	305.1	320.3	270.1	.95	1.13
S4	314.6	302.4	318.0	1.04	.99
S5	113.4	110.0	85.0	1.03	1.33
S6	288.0	273.0	328.5	1.06	.88
		Average =		1.04	1.05
		S. D. =		0.04	0.16

V_{exp}= Experimental Ultimate Failure Load

V_{theo}= Theoretical Ultimate Failure Load

V_{ACI}= Predicted Failure Load by ACI code.

8.5 Theoretical Investigation of Parameters of Study (Numerical Experiments)

8.5.1 Introduction

In sections 8.3 and 8.4 it was shown that the three-dimensional finite element method is capable of predicting well the ultimate failure load and overall behaviour of prestressed flat slabs at both internal and external column-slab connections. In this section, the three parameters which were described in Chapter Six are investigated. This investigation is about their effects on the strength of prestressed flat slabs at edge column-slab connections. For this purpose, all the parameters involved in the strength of the connections presented in Table 6.1 were kept constant except the parameter in question. Then the analysis is carried out for different values for that parameter. The parameters which are studied in this work are :

a) Prestress level.

b) Ratio of wind shear moment to wind shear (M_W/V_WL).

c) Column aspect ratio.

d) Effective depth

The plan, layout of the tendons and reinforcing bars for all the models are shown in Figures 8.82, 8.83a and 8.83b respectively

8.5.2 Prestress Level

For a study of this parameter three theoretical models of prestressed flat slab at edge column connection TS1, TS2 and TS3 with concrete compressive stress of 4.8, 6.0 and 7.2 N/mm2 respectively due to prestressing were considered keeping all other parameters constant. The model TS3 corresponds to full prestressing case which means that cracking is not allowed at the serviceability load (corresponding to 'class 1' in the BS8110). In the analysis of the model TS3 the first cracks occurred at 80% of design load which is higher than the service load. In the two other cases the slab was considered as partially prestressed which means some small cracks are allowed. The first cracks were observed at 58% and 65% of design load respectively in models TS1 and TS2 (corresponding to 'class 3' and 'class 2' in the BS8110 respectively).

Figure 8.84 shows the load–deflection curves for this group of models. These curves show that by increasing the prestressing level, the load–carrying capacity of the connection increases while the deflection of the slab decreases.

Figure 8.85 shows the load–strain curves for unstressed reinforcement which passed through the column head. It is seen that for model TS3 with the maximum prestressing level in this group the maximum tensile strain of the bar is 26% of the yield strain while for the two other models they are 23% and 11%.

The maximum increase of the tendon force which passed through the column head is 18%, 10% and 6% of the initial prestressing force respectively for models TS1, TS2 and TS3. Therefore, it can be concluded that when the prestressing level increases, the increase in tensile stress in steel bars (tendons and unstressed bars) decreases. Table 8.11 shows variation of the ultimate failure load versus the prestressing level.

Table 8.11

Model	Parameter of Prestressing Level (N/mm^2)	Ultimate Failure Load (KN)
TS1	4.8	74.7
TS2	6.0	81.6
TS3	7.2	86.4

8.5.3 Ratio of (M_w/V_wL)

Three theoretical models were selected to study the effect of this parameter on the strength and overall behaviour of the models. Considering model TS1 as a base model, the two other models TS4 and TS5 were analysed. The cantilever span of models TS4 and TS5 are 0.78 and 1.20 of TS1 respectively.

Figures 8.86 and 8.87 show the differences in the behaviour of these models. It shows that the ultimate failure load of the connection has increased due to the reduction of the moment– shear ratio and the connection is stiffer. Table 8.12 shows the variation of the ultimate failure load versus the ratio of (M_W/V_WL).

Table 8.12

Model	Parameter of $(M_W/V_WL)^*$ Ratio	Ultimate Failure Load (KN)
TS4	0.78	96.5
TS1	1.0	74.7
TS5	1.2	64.5

* L is the cantilever span of model TS1.

8.5.4 Column Aspect Ratio

Three theoretical models of prestressed flat slab at edge column connection TS1, TS6 and TS7 were analysed corresponding to the column aspect ratios of 1.67, 1.33 and 2.0 respectively keeping all other parameters constant. Figures 8.88 and 8.89 show the differences in the behaviour of these models. The ultimate load of 89.5 KN for model TS7 with the high column aspect ratio was the highest among these models while model TS6 with low column aspect ratio had the lowest ultimate load (64.5 KN) in this group. As a result, the ultimate failure load of the connection increased in proportion to the aspect ratio of the column.

A study of the results corresponding to this group of models shows that increasing the column aspect ratio in windward direction increases the strength and stiffness of the connection. The reason for this behaviour is the mechanism of moment transfer from slab to the edge column connection. The wind shear moment is transferred from the slab to the column by means of bending moment at the front face of the column and twisting moment at the two side faces of the column. The failure mode of these models were torsional shear failure. It can therefore be said that for edge column–slab connection the twisting moment resisting capacity makes a significant contribution to the punching shear strength of the connection and it increases in proportion to the column aspect ratio. Table 8.13 shows the variation of the ultimate failure load versus the column aspect ratio.

Table 8.13

Model	Parameter of Column Aspect Ratio	Ultimate Failure Load (KN)
TS6	1.33	72.3
TS1	1.67	74.7
TS7	2.0	91.6

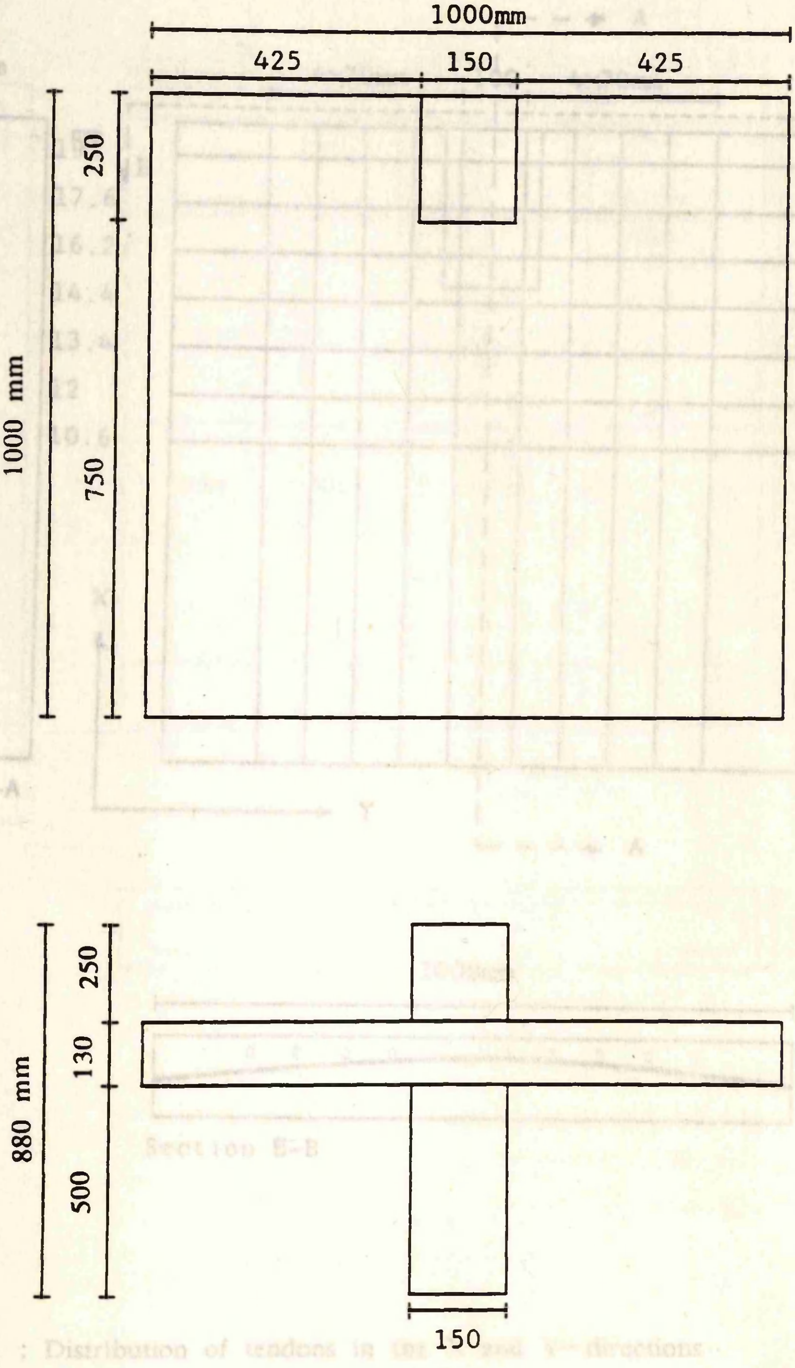

Figure 8.82 : Plan and dimensions of the models

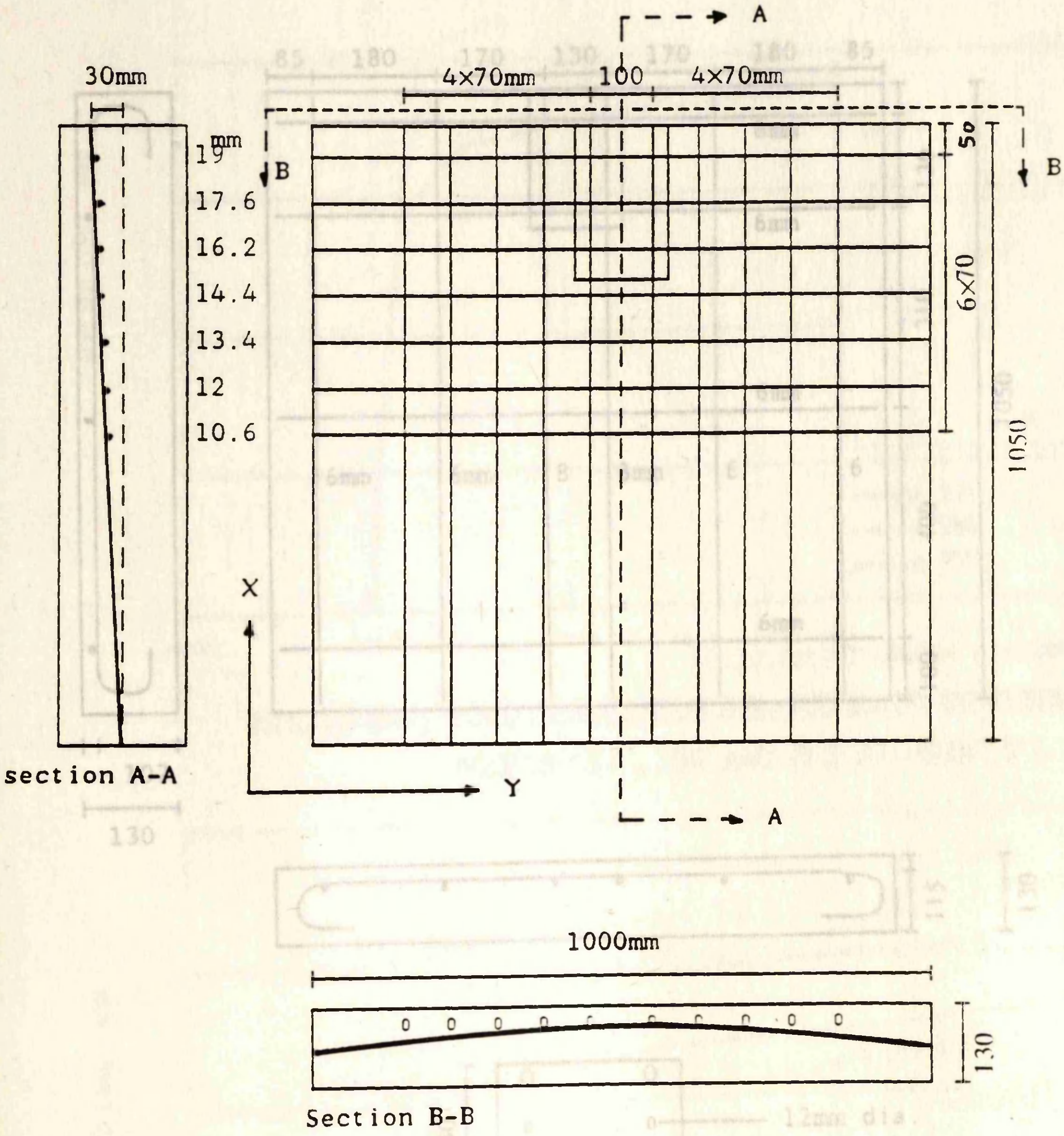

Figure 8.83a : Distribution of tendons in the X and Y– directions

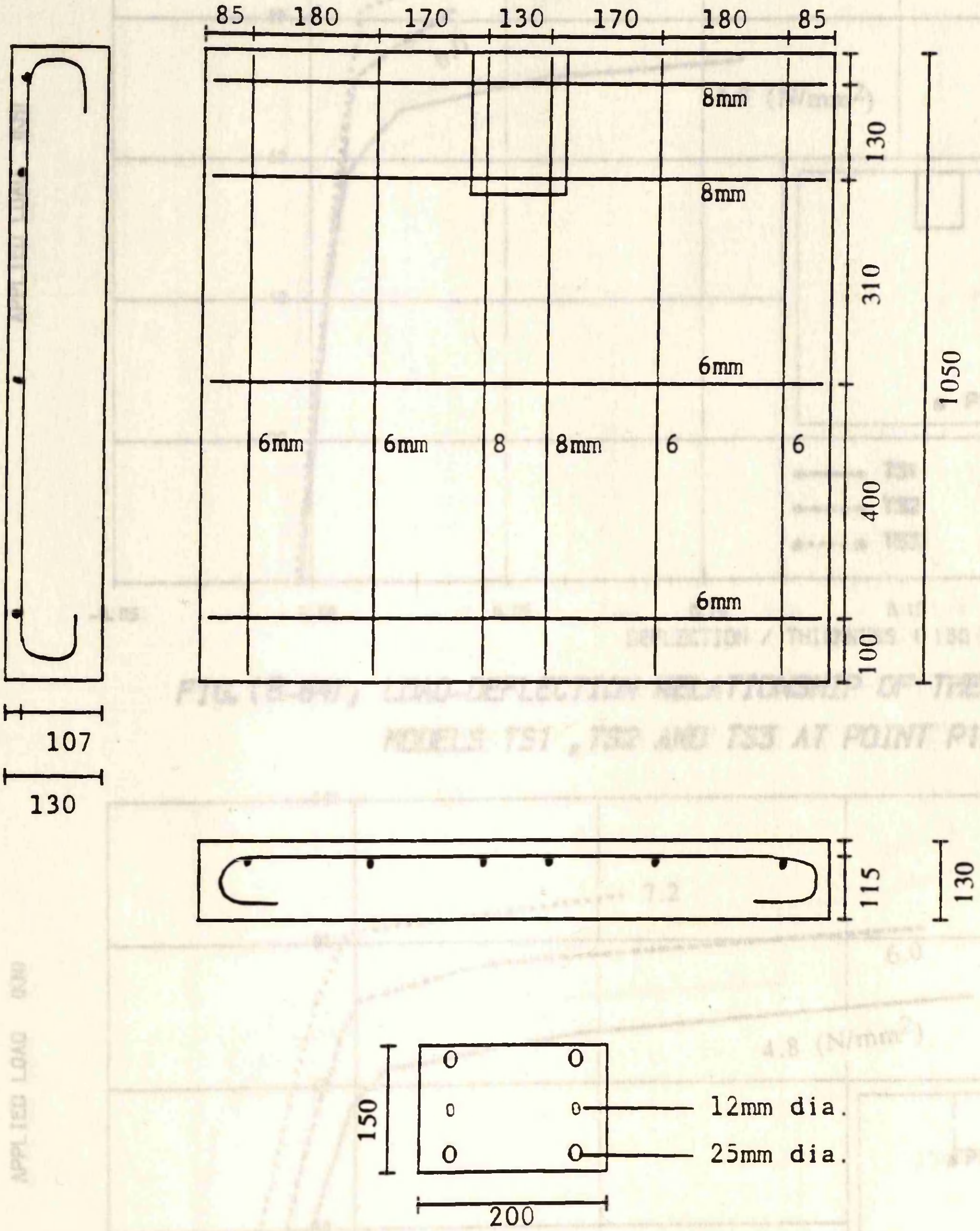

Figure 8.83b : Arrangement of steel bars in the slab and column

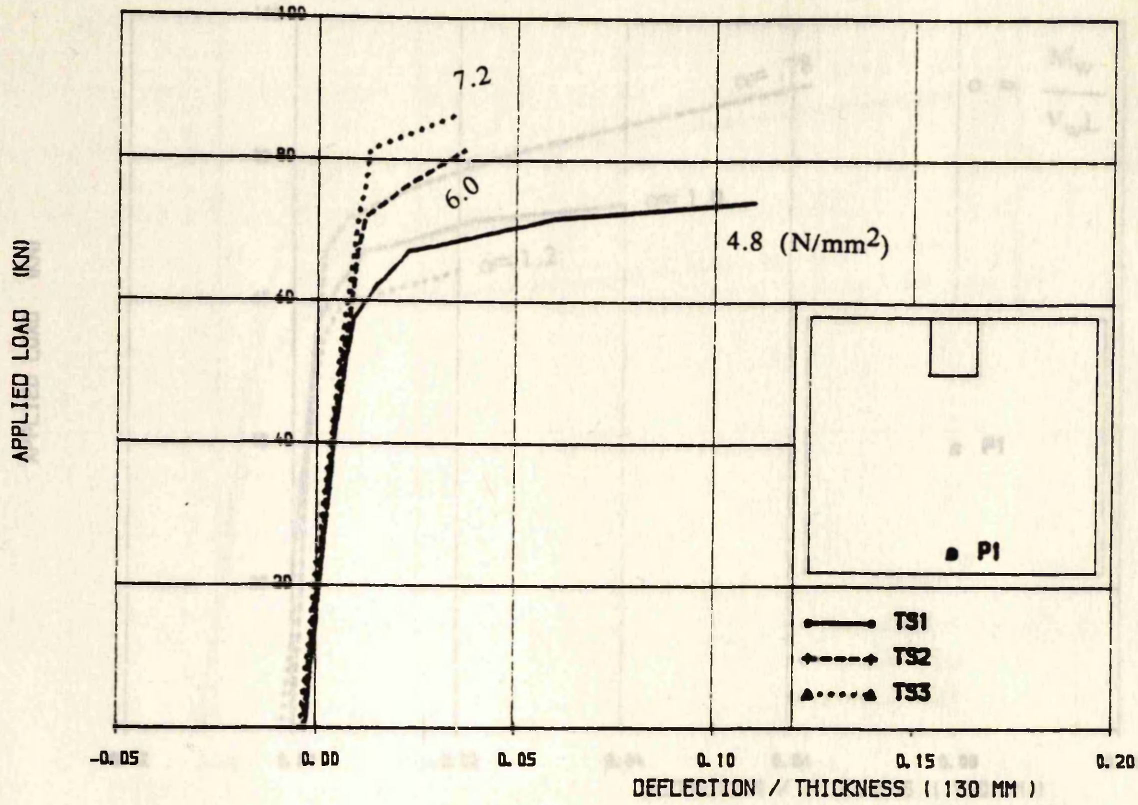

FIG. (8-84), LOAD-DEFLECTION RELATIONSHIP OF THEORETICAL MODELS TS1 ,TS2 AND TS3 AT POINT P1.

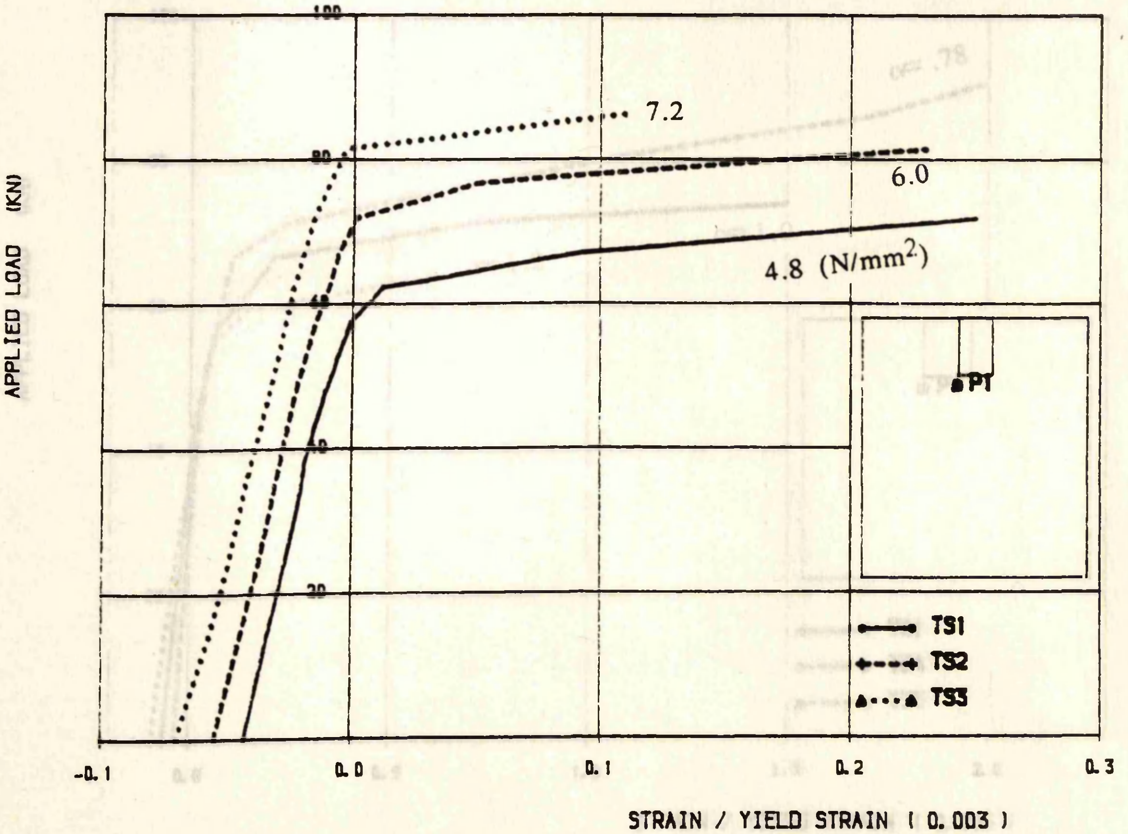

FIG. (8-85), LOAD-STRAIN CURVE FOR REINFORCING BAR IN X-DIRECTION FOR MODELS TS1 TO TS3.

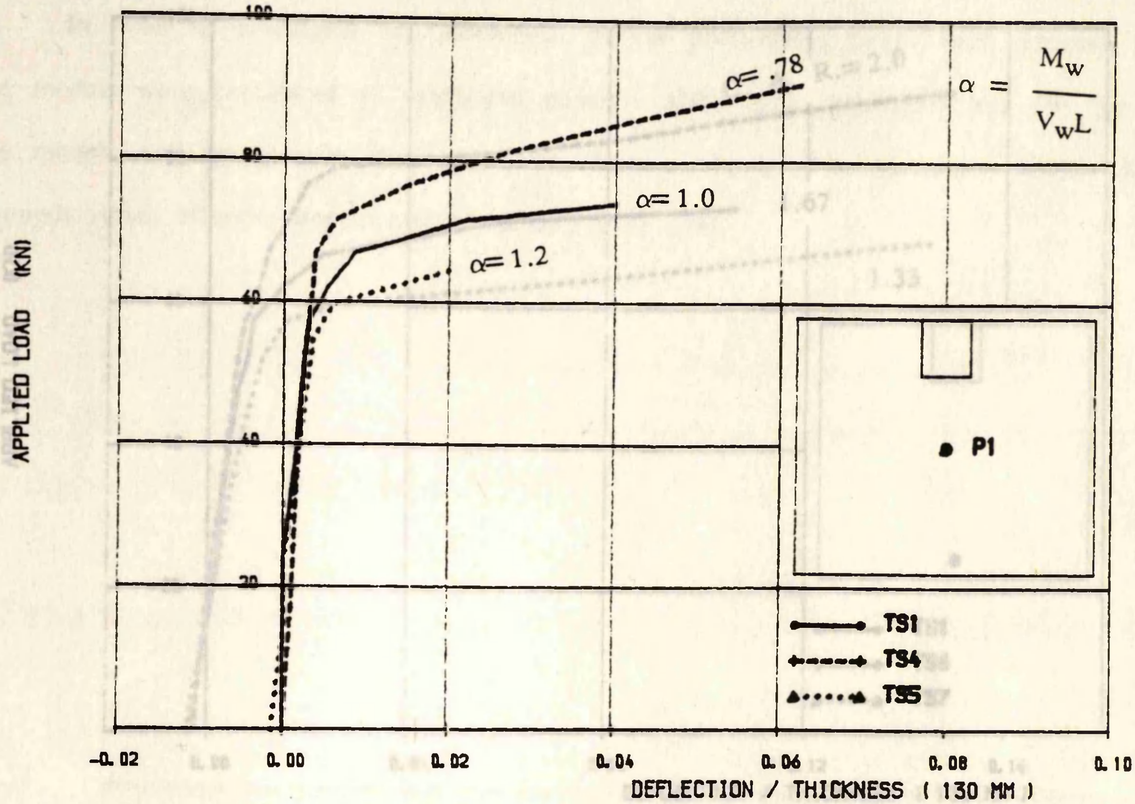

FIG. (8-86), LOAD-DEFLECTION RELATIONSHIP OF THEORETICAL MODELS TS1 ,TS4 AND TS5 AT POINT P1.

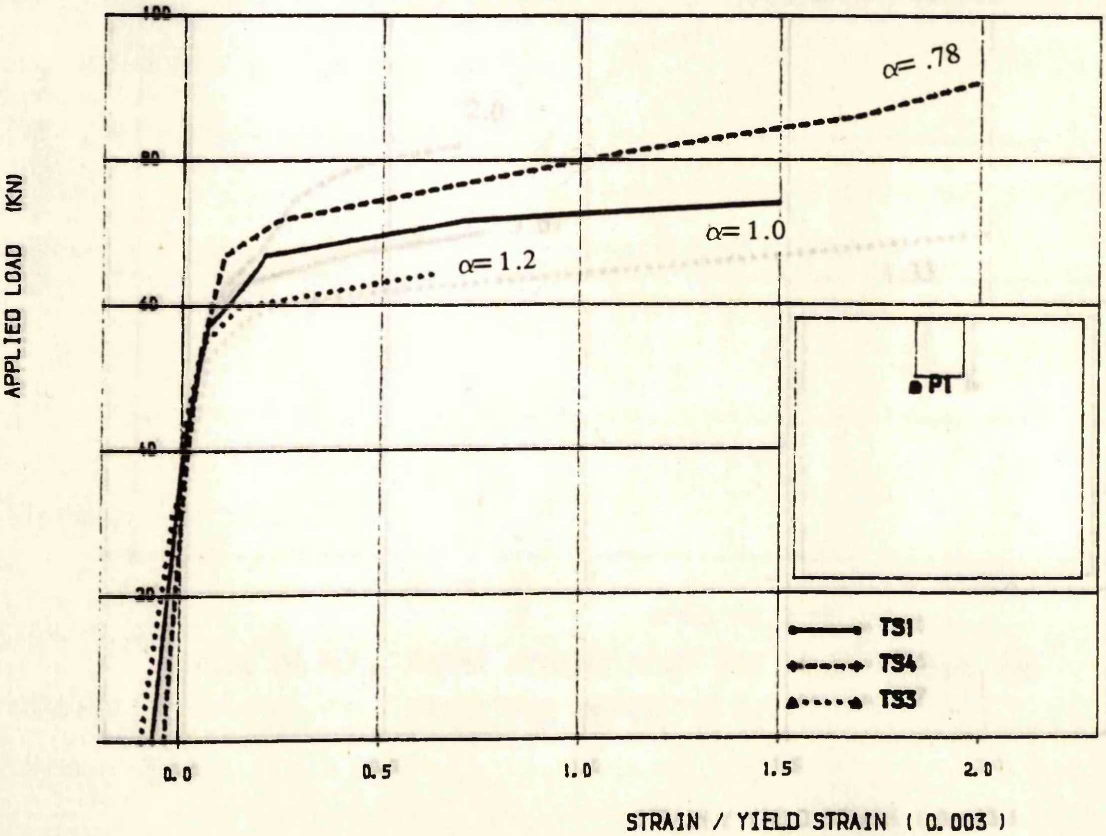

FIG. (8-87), LOAD-STRAIN CURVE FOR REINFORCING BAR IN X-DIRECTION FOR MODELS TS1 TO TS3.

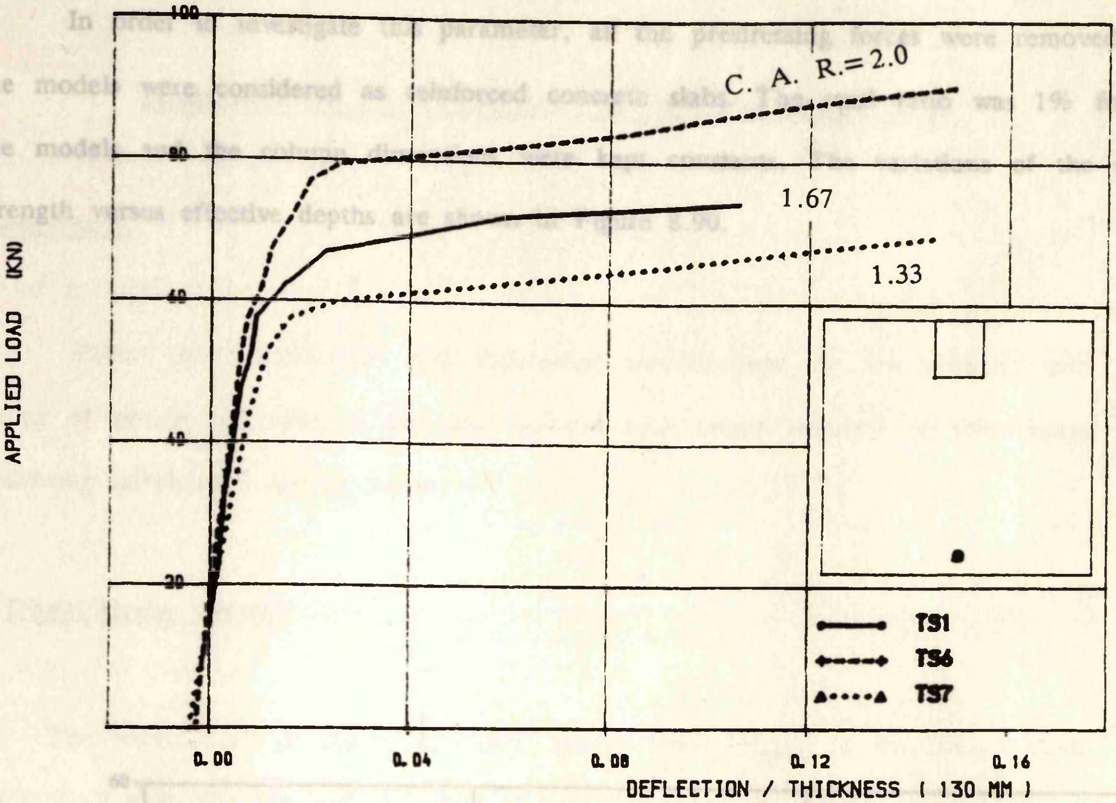

FIG. (8-88), LOAD-DEFLECTION RELATIONSHIP OF THEORETICAL MODELS TS1 ,TS6 AND TS7 AT POINT P1.

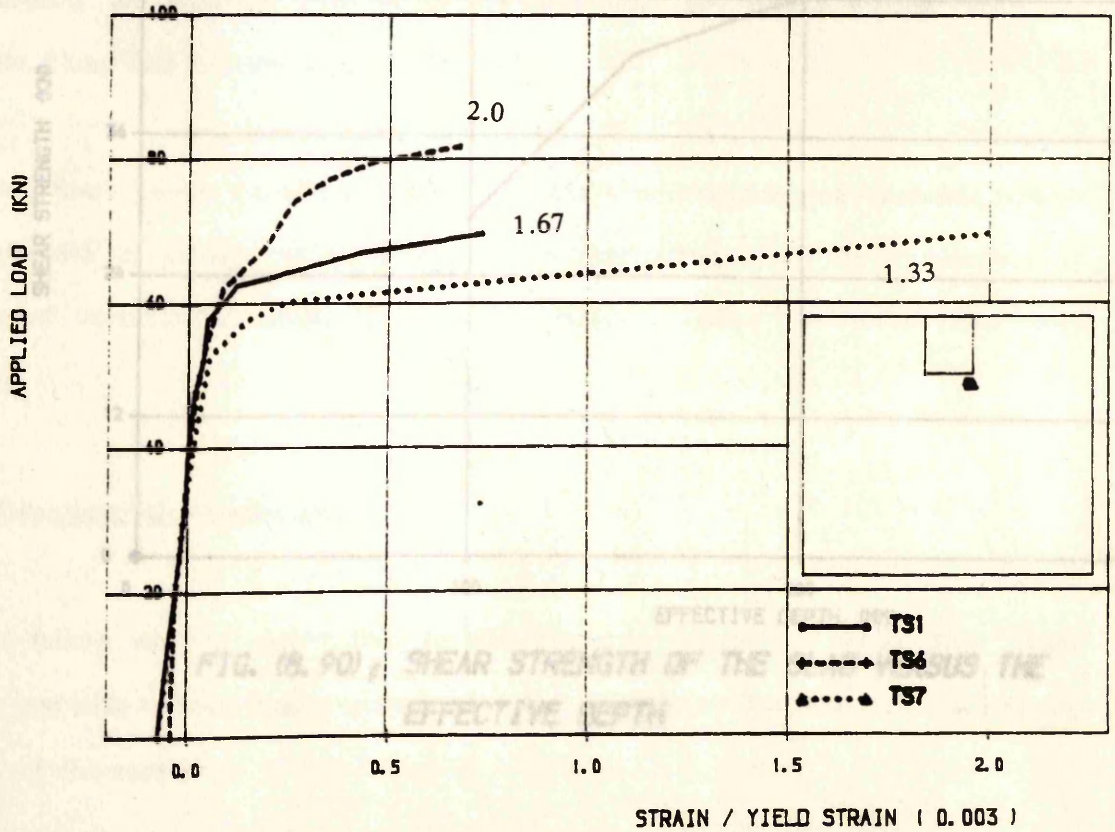

FIG. (8-89), LOAD-STRAIN CURVE FOR REINFORCING BAR IN X-DIRECTION FOR MODELS TS1 TO TS3.

8.5.5 Effective Depth of Slab

In order to investigate this parameter, all the prestressing forces were removed and the models were considered as reinforced concrete slabs. The steel ratio was 1% for all the models and the column dimensions were kept constants. The variations of the shear strength versus effective depths are shown in Figure 8.90.

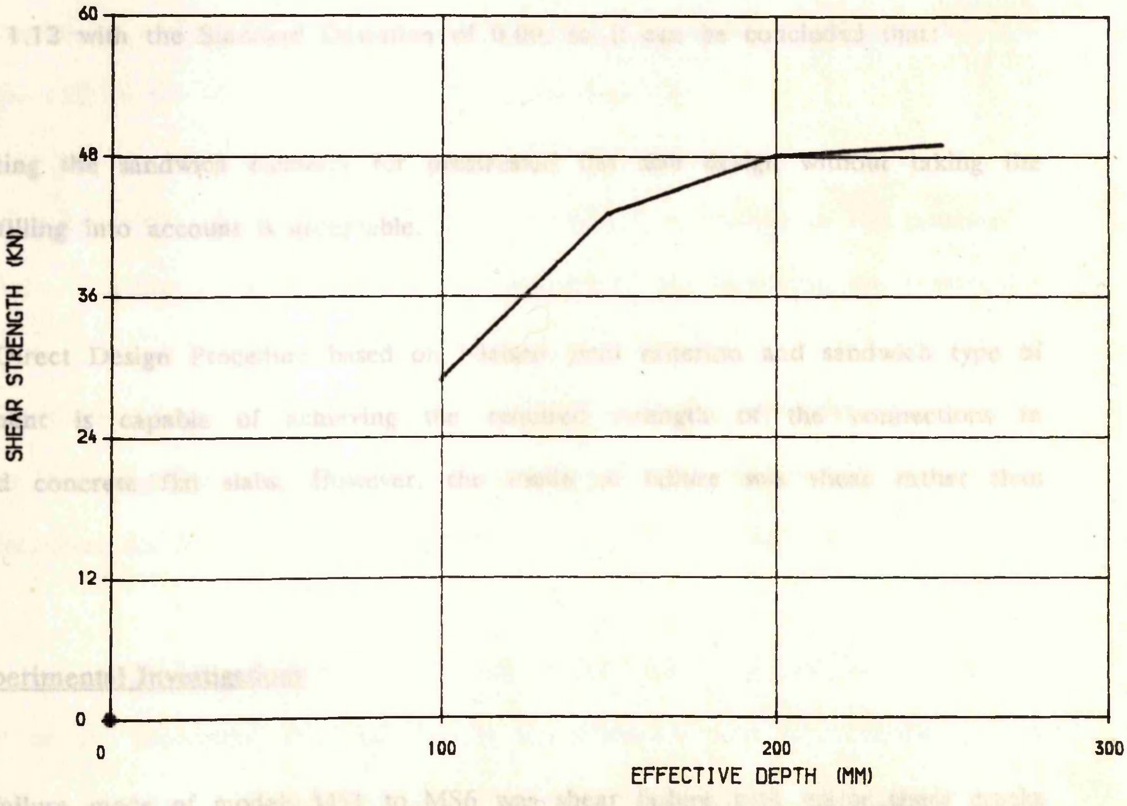

FIG. (8.90), SHEAR STRENGTH OF THE SLAB VERSUS THE EFFECTIVE DEPTH

CHAPTER NINE

SUMMARY OF CONCLUSIONS AND RECOMMENDATIONS

9.1 Conclusions

From the experimental and theoretical investigations on the strength and behaviour of prestressed concrete flat slab– column connections reported in this thesis, the following conclusions can be drawn.

9.1.1 Direct Design Method

The mean ratio of the experimental failure loads (V_{exp}) to the design loads (V_{des}) is 1.12 with the Standard Deviation of 0.09, so it can be concluded that:

1– Adopting the sandwich elements for prestressed flat slab design without taking the concrete filling into account is acceptable.

2– The Direct Design Procedure based on Nielsen yield criterion and sandwich type of slab element is capable of achieving the required strength of the connections in prestressed concrete flat slabs. However, the mode of failure was shear rather than flexural.

9.1.2 Experimental Investigations

1– The failure mode of models MS1 to MS6 was shear failure with major shear cracks at the rear side of the models accompanied by insignificant flexural cracks on the top surface of the models.

2– On average, the first flexural cracks occurred at 78% of the design load. The minimum value was for model MS1 at 69% and the maximum was for model MS6 at 89% of the design load.

3– On average, the first torsional shear cracks occured at 87% of design load. The minimum value was 82% and maximum value was 95% corresponding to models MS3 and MS5 respectively

4– The mean value of the ratios of maximum concrete compressive strains at experimental failure load to the compressive yield strain for all the models was 0.55.

5– The maximum variation from the initial tendon force due to the applied loads was on average 9% of initial tendon force.

6– The maximum tensile stress of the unstressed steel normalized to the yield stress is on average 0.88 in the X–direction and 0.28 in Y–direction.

7– from the behaviour of models MS1, MS2 and MS3 corresponding to the prestressing level of 1.5 , 2.3 and 4.8 N/mm^2. It can be concluded that increasing the prestressing level:

i) increases the load–carrying capacity and rigidity of the connection due to increasing the compressive stress of concrete around the column.

ii) decreases the deflection of slab and strains of steel and concrete.

8– From the comparison of behaviour between models MS3 and MS4 with respect to the effect of the parameter (M_w/V_w), it can be concluded that the reduction of the parameter ;

i) increases the lateral load–carrying capacity of the connection due to reducing the lateral load moment transferred to the column.

ii) reduces the deflection of the slab and strains of concrete and steel.

9– To study the effect of the column aspect ratio models MS3, MS5 and MS6 were tested. Comparison of the results indicated that, increasing the column aspect ratio has the following effects;

i) increases the load– carrying capacity and strength of the connection due to increasing the twisting moment resisting capacity.

ii) reduces deflection of the slab and strains of steel bars and concrete.

10– In cyclic loading model RCS8, the prestressing level was 65% of that in model RCS7. This 35% reduction of prestressing level caused 9% reduction in ultimate failure load of model RCS8.

11– The failure mode of both cyclic loading models RCS7 and RCS8 was flexural and according to Figures 8.25 to 8.27 the stiffness degradation in model RCS8 was more than that in model RCS7 especially after the 8^{th} cycle of loading.

9.1.3 Theoretical Investigation

9.1.3.1 Edge– Column Connections

1– The 3–dimensional finite element programme is capable of providing a good prediction of the ultimate failure load and overall behaviour of the models under monotonic loading. The mean ratio of (V_{theo}/V_{exp}) for all the models was 1.01 with a Standard Deviation of 0.08.

2– The displacement and strain of steel and concrete were not affected by the variation of shear retention factor up to about 90% of the design load. But the ultimate failure load increased in proportion with the shear retention factor (*Beta*). The range of this variation was between 89% to 113% of the experimental failure load and result of the analysis due to *Beta* = 0.30 gave good agreement with the experimental results.

3– Comparison between proportional and experimental sequence of loading showed that there is no significant difference in predicting of behaviour of the models by these two procedures. However in predicting the ultimate failure load, the proportional sequence method gives on average 10% higher ultimate load than does the experimental sequence.

4– Two following methods were used to simulate the column support of the connections;

a) The column stub was not taken into the finite element analysis.

b) The column stub was taken into the analysis as additional elements.

From comparison of the results (Table 8.3 and Figures 8.11 to 8.14), it can be concluded that there is insignificant difference between above–mentioned methods in predicting the displacements and strains of steel and concrete. In predicting the ultimate failure load the analysis with the column elements gave better agreement with the experimental results. Therefore, this method was used for the theoretical study of the models.

5– In the analysis, small increase in the initial tendon force was observed. The increase of the initial force in the tendons passing through the column head at 90% of design load was on average 4% of the initial load and at the ultimate failure load was on average 13% for all the models. The experimental counterparts of these figures were 2% and 10% respectively.

6– For the parameters investigation three models for each parameter were analysed. The conclusions were similar to that in the experimental study (items 7, 8 and 9 in previous section).

9.1.3.2 <u>Internal– Column Connections</u>

1– In the analysis of Smith and Burn's tests[10] by three–dimensional finite element method using sixteen–element mesh and *Beta*= 0.3 (shear retention factor), the mean ratio of the experimental ultimate failure loads (V_{exp}) to the theoretical one (V_{theo}) was 1.05.

2– In the analysis of Long and Franklin's tests using 28–element mesh, the mean ratio of (V_{exp}/V_{theo}) was 1.1 with a Standard Deviation of 0.05.

3– In the analysis of Regan's work, fifteen tests were analysed using sixteen–element mesh for quarter of the slab and *Beta*= 0.30. The mean ratio of (V_{exp}/V_{theo}) was 1.0 with Standard Deviation of 0.06.

4– Therefore, considering the above theoretical predictions from the analysis of 33 experimental models, it can be concluded that the finite element method can predict failure load and behaviour of the connections satisfactorily.

9.2 Recommendations for future work

9.2.1 Experimental Study

1– Repetition of the tests MS1 to MS8 using shear reinforcement and keeping all the other parameters constant, for investigation of the effect of shear reinforcement on the ultimate failure load and overall behaviour of the post–tensioned flat slabs at edge column connections.

2– Experimental work on post–tensioned concrete flat slabs consist of the two edge columns subjected to the gravity loads only (Figure 9.1). The reason for this experimental work is that the punching failure mode expected might be different from that of models MS1 to MS8.

3– Experimental investigation on punching shear behaviour of post–tensioned concrete slabs with the restrained edges. The investigation which has been done by Kuang and Morely[17] may be a suitable base for this study.

9.2.2 Theoretical Studv

Three–dimensional finite element analysis of the tests mentioned in section 9.2.1 and comparison between the tests and the analytical results.

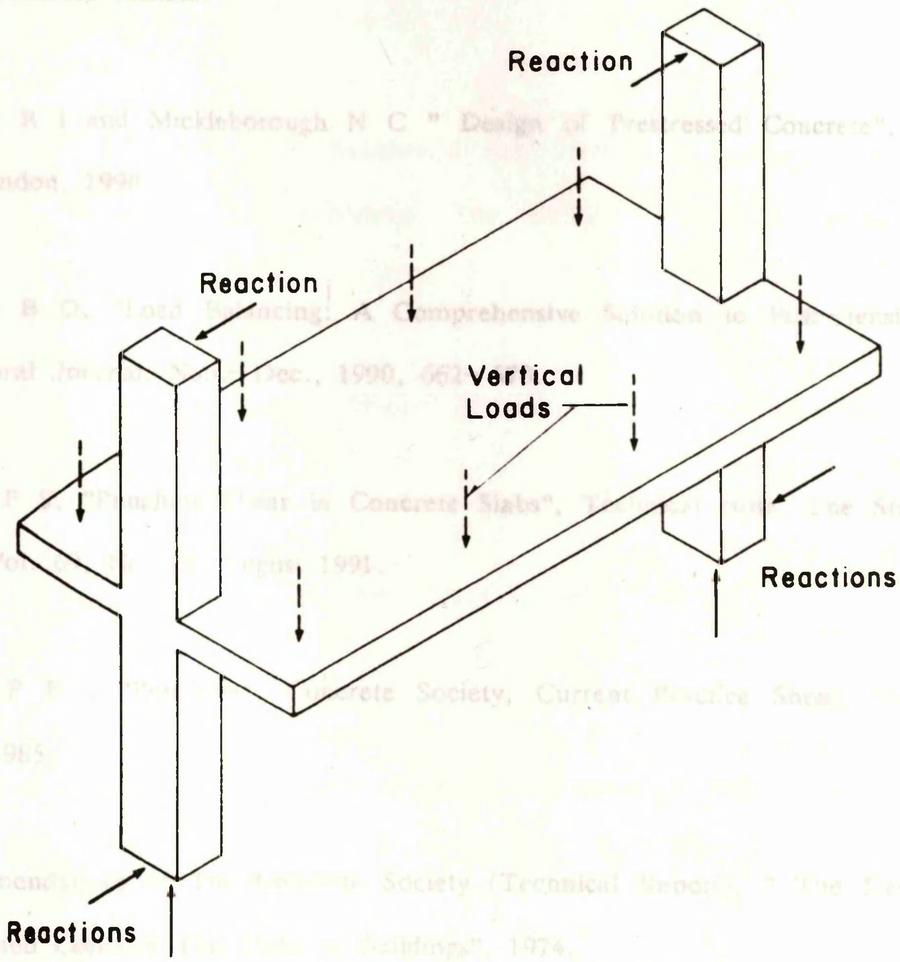

Figure 9.1

REFERENCES

1– British Standards Institution, "The Structural Use of Concrete" , Unified British Code for Structural Use of Concrete in Building, BS8110, London, 1985.

2– ACI 318–83 1983, Building Code Requirements for Reinforced Concrete, Detroit, American Concrete Intitute.

3– Gilbert R I and Mickleborough N C " Design of Prestressed Concrete", Unwin Hyman, London, 1990.

4– Aalami B O, "Load Balancing: A Comprehensive Solution to Post–tensioning", ACI Structural Journal, Non.–Dec., 1990, 662–670.

5– Chana P S, "Punching Shear in Concrete Slabs", Technical Note, The Structural Engineer, Vol. 69, No. 15, August 1991.

6– Regan P E , "Punching", Concrete Society, Current Practice Sheet, No. 106, December 1985.

7– Recommendations of The Concrete Society (Technical Report), " The Design of Post–tentioned Concrete Flat Slabs in Buildings", 1974.

8– ASCE–ACI Committee 426, "The Shear Strength of Reinforced Concrete member–slab", Journal of the Structural Division, ASCE, Vol. 100, No.ST8, August 1974, pp.1543–1591.

9– Akiyama H and Hawkins N M ,"Response of Flat Plate Concrete Structures to Seismic and Wind Forces", Progress Report on National Science Foundation Earthquake Hazards Mitigation Program, Grant No. ENN 72–03585, University of Washington, Seattle, July 1984.

10– Di Stasio J and Van Buren M R," Transfer of Bending Moment Between Flat Plate Floor and Column", Journal of American Concrete Institue, Proceeding, Vol.53, No.3, Sept. 1960, PP.299–314.

11– Regan P E, "Behaviour of Reinforced and Prestressed Concrete Subjected to shear forces", Paper 7441 S, Proceedings, The Institute of Civil Engineers, Vol.50, Dec.1971.

12– Kotsovos M D, "Mechanisms of 'Shear' Failure", Magazine of Concrete Research, Vol. 335, No. 123, June 1983.

13– Mast P E, "Stresses in Flat Plate Near Columns", ACI Journal, Oct. 1970, 761–768.

14– Long A E, "Punching Failure of Slabs, Transfer of Moment and Shear", Journal of Structural Division, ASCE, Vol.99, No.ST4, April 1973, PP. 663–685.

15– Long A E and Bond D, "Punching Failure of Reinforced Concrete Slabs", Paper No. 7002, Proceedings of the Institution of Civil Engineers, Vol.37, May 1967, PP. 109–136.

16–Timoshinko S and Woinowsky K S, "Theory of Plates and Shells", M^{c}Graw Hill, New York, 1959.

17– Kuang J S and Morely C T, "Punching Shear Behavior of Restrained Reinforced Concrete Slabs", ACI structural Journal, Jan.– Feb. 1992, PP. 13– 19.

18– Hawkins N M ,Aibin B and Yamazaki J, "Moment Transfer from Concrete Slabs to Columns", ACI Structural Journal, Nov.– Dec. 1989, PP. 705–716.

19– Rangan B V and Hall A S, "Moment and Shear Transfer Between Slab and Edge Column", ACI Structural Journal, May– June 1983, PP. 183– 191.

20– Hawkins N M, "Shear and Moment Transfer Between Concrete Flat Plates and Columns", Progress Report on National Science Foundation Grant No. 16375, University of Washington, Seattle , Washington, Dec. 1971.

21– Shehata I A, "Punching of Prestressed and Non– Prestressed Concrete Flat Slabs", MPhil thesis, Polytechnic of Central London, Sept. 1982.

22– Collins M P and Mitchell, "A Rational Approach to Shear Design – The 1984 Canadian Code Provisions", ACI Journal, Nov.– Dec. 1986, PP. 925– 933.

23– Elnounu G F R, "Design of Shear Wall– Floor Slab Connections", PhD Thesis, University of Glasgow, Glasgow, 1985.

24– Bari M S, " Design of Shear Wall– Floor Slab Connection Using Shear Reinforcement", PhD Thesis, University of Glasgow, Glasgow, Oct. 1987.

25– Smith S W and Burns N H, "Post– tensioned Flat Plate to Column Connection Behaviour", J. Prestr. Concr. Inst., 1974, 19, No. 3, May, 74– 91.

26- Hawkins N H, "Lateral Load Resistance of Unbonded Post-tensioned Flat Plate Construction", PCI Journal, Jan.-Feb. 1981, P. 94-116.

27- Franklin S O and Long A E, "The Punching Behaviour of Unbonded Post-tensioned Flat Plates", Proc. Instn Civ. Engrs, Part 2, 1982, 73, Sept.,609-631.

28- ACI- ASCE Committee-352, "Recommendations for Design of Slab-Column Connections in Monolithic Reinforced Concrete Structures", ACI Structural Journal, Nov.-Dec. 1988, PP. 675-695.

29- American Concrete Institute and American Society of Civil Engineers Commitee 423, "Tentative Recommendations For Prestressed Concrete Flat Slabs", Journal of ACI, 1974, 71, Feb., No. 2, 61-71.

30- Franklin S O , Cleland D J and Long A E, "A Flexural Method for the Prediction of the Punching Capacity of Unbonded Post-tentioned Flat Slabs at Internal Columns", Proc. Instn Civ. Engrs, Part2, 1982, 73, June, 277-298.

31- Cleland D J, "An Experimental and Analytical Study of The Behaviour of Post-tensioned Unbonded Concrete Flat Slabs at Edge Columns", PhD thesis, Queen University of Belfast, 1979.

32- Ngo D and Scordelis A C, "Finite Element Analysis of Reinforced Concrete Beams", Journal of the American Concrete Institute, Vol. 64, No. 3, March 1967, 152-163.

33- Gupta A K and Akbar H, "Cracking in Reinforced Concrete Analysis", Journal of Structural Division, ASCE, Vol.110, No. ST8, August 1984, 1735-1746.

34– Cook R D, "Concepts and Applications of Finite Element Analysis", John Wiley & Sons, 1981.

35– Al– Manaseer A A, "A Nonlinear Finite Element study of Reinforced Concrete Beams", PhD Thesis, Glasgow University, 1983.

36– Al– Mahaidi R S H, "Nonlinear Finite Element Analysis of Reinforced Concrete Deep Members" Report No. 79–1, Department of Structural Engineering, Cornell University, Jan. 1979.

37– Cedolin L and Poli S D, "Finite Element Studies of Shear Critical Reinforced Concrete Beams", Journal of Engineering Mechanics Division, ASCE, Vol. 103, No. EM3,June 1977, 395–410.

38– Owen D R J and Hinton E, "Finite Element in Plasticity – Theory and Practice", Pineridge Press, Swansea, 1980.

39– Notebook, "Experimental Stress Analysis", Measurements Group Inc., Raleigh, NC27611, May 1987.

40– Regan P E, "The Punching Resistance of Prestressed Concrete Slabs", Proc. Instn Civ. Engrs, Part2, 1985, 79, Dec., 657–680.

41– Bortolotti L, "Punching Shear Strength in Concrete Slabs", ACI Structural Journaal, March– April 1990, PP. 208–219.

42– Rangan B V, "Tests on Slabs in the Vicinity of Edge Columns", ACI Structural

Journal, Nov.– Dec. 1990, PP. 623– 629.

43– Grow J B and Vanderbilt M D, "Shear Strength of Lightweight Aggregate Concrete Flat Plates", J. Prestr. Concr.Inst., Aug. 1972, 2, No. 4, 18– 28.

44– Regan P E, "Symmetric Punching of Reinforced Concrete Slabs", Magazine of Concrete Research, Vol 38, No. 136, Sept. 1986.

45– Gerber L L and Burns N H, "Ultimate Strength Tests of Post– tensioned Flat Plates", PCI Journal, Nov.– Dec. 1971, P. 40– 58.

46– Johannes U G and Alexander C S, "Nonlinear Analysis of Prestressed Concrete Slabs", Journal of Structural Engineering, ASCE, Vol. 109, No. 7, July 1983, 1742– 1760.

47– Moehle J P, "Strength of Slab– Column Edge Connection", ACI Structural Journal, Jan.– Feb. 1988, PP. 89– 98.

48– Vidosa F G, Kotsovos M D and Povlovic M N, "Symmetrical Punching of Reiforced Concrete Slabs: An Analytical Investigation Based on Nonlinear Finite Element Modeling", ACI Structural Journal, May– June 1988, PP. 241– 250.

49– Islam S and Park R, "Tests on Slab– Column Connections with Shear and Unbalanced Flexure" Journal of Structural Division, ASCE, Vol. 102, No. ST3, March 1976, PP. 549– 568.

50– Ahmadi H and Gilbert S, "Behaviour of Reiforced Concrete Slab– Column Models Subject to Cyclic Lateral Loading", Proc. Instn Civ. Engrs, Part 2, 1990, 89, Dec., 543–563.

51– Derbal R, "An Experimental Investigation of The Flat Slab to The Edge Column Connection Subjected to Lateral Cyclic Loading", Queen's University of Belfast, MSc thesis, Oct. 1987.

52– Whittle R T, "Design of Reinforced Concrete Flat Slabs to BS8110", CIRIA, Report No. 110, 1985.

53– Hinton E and Owen D R J, "Finite Element Programming", Academic Press, London, 1977.

54– Nielsen T B, "Optimum Design of Reinforced Concrete Shells and slabs", Technical University of Denmark, Report NR. R 44, 1974.

55– Gulvanessian H, "Optimum Reinforcement of Concrete Slab Elements", Printout No. 20, 1976, P. 13–15.

56– BSI, " Code of Basic Data for The Design of Buildings, Loading", CP3: Chapter v, Part 2, 1972.

57– Zienkiewicz O C, "The Finite Element Method", McGraw Hill, 3rd. Edition, 1977.

58– Douglas A F, William L G and Harianto S, "Tests of Post– tensioned Concrete Slab– Edge Column Connections", ACI Structural Journal, March– April 1990, pp. 167–179.

59– Mohamed M S , "A Finite Element and Experimental Study of Reinforced Concrete in Torsion", PhD thesis, University of Glasgow, 1986.

60– Durelli A J, Phillips E A and Tsao C H, "Analysis of Stress and Strain", McGraw Hill, 1958.

61– Suidan M and Schnobrich W C, "Finite Element Analysis of Reinforced Concrete", Journal of the Structural Division, ASCE, Vol. 99, No. ST10, October 1973, PP. 2109– 2122.

62– Alexander S D B and Simmonds S H, "Ultimate Strength of Slab– Column Connections", ACI Structural Journal, May– June 1987, PP.255– 261.

63– Phillips D V and Zeinkiewicz O C, "Finite Element Nonlinear Analysis of Concrete Structures" Proceedings, Institution of Civil Engineers, Vol 61, Part 2, 1976. PP. 59– 88.

64– The Concrete Society, " Post– tensioned Flat– Slab Design Handbook", Concrete Society Technical Report No. 25, 1984.

65– Mohamed M S, "A Finite Element and Experimental Study of Reinforced Concrete in Torsion", PhD Theis, University of Glasgow, Glasgow, 1986.

66– Rankin G I B and Long A E " Predicting The Punching Strength of Conventional Slab– Column Specimens" Proc. Instn Civ. Engrs, Part1, 82, 1987, April, 327– 346.

67– Rankin G I B and Long A E " Predicting The Enhanced Punching Strength of

Interior Slab–Column Connections" Proc. Instn Civ. Engrs, Part1, 1987, 82, Dec., 1165–1186.

68– Chen W F, "Plasticity in Reinforced Concrete ", McGraw Hill, 1982.

69– Chen W F and Ting E C, "Constitutive Models for Concrete Structures", Journal of Engineering Mechanics Division, ASCE, Vol. 106, No. EM1, Feb. 1980, pp. 1–19.

70– Kotsovos M D and Newman J B, "A Mathematical Description of the Deformational Behaviour of Concrete Under Complex Loading", Magazine of Concrete Research, Vol. 31, No. 107, June 1979, pp. 77–90.

71– Kotsovos M D, "A Mathematical Description of the Strength Properties of Concrete Under Generalised Stress", Magazine of Concrete Research , Vol. 31, No. 108, Sept. 1979, pp. 151–158.

72– Kotsovos M D and Newman J B, "Behaviour of Concrete Under Multiaxial Stress", Journal of the American Concrete Institute ,Sept. 1977, pp. 443–446.

73– Kotsovos M D , "Concrete, A Brittle Fracturing Material", Materials and Structures , RILEM, Vol. 17, No. 98, pp. 107–115, 1984.

APPENDIX 'A'

Calculations of the shear strengths of connections according to the codes formulae were carried out as follows;

a) According to BS8110

From equation 2.10 the shear strength of an edge column connection is given by:

$$V_{BS} = 0.8\ v_c\ A_c \qquad \text{(A.1)}$$

where:

$v_c = 0.79(100A_s/A_c)^{1/3}(f_{cu}/25)^{1/3}(400/d)^{1/4}$

A_s= Area of all the tension reinforcement crossing the critical area

A_c= Critical area = $d(2c_1 + c_2 + 6d)$ for an edge column shown in Fig. A1

f_{cu}= Cube strength of concrete

d = Effective depth of slab

Since we have two kinds of steel (unstressed and prestressed) with different effective depths so an equivalent effective depth of slab and an equivalent steel area are defined as follows:

$$d = \frac{A_{so}f_y d_o + A_{sp}f_{0.2}d_p}{A_{so}f_y + A_{sp}f_{0.2}} \qquad \text{(suggested by P E Regan, Ref.(40))}$$

and $$A_s = A_{so} + A_{sp}\frac{f_{0.2}}{f_y}\frac{d_p}{d_o}$$

where : A_{so} is ordinary steel area and A_{sp} is prestressed steel area.

d_o and d_p are effective depths of ordinary steel and tendons respectively.

$f_{0.2}$ is proof stress of tendons.

EXAMPLE : For Model MS3

In the X- direction : A_{so}= 100.6 mm^2 and d_o= 110 mm

A_{sp}= 154 mm^2 and d_p= 75 mm

In the Y- direction : A_{so}= 100.6 mm^2 and d_o= 102 mm

A_{sp}= 192.5 mm^2 and d_p= 75 mm

therefore ; $d = (d_x + d_y)/2$

$= (82+79)/2 = 80$ mm

<u>Calculation of equivalent steel area:</u>

$$A_{sx} = 100.6 + 154 \times 2.6 \times 0.68 = 372 \text{ mm}^2$$

$$A_{sy} = 100.6 + 192.5 \times 2.6 \times 0.74 = 471 \text{ mm}^2$$

$$A_s = A_{sx} + 2A_{sy} = 1314 \text{ mm}^2$$

In the Y-direction the steel bars cross the critical section twice so A_{sy} is multiplied by 2.

<u>Calculation of critical area</u>

$$A_c = d(2c_1 + c_2 + 6d)$$

c_1= 250 mm , c_2= 150 mm , d= 80 mm

so; $A_c = 90400$ mm^2

<u>Calculation of 'v_c'</u>

$$v_c = .79(1314 \times 100/90400)^{1/3}(40/25)^{1/3}(400/80)^{1/4}$$

$$= 1.55$$

Finally from equation (A.1) shear strength of the connection will be;

$$V_{BS} = .8 \times 1.55 \times 90400 = 112 \text{ KN}$$

b) <u>According to ACI-83</u>

From equation 2.8 the shear strength of the connection is given by:

$$V_{ACI} = \frac{v_c A_c}{1 + \dfrac{M}{V}\dfrac{\nu A_c}{(J/C)}} \tag{A.2}$$

where ; $v_c = 0.29\sqrt{.8f_{cu}} + 0.3f_{cp} + V_p/A_c$

$$A_c = d(c_1 + c_2 + 2d)$$

$$\nu = 1 - \frac{1}{1 + 0.67\sqrt{(c_1+d)/(c_2+d)}}$$

$$J/C = (1/6)\left[2d(c_1+.5d)(c_1+2c_2+2.5d) + d^3(2c_1+c_2+2d)/(c_1+.5d)\right]$$

EXAMPLE: For Model MS3

V_p is the vertical component of prestressing force at the critical section. Because the tendons above the column head are nearly horizontal, we can assume that $V_p = 0.0$

$f_{cp} = 4.8$ N/mm^2

$f_{cu} = 56$ N/mm^2

$d = 82$ mm

$c_1 = 250$ mm

$c_2 = 150$ mm

therefore,

$A_c = 82(2\times250 + 150 + 164) = 66748$ mm^2

$\nu = .44$

$M/V = 800$

$J/C = 6722917$

$v_c = 3.44$ N/mm^2

substituting above values in equation (A.2), the shear strength of the connection will be:

$V_{ACI} = 51.1$ KN

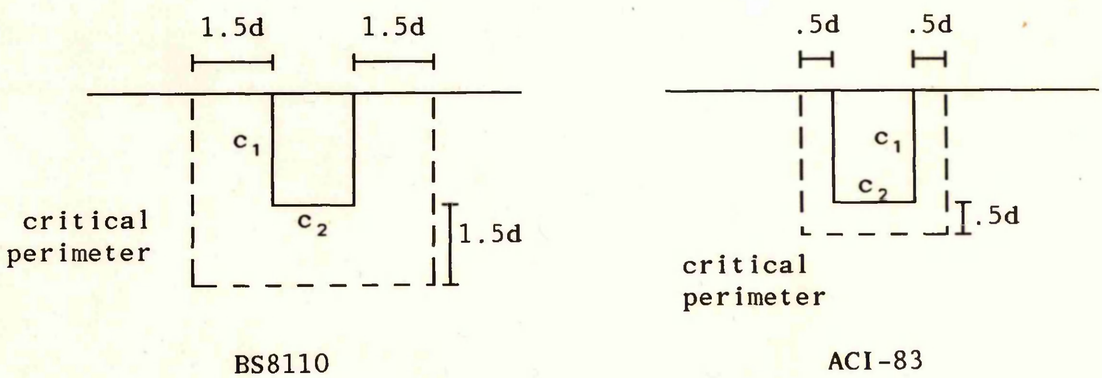

Fig.(A.1)